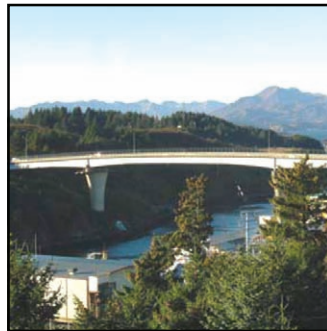**MCEER**
EARTHQUAKE ENGINEERING TO EXTREME EVENTS

Performance of Seismic Isolation Hardware under Service and Seismic Loading

by

M.C. Constantinou, A.S. Whittaker, Y. Kalpakidis, D.M. Fenz and G.P. Warn

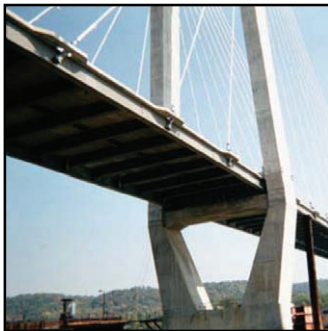# NOTICE

MCEER
EARTHQUAKE ENGINEERING TO EXTREME EVENTS

Performance of Seismic Isolation Hardware Under Service and Seismic Loading

by

M.C. Constantinou,[1] A.S. Whittaker,[1] Y. Kalpakidis,[2] D.M. Fenz[2] and G.P. Warn[3]

1   Professor, Department of Civil, Structural and Environmental Engineering, University at Buffalo, State University of New York
2   Ph.D. Student, Department of Civil, Structural and Environmental Engineering, University at Buffalo, State University of New York
3   Post-Doctoral Researcher, Department of Civil, Structural and Environmental Engineering, University at Buffalo, State University of New York

MCEER
University at Buffalo, The State University of New York
Red Jacket Quadrangle, Buffalo, NY 14261
Phone: (716) 645-3391; Fax (716) 645-3399
E-mail: *mceer@buffalo.edu*; WWW Site: *http://mceer.buffalo.edu*

Preface

The Multidisciplinary Center for Earthquake Engineering Research (MCEER) is a national center of excellence in advanced technology applications that is dedicated to the reduction of earthquake losses nationwide. Headquartered at the University at Buffalo, State University of New York, the Center was originally established by the National Science Foundation in 1986, as the National Center for Earthquake Engineering Research (NCEER).

Comprising a consortium of researchers from numerous disciplines and institutions throughout the United States, the Center's mission is to reduce earthquake losses through research and the application of advanced technologies that improve engineering, pre-earthquake planning and post-earthquake recovery strategies. Toward this end, the Center coordinates a nationwide program of multidisciplinary team research, education and outreach activities.

MCEER's research is conducted under the sponsorship of two major federal agencies, the National Science Foundation (NSF) and the Federal Highway Administration (FHWA), and the State of New York. Significant support is also derived from the Federal Emergency Management Agency (FEMA), other state governments, academic institutions, foreign governments and private industry.

The Center's Highway Project develops improved seismic design, evaluation, and retrofit methodologies and strategies for new and existing bridges and other highway structures, and for assessing the seismic performance of highway systems. The FHWA has sponsored three major contracts with MCEER under the Highway Project, two of which were initiated in 1992 and the third in 1998.

Of the two 1992 studies, one performed a series of tasks intended to improve seismic design practices for new highway bridges, tunnels, and retaining structures (MCEER Project 112). The other study focused on methodologies and approaches for assessing and improving the seismic performance of existing "typical" highway bridges and other highway system components including tunnels, retaining structures, slopes, culverts, and pavements (MCEER Project 106). These studies were conducted to:

- assess the seismic vulnerability of highway systems, structures, and components;
- develop concepts for retrofitting vulnerable highway structures and components;
- develop improved design and analysis methodologies for bridges, tunnels, and retaining structures, which include consideration of soil-structure interaction mechanisms and their influence on structural response; and
- develop, update, and recommend improved seismic design and performance criteria for new highway systems and structures.

iii

The 1998 study, "Seismic Vulnerability of the Highway System" (FHWA Contract DTFH61-98-C-00094; known as MCEER Project 094), was initiated with the objective of performing studies to improve the seismic performance of bridge types not covered under Projects 106 or 112, and to provide extensions to system performance assessments for highway systems. Specific subjects covered under Project 094 include:

- development of formal loss estimation technologies and methodologies for highway systems;
- analysis, design, detailing, and retrofitting technologies for special bridges, including those with flexible superstructures (e.g., trusses), those supported by steel tower substructures, and cable-supported bridges (e.g., suspension and cable-stayed bridges);
- seismic response modification device technologies (e.g., hysteretic dampers, isolation bearings); and
- soil behavior, foundation behavior, and ground motion studies for large bridges.

In addition, Project 094 includes a series of special studies, addressing topics that range from non-destructive assessment of retrofitted bridge components to supporting studies intended to assist in educating the bridge engineering profession on the implementation of new seismic design and retrofitting strategies.

This report presents state-of-the-art knowledge on the behavior of contemporary seismic isolators (elastomeric and lead-rubber bearings; sliding isolators) and fluid viscous dampers, under both service and seismic loads. Specific problems addressed include the effects of ambient temperature, aging and history of loading, and the effects of frictional or hysteretic heating. The study focused on developing an understanding of the impact of these parameters on seismic isolators and dampers, to better understand how these devices will respond over a lifetime of use in seismically protected structures. Reviews of seismic protective systems as well as analysis and design methods for hardware are presented. The information presented herein may also form the basis for the development of a contemporary "Guide Specifications for Seismic Isolation Design."

ABSTRACT

This report presents a comprehensive description of the current stage of knowledge on the behavior of hardware used in seismic isolation and in seismic damping systems. Particular emphasis is placed on the description of fundamental behavior under both non-seismic, service-type of loading conditions and under high-speed seismic conditions. Specific problems described and addressed in this report include the following: (a) Aging of elastomeric and sliding bearings, (b) effect of ambient temperature on the behavior of elastomeric and sliding bearings, (c) prediction and experimental verification of effects of frictional heating on the sliding bearings, (d) prediction and experimental verification of effects of hysteretic heating on the lead-rubber bearings, (e) analysis of elastomeric and sliding bearings, (f) design of elastomeric and sliding bearings based on principles of LRFD and ASD, (g) establishment of upper and lower bound values of properties of seismic isolation bearings for use in the analysis and design and (h) detailed new testing protocols for seismic isolators and dampers.

The presented information may represent the basis for the development of contemporary Guide Specifications for Seismic Isolation Design.

ACKNOWLEDGEMENTS

DISCLAIMER

❖   This document has been reproduced from the best
copy furnished by the sponsoring agency.

TABLE OF CONTENTS

TABLE OF CONTENTS (CONT'D)

TABLE OF CONTENTS (CONT'D)

xi

TABLE OF CONTENTS (CONT'D)

TABLE OF CONTENTS (CONT'D)

TABLE OF CONTENTS (CONT'D)

xiv

LIST OF ILLUSTRATIONS

LIST OF ILLUSTRATIONS (CONT'D)

LIST OF ILLUSTRATIONS (CONT'D)

LIST OF ILLUSTRATIONS (CONT'D)

LIST OF ILLUSTRATIONS (CONT'D)

LIST OF ILLUSTRATIONS (CONT'D)

LIST OF ILLUSTRATIONS (CONT'D)

LIST OF ILLUSTRATIONS (CONT'D)

LIST OF ILLUSTRATIONS (CONT'D)

LIST OF ILLUSTRATIONS (CONT'D)

LIST OF TABLES

LIST OF TABLES (CONT'D)

LIST OF TABLES (CONT'D)

SECTION 1
INTRODUCTION

Numerous studies have demonstrated the benefits of seismic isolation and supplemental damping devices for the mitigation or elimination of damage in structural and nonstructural components and systems during severe earthquake shaking. Naeim and Kelly (1999) correctly note that it is the *proper* application of these protective devices that leads to "…better performing structures." Proper application should mean appropriate consideration of the design seismic hazard (providing sufficient displacement capacity in the isolators), a thorough understanding of the mechanical properties of the devices and how the properties can change with time, the use of appropriate methods of response analysis, and adequate detailing so as to permit the protective devices to function as intended.

Only a few seismically isolated structures have experienced significant earthquake shaking. Stewart et al. (1999), Nagarajaiah and Sun (2000) and Kani et al. (2006) documented good performance of isolated structures although Stewart noted that actual responses differed somewhat from those assumed in design. Poor performance has been observed in two applications: 1) the failure of the Bolu Viaduct in the 1999 Ducze earthquake because the displacement capacity of the isolation system was exceeded substantially (see Roussis et al., 2003), and 2) overload of bridge piers in the 1993 Kushiro-Oki earthquake because of stiffening of the seismic isolators due to very cold temperatures (Sato et al, 1994).

Most of the studies on the utility of seismic protective systems have been based on best estimates of the mechanical properties of the isolation and energy dissipation devices, with no consideration given to the effects of aging, history of loading and environment over the lifetime of the devices on the mechanical properties. Such changes can negatively impact the utility of the protective systems and perhaps render them by-and-large ineffective.

A study was conducted in the mid-1990s by Constantinou et al. (1999) to collect and synthesize data and knowledge on the effects of temperature, loading history and aging on the mechanical properties of selected seismic isolators. The study proposed an analysis procedure to account for the effects of changing mechanical properties–a procedure that was implemented subsequently in specifications for seismic isolation design, including the AASHTO Guide Specification for Seismic Isolation Design (AASHTO, 1999), ASCE-7-05 (ASCE, 2005) and EN1998 (European, 2005).

This report updates the 1999 study with new information on the effects of temperature, loading history and aging on the mechanical properties of seismic isolators and their impact on the response of seismically isolated structures. Reviews of contemporary protective-systems hardware and analysis and design methods are presented. The report seeks to develop a scientific understanding of the effects of heat, loading and aging on seismic isolators and dampers to enable predictions of response over the lifetime of seismically protected structures–predictions that can then be validated by experiments and observations.

1

SECTION 2
BASIC PRINCIPLES OF SEISMIC ISOLATION AND DAMPING SYSTEMS

2.1 Conventional Earthquake Resistant Bridge Construction

Conventionally constructed earthquake-resistant bridges rely on significant inelastic action (energy dissipation) in selected components of the piers and bent caps for design earthquake shaking. For the single-level moment-resisting frame construction (see Figure 2-1) and the hammerhead pier-bent-cap construction (see Figure 2-2), inelastic action should occur in the column at the underside of the bent cap or at the bottom of the column immediately above the footing. The inelastic action results in damage, which is often substantial in scope and difficult to repair. Importantly, structural damage will generally result in bridge closure with the attendant direct and indirect economic losses.

FIGURE 2-1 Reinforced Concrete Moment-Resisting Frame Construction

FIGURE 2-2 Reinforced Concrete Pier-Bent Cap Construction

Conventional bridges are typically analyzed and designed for earthquake effects using elastic force-based procedures that rely on the specification of an elastic response spectrum and a response modification factor, R, greater than 1.0, that indirectly accounts for the reserve strength, ductility and redundancy in the lateral-force-resisting system. Pier, beam and girder sizes are based on the results of such analysis. Prescriptive details (e.g., hoop spacing in reinforced concrete columns) are then imposed on the design with the expectation that these details will allow the bridge to deform far into the inelastic range without collapse. No specific calculations of deformation capacity are typically prepared for conventional bridge construction. The level of expected damage in the design earthquake is not computed.

2.2 Performance Based Earthquake Engineering

2.2.1 First Generation Tools for Performance Based Earthquake Engineering

The traditional prescriptive provisions for seismic design contained in U.S. bridge and building codes and under development since the late 1920s could be viewed as performance-oriented in that they were developed with the *intent* of achieving specific performance, that is, avoidance of collapse and protection of life safety. It was assumed by those engineers preparing the building codes that building structures designed using prescriptive code provisions would (1) not collapse in very rare earthquake; (2) provide life safety for rare earthquakes; (3) suffer only limited repairable damage in moderate shaking; and (4) be undamaged in more frequent, minor earthquakes. There were similar expectations for conventional bridge construction. The shortcomings of the prescriptive procedures include fuzzy definitions of performance and hazard and the fact that the procedures do not include an actual evaluation of the performance capability of a design to achieve any of these performance objectives. Further, records of earthquake damage to buildings and bridges over the past 70+ years following minor, moderate and intense earthquake shaking has demonstrated that none of the four performance objectives has been realized reliably. Deficiencies in the prescriptive provisions in terms of accomplishing the four target objectives have been identified following each significant earthquake in the United States and substantial revisions to the prescriptive provisions have then been made.

Performance expectations for critical bridges and buildings began to evolve in the mid-1970s following severe damage to such structures in the 1971 San Fernando earthquake. Since that time, the prescriptive provisions have evolved slowly but still include few direct procedures for predicting the performance of a particular bridge or building design, or for adjusting the design to affect the likely performance, other than through application of arbitrary importance factors that adjust the required strength.

Large economic losses and loss of function in critical bridges and buildings following the 1989 Loma Prieta and 1994 Northridge earthquakes spurred the development of performance-based seismic design procedures. In the early 1990s, expert design professionals and members of the academic community, ostensibly structural and geotechnical engineers, recognized that new and fundamentally different design

4

approaches were needed because the prescriptive force-based procedures were a complex compendium of convoluted and sometimes contradictory requirements, were not directly tied to the performance they were intended to achieve, were not reliable in achieving the desired protection for society, were sometimes excessively costly to implement, and were not being targeted at appropriate performance goals in most cases.

Funding in the early to mid-1990s from the Federal Emergency Management Agency (FEMA) to the Applied Technology Council (ATC) and the Building Seismic Safety Council (BSSC) led to the development of the *NEHRP Guidelines and Commentary for Seismic Rehabilitation of Buildings* (FEMA 273/274, Applied Technology Council, 1997): the first generation of tools for performance based earthquake engineering of buildings. This development effort marked a major milestone in the evolution of performance-based seismic design procedures and articulated several important earthquake-related concepts essential to a performance-based procedure. The key concept was that of a performance objective, consisting of the specification of the design event (earthquake hazard), which the building is to be designed to resist, and a permissible level of damage (performance level) given that the design event is experienced. Another important feature of the *NEHRP Guidelines* (FEMA 273/274) was the introduction of standard performance levels, which quantified levels of structural and nonstructural damage, based on values of standard structural response parameters. The *NEHRP Guidelines* also specified a total of four linear and nonlinear analysis procedures, each of which could be used to estimate the values of predictive response parameters for a given level of shaking, and which could then be used to evaluate the building's predicted performance relative to the target performance levels contained in the performance objective. Figure 2-3 below illustrates the qualitative *performance levels* of FEMA 273/274 superimposed on a global force-displacement relationship for a sample building. The corresponding levels of damage are sketched in the figure.
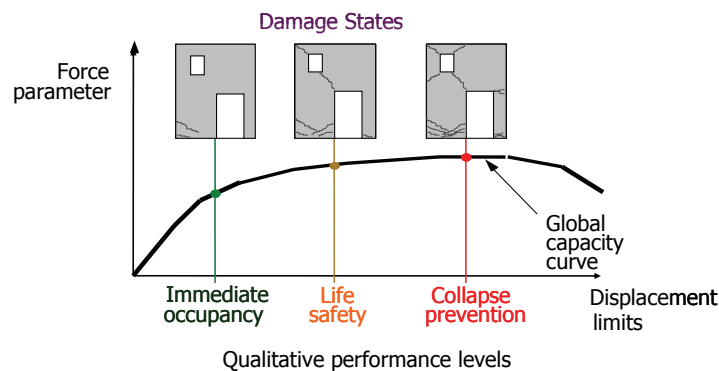
FIGURE 2-3 Qualitative Performance Levels of FEMA 273/274/356

Other projects including *ATC-40, Methodology for Evaluation and Upgrade of Concrete Buildings and Vision-2000 Framework for Performance-based Seismic Design Project* further developed and extended the technology developed in FEMA-273/274. These technologies were further refined by the American Society of Civil Engineers in their conversion of the FEMA-273/274 reports into the *Prestandard for Seismic Rehabilitation*

of Buildings, FEMA-356 (Federal Emergency Management Agency, 2000). Together, the *FEMA-356*, *ATC-40*, and *Vision-2000* documents define the current state of practice of performance-based seismic engineering of buildings. Companion documents for bridge construction do not exist at the time of this writing.

Hamburger et al (2004) identified key shortcomings with the state of practice characterized by FEMA 273/356, including (1) the current procedures predict structural response and demands based on the global behavior of the structure but evaluate performance on the basis of damage sustained by individual components with the result that the poorest performing elements tend to control the prediction of structural performance, (2) much of the acceptance criteria contained in the documents, and used by engineers to evaluate the acceptability of a structure's performance is based on judgment, rather than laboratory data or other direct substantiating evidence, leading to questions regarding the reliability of the procedures, (3) many structural engineers view the guidelines as excessively conservative, when compared against designs developed using prescriptive criteria, however, the reliability of the guidelines and their ability to actually achieve the desired performance has never been established, and (4) the performance levels of FEMA 273/356 do not directly address some primary stakeholder concerns, that is probable repair costs and time of occupancy loss in the building, due to earthquake induced damage.

2.2.2 Second Generation Tools for Performance Based Earthquake Engineering

FEMA has contracted with the Applied Technology Council (ATC) to develop a next generation of performance-based seismic design guidelines for buildings, a project known as ATC-58. The guidelines are to be applicable to new and retrofit building construction and will address structural and non-structural components. Although focused primarily on design to resist earthquake effects, the next generation performance guidelines will be compatible with performance-based procedures being developed at this time for other hazards including fire and blast. The framework being developed at this time will be applicable in principle to bridge construction.

The ATC-58 project will utilize performance objectives that are both predictable (for design professionals) and meaningful and useful for decision makers. Preliminary project work tasks have revealed that these decision makers (or stakeholders) are a disparate group, representing many constituencies and levels of sophistication (Hamburger 2004). Decision makers include building developers, corporate facilities managers, corporate risk managers, institutional managers, lenders, insurers, public agencies and regulators. Each type of decision maker views performance from a different perspective and select performance goals using different decision making processes. The performance-based design methodology will include procedures for estimating risk on a design-specific basis, where risk will be expressed on either a deterministic (scenario basis or event) or a probabilistic basis. Risk will be expressed in terms of specific losses (e.g., cost of restoration of a facility to service once it is damaged, deaths and downtime) rather than through the use of traditional metrics (e.g., life safety in a design-basis earthquake).

The performance prediction process is similar to that utilized in the HAZUS national loss estimation software, although the individual steps in the process will be implemented differently. Figure 2-4 from Hamburger et al (2004) is the flow chart for the ATC-58 performance prediction methodology. Much of the methodology is based on procedures currently under development by the Pacific Earthquake Engineering Research (PEER) Center (Moehle, 2003) with funding from the U.S. National Science Foundation.
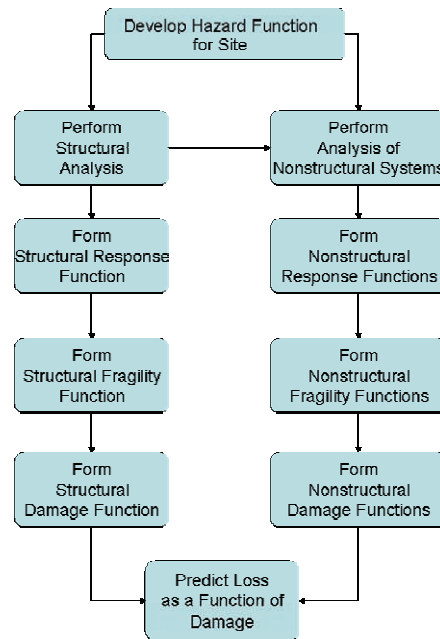
FIGURE 2-4 Performance Prediction Flowchart (Hamburger et al. 2004)

The PEER performance-based methodology is formalized on a probabilistic basis and is composed of four sequential steps: hazard assessment, structural/nonstructural component analysis, damage evaluation and loss analysis or risk assessment. The product from each of these four steps is characterized by a generalized variable: Intensity Measure (IM), Engineering Demand Parameter (EDP), Damage Measure (DM), and Decision Variable (DV), for each of the steps, respectively. Figure 2-5 illustrates the methodology and its probabilistic underpinnings. The variables are expressed in terms of conditional probabilities of exceedance (e.g., $p(EDP \mid IM)$) and the approach of Figure 2-5 assumes that the conditional probabilities between the parameters are independent. Moehle (2003) and Hamburger et al. (2004) describe the performance-based methodology that has been adopted for the ATC-58 project.

The following section introduces seismic protective systems, which are systems of isolators and/or energy dissipation devices that *substantially improve* the seismic response of bridges, buildings and infrastructure, measured here in terms of damage and direct and indirect economic loss. Much of the work of the PEER Center and the ATC-58 project is directly applicable to bridges with the only notable exception being nonstructural components and systems, which are typically found only in buildings and infrastructure.

7
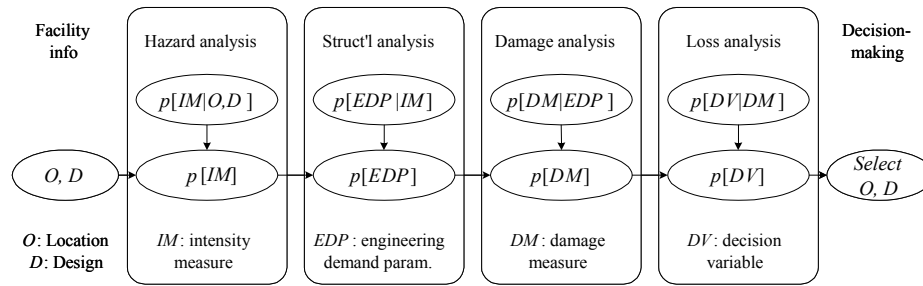
FIGURE 2-5 PEER and ATC-58 Performance Methodologies (Moehle 2003)

2.3 Seismic Protective Systems

The seismic design of conventionally framed bridges and buildings relies on the dissipation of earthquake-induced energy through inelastic (nonlinear) response in selected components of the structural frame. Such response is associated with structural damage that produces direct (capital) loss repair cost, indirect loss (possible closure, re-routing, business interruption) and perhaps casualties (injuries, loss of life). Importantly, traditional seismic analysis and design procedures do not permit the accurate estimation of structural deformations and damage, making it impossible to predict the likelihood of direct and indirect losses and casualties.

Seismic protective systems, herein assumed to include seismic (base) isolators and damping (energy dissipation) devices, were developed to mitigate the effects of earthquake shaking on bridges and buildings. Seismic isolators are typically installed between the girders and bent caps (abutments) in bridges and the foundation and first suspended level in a building. Figure 2-6 shows a typical bridge installation of seismic isolators; the isolators were installed at the top of the pier as shown in Figure 2-6b (the steel plate on the side of the isolator is part of lateral wind-restraint system). For bridge construction, the typical design goals associated with the use of seismic isolation are a) reduction of forces (accelerations) in the superstructure and substructure, and b) force redistribution between the piers and the abutments.
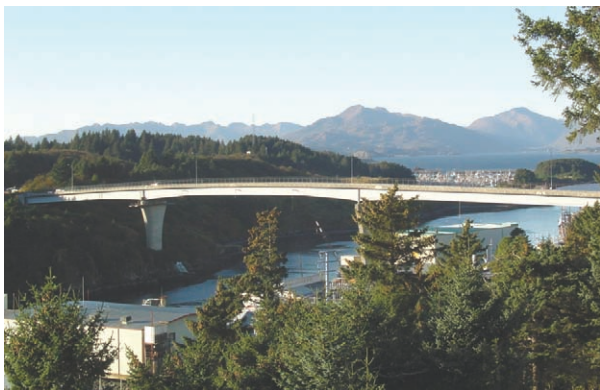
a. bridge elevation   b. Friction Pendulum seismic isolator

FIGURE 2-6 Typical Installation of a Seismic Isolation Bearing in a Bridge

Contemporary seismic isolation systems for bridge applications are described in Section 2.4. Each of these systems provides a) horizontal isolation from the effects of earthquake shaking, and b) an energy dissipation mechanism to reduce displacements. Figure 2-7a illustrates the effect of horizontal isolation on the inertial forces that can develop in a typical bridge. The elongation of the fundamental period (period shift in Figure 2-7a) of the bridge can substantially reduce, by a factor exceeding 3 in most cases, the accelerations that can develop in a bridge superstructure. Such significant reductions in force (acceleration) enable the cost-effective construction of bridges that respond in the elastic range (no damage) in design earthquake shaking. Figure 2-7b illustrates the effect of isolation on the displacement response of the bridge. It must be noted that nearly all of the displacement will typically occur over the height of the isolator and not in the superstructure, piers or abutments.

a. reduction in spectral accelerations   b. increase in spectral displacements
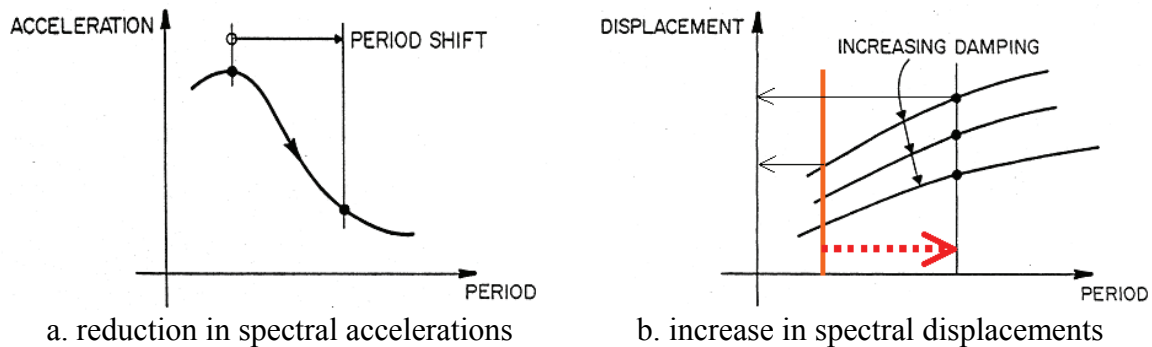
FIGURE 2-7 Principles of Seismic Isolation

The increase in displacement response associated with the use of seismic isolators has a deleterious impact on expansion joints in bridges. To control displacements, and thus reduce demands on joints and the cost of the isolators, damping (energy dissipation) is typically introduced in the isolator as noted in Section 2.5. Damping in the two most common bridge seismic isolators in use in the Western United States, the Lead-Rubber (LR) Bearing and the Friction Pendulum (FP) bearing, is achieved through hysteretic energy dissipation, leading to the shear force-lateral displacement relationship of Figure 2-8.
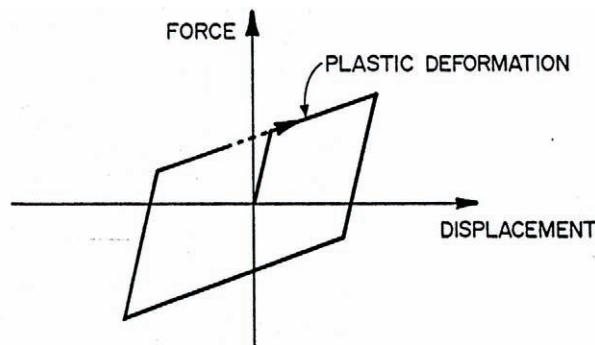
FIGURE 2-8 Hysteretic Damping in LR and FP Bearings

9

Energy dissipation devices (dampers) serve to protect structural components of a bridge from damage by reducing deformations and earthquake-induced damage. Energy is dissipated by either hysteretic or viscous damping in components that are specifically designed for this function. Dampers do not form part of the gravity-load-resisting system in a bridge. Contemporary dampers for bridge applications are described in Section 2.5.

Dampers require relative displacement or velocity to be activated and dissipate energy. Large relative displacements can be achieved in only limited locations in bridge construction, for example, as part of a hybrid seismic isolation system, and b) in cable-stayed and suspension-cable bridge construction. Figure 2-9 shows one application of fluid viscous dampers in a cable-stayed bridge, where the dampers are installed between the bridge deck and the towers.

| a. between bridge deck and tower | b. damper installation |

FIGURE 2-9 Typical Installation of a Dampers in a Cable-Stayed Bridge

The use of seismic protective systems for bridge applications in the United States received a significant boost in the 1990s with the publication of guidelines, resource documents and standard testing procedures. The 1991 *Guide Specification for Seismic Isolation Design* (AASHTO, 1991) presented procedures for the analysis and design of bridges isolated with elastomeric bearings. This specification was substantially re-written and re-published in 1999 to be consistent with the AASHTO Standard Specification for Highway Bridges, provide procedures for the design of sliding isolation bearings, and to introduce methods for bounding the response of seismically isolated bridges. Other important developments in the 1990s and early 2000s that spurred the implementation of seismic protective systems included the HITEC *Guidelines for the Testing of Seismic Isolation and Energy Dissipation Devices* (HITEC, 1996) and the HITEC *Guidelines for the Testing Large Seismic Isolator and Energy Dissipation Devices* (HITEC, 2002).

10

2.4 Seismic Isolation Devices and Systems

2.4.1 A Brief History of Seismic Isolation

Although patents on seismic isolators can be traced back to the 1800s, the use of seismic isolation for protecting bridges and buildings is somewhat recent in the United States, with the first application being completed in 1985 for the retrofit of the Sierra Point Overpass, in San Francisco, California. Lead-rubber bearings (see Section 2.4.2) were used for this retrofit project.

Isolation-system design practice in the United States differs from that in some other countries because a significant restoring force is required to reduce or eliminate permanent lateral displacements after earthquake shaking. The discussion that follows in the remainder of this chapter addresses only those seismic isolators that meet the intent of the AASHTO *Guide Specification for Seismic Isolation Design* (AASHTO, 1999), which mandates a significant restoring force.

2.4.2 Contemporary Seismic Isolation Systems

There are two common types of seismic isolation bearings used the United States at this time, namely, elastomeric bearings (low- and high-damping rubber; lead rubber) and sliding bearings (spherical sliding or Friction Pendulum bearings; flat sliding or EradiQuake bearings). Each type of bearing is described below. A typical hysteretic (force-displacement) loop for a seismic isolation bearing is shown in Figure 2-8.

Elastomeric, non-lead-rubber bearings are available as either low-damping natural rubber bearings (manufactured principally by Andre, Bridgestone, Dynamic Isolation Systems (DIS: www.dis-inc.com), Scougal Rubber (www.scougalrubber.com) Seismic Energy Products (SEP: www.sepbearings.com) or high-damping (filled) bearings (manufactured principally by Andre and Bridgestone). A section through a 1980s-vintage elastomeric bearing is presented in Figure 2-10 below. The maximum shear-strain range for a high-damping rubber bearing varies as a function of compound and manufacturer but is generally between 200% and 350%. Since these bearings have low elastic stiffness and this provides little resistance to service-level loads such as braking and wind forces, they have not been used for bridge applications in the United States.

Energy dissipation in high-damping rubber bearings is achieved by special compounding of the elastomer. Damping ratios generally range between 7% and 14% of critical. The shear modulus of high-damping elastomers generally ranges between 0.35 MPa (50 psi) and 1.4 MPa (200 psi). Techniques to manipulate mechanical properties are generally considered proprietary. The effective stiffness (a function of the modulus, bonded area, and total rubber thickness) and damping of an elastomeric bearing will depend on:

- Elastomer (including fillers) and vulcanization profile
- Contact pressure (supported load divided by bonded area)
- Velocity of loading

11

- Load history
- Strain history
- Temperature (especially below -7°C or 20°F)

FIGURE 2-10 Section Through an Elastomeric Bearing

Information on the mechanical properties of elastomers and elastomeric bearings is presented in Section 7.

Elastomeric, lead-rubber bearings are manufactured in the United States by Dynamic Isolation Systems (DIS: www.dis-inc.com) and Seismic Energy Products (SEP: www.sepbearings.com). A cut-away view through a lead rubber (LR) bearing is presented in Figure 2-11 below. Shown in this figure are the alternating layers of elastomer and steel shims and the central lead core.

Lead-rubber bearings are generally constructed with low-damping (unfilled) elastomers (with shear moduli in the range of 65 to 100 psi at 100% shear strain) and lead cores with diameters ranging between 15% and 33% of the bonded diameter of the bearing. The elastomer provides the isolation component and the lead core provides the energy dissipation or damping component. The maximum shear-strain range for LR bearings varies as a function of manufacturer but is generally between 125% and 200%.
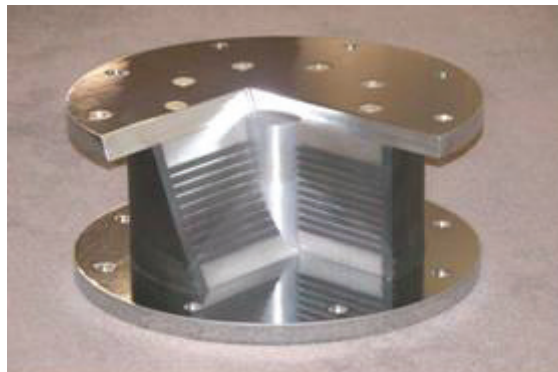
FIGURE 2-11 Construction Details for a Lead-Rubber Bearing

Information on the mechanical properties of LR bearings is presented in Section 8.

The Friction Pendulum (FP) bearing is manufactured in the United States by Earthquake Protection Systems (www.earthquakeprotection.com). The key components of the FP bearing are shown on Figure 2-12[1], including:

- Concave dish and housing plate (ductile cast iron, steel or cast steel)
- Articulated slider (typically of 304 austenitic stainless steel)
- Bearing material (high load, low friction composite)
- Stainless steel overlay (typically of 316 austenitic stainless steel)

Isolation is achieved through sliding of the articulated slider on the concave surface. Energy dissipation (damping) is provided by friction between the composite bearing material and the stainless steel overlay that is not shown in the figure. The stainless steel overlay is attached to the concave dish. The sliding interface plays a crucial role in the response of the FP bearing and the frictional resistance of the interface is a function of:

- Slider diameter (affecting the confinement of the composite)
- Contact pressure
- Sliding velocity
- Temperature
- Wear (due to extended travel in bridge bearings due to thermal cycling)

The Double Concave Friction Pendulum bearing is a derivative of the FP bearing shown in Figure 2-12. Information on the mechanical properties (isolation and energy dissipation) of FP bearings is presented in Sections 4, 5 and 6. The FP bearing is capable of supporting very high axial loads at large lateral displacements.
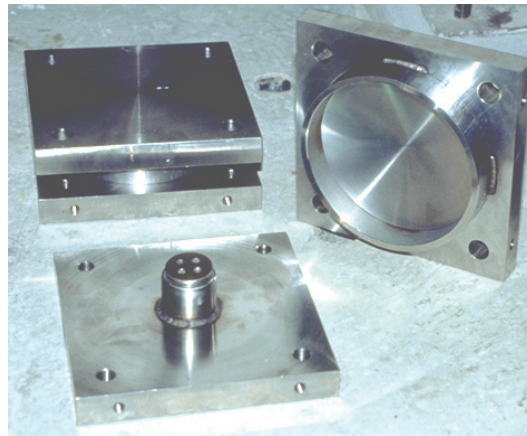
FIGURE 2-12 Views of Friction Pendulum Bearings

---

[1] The bearing of Figure 2-12 is a small-scale isolator produced for earthquake-simulator testing. In prototype bearings, the composite material is bonded to the articulated slider rather than screwed to the slider as seen in the figure.

13

The EradiQuake bearing is manufactured in the United States by R. J. Watson, Inc. (www.rjwatson.com) and is composed of a disk bearing with restoring force elements in the form of urethane springs. Energy dissipation is via sliding friction on the PTFE-stainless steel interface. The EradiQuake bearing is suitable for small to moderate seismic displacements and has been used for isolating bridges primarily in the central and eastern United States. Figure 2-13 provides views of a EradiQuake bearing.
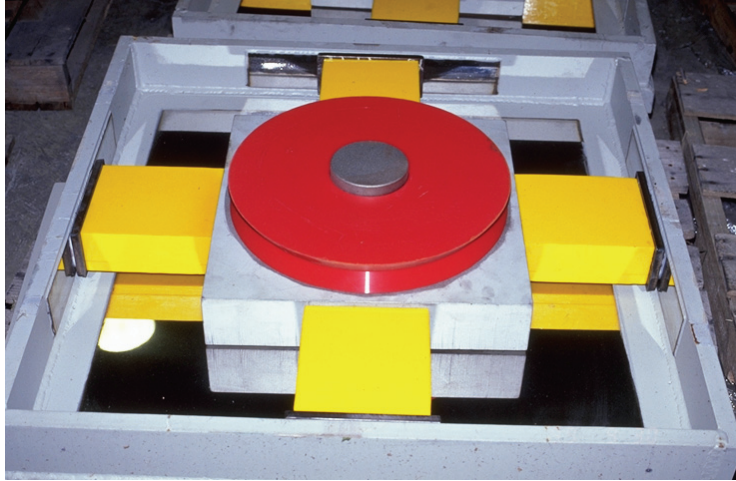
FIGURE 2-13 Internal Construction of an EradiQuake Bearing

Information on the mechanical properties of PTFE-polished stainless steel interfaces is presented in Section 5.

2.5 Energy Dissipation Devices and Systems

2.5.1 A Brief History of Energy Dissipation Devices

Energy dissipation devices have been used in mechanical systems for over one hundred years. Of relevance to this presentation is the first use of fluid viscous dampers by the French Army in the 1890s to dampen the shock loadings from artillery pieces. Many of the components in those dampers can be found in the most modern of fluid viscous dampers today.

The use of discrete energy dissipation devices for earthquake engineering applications is somewhat recent with the first applications in New Zealand in the 1970s. Yielding steel devices were used in these applications. The first applications of seismic energy dissipation devices in North America date to the late 1980s where use was made of yielding steel and fluid viscous dampers. However, the use of fluid damping devices for shock and vibration isolation dates back to the beginning of the 20th century.

The use of energy dissipation devices for buildings, bridges and infrastructure was spurred by the publication in the late 1980s of a draft guideline for the implementation of damping devices in buildings (Whittaker et al., 1993), which provided regulators with a

14

means by which to judge the efficacy of a design using dampers. The draft guideline was superseded in mid 1990s with the publication of FEMA 273 and FEMA 274 (ATC, 1997) and lately with the publication of the 2003 NEHRP (BSSC, 2003) and Standard ASCE/SEI 7-05 (ASCE, 2005).

2.5.2   Contemporary Energy Dissipation Devices and Systems

Energy dissipation or damping devices are generally divided into three categories: displacement-dependent, velocity-dependent, and other. Examples of displacement-dependent or hysteretic systems include devices based on yielding of metal and friction. Figure 2-14a presents sample force-displacement loops of hysteretic dampers. Examples of velocity-dependent systems include dampers consisting of viscoelastic solid materials, dampers operating by deformation of viscoelastic fluids (e.g., viscous shear walls), and dampers operating by forcing fluid through an orifice (e.g., viscous fluid dampers). Figure 2-14b illustrates the behavior of these velocity-dependent systems. Other systems have characteristics that cannot be classified by one of the basic types depicted in Figures 2-14, including dampers made of shape memory alloys, frictional-spring assemblies with re-centering capabilities, and fluid restoring force/damping dampers. For information on these dampers, the reader is referred to ATC (1993), Constantinou et al. (1998), EERI (1993), Soong and Constantinou (1994), Soong and Dargush (1997) and Hanson and Soong (2001). Only displacement-dependent and velocity-dependent dampers are introduced in this report, and only those dampers suitable for bridge applications are described in detail below.

a. hysteresis loops for displacement-dependent dampers

b. hysteresis loops for velocity-dependent dampers
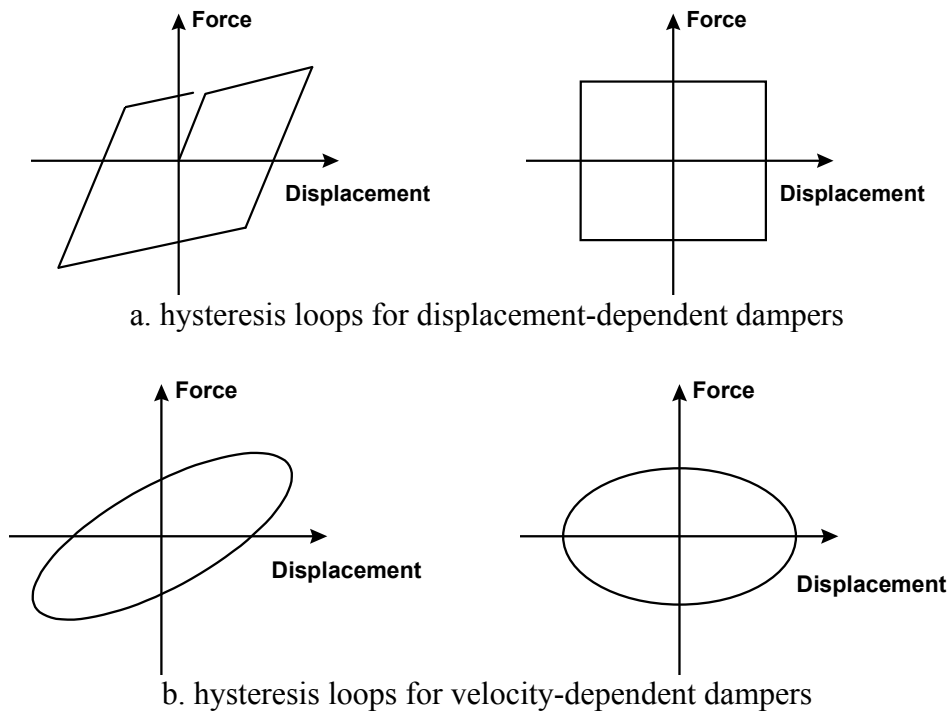
FIGURE 2-14 Force-displacement Loops for Energy Dissipation Devices

15

Of all the energy dissipation devices available in the marketplace, only two, the displacement-dependant unbonded (buckling-restrained) brace and the fluid viscous damper are suitable for bridge applications. Note that the unbonded brace is not suitable for installation across expansion or contraction joints in bridge decks because these dampers will generally a) have insufficient displacement capacity, and b) prevent the thermal expansion and contraction. Unbonded braces are suitable for incorporation in bridge substructures to augment the stiffness, strength and energy dissipation capacity of the substructure.

A schematic drawing of the unbonded (or buckling restrained) brace is shown in Figure 2-15. This brace damper was developed in Japan in the mid-1980s (Watanabe et al., 1988) and has been used on a number of building projects in the United States. The schematic of Figure 2-15 illustrates the key components of the Nippon Steel brace, namely, a cruciform cross section of welded steel plate (often low-yield steel) that is designed to yield in tension and compression, and an exterior steel tube of circular or rectangular cross section that is selected such that the buckling capacity of the tube exceeds the squash load of the cruciform cross section. The space between the cruciform cross section and the steel tube is filled with a concrete-like material to delay local buckling of the cruciform cross section outstands. Proprietary materials are used to de-bond the cruciform cross section from the concrete-like material. The unbonded brace is designed to have approximately equal strength in tension and compression, and is conceptually superior to the concentrically braced frame.
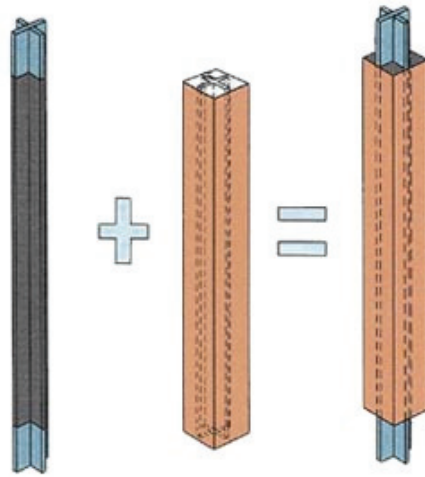
FIGURE 2-15 Schematic Construction Information for the Unbonded Brace

Unbonded braces are supplied in the United States by Corebrace (www.corebrace.com), Star Seismic (www.starseismic.net) and Nippon Steel.

Fluid viscous dampers are widely used in the United States at this time for bridge (see Figure 2-9) and building construction. Much of the technology used in this type of damper was developed for military, aerospace and energy applications.

Pure viscous behavior may be produced by forcing fluid through an orifice (Constantinou and Symans, 1992; Soong and Constantinou, 1994; Hanson and Soong, 2001). This principle is used by both manufacturers of seismic fluid viscous dampers in the United States, namely, Jarret and Taylor Devices. Figure 2-16 shows the internal construction of a Taylor fluid viscous damper. As shown in this figure, fluid flows from one side of the piston head to the other via annular orifices and orifices in the piston head. The design of such orifices is proprietary. The damper design shown in Figure 2-16 consists of a run-through piston rod with two seals. It is typical of what is currently used in seismic isolation and damping systems because such designs are generally reliable and do not develop restoring force. Alternate constructions with accumulators are discussed in Section 10.
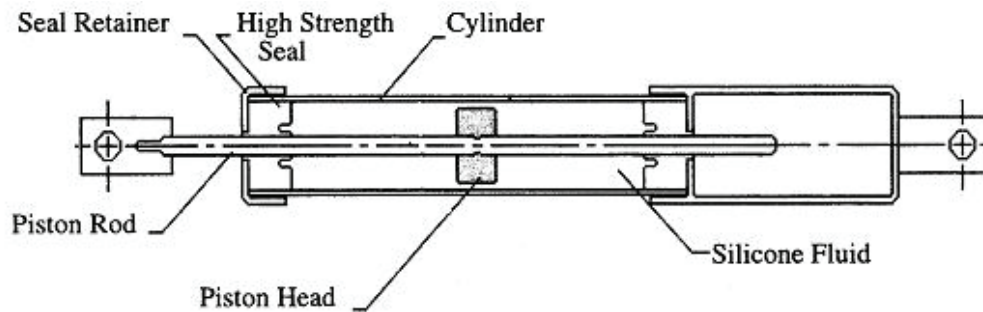
FIGURE 2-16 Internal Construction of a Fluid Viscous Damper

Figure 2-17 shows the use of a fluid viscous damper as part of a hybrid seismic isolation system. In such a system, the fluid viscous dampers augment the damping provided by the seismic isolation bearings. The stroke of the damper must exceed the expected displacement capacity of the seismic isolator in maximum considered earthquake shaking. Section 10 of this report provides additional information on the mechanical properties of fluid viscous dampers.
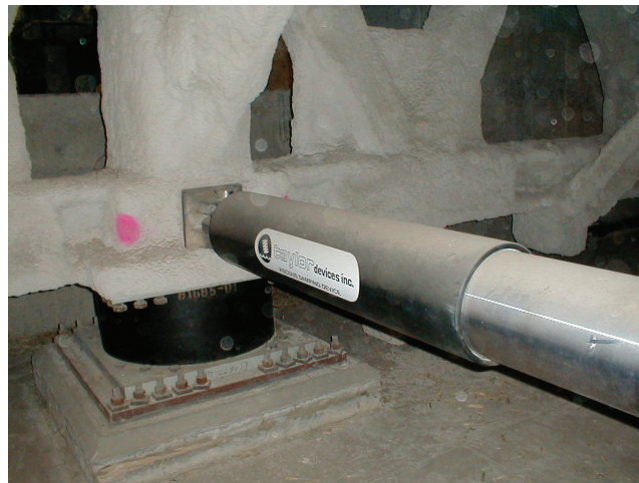
FIGURE 2-17 A Fluid Viscous Damper in a Hybrid Isolation System

17

2.6 Applications of Seismic Isolation and Damping Systems

There are numerous applications of seismic isolation and energy dissipation for bridges and buildings in the United States and abroad. No comprehensive and current list of applications exists at this time. A list of applications prior to 2000 can be found at the PROSYS website: www.nisee.berkeley.edu/prosys/usbridges.html. For a listing of more recent applications in the United States, the reader is referred to the websites of the manufacturers of seismic isolation and energy dissipation devices, including the U.S. manufacturers listed below.

- www.corebrace.com
- www.dis-inc.com
- www.earthquakeprotection.com
- www.jarretstructures.com
- www.scougalrubber.com
- www.sepbearings.com
- www.starseismic.net
- www.taylordevices.com

International manufacturers have supplied seismic isolators and energy dissipation devices to projects in the United States, including:

- Alga
- Andre Rubber
- Bridgestone
- FIP Industriale
- Nippon Steel
- Oiles Corporation
- Skellerup

The interested reader should visit the websites of these overseas suppliers for information on their seismic protective technologies.

SECTION 3
METHODS OF ANALYSIS OF SEISMICALLY ISOLATED BRIDGES

3.1 Introduction

Methods of analysis of seismically isolated bridges consist of (a) the single mode or simplified method, (b) the multimode or response spectrum method, and (c) the response history analysis method. The latter is the most accurate method of analysis and can be implemented in a variety of computer software.

The single mode and the multimode methods of analysis are based on representing the behavior of isolators by linear elastic elements with stiffness equal to the effective or secant stiffness of the element at the expected displacement. The effect of energy dissipation of the isolation system is accounted for representing the isolators as equivalent linear viscous elements on the basis of the energy dissipated per cycle at the expected displacement. The response is then calculated using a response spectrum that is modified for the effect of damping larger than 5 percent of critical. Given that the expected displacement is unknown until the analysis is performed, these methods require some iteration until the assumed and calculated values of isolator displacement are equal.

The following sub-sections briefly describe methods of analysis for seismically isolated bridges and provide information on the following related topics:

- Modification of a response spectrum for higher damping
- Calculation of maximum velocity and maximum force in isolation systems with viscous damping devices
- Response modification factors
- Re-centering capability in isolation systems

3.2 Modification of a Response Spectrum for Higher Damping

A 5%-damped elastic response spectrum is typically used to represent the seismic hazard for bridge design. Spectra for higher levels of damping need to be constructed for the application of simplified (single or multimode) methods of analysis. Elastic spectra constructed for higher levels of viscous damping are useful for the analysis of linear elastic structures with linear viscous damping systems. Moreover, they are used in the simplified analysis of yielding structures or structures exhibiting hysteretic behavior since simplified methods of analysis are based on the premise that these structures can be analyzed by using equivalent linear and viscous representations.

The typical approach of constructing an elastic spectrum for damping greater than 5 percent is to divide the 5%-damped spectral acceleration by a damping coefficient or damping reduction factor B:

$$S_a(T, \beta) = \frac{S_a(T, 5\%)}{B}$$

(3-1)

19

where $S_a(T, \beta)$ is the spectral acceleration at period T for damping ratio β. Note that the spectral acceleration is the acceleration at maximum displacement and is not necessarily the maximum acceleration (it does not contain any contribution from the viscous force) Therefore, it is related directly to the spectral displacement S_d through

$$S_d = \frac{T^2}{4\pi^2} S_a \qquad (3\text{-}2)$$

where all terms are defined above. The damping reduction factor B is a function of the damping ratio and can be a function of the period.

Lin et al. (2005) recently presented a comparison of values determined by various researchers. Equation (3-1) is typically used to obtain values of coefficient B for a range of values of period T and for selected earthquake motions. The results for the selected earthquake motions are statistically processed to obtain average or median values, which upon division of the value for 5% damping to the value for damping β results the corresponding value of B. The results are affected by the selection of the earthquake motions and the procedures used to scale the motions in order to represent a particular smooth response spectrum. Furthermore, the values of B used in codes and specifications are typically conservative, are rounded and are based on simplified expressions. The interested reader is referred to Ramirez et al. (2001) for more details.

Table 3-1 presents values of B in the following codes and specifications: (a) 1999 AASHTO (American Association of State Highway and Transportation Officials, 1999), 2003 NEHRP Recommended Provisions (Building Seismic Safety Council, 2003), 2001 California Building Code (CBC) (California Building Standards Commission, 2001), draft of Eurocode 8 (European Committee for Standardization, 2005) and recommendations in FEMA 440 (Applied Technology Council, 2005). FEMA 440 and the draft of Eurocode 8 present equations for B, whereas the other documents present values of B in tabular format. The equation in FEMA 440 is

$$B = \frac{4}{5.6 - ln(100\beta)} \qquad (3\text{-}3)$$

where β is presented as a decimal fraction (not a percentage). The equation in Eurocode 8 is

$$B = \sqrt{\frac{0.05 + \beta}{0.10}} \qquad (3\text{-}4)$$

The values of B in Table 3-1 calculated using equations (3-3) and (3-4) were rounded to the nearest number with one decimal digit of accuracy.

TABLE 3-1 Values of Damping Reduction Factor _B_ in Codes and Specifications

$\beta(\%)$	1999 AASHTO, 2001 CBC	2003 NEHRP	FEMA 440	EUROCODE 8
≤2	0.8	0.8	0.8	0.8
5	1.0	1.0	1.0	1.0
10	1.2	1.2	1.2	1.2
20	1.5	1.5	1.5	1.6
30	1.7	1.7 or 1.8[1]	1.8	1.9
40	1.9	2.1	2.1	2.1
50	2.0	2.4	2.4	2.3

1. 1.7 for isolated structures and 1.8 for structures with damping systems

The values of _B_ in various codes and specifications are nearly identical for values of damping ratio less than or equal to 30%. This is the limit of damping ratio for which simplified methods of analysis can be used. The values of _B_ for larger damping ratio in 1999 AASHTO and 2001 CBC are more conservative than in more recent codes and specifications.

3.3 Maximum Velocity and Maximum Force in Isolation Systems with Viscous Damping Devices

Consider a seismically isolated structure represented as a single degree of freedom (SDOF) system with mass m , weight W and lateral force-displacement relationship having the bilinear hysteretic characteristics shown in Figure 3-1. The system is characterized by characteristic strength Q_d and post-elastic stiffness K_d . For the FP system (see Section 6), $Q_d = \mu W$ and $K_d = W / R_e$, where μ is the coefficient of friction at large sliding velocity and R_e is the effective radius of curvature. For LR systems, the characteristic strength is the product of the area of the lead cores and the (dynamic) yield stress of the lead and the post-elastic stiffness is the product of the bonded area of the bearings and the shear modulus, divided by the total thickness of the rubber in one bearing (assuming the rubber thickness is identical for all bearings).
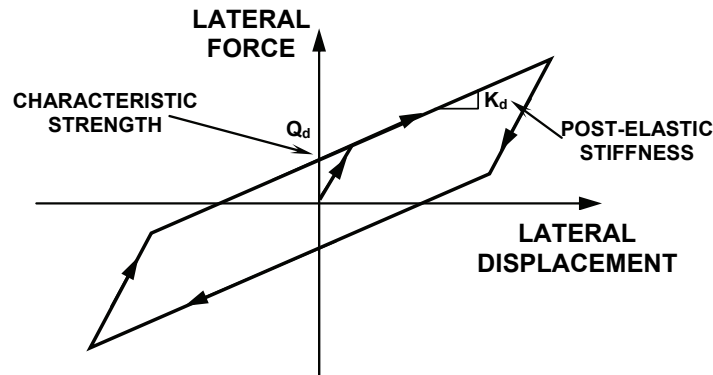
FIGURE 3-1   Idealized Force-Displacement Relation of Typical Seismic Isolation System

21

Let the displacement of the isolation system for a given level of earthquake shaking described by smoothed response spectrum, be D. The effective period and effective damping of the system are given by (1999 AASHTO, 2001 CBC)

$$T_{eff} = 2\pi \sqrt{\frac{W}{K_{eff}g}} \tag{3-5}$$

$$K_{eff} = K_d + \frac{Q_d}{D} \tag{3-6}$$

$$\beta_{eff} = \frac{1}{2\pi} \left[\frac{E}{K_{eff}D^2} \right] \tag{3-7}$$

where E is the energy dissipated per cycle at displacement D and period T_{eff}. For the behavior depicted in Figure 3-1, the energy dissipated per cycle is given by

$$E = 4Q_d(D-Y) \tag{3-8}$$

where Y is the yield displacement of the system.

The peak dynamic response of this system may be obtained from the response spectrum by assuming that the system is linear elastic with effective period T_{eff}. Based on the value of effective damping β_{eff}, the damping reduction factor B is calculated. The response of the system (in terms of spectral displacement and spectral acceleration) is calculated as the response obtained for 5% damping divided by B. However, since the calculation is based on an assumed value of displacement D, the process is repeated until the assumed and calculated values of displacement are equal. This procedure represents a simplified method of analysis that is typically used for seismically isolated structures. (We will later modify the method to account for the flexibility of a bridge's substructure). Note that the calculated spectral acceleration represents the maximum acceleration because the system has hysteretic behavior. Also, note that the maximum velocity was not calculated. We will address this problem later on in this section.

For other simplified methods of analysis, the interested reader is referred to FEMA 440 (Applied Technology Council, 2005). The accuracy of the simplified method of analysis is discussed later on this section. Moreover, FEMA 440 (Applied Technology Council, 2005) presented an evaluation of accuracy of several methods of simplified analysis.

Consider that viscous damping devices (say N in number oriented at an angle ϕ_j with respect to the direction of displacement considered) are added to this system so that the damping force in each device is described by (Constantinou et al., 1997)

$$F_{Dj} = C_{Nj} |V|^a \, \text{sgn}(V) \tag{3-9}$$

22

where V is the velocity and a is an exponent typically with a value of less than or equal to 1. To calculate the displacement response of the system with the damping devices one has to account for the effect of the damping devices on effective damping (the damping devices are purely viscous so that they do not affect the effective stiffness of the system). The analysis that follows is based on Constantinou et al. (1997) and Ramirez et al. (2001) and has been incorporated in FEMA 273/274 (Applied Technology Council, 1997) and the 2003 NEHRP Recommended Provisions (Building Seismic Safety Council, 2003).

The effective damping of the isolation system incorporating fluid viscous dampers is

$$\beta_{eff} = \frac{1}{2\pi} \left[\frac{E + E_D}{K_{eff} D^2} \right]$$
(3-10)

where E_D is the energy dissipated in the viscous damping devices given by

$$E_D = \sum_{j=1}^{N} \left(\frac{2\pi}{T_{eff}} \right)^a C_{Nj} \lambda D^{1+\alpha} \cos^{1+a} \phi_j$$
(3-11)

In (3-11), parameter λ is given by (Constantinou et al., 1997)

$$\lambda = 4(2^a) \frac{\Gamma^2 (1 + a/2)}{\Gamma(2 + a)}$$
(3-12)

where Γ is the gamma function. Table 3-2 presents values of parameter λ.

TABLE 3-2 Values of parameter λ

					a				
	0.00	0.25	0.50	0.75	1.00	1.25	1.50	1.75	2.00
λ	4.000	3.723	3.496	3.305	3.142	3.000	2.876	2.765	2.667

Analysis for the calculation of the displacement and spectral acceleration is identical that described previously but the calculated value of acceleration is not the maximum acceleration.

Ramirez et al. (2001) have shown that the maximum velocity of the system may be accurately calculated by

$$V = \left(\frac{2\pi}{T_{eff}} \right) (D) CFV$$
(3-13)

where *CFV* is a velocity correction factor given in Table 3-3. Is should be noted that equation (3-13) calculates the velocity as pseudo-velocity multiplied by a correction factor. A study by Peckan et al. (1999) resulted in an expression for *CFV* with results that are in good agreement with those of Table 3-3.

TABLE 3-3 Velocity Correction Factor *CFV*

Effective Period (sec)	Effective Damping									
	0.10	**0.20**	**0.30**	**0.40**	**0.50**	**0.60**	**0.70**	**0.80**	**0.90**	**1.00**
0.3	0.72	0.70	0.69	0.67	0.63	0.60	0.58	0.58	0.54	0.49
0.5	0.75	0.73	0.73	0.70	0.69	0.67	0.65	0.64	0.62	0.61
1.0	0.82	0.83	0.86	0.86	0.88	0.89	0.90	0.92	0.93	0.95
1.5	0.95	0.98	1.00	1.04	1.05	1.09	1.12	1.14	1.17	1.20
2.0	1.08	1.12	1.16	1.19	1.23	1.27	1.30	1.34	1.38	1.41
2.5	1.05	1.11	1.17	1.24	1.30	1.36	1.42	1.48	1.54	1.59
3.0	1.00	1.08	1.17	1.25	1.33	1.42	1.50	1.58	1.67	1.75
3.5	1.09	1.15	1.22	1.30	1.37	1.45	1.52	1.60	1.67	1.75
4.0	0.95	1.05	1.15	1.24	1.38	1.49	1.60	1.70	1.81	1.81

Ramirez et al. (2001) developed a theory for calculating the maximum force or base shear in the isolation system when accounting for the effects of viscous forces. The results of the theory have been incorporated in the 2003 NEHRP Recommended Provisions for structures with damping systems (Building Seismic Safety Council, 2003). For the general case of nonlinear viscous behavior, the base shear is given by

$$V_b = K_{eff}D\left[\cos\delta + \frac{2\pi\beta_V}{\lambda}(CFV)^a(\sin\delta)^a\right] \geq K_{eff}D \qquad (3\text{-}14)$$

where

$$\delta = \left(\frac{2\pi a\beta_V}{\lambda}\right)^{1/(2-a)} \qquad (3\text{-}15)$$

In these equations, β_V is the portion of the effective damping contributed by the viscous dampers:

$$\beta_V = \frac{\lambda}{(2\pi)^{1-a}T_{eff}^a K_{eff}D^{1-a}}\sum_j^N C_{Nj}\cos^{1+a}\phi_j \qquad (3\text{-}16)$$

24

For the case of linear viscous dampers ($\alpha = 1$),

$$\delta = \tan^{-1}(2\beta_V) \tag{3-17}$$

and

$$\beta_V = \frac{\pi}{T_{eff} K_{eff}} \sum_j^N C_j \cos^2 \phi_j \tag{3-18}$$

where C_j is the damping constant of the linear dampers. Note that the maximum acceleration is given by

$$a_{max} = \frac{V_b}{W} g \tag{3-19}$$

By virtue of (3-2) and (3-5), and using $S_d = D$, the maximum acceleration may be written as function of the spectral acceleration S_a:

$$a_{max} = S_a [\cos \delta + \frac{2\pi\beta_V}{\lambda}(CFV)^a (\sin \delta)^a] \tag{3-20}$$

Equations (3-14) and (3-20) imply that the peak force may be calculated as the peak restoring force times $\cos \delta$ plus the peak viscous force times $(\sin \delta)^a$.

3.4 Re-centering Capability

Contemporary seismic isolation systems that have been applied to buildings are characterized by strong restoring force capability. However, for bridge applications, two competing seismic isolation design strategies have been developed: (1) a strategy championed by engineers in New Zealand, the United States and Japan that requires strong restoring force in the isolation system, and (2) the Italian strategy in which the isolation system exhibits essentially elastoplastic behavior.

Specifications in the United States presume that the isolation system has, excluding any contribution from viscous devices, a bilinear hysteretic behavior characterized by the zero-force intercept or characteristic strength and the post-elastic stiffness. The 2001 California Building Code (California Building Standards Commission, 2001) specifies a minimum required stiffness as follows as such that the force at the design displacement D minus the force at half the design displacement ($D/2$) is greater than $0.025W$. Based on the typical behavior of isolation systems shown in Figure 3-1, the requirement may be expressed in the following two ways:

$$K_d D \geq 0.05W \tag{3-21}$$

or

$$T \leq 28 \left(\frac{D}{g} \right)^{1/2} \qquad \qquad (3\text{-}22)$$

where D is the design displacement of the isolation system and the period T calculated on the basis of the post-elastic stiffness:

$$T = 2\pi \sqrt{\frac{W}{g K_d}} \qquad \qquad (3\text{-}23)$$

For example, a displacement $D = 300\,\text{mm}$, which is characteristic of applications in California, would have resulted a requirement for $T \leq 4.9\,\text{sec}$, which has been already implemented. Moreover, the 2001 California Building Code allows the use of systems with insufficient restoring force provided that they are designed with a displacement capacity that is three times larger than the calculated demand.

The 1999 AASHTO Guide Specifications for Seismic Isolation Design (AASHTO, 1999) have a more relaxed specification for the minimum restoring force but subject to a constraint on period T

$$K_d D \geq 0.025 W \qquad \qquad (3\text{-}24)$$

and

$$T \leq 40 \left(\frac{D}{g} \right)^{1/2} \leq 6\,\text{sec} \qquad \qquad (3\text{-}25)$$

Moreover, AASHTO does not permit the use of systems that do not meet this requirement.

The design strategy of requiring strong restoring force is based on the experience that bridge failures in earthquakes were primarily the result of excessive displacements. By requiring strong restoring force, cumulative permanent displacements are avoided and the prediction of displacement demand is accomplished with less uncertainty. By contrast, seismic isolation systems with low restoring force ensure that the force transmitted by the bearing to the substructure is predictable with some certainty. However, this is accomplished at the expense of uncertainty in the resulting displacements and the possibility for significant permanent displacements. Tsopelas and Constantinou (1997) demonstrated the potential for significant permanent displacements in earthquake-simulator testing of bridge models with seismic isolation systems having weak restoring force capability. Moreover, Section 15.2 herein and Roussis et al. (2003) describe the failure of an elastoplastic isolation system in an earthquake.

The draft of Eurocode 8, EN1998-2 for seismically isolated bridges (European Committee for Standardization, 2005) presents a different approach for ensuring sufficient re-centering capability. The code defines the permanent displacement D_R as

26

the displacement at the intersection of the descending branch of the hysteresis loop with the zero-force axis. For systems with bilinear hysteretic behavior, the permanent displacement is given by

$$D_R = \frac{Q_d}{K_d} \tag{3-26}$$

This equation is valid when $D_R \leq D - 2Y$, which is the typical case. Eurocode 8 requires that the force at the design displacement D minus the force at half the design displacement ($D/2$) is greater than $0.025WD_R/D$. Based on the typical behavior of isolation systems shown in Figure 3-1, the requirement may be expressed in the following two ways:

$$K_d D \geq W\sqrt{0.05\mu} \tag{3-27}$$

or

$$T \leq 28\left(\sqrt{\frac{0.05}{\mu}}\right)\left(\frac{D}{g}\right)^{1/2} \tag{3-28}$$

In these equations μ is the ratio of the characteristic strength to weight

$$\mu = \frac{Q_d}{W} \tag{3-29}$$

It should be noted that (3-28) collapses to (3-22) of the 2001 CBC when $\mu = 0.05$, it is more conservative when $\mu \geq 0.05$ and is less conservative otherwise. Note that in assessing the re-centering capability of isolation systems, the characteristic strength should be evaluated under conditions of very slow motion as those experienced just prior to reaching the permanent displacement. For sliding systems (see Section 5), the parameter μ is the coefficient of sliding friction at near zero velocity or f_{min}. Similarly, in lead-rubber systems (see Section 8) the characteristic strength used in (3-29) should be the value under quasi-static conditions, which is approximately two to three times smaller that the value under dynamic, high speed conditions.

Equations (3-27) and (3-28) recognize the importance of the characteristic strength in defining the re-centering capability. As such, Eurocode 8 (European Committee for Standardization, 2005) provides a more rational basis for establishing sufficient re-centering capability than either the 2001 CBC or the 1999 AASHTO Guide Specification.

A recent study (Katsaras et al., 2006) funded by the European Union addressed the requirement for restoring force capability and proposed changes to the Eurocode. The study was based on dynamic analysis of a large number of single degree of freedom systems with bilinear hysteretic behavior and statistical processing of results on

27

displacement response, including permanent displacement and accumulated displacement. The main conclusion of the study is that seismic isolation systems has sufficient restoring force capability (no accumulation of permanent displacements in sequential earthquakes and small permanent displacements) when

$$\frac{D}{D_R} \geq 0.5 \tag{3-30}$$

where parameters D and D_R have been previously defined. It may be easily shown that this requirement is equivalent to

$$T \leq 28 \left(\sqrt{\frac{0.05}{\mu/2}} \right) \left(\frac{D}{g} \right)^{1/2} \tag{3-31}$$

where all parameters have been previously defined (with μ being the high velocity value of the normalized strength). Interestingly, Tsopelas et al. (1994) proposed on the basis of observations in the shake table testing of seismic isolation systems that systems with sufficient restoring force capability have ratio of characteristic strength (at high velocity) to peak restoring force less or equal to 3.0. This requirement is equivalent to $D/D_R \geq 0.33$, which can also be written as

$$T \leq 28 \left(\sqrt{\frac{0.05}{\mu/3}} \right) \left(\frac{D}{g} \right)^{1/2} \tag{3-32}$$

where again μ is the high velocity value of the normalized strength. The difference between (3-32) and (3-31) is likely due to the fact that the tested systems of Tsopelas et al. (1994) had velocity dependent strength, whereas the analyzed systems of Katsaras et al. (2006) were not. Nevertheless, these studies demonstrate the validity of equation (3-28) but with μ interpreted as the low velocity value of the normalized strength (about one half to one third of the high velocity value).

3.5 Response-Modification Factor

Response-modification factors (or R factors) are used to calculate the design forces in structural components given the elastic force demand. That is, the demand is calculated on the assumption of elastic structural behavior and subsequently the design forces are established by dividing the elastic force demand by R. Figure 3-2 illustrates the structural response of a yielding system. The elastic force demand is F_e; the yield force of an idealized representation of the system is F_Y. The design force, F_D, is given by

$$F_D = \frac{F_e}{R} \tag{3-33}$$

28
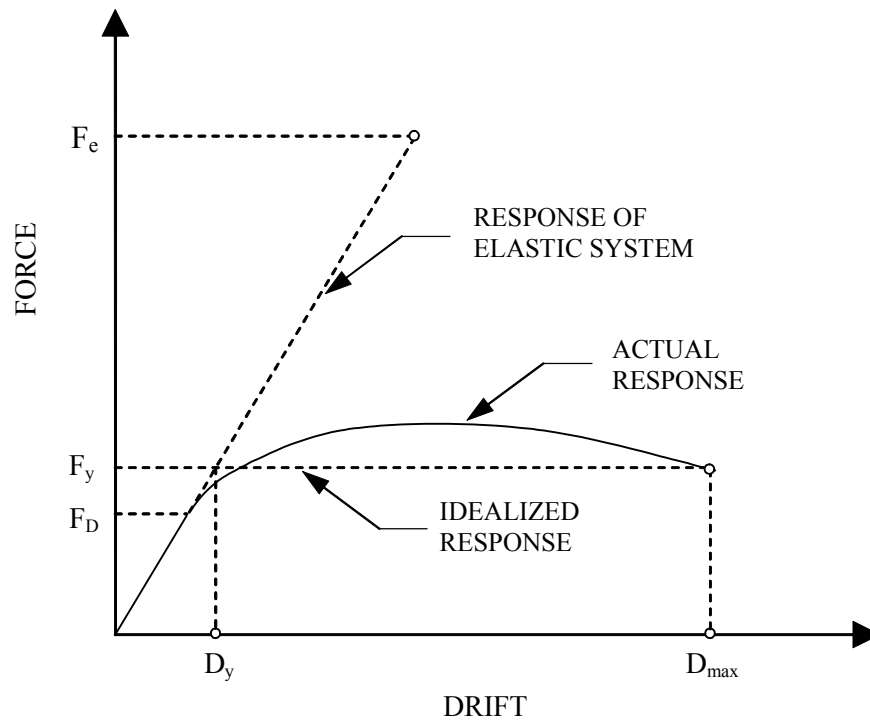
FIGURE 3-2 Structural Response of a Yielding System

The response modification factor contains two components (Uang and Bertero, 1987; Whittaker, Uang and Bertero, 1988):

$$R = \frac{F_e}{F_D} = \frac{F_e}{F_Y} \cdot \frac{F_Y}{F_D} = R_\mu \cdot R_s \tag{3-34}$$

where R_μ is the ductility-based portion of the factor and R_S is the overstrength or strength factor. The ductility-based portion of R is a measure of the inelastic deformation capacity of the structural system. The strength factor is a measure of the reserve strength of the system beyond the design strength.

In strength design, the design force corresponds approximately to the level at which yielding develops in the frame and the structural response deviates from linearity (as illustrated in Figure 3-2). In this case, the overstrength factor results from redundancy, material overstrength, over-sizing of members, strain hardening, strain rate effects and code-specified prescriptive requirements related to drift, detailing, etc.

Codes (such as the California Building Code), specifications (such as the AASHTO Standard Specification for Highway Bridges) and resource documents and guidelines (such as the NEHRP Recommended Provisions) specify values for R that are empirical. In general, the value assigned to R is dependent only on the type of structural system

29

without consideration of fundamental period, framing layout, height and ground motion characteristics.

The 1991 AASHTO Guide Specifications for Seismic Isolation Design (American Association of State Highway and Transportation Officials, 1991) specified the response modification factors for isolated bridges to be the same as those for non-isolated bridges. For substructures (piers, columns and column bents) this factor has values in the range of 2 to 5 (American Association of State Highway and Transportation Officials, 2002). While not explicitly stated in the 1991 AASHTO Guide Specifications, it is implied that the use of the same R factors would result in comparable seismic performance of the substructure of isolated and non-isolated bridges. Accordingly, the 1991 AASHTO Guide Specifications recommended the use of lower R factors when lower ductility demand on the substructure of the isolated bridge is desired. The assumption that the use of the same R factor would result in comparable substructure seismic performance in isolated and non-isolated bridges appeared rational. However, it has been demonstrated by simple analysis (Constantinou and Quarshie, 1998) that when inelastic action commences in the substructure, the effectiveness of the isolation system diminishes and larger displacement demands are imposed on the substructure.

One significant change in the 1999 edition AASHTO Guide Specifications for Seismic Isolation Design is the specification of smaller values for R for substructures of isolated bridges; the values range of 1.5 to 2.5. The following commentary from the 1999 AASHTO Guide Specifications provide the rationale for the changes from the 1991 edition:

Preface:

"…The response modification factors (R factors) have been reduced to values between 1.5 and 2.5. This implies that the ductility-based portion of the R factor is unity or close to unity. The remainder of the factor accounts for material overstrength and structural redundancies that are inherent in most structures. The specification of lower R factors has been based on the following considerations: (i) Proper performance of the isolation system, and (ii) Variability in response given the inherent variability in the characteristics of the design basis earthquake.

The lower R factors ensure, on the average, essentially elastic substructure response in the design basis earthquake. However, they do not necessarily ensure either proper behavior of the isolation system or acceptable substructure performance in the maximum capable earthquake (e.g., described as an event with 10% probability of being exceeded in 250 years). Owners may opt to consider this earthquake for the design of important bridges. This approach is currently utilized for the design of isolated bridges by the California Department of Transportation….."

30

Section C6. Response Modification Factor:

"…The specified R factors are in the range of 1.5 to 2.5, of which the ductility based portion is near unity and the remainder accounts for material overstrength and structural redundancy that are inherent in most structures. That is, the lower R factors ensure, on the average, essentially elastic substructure behavior in the design basis earthquake. It should be noted that the calculated response by the procedures described in this document represents an average value, which may be exceeded given the inherent variability in the characteristics of the design basis earthquake…."

The intent of the 1999 AASHTO Guide Specifications is to essentially eliminate inelastic action in the substructure of seismically isolated bridges for the proper performance of isolated bridges. The interested reader is referred to Constantinou and Quarshie (1998) for details of the study that established values of R for isolated bridges.

3.6 Single Mode Method of Analysis

Section 3.3 presented a detailed description of the single mode method of analysis, which applies if the bridge substructure (that part of the bridge below the isolators) is sufficiently stiff to be considered rigid. This assumption is not always valid. In such cases, the effect of substructure flexibility is to lengthen the effective period of the isolated bridge and to reduce the effective damping. The 1999 AASHTO Guide Specification (American Association of State Highway and Transportation Officials, 1999) and the draft of Eurocode 8 (European Committee for Standardization, 2005) provide some direction on how to incorporate the effects of substructure flexibility in the single mode method of analysis.

As an example, consider the simple model shown in Figure 3-3. It shows a bridge represented by a rigid deck of tributary weight W, an isolator with effective stiffness at displacement D equal to K_{IS} and a column below the isolator with horizontal stiffness K_C (stiffness derived for elastic behavior, assuming fixity at the base and applying a force at the centroidal axis of the deck). If the column is of a constant section with modulus of elasticity E and moment of inertia I, the stiffness is given by $K_C = \left[l^2(h-l)/2EI + l^3/3EI \right]^{-1}$ if shear deformations are ignored. The foundation is represented with horizontal stiffness K_F and rotational stiffness K_R. Inertial effects in the substructure are neglected. This model would be representative of the behavior of a long bridge with identical piers and isolators at each pier. The extension of this model to the case of a bridge with piers of variable properties is straightforward.

FIGURE 3-3   Seismically Isolated Bridge with a Flexible Substructure and its Deformation under Lateral Force

An inertial force F acts at the centroidal axis of the deck. The deck undergoes a total displacement equal to D_{DECK}. The effective stiffness of this system is

$$K_{eff} = \frac{F}{D_{DECK}} = \left(\frac{1}{K_F} + \frac{hl}{K_R} + \frac{1}{K_C} + \frac{1}{K_{IS}} \right)^{-1} \tag{3-35}$$

The components of displacement (see Figure 3-3 for definitions) are given by

$$u_F = \frac{F}{K_F}, \quad \phi = \frac{Fh}{K_R}, \quad u_C = \frac{F}{K_C}, \quad D = \frac{F}{K_{IS}} \tag{3-36}$$

The effective period of the isolated bridge is given by

$$T_{eff} = 2\pi \sqrt{\frac{W}{K_{eff} g}} \tag{3-37}$$

The effective damping is given by

$$\beta_{eff} = \frac{1}{2\pi} \left[\frac{EDC}{K_{eff} D_{DECK}^2} \right] \tag{3-38}$$

32

The energy dissipated per cycle, EDC, can be calculated using equation (3-8) when damping in the column and foundation is neglected (conservative) and the isolator behavior is as shown in Figure 3-1.

The total displacement of the deck D_{DECK} can be directly obtained as the spectral displacement from the response spectrum for period T_{eff} upon division by the damping reduction factor appropriate for damping β_{eff}. The isolator displacement D is then calculated from

$$D = \frac{K_{eff}}{K_{IS}} D_{DECK} \qquad (3\text{-}39)$$

The accuracy of simplified methods of analysis has been the subject of many studies. For example, FEMA 440 (Applied Technology Council, 2005), Tsopelas et al (1997), Ramirez et al (2001) and Pavlou and Constantinou (2004) presented such studies. In general, these studies confirm that the simplified method of analysis produces results of acceptable agreement with the median results of response history analyses for suites of one-directional seismic motions representing particular smoothed response spectra. However, the accuracy of the simplified method to predict the resultant displacement of isolators when the structure is excited by bi-directional seismic excitation is still a subject of study. Examples of such studies are found in Winters and Constantinou (1993) and Warn and Whittaker (2004). Such studies are difficult due to (a) the complexity of selecting bi-directional ground motions that are representative of code-specified response spectra, and (b) the complexity of defining the average of resultant displacements that occur in different directions for different seismic excitations.

3.7 Multimode Method of Analysis

The multimode method of analysis is typically implemented in a computer program capable of performing response-spectrum analysis. Each isolator is represented by its effective horizontal stiffness that is calculated on the basis of the single mode method of analysis. The response spectrum specified for the analysis is the 5 percent damped spectrum that is then modified for the effects of higher damping. The ordinates of the 5 percent damped response spectrum for periods larger than $0.8T_{eff}$ are divided by the damping reduction factor B for the effective damping of the isolated bridge. The reductions in demand due to higher damping apply only to the isolated modes; the non-isolated modes are assumed to be damped at 5 percent of critical. The modification of the spectrum for higher damping requires that the effective period and effective damping in each principal direction be calculated using the single mode method of analysis.

Figure 3-4 below presents the response spectrum used in multimode analysis of a seismically isolated bridge. The effective period is $T_{eff} = 2.75$ sec, the effective damping is $\beta_{eff} = 0.3$ and the damping reduction factor $B = 1.8$. The ordinates of the 5 percent damped spectrum for periods larger than 2.2 sec were divided by 1.8.

33
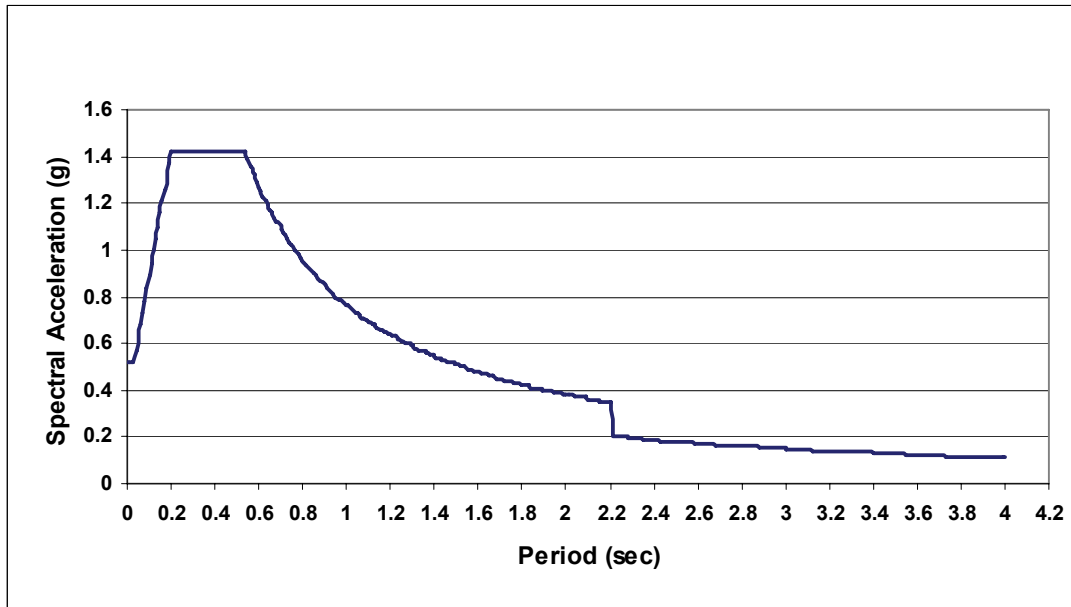
FIGURE 3-4 Response Spectrum for Multimode Analysis of a Seismically Isolated Bridge

3.8 Response History Analysis Method

The response-history analysis method incorporating nonlinear representations of the isolators is the most accurate method of analysis. Computer programs capable of such analysis are the 3D-BASIS family of programs (Nagarajaiah et al, 1989), SAP2000 (CSI, 2002), ANSYS (Swanson Analysis Systems, 1996) and ABAQUS (Hibbitt, Karlsson and Sorensen, 2004). For examples of analysis of isolated structures using programs ANSYS and ABAQUS the interested reader is referred to Roussis et al. (2003), Clarke et al. (2005) and Tsopelas et al. (2005).

SECTION 4
A DESCRIPTION OF FRICTION IN SLIDING INTERFACES

4.1 Introduction

The use of sliding bearings in seismic isolation applications requires the collection of experimental data on the frictional properties of sliding interfaces under conditions of relevance to both service and seismic loading conditions, namely, conditions of both low and high velocity motion. Moreover, it requires that an understanding of the origin of friction in these interfaces is developed so that the results are properly interpreted.

This section presents a physical interpretation of the phenomenon of friction in selected sliding interfaces. The presentation is limited to aspects of frictional behavior that are relevant to the interpretation of experimental results at the macroscopic level. While the focus is PTFE-stainless steel interfaces, it is assumed that composites containing PTFE exhibit similar behavior. Bimetallic interfaces are also discussed.

4.2 Friction

Friction is the resistance to movement of one body relative to another. Our interest is for sliding movements between solid bodies, that is, *sliding solid friction*. Moreover, we have an interest in the description of the frictional behavior of sliding interfaces as they are used in sliding bearings for structural applications. We will refer to this as friction at the macroscopic level, as opposed to friction at the microscopic and atomic levels.

The frictional force, F, at the sliding interface of a bearing will be described as

$$F = \mu N \tag{4-1}$$

where μ is the coefficient of friction and N is the normal load on the interface. We will distinguish between the sliding coefficient of friction and static (or breakaway) coefficient of friction, the latter been defined as the ratio F/N at the initiation of movement. The classical laws of friction (named for Coulomb who built his work on earlier works by Amontons and Leonardo da Vinci) postulate a friction coefficient that is independent of sliding velocity and contact area. While these laws are applicable in many cases, they do not, in general, apply to sliding bearings. Nevertheless, there is value in the use of (4-1) with the coefficient of friction being dependent on the most influential parameters, that is, velocity of sliding and apparent pressure.

4.3 Basic Mechanisms of Friction

Our interest is the understanding of the basic mechanisms of friction, that is, the microscopic events that cause friction. The overview given in this section is limited to those aspects that may provide physical insight into the frictional behavior of sliding bearings. It is largely based on the work of Bowden and Tabor (1950, 1964 and 1973)

35

and their Cambridge University students, and others over the past half century (American Society for Metals, 1992).

The basic mechanisms of friction were proposed and studied before an understanding of the atomic nature of friction was achieved. The study of friction at the atomic level, or nanotribology, is of very recent origin given that experimental techniques to measure the frictional force of one-atom-thick films were developed in the 1980s. The atomic nature of sliding contact is not yet known. Even if it was completely known, tribologists are still unable to predict the friction force at the atomic level (Krim, 1996).

Various mechanisms of friction have been proposed over the past several years. It is believed that all these mechanisms contribute in the generation of friction in various degrees depending on the particular situation. These mechanisms are described below.

4.3.1 Adhesion

When two clean solid materials come into contact they form intimate atomic bonds across the contact interface. These regions of contact are called junctions, and the sum of the areas of all the junctions constitutes the real (or true) area of contact. By comparison to the apparent area of contact, the real area of contact is very small (Figure 4-1). The junctions are characterized by interfacial forces caused by adhesion. That is, the friction force is given by the product of the real area of contact, A_r, and the shear strength of the junctions, s:

$$F_a = sA_r \qquad\qquad (4\text{-}2)$$

Adhesion between sliding interfaces is dominant for very clean surfaces in a high vacuum. It is now generally recognized that adhesion does not contribute a clearly separate component of friction. Rather, it is thought to be a component of the deformation of asperities on the sliding surfaces.
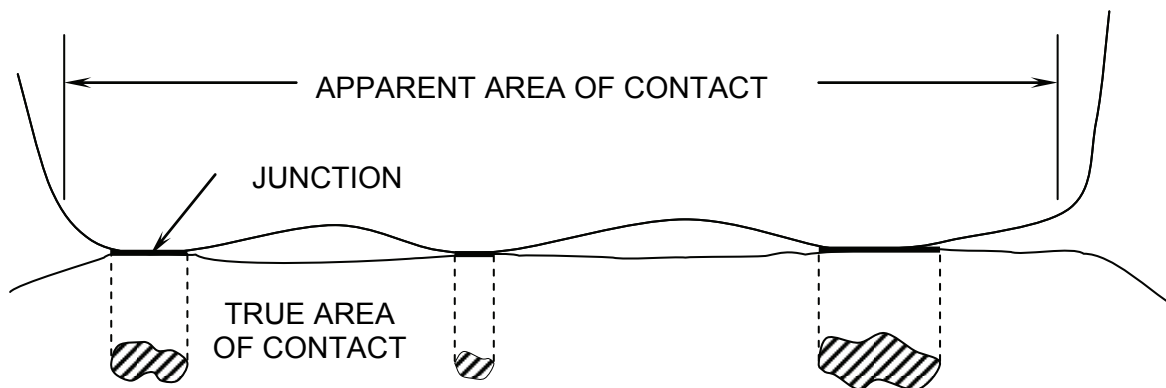
FIGURE 4-1 View of Interface Showing Apparent and Real (True) Areas of Contact

36

4.3.2 Plowing

Surfaces are characterized by asperities. When in contact, these asperities undergo elastic and plastic deformations. The plowing component of friction is due to energy dissipation during plastic deformation. This is better explained by considering a hard spherical asperity over a softer flat surface. On application of axial load on the asperity the softer surface below yields, junctions are formed and the asperity sticks to the surface below. On application of a shear force, the asperity moves horizontally, pushing a wall (or bow wave) of softer material in its path and creating a groove. The plowing component of friction results from the effort to push the wall of material.

4.3.3 Third-Body Effects

Wear debris and contaminants at the sliding interface contribute an additional term to the friction force. The contribution is due to plastic deformation as agglomerates of debris and contaminants roll between the surfaces or as they indent these surfaces.

4.3.4 Viscoelastic Effects

Polymers, such as PTFE, exhibit viscoelastic behavior. As asperities of a harder material slide over a viscoelastic material, energy is dissipated due to viscoelastic deformation, contributing an additional component to friction.

In general, it is believed that several mechanisms contribute to friction. Their relative roles are the subject of much debate. However, we assume that adhesion and mechanical deformation (elastic, plastic or viscoelastic) are collectively responsible for friction. Moreover, we shall recognize that the real area of contact is of paramount importance in the qualitative description of friction at the macroscopic scale.

4.4 Static (or Breakaway) and Sliding (or Kinetic) Friction

The static friction is the maximum force that must be overcome to initiate macroscopic motion. We define this force as the breakaway friction force. Upon initiation of motion, the friction force generally drops, that is, the static friction is typically higher than the sliding friction force, the latter being measured at a very low velocity of sliding, immediately following initiation of motion.

Figure 4-2 shows a result obtained from the testing of a sliding bearing consisting of unfilled PTFE in contact with a mirror finished stainless steel. The interface was at constant average pressure of 20.7 MPa (normal load divided by apparent area) and the temperature at the start of the experiment was 19°C. A cycle of sinusoidal motion of 12.5 mm amplitude at frequency of 0.0318 Hz was imposed (peak velocity of 2.5 mm/sec) in the test. The recorded friction force was divided by the normal load and plotted against the sliding displacement. The difference between the static and sliding values of the coefficient of friction are apparent.
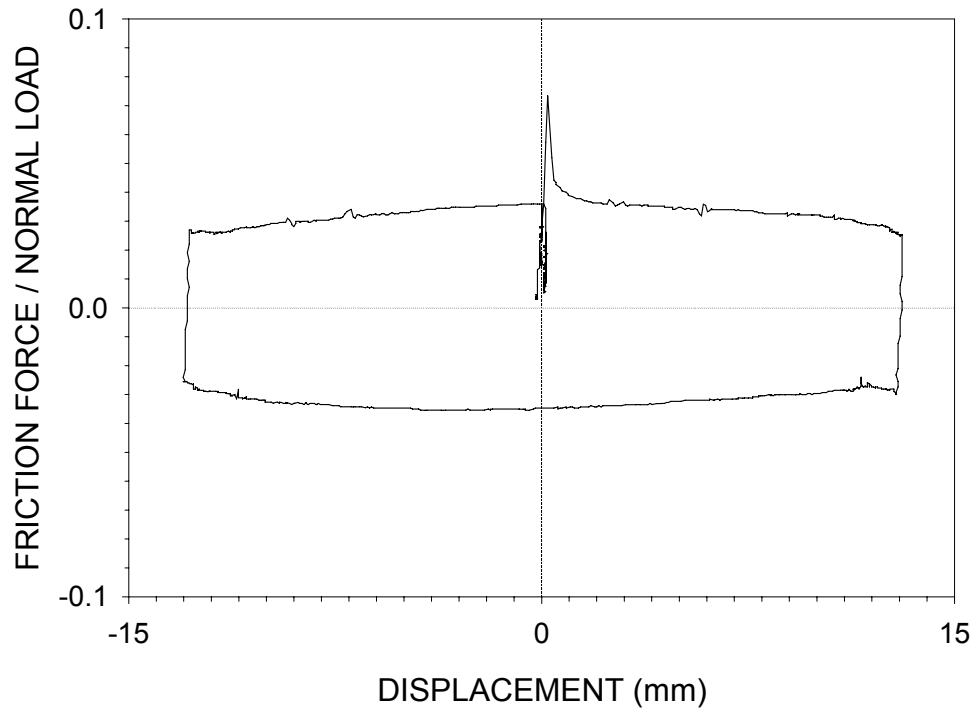
FIGURE 4-2 Typical Friction Force-Sliding Displacement Loop of PTFE-Stainless Steel Interface, Pressure=20.7 MPa, Peak Velocity=2.5 mm/sec

The static friction is real but can also be a product of the experimental technique employed or the measuring system utilized. In many civil engineering applications the experimental technique involves a system in which motion is imposed in a displacement controlled experiment: the motion being either a sine wave or a saw-tooth wave (constant velocity motion with reversal). In either case, initiation of motion requires an abrupt change of velocity from zero to a high value within extremely short time. This situation is unrealistic given that in actual applications motion initiates at essentially quasi-static conditions. This is corroborated by observations in the earthquake-simulator testing of seismically isolated structures (e.g., Mokha et al., 1990; Constantinou et al., 1990; Constantinou et al., 1993; Al-Hussaini et al., 1994). That is, while breakaway friction exists, it does not have any measurable effect because the sliding value of friction is much higher at the velocities attained under seismic conditions. In fact the concept of static friction is meaningless when the sliding friction exhibits a substantial increase with increasing velocity of sliding (Rabinowicz, 1995). It is important to measure the breakaway friction under quasi-static conditions.

The origin of the difference between static and sliding friction can be explained by the presumption of either a rapid drop in the real area of contact or the strength of the junctions following initiation of sliding. In the case of PTFE, this is likely caused by the transfer of a very thin film of PTFE on the stainless steel plate.

38

4.5 Stick-Slip Motion

Jerky motion sometimes results when one object slides on another. In displacement-controlled testing of a sliding bearing (i.e., motion is imposed by an actuator and the force is measured), stick-slip behavior is manifested as a fluctuation in the recorded friction force versus time. Conversely, in a force-controlled test the behavior is manifested as motion with stops.

Stick-slip may be an intrinsic property of the sliding interface or more often is the result of inertial effects and the flexibility in the testing arrangement, although the phenomenon might be aggravated by the frictional behavior of the interface. Figure 4-3 illustrates a testing machine that the authors have used in some of their experiments. A simplified diagram of the machine is shown in Figure 4-4. The testing arrangement is characterized by mass (hence inertial effects) and finite stiffness, both of which will affect the measurement of friction.

As an example, Figure 4-5 shows the histories of movement and axial load imposed in the testing of a sliding bearing with an unfilled PTFE-polished stainless steel interface. Recorded friction force-displacement loops are shown in Figure 4-6. In the hysteresis in the upper panel, the friction force was measured by the reaction load cell so that the inertial effects of the large mass are excluded. The friction force is smooth except following reversals of motion (where displacement is maximized) where some small fluctuation in the force is seen: true stick-slip motion at the sliding interface. It is manifested by the flexibility of the supporting part of the sliding interface. The bearing contains a flexible element to accommodate rotation; this element allows for very small translational movement.

When the actuator load cell is used to measure friction, the recorded loops exhibit significant fluctuations that result from inertial effects. An attempt was made to correct for the inertial effects by utilizing records of acceleration of the moving mass (bottom panel). While this succeeded in removing much of the fluctuation, it did not so at the start of the experiment where the corrected friction force exhibits wild fluctuations. These fluctuations could be mistakenly interpreted as resulting from stick-slip.

Consider the upper panel in Figure 4-6 and focus on the observed small fluctuation of the friction force following reversals of motion. We note that what we truly measure is not the friction force at the sliding interface but it is force in the spring (see Figure 4-4) representing the bearing and the load-cell body. Upon reversal of motion, the interface undergoes a momentary stop (movement changes direction). On initiation of motion the static (or breakaway) friction is mobilized. This is identified as point A on the force-displacement plot of Figure 4-7. Subsequently, the friction force drops (smoothly) with increasing displacement (sliding friction) and later on it increases due to increases in the velocity of sliding (a property of PTFE-stainless steel interfaces). The spring cannot adjust its position accordingly. Rather it follows the straight dashed line that represents its stiffness. The excess energy, represented by the shaded area, is kinetic energy of the supporting part of the sliding interface. That is, the supporting part is set into motion until

point B is reached, when all the kinetic energy is consumed. The result is an abrupt drop in the spring force and a subsequent increase in this force.

FIGURE 4-3 Machine Used in Testing of Sliding Bearing
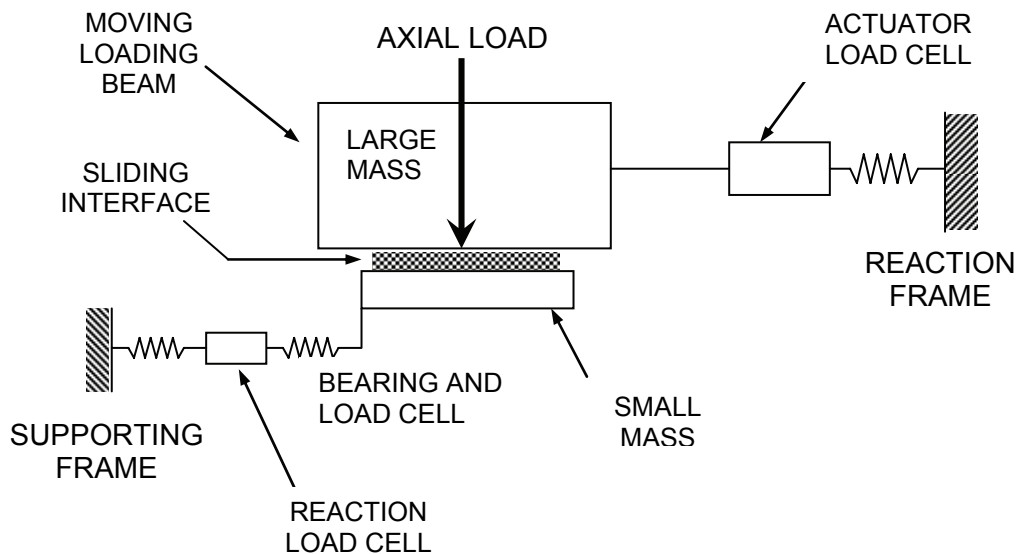
FIGURE 4-4 Simplified Diagram of the Testing Machine
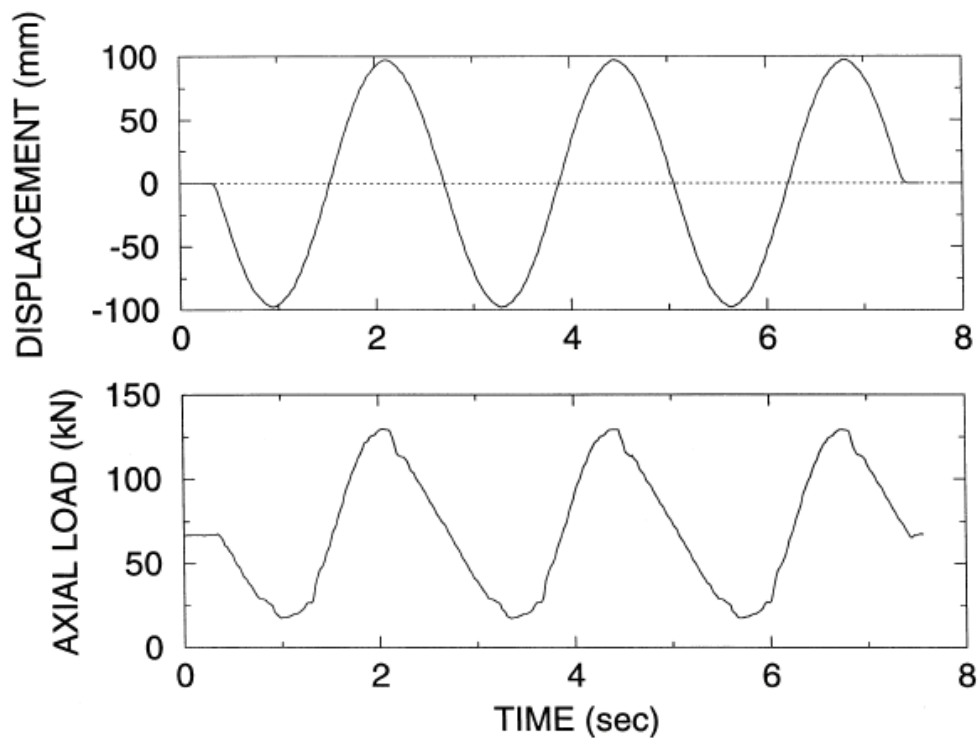
FIGURE 4-5 Histories of Imposed Motion and Axial Load on the Tested Sliding Bearing
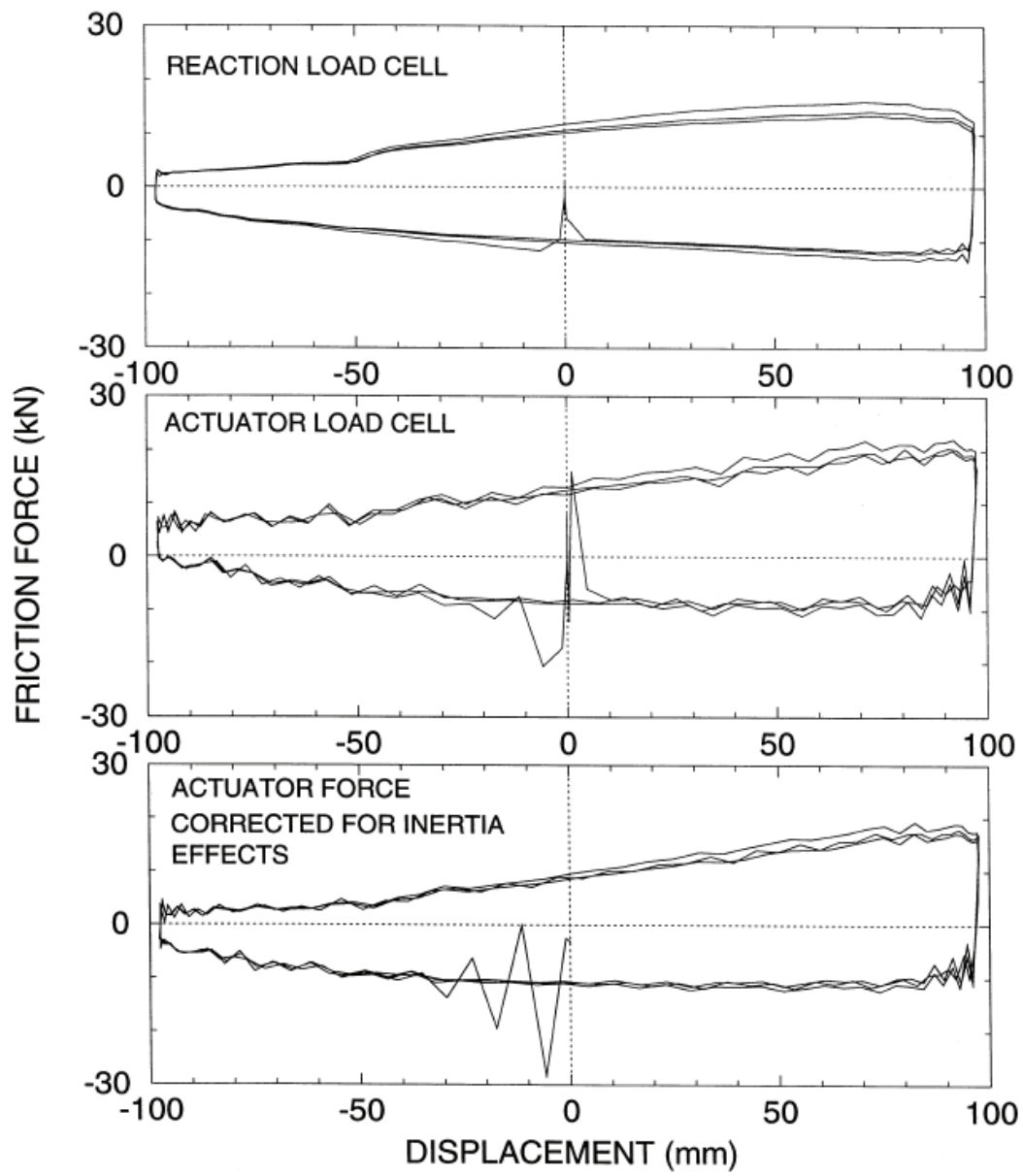
FIGURE 4-6 Recorded Friction Force-Displacement Loops from Testing of a Sliding Bearing
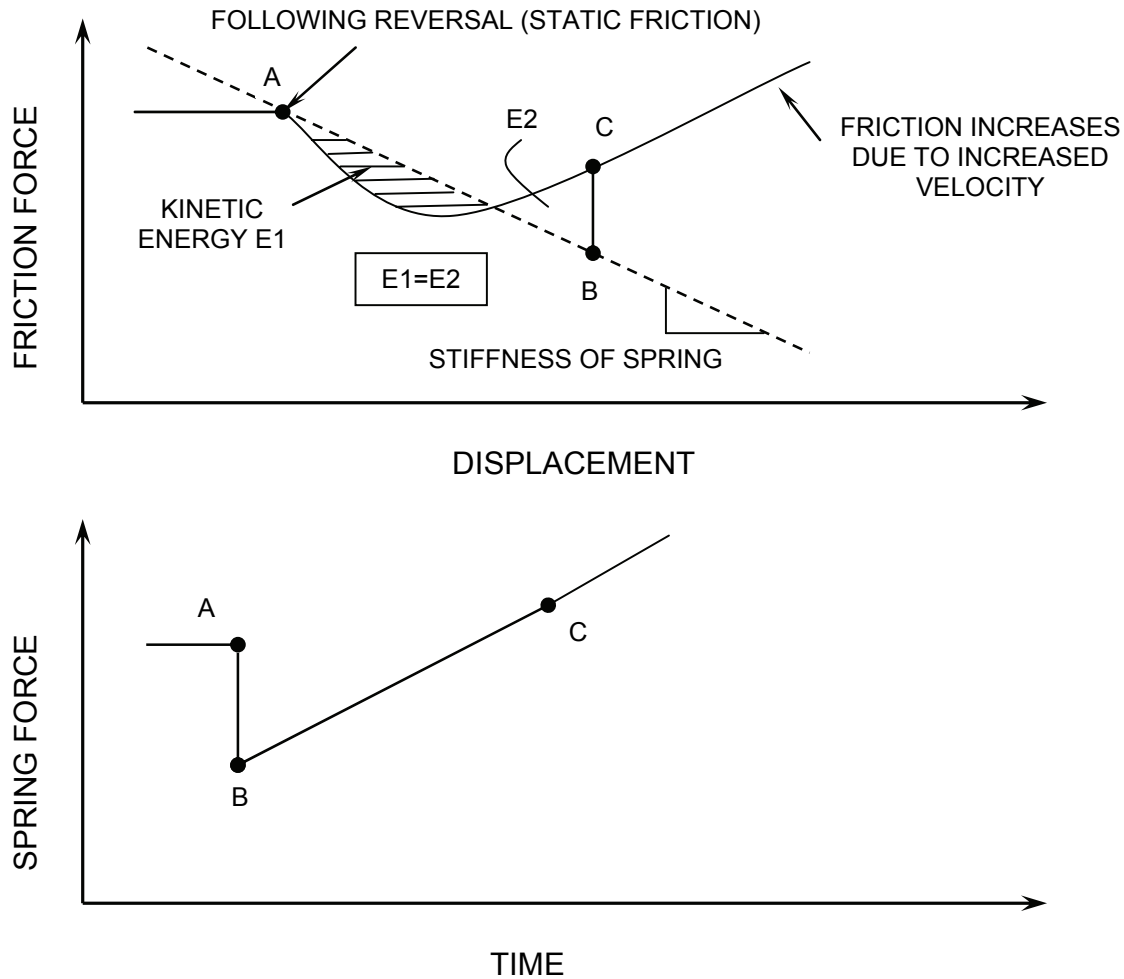
FIGURE 4-7   Friction Force and Spring Force-Displacement Plots Following Reversal of Motion

It is important to note that the phenomenon is manifested by the finite stiffness of the sliding bearing and the load cell below it (i.e., the testing arrangement), as well as the actual frictional characteristics of the interface. The magnitude of the drop in the spring force is dependent on the stiffness, the difference between static and sliding friction and the rate of increase of the sliding friction with velocity. Note that if there was no increase in the friction with increasing velocity, the same phenomenon would have been observed but with a larger drop AB in the spring force.

This classical explanation of stick-slip motion was considered to be the only interpretation of behavior until recently. Studies by Yoshizawa and Israelachvili (1993) demonstrated the possibility for another, truly intrinsic mechanism for stick-slip motion. When an interface is characterized by a thin interfacial film of polymeric fluid, phase transition between liquid-like and solid-like states of the film are possible, that is, abrupt changes in the flow characteristics of the film produce stick-slip motion.

The described stick-slip phenomenon is different, although related, to the phenomenon of motion with stops of a frictional oscillator driven by a dynamic force. Den Hartog (1931) demonstrated in a classic paper that motion with an arbitrarily large number of stops is possible. This phenomenon is the result of the requirements for dynamic equilibrium and it is completely unrelated to variations in the frictional force. Actually the stick-slip phenomenon can occur only when there is a natural variation in the friction force, whereas the analysis of Den Hartog was based on the assumption of constant friction. Makris and Constantinou (1991) demonstrated that the motion of a frictional oscillator exhibits a substantially smaller number of stops when the friction force reduces with decreasing sliding velocity.

4.6 Friction in PTFE-Polished Stainless Steel Interfaces

We will provide in this section a brief description of the macroscopic frictional properties of PTFE-polished stainless steel interfaces and we will attempt to provide a physical interpretation of these properties. It should be noted that PTFE or PTFE-based materials in contact with polished stainless steel represent, by far, the most frequently used interface in sliding bearings.

We will provide in this section a brief description of the macroscopic frictional properties of PTFE-polished stainless steel interfaces and we will attempt to provide a physical interpretation of these properties. It should be noted that PTFE or PTFE-based materials in contact with polished stainless steel represent, by far, the most frequently used interface in sliding bearings.

4.6.1 Dependency on Velocity of Sliding and Pressure

Figure 4-8 illustrates the dependencies of the coefficient of friction (friction force divided by normal load) on the velocity of sliding and normal load. The behavior is characteristic of clean, unlubricated interfaces at normal ambient temperature ($\sim$20$^{\mathrm{o}}$C). The static (or breakaway) value, is shown at zero velocity of sliding (as it should be the conditions at which is determined). The sliding value is characterized by a low value immediately following initiation of sliding, f_{min}, and a progressively increasing value as the velocity increases. At large velocities the sliding value attains a constant value, f_{max}. Increases in normal load result in reduction of the coefficient of friction; the percentage rate at which f_{max} reduces diminishes at some limiting value of the normal load. It should be noted that the illustrated behavior is obtained in testing of sliding bearings under cyclic harmonic displacement and that measurements of the sliding friction are obtained within the first cycle at the first instant in which the peak sliding velocity is attained. The sliding friction is known to decrease with increasing number of cycles as a result of heating of the interface. The effect of temperature is discussed later in this section.

In discussing this behavior it is important to note that (a) the PTFE is in the form of a large sheet (typically larger than 250 mm in diameter) with small thickness (confined within a recess and projecting out about 2 mm) and compressed by a larger size rigid stainless steel plate, (b) the stainless steel is highly polished with a surface roughness of

44

about 0.05 μm on the arithmetic average scale, and (c) the PTFE is very soft by comparison to steel. We assume that the PTFE surface is covered by asperities which on application of the normal load deform to form junctions with the stainless steel. Due to the very soft nature of PTFE the real contact area will be large (by comparison, in metal-to-metal contact, the true area of contact is much smaller than the apparent area).
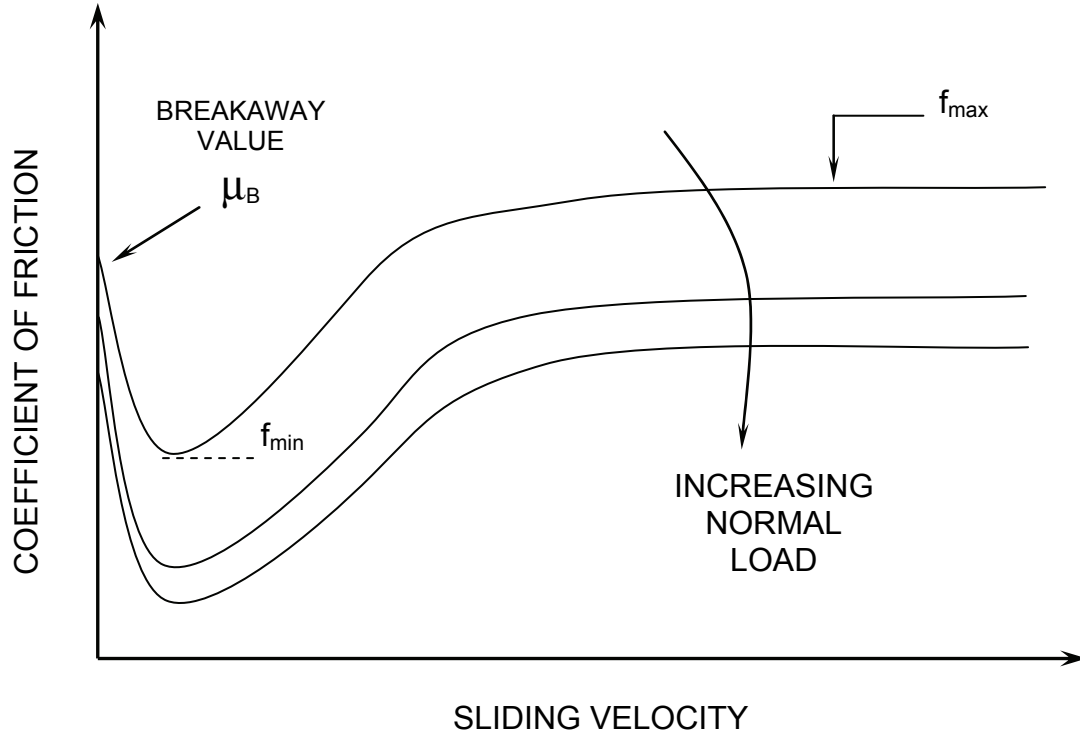
FIGURE 4-8 Dependency of Coefficient of Friction of PTFE-Polished Stainless Steel Interface on Sliding Velocity and Normal Load

Friction in this interface is primarily the result of adhesion, with the plowing contribution being insignificant. While in polymers the tendency is to shear in their bulk, PTFE is one of the few marked exceptions in which sliding occurs truly at the interface (Tabor, 1981). We write as before:

$$F = sA_r \tag{4-3}$$

where s is the shear strength of the interface. To a first approximation, the shear strength is a linear function of the actual pressure (pressure over the real area of contact) (Tabor, 1981)

$$s = s_o + \alpha \, p_r \tag{4-4}$$

The coefficient of friction is

$$\mu = \frac{F}{N} = \frac{(s_o + \alpha p_r)A_r}{p_r A_r} = \frac{s_o}{p_r} + \alpha \tag{4-5}$$

45

where all terms have been defined previously. In discussing (4-5), we utilize results on the real area of contact (Bowden and Tabor, 1964). Assuming elastic deformation of asperities, the real area of contact is proportional to some power $\eta < 1$ of the normal load N:

$$A_r = kN^\eta \tag{4-6}$$

As load increases the deformation may be mainly plastic and the real area of contact will be

$$A_r = \frac{N}{p} \tag{4-7}$$

where p is the resistance of PTFE to plastic flow in bulk compression. If plastic deformation occurs the actual pressure ($= p$) remains constant and the real area of contact increases in proportion to the normal load. Thus by considering only elastic and plastic deformation of the PTFE asperities it is possible to explain the reduction in the coefficient of friction with increasing normal load and the eventual attainment of a nearly constant value (Campbell and Kong, 1987; Mokha et al., 1988; Taylor, 1972). Figure 4-9 illustrates the variation of real area of contact, contact pressure and coefficient of friction with normal load as determined by (4-5) to (4-7).

While this theory provides an explanation for the observed dependency of the coefficient of friction on normal load, we can find a number of arguments against it. Specifically:

a) The interface consists of a large highly polished stainless steel surface in contact with a soft material having also a large smooth surface. The conditions are ideal for elastic contact with very large contact area (Rabinowicz, 1995).
b) The PTFE is essentially under conditions of hydrostatic compression, which should greatly increase its resistance to plastic flow in compression.
c) The PTFE exhibits viscoelastic behavior with the real area of contact expected to grow with time.

It should be noted that experimental results on friction are obtained following compression of the sliding bearing for several minutes to several hours. Accordingly, very large contact areas can be produced.

Therefore, it is possible that the real area of contact is essentially equal to the apparent area of the bearing, A_o. That is, $A_r \approx A_o$ and $p_r \approx N / A_o$. Equation (4-5) can then be written as

$$\mu = \frac{A_o s_o}{N} + \alpha \tag{4-8}$$

46
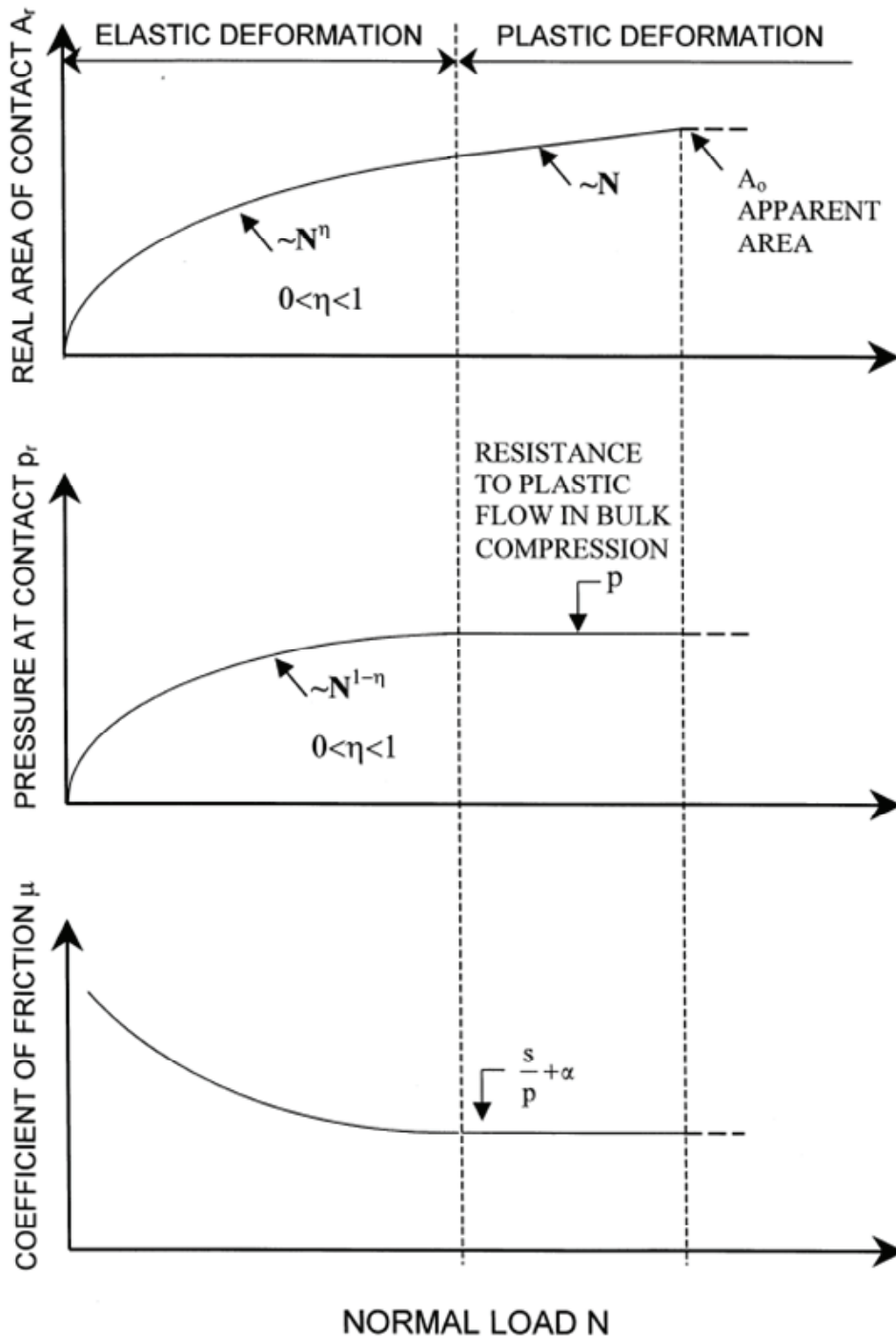
FIGURE 4-9 Variation of Real Area of Contact, Pressure at Contact Area and Coefficient of Sliding Friction with Increasing Normal Load

Considering that α is small by comparison to the other term in (4-8), (4-8) predicts that $1/\mu$ is essentially a linear function of the normal load. Indeed, this behavior is consistent with experimental results. Figure 4-10 presents the inverse of the coefficient of sliding friction at very low velocity of sliding (f_{min} in Figure 4-8) versus the apparent pressure (N/A_o) from four different experimental studies (Thompson et al., 1955; Mokha et al.,; 1988; Campbell et al., 1991; and Hwang et al., 1990). The presented data are for unlubricated PTFE in contact with polished stainless steel with a surface roughness of about 0.05 μm or less on the arithmetic average scale. The data clearly demonstrate a linear relation between the inverse of the sliding coefficient of friction and the normal load.

This linear relationship was first observed by Hwang et al. (1990) who included in their study data from Taylor (1972) and Long (1974) on the breakaway (or static) friction, as well as data for rougher stainless steel surfaces (roughness of up to 0.25 μm on the arithmetic average scale). That is, the linear relation is valid for a range of conditions that include the velocity and apparent pressure ranges indicated in Figure 3-10, surface roughness of up to 0.25 μm on the arithmetic average scale and specimen size (on this we note that the data in Figure 4-10 were generated from PTFE specimens having an area of between 887 mm^2 and 50,670 mm^2).
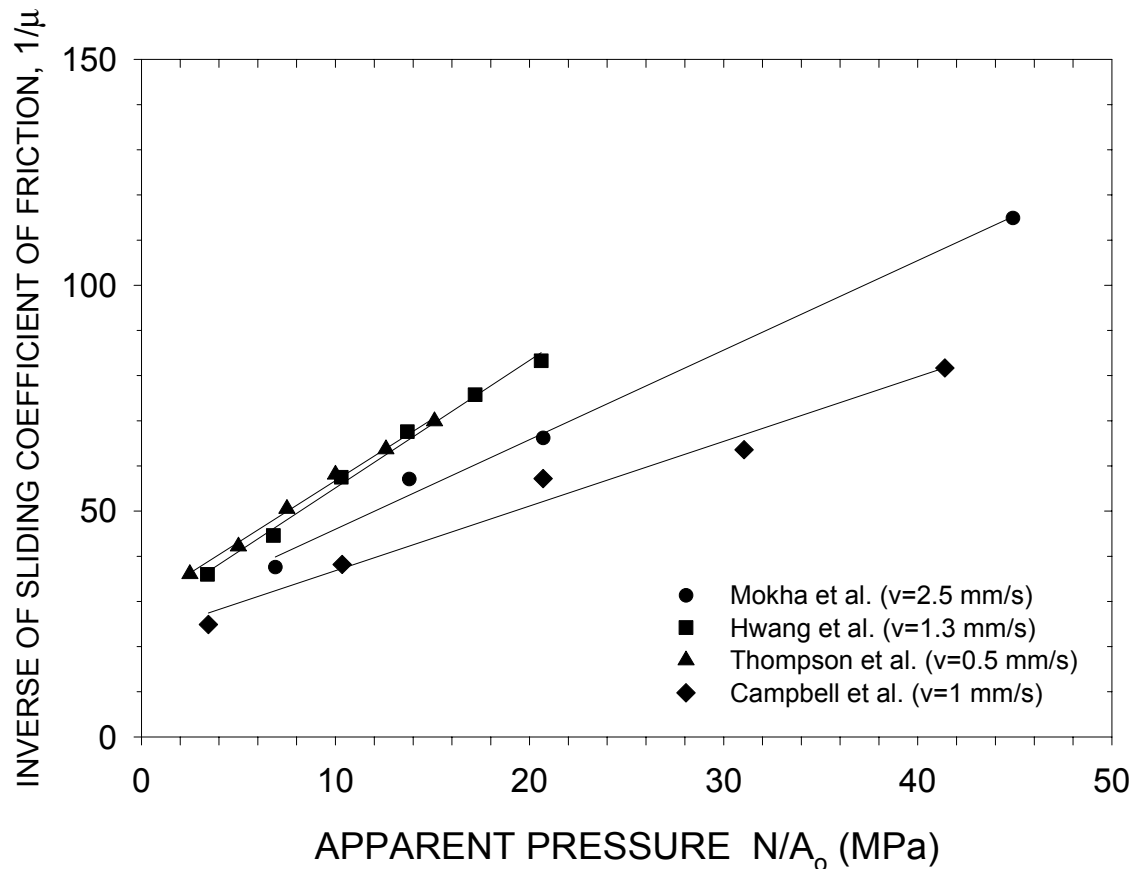
FIGURE 4-10 Relation Between Inverse of Sliding Coefficient of Friction and Apparent Pressure

At this point it is of interest to review the work of others on the dependency of the friction coefficient on normal load. Taylor (1972), Long (1974) and Campbell and Kong (1989) observed that

$$\mu = Q\left(\frac{N}{A_o}\right)^{\eta-1} \tag{4-9}$$

where all terms were defined previously and for which η is generally small. For example, Taylor (1972) reports a value for η equal to 0.58, Long, (1974) reports 0.50, and Campbell and Kong (1989) report values of 0.13 to 0.45 for normal temperature. Indeed, the adhesion theory of friction predicts for elastic contact, per (4-5) and (4-6) with $\alpha = 0$:

$$\mu = k s_o N^{\eta-1} \tag{4-10}$$

where all terms were defined previously. However, the theory predicts also that η is larger than 0.67 (when asperities are spherical) and close to unity when the asperities have complex or random shapes (Bowden and Tabor, 1964). Specifically, if we concentrate on the conditions of highly polished stainless steel, normal temperature and very low velocity (conditions for which the adhesion component of friction is expected to dominate), Campbell and Kong (1989) report a value of $\eta = 0.13$. This is inconsistent with the theory of elastic or plastic deformation of asperities for which $0.67 \leq \eta \leq 1.0$).

In conclusion, it appears that (4-8) is in agreement with experimental data and is consistent with the theory of adhesion. This implies that the real area of contact is approximately equal to the apparent area of the bearing.

Before proceeding with a discussion on the effects of sliding velocity on the coefficient of friction, it is necessary to discuss the origin of the very low value of the sliding coefficient of friction at very low speed. For example, for the conditions of the test data in Figure 4-10, the value of the coefficient of friction is in the range of 0.01 to 0.03. It was once thought that this low friction is due to poor adhesion. In reality, the junctions are firmly attached to the surface and thus the higher static or breakaway friction). However, on sliding, a very thin (of the order of a few hundred Angstrom) highly oriented and crystalline film of PTFE is deposited on the stainless steel surface. Sliding occurs at the interface of this film and the bulk of PTFE. The low friction is attributed to the easy shear of this thin film under tangential traction (Makison and Tabor, 1964; Sarkar, 1980).

The coefficient of sliding friction increases with increasing velocity of sliding. The increase above the low velocity value (f_{min} in Figure 4-8) is dependent on the velocity of sliding and it is approximately 5 to 6 times f_{min} at speeds of interest in seismic applications (500 mm/s or larger). Under these conditions of intense loading there is considerable frictional heating. When heating is significant, some local melting of PTFE can occur and under these conditions the friction force should reduce considerably. Thus

while not shown in Figure 4-9, there must be some very high velocity for which the coefficient of friction drops.

Frictional heating is not responsible for the increase in friction because it is not observed in low velocity tests that are carried out at high temperatures (Bowden and Tabor, 1964). Rather the viscoelastic properties of PTFE and the massive transfer of PTFE are responsible for the observed increase in friction (Makison and Tabor, 1964). As the speed of sliding is increased, the viscous force needed to shear the very thin film of PTFE increases. This process continues until the shear force exceeds the strength of the boundaries between the crystals of PTFE and massive transfer of PTFE then occurs. At this stage, the friction force exhibits small increases with increasing velocity, likely due to the fact that the strain rate in the bulk of the PTFE is much smaller than that at the very thin film on the stainless steel surface.

4.6.2 Effect of Temperature

Figure 4-11 illustrates the coefficient of friction as function of the sliding velocity for various temperatures. This is the temperature at the interface at the start of the experiment, or otherwise is the temperature in the bulk of the testing arrangement far away of the sliding interface. Results of the form of Figure 4-11 have been produced by the authors and will be presented in more detail in Section 4.8. These results are in general agreement with results obtained at low velocity of sliding by Campbell et al. (1991).

Temperature has a dramatic effect on the static (or breakaway) and the very low velocity coefficients of friction (μ_B and f_{min} in Figure 4-11). For unfilled PTFE, there is approximately a 7-fold increase in these values between the temperatures of 50°C and minus 40°C. This substantial increase is the effect of the changing viscoelastic properties of PTFE due to temperature. We should note that the friction values in Figure 4-11 are obtained at the first instant at which a particular value of sliding velocity is achieved (note that the experiments are conducted with cyclic motion) so that for very low velocity the heat input is not sufficient to substantially change the temperature.

The heat flux generated by friction is proportional to the coefficient of friction, the average pressure and the velocity of sliding. Accordingly, the heat flux at large velocity (say 500 mm/s) is several thousand times larger than the heat flux at very low velocity (≤ 1 mm/s). Substantial frictional heating of the sliding interface occurs at large velocities which, in turn, substantially moderate the effects of low temperature on the viscoelastic properties of PTFE. The result is that the value of the coefficient of friction at high velocity (f_{max} in Figure 4-11) increases by only 50 percent or thereabouts as the temperature decreases from 20°C to –40°C.
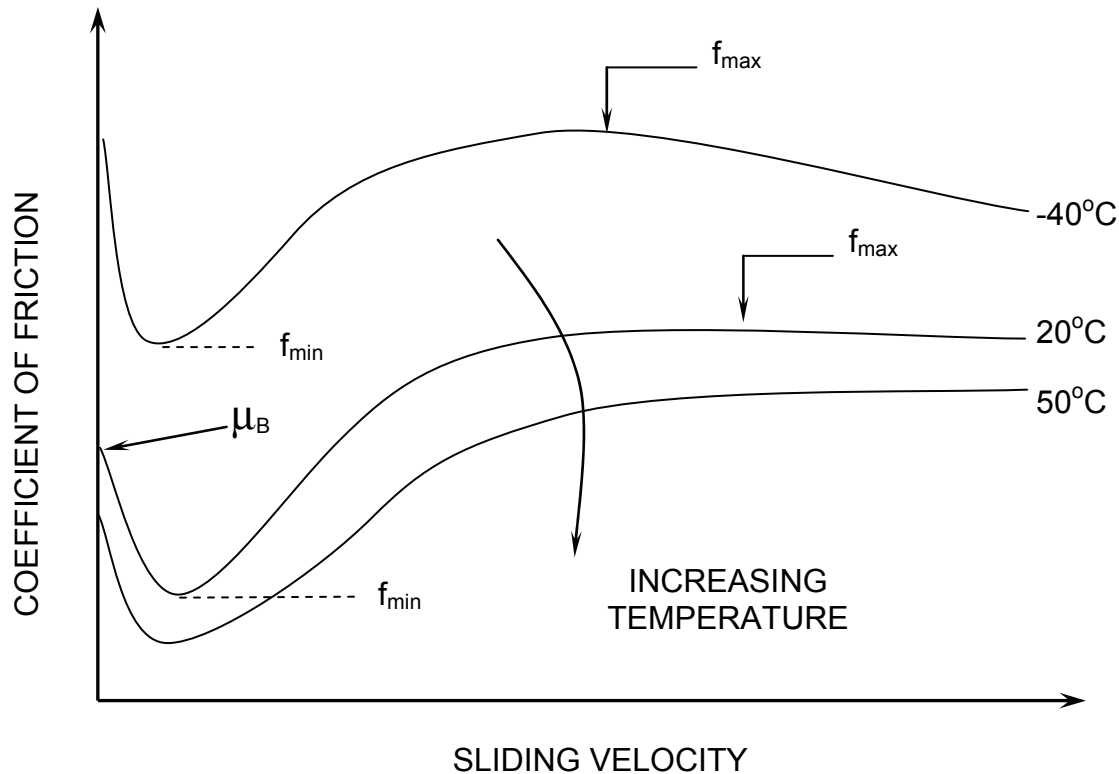
FIGURE 4-11 Effect of Temperature on the Frictional Properties of PTFE-Polished Stainless Steel Interfaces

4.6.3 Effect of Time of Loading (Load Dwell)

Since PTFE is a viscoelastic material we should expect the real area of contact and hence friction to depend on the load dwell (Bowden and Tabor, 1964). Indeed, experiments conducted with a steel sphere on a block of plastic demonstrated increases in both the real area of contact and the friction force over loading times of 6 to 1000 sec.

Testing of PTFE sliding bearings for the effect of load dwell has been conducted over much longer times, of up to 594 days. Paynter (1973) reported on tests conducted by the Glacier Company in England for dwells of up to 120 hours. Specific results are not reported other than that the static friction increased rapidly up to about 24 hours of load dwell, and then leveled off. Paynter (1973) speculated (and this was repeated in Campbell and Kong, 1987) that such an increase is an anomaly since one would expect increasing time and increasing load to have the same effect, namely, a reduction in friction. He suggested that the increase is likely caused by changes in the crystalline structure of PTFE.

Mokha et al. (1990) tested large specimens for load dwells of 0.5 hour and 594 days; the values of the static coefficient of friction were virtually identical. Many more tests were conducted by these authors for load dwells of a few minutes to 120 hours. The results for static friction exhibit fluctuations that couldn't be correlated to load dwell. Rather, it was observed that static friction is higher in the first test conducted on a new specimen

51

regardless of load dwell. The static friction was lower in any subsequent test, again regardless of load dwell. This might be explained by the existence of a film of PTFE on the stainless steel surface which was deposited by prior cycles of testing.

We conclude that the time-dependent deformation of PTFE is ostensibly complete within a very short time interval, likely of the order of a few minutes or hours, resulting in a constant real area of contact thereafter. As discussed previously, the experimental results for the dependency of the low velocity friction on normal load suggest that the real area of contact is approximately equal to the apparent area of contact.

A question to be answered is whether it is possible to complete the time-dependent deformation of PTFE in a short time interval. If a satisfactory explanation is found, we can conclude that for the purpose of design, the real area of contact is equal to the apparent area of contact. The observed dependency of the low velocity friction on normal load and the observed insignificance of load dwell on the static friction can then be explained.

One such explanation can be found by investigating the rate of deformation of PTFE under conditions of confined compression. We assume that PTFE can be reasonably modeled as a Kelvin viscoelastic material (Shames and Cozzarelli, 1992). The one-dimensional behavior of the material is described by

$$\sigma = E(\varepsilon + \tau\dot{\varepsilon}) \tag{4-11}$$

where σ is stress, ε is strain, E is Young's modulus and τ is the retardation time (a dot denotes differentiation with respect to time).

In the three dimensional theory of linear viscoelasticity, it is common to consider separately the viscoelastic behavior under conditions of pure shear and pure dilatation. This is handled by resolving the stress and strain tensors into their deviatoric and spherical parts and the viscoelastic constitutive relations are written for each. The decomposition of the stress tensor σ_{ij} is given by

$$\sigma_{ij} = s_{ij} + \delta_{ij}\sigma_{kk}/3 \tag{4-12}$$

where s_{ij} is the deviatoric part of the tensor, σ_{kk} is the spherical part of the tensor and δ_{ij} is equal to 1 if $i = j$ and 0 otherwise. The small strain tensor ε_{ij} is given by

$$\varepsilon_{ij} = e_{ij} + \delta_{ij}e_{kk}/3 \tag{4-13}$$

where e_{ij} is the deviatoric part of the tensor and e_{kk} is the spherical part of the tensor.

A three dimensional generalization of the viscoelastic constitutive equation, (4-11), is

$$s_{ij} = 2\{Q\}e_{ij} \tag{4-14}$$

52

$$\sigma_{ii} = 3K\varepsilon_{ii} \tag{4-15}$$

where $\{Q\}$ is the differential operator

$$Q = G\left\{1 + \tau\frac{\partial}{\partial t}\right\} \tag{4-16}$$

and K is the bulk modulus and G is the shear modulus. Note that in (4-14) to (4-16) we considered a material with elastic compressibility for bulk behavior and Kelvin-type viscoelasticity for multidimensional distortion. This behavior, while seemingly anomalous, is mathematically possible.

We now consider that a *creep test* conducted on a column of Kelvin material, namely, a stress σ_0 is applied along direction 1 at time $t = 0$ and then kept constant thereafter. For the case of uniaxial compression, all stresses other than σ_{11} are zero. The strain in direction 1 is

$$\varepsilon_{11} = \frac{\sigma_o}{E}\left(1 - e^{-\frac{t}{\tau}}\right) \tag{4-17}$$

where all terms have been defined previously. That is, the time dependent deformation of the column is exponentially dependent on the negative of the ratio of time to retardation time.

We consider now a block of Kelvin material compressed in a container under confined conditions so that $\varepsilon_{22} = \varepsilon_{33} = 0$. These would approximately be the conditions of a specimen partially retained in a recess and with large shape factor (small thickness, very large diameter) under compression. A solution of (4-11) to (4-16) results in

$$\varepsilon_{11} = \frac{3\sigma_0}{4G + 3K}\left\{1 - e^{-(1 + \frac{3K}{4G})\frac{t}{\tau}}\right\} \tag{4-18}$$

where all terms have been defined previously. Evidently, deformation proceeds with a rate which is exponentially dependent on the negative of time and $(1 + 0.75K/G)/\tau$. This parameter is related to Poisson's ratio so that estimates of its order can be made:

$$1 + 0.75\frac{K}{G} = \frac{3(1 - \nu)}{2(1 - 2\nu)} \tag{4-19}$$

For PTFE, $\nu = 0.46$ (du Pont, 1981) for which (4-19) yields an answer of approximately 10. That is, the creep function of the confined material is proportional to $1 - \exp(-10t/\tau)$. Evidently, the confined PTFE creeps at a substantially faster rate than the unconfined PTFE. Experimental data on the creep of PTFE with and without retention

in a recess demonstrate these substantially different rates of creep (Kauschke and Baigent, 1986; Campbell and Kong, 1987).

We have demonstrated that confined PTFE creeps at very fast rate. It is thus likely that the condition of the real area of contact being approximately equal to the apparent area of the bearing is reached within very short time. If so, we have a rational explanation for (a) the observed insignificant effect of load dwell on the static coefficient of friction, and (b) the observed dependency of the very low velocity sliding friction on the inverse of the normal load.

4.7 Friction in Bimetallic Interfaces

Bimetallic interfaces used in sliding bearings and other elements in isolation systems consist of stainless steel in contact with bronze that is impregnated with some form of solid lubricant. The paragraphs below present descriptions of applications and summarize relevant studies and observations.

Stainless steel in contact with bronze that was impregnated with lead was used in the sliding isolation system of the Koeberg Nuclear Power Station in South Africa (Pavot and Polust, 1979; Lee, 1993). The selection of this interface appears to have been based on considerations of the compatibility of the metals used. Rabinowicz developed in 1971 (see Rabinowicz, 1995) compatibility charts for metal combinations based on their solid and liquid solubility. Rabinowicz determined that two metals that can form alloy solutions or alloy compounds with each other have strong adhesion. Of the readily available and inexpensive metals only iron and lead have no liquid solubility and very low solid solubility, hence they exhibit low adhesion. Stainless steel and bronze have been selected on the basis of preventing bimetallic corrosion. Lead is extruded from pockets within the bronze during the sliding process so that it and its oxide lubricate the interface. Pavot and Polust (1979) reported values of the coefficient of friction for this interface in the range of 0.15 to 0.22 for apparent pressures of 2 to 15 MPa, low and high sliding velocity and load dwell of up to 30 days. In service, the apparent pressures were in the range of 2 to 8 MPa and the design was based on the assumption that the bearings obey Coulomb's law with a coefficient of friction in the range of 0.15 to 0.25. Following 14 years of service, 60 sample bearings that were stored in prestressed rigs in the same environment as the isolation bearings were retested (Lee, 1993). Marked increases in the static (or breakaway) coefficient of friction were reported over the baseline test results: the friction coefficient increased to a value of about 0.4 from the baseline value of about 0.2. This increase, which occurred in the absence of any significant corrosion, is likely the result of an increase in the real area of contact due to creep.

Stainless steel in contact with DU material has been used in the seismic isolation bearings of a pair of highway bridges over the Corinth Canal in Greece (Constantinou, 1998). The DU material consists of bronze powder that was sintered onto a steel backing plate. The porous structure of this material was impregnated with a mixture of lead and PTFE. On sliding, the lead and PTFE mixture is drawn from the porous bronze and lubricates the contact surface. The interface can sustain high pressures and exhibits low sliding friction

54

following a typically high static (or breakaway) coefficient of friction (Taylor, 1972). DU bearings have been extensively used in automotive, machine and other industrial applications where load dwells are typically very short. Manufacturers of DU bearings for these applications warn of the significant effect of load dwell on the static coefficient of friction. For example, Garlock Bearings, Inc. (1987) note that load dwell of between a few hours and a few days can result in a 50 to 200 percent increase in the static (breakaway) coefficient of friction. Again these increases in the static friction are likely caused by increases in the real area of contact due to creep.

Steel-on-steel, bronze-on-steel and steel-on-bronze interfaces have been used as bridge expansion bearings, typically with lubricants such as grease and graphite, (Transportation Research Board, 1977). Steel-on-steel and bronze-on-bronze interfaces experience cold welding: an expected result given that identical metals exhibit very high adhesion. Corrosion has been reported as the main source of problems for the steel-on-steel and steel-on-bronze interfaces (Transportation Research Board, 1977; Jacobsen, 1977). It is somewhat surprising that steel-on-bronze interfaces have been used given that this interface can suffer severe bimetallic corrosion (Military Standards, 1976; British Standards Institution, 1990). The British Standards Institution (1990) classified the additional corrosion of carbon and low alloy steel in contact with copper, brass or bronze as moderate-to-severe.

Lubricated bronze-steel interfaces are now commonly used for accommodating rotation in bridges. Bronze in these interfaces is impregnated with graphite in a variety of patterns. The graphite projects above the bronze approximately 1.5 mm and it spread upon load and movement application, thus lubricating the contact surface. This interface was used more than 20 years ago in sliding bearings (Transportation Research Board (1977). While this interface can maintain the solid lubricant much more effectively than when it is spread at the interface, eventually a condition is reached in which steel bears directly on bronze. Corrosion and a significant increase in friction are then encountered. The Transportation Research Board (1977) reports on such experiences, of which specific mention is made of a State that experienced a number of corrosion cases of galvanized steel-lubricated bronze interfaces. This observation is also expected because galvanized steel is coated with zinc that can suffer moderate-to-fairly severe additional corrosion if in contact with bronze (British Standards Institution, 1990).

A number of bimetallic interfaces have been used or proposed for use in energy dissipation devices (Soong and Constantinou, 1994; Soong and Dargush, 1996; Constantinou et al., 1997). These are in the form either of graphite-impregnated bronze in contact with stainless steel or of brass in contact with steel (Grigorian and Popov, 1993). The latter is clearly susceptible to severe corrosion due to bimetallic contact (British Standards Institution, 1990) and 1997 AASHTO (American Association of State Highway and Transportation Officials, 1997) strongly discourages its use. The graphite-impregnated bronze-to-stainless steel interface, while much more reliable in terms of corrosion resistance, can suffer from the aforementioned load dwell-creep induced increase in the static coefficient of friction.

Field observations, laboratory experiments and data from industrial applications show the potential for substantial increases in the static coefficient of friction of bi-metallic interfaces with load dwell. The likely explanation for this observation is the very small real contact area in bimetallic interfaces and resulting potential for increase in the contact area under prolonged loading.

4.8 Frictional Heating

4.8.1 Theory

To maintain sliding motion, mechanical work must be done to overcome the friction forces. This work is converted into thermal energy, which is manifested as a temperature rise. Herein we attempt to quantity the temperature rise at the sliding interface based primarily on the seminal work of Carslaw and Jaeger (1959).

The sliding contact problem of interest here is illustrated in Figure 4-12. Body 1 (PTFE) is stationary, whereas body 2 (stainless steel) moves with a known displacement history. The contact surface is the surface of the PTFE (presumed to be in full contact with the stainless steel). This surface represents the heat source, which has a heat flux distribution q. A portion, q_1, of this heat flux enters body 1 and the remaining flux, q_2, enters the body 2. It is reasonable (and conservative in the estimation of the surface temperature) to assume that $q_1 = 0$ and $q_2 = q$. That is, all of the generated heat is supplied to body 2 (stainless steel). Detailed calculations for the heat partitioning problem (see American Society for Metals, 1992 for a review of frictional heating calculations) for a wide range of velocities of motion and contact area dimensions confirm that for PTFE-stainless steel interfaces, the heat partition factor q_1 / q is very small. The reason for this is the large values of the thermal conductivity and thermal diffusivity of stainless steel by comparison with those of PTFE. Table 4-1 presents the thermal properties of these materials (from American Society for Metals, 1992). Further information can be found in Linde (1993).

Carslaw and Jaeger (1959) analyzed the problem of a semi-infinite solid with constant heat flux q at the free surface (see Figure 4-13). The solution for the temperature rise as function of depth x and time t, noting that this is a one-dimensional problem, is

$$T(x,t) = \frac{2q}{k}\left\{\left(\frac{Dt}{\pi}\right)^{1/2}\exp\left(-\frac{x^2}{4Dt}\right) - \frac{x}{2}erfc\left(\frac{x}{2D^{1/2}t^{1/2}}\right)\right\} \qquad (4\text{-}20)$$

where k is the thermal conductivity of the solid, D is the thermal diffusivity of the solid and *erfc* is the complementary error function. At the surface ($x = 0$) the temperature rise is

$$T_s = \frac{2q}{k}\left(\frac{Dt}{\pi}\right)^{1/2} \qquad (4\text{-}21)$$
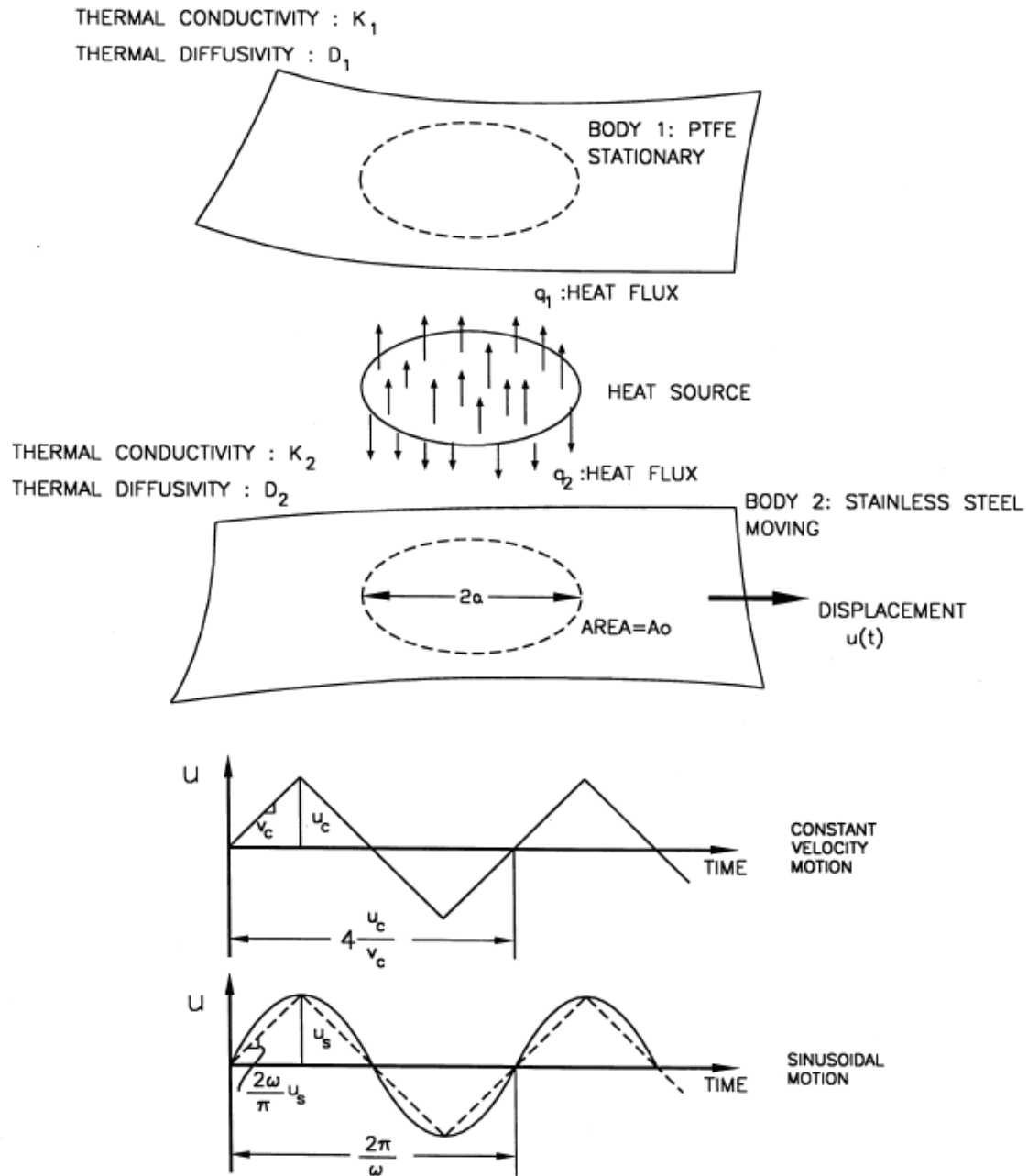
FIGURE 4-12 Schematic of Two Bodies in Sliding Contact

TABLE 4-1 Thermal Properties of PTFE and Stainless Steel

Material	Thermal Conductivity (k) W/ (m.^{o}C)[1]						Thermal Diffusivity (D) m^2/s
	0°C	20°C	100°C	300°C	600°C	1000°C	20°C
Unfilled PTFE	-	0.24	-	-	-	-	0.010 x 10^{-5}
18%Cr, 8%Ni Steel	16.3	16.3	17	19	26	31	0.444 x 10^{-5}
15% Cr, 10% Ni Steel	-	19	-	-	-	-	0.526 x 10^{-5}

1) W = 1 N.m/s

In utilizing this solution (particularly equation 4-21) for the problem of Figure 4-12, we recognize the following:

a) The solution is for a half-space with heat flux over the entire free surface, whereas the problem is for a body of finite plan dimensions and depth. However, when the interest is for the temperature generated by friction at the surface of a large contact area the solution should be valid. Evidence for this can be found in the solution of the problem of a slab with prescribed heat flux at one surface (Carslaw and Jaeger, 1959, p. 113). Although this solution is too complex to be of practical value, we note that its leading term for the temperature rise at the surface is exactly that of (4-21).

b) The heat flux generated by friction is not, in general, constant but rather it exhibits dependencies on both time and space (dependency on *y* and *z*). This is due to dependencies of the friction force (per unit area) on the history of motion and on the normal load distribution. To bypass this problem we shall utilize an average constant value of the heat flux so that the estimate for the temperature rise will be on an average over the apparent area of contact.

c) We will consider motion of body 2 such that the amplitude is small by comparison to the radius of the apparent area of contact. Accordingly, we can assume that, on the average, body 2 is supplied with a constant heat flux over the duration of the motion. We will later relax this limitation and consider large amplitude motions.

d) We will consider short time intervals so that the solution for the heat applied over the entire free surface of a half-space is valid. Note that for very long time intervals heat will flow laterally to the cooler parts of the moving body, heat will be lost by radiation and convection, and eventually a stable condition may be reached.
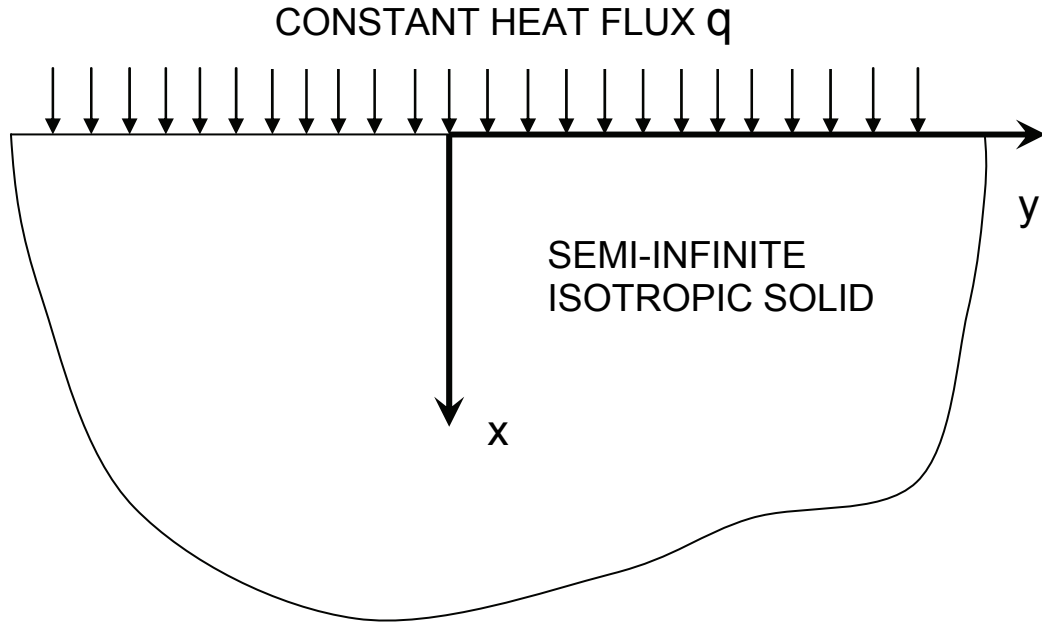
FIGURE 4-13 Semi-infinite Solid with Constant Heat Flux at x=0

Consider now that the motion is as illustrated in Figure 4-12, that is, as it would have been in a constant velocity test (sawtooth displacement). Time t is the total exposure time (for $u_c < a$), that is,

$$t = \frac{4u_c}{v_c} N \tag{4-22}$$

where u_c is the peak displacement, v_c is the constant velocity and N is the number of cycles. Moreover, the average heat flux is equal to the energy dissipated in N cycles ($= 4NF_f u_c /(A_0 t)$), that is,

$$q_{av} = \frac{F_f v_c}{A_o} = \mu p v_c \tag{4-23}$$

where F_f is the friction force, μ is the coefficient of sliding friction and p is the apparent pressure (assumed to be constant). Substituting (4-22) and (4-23) into (4-21) we obtain

$$T_s = 2.26 N^{1/2} \frac{\mu p u_c v_c}{k} \left(\frac{D}{u_c v_c} \right)^{1/2} \tag{4-24}$$

where all terms have been defined previously. The dimensionless quantity $u_c v_c / D$ is the Peclet number: the ratio of the velocity of the surface to the rate of thermal diffusion into the moving body.

59

Consider now the case of sinusoidal motion of body 2 as illustrated in Figure 4-12. Using (4-21) with

$$q_{av} = \frac{2\mu p u_s \omega}{\pi}$$ (4-25)

and

$$t = \frac{2\pi N}{\omega}$$ (4-26)

we arrive at

$$T_s = 1.8 N^{1/2} \frac{\mu p u_s^2 \omega}{k} \left(\frac{D}{u_s^2 \omega} \right)^{1/2}$$ (4-27)

The utility of (4-27) is seen when the sinusoidal motion is replaced by an equivalent constant velocity motion as shown in Figure 4-12 with a dashed line. If we set $u_c = u_s$ and $v_c = 2u_s \omega / \pi$ (a reasonable representation of the sinusoidal motion by a constant velocity motion) in (4-24), we recover (4-27).

Equations (4-24) and (4-27) are similar in form to equations used by tribologists to estimate flash temperature (American Society for Metals, 1992), which is the rise in temperature at the real area of contact. However, (4-24) and (4-27) are based on the use of the apparent area so that the calculated temperature is a representative average value of the temperature rise at the sliding interface. It is useful for assessing the structural effects of frictional heating on the stainless steel overlay, in estimating average wear, and in establishing scaling principles for reduced-scale sliding bearings. Moreover, it can be compared with direct measurements of the temperature rise at some small depth inside the stainless steel plate (although the measurement is expected to be less than the actual average value at the surface). Furthermore, we expect the actual maxima and minima of the temperature rise to differ by relatively small amounts from the average temperature rise because in PTFE-polished steel interfaces the real area of contact is large and likely equal to the apparent area (see section 4.6).

The presented solution (4-24 and 4-27) is valid when the amplitude of motion, u_c or u_s, is less (in theory, much less) than the radius a of the apparent contact area. Under these conditions, the average exposure time of any point within the apparent area is equal to the duration of the motion of body 2.

However, a more interesting situation is when the amplitude of motion is larger than the radius a of the apparent contact area. This is a typical situation in sliding seismic isolation bearings. To illustrate the difference between this case and the previously studied case of small amplitude motion consider that body 2 in Figure 4-12 moves at constant velocity v_c in a motion described by $u = v_c t$. The time during which any point on body 2 is exposed

to heat flux is somehow less than $2a/v_c$ (it will be exactly that amount if the apparent area is square). We will show that the average exposure time is $\pi a/(2v_c)$. Now consider that the motion is as illustrated in Figure 4-12 with $u_c > a$. In each half cycle of motion there will be heat flux on the surface of body 2 for a duration $\pi a/(2v_c)$ followed by an interval of zero flux (the surface of body 2 moves beyond the heat source). That is, we have a case of intermittent heat flux, as if a heating element is periodically switched on and off. The use of (4-24) or (4-27), which are based on the assumption of continuous heat flux, would yield a conservative estimate of the temperature rise.

We start the analysis of this problem by evaluating the average time that any point on body 2 is exposed to heat flux from the circular heat source. Assume that the circular heat source is described by $y^2 + z^2 = a^2$ and that motion is along the y axis and is of constant velocity. The average exposure time is

$$t_{av} = \frac{1}{a} \int_{-a}^{a} \frac{(a^2 - z^2)^{1/2} dz}{v_c} = \frac{\pi a}{2v_c} \qquad (4\text{-}28)$$

where all terms have been defined previously. The distance traveled during this time is $\pi a/2$.

The average heat flux during the average exposure time is equal to the friction force times distance traveled and divided by the area of the heat source (πa^2) and the average exposure time, namely,

$$q_{av} = \mu p v_c \qquad (4\text{-}29)$$

where all terms have been defined above. Again we assume that this heat flux is supplied entirely to body 2.

Figure 4-14 (a) illustrates the configuration of the two bodies and the considered periodic constant velocity motion. Figure 4-14(b) shows the resulting history of heat flux; part (c) shows the heat flux history shifted in time to simplify the analytical solution. During the time intervals t_0 the heat flux is assumed to be zero (as if the exposed-to-air surface of body 2 is insulated). In reality there is loss of heat due to convection and radiation, but this is assumed to be negligible.

Carslaw and Jaeger (1959) presented the solution for the isotropic semi-infinite body subjected at $x = 0$ to *constant* heat flux, q, of duration T. The solution for the temperature rise if $t < T$ is given by (4-20), whereas for $t > T$, the temperature rise is given by

$$T(x,t) = \frac{2qD^{1/2}}{k} \left\{ t^{1/2} ierfc\left(\frac{x}{2D^{1/2}t^{1/2}}\right) - (t-T)^{1/2} ierfc\left(\frac{x}{2D^{1/2}(t-T)^{1/2}}\right) \right\} \qquad (4\text{-}30)$$

61
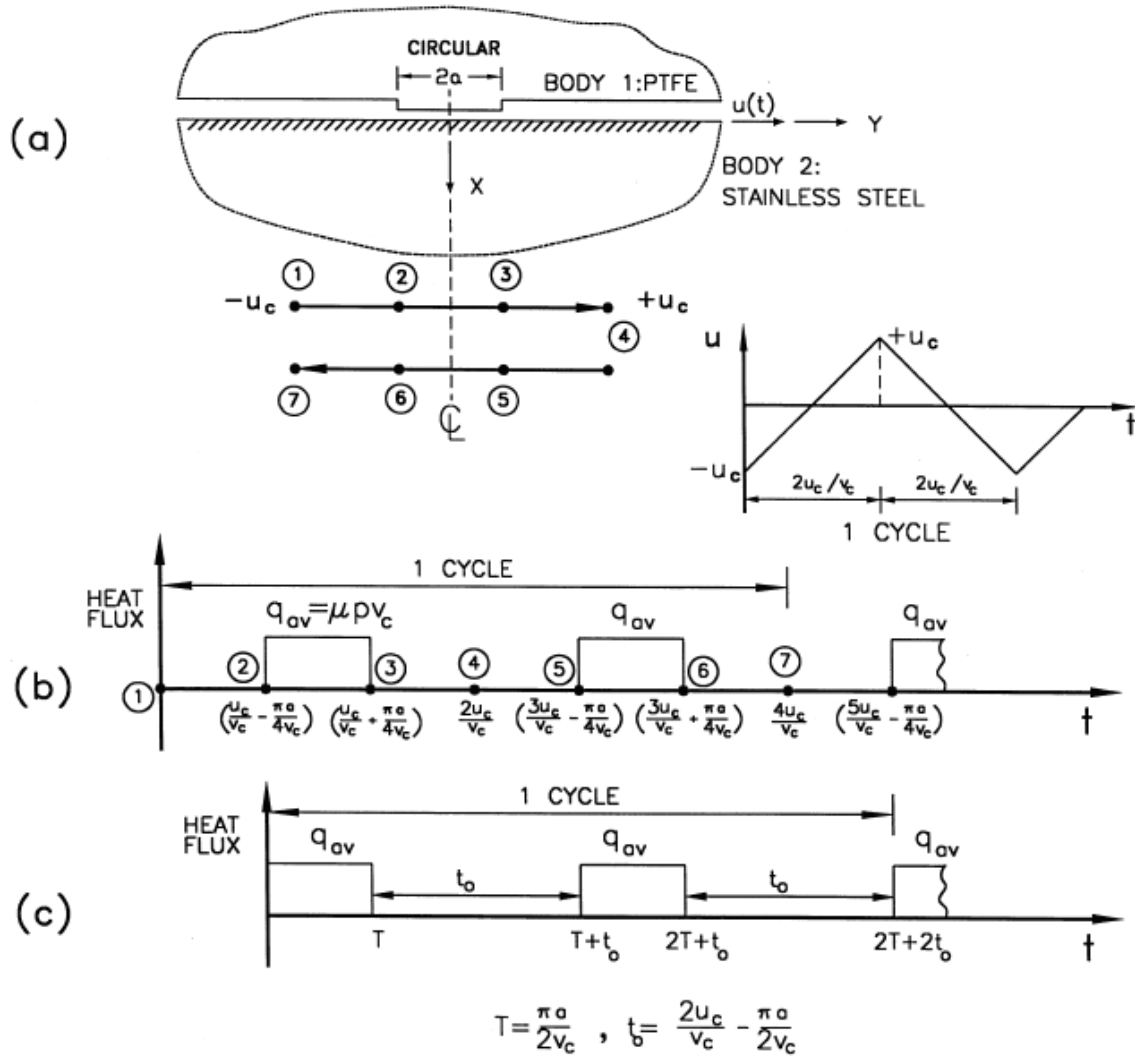
FIGURE 4-14 History of Heat Flux Input for Periodic Constant Velocity Motion of Large Amplitude

where

$$ierfc(x) = \int_{x}^{\infty} erfc(\zeta)d\zeta = \frac{e^{-x^2}}{\pi^{1/2}} - xerfc(x) \qquad (4\text{-}31)$$

and all terms have been defined previously. This function takes the value of $1/\pi^{0.5}$ for $x = 0$. Accordingly, the solution for the surface ($x = 0$) temperature rise takes the simple form

$$T_s = \frac{2qD^{1/2}}{\pi^{1/2}k}\left\{ t^{1/2} - (t-T)^{1/2}\right\} \qquad (4\text{-}32)$$

62

The solution for the intermittent heat flux of Figure 4-14(c) may be now constructed using (4-32):

For $t = 2T + t_0$ (first cycle)

$$T_{s1} = \frac{2q_{av}D^{1/2}}{\pi^{1/2}k}\left\{(2T+t_o)^{1/2} - (T+t_o)^{1/2} + T^{1/2}\right\} \tag{4-33}$$

For $t = 4T + 3t_0$ (second cycle)

$$T_{s2} = \frac{2q_{av}D^{1/2}}{\pi^{1/2}k}\left\{(4T+3t_o)^{1/2} - (3T+3t_o)^{1/2} + (3T+2t_o)^{1/2} - (2T+2t_o)^{1/2}\right\} + T_{s1} \tag{4-34}$$

For $t = 6T + 5t_0$ (third cycle)

$$T_{s3}\frac{2q_{av}D^{1/2}}{\pi^{1/2}k}\left\{(6T+5t_{o)})^{1/2} - (5T+5t_o)^{1/2} + (5T+4t_o)^{1/2} - (4T+4t_o)^{1/2}\right\} + T_{s2} \tag{4-35}$$

For $t = 8T + 7t_0$ (fourth cycle)

$$T_{s4} = \frac{2q_{av}D^{1/2}}{\pi^{1/2}k}\left\{(8T+7t_o)^{1/2} - (7T+7t_o)^{1/2} + (7T+6t_o)^{1/2} - (6T+6t_o)^{1/2}\right\} + T_{s3} \tag{4-36}$$

For $t = 2nT + (2n-1)t_0$ (nth cycle)

$$T_{sn} = \frac{2q_{av}D^{1/2}}{\pi^{1/2}k}\left\{\left[2nT+(2n-1)t_o\right]^{1/2} - \left[(2n-1)(T+t_o)\right]^{1/2} + \right.$$
$$\left.\left[(2n-1)T+(2n-2)t_o\right]^{1/2} - \left[(2n-2)(T+t_o)\right]^{1/2}\right\} + T_{s(n-1)} \tag{4-37}$$

where all terms have been defined previously. Equations similar to (4-33) to (4-37), albeit more complex, can be written for the temperature rise at depth $x > 0$ using (4-30). Moreover, a general solution for the problem of the semi-infinite body with heat flux $q(t)$ at $x = 0$ can be deduced from the solution of the problem of constant heat flux (eq. 4-20) and use of Duhamel's theorem (Carslaw and Jaeger, 1959):

$$T(x,t) = \frac{D^{1/2}}{\pi^{1/2}k}\int_o^t q(t-\tau)\exp(-\frac{x^2}{4Dt})\frac{d\tau}{\tau^{1/2}} \tag{4-38}$$

In summary, the temperature rise at the sliding contact of sliding bearings depends on:

a) The heat flux generated at the contact surface. In general, the heat flux is given by

$$q = \mu p\dot{u} \tag{4-39}$$

where $\dot{u}$ is the velocity of body 2 (see Figure 4-12) and noting that all variables in (4-39) can be functions of time.

b) The heat flux partitioning between bodies 1 and 2. For unfilled PTFE-stainless steel interfaces it is appropriate to assume that all of the generated heat flux is supplied to the steel part.

c) The exposure time, that is, the duration of the heat flux.

d) The time between intermittent heat fluxes.

In large amplitude uni-directional periodic motion, (as typically developed in testing of bearings) the heat flux history is periodic and intermittent as shown in Figure 4-14. However, the actual motion in an earthquake is multi-directional, in which the time between intermittent heating is generally longer than in uni-directional motions. To demonstrate this, consider a motion that consists of six segments of constant velocity v_c, each with duration u_c / v_c where u_c is the distance traveled in each segment. Figure 4-15 illustrates the history of this motion when it is uni-directional and periodic along the y axis. The figure also presents a schematic of the bearing in which the small circular area (of radius a) is the PTFE surface (shown moving with respect to the steel surface rather the other way around). The heat flux input at positions A (starting position) and B (extreme right, which is traversed twice) of the steel part are also shown in Figure 4-15. Note that as the contact area moves the heat flux is supplied to a new portion of the steel surface resulting in different intermittent heat fluxes at different positions.

We assume next that the motion (again consisting of six segments, each of travel u_c, duration u_c / v_c and constant velocity v_c) is multi-directional as shown in Figure 4-16. Note that all positions of the contact area are fully traversed once, except for the starting position (A), which is fully traversed twice. The heat flux input at positions A and B is shown in Figure 4-16 and, as expected, has longer intermissions than that of the uni-directional motion.
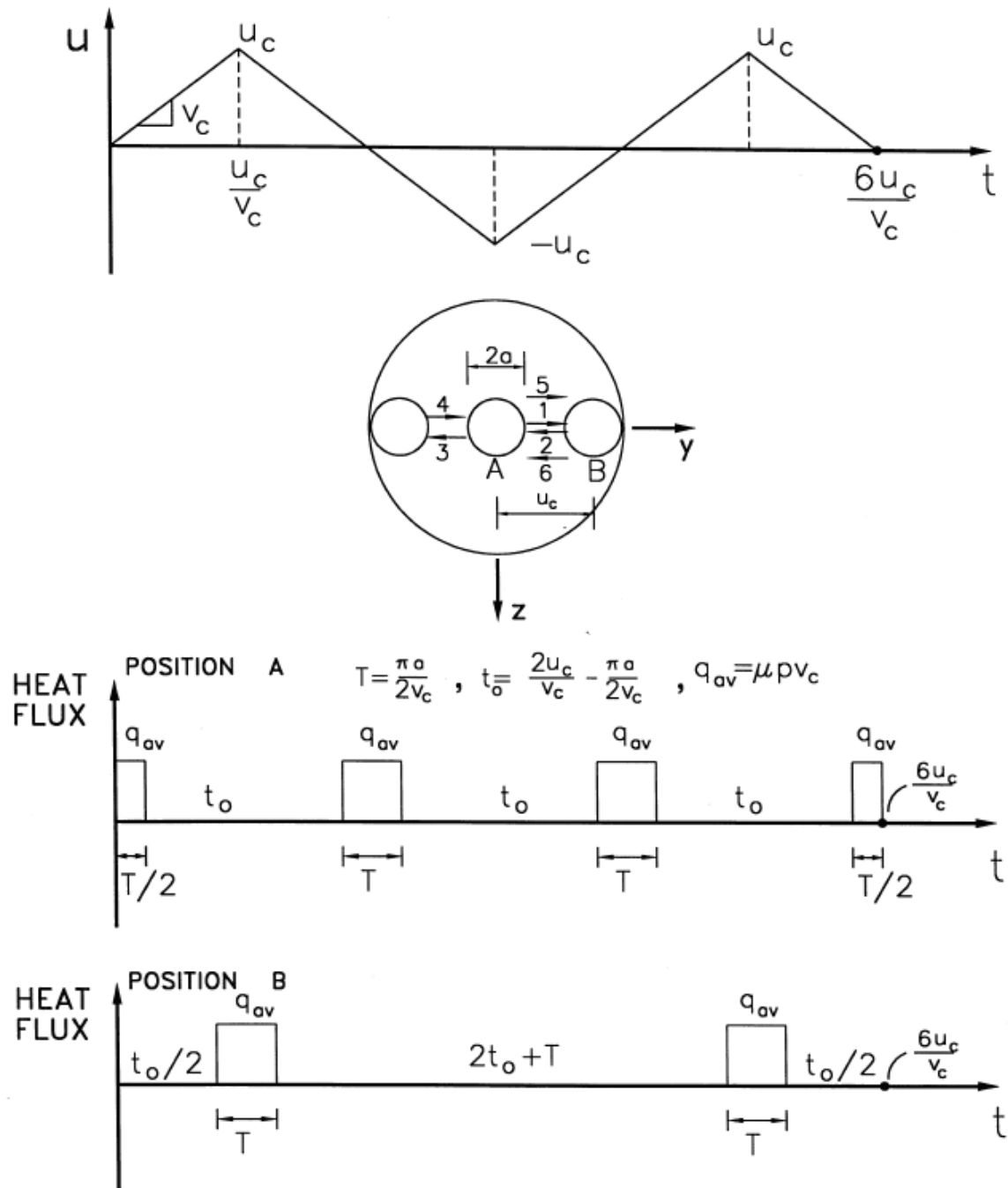
FIGURE 4-15 Heat Flux Input at Various Positions of Steel Body in Uni-directional Periodic Constant Velocity Motion

65
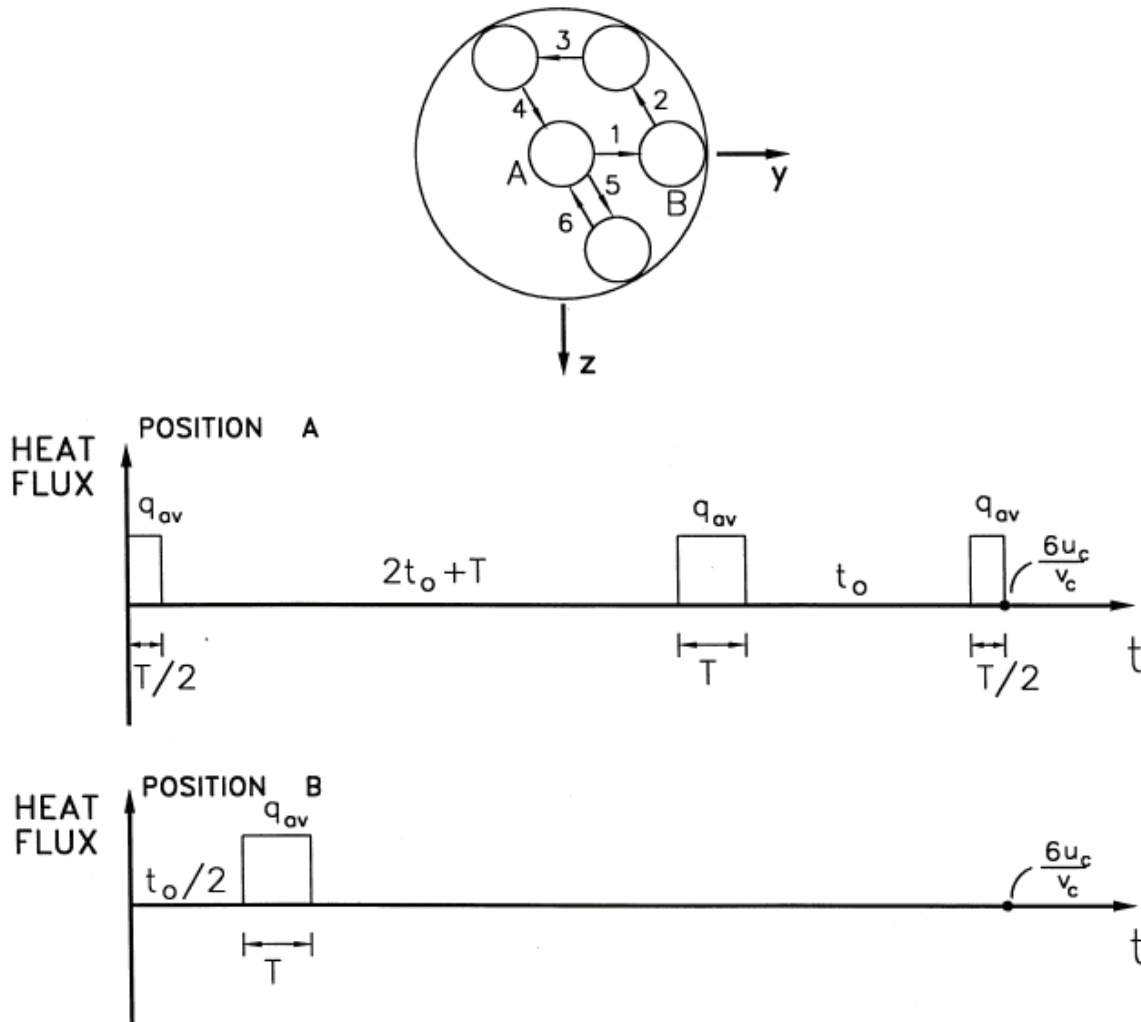
FIGURE 4-16   Heat Flux Input at Various Positions of Steel Body in Multi-directional Constant Velocity Motion

4.8.2 Test Results on Temperature Rise Histories due to Frictional Heating

A series of tests have been conducted for the specific purpose of measuring the temperature rise at the interface of sliding bearings (Wolff, 1999). The tests were conducted in the machine of Figure 4-3 utilizing flat sliding bearings. The sliding interface considered of unfilled PTFE in contact with polished stainless steel. The apparent contact area had a diameter of 95.25 mm. Thermocouples were embedded in the stainless steel plate at depth of 1.5 mm. One thermocouple was located at the center of the bearing directly below the contact area. T-type thermocouples with a wire diameter of 0.025 mm were utilized in an attempt to increase the sensitivity of the instrument and obtain reliable measurements of temperature histories under conditions of high speed motion.

66

The tests consisted of five cycles of sinusoidal motion with amplitude of either 25.4 mm ($u_s / a = 0.27$) or 96.5 mm ($u_s / a = 1.01$). The frequency varied so that the peak velocity was in the range of 40 mm/s to 320 mm/s. The apparent bearing pressure was 13.8 MPa in the small amplitude tests and 12 MPa in the large amplitude tests.

Figure 4-17 presents the recorded histories of temperature at the central thermocouple in four small amplitude tests ($u_s = 25.4$ mm). In these small amplitude tests the conditions of continuous (uninterrupted) heat flux prevailed. This is observed in the monotonic increase of temperature with time as predicted by (4-20) and (4-21). Prediction of the temperature rise and drop following the conclusion of testing was made using (4-20) and (4-30), respectively, in which the heat flux was calculated by (4-25) using the measured coefficient of friction. Moreover, $x = 1.5$ mm, $k = 16.3$ W/(m·$^{\circ}$C) and $D = 0.444 \times 10^{-5}$ m^2/s, which are appropriate thermal properties for the stainless steel. In (4-30), T is the duration of testing (e.g., 20 sec in the test at frequency of 0.25 Hz). The analytical prediction is very good.

It is of interest to note that the recorded peak temperature rises in the four tests differ by small amounts despite the 8-fold difference in the peak velocities. There are two reasons for this behavior. The first is revealed by examination of (4-27), which applies in this case. The temperature rise is proportional to the square root of the frequency when all other parameters are fixed (the case for the tests at frequencies of 0.5, 1.0 and 2.0 Hz, in which the coefficient of friction was essentially the same). The second reason is that the temperature was recorded at a depth of 1.5 mm below the surface. Despite the small depth, the reduction of temperature with depth is significant in the higher velocity tests as revealed in the temperature profiles of Figure 4-14.

The peak surface temperatures could not be measured but could be analytically predicted and are shown in Figure 4-17. These temperatures are significantly higher than the recorded ones at the depth of 1.5 mm in the high velocity motions.

Figure 4-18 presents the recorded histories of temperature in three large amplitude tests ($u_s = 96.5$ mm). The conditions in these tests are those of intermittent heat flux for which the history of temperature is predicted to have consecutive build-up and decay intervals, which was the recorded behavior.

Prediction of the temperature histories has been made by repeated use of (4-20) and (4-30) and superposition of the results. Again, the heat flux was calculated by (4-25) using the measured coefficient of friction. Moreover, the duration of each heat flux and the duration of each intermediate interval of zero heat flux were calculated on the basis of the theory presented in section 4.8.1. The thermal properties of $k = 16.3$ W/(m·$^{\circ}$C) and $D = 0.444 \times 10^{-5}$ m^2/s were used for the stainless steel.
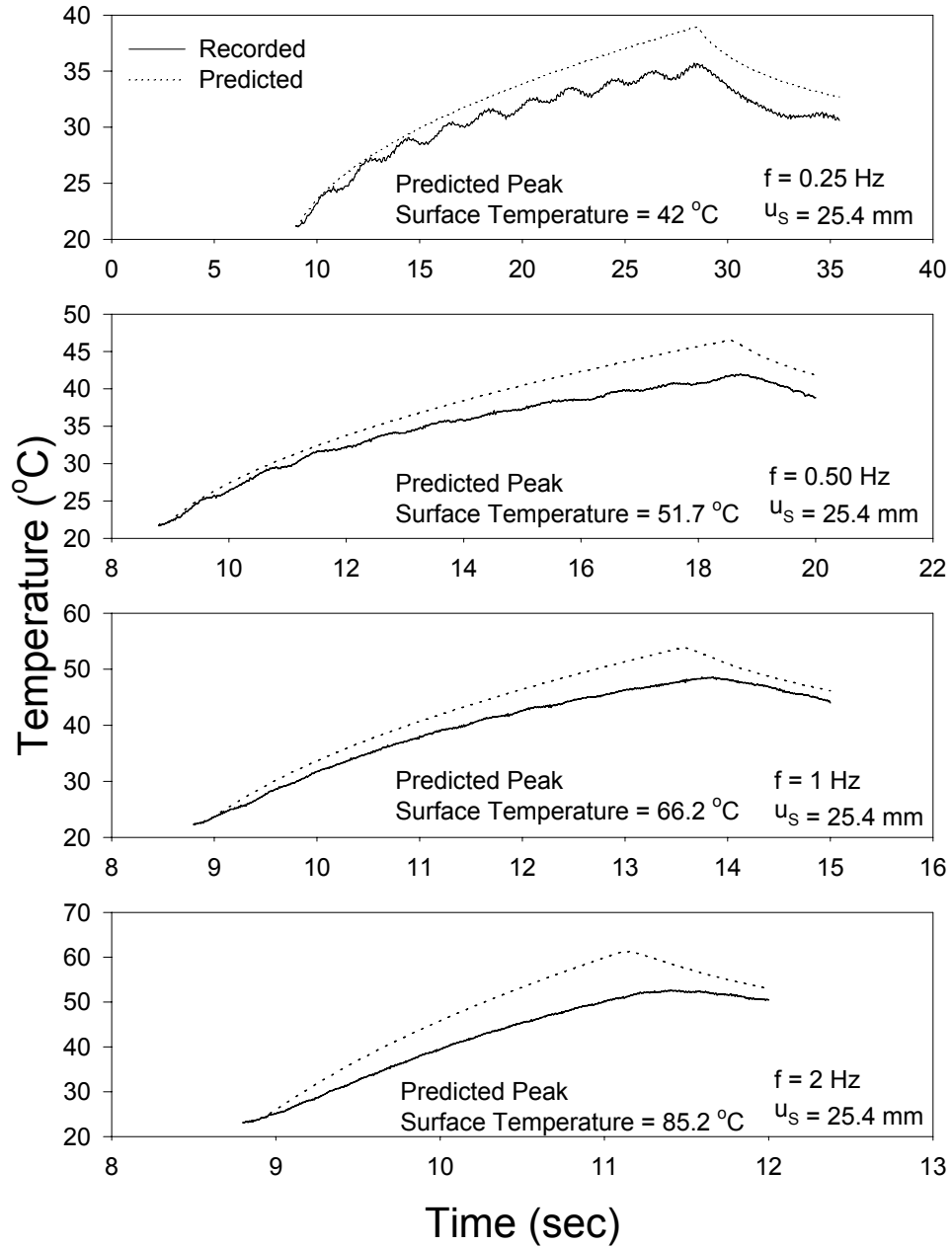
FIGURE 4-17 Recorded and Predicted Histories of Temperature at the Middle Thermocouple (Depth of 1.5 mm) in the Small Amplitude Tests
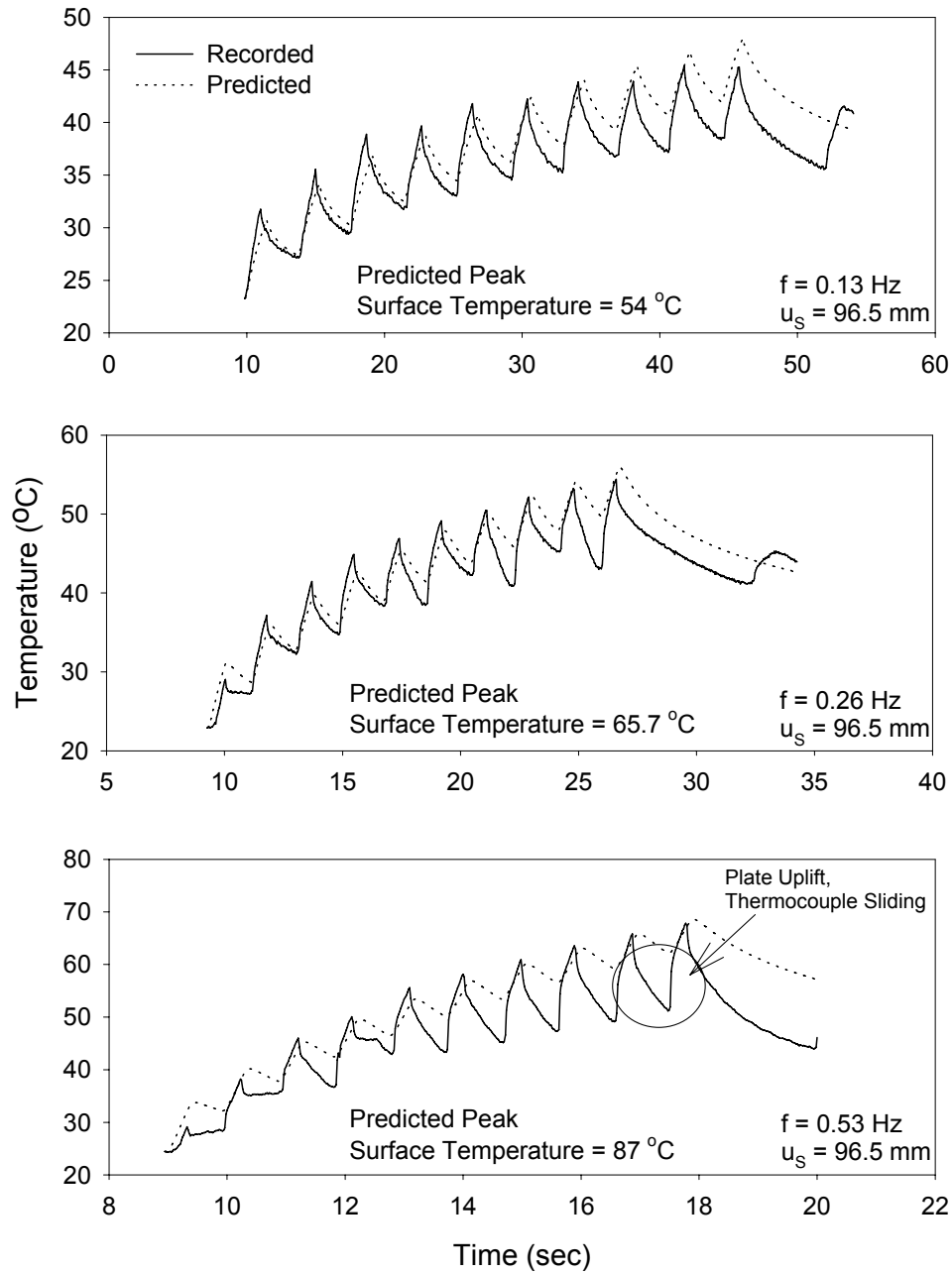
FIGURE 4-18   Recorded and Predicted Histories of Temperature at the Middle Thermocouple (Depth of 1.5 mm) in the Large Amplitude Tests

In discussing the accuracy of the analytical prediction, we make the following observations:

a) The prediction is, in general, good in terms of both the peak temperature values and the trends in the histories of temperature.
b) There is a small difference between the analytical and experimental values of time at which the peak temperatures occur. This is the result of the calculation of the exposure time as an average time given by (4-28).
c) There is a difference in the calculated and measured histories of temperature during the intervals of zero heat flux. This difference appears to increase with increasing frequency of motion. One reason for this difference is conservatism in the analytical solution, in which losses of heat due to radiation and the lateral conduction of heat (solution is for half space with heat flux at $x = 0$) are neglected. Another reason is related to limitations in the experimental setup. It has been observed that as the displacement approached its peak value, the stainless steel plate uplifted resulting in movement of the thermocouple and likely loss of contact. This behavior was more pronounced in the high frequency tests.

4.8.3 Example of Temperature Rise Calculation in Bi-directional Sliding Motion

The analytical solution for the temperature rise due to frictional heating can be used for arbitrary history of heat flux (though still restricted to the half space subject to heat flux at x = 0) either by utilizing the convolution integral of (4-38) or by repeatedly utilizing (4-20), (4-21), (4-30) and (4-32). The latter is equivalent to the use of (4-38) but with an incremental summation process involving gross time steps rather than "infinitesimal" time steps. This procedure is used below for the prediction of the temperature rise at the surface of a large sliding bearing (see Figure 4.19) subjected to dynamic vertical load and high speed bi-directional motion.
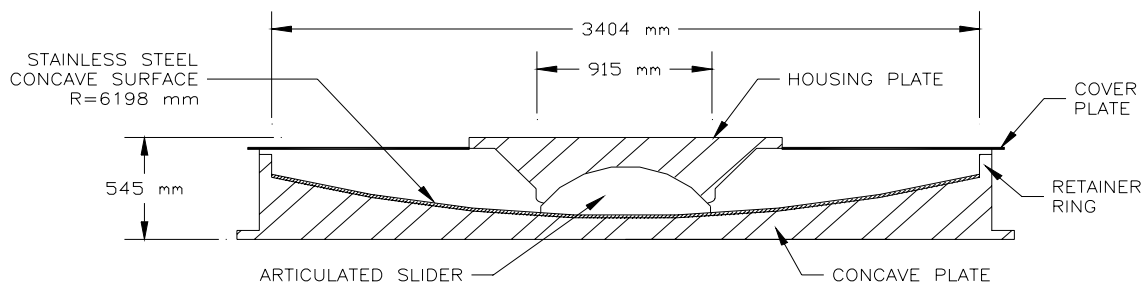
FIGURE 4-19 FPS Bearing for the Benicia-Martinez Bridge, California

The presented example is for one of the FP bearings used in the seismic rehabilitation of the Benecia-Martinez bridge in California (Mellon and Post, 1999). Figure 4-19 presents a schematic of this bearing and Figure 4-20 presents histories of the vertical load and bi-directional motion of the bearing as calculated in the dynamic analysis of the bridge. This bearing was tested at the Caltrans Seismic Response Modification Device Test Facility at the University of California, San Diego (Benzoni and Seible, 1999). The

70

bearing was tested with a unidirectional motion within the peak velocity capability of the machine. To establish the equivalent one-directional motion, the power input and heat flux input at the most traversed part of the bearing were considered. Particularly, calculations of the history of temperature rise in the calculated bi-directional motion and in the equivalent one-directional motion were key to establishing the equivalent unidirectional motion.
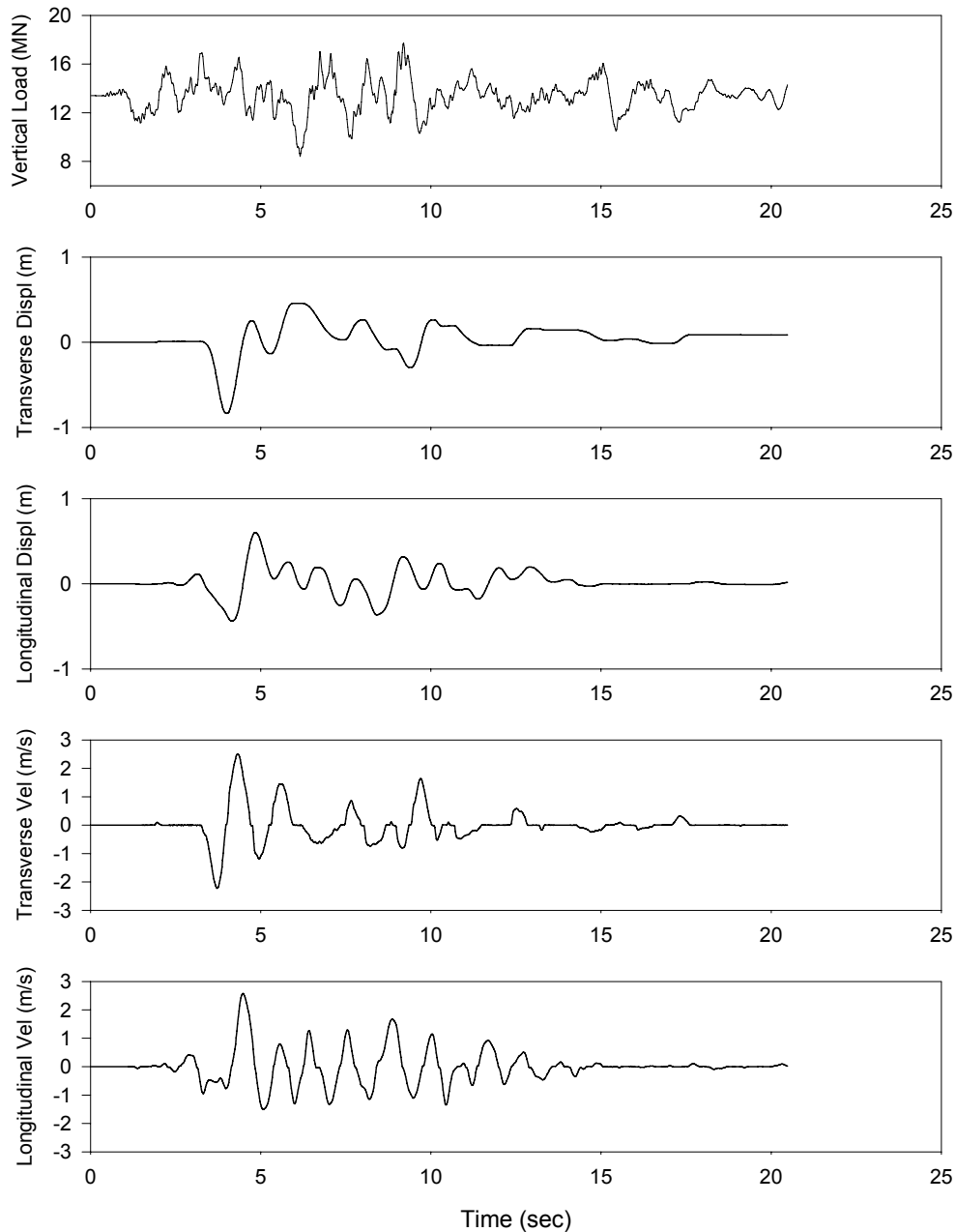
FIGURE 4-20 Calculated Histories of Vertical Load and Bi-directional Horizontal Motion of a FP Bearing for the Benicia-Martinez Bridge, California

71

To perform calculations for the temperature rise, one has to first identify the most traversed part of the bearing and then calculate the heat flux supplied to that part. Figure 4-21 shows the displacement path in the bi-directional motion. It is apparent that the most traversed part is the neighborhood of the center of the bearing. The heat flux generated at the sliding interface is given by (4-39) with p being the instantaneous apparent pressure, $\dot{u}$ being the amplitude of the instantaneous velocity vector and μ being the coefficient of friction. The heat flux history has been calculated using the nominal value of the coefficient of friction (= 0.06) and it is shown at the top panel of Figure 4-22. This heat flux history is that supplied to the instantaneous apparent contact area. The next step is to calculate the heat flux history at the selected fixed area of the steel part (in this case, the neighborhood of the bearing center).
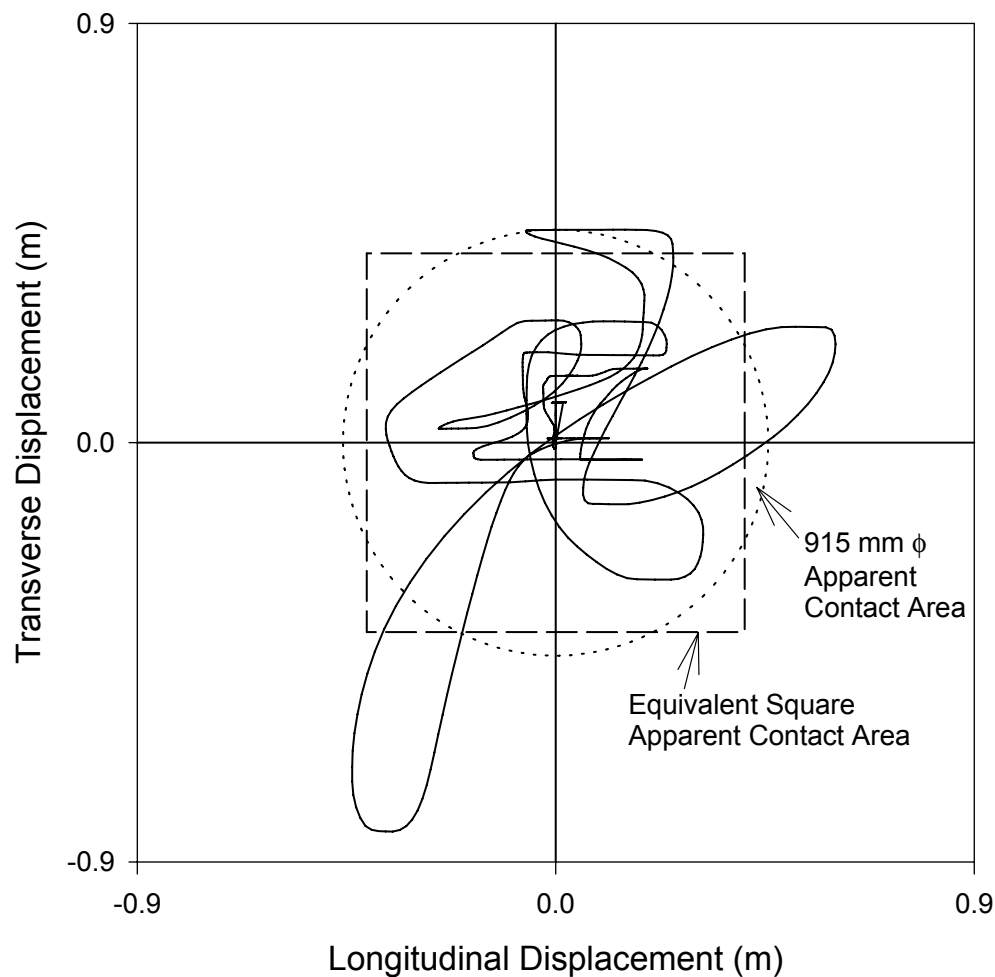
FIGURE 4-21   Displacement Path in Bi-directional Motion and Actual and Equivalent Apparent Contact Areas

The heat flux history at the selected fixed area of the steel part depends on the history of displacement and the size of the apparent contact area. In general, this heat flux history is similar to the history of heat flux supplied at the instantaneous apparent contact area except for some intervals of zero flux when the contact area moves away of the selected fixed area. Options for identifying the intervals of zero flux are:

a) On the basis of calculations of average exposure times during each passage (similar to 4-28). This is a complex procedure given that the velocity varies and it is difficult to define the average exposure time.

b) By simply defining the intervals of zero flux as those for which the resultant displacement u_r is larger than a, where a is the radius of the apparent contact area. This is a conservative approach since it neglects the effect of the diminishing width of the apparent contact area as u_r approaches a.

c) By replacing the circular apparent contact area with an equal square area of which one side is always perpendicular to the direction of motion. This leads to the condition of zero heat flux when

$$u_r > \frac{\pi^{1/2}a}{2} \qquad (4\text{-}40)$$

We prefer option (c) because of its simplicity. Note that when the velocity is constant and equal to v_c (4-40) results in an average exposure time given by

$$t'_{av} = \frac{\pi^{1/2}a}{v_c} \qquad (4\text{-}41)$$

which is larger than that predicted by (the more accurate) (4-28). The ratio $t'_{av}/t_{av} = 1.1284$ and so for a constant heat flux, the temperature rise is overestimated by $\sqrt{1.1284} = 1.06$: the procedure is slightly conservative.

The heat flux history at the bearing center was calculated on the basis of (4-40) and is shown in Figure 4-22. It should be noted that this history contains a small number of zero flux intervals due to the large radius of the apparent contact area by comparison to the amplitude of motion. It is clear from the lower panel in Figure 4-22 that there is continuous heat flux supply for $t > 7$ seconds.

The temperature rise can be calculated using the convolution integral of (4-38). More convenient, however, is the repeated use of (4-21) and (4-32) following replacement of the actual heat flux history with an equivalent series of rectangular heat flux pulses as shown in Figure 4-22 (a simple process that can be carried out with a spreadsheet). In this case, each of the actual heat flux pulses was replaced by a rectangular pulse of the same "area". The calculation of the temperature rise at the surface was based on the use of (4-21) and (4-32) for each of the rectangular heat flux pulses and superposition of results. Figure 4-23 shows the calculated history of temperature rise. The calculation was based on the thermal property values of $D = 0.444 \times 10^{-5}\,\mathrm{m^2/s}$ and $k = 18$ W/(m·°C), which are

approximately valid for a temperature of 200°C (that is, the average temperature conditions).
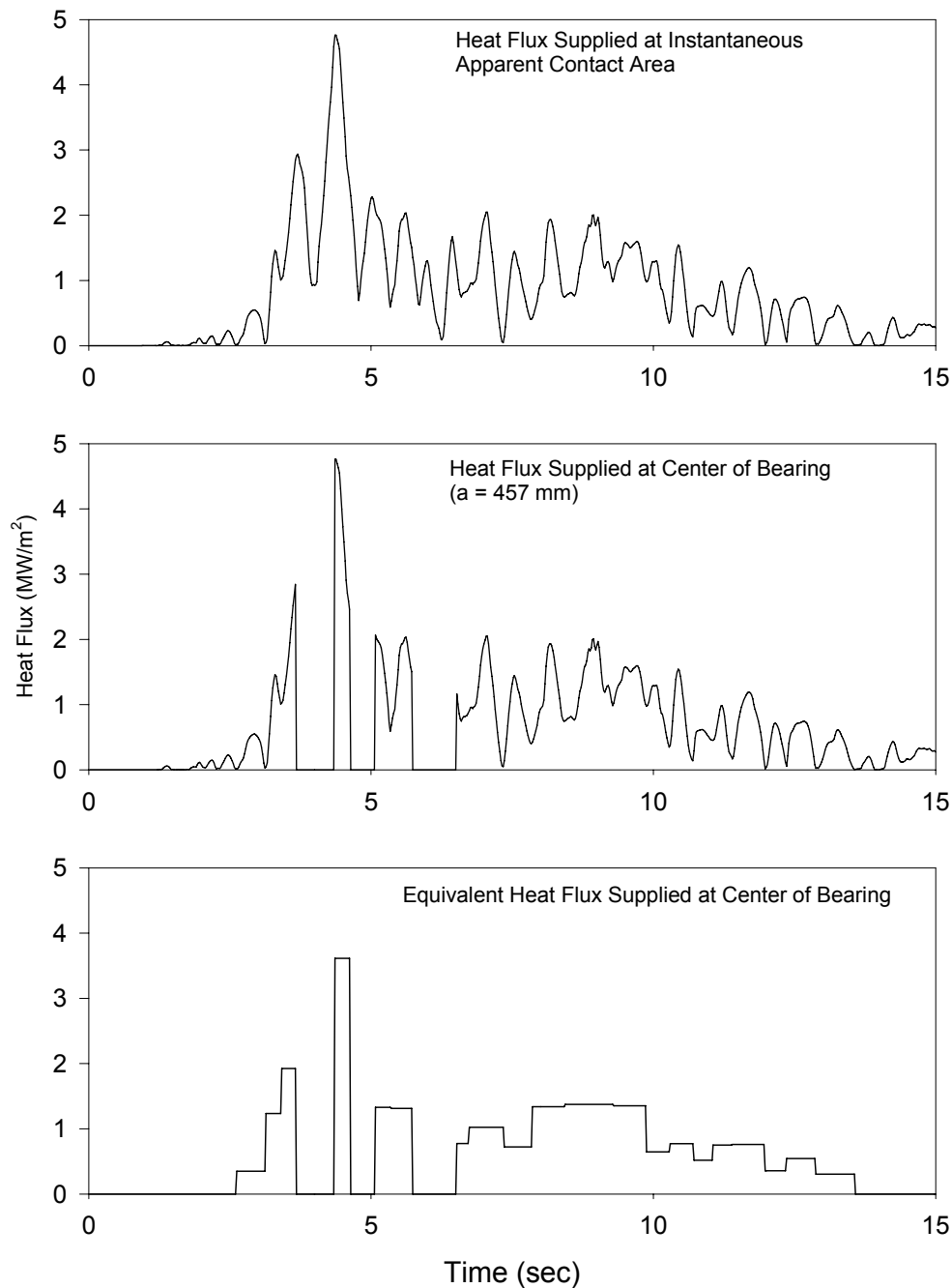
FIGURE 4-22 Histories of Heat Flux

The temperature rise at a depth of 1.5 mm was calculated and is shown in Figure 4-23. The calculation was based on the use of (4-20) and (4-30) for each of the rectangular heat flux pulses. The temperature rise at the depth of 1.5 mm is much less than that at the surface. This temperature is of little practical significance. Rather, the surface

temperature is important since it is equal to the surface temperature of the bearing material, which is the temperature to be used to assess the potential for wear of the bearing material. However, the temperature at some small depth below the surface of the stainless steel is what could be recorded by thermocouples in an experiment.
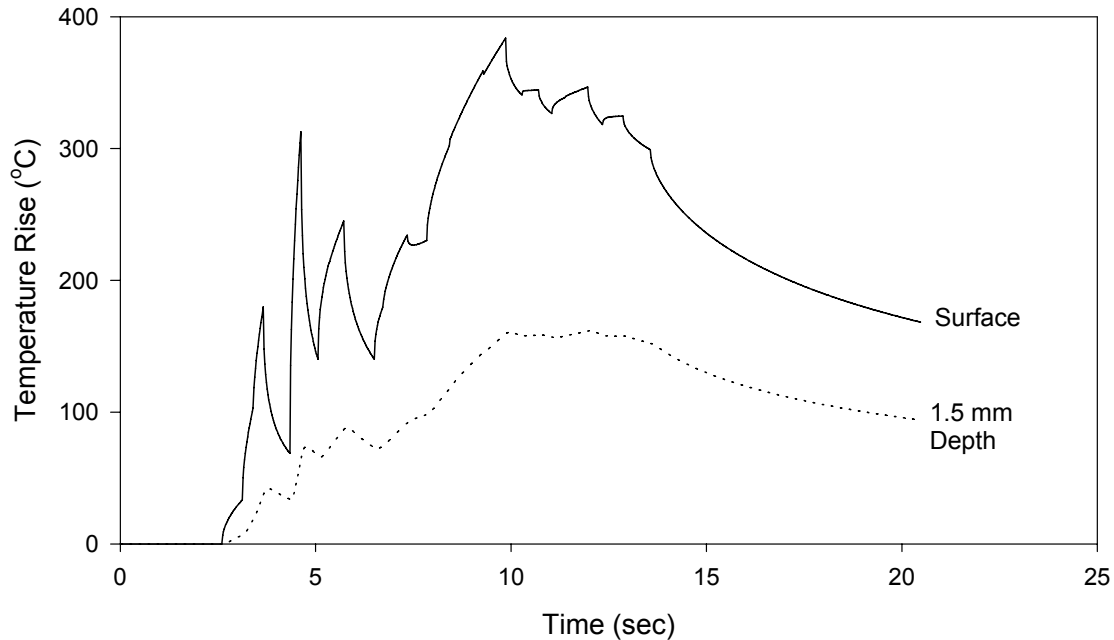
FIGURE 4-23 Predicted Histories of Temperature Rise at the Surface and at Depth of 1.5mm of Stainless Steel Overlay at its Center

4.8.4 Example of Selection of One-directional Motion to Simulated Frictional Heating Effects of Bi-directional Motion with Variable Axial Loading

In-service (production) bearings are subjected to bi-directional horizontal seismic motion with varying axial load during earthquake shaking. Often these bearings are too large to test under the calculated conditions of bi-directional high speed motion and varying axial load. The bearing shown in Figure 4-24 is a FP bearing designed to carry a gravity load of 75.4MN in an offshore platform (Clarke et al., 2005). This bearing could not be tested under high speed motion. Reduced-size prototype bearings were developed as shown in Figure 4-25 and subjected to a variety of tests with unidirectional sinusoidal motion under constant axial load. One of the prototype tests was a high-speed test that was designed to replicate the heat-flux history and temperature rise at the sliding interface in the production bearings under maximum considered earthquake shaking. The equivalency of the high speed sinusoidal prototype tests and the high-speed bi-directional response of the production bearings to maximum considered earthquake shaking is demonstrated below using calculations of heat flux history and temperature rise at the sliding interface.

75

The calculations presented below are based on the theory of presented previously. For these bearings, the peak bearing displacement in the worst case scenario is less than half the diameter of the contact area and so the entire heat flux is supplied at the center of the bearing without intervals of zero heat flux. The calculations are based on dynamic analysis results for the maximum earthquake. It was determined that the critical case for temperature rise was a particular earthquake excitation considered in the analysis when using the upper bound friction properties of the bearings: a coefficient of friction of 0.095 under high speed motion. (The lower bound value of the coefficient considered in the analysis was 0.040 under high speed motion.)

Figure 4-26 presents the calculated displacement histories for the critical bearing. Figure 4-27 presents the calculated relative velocity and axial load histories for the bearing of Figure 4-26. The heat flux history for this bearing and an equivalent representation of that history is shown in Figure 4-28. The equivalent history consists of rectangular heat flux pulses so that the total energy per unit area is the same over the duration of the response history.

The temperature-rise history at the surface of the stainless steel overlay was computed numerically using equation (4-38). Results for $x = 0$ are presented in Figure 4-28c assuming that the thermal conductivity is 22 W/m°C and that the thermal diffusivity is 4.44×10^{-6} m^2/sec. To replicate the temperature rise history in the production FP bearings using unidirectional sinusoidal motions that could be replicated by a test machine, analyses were undertaken using a semi-infinite solid with a constant heat flux at the surface. The solution to this problem relating temperature rise to distance and time is given by (4-20) and by (4-21) for the case of $x = 0$. The value of the constant heat flux that best replicated the temperature-rise history of Figure 4-28c was back-calculated using the temperature-rise time of Figure 4-28c (16.7 seconds: from $t = 7.4$ sec to $t = 24.1$ sec), a distance of $x = 0$ for the surface calculation, and the values of thermal conductivity and thermal diffusivity given above. This value is termed the equivalent constant heat flux below and is denoted by q_e. For $q_e = 0.89$ MW/m^2, (4-21) provides a good representation of the calculated rise in temperature at the surface of the bearing. The equivalent unidirectional sinusoidal motion can then be established as follows, noting that the equivalent constant heat flux is given by (4-25).

The displacement amplitude was selected as 240 mm: less than one-half of the diameter of the contact area in the reduced-size prototype bearing (=520 mm). The frequency of motion was then calculated using (4-25) assuming a constant heat flux $q_e = 0.89$ MW/m^2, a coefficient of sliding friction of 0.05, a contact pressure of 30.8 N/mm^2 and a frequency of 0.60 Hz. The calculation of the equivalent unidirectional sinusoidal motion was based on a nominal coefficient of friction of 0.05 but the temperature-rise history was based on a coefficient of friction of 0.095. This approach was adopted because the prototype bearings were tested at room temperature and in the non-aged condition: conditions for which the coefficient of friction should have been close to the target value of 0.05.
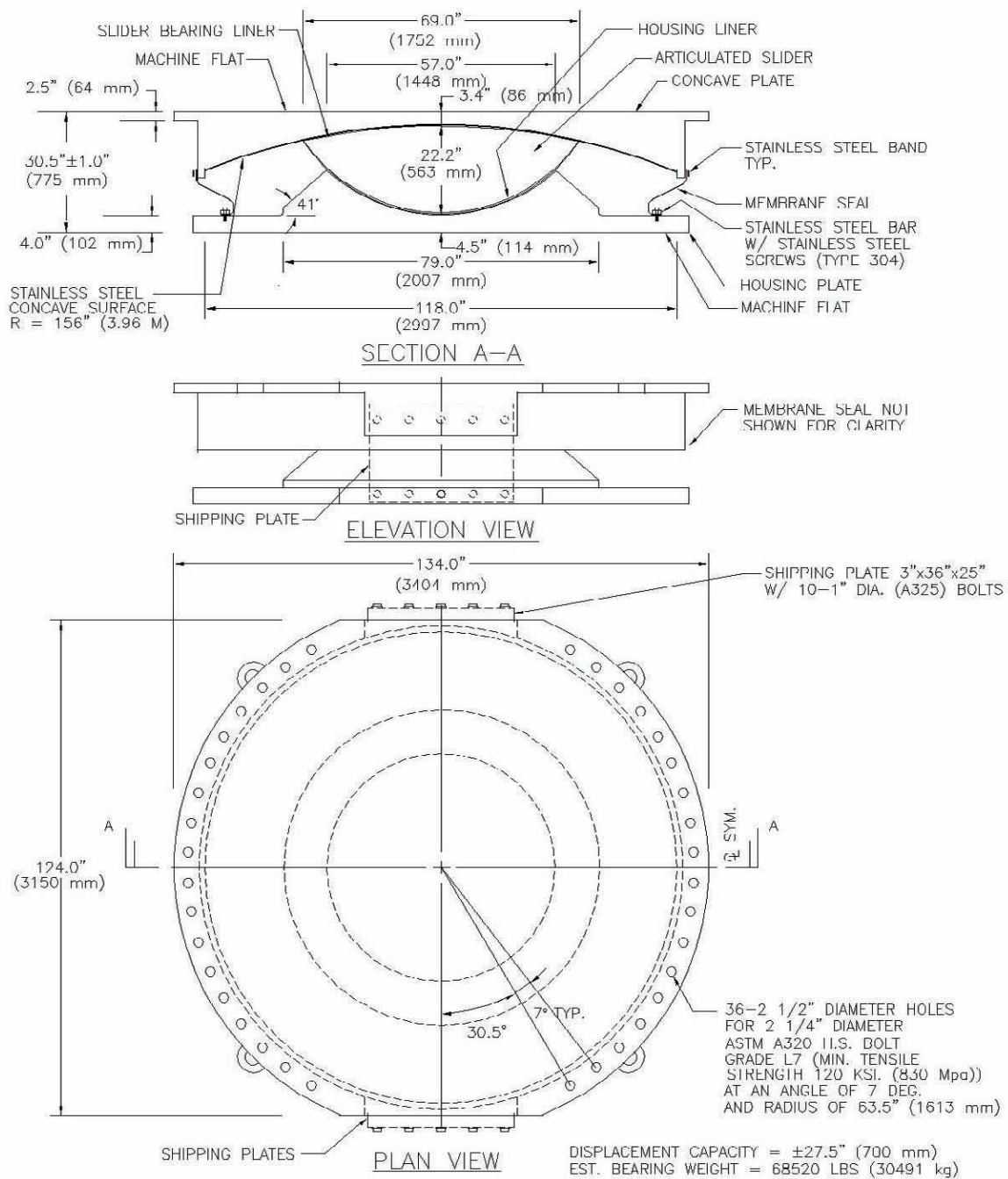
FIGURE 4-24 Details of Large Size Production FP Bearing
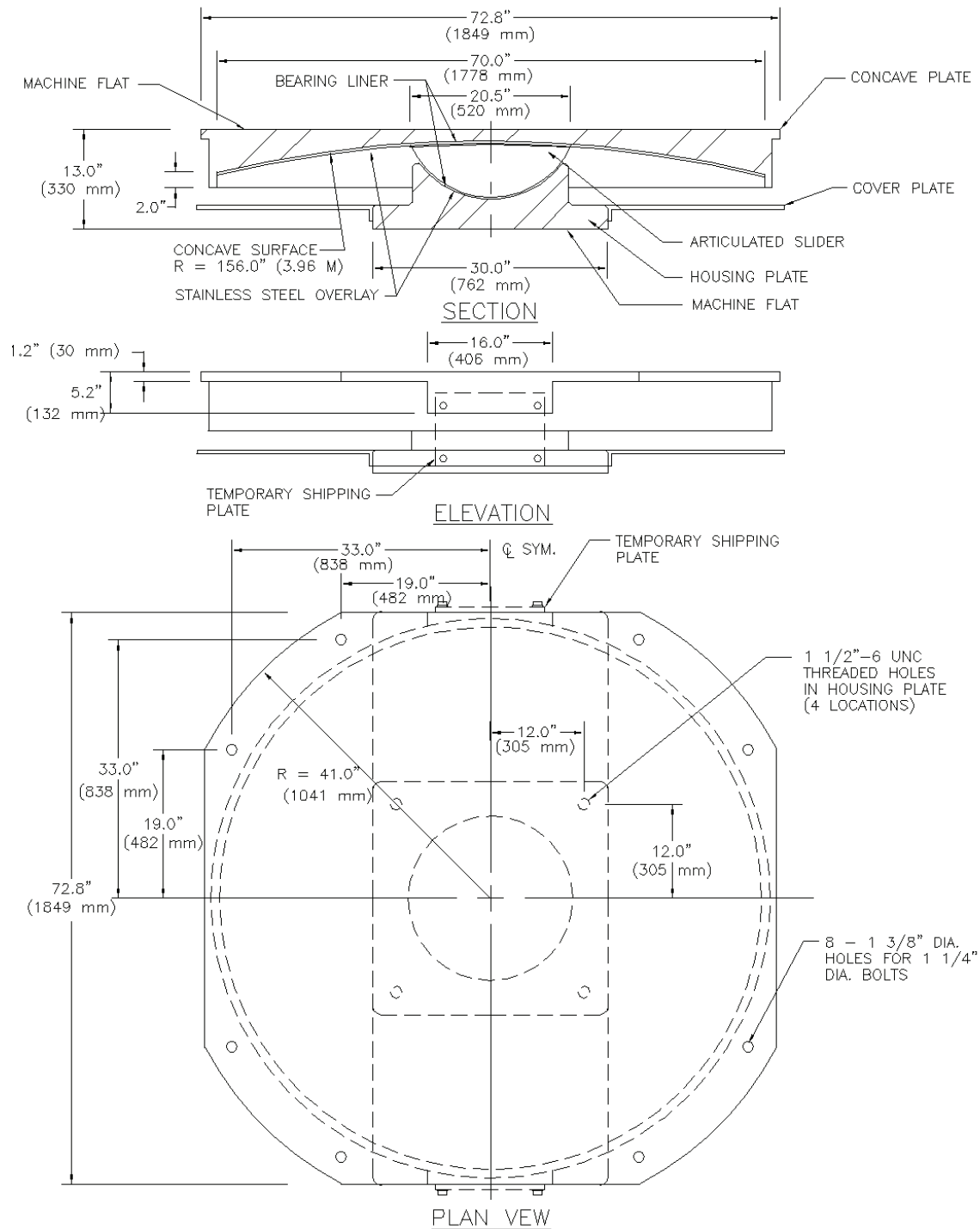
FIGURE 4-25 Details of Reduced-Size Prototype Bearing

78
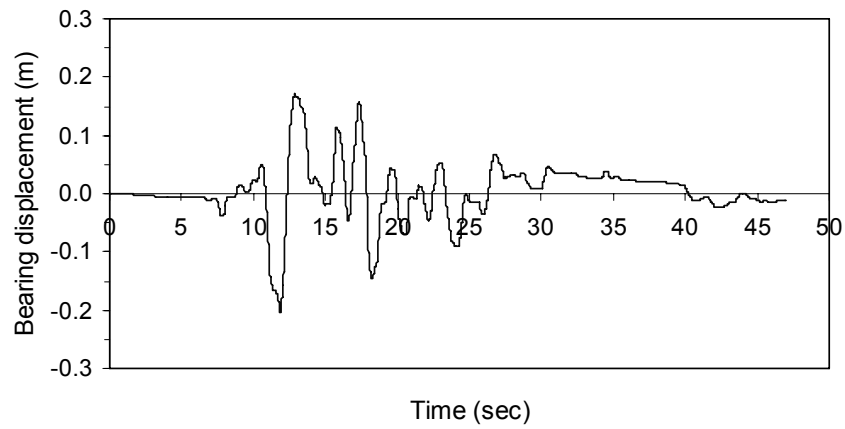
a. bearing displacement history, x-direction
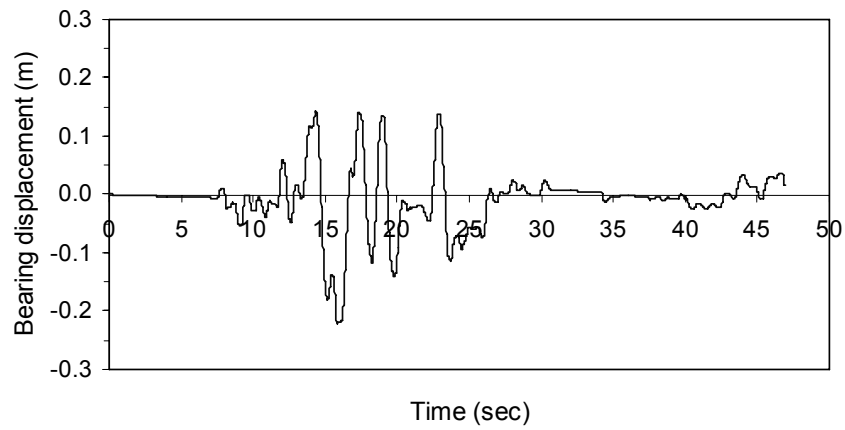
b. bearing displacement history, y-direction
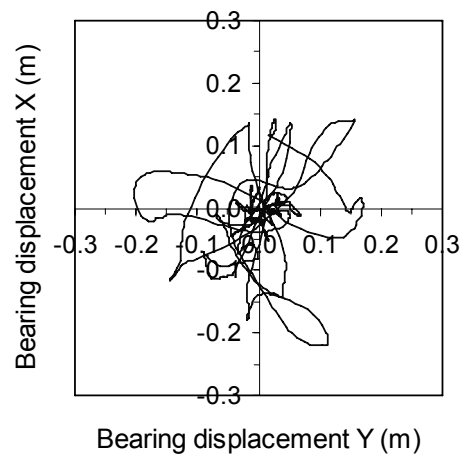
c. bearing displacement orbit

FIGURE 4-26 Displacement History Data for Full-Size FP Bearing

79
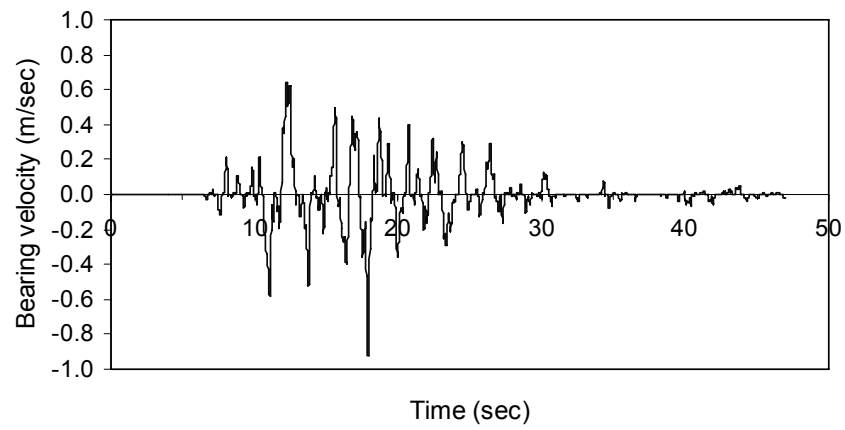
a. velocity history in x direction
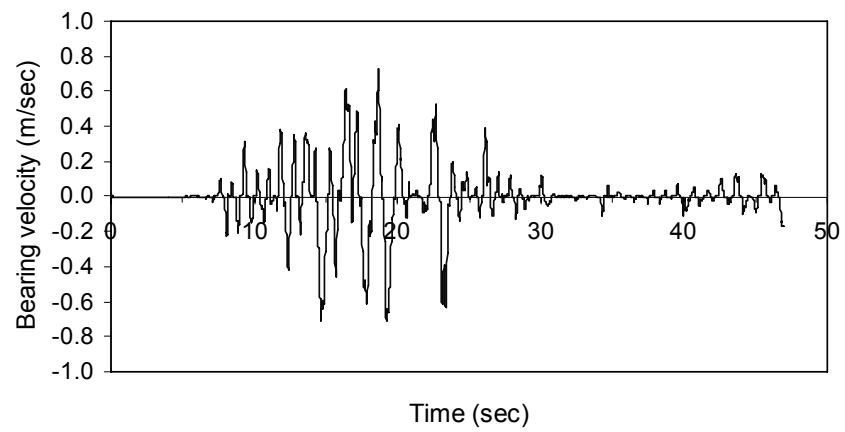
b. velocity history in y direction
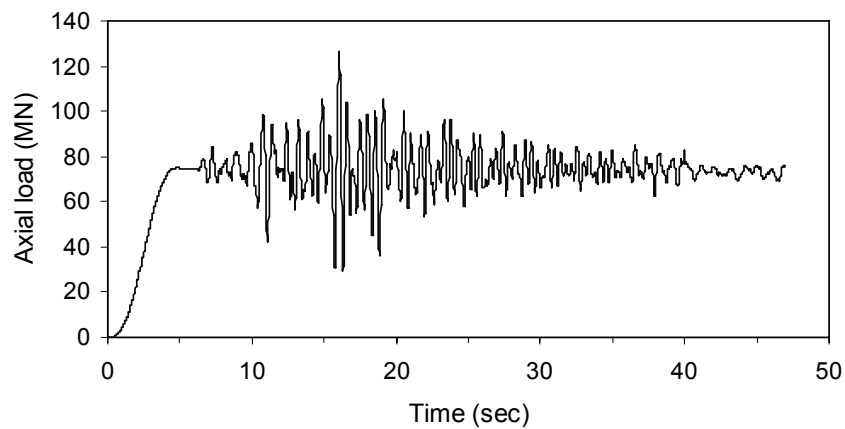
c. axial load history

FIGURE 4-27 Velocity and Axial Load History Data for Full-Size FP Bearing

80
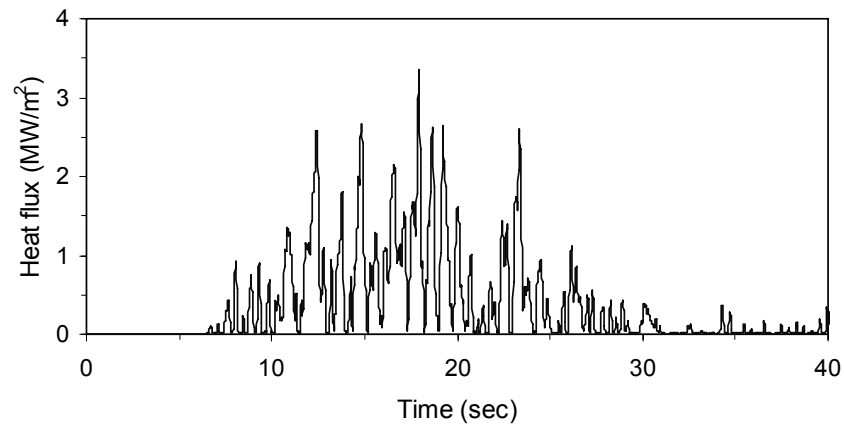
a. heat flux history at center of production bearing
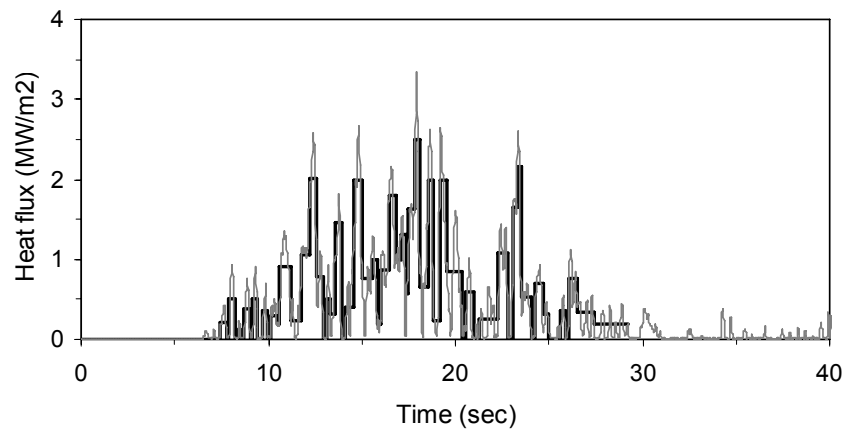
b. equivalent heat flux history at center of production bearing
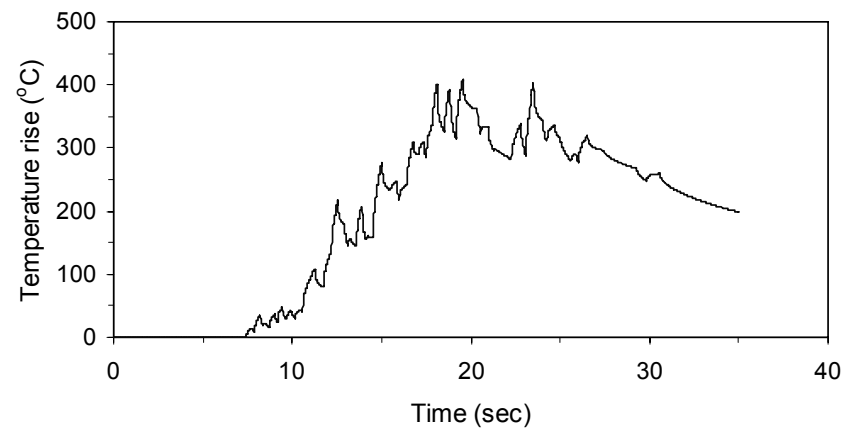
c. temperature-rise histories

FIGURE 4-28 Heat Flux and Temperature History Data for Full-Size FP Bearing

81

The resulting peak velocity was 0.90 m/sec ($0.240 \times 0.6 \times 2 \times \pi$) and the number of fully reversed cycles was 10 ($= 16.7 \times 0.6$), noting that the time from the first increase in temperature to the time after which the temperature dropped permanently (see Figure 4-29) was 16.7 seconds and the frequency of loading was 0.6 Hz. The resulting temperature rise history is shown in Figure 4-29 together with the calculated temperature rise due to bi-directional seismic motion of the production FP bearing. The temperature rise is reported for the surface of the stainless steel overlay. There is good correlation between the two histories in this figure and it is clear that the unidirectional sinusoidal history with displacement amplitude of 240 mm, frequency of 0.6 Hz, and duration of 16.7 seconds (equivalent to 10 cycles) was essentially equivalent, in terms of temperature increase, to the critical earthquake history for the full size bearings.
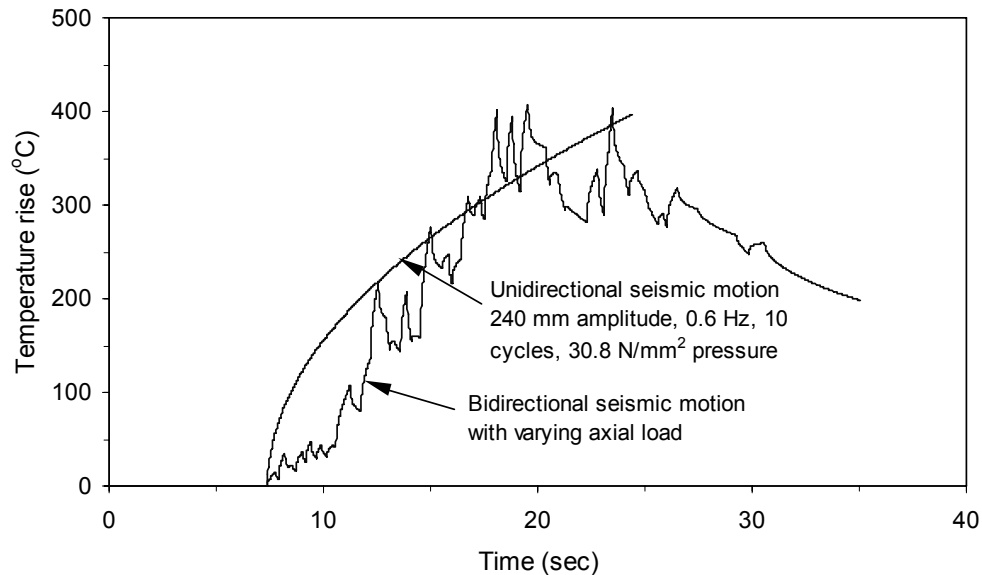
FIGURE 4-29 Predicted Temperature Histories for the Worst Case Bidirectional Seismic Motion and the 10-Cycle Prototype Test

Equation (4-20) for constant (non-intermittent) heat flux was used to solve for the temperature profile below the surface of the overlay as a function of time. The time-varying temperature profile for the 16.7-second-duration test was established for $t = 5$ seconds (3 cycles), 8.3 seconds (5 cycles), and 16.7 seconds (10 cycles), by replacing q with q_e in that equation, assuming $q_e = 0.89$ MW/m^2 and the values for thermal conductivity and diffusivity for stainless steel given previously. The results are presented in Figure 4-30. In that figure it can be seen the temperature rise drops rapidly below the surface with the significant temperature increases being observed in the stainless steel only. Thirty millimeters below the surface of the stainless steel overlay, there is no discernable temperature increase. Note that the thickness of the overlay-casting assembly is much greater than 30 mm and that the temperature rise near the base of the casting is nearly zero. Further, note that the contact-area diameter for both the reduced-size prototype and production FP bearings (520 mm and 1,752 mm, respectively) is substantially larger than the depth over which heat conduction occurs (30 mm per Figure 4-30). This observation proves that the initial assumption of heat flux over the entire surface of a half space is valid.
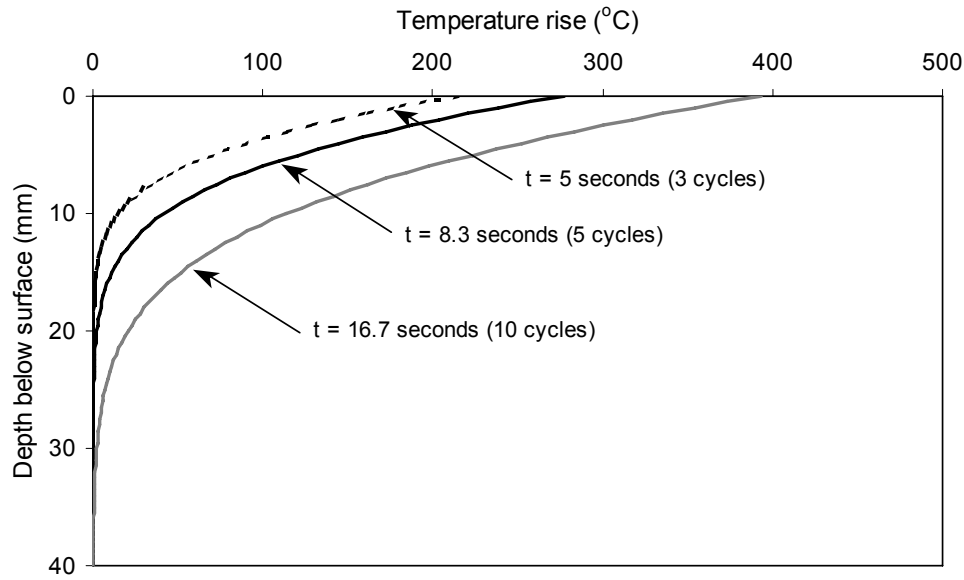
FIGURE 4-30 Temperature-rise Below the Surface of the Stainless Steel Overlay

4.8.5 Concluding Remarks on Frictional Heating

A theory has been presented to calculate the temperature rise at the contact surface of a sliding bearing and at small depths below the surface of sliding bearings. The important assumptions in this theory are that 100 percent of the heat generated at the contact surface is supplied to the steel part (i.e., the bearing material is a perfect thermal insulator), heat conduction is one-dimensional, loss of heat due to radiation is negligible, conditions of half space prevail (a good assumption for large contact area and high speed motion) and that the true contact area is essentially the same as the apparent contact area. The latter assumption is based on the theory presented in section 4.6 that appears to be valid for PTFE and the like materials in contact with highly polished stainless steel.

The theory predicted well the temperature rise recorded in various experiments, although the experimental results were restricted to measurements of temperature at some small depth in the stainless steel and not at the surface. Nevertheless, the correlation of experimental data and calculated values provides confidence in the use of this rather simple theory for the prediction of the temperature rise due to frictional heating in PTFE-stainless steel interfaces.

It is important to note that large temperature increases are predicted at the contact surface of bearings subjected to high speed seismic motions. However, temperature increases at even small depths below the steel surface are significantly less. This fact should be considered when measurements of temperature are made by embedding thermocouples at small depths below the contact surface.

Frictional heating causes substantial increases in temperature at the sliding interface, which in turn affects the effective friction coefficient. The latter is defined as the average value of the coefficient of friction obtained in a number of cycles representative of the seismic environment in which the bearing operates and it is the value useful in analysis. As an example, Figure 4-31 presents the histories of displacement and velocity and the lateral force versus displacement loops recorded in the testing of the bearing of Figure 4-25. The bearing was subjected to vertical load of 6,540kN (resulting in apparent pressure of 30.8MPa) and 10 cycles of harmonic motion as described in Section 4.8.3 (also see Fig. 4-29). The effects of high temperature at the sliding interface are seen in the reduction of friction with increasing number of cycles.

4.9 Friction in Lubricated Interfaces

Lubrication of the PTFE-stainless steel interface reduces the coefficient of friction. The lubricant, typically in the form of grease, is stored in dimples under hydrostatic pressure from where it is extruded to the sliding interface. Dimpling is important for prolonging the effective life of the lubricant (Campbell and Kong, 1987). Dimples cover approximately 30 percent of the apparent contact area. Grease consists of primarily oil or synthetic fluid (approximately 80 percent or more), a thickening agent (typically soap at approximately 10 percent) and additives (antioxidants, anticorrosion agents, etc. at less than 10 percent).

In unlubricated PTFE-stainless steel interfaces the friction at low velocity of sliding is primarily the result of shearing at the junctions. Moreover, at a high velocity of sliding significant contributions to the sliding friction are provided by third body effects (agglomerates of wear debris) and the viscoelastic deformation of PTFE (see section 3). For these interfaces it is also likely that the real area of contact (that is, the area of the junctions) is approximately equal to the apparent area of contact (see sections 3.6.1 and 3.6.3).

For dimpled, lubricated PTFE-stainless steel interfaces there is total separation of junctions by the lubricant over the area of the dimples (approximately 30 percent of the apparent area). For the rest of the apparent area the conditions are not exactly known, but it is reasonable to assume that major part of the load is carried by junctions which are separated by a very thin film of lubricant. Nevertheless, the result is substantial reduction in the friction. For wide ranges of apparent pressure and sliding velocities, the sliding coefficient of friction for highly polished stainless steel and for normal temperature is of the order of 0.02 or less.

4.10 Aging of Sliding Bearings

In the past, bearings used in bridges for non-seismic applications consisted primarily of rockers, rollers and sliding plates. All of these types of bearings have experienced problems such as flattening of rollers, tilting of rockers and, more commonly, severe corrosion of contact surfaces. The latter problem, which is typically the result of the use of unsuitable materials in the presence of leaking expansion joints, might have been the

84
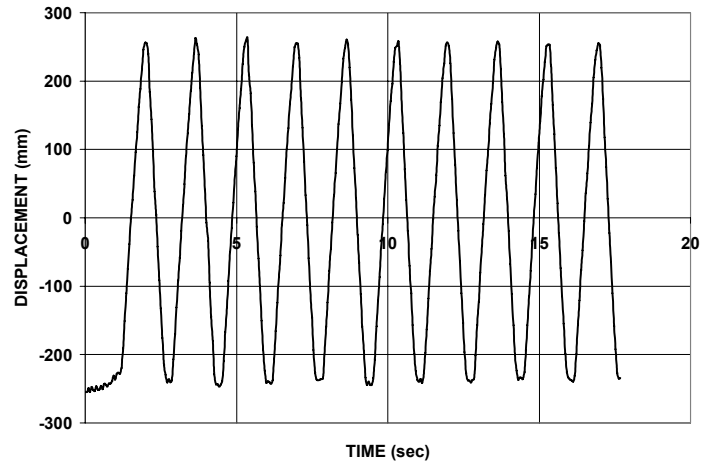
a. displacement history
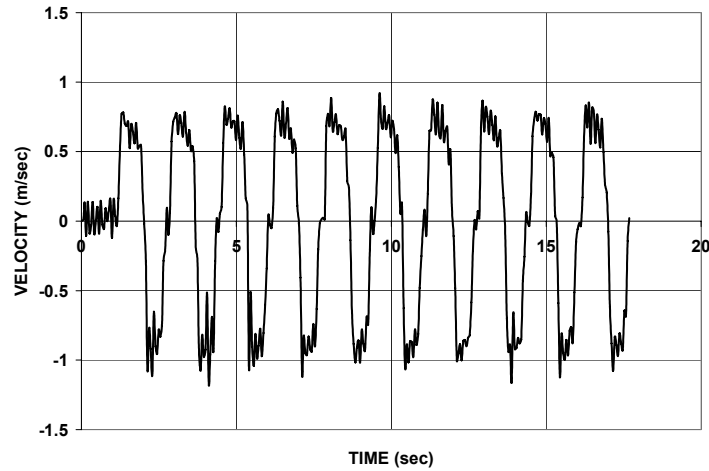
b. velocity history

c. lateral force-displacement loop

FIGURE 4-31 Displacement and Velocity History Data and Force-displacement Loops Recorded in Testing of FP Bearing of Figure 4-25

85

prime contributor to the perception among many engineers that sliding bearings exhibit poor aging characteristics.

The presentation in this section concentrates on modern sliding bearings that have very different characteristics, and also different aging problems, than those deficient old types of bearings. Modern sliding bearings consist of a sliding interface and a rotational element that is needed for maintaining full contact at the sliding interface. The rotational element may take various forms such as in the pot bearing, the spherical bearing, the disc bearing, the articulated slider in the Friction Pendulum bearings or an elastomeric bearing (Campbell and Kong, 1987; Mokha et al., 1988; Constantinou, et al., 1993). The sliding interface can take a variety of forms, but those of interest herein are those that have found applications in seismic isolation bearings, namely,

a) PTFE (polytetrafluoroethylene) in contact with polished stainless steel, under either dry or lubricated conditions,
b) Various forms of composites (which typically contain some PTFE) in contact with polished stainless steel as used in the Friction Pendulum bearings, and
c) Certain forms of bimetallic interfaces that consist of stainless steel in contact with bronze that is impregnated with a lubricant such as lead, PTFE or graphite

A number of reports provide information on the field performance of modern sliding bearings used in non-seismic bridge applications (e.g., Lee, 1981; Manning and Bassi, 1986; Transportation Research Board, 1989). Moreover, other publications provide related general information on sliding bearings (e.g., Campbell and Kong, 1987; Kauschke and Baigent, 1986). These documents deal with non-specific reports of failures or problems. Nevertheless, it is possible to classify the observed problems as follows:

a) *Leakage of elastomer*: A significant number of problems occurred due to leakage of the elastomer in pot bearings. Typically, this problem is the result of inferior bearing design, improper installation, miscalculation of bearing rotation, or inappropriate use (e.g., use in locations where live loadings cause significant fluctuation in the axial load on the bearing).
b) *Metal-to-metal contact due to excessive bearing rotation:* Excessive rotations are often the result of improper bearing installation or of underestimation of bridge movement.
c) *PTFE deformation and extrusion*: This problem has been observed for cases where the PTFE was either not bonded or not recessed, or the recess had inadequate depth, or the free height of PTFE was excessive, or the stainless steel surface was not flat.
d) *Corrosion:* Corrosion of external metal parts with inadequate corrosion protection has been reported often. In some cases crevice corrosion between the stainless steel and its backing steel plate has been reported. This problem is easily prevented by continuous welding around the perimeter of the stainless steel plate. Chrome-plated structural steel was tried in Germany in place of stainless steel but the surface developed small pockets of rust in time. This was also observed by the authors for chrome-plated steel after about one year of outside exposure. Reports

on corrosion of stainless steel (particularly ASTM 240, Type 304 or better) in sliding bearings could not be found. However, the authors located several studies on corrosion of metals that document corrosion of stainless steel (e.g., Davison et al., 1987). The authors have also observed mild corrosion on ASTM 240, Type 304 stainless steel on one of their bearings after about nine years of indoor exposure. The bearing was extensively tested during this period and stored disassembled. The stainless steel exhibited mild corrosion over a small portion of the surface. This had an effect of increased surface roughness and, thus, could affect the friction coefficient. (The issue of corrosion is further discussed later in this report.)

e) *Contamination*: Significant increases in friction and even seizure have been reported in bearings contaminated by ferrous and cementitious materials (Lee, 1981; Tyler, 1977; Campbell and Fatemi, 1989). All these cases were either observed in the laboratory where contaminants were artificially introduced or in the field when the bearings were disassembled prior to installation. Contamination of bearings in service in dust-laden environments is unlikely and any dust that settles on the stainless steel plate is likely to be swept off by the moving PTFE part. Nevertheless, it is possible for contaminants to enter the sliding interface during service, particularly in lubricated bearings.

f) *Total sliding movement*: Bearings of bridges carrying heavy live loads experience significant total movements that may amount to several kilometers over their lifetime. Wear reduces the useful thickness of the PTFE and limits the operational lifetime of the bearings. Moreover, the coefficient of friction is affected by the total sliding movement experienced by the bearing. Laboratory studies have produced mixed results. Studies of German origin (summarized in Kauschke and Baigent, 1986) show substantial increases in the very low velocity coefficient of friction of lubricated PTFE bearings after 20 km travel. More recent studies by Campbell and Kong (1989) on lubricated PTFE bearings show similar results over the shorter travels of 0.5 to 0.75 km. Studies by the authors (reported later in this report) on unlubricated bearings made of either PTFE or PTFE composites and highly polished stainless steel demonstrated small changes in the sliding coefficient of friction at very low (0.4 mm/s) and at high (160 mm/s) velocities over a 0.5 km travel.

These reports deal primarily with sliding interfaces consisting of PTFE in contact with stainless steel because this has been by far the most frequently used interface. Lee (1993) reported on the frictional properties of a bimetallic interface utilized in the seismic isolation bearings of the Koeberg nuclear power station in South Africa, This interface consisted of stainless steel in contact with leaded bronze. After 14 years of service, 60 of a total of 1829 bearings were removed and tested. The bearings did not show any noticeable corrosion or contamination and had not been subjected to any movement during service. On average, the bearings exhibited a 68 percent increase in the initial (static or breakaway) coefficient of friction. It appears that this increase in friction was the result of the motionless state of the bearings; an observation corroborated by field observations of graphite-impregnated bronze bearings in Illinois (Jacobsen, 1997).

The effect of load dwell (i.e., loading without movement) is of interest for sliding seismic isolation bearings. Although this is primarily an issue for building applications, there are cases in bridge applications in which a sliding bearing might not experience any movement for a long period of time. This case might arise in bearings on top of flexible piers, which can accommodate thermal and traffic-induced movement by deformation of the pier rather than by sliding of the bearing. Tests performed on PTFE-stainless steel interfaces following a two-year load dwell (Mokha et al., 1991), resulted in no increase of the static coefficient of friction. The difference between this observation and that of Lee (1993) on bimetallic interfaces is, we will claim elsewhere in this report, likely the result of the very different mechanisms of friction in the two interfaces, namely, bimetallic interfaces are susceptible to the effects of load dwell whereas PTFE-stainless steel interfaces are not.

In summary, we group the potential problems of sliding bearings into the following categories:

a) Problems that can be prevented through the use of detailed specification requirements and quality control for the design, material selection, manufacture and installation of the bearings. These problems are those of corrosion of external parts, crevice corrosion, metal-to-metal contact, squeezing out of PTFE, contamination at the site (by disassembly) and some of the problems related to leakage in pot bearings.

b) Problems that may not affect the performance of the bearings but which may limit their operational lifetime. These problems include wear at the sliding interface that reduces the useful thickness of PTFE, and wear of the rotational part. This part might be the weakest component in some types of bearings under certain conditions. Mayrbaurl (1986) describes tests conducted on the replacement bearings for the Manhattan Bridge in New York. These bearings are subjected to an average of 500 train crossings per day that induces sliding, rotation and uplift. Testing under in-service conditions resulted in unacceptable performance of the rotational part of the pot bearings. Disc bearings performed well. However, the estimated operational lifetime of the rotational part, after extrapolation of test data over the equivalent of about 6 years of service, was a mere 13.5 years: in sharp contrast to the expected lifetime of the sliding interface that showed only minor wear.

c) Certain conditions that are likely to occur are either known or are potentially capable of affecting the frictional properties of the sliding interface. Therefore, they have to be considered in the analysis and design of structures incorporating sliding bearings. These conditions include (a) corrosion of stainless steel, (b) contamination of the sliding interface while the bearing is in service, (c) accumulated movement (travel), and (d) loading without movement. The effects of these conditions are investigated in more detail later in this report.

It is of interest to review attempts to obtain information on the *lifetime* of sliding bearings in the laboratory environment. These attempts may be classified as follows:

88

a) Testing of full size bearings under the actual conditions of loading but applied at an increased rate. A notable example of such testing was that for the Manhattan Bridge bearings (Mayrbaurl, 1986). The bearings were subjected to the actual cycle of loading (as monitored at the bridge) at a rate of about 360 cycles per hour, whereas the actual rate was about 20 cycles per hour. It was thus possible to conduct testing over few months that was equivalent to about 6 years of actual service. Such tests are time consuming and expensive and can only be performed in rare cases. However, such tests can produce invaluable results provided that the data are interpreted carefully. Application of the load at an increased rate can accelerate fatigue (particularly in the rotational part) and wear. Conversely, accelerated testing cannot account completely for the effects of time.

b) Testing of either full-size or reduced-size bearings under artificial conditions to provide information on a particular effect. This has been the approach followed by the writers in generating some results on the effects of corrosion, travel, load dwell and temperature on the frictional properties of sliding bearings. It is also expected to be the procedure for establishing property modification factors for seismic isolation bearings. The procedure is complicated by the fact that the generation of an artificial condition (a) requires understanding of the fundamental behavior of the materials that make up the bearing, (b) might require complex analysis for interpretation of the results, and (c) does not truly account for the actual, in-service conditions. Another issue with this type of testing is the use of results generated by accelerated testing to predict lifetime by extrapolation. For example, consider that testing is performed in order to establish the lifetime of a bearing as related to wear of the PTFE. Apart from the apparent complexities in determining representative histories of loading and movement, let us assume that testing is conducted over a specific length of travel. A direct result of this test is a measurement of wear and coefficient of friction, which is useful information for the tested travel. Another result might be the wear rate (i.e., wear per unit of travel) or the wear factor (Predicting Bearing Wear, 1968). Could this information be used to predict the condition of the bearing after travel significantly longer than that imposed on a test specimen? Do the wear rate and wear factor remain unchanged? In the opinion of these authors, extrapolation of experimental results without a solid physical interpretation is inappropriate.

c) The writers have noted the publication of testing requirements for seismic isolation bearings that include some form of artificial aging. The State of New York specifies testing of bearings following exposure for 1000 hours in a salt spray chamber (per ASTM B117) under the title *Environmental Aging*. The purpose of the test is described as "…to verify performance of the selected bearing assembly in a salt spray environment such as that encountered over a long period of time under an expansion deck joint which is subject to salting…" The test seeks to acceleration corrosion of the stainless steel surface of sliding bearings. However, the salt spray fog does not truly simulate the environment of a bearing over say a period of 30 years in service. The effects of loading, movement, temperature and, more importantly, the various chemicals in the atmosphere and on the road are not addressed. The authors have observed specimens of stainless steel to be in excellent condition following salt spray

chamber testing. They have also collected information (to be presented later in this report) that shows that even the most corrosion-resistant stainless steel can suffer some atmospheric corrosion in aggressive environments. A single, simple test to assess the aging characteristics of a bearing cannot provide much useful information and perhaps can only serve to increase the confidence of the engineer in the use of the selected product.

4.11 Summary

Friction is an extremely complex phenomenon of which the exact mechanism is not known. Rather, several mechanisms are believed to contribute in the generation of friction. One particularly important aspect of frictional behavior is that when solid materials come into contact, the true area of contact is, in general, less than the apparent contact area. The size of the true contact area depends on the materials in contact, the load and time.

Concentrating only on interfaces consisting of PTFE or similar soft materials and highly polished stainless steel, we have argued that the true area of contact is nearly equal to the apparent contact area. In support of this theory we have presented theoretical solutions on the rate of creep and experimental results on the dependency of friction on normal load and on the dependency of the breakaway (or static) friction on the load dwell. An important prediction of this theory is that load dwell does not have an effect on the breakaway friction except likely for short time intervals of the order of minutes to hours.

The macroscopic behavior of PTFE-stainless steel interfaces has been described and effects such as those of velocity of sliding, apparent bearing pressure and temperature have been discussed. Moreover, the so-called phenomenon of stick-slip has been described as the result of the flexibility of the testing arrangements and not as an intrinsic property of sliding bearings.

Seismic isolation bearings are likely to experience changes in their mechanical properties over time. Depending on the bearing type, materials used, design procedures, installation procedures, loading history, and environment, these changes may be significant enough to limit the operational life of the bearing.

Sliding bearings have experienced problems, such as corrosion, metal-to-metal contact, squeezing out of PTFE, contamination and failure of the rotational part. Currently, there is sufficient knowledge and experience in the design, material selection, manufacture and installation of these bearings to prevent or minimize the potential for these problems. However, this would require the use of detailed specification requirements and rigorous quality control. Nevertheless, it should be recognized that sliding bearings are complex structural arrangements that are sensitive to the quality of manufacturing.

Changes in the mechanical properties of sliding bearings (specifically the coefficient of friction) can be caused by corrosion of the stainless steel, contamination of the sliding

interface while in service, history of movement, and loading without movement (load dwell).

A major part of this section was devoted to the problem of frictional heating and an analytic solution for the temperature rise at the sliding interface has been presented. Experimental results confirmed the validity of the theoretical solutions.

SECTION 5
FRICTIONAL PROPERTIES OF INTERFACES OF PTFE AND POLISHED STAINLESS STEEL

5.1 Introduction

This section presents the frictional properties of interfaces constructed of unfilled PTFE and one type of PTFE-based composite in contact with polished stainless steel. The effects of apparent pressure, sliding velocity, temperature, load dwell, corrosion of stainless steel, contamination, travel and wear on the frictional properties are presented. The data presented herein was collected from the literature or generated by the authors. Much of the data are for unlubricated conditions.

Most of the presented data have been generated by the authors at the University at Buffalo and by Professor Campbell's group at Queen's University, Kingston, Ontario, Canada (Campbell and Kong, 1989; Campbell and Fatemi, 1989; Campbell et al., 1991). Although the machines used in these testing programs were most different, the sizes of the test specimens were similar.

In the Queen's University testing apparatus a single sliding interface was used. Rollers were utilized below the sliding platform. Vertical load was developed with a hydraulic ram. Load cells monitor the friction force at the interface, excluding the inertia effects and the friction in the supporting rollers. Concentric normal loads are applied through the use of spherical bearings between the hydraulic ram and the sliding interface. The diameter of the PTFE specimens was 75 mm.

Two different machines were used for the tests at the University at Buffalo. The first machine is illustrated in Figure 4-3. This machine can apply a variable normal load and rotate and horizontally translate a bearing. The machine can test a single horizontal force is measured by a reaction load cell so that inertial effects are eliminated from the recorded forces. The tested sliding bearing included a rotational element (standard disc bearing with a soft adiprene disc) to ensure concentric application of the load and to accommodate rotation. The diameter of the PTFE specimens was 95 mm diameter, their thickness was 3.2 mm and the specimens were recessed to a depth of 1.6 mm. The bearings were identical to those utilized in earthquake-simulator testing (Tsopelas et al., 1994). Most of the data generated by the authors were produced with the second machine, which allowed for large load dwells and testing at low temperatures. Figure 5-1 illustrates this testing arrangement that utilizes two sliding interfaces, supported by disc bearings, which bear against a moving plate that is faced with stainless steel. The two sliding interfaces and the moving plate can be enclosed in a styrofoam box that was filled for the experiments with small sealed plastic bags containing solid carbon dioxide (dry ice) for low temperature testing. The temperature was monitored for these tests by a thermocouple embedded in the moving plate just below the stainless steel overlay.
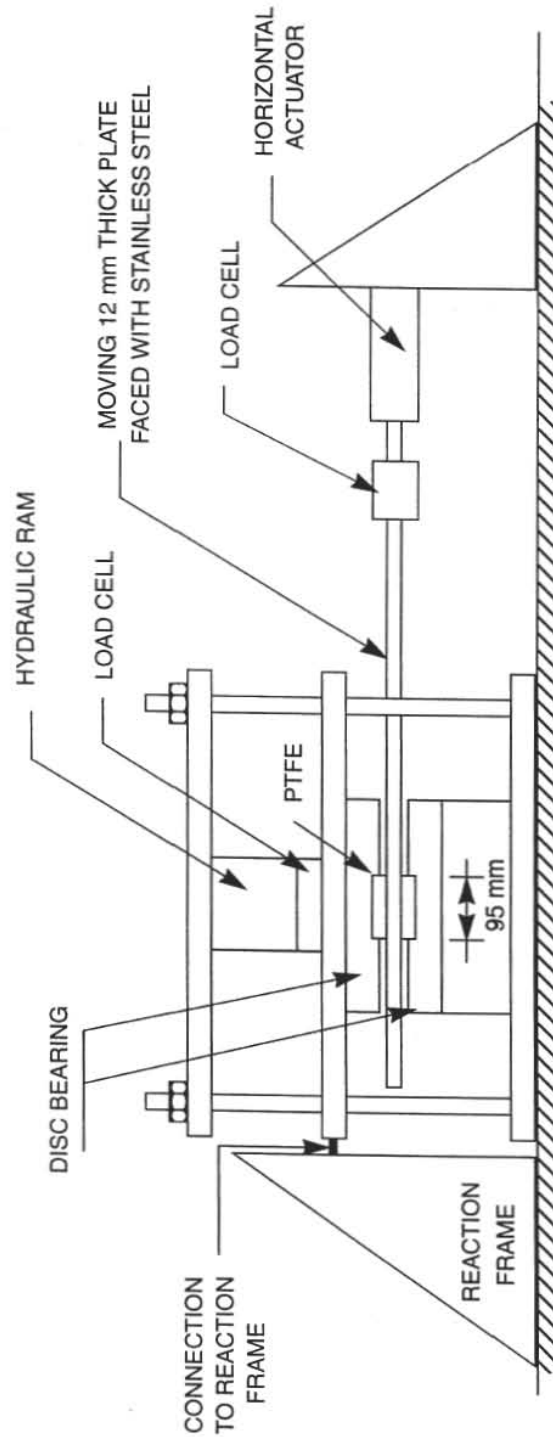
FIGURE 5-1 Testing Arrangement Used in Testing of Sliding Bearings

In the testing fixture of Figure 5-1, the friction force was obtained from two sliding interfaces (presumed to be identical) and then divided by two to obtain the friction force for a single interface. The friction force was measured by the actuator load cell; the measured force included the inertial force of the moving plate. No correction was made for the inertial force since it introduced negligible error: for the test under the smallest normal load and highest sliding velocity, the error was about 2 percent of the friction force. The fixture of Figure 5-1 was also used in the testing of a PTFE-based composite which has been used in Friction Pendulum (FP) bearings. We denote this material as PTFE composite No. 1. It is identical to the material used in the earthquake-simulator tests of Constantinou et al. (1993) and also utilized in many building applications of FP bearings. For testing, the two disc bearings in the arrangement of Figure 5-1 were replaced with the two housing plates of the FP bearings used in Constantinou et al. (1993). These plates included the standard column with a spherical cavity and the articulated slider of the FP bearings. However, the slider was machined flat to bear against the moving plate of the testing arrangement. The slider was 50 mm in diameter and was faced with the composite material at a thickness of 0.25 mm. This thickness is about three times thinner than that utilized in applications of FP bearings in building-type structures (e.g., U.S. Court of Appeals, LNG tank facility in Greece and the San Francisco International Airport Terminal). This material is not identical to that used in recent applications of FP bearings in bridges.

5.2 Effect of Load Dwell on Breakaway (or Static) Friction

It is common practice to sustain load on PTFE bearings for some time prior to imposing sliding. Campbell and Kong (1989) and Campbell et al. (1991) used a 12 hour load dwell in all of their experiments. The 12 hour load dwell is required by the AASHTO Standard Specifications (American Association of State Highway and Transportation Officials, 1992). The origin of the 12-hour load dwell requirement is unknown. However, it might be related to data obtained at the factory of Glacier Bearings in 1971 and reported by Paynter (1973). Paynter provided a brief description based on his personal communication with the technical manager of Glacier Bearings. These load dwell tests were conducted on interfaces consisting of Glacier DZ material (reported as pure PTFE) in contact with polished stainless steel of surface roughness of about 0.05 to 0.10 µm on the arithmetic average scale, and at an apparent pressure of 28 MPa. Load dwells of up to 24 hours are reported as having an effect on properties but the extent of the effect was not reported. We note that the surface roughness of the stainless steel in these tests is approximately twice that used in the tests at Queen's University and at the University at Buffalo.

The authors have conducted a number of tests to assess the effect of load dwell on the static (breakaway) friction of PTFE bearings. Prior to these tests Mokha et al. (1990) reported on the effect of load dwell on the frictional properties of such bearings. Mokha et al. (1990) observed nearly identical breakaway friction following 30 minutes and 594 days of load dwell. In the tests reported herein, we used the testing fixture of Figure 5-1 and 95-mm diameter unfilled PTFE specimens in contact with polished stainless steel (ASTM A240, Type 304) of surface roughness equal to 0.03 µm on the arithmetic

average scale (R_a or CLA) (American Society of Mechanical Engineers, 1985). Testing was conducted at an apparent pressure of 6.9 MPa using three specimens and at an apparent pressure of 20.7 MPa using one specimen. The ambient temperature during testing was about 20°C and the relative humidity was in the range 25 to 30 percent. Lateral motion on the tested interfaces was imposed as a sine wave of frequency of 0.0318 Hz and amplitude of 12.5 mm so that the peak sliding velocity was 2.5 mm/s.

Table 5-1 presents the results for the apparent pressure of 6.9 MPa. The first specimen (actually pair of specimens) was loaded for 0.2 hours and then lateral motion was imposed. The specimen was then kept under load for another hour and the test was repeated. This process was repeated seven times for a cumulative loading time of 167.0 hours. Subsequently, new specimens were tested as presented in Table 5-1. The test results demonstrate that for new specimens (not previously tested) load dwells in the range of 0.2 to 118.4 hours results in static friction values that are unaffected by load dwell. There is, of course, some variability in the obtained results but there is no systemic increase in the static friction with increasing load dwell, rather the opposite is observed.

TABLE 5-1 Test Results on Effect of Load Dwell on Static (Breakaway) Friction of Unfilled PTFE in Contact with Polished Stainless Steel at an Apparent Pressure of 6.9 MPa

Specimen	Cumulative Loading Time (hrs)	Static Friction Coefficient	Comments
1	0.2	0.116	Tests were conducted in the sequence presented without unloading of the interface.
	1.2	0.056	
	6.5	0.050	
	19.7	0.052	
	45.9	0.062	
	164.7	0.068	
	167.0	0.066	
2	118.4	0.095	Two high velocity tests were conducted immediately after the second and prior to the third test.
	128.9	0.031	
	153.3	0.073	
3	0.3	0.092	

Another observation in these tests is the marked reduction in the static friction following the first test. This is best illustrated in the recorded loops of Figure 5-2. It is likely caused by the deposition of a film of PTFE on the stainless steel plate in the previous tests.

One specimen was tested at an apparent pressure of 20.7 MPa; the results are presented in Table 5-2. The specimen was initially loaded for 0.2 hours and tested; the process was repeated for other load dwells without unloading the interface. The behavior is very

similar to the one observed at the apparent pressure of 6.9 MPa, that is, friction is lower in the tests following the very first test. Subsequently, the specimen was unloaded and was allowed to relax overnight. Without cleaning the interface, the specimen was reloaded for 24.2 hours and retested; a higher static friction was recorded with a value close to that obtained in the first test. The specimen was then unloaded, cleaned of the PTFE film deposited on the slider and allowed to relax overnight. It was the reloaded for 50.2 hours and retested. The measured static coefficient of friction was higher (=0.073) than in the very first test at a load dwell of 0.2 hours (=0.057).

TABLE 5-2 Test Results on Effect of Load Dwell on Static (Breakaway) Friction of Unfilled PTFE in Contact with Polished Stainless Steel at an Apparent Pressure of 20.7 MPa

Cumulative Loading Time (hrs)	Static Friction Coefficient	Comments
0.2[*]	0.057	[*]First test on new specimen
1.2	0.039	
6.0	0.043	
16.2	0.025	
29.4	0.030	
24.2[**]	0.047	[**]Same specimen as in first sequence. However, the interface was unloaded and allowed to relax overnight. Interface was not cleaned prior to re-loading.
118.7	0.045	
139.8	0.031	
50.2[***]	0.073	[***]Same specimen as in previous tests. Interfaces unloaded and allowed to relax overnight. Interface was cleaned prior to re-loading.
118.9	0.045	

Figure 5-3 presents the recorded loops in the very first test and the two subsequent tests following unloading of the specimen. We note in this figure that the true peak in the recorded friction in the first test might have been missed due to low data acquisition speed (at 30 points per second or about 1000 points for the duration of the imposed single cycle of movement). Nevertheless, the data on the static friction in the three tests of Figure 5-3 are within ± 30-percent of the value recorded in the first test. This range appears to be the result of natural variability in properties and measurement errors rather than the effect of load dwell (see also data in Table 5-1).

The experimental data presented herein and the data from two tests by Mokha et al. (1990) indicate that when considering the natural variability in the frictional properties obtained from different specimens or different tests of the same specimen and when considering likely measurement errors, the static friction of PTFE-polished stainless steel interfaces is unaffected by load dwell. A rational explanation for this phenomenon was presented in section 4. However, do not consider this issue to be settled. On this, we note
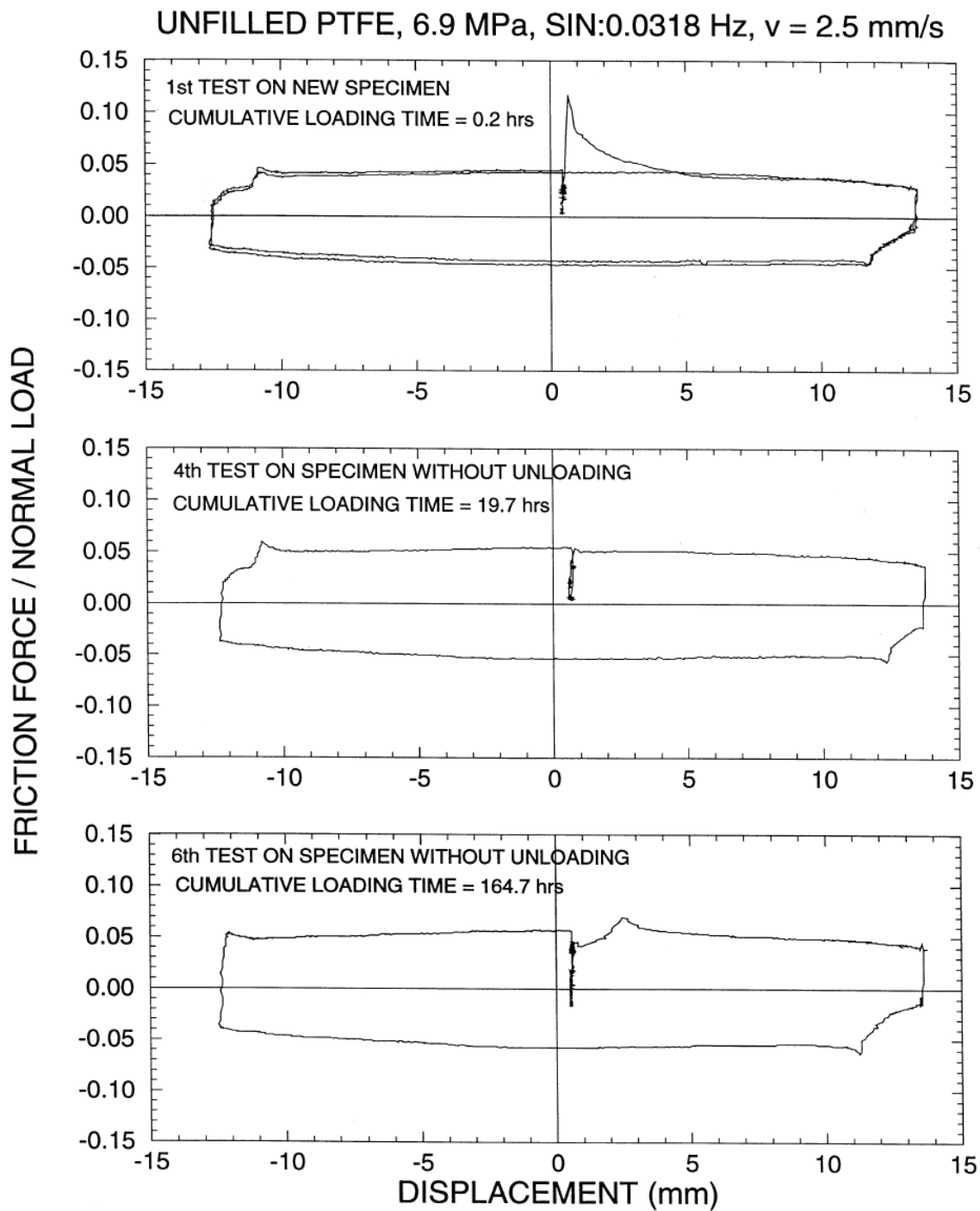
FIGURE 5-2 Recorded Loops of Friction Force Divided by Normal Load Versus Displacement in Load Dwell Tests at an Apparent Pressure of 6.9 MPa

98
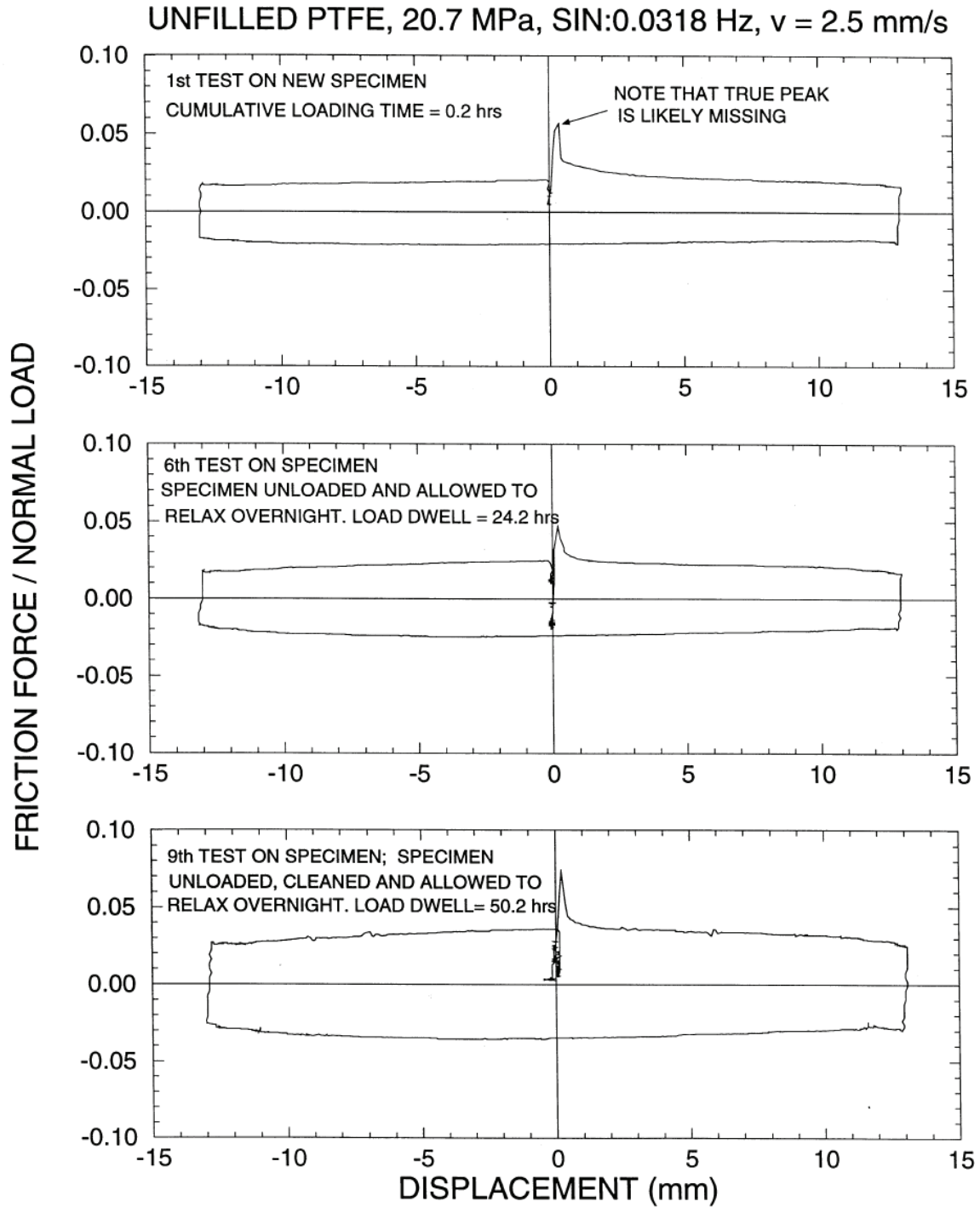
FIGURE 5-3 Recorded Loops of Friction Force Divided by Normal Load Versus Displacement in Load Dwell Tests at an Apparent Pressure of 6.9 MPa

that the explanation is not based on direct observation (as it would have been one based on measurements of the real area of contact). Rather it is an assumption that explains both the observed dependency of sliding friction on the inverse of normal load (pressure) and the apparent insignificance of the effect of load dwell on the static friction.

5.3 Effect of Apparent Pressure and Sliding Velocity

The published data on the coefficient of friction of PTFE-polished stainless steel interfaces over a large range of sliding velocities is limited. The tests of Campbell and Kong (1989) were limited to sliding velocities of 20 mm/s or less, apparently because this velocity range is relevant to the temperature and traffic induced movement of bridge bearings.

Tyler (1977), Mokha et al. (1988, 1990), and Bondonet and Filiatrault (1997) performed tests at high velocities of sliding, up to 0.8 m/s, apparent pressures in the range of 5 to 45 MPa, and with PTFE specimens having areas of approximately 12,500 mm^2 to 50,7000 mm^2. Testing was conducted by imposing either sinusoidal or constant velocity (sawtooth displacement) motion of specified displacement amplitude, d, and frequency, ω. This requires that immediately upon initiation of motion a large sliding velocity be attained. For example, in sinusoidal testing, the imposed displacement history is $d \sin \omega t$, the velocity history is $\omega d \cos \omega t$, and the acceleration history is $-\omega^2 d \sin \omega t$. However, at time $t = 0$, the actuator is motionless; it is required to achieve a velocity of ωd within an extremely short time interval. Accordingly, a large acceleration shock (jerk) is imposed at the start of the experiment. The magnitude of this acceleration depends largely on the available hydraulic power. The authors have measured this acceleration to be several times (between 2 and 13 times) the acceleration $\omega^2 d$ (see the data of Mokha et al., 1988, for information). For example, in a test at a frequency of 2.0 Hz and an amplitude of 70 mm (as in some of the tests conducted by Bondonet and Filiatrault, 1997), $\omega^2 d = 1.1$ g and the acceleration at the start of the experiment will exceed, and likely substantially exceed, 2.0 g.

Accelerations of this magnitude on initiation of motion in in-service isolation bearings are unrealistic. Figure 5-4 presents an example of histories of motion of isolation bearings from the tests of Constantinou et al. (1993) and Tsopelas et al. (1996). A 143 kN bridge model, supported by four FPS bearings on top of flexible piers, was tested at quarter length scale and half time scale. The input excitation was the N21E component of the 1952 Taft motion, scaled to a peak acceleration of 0.71 g and peak velocity of 0.54 m/s (at the prototype scale). The record of bearing relative displacement was numerically differentiated to obtain the sliding velocity and the relative acceleration histories at the sliding interface. They are presented in Figure 5-4 after conversion to the prototype scale. Moreover, a record of relative acceleration (obtained as the difference of records from accelerometers placed above and below the sliding interface) is shown to demonstrate the accuracy of the numerical differentiation. It can be observed that gross sliding occurs at 4 seconds after the start of the experiment. Following initiation of significant movement, a large sliding velocity of about 200 mm/s is reached within about 0.1 sec. However, the
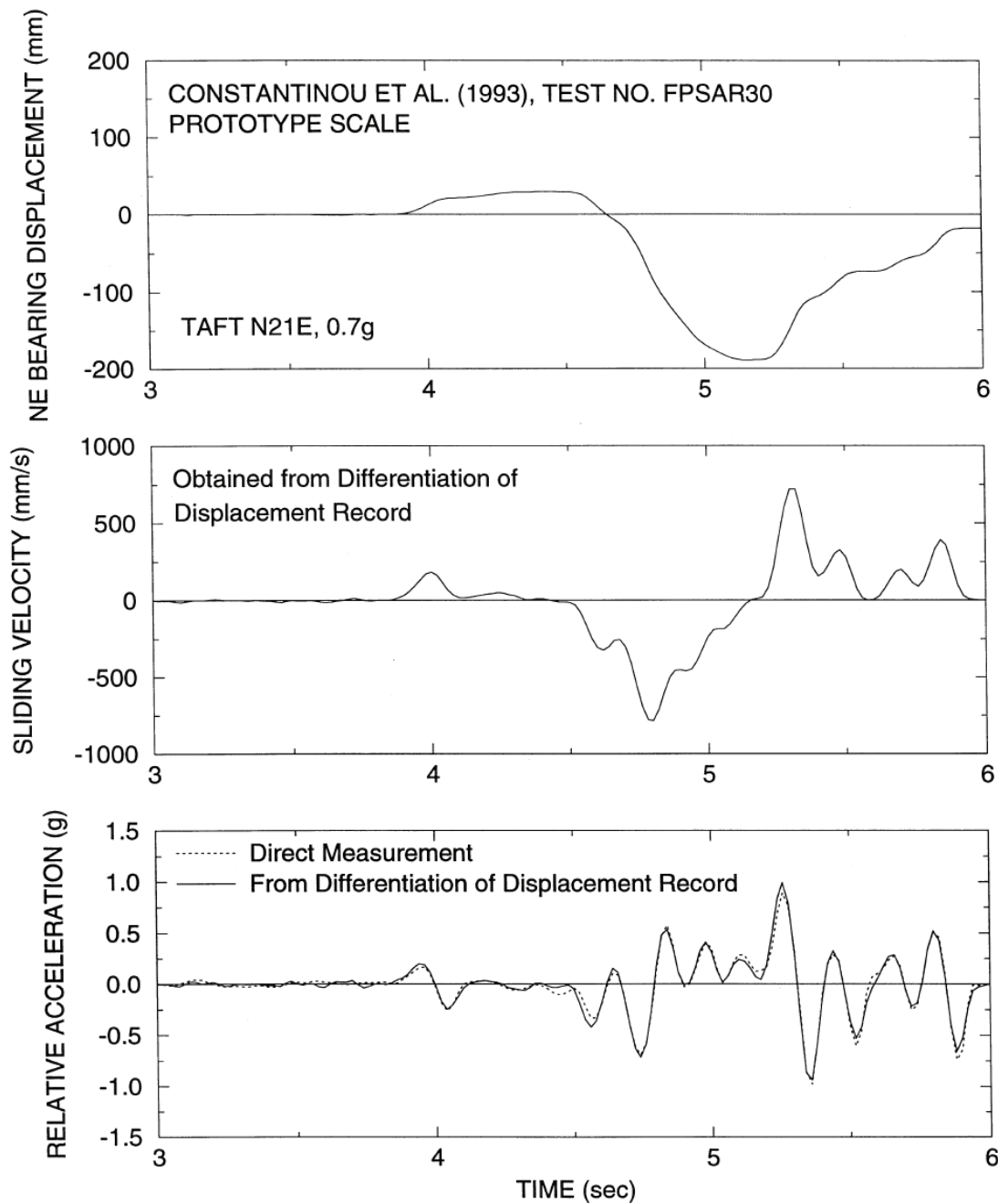
FIGURE 5-4   Recorded Response of Sliding Bearings in Earthquake Simulator Testing of a Model Bridge Structure by Constantinou et al. (1993)

relative acceleration is only about 0.2 g, which is far less than the initial acceleration in displacement controlled, high frequency testing of sliding bearings.

Although not evident in Figure 5-4, sliding at the interface of the isolation bearings occurred well before $t = 4$ seconds. Figure 5-5 shows the responses of the bearings in the time period between 2 and 4 seconds. Sliding displacements of about 0.5 mm are observed starting at $t = 2$ seconds (actual measurement at the scale of the experiment was 0.14 mm with the instrument resolution being at 0.025 mm). The recorded shear force-displacement loop in this time period clearly shows sliding with the breakaway friction coefficient of approximately 0.08. The high velocity coefficient of sliding friction was approximately 0.10. Sliding commences at quasi-static conditions.

The second example is from the earthquake-simulator testing of the same bridge model equipped with a different sliding isolation system (Tsopelas et al., 1994, 1996). Figures 5-6 and 5-7 present the recorded response of one of four flat PTFE bearings (the isolation system consisted of these bearings and rubber restoring force devices) in a test with the S16E component of the Pacoima Dam record from the 1971 San Fernando earthquake. The earthquake history was scaled to a peak acceleration of 0.6 g (peak velocity of 0.73 m/s) at the prototype scale. This earthquake record includes a high velocity shock of near-source characteristics (the recording site was essentially at the surface projection of the rupture).

Motion commences (see the zoomed view in Figure 5-7) occurs at $t = 5.8$ at near static conditions (the peak velocity of 12 mm/s is achieved within about 0.1 second with a peak relative acceleration of about 0.02 g), that is, the breakaway friction force is mobilized at very low relative accelerations. Subsequently, and following momentary stops, conditions of high speed motion are achieved. However, these data show that the high initial value of the breakaway friction measured from sinusoidal tests of bearings in test machines is not developed. Rather, the prevailing friction force is that under sliding conditions, which depends on the velocity of sliding.

The effect of apparent pressure and sliding velocity on the coefficient of friction is as illustrated in Figure 4-8. Note that the breakaway friction coefficient (denoted as μ_B) is shown in this figure to be the value at a velocity of sliding: the value mobilized at initiation of motion under quasi-static conditions. The value of the sliding friction coefficient under very low sliding velocity is denoted in Figure 4-8 as $f_{\min}$. Mokha et al. (1988, 1990) and Constantinou et al. (1990) reported values of the ratio $\mu_B / f_{\min}$ for unfilled and glass filled PTFE in contact with polished stainless steel (surface roughness of 0.03 to 0.04 μm R_a), at temperature of about 20°C, to be in the range of 1.3 to 4.4. Moreover, test data from Campbell et al. (1991) on a variety of PTFE-polished stainless steel interfaces indicate values of the ratio $\mu_B / f_{\min}$ to be in the range of about 2.0 to 7.0.
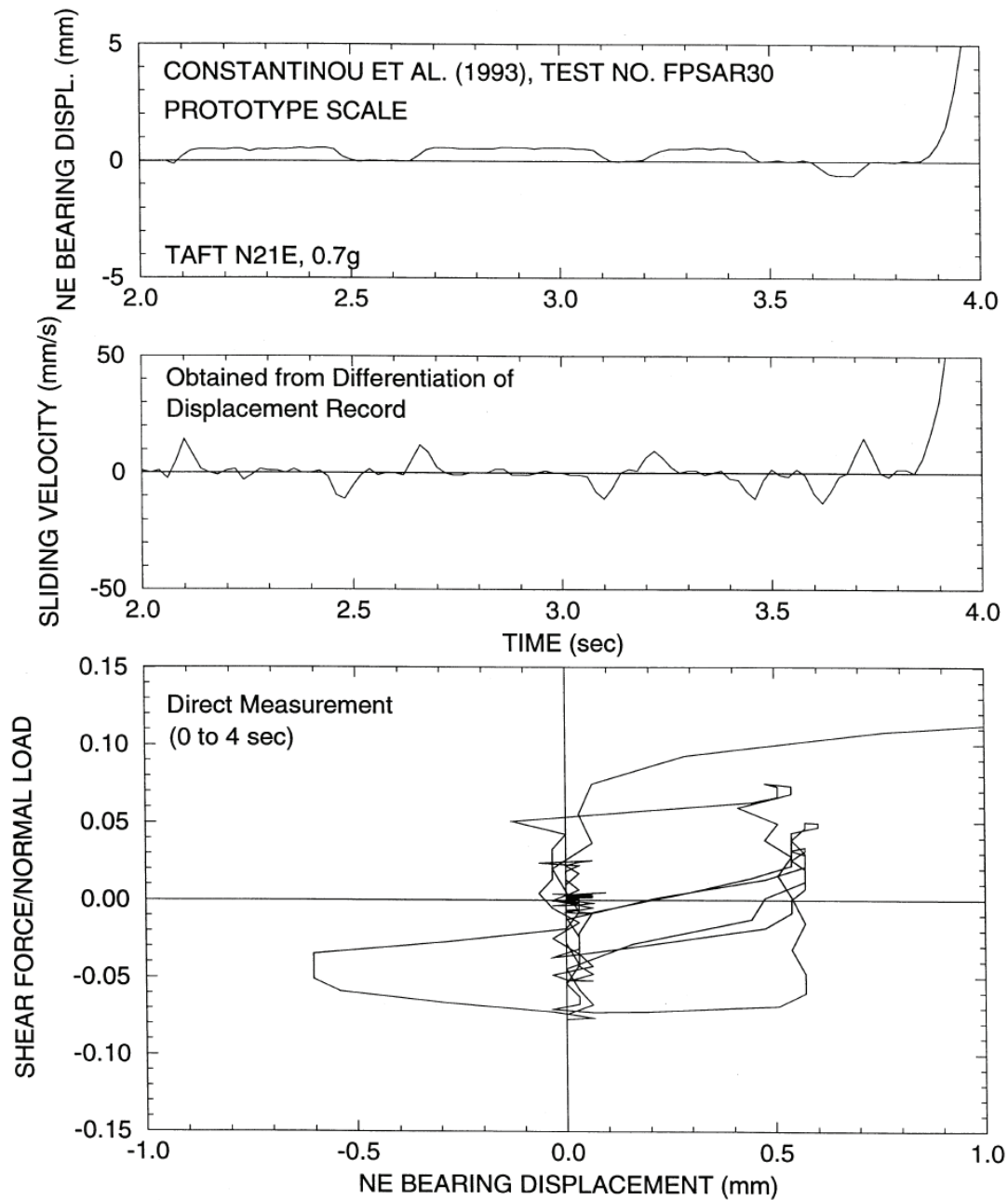
FIGURE 5-5 Recorded Response of Sliding Bearings in the Earthquake Simulator Testing of a Model Bridge Structure by Constantinou et al. (1993)
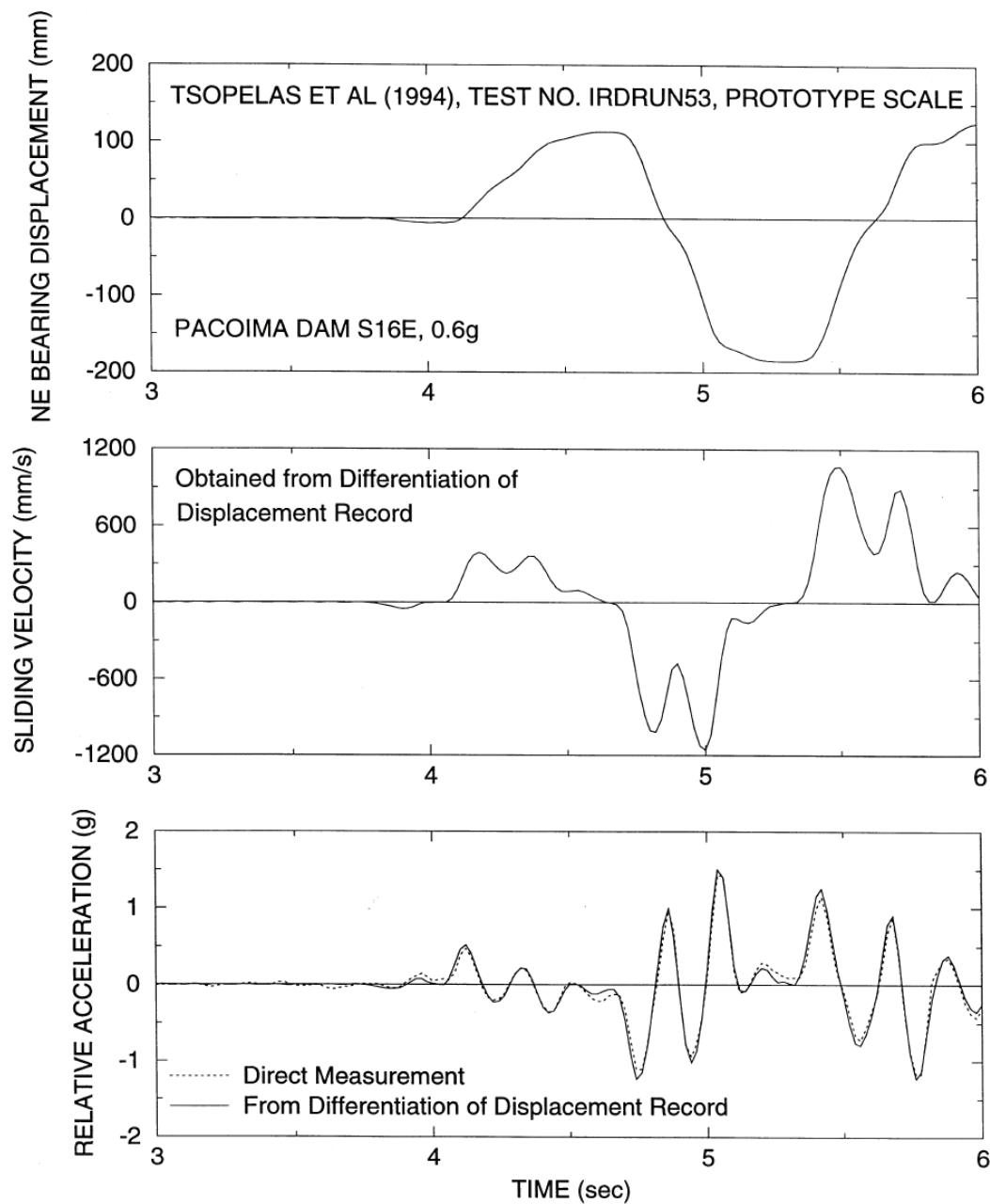
FIGURE 5-6 Recorded Response of Sliding Bearings in the Earthquake Simulator Testing of a Model Bridge Structure by Tsopelas et al. (1994)
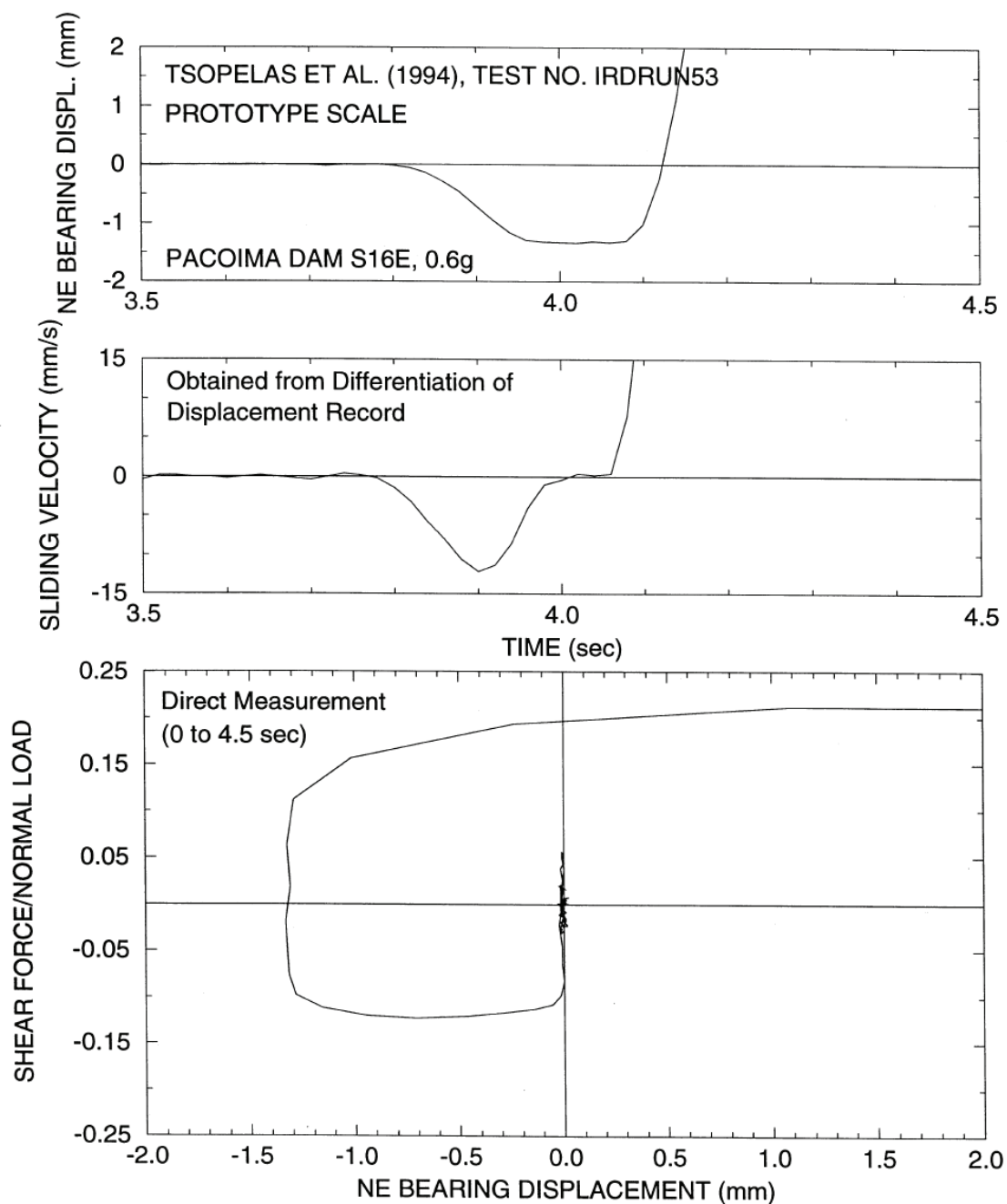
FIGURE 5-7 Snap Shot View of Recorded Response of Sliding Bearings in Shake Table Testing of a Model Bridge Structure by Tsopelas et al. (1994)

105

Mokha et al. (1990) and Campbell et al. (1991) reported data on the frictional properties of woven PTFE, for which values of the ratio μ_B / f_{min} are in the range of 2.0 to 3.0. However, data on the frictional properties of the PTFE composite used in FP bearings (data are reported in Section 5.4 herein where the effect of temperature is discussed) indicate smaller values of this ratio, typically of the order of 1.2. Although we have observed this behavior in many test programs (e.g., Mokha et al., 1990; Constantinou et al., 1993; Al-Hussaini et al., 1994), we are unable to provide an explanation for the observed difference between this material and unfilled and woven PTFE.

Published data in the literature on the frictional properties of PTFE bearings at large sliding velocities is limited. To our knowledge, Tyler (1977) was the first to report such data. Although the focus of his study was the breakaway coefficient of friction at a (unrealistic) high rate of motion, he reported data on the sliding coefficient of friction. These data are in general agreement with the data of Mokha et al. (1988, 1990) who conducted tests for a wider range of conditions.

Figure 5-8 presents data from Mokha et al. (1988) on the sliding coefficient of friction of unfilled PTFE in contact with polished ASTM A240, Type 304 stainless steel (surface roughness of 0.03 μm R_a) at a temperature (at the start of the experiments) of about 20^oC. The data reveal the dependency of this coefficient on the apparent pressure and velocity of sliding. However, the values of the coefficient of friction cannot be regarded as absolute. Rather, the values presented were extracted from the first cycle of testing and it is well established that the coefficient of friction can diminish with increasing travel at high speeds due to the effects of frictional heating. Moreover, specimen size has an effect (typically, slightly lower values are obtained in tests of very large specimens). Finally, there is variability in the recorded values of friction that might be the result of yet unknown effects such as the type of stainless steel (the authors have observed small differences between stainless steels of types 304 and 316) and humidity.

Figure 5-9 presents data on the frictional properties of the PTFE composite used in FP bearings from the tests of Constantinou et al. (1993) and Tsopelas et al. (1994). The values of the sliding coefficient of friction were obtained from the earthquake-simulator testing of a bridge model with either FP bearings (Constantinou et al., 1993) or flat sliding bearings (Tsopelas et al., 1994). The data were extracted from either displacement controlled tests (open circle and square symbols) or seismic motion tests (dark symbols). In all tests the normal load on the bearings was about 35 kN. Note again that the values should be regarded as representative and not absolute.

106
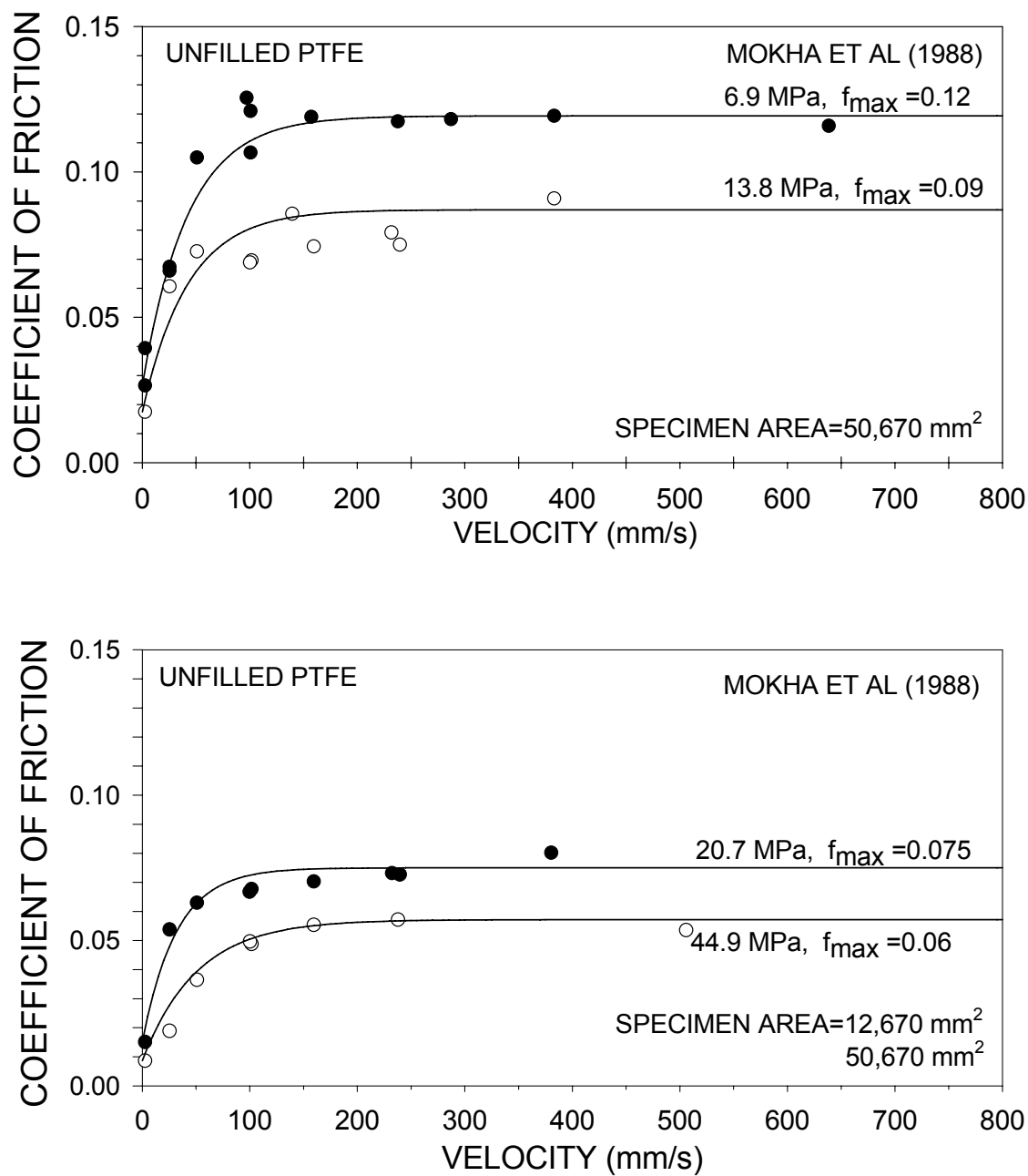
FIGURE 5-8   Coefficient of Sliding Friction of Unfilled PTFE-Polished Stainless Steel Interfaces (0.03 μm Ra), Ambient Temperature of 20°C
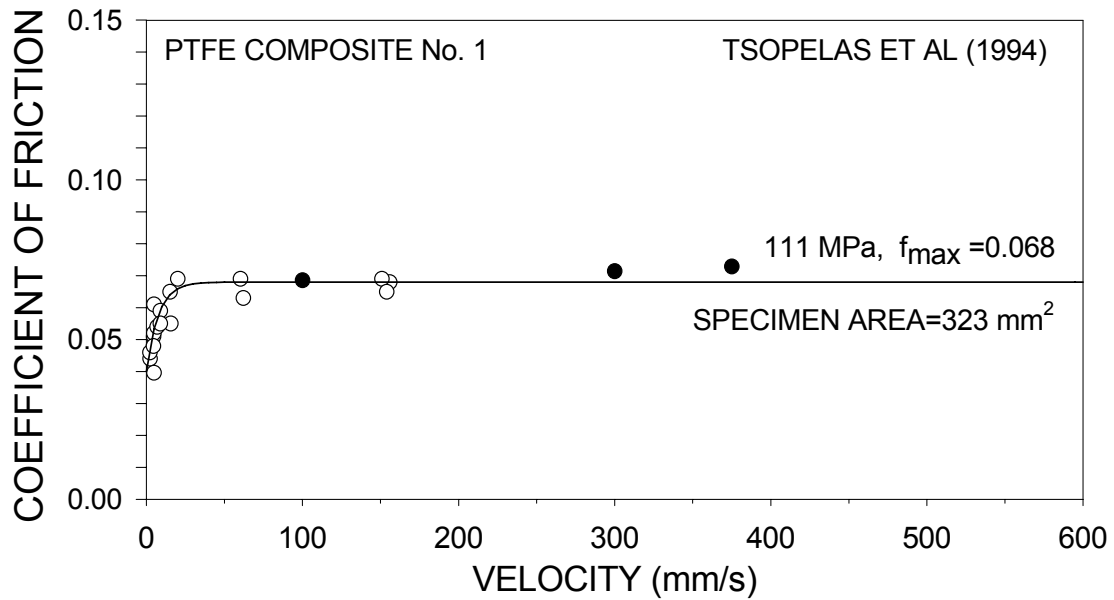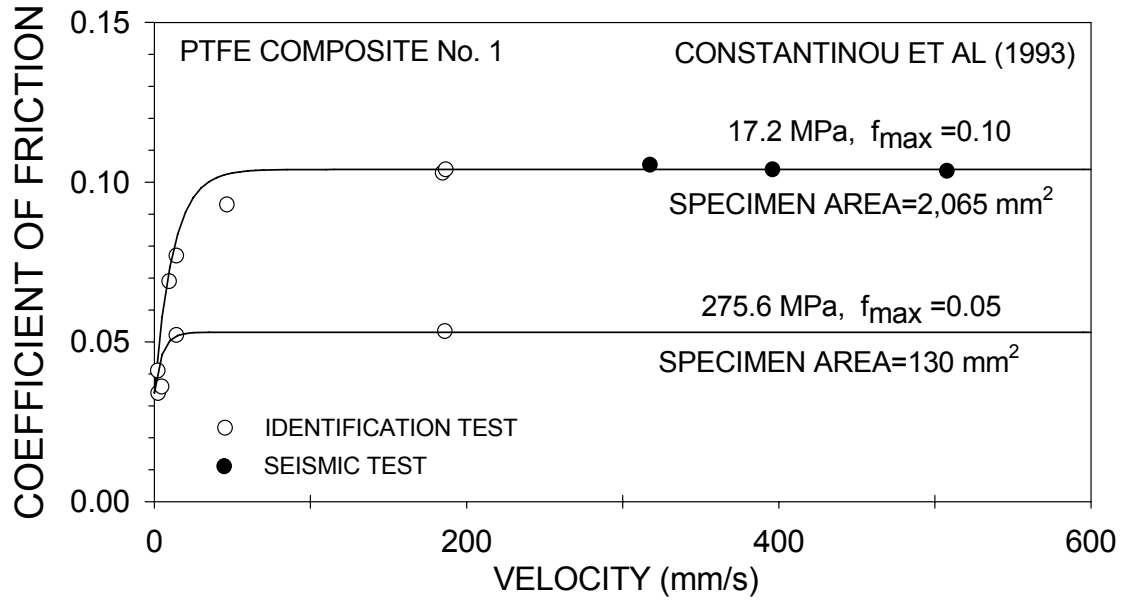
FIGURE 5-9 Coefficient of Sliding Friction of Composite No.1-Polished Stainless Steel Interfaces, Ambient Temperature of 20°C (all tests conducted under normal load of about 35 kN)

In general, for a fixed value of the apparent pressure the sliding coefficient of friction depends on the velocity, V, in a fashion that can be described by (Mokha et al., 1988; Constantinou et al., 1990).

$$\mu = f_{max} - (f_{max} - f_{min})e^{-aV} \qquad (5\text{-}1)$$

where f_{max} and f_{min} are defined in Figure 4-8 and a is a parameter with values of 20 to 30 s/m for unfilled PTFE and about 100 s/m or larger for the PTFE composite. The curves shown in Figures 5-8 and 5-9 are based on (5-1) with values of the parameters (see Mokha et al. 1988; Constantinou et al., 1993, and Tsopelas et al., 1994); (5-1) describes well the observed dependency of the sliding coefficient of friction on velocity.

Parameter a controls the transition of the coefficient of friction from its minimum value to its maximum value at a high velocity of sliding. Figure 5-10 illustrates the effect of parameter a for two values of f_{max} / f_{min} : 2.5 and 5. The smaller value is representative of the PTFE composite and the upper value is representative of unfilled PTFE. Figures 5-8, 5-9 and 5-10 demonstrate that testing at a sliding velocity of greater than about 150 mm/s is sufficient to obtain the maximum value of the sliding coefficient of friction of all PTFE and PTFE-based materials at normal temperatures.
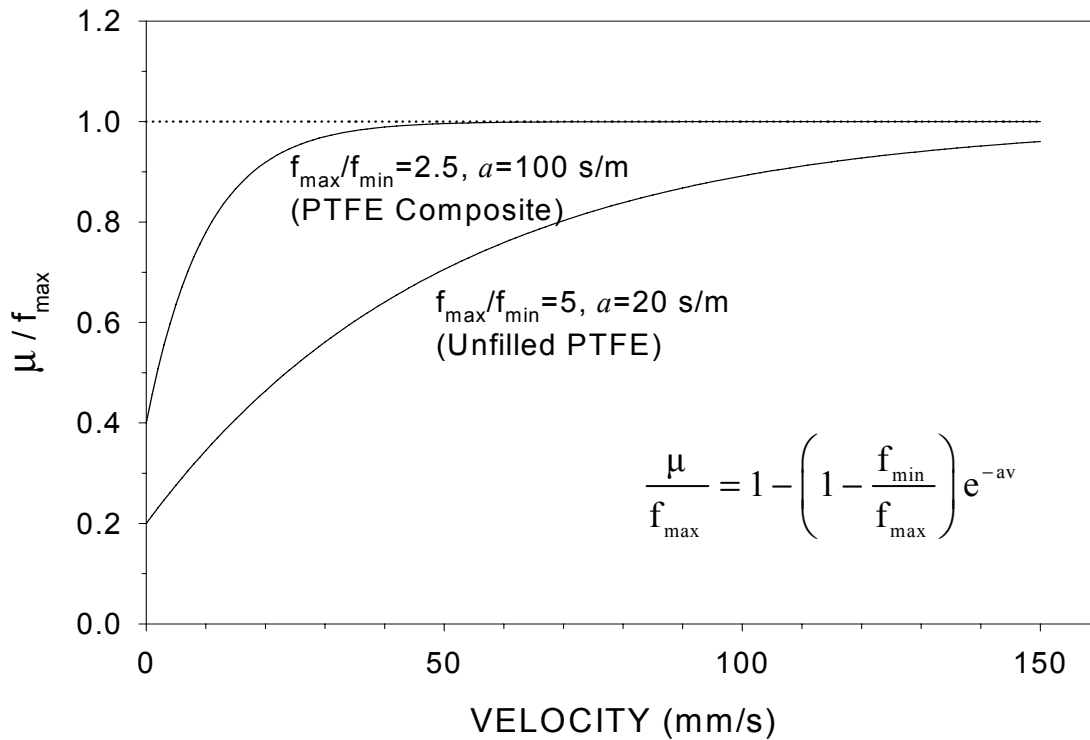
FIGURE 5-10 Effect of Parameter a on Variation of Coefficient of Friction with Velocity

5.4 Effect of Temperature

Campbell et al. (1991) report data on the effect of temperature on the breakaway and the low velocity coefficient of sliding friction of unlubricated unfilled, glass filled and woven PTFE in contact with highly polished stainless steel at an apparent pressure of 20.7 MPa. Table 5-3 presents the results of Campbell et al. (1991) as extracted by the authors from the graphs of Campbell et al. The parameter f_{min} is the sliding coefficient of friction in the first cycle of movement. All tests were conducted at a peak sliding velocity of 1 mm/s. Temperature has a substantial effect on the breakaway and the low velocity coefficients of sliding friction.

TABLE 5-3   Effect of Temperature on the Breakaway and the Sliding Coefficient of Friction (v = 1 mm/s) of Unfilled PTFE in Contact with Highly Polished Stainless Steel at Apparent Pressure of 20.7 MPa (from Campbell et al., 1991).

Temperature ^{o}C	Breakaway Coefficient of Friction	Sliding Coefficient of Friction (v = 1mm/s)
20	0.066	0.016
10	0.125	0.016
0	0.132	0.020
-10	0.149	0.039
-15	0.154	0.057
-20	0.136	0.074
-25	0.157	0.086

We conducted tests on unfilled PTFE and the PTFE composite No. 1 over a wide range of sliding velocities and temperatures in the range of 50^oC to -50^oC using the test fixture of Figure 5-1. Testing was conducted at an apparent pressure of 20.7 MPa for the unfilled PTFE and 69 MPa for the PTFE composite. The stainless steel used in these tests was ASTM A240, Type 304 with a measured surface roughness of 0.03 μm R_a.

Experimental results from this testing program were presented in Appendix A of Constantinou et al. (1999). Each page in that appendix presents the imposed displacement history, the recorded friction force history from the two interfaces and the normalized friction force-to-normal load versus displacement loops for each experiment. Moreover, information on the materials (UF for unfilled PTFE and C1 for the composite PTFE No. 1), apparent pressure, frequency of harmonic motion and temperature at the start of each experiment was presented. The imposed history of displacement is presented in Figure 5-11. The history starts with an idle time in which data acquisition is performed to capture the breakaway friction force in the case of unforeseen movement of the actuator. A build-up time of 60 to 80 sec follows, in which the displacement amplitude, u_0, is reached at a very low sliding velocity (less than 0.8 mm/s). During this part of the imposed motion, measurements of the breakaway and minimum sliding friction (f_{min}) could be made

under truly quasi-static conditions. An idle time of 10 sec was then imposed to allow the temperature at the sliding interface to stabilize. The idle time was followed by 2.25 to 3.25 cycles of harmonic displacement as shown in Figure 5-11.

$$u_o=12.7 \text{ mm}, f=0.0318, 0.318, 1, 2 \text{ Hz}$$
$$u_o=25.4 \text{ mm}, f=2 \text{ Hz}$$
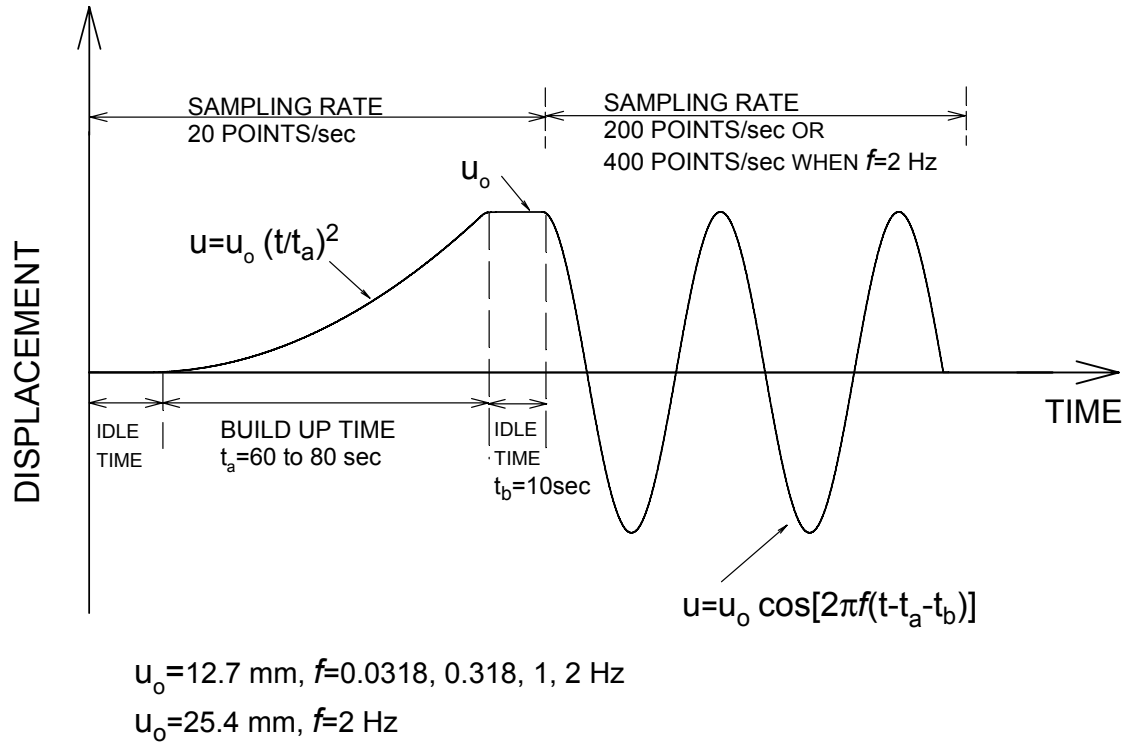
FIGURE 5-11 Imposed Displacement History in Testing of Sliding Interfaces for Determining Temperature Effects on Frictional Properties

The recorded friction force histories in those tests were biased as a result of preloading in the horizontal actuator of the testing arrangement. The amount of preload was determined from the average of the positive and negative normalized friction forces (divided by normal load that slightly varied during testing) at zero displacement in the last cycle of imposed harmonic motion. Once the value of the preload had been established, the normalized friction-displacement loops were adjusted to achieve symmetry as illustrated in Figure 5-12. These loops were then used to obtain the breakaway friction coefficient, the minimum sliding friction coefficient (f_{min}, at a velocity of less than 0.6 mm/s), and the sliding coefficient of friction at the first instant at which the largest velocity of sliding was attained (typically after 12.7 mm or 25.4 mm of travel) as shown in Figure 5-12.

Constantinou at al. (1999) presents a complete set of results on the testing of unfilled PTFE at temperature of about –40°C (tests UF-TEST58 to UF-TEST62). Of those, test No. 58 was conducted on new specimens of PTFE with a clean stainless steel plate. The specimens were loaded with a normal load of 147 kN at 4 pm on February 1, 1995, and were continuously maintained under load until testing on February 14, 1995 (load dwell of 311 hours). At 10 am on that day the insulating box around the testing arrangement

111
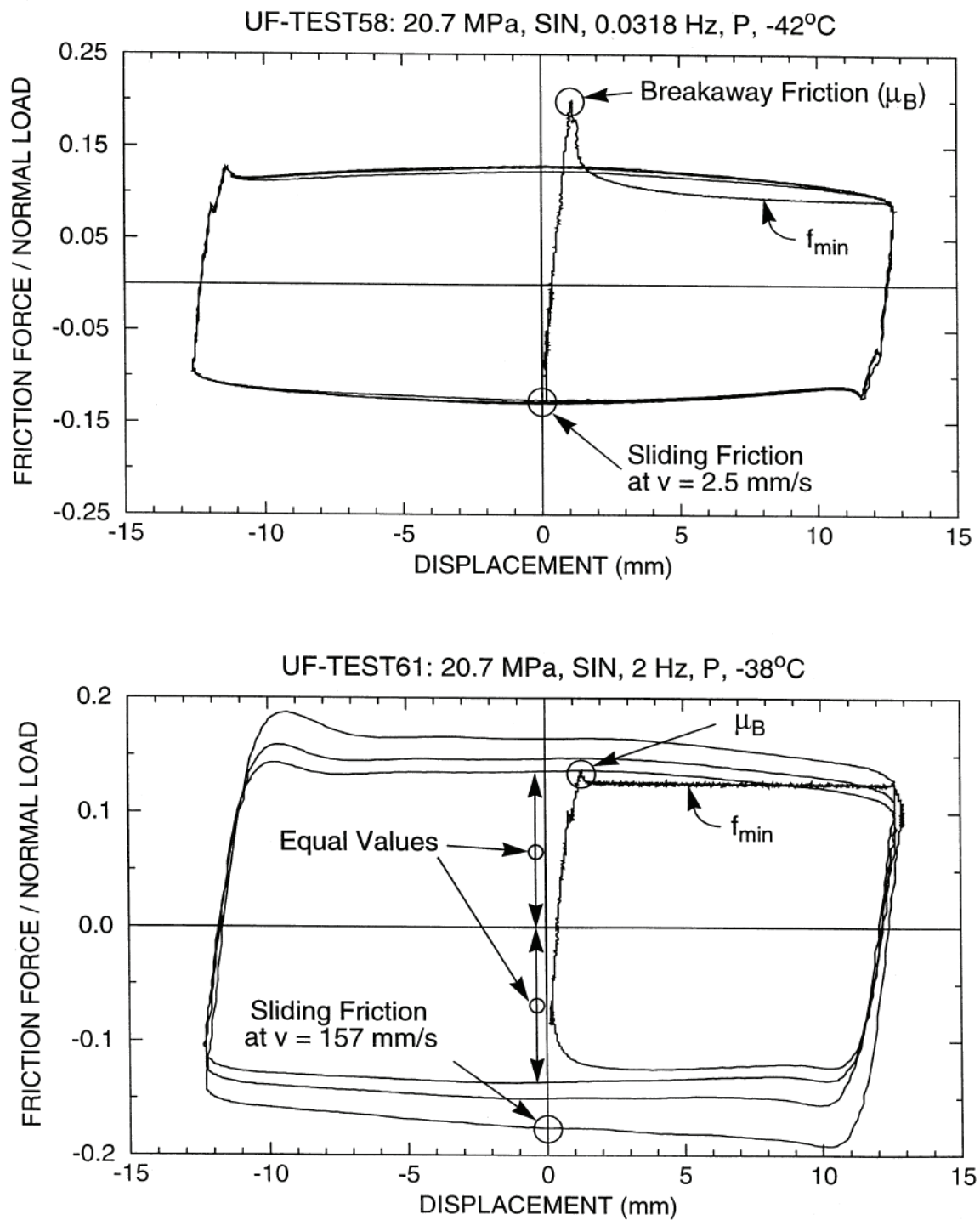
FIGURE 5-12 Example of Determination of Frictional Properties

was filled with sealed bags containing solid carbon dioxide (dry ice). Following five hours of conditioning, the temperature was stable at –42°C and test No. 58 was conducted. At the conclusion of the test, the temperature had increased to –32°C. The specimen was left undisturbed for one more hour until the temperature reached –39°C and then test No. 59 was conducted (note that during testing the insulating box was filled with sealed bags of dry ice including some directly on the moving plate except for a 30 mm strip around the specimen). This procedure was repeated for a total of nine tests and then a new specimen was installed.

For testing at elevated temperatures, heating elements were installed around the testing arrangement and directly on the moving plate.

Testing of the unfilled PTFE material was conducted during the months of January and February 1995. During this period the average conditions in the laboratory were 22^oC and 20 percent relative humidity. The PTFE composite material was tested in April and May 1995 when the average conditions were 22^oC and 25 to 40 percent relative humidity. However, for the low temperature tests, the relative humidity in the insulated box was extremely low.

It can be observed from the results of Constantinou et al. (1999) that at very low temperature and for the high frequency tests, the loops exhibit higher friction on reversal of motion during the first cycle. Particularly, the friction is highest at initiation of the harmonic portion of the imposed motion. In some of the tests (e.g., tests UF-TEST 59 to UF-TEST 62) the friction force on initiation of the harmonic motion is essentially constant and independent of the characteristics of the imposed motion (e.g., in these tests the peak velocity varied between 25 mm/s and 320 mm/s). This observation can be interpreted as breakaway friction following the brief (10 second) stop (see Figure 5-11), albeit influenced by the dynamic conditions at initiation of motion. In the presentation that follows, the value of friction at the initiation of motion (and at each reversal of motion) has not been used. Rather, the value at the first instant of peak velocity (see Figure 5-12) is used for the following reasons:

a) The reported value is truly the sliding value at some known velocity and following some small travel.
b) There is design-professional interest in using (5-1) to describe the dependency of the sliding coefficient of friction on velocity. However, at low temperatures, the maximum value of sliding friction, f_{max}, occurs not at a high sliding velocity but rather at relatively low velocities (see Figure 4-11) at which the friction on initiation of harmonic motion is essentially the same as the sliding value (e.g., see test UF-TEST 60).
c) The interest is primarily in establishing values of the ratio of parameter f_{max} at various temperatures and at a reference temperature (20^oC), which will be used for defining property modification factors (λ) for temperature. We will use values of f_{max} that occur at different velocities to establish these ratios: a conservative approach. For example, consider that the λ factor for a temperature of –40^oC is established from the ratio of the values of f_{max} at –40^oC and 20^oC.

113

Based on the results of Appendix A of Constantinou et al. (1999) for unfilled PTFE, f_{max} are 0.178 at -39^oC (test No. 60 at velocity of 80 mm/s) and 0.113 at 22^oC (test No. 43A at velocity of 320 mm/s). The ratio of the values of f_{max} is $0.178/0.113 = 1.58$. This will be the value reported for λ. Alternatively, if we use the values of f_{max} at the reversal of motion: f_{max} at -40^oC is 0.189 (test No. 62) and at 22^oC is 0.118 (test No. 43A) for a value of $\lambda = 0.189/0.118 = 1.60$: essentially the same value as before.

Figures 5-13 to 5-15 present data on the effect of temperature on the frictional properties of unfilled, unlubricated PTFE. Figure 5-13 presents the breakaway coefficient of friction as measured in the various tests. Temperatures are reported in the range of -40^oC to 50^oC: the temperature at the start of each experiment, rounded to the nearest multiple of ten. For each of the first tests in each sequence, the load dwell in hours is shown next to the data point. Each of the subsequent tests was conducted after a load dwell of less than one hour.

Figure 5-14 presents the measured breakaway friction, the minimum sliding friction, f_{min}, and the sliding friction at three different velocities as function of the temperature at the start of each experiment. The figure demonstrates the substantial effect of temperature on the low velocity coefficient of friction, f_{min}, and breakaway coefficient of friction and the limited effect on the high velocity coefficient of friction. The latter is clearly the result of frictional heating. The values of friction in this figure are consistent with those reported by Campbell et al. (1991); see Table 5-3. For example, the values for the sliding coefficient of friction at very low velocity (f_{min}) in Figure 5-14 are 0.016 to 0.03 at 20^oC and about 0.09 (interpolated) at -25^oC. Campbell et al. (1991) report values of 0.016 and 0.086, respectively.

Figure 5-15 presents the measured coefficient of friction as function of sliding velocity for various temperatures at the start of each experiment (rounded to the nearest multiple of ten). When data points for the same temperature are connected by a curve, as presented in the figure for two cases, a clear picture of the effect of temperature emerges. For example, between the temperatures of 20^oC and -40^oC, we observe a 4 to 5 fold increase in the breakaway and low velocity coefficients of sliding friction (f_{min}) but only about a factor of 1.6 increase in the high velocity value (f_{max}). Note that at a sufficiently large velocity, the temperature at the start of the experiment has a minor effect on friction because of frictional heating.
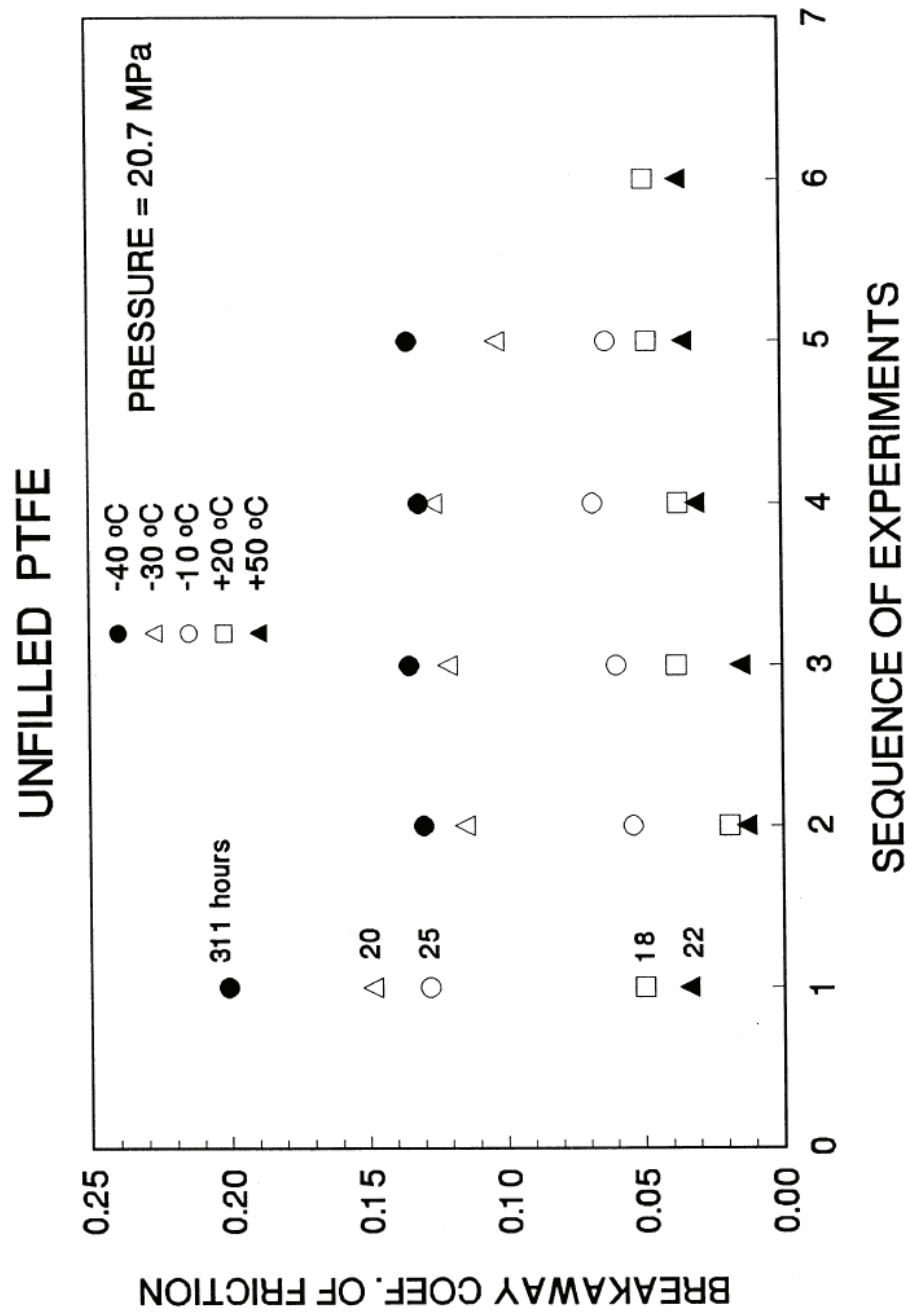
FIGURE 5-13 Breakaway (or Static) Friction of Unfilled PTFE-Polished Stainless Steel Interfaces as Function of Temperature and Sequence of Testing
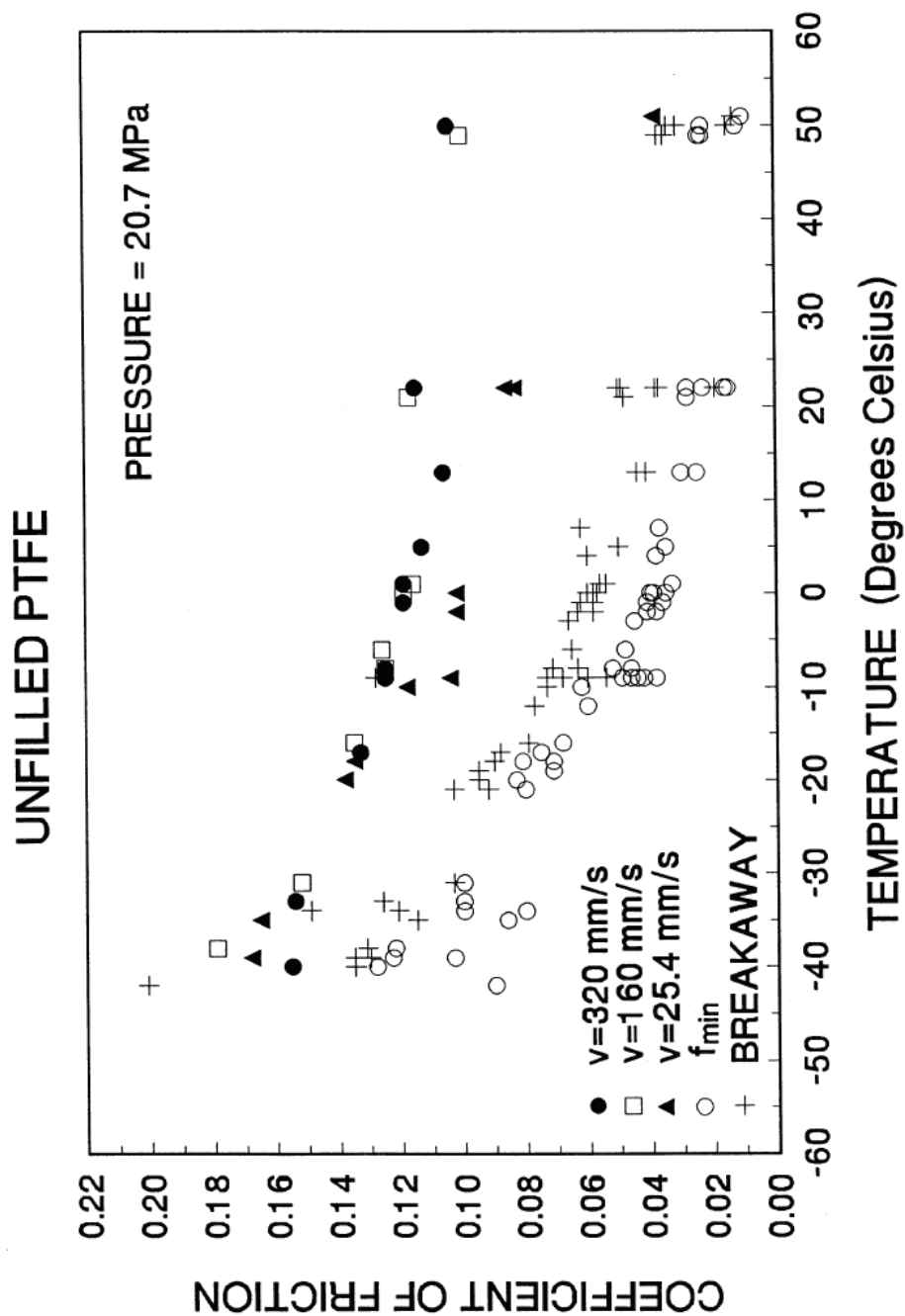
FIGURE 5-14   Friction of Unfilled PTFE-Polished Stainless Steel Interfaces as Function of Temperature

FIGURE 5-15   Friction of Unfilled PTFE-Polished Stainless Steel Interfaces at Various Temperatures as Function of Sliding Velocity

Since we have now a theory to predict the temperature rise due to frictional heating (section 4.8), it is instructive to perform some representative calculations. Consider the test at which the f_{max} was determined at temperature of -40°C. In Figure 5-15, the data point is associated with a velocity of about 80 mm/s. In this test, the imposed amplitude was 12.7 mm at a frequency of 1 Hz. The value of f_{max} was recorded after a quarter cycle of motion, that is, at time $t = 0.25$ second. The motion is equivalent to one of constant velocity $v_c = 0.051$ m/s. Using $\mu = 0.18$, $p = 20.7$ MPa and the thermal properties of steel that are appropriate for about -30°C (see Table 4-1 and Lide, 1993 for further information), and using (4-21) and (4-29), we calculate a surface temperature rise of about 16°C. Repeating the calculation for the same temperature and the highest velocity (test at frequency of 2Hz and amplitude of 25.4 mm), we have $t = 0.125$ sec, $v_c = 0.20$ m/s, $\mu = 0.16$ and the surface temperature rise is about 35°C: a temperature rise that is sufficiently large to affect the frictional properties.

Figures 5-16 to 5-18 present data on the effect of temperature on the frictional properties of the PTFE-based composite. After comparing these results to those for unfilled PTFE, we make two observations:

a) The breakaway friction is nearly the same as the low velocity sliding friction (f_{min}).
b) The effect of temperature is, in general, much less than in the case of unfilled PTFE.

An explanation for the smaller effect of temperature is related to the generated heat flux. Friction in the composite material is about half that of the unfilled PTFE, whereas the apparent pressure is 3.3 times larger. Given that the imposed motions were identical, the heat flux (see 4-29) in the test of the composite material was about 1.7 times greater than that for the unfilled PTFE. However, the measurements of the temperature rise, which were made using a thermocouple embedded in the stainless steel plate, were much less than those recorded for identical motions in the testing of unfilled PTFE. Therefore, there must have been a substantial heat flux into the composite material, whereas in the case of unfilled PTFE nearly all of the generated heat was supplied to the stainless steel surface. The main reason for this must have been the very small thickness of the composite material (0.25 mm, which was selected on the basis of considerations for wear for the wear tests that followed the temperature testing). The results for the composite material must be viewed in this light. It is likely that the effect of temperature for thicker materials (as those expected to be used in bridge applications) will be larger than what is shown in Figures 5-16 to 5-18.
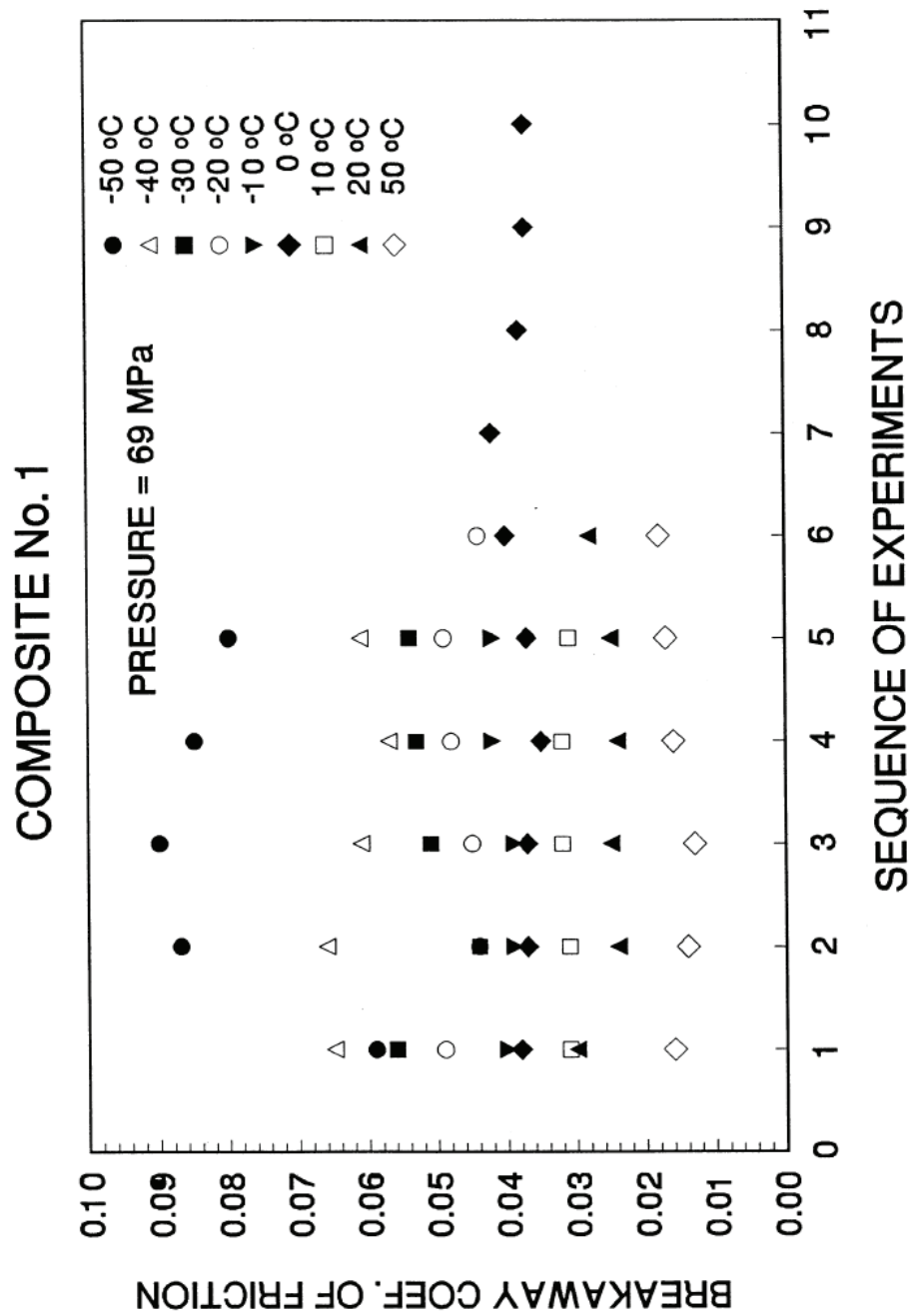
FIGURE 5-16 Breakaway (or Static) Friction of PTFE-based Composite-Polished Stainless Steel Interfaces as Function of Temperature and Sequence of Testing
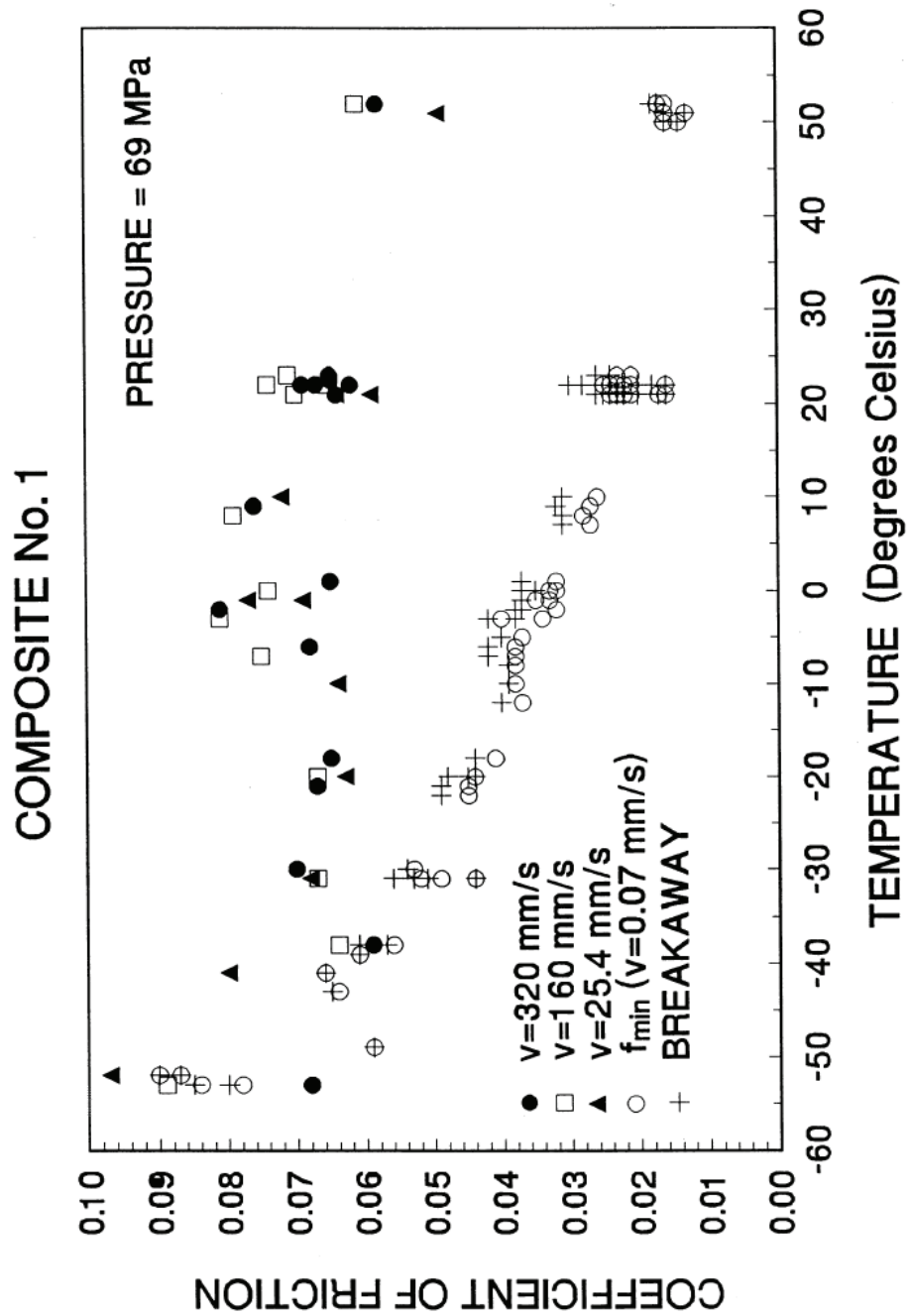
FIGURE 5-17   Friction of PTFE-based Composite-Polished Stainless Steel Interfaces as Function of Temperature

120
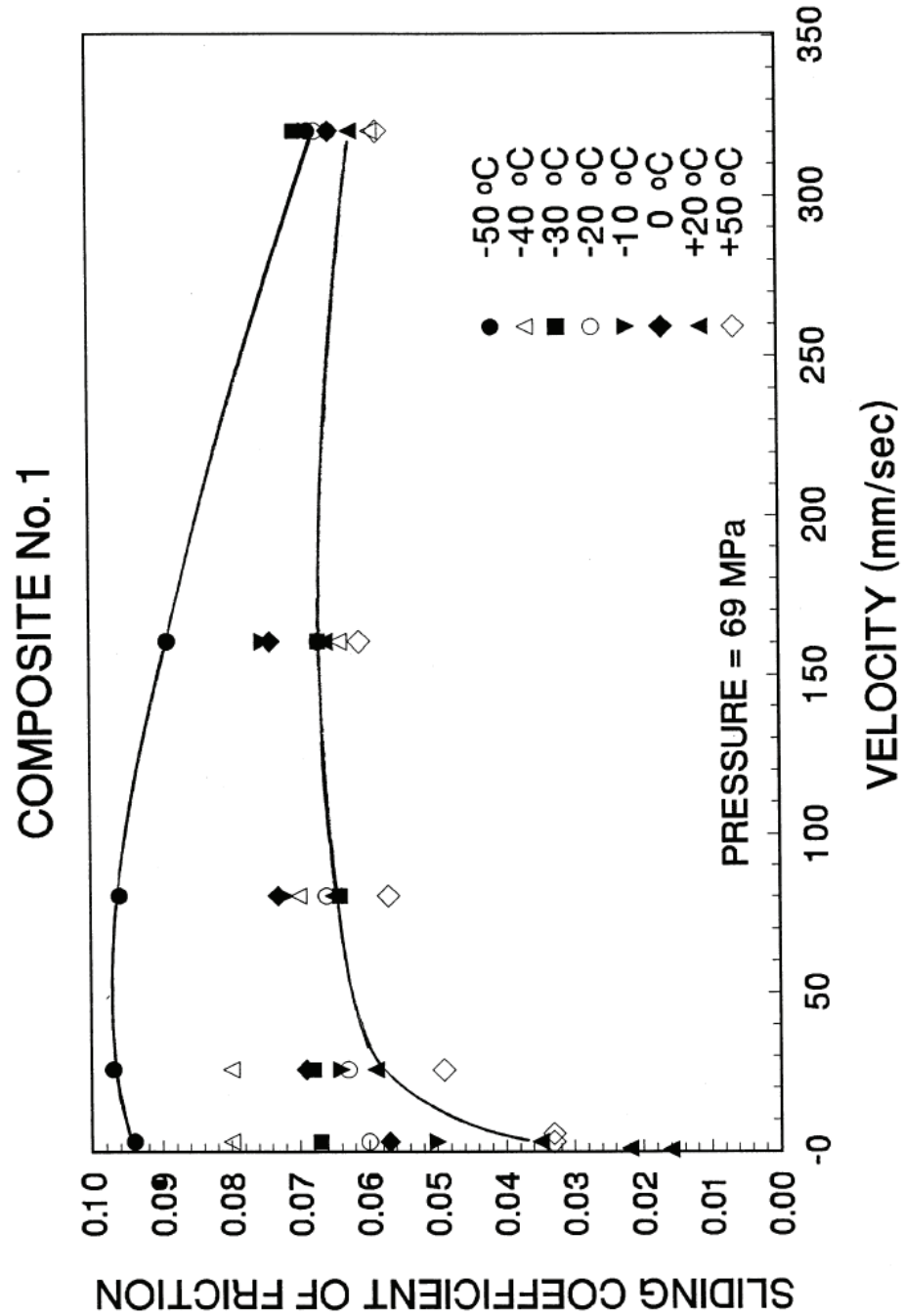
FIGURE 5-18 Friction of PTFE-based Composite-Polished Stainless Steel Interfaces at Various Temperatures as Function of Sliding Velocity

121

5.5 Effect of Cumulative Movement

A review of the literature on the effect of cumulative movement (travel) on the coefficient of friction of PTFE-stainless steel interfaces produced conflicting results. The report of Campbell and Kong (1987) contains two figures (Figures 21 and 23) that show a substantial increase in the low velocity coefficient of sliding friction with cumulative travel: a 3 fold increase over a travel of 20 km. Although not mentioned in the report, the results are for lubricated bearings and are of German origin. A more detailed presentation of such results can be found in Kauschke and Baigent (1986) and Eggert and Kauschke (2002), who document the effect of travel of up to 20 km and temperature in the range of $20^{o}C$ to $–35^{o}C$ on the coefficient of sliding friction at low velocity (0.4 to 2.0 mm/s) for lubricated PTFE-stainless steel bearings. The stainless steel (type X5CrNiMo 1810) is equivalent to ASTM 240, Type 316; test results are presented for polished and as-rolled (rough) stainless steel.

Kauschke and Baigent (1986) also present results for unlubricated bearings, of which one set of results apply for Polyoxymethylene (a form of acetal plastic) in contact with PTFE (the results for this case are presented in Campbell and Kong, 1987, as Figure 7, without mentioning the nature of the interface) and another for polished, Type 316 stainless steel (respectively, Figures 9 and 10 in Kauschke and Baigent, 1986). The first set of results is of no interest whereas the results of the second set apply for temperature of $21^{o}C$, an apparent pressure of 30 MPa and a travel of 2 km. The sliding coefficient of friction changed little (0.05 to 0.06) for this travel.

Long (1969, 1974) reported on the effect of travel on the friction of unlubricated PTFE-polished stainless steel interfaces at an apparent pressure of 24 MPa. The stainless steel was highly polished (0.05 μm arithmetic average). Periodic constant velocity motion was imposed at an amplitude of 25 mm and a velocity of 2.5 mm/s for a total travel of just over 5 km. Long reported the static coefficient of friction that should be interpreted as the friction upon reversal of motion. Excluding the higher value on initiation of motion (the breakaway value), the reported value is essentially the same as the value of the sliding coefficient of friction. Long reported a value of the breakaway coefficient of friction of 0.017 that dropped to 0.010 after short travel (50 m) stabilized at 0.008, and dropped to 0.007 after 5 km of travel.

The results of Long (1969, 1974) differ from those of German origin (reported by Kauschke and Baigent, 1986) in two respects:

   a) The values of friction for approximately the same values of apparent pressure (24 to 30 MPa) and sliding velocity (2.0 to 2.5 mm/s) are substantially different (about 0.05 in the German origin tests and about 0.01 in the tests of Long). This substantial difference might be the effect of specimen size (typically 75 mm diameter in the German tests and about 20 mm in the tests of Long) but more likely the composition and surface condition of the stainless steel. Long (1969) obtained and tested the German steel and observed a higher surface roughness

122

(about 0.18 μm arithmetic average) and substantially higher friction values than those of his tests.

b) The results of Long demonstrate a reduction of friction with increasing travel, whereas the results of German origin demonstrate the opposite trend. There is notapparent explanation for this difference. Possibilities are the effect of composition and surface roughness of the stainless steel and the effect of frictional heating. It is not known whether the temperature at the sliding surface was monitored in either test program and whether measures were taken to prevent temperature rise (e.g., by conducting intermittent testing).

Regardless of these differences, both sets of results show rather small changes (either increases or decreases) of the low velocity coefficient of friction with travel in the range of 2 to 5 km. Campbell et al. (1991) reported test results on unfilled PTFE in contact with highly polished stainless steel at various apparent pressures and temperatures that show marked increases in the low velocity coefficient of friction after short travel. Testing was conducted with 75 mm diameter specimens using periodic constant velocity motion of 12.5 mm amplitude and 1 mm/s velocity. Typically, the initial coefficient of friction was high (the breakaway value); the coefficient of friction then dropped and remained stable until the cumulative travel equaled about 10 m after which it increased. For example, at temperature of 20°C and an apparent pressure of 20.7 MPa, the friction was stable at 0.015 for travel up to 10 m and then gradually increased to 0.025 at a travel of 15 m. Moreover, at temperature of –10°C the friction was stable at 0.030 up to a travel of 5 m but rapidly increased thereafter to a value of 0.072 at the travel of 25 m. These increases are disappointingly large for a very short travel distance. These results contradict those of Long (1969, 1974) and of German origin as reported by Kauschke and Baigent (1986). Clearly, there is a need for further study of the effects of cumulative movement.

In an attempt to provide further information on the effect of cumulative movement, we conducted testing of two interfaces, one of unfilled PTFE and the other of PTFE composite, for travel up to 500 m. The testing was conducted with the arrangement of Figure 5-1 and used periodic constant velocity motion of 6.4 mm amplitude and a velocity of either 0.8 or 2.4 mm/s. This range of velocities is consistent with the conditions of testing in earlier studies (about 2.0 to 2.5 mm/s in the German tests and in Long, 1969, and 1 mm/s in Campbell et al., 1991). Furthermore, it is consistent with field observations (Muller-Rochholz et al., 1986a, 1986b) and calculations.

At this point it is of interest to present sample calculations. Bearing movement is primarily caused by traffic and secondarily by temperature changes. Extreme temperature changes are too rare to be of any significance in the calculation of cumulative movement. Rather, a more representative temperature change for such calculation is the difference between the average high and the average low temperature over a specific period of time and a particular location. Utilizing widely available data for the United States, the difference between the monthly average high and average low for most locations is approximately 20°F. It is reasonable to consider this value to be, on the average, the temperature change within a day. Considering steel girder bridges and a representative

span of 100 feet (30.5 m), the cumulative movement in 30 years of service is about 90 m. This travel is insignificant by comparison to the one induced by traffic.

Estimating the bearing movement caused by traffic is difficult. However, for certain types of bridges one can obtain a reasonable estimate of the movement. Steel girder (I-beam) bridges are typically designed to have a beam depth, d, to span length, L, ratio of about 1/30 (here the span length is considered to be the distance between the inflection points under dead load). Moreover, the beams are designed to have a maximum deflection, Δ, under live load (including lateral distribution and impact) of about 1/1,000th of the span length (Xanthakos, 1994). To obtain the average bearing movement, we exclude the lateral distribution and impact effect and compute a value $\Delta/L = 1/1500$. The relationship between maximum support rotation, θ, and maximum deflection is $\theta = \alpha\Delta/L$, where α is approximately 3.0 for single span girders and less for continuous multi-span girders (for example, a two span equal length girder loaded in one span has a value of approximately 2.5). Moreover, the bearing movement has an amplitude $u = \theta d/2$.

A conservative estimate of the average bearing amplitude of movement in a single crossing is obtained using $\alpha = 3.0$:

$$u = \frac{L}{30,000} \qquad (5\text{-}2)$$

The cumulative movement u_T is

$$u_T = \left(\frac{L}{15,000}\right) \times C \times H \qquad (5\text{-}3)$$

where C is the number of crossings per hour and H is the total number of hours. Furthermore, an estimate of the velocity of movement v can be obtained by assuming that the time to traverse the span length L is L/v_T, where v_T is the average speed of traffic. Accordingly,

$$v = \frac{v_T}{15,000} \qquad (5\text{-}4)$$

Considering a typical span length of 100 feet (30.5 m) and an average speed of traffic of 60 km/h, we calculate $u \sim 1$ mm and $v \sim 1$ mm/s. To estimate the cumulative movement, we consider 30 years of service and 10 crossings per hour (these are crossings of the full traffic load) to obtain $u_T = 5.3$ km. This estimate depends largely on the assumed number of crossings per hour. Moreover, a portion of this movement could be consumed as deformation of the bearing itself (rather than just sliding). Nonetheless, on average, the velocity of movement is of the order of 1 mm/s and the cumulative movement is large and of the order of several kilometers. The European Standard on Structural Bearings EN1337 (European, 2004) describes a *Long Term Friction Test* for sliding bearings for

124

which the cumulative travel is 10.2 km. This test is conducted on a small scale specimen (contact area of 75mm diameter) as part of a qualification program for sliding bearings. The test is conducted at an apparent pressure of 30 MPa, a peak velocity in the range of 0.4 to 3.8 mm/sec and a fluctuating temperature in the range of 35 to -35°C, with the nearly 98% of the total travel conducted at the temperature of 21°C. Larger cumulative travel tests were conducted in Germany using the same history of travel and temperature as the EN1337 test but with a total travel of over 20 km. The interested reader is referred to Eggert and Kauschke (2002) for these results for lubricated PTFE in contact with stainless steel.

Testing for the effects of cumulative movement on friction was conducted with periodic constant velocity motion of 0.8 mm/s for a travel of about 260 m, followed by a motion at velocity of 2.4 mm/s for an additional travel of about 240 m: a velocity that is consistent with the expected average conditions in steel girder bridges, however, the cumulative movement is representative of about 3 years of service for such bridges. Testing of the PTFE composite was conducted first. The apparent pressure was 69 MPa. Figure 5-19 presents test results that were obtained as follows

    a) Three cycles of periodic constant velocity motion of 0.8 mm/s were imposed and measurements of the sliding friction were made. This test was conducted in intervals following travel of between 5 and 25 m. The measured values of friction are shown in the figure with square symbols. Each of these tests was conducted immediately following the interruption of motion so that the sliding interface was at a temperature higher than the starting temperature of 24°C. Measurements of the temperature by the thermocouple embedded in the steel plate were about 28°C.

    b) A high velocity test was conducted at intervals following travel of 25 m. The test consisted of a displacement history as shown in Figure 5-11 with $u_0 = 12.7$ mm and frequency of 2 Hz. The test allowed for the measurement of the very low velocity coefficient of sliding friction, f_{min}, and the sliding friction at a velocity of 160 mm/s (as described in section 4.4). The measured values of friction are shown in the figure with circular and triangular symbols. Some of these tests were conducted after some idle time so that the temperature at the sliding interface, as monitored by the embedded thermocouple, was at about 24°C (dark symbols), whereas the rest were conducted without idle time so that the temperature at the start of each experiment was higher, typically about 28°C.

During testing and following a cumulative movement of about 125 m, it was detected that part of the normal load as applied by the hydraulic ram (see Figure 5-1) was not directly transferred to the specimen. The cyclic motion was interrupted and without unloading the specimen, the connection to the reaction frame was released (see Figure 5-1), which resulted in a drop in the load measured by the load cell in the hydraulic ram by 15 percent (from 146.7 kN to 124.7 kN). Accordingly, the measured values of friction up to the cumulative movement of 125 m were about 83 percent of the actual values. That is, the initial value of the high velocity friction is not 0.064, as shown in Figure 5-19 but rather
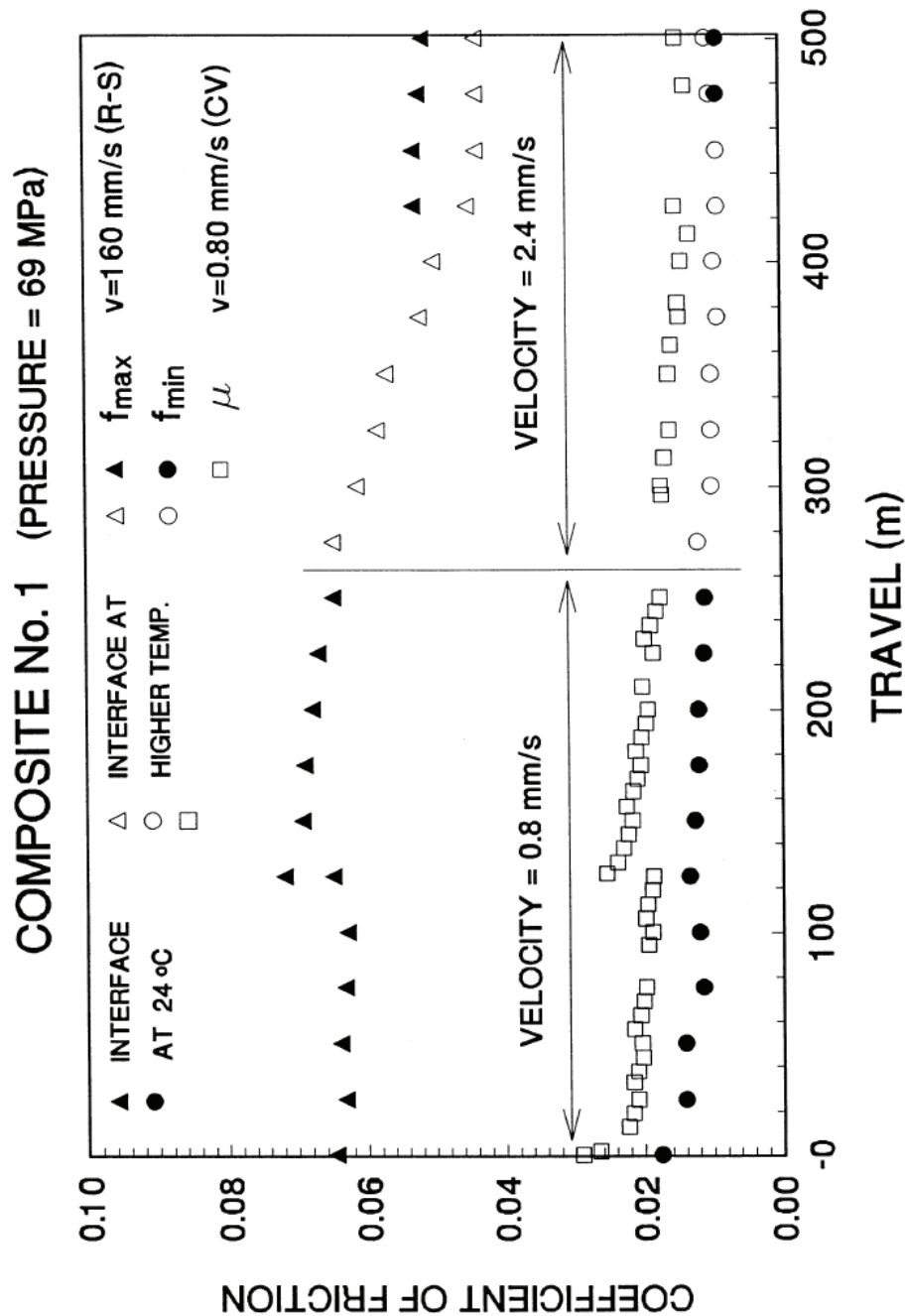
FIGURE 5-19 Effect of Cumulative Movement (Travel) on Sliding Coefficient of Friction of PTFE Composite in Contact with Polished Stainless Steel

0.075. The problem was corrected by increasing the normal load to the appropriate value, connecting the loading plate to the reaction frame and restarting the experiment. The data, following correction for the aforementioned problem with the normal load path, demonstrate that the coefficients of sliding friction at very low velocity and at some representative high velocity reduce with increasing cumulative movement and appear to stabilize after a 500 m of travel. The initial value of f_{max} was 0.075 and it stabilized at about 0.052, that is, the reduction is about 30 percent.

A similar test was conducted on unfilled PTFE specimens at apparent pressure of 20.7 MPa. The results are presented in Figure 5-20. In this case, measurements of the sliding friction were obtained for a range of very low velocities and again at a velocity of 160 mm/s. All of the results were obtained at a temperature of $24^{o}C$ at the start of each test (idle time was imposed until the embedded thermocouple recorded a temperature of about $24^{o}C$). Figure 5-21 presents three recorded loops of normalized friction force versus displacement for the high velocity tests (per Figure 5-11 and a frequency of 2 Hz) following travel of 0.5, 254 and 510 m.

The results of Figure 5-20 demonstrate that the coefficient of sliding friction, in general, reduces with increasing travel and that after a travel of about 300 m it shows a mild tendency to increase. The low velocity coefficient of sliding friction exhibits fluctuations in the travel range of 0 to 40 m. The initial value of the high velocity coefficient of sliding friction is 0.125 but drops to 0.100 after 40 m of travel (interestingly, this value is also attained after a travel of 510 m), the low velocity coefficient of friction shows a sharp increase for a travel of less than 15 m: consistent with the results of Campbell et al. (1991).

In summary, the available data on the low velocity friction of unfilled PTFE in contact with stainless steel are either of German origin and show a mild increase over a travel of 2 km or are of British origin (Long, 1969) and show a reduction over a travel of 5 km. It is likely that the difference is due to differences in the roughness and composition of the stainless steel plates used. The test results reported herein for unfilled PTFE and a PTFE composite material demonstrate a general reduction of both the high velocity and the low velocity sliding friction with increasing travel up to about 0.5 km.

It is likely that the high velocity friction increases beyond the initial value after about 1 to 2 km of cumulative movement. If we accept that the trend for the high velocity coefficient of friction is the same as that for the low velocity coefficient of friction (and this appears to be the case for unfilled PTFE, see Figure 5-20), we should expect a 20 percent increase in the high velocity coefficient of friction after about 2 km of travel. This conclusion is based on the German data as reported by Kauschke and Baigent (1986).

Certain phenomena were observed during testing that are worthy of reporting. In tests of unfilled PTFE, after travel of 0.5 km, the PTFE surface contained very small dark particles that could be removed by scratching of the surface. These particles were either fine steel particles removed from the steel surface by rubbing or residuals of the abrasive

127
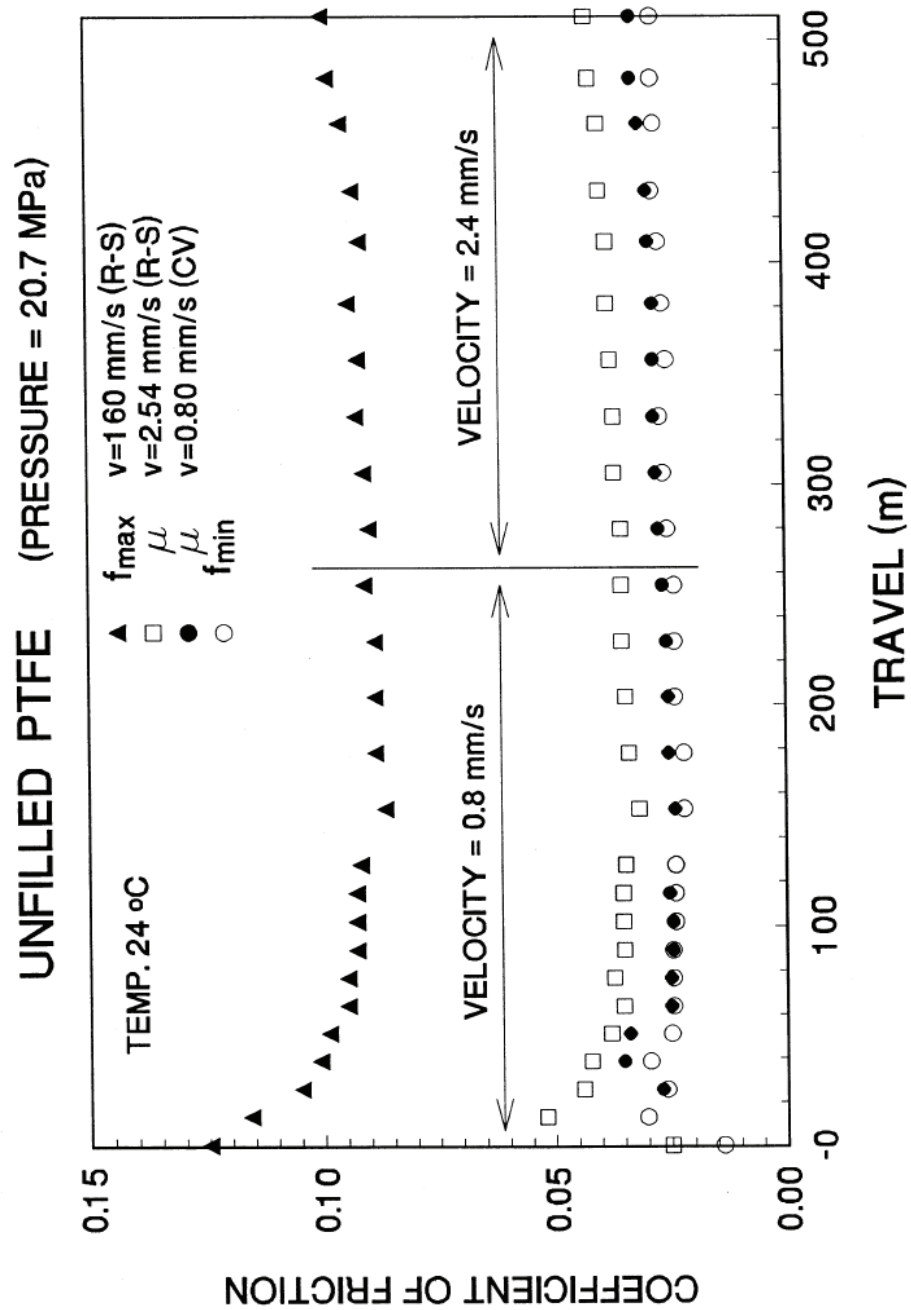
FIGURE 5-20 Effect of Cumulative Movement (Travel) on the Sliding Coefficient of Friction of Unfilled PTFE in Contact with Polished Stainless Steel

128
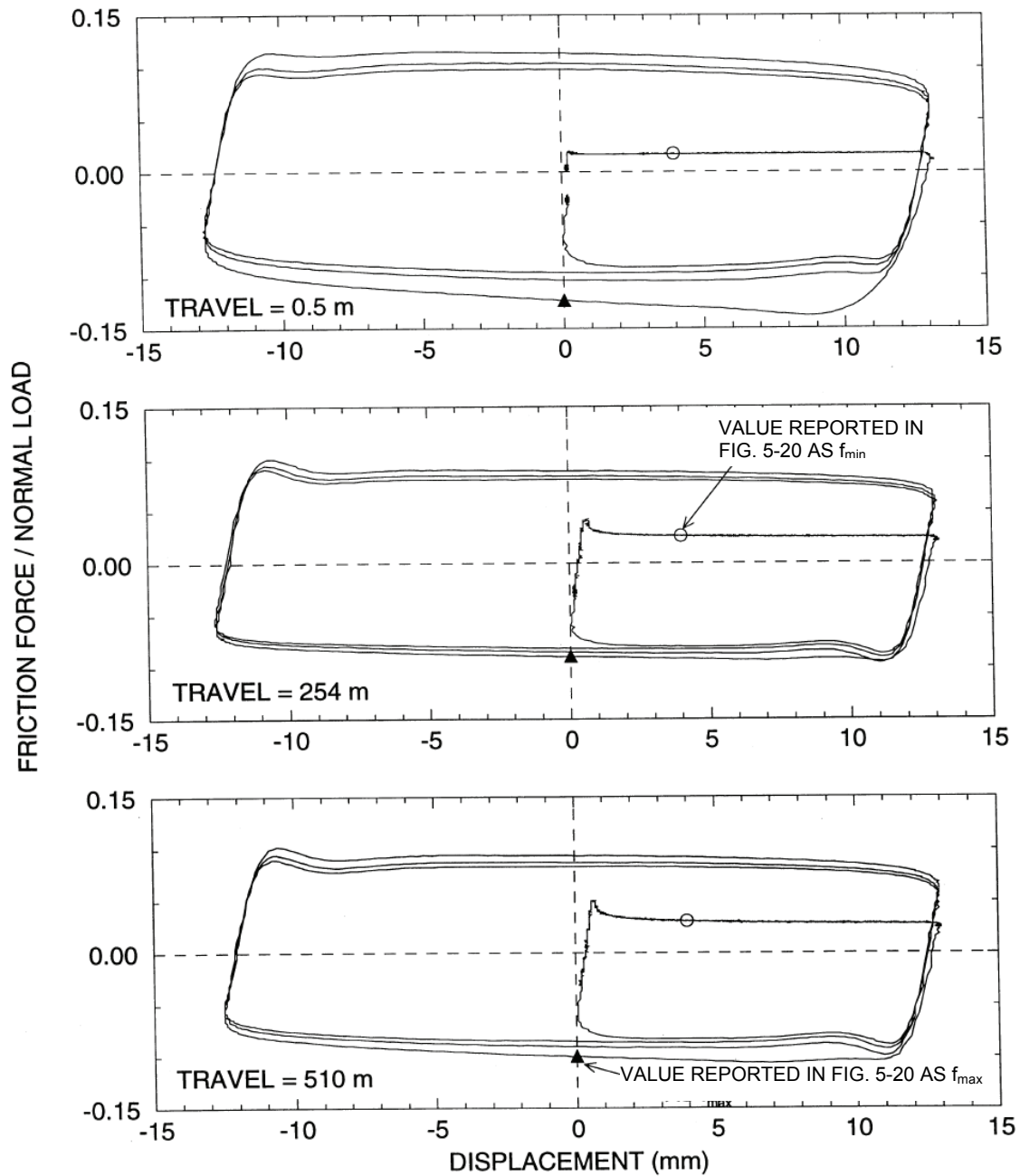
FIGURE 5-21 Recorded Loops of Friction Force / Normal Load vs. Displacement of Unfilled PTFE-Polished Stainless Steel Interfaces Following Travel of 0.5m to 510m, Testing Conducted with the Motion of Figure 5-11 at a Frequency of 2 Hz

129

used to polish of the plate, or both. It is likely that these particles increase in density with increasing travel and eventually cause an increase in friction. If so, the effect could be mitigated by the use of a highly polished, high strength stainless steel, cleaned to remove all abrasive residues. Perhaps this is the reason for the differences in the trends observed in the British and German tests.

This phenomenon could not be observed in the testing of the PTFE composite because of its dark color. However, observations on wear of the composite were made. The material was very thin, with a thickness of 0.25 mm. Figure 5-22 shows views of the material prior to and after testing. The disc on the right shows the material prior to testing. The disc in the middle of the figure was tested extensively using high amplitude motion but the cumulative movement was only a few meters: the material is evenly distributed over the surface (flakes of material from the edges were removed prior to taking the photograph). The disc on the left shows the composite following a travel of 500 m (again flakes from the edges have been removed): the material is unevenly distributed. This wear was caused by transport of particles of the material and their subsequent re-integration into the matrix of the composite during the low amplitude movement of the long travel test. It appears that this mechanism is fundamental for this material (and likely also for woven PTFE) in reducing wear in small amplitude motion.

Section 5-10 herein is devoted to a description of available results on wear of sliding bearings.
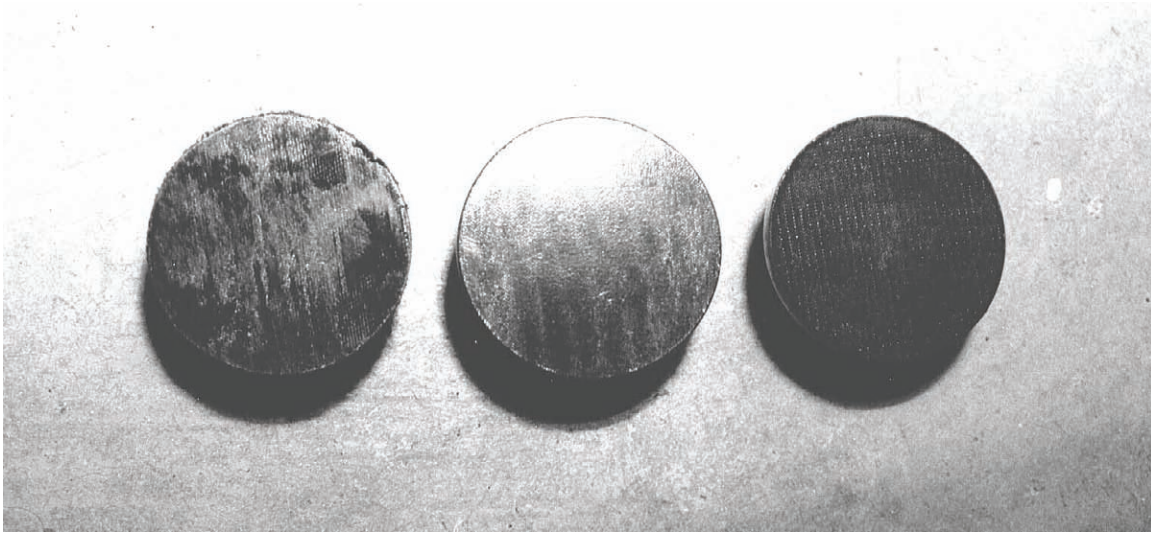
FIGURE 5-22 Views of PTFE Composite Material Following Travel of 500 m (left), Following Short Travel and High Amplitude Motion (center) and Prior to Testing (right)

130

5.6 Effect of Surface Roughness of Stainless Steel

The surface roughness of stainless steel has an effect on friction. Surface roughness was mentioned previously as a likely contributor to the differences in the results obtained in Germany (reported by Kauschke and Baigent, 1986) and England (Long, 1969, 1974). Taylor (1972) documented the effect of surface roughness on the very low velocity coefficient of friction in tests conducted on unfilled PTFE in contact with stainless steel at an apparent pressure of 35 MPa, velocity of 0.02 mm/s and temperature of 20°C. He reported 3- to 5-fold differences between the coefficient of friction obtained with a standard finish and with a mirror finish stainless steel. The results of Long (1969) and Taylor (1972) are likely the reason for the near-exclusive use today of mirror finish stainless steel in PTFE sliding bearings.

Although mirror finished stainless steel (surface roughness of about 0.03 μm arithmetic average) is used almost exclusively today, data on the effect of roughness of friction (and particularly the high velocity friction) are of interest if we assume that the effects of corrosion are equivalent to those of roughness. The subject of corrosion of stainless steel is addressed in Section 5.7. Herein we assume that with time, and depending on the environment, stainless steel can corrode, which we will further assume to be uniform on the surface of the stainless steel. Accordingly, we relate corrosion to surface roughness and thus assume that corrosion is equivalent to an increase in the surface roughness.

We conducted tests of unfilled PTFE and the PTFE composite in contact with stainless steel (ASTM 240, type 304) having surface roughness of 0.03, 0.30 and 0.50 μm R_a. The lowest roughness is that in the lay direction of a commercially polished to mirror finished (or No. 8) sheet. The intermediate roughness is that of an as-rolled sheet of stainless steel. The maximum roughness was created by uniformly roughening an as-rolled sheet using a wire brush.

Testing was conducted using the motions shown in Figure 5-11. Load dwell prior to imposing the motion was generally less than one hour; the temperature at the start of each experiment was 24°C. The apparent contact pressures were 20.7 MPa (unfilled PTFE) and 69 MPa (PTFE composite).

Figures 5-23 and 5-24 present the results on the coefficient of sliding friction as measured at the first instant at which the indicated velocity was reached (i.e., after travel equal to the amplitude of the imposed motion as illustrated in Figure 5-12). For each roughness, a new unfilled PTFE specimen was tested. However, only one specimen was constructed with the PTFE composite and was used for all tests. Most of the tests were conducted without unloading the specimen and cleaning of the sliding interface, that is, the stainless steel was coated with PTFE from the previous test. However, selected tests (particularly in the case of the maximum roughness) were repeated after cleaning the interface. The test data for these cases are shown in the figures with dark symbols, whereas the rest of the data are shown with open symbols.

131
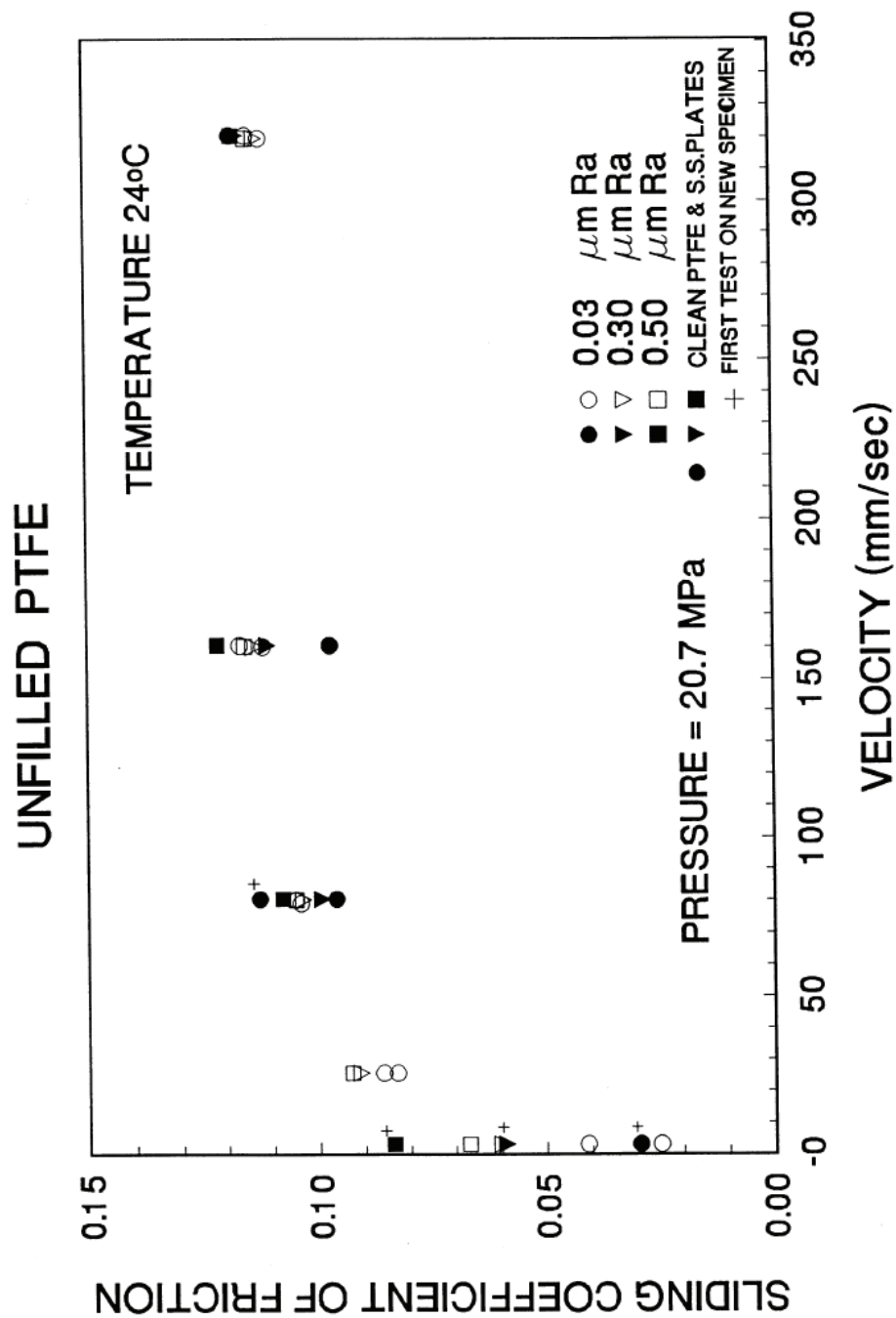
FIGURE 5-23 Effect of Surface Roughness of Stainless Steel on the Sliding Friction of Unfilled PTFE
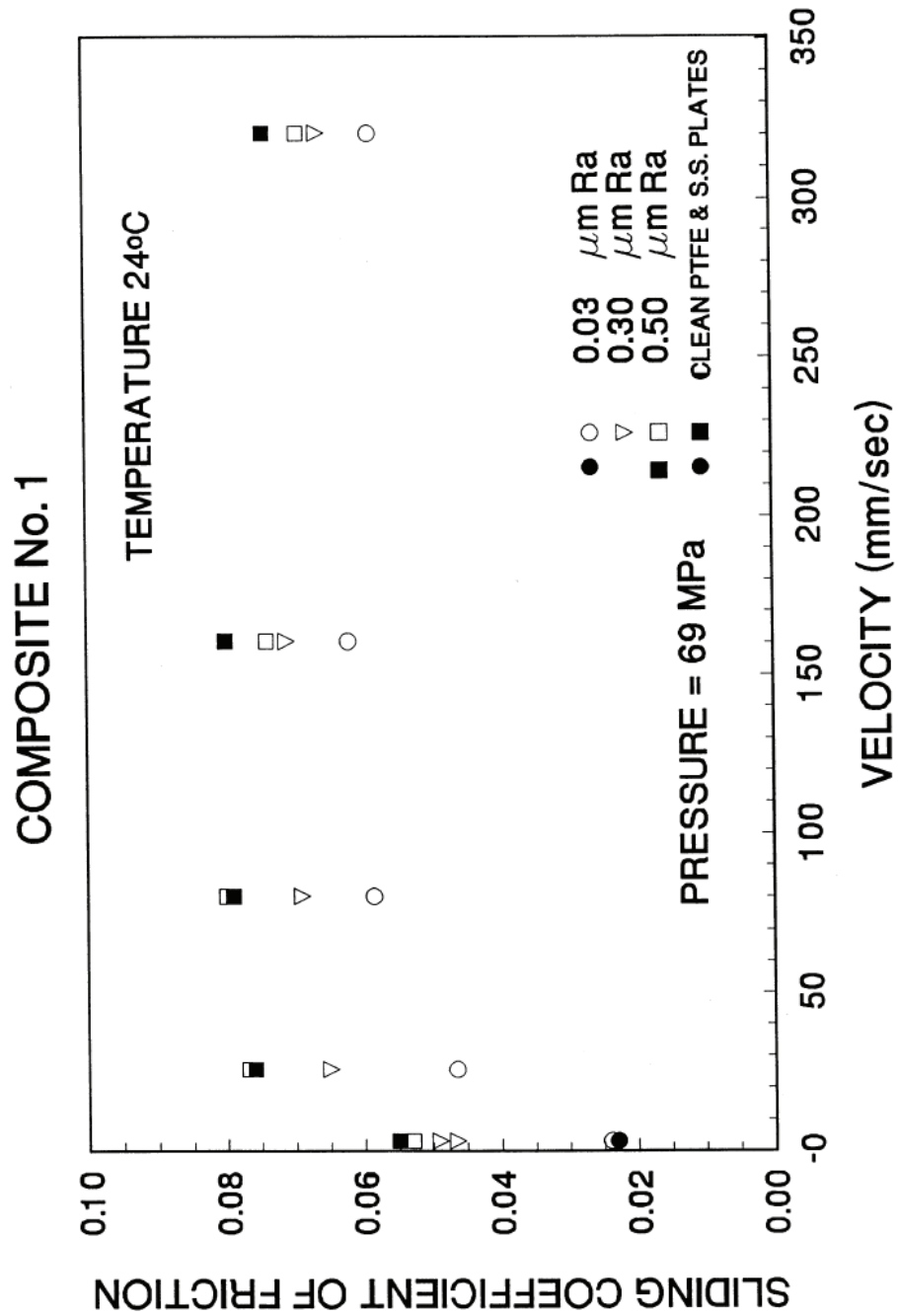
FIGURE 5-24 Effect of Surface Roughness of Stainless Steel on the Sliding Friction of PTFE Composite

The results in Figures 5-23 and 5-24 demonstrate an increase of the sliding friction with increasing roughness. The increase is substantial at very low velocities of sliding and is, in general, consistent with the observations of Taylor (1972). This increase is likely caused by:

a) The introduction of a component of friction due to plowing of the PTFE by the rough stainless steel, and

b) The effects of increased number of wear particles trapped between the sliding surfaces.

Per Figures 5-23 and 5-24, it can be seen that the effect of surface roughness on the sliding coefficient of friction reduces with increasing velocity of sliding. This phenomenon is particularly pronounced for unfilled PTFE, for which the high velocity sliding friction (f_{max}) is nearly unaffected by roughness. An explanation for this observation is related to the effect of third body particles (wear debris) that dominate friction at high velocities of sliding. The effect of third body particles is limited and the coefficient of friction attains a constant value beyond some large velocity (except for the effect of frictional heating). High roughness generates more wear particles but the effect is minor at a large velocity of sliding.

As seen in Figure 5-24 the effect of surface roughness on the sliding coefficient of friction of the PTFE composite is more than that of unfilled PTFE at high velocities. The data have been carefully examined to identify likely contributors to this effect. For example, it was observed that the tests were conducted over a period in which the relative humidity in the laboratory was either at about 20 percent or 45 percent. However, even when some of the data were ignored, the effects of roughness remained at the level depicted in Figure 5-24. It is likely that the third body particle effects for this interface are not as important as for the unfilled PTFE due to the woven nature of the material (a significant part of the wear debris is re-integrated in the matrix of the material). Accordingly, some other mechanism (likely plowing) might be responsible for this phenomenon.

5.7 Effect of Corrosion of Stainless Steel

Stainless steels are alloys containing iron, at least 10 percent chromium and some 10 to 15 other elements that can provide a range of corrosion resistance. There are five major families of stainless steels: Ferritic, Austenitic, Martensitic, Precipitation-Hardening and Duplex. Of these, austenitic stainless steels of the AISI (American Iron and Steel Institute) types 304 and 316 are used in sliding bearings (Davison et al., 1987).

The mechanism of corrosion protection of stainless steel differs from that of most metals, including that of carbon steel. Unlike other metals, stainless steels do not form a layer of true oxide. Rather, they form a passive film that if maintained enable stainless steels to exhibit outstanding corrosion resistance. This film forms immediately in the presence of oxygen.

The basic elements of stainless steels that are important for corrosion resistance are chromium for forming the passive film and molybdenum, which in combination with chromium is effective in stabilizing the passive film in the presence of chlorides. Moreover, carbon is detrimental to corrosion resistance through its reaction with chromium.

The most commonly used stainless steel is the AISI type 304 austenitic stainless steel due to its high ductility, ease of fabrication, availability and good corrosion resistance. Type 316 stainless steel which contains molybdenum and particularly type 316L with low carbon content have superior corrosion resistance and should be utilized in sliding bearings in chloride-rich environments.

The corrosion of stainless steel can take various forms (Davison et al., 1987). However, the most common form is pitting that is associated with local discontinuity of the passive film. Chloride is the typically responsible for the initiation of pitting. Uniform corrosion of stainless steel is very rare and its occurrence generally indicates an error in the selection of the stainless steel.

Data on the corrosion resistance of stainless steels are presented in Davison et al. (1987). However, the most comprehensive collection of data that are of interest for sliding bearings can be found in International Nickel Company (1970). This collection of data is specifically for austenitic stainless steels in atmospheric environments. The data are typically in the form of qualitative statements on the appearance of stainless steels following lengthy exposure in known environments. Table 5-4 presents information from International Nickel Company (1970) for types 304 and 316 austenitic stainless steels.

The information in Table 5-4 reveals that:

a) Corrosion of stainless steel in atmospheric environments is possible and is typically manifested as light rust stains over small part of the surface.
b) Type 316 stainless steel has significantly better corrosion resistance than type 304 in all environments.
c) Industrial-chemical environments can cause unacceptable corrosion of type 304 stainless steel due, apparently, to the existence of chlorides.

Data are presented in Table 5-4 for the case of specimens exposed to industrial environment under sheltered and unsheltered conditions. The sheltered specimens were kept under a roof so that rain could not wash away deposits that accumulated over a 12 years period. The other specimens were exposed so that rain regularly removed any deposits. These protected specimens corroded but those exposed to rain (regular cleaning) did not: the accumulated deposits depleted the stainless steel under the covered portion of oxygen and prevented the restoration of the passive film.

This observation raises the question as to whether sliding bearings should be sealed to prevent contamination. The authors strongly believe that bearings should be sealed for the following reasons: (1) to prevent contamination; heavy contamination depletes the

stainless steel of oxygen and, (b) to prevent exposure of the surface to de-icing salts (chlorides). Moreover, the stainless steel surface should be installed facing downwards to prevent contamination from within the bearing (e.g., from falling rust debris from the carbon steel parts of the bearings). The ideal situation for sliding bearings to prevent corrosion over prolonged time intervals is the use of type 316 stainless steel (preferably 316L with the stainless steel surface facing down and with a seal that prevents contamination but allows airflow.

TABLE 5-4 Information on Performance of Austenitic Stainless Steels in Various Atmospheric Environments

Location	Environment	Duration (Years)	Condition	
			Type 304	Type 316
New York City	Industrial-Urban	26 23	No rust stains -	- No rust stains
Niagara Falls, NY	Industrial-Chemical	6	Covered with rust, pitted	Slight rust spots, slightly pitted
Panama Canal	Tropical	8	-	No rust, no pitting
Bayonee, NJ	Industrial[1] (sheltered)	12	Pitted to depth of 0.18 mm	Pitted to depth of less than 0.025 mm
Bayonee, NJ	Industrial[1] (not sheltered)	12	No rust, no pitting	No rust, no pitting
Kure Beach, NC	Marine	15	Spotted with slight rust stain over 15% of surface	Extremely light rust stain over 15% of surface

1. Likely chemical environment

The superiority of type 316 stainless steel is documented for a number environments. Romanoff (1957) documents extensive data on the underground corrosion of some 37,000 specimens for exposures of up to 18 years. While not directly relevant to sliding bearings, the data are highly informative. Type 304 and 316 stainless steels exposed for 14 years in soil containing 2 percent sodium chloride exhibited significantly different levels of corrosion: the type 316 specimens did not corrode but the type 304 specimens developed significant pitting.

Despite the wealth of information on the corrosion of stainless steels there is still lack of data that relate corrosion to the coefficient of friction and particularly the high velocity coefficient of friction. To provide some quantitative information on this subject we have

to relate the information on the appearance of stainless steel to some relevant quantity, such as surface roughness. After this task is accomplished, data such as those presented in Figures 5-23 and 5-24 can be used to assess the effect of corrosion on friction.

The authors were able to obtain information from sliding bearings tested at the University at Buffalo. The bearings were faced with type 304 austenitic stainless steel that was welded onto a carbon steel plate. The bearings were extensively tested over a period of 9 years and were stored disassembled in the laboratory. One of these bearings (of a total of 4) exhibited light rust stains over the perimeter of the stainless steel sheet for a distance of about 20 mm from its edge. The rust stains covered an area of about 15 percent of the stainless steel surface. The observed corrosion was the result of contamination of the perimeter of the stainless steel plate by iron particles due to grinding of the carbon steel plate. Nevertheless, the area with light rust stains appeared to the touch as having a rougher surface than that of the remaining stainless steel. Measurements of surface roughness of the rusted sheet were about 0.30 μm on the arithmetic average. The rest of this surface, as well the entire surface of the other three bearings, was rust free and had a measured surface roughness of about 0.03 μm arithmetic average after 9 years of exposure.

We make the assumption that a surface roughness of 0.3 μm arithmetic average is representative of the surface condition of type 304 stainless steel after 30 years of exposure in an industrial/urban (but not chemical) environment under conditions that prevent contamination and direct exposure to salts. Note that the assumption might be very conservative because (a) observations after 26 years exposure in such an environment (see Table 5-4) show no rust stains, and (b) even when rust stains develop, they are over a small portion of the surface and do not represent uniform corrosion as we have assumed. Moreover, we assume that a surface roughness of 0.5 μm arithmetic average is representative of the condition of type 304 stainless steel in an industrial/chemical environment.

Table 5-5 was prepared on the basis of these assumptions. The table presents assumed values of the surface roughness of type 304 stainless steel for different environmental conditions and methods of installation of the stainless steel plate. Of these values only the value of 0.3 μm (underlined in the table) is supported by data. The values in the table might be very conservative but represent a starting point for assessing the effects of corrosion on friction. Moreover, they reflect the effects of environmental conditions and methods of installation as they are understood from the study of the mechanisms of corrosion of stainless steel.

Table 5-6 was developed using the values of surface roughness in Table 5-5 and the coefficients of friction presented in Figures 5-23 and 5-24. The table lists factors for increasing the high velocity coefficient of friction of unlubricated unfilled PTFE and PTFE composites in contact with type 304 austenitic stainless steel after 30 years of exposure in different environments. Use was made of the data in Figures 5-23 and 5-24 at velocities of approximately 75 mm/s (values shown underlined). The factor should be less (closer to 1.0) at velocities exceeding 75 mm/s.

137

Austenitic type 316 stainless steel exhibits corrosion resistance that is superior to that of type 304 stainless steel. Accordingly, the factors for adjusting the friction for the effects of corrosion should be less than those presented in Table 5-6 for type 316 stainless steel. One could assume midpoint values between those in Table 5-6 and 1.0.

TABLE 5-5 Suggested Surface Roughness Values (in µm arithmetic average) of Type 304 Austenitic Stainless Steel (originally polished to roughness of 0.03 µm arithmetic average) After 30 Years of Exposure Within Unlubricated Sliding Bearings

Environment	Installation Method of Stainless Steel Plate in Sliding Bearing			
	Sealed Facing Down	**Sealed Facing Up**	**Unsealed Facing Down**	**Unsealed Facing Up**
Rural	0.10	0.30	0.30	Unacceptable[1]
Industrial/ Urban	0.30	0.40	0.40	Unacceptable
Marine	0.40	0.50	0.50	Unacceptable
Industrial/ Chemical	0.50	>0.50	>0.50	Unacceptable

1. Installation method is unacceptable due to potential for significant contamination.

TABLE 5-6 Proposed Factors for Increasing the High Velocity Sliding Coefficient of Friction (fmax) of Unlubricated Unfilled PTFE and PTFE Composites in Contact with Type 304 Austenitic Stainless Steel After 30 Years of Exposure in Various Environments

Environment	Installation Method of Stainless Steel Plate in Sliding Bearing		
	Sealed Facing Down	**Sealed Facing Up**	**Unsealed Facing Down**
Rural	1.10	1.20	1.20
Industrial/ Urban	1.20	1.30	1.30
Marine	1.30	1.40	1.40
Industrial/ Chemical	1.40	>1.40	>1.40

5.8 Effect of Contamination

Contamination of the sliding interface will cause an increase in friction. A number of experimental studies have documented this phenomenon, which is apparently caused by the introduction of an additional component of friction due to third body effects (see section 3.3) and due to abrasion of the stainless steel.

Long (1969) reported satisfactory performance of unfilled PTFE bearings following deliberate contamination of the PTFE with dust. Neither the satisfactory performance nor the amount of contamination is quantified, other than that the bearing was subjected to cumulative travel of about 5.7 km. The contamination was likely light and of very small particle size so that it was absorbed by the soft PTFE. Long (1969) reports that it was impossible to contaminate the sliding interface while the bearing was under load and it was necessary to disassemble the bearing and introduce contaminants. He reported on a substantial increase in the static (breakaway) coefficient of friction (approximately 6-fold, from 0.017 to 0.100) when dry cement dust was introduced as a contaminant.

Jacobsen (1977) reported similar results to Long. Jacobsen's tests were conducted on unfilled PTFE-stainless steel interfaces (the type of stainless steel and its surface condition were not reported) at an apparent pressure of 6.5 MPa and for slow constant velocity motion (4 mm/s) to obtain a static (breakaway) value of the coefficient of friction of 0.05 and a sliding value of 0.06 after about 950 m of travel. The same specimen was contaminated with sand particles (the amount is not given) and tested at an apparent pressure of 4.3 MPa. The static coefficient of friction was measured at 0.27 and the sliding value at 0.14 after about 870 m of travel. In another test on unfilled PTFE at an apparent pressure of 4.1 MPa, the static coefficient of friction of the uncontaminated interface was 0.08 whereas the value for specimen contaminated with sand particles was 0.29.

Jacobsen also reported test results on woven PTFE in contact with bronze. At an apparent pressure of 13.8 MPa the static coefficient of friction was at 0.065 for the uncontaminated specimen and at 0.125 for specimen contaminated with sand particles. After 130 m of travel, the value of the sliding coefficient of friction reduced to that of the uncontaminated specimen: the sand particles likely were into the woven fibers of the PTFE , reducing the impact of the contamination.

Tyler (1977) tested contaminated and uncontaminated lubricated, dimpled PTFE-stainless steel interfaces at a large velocity of sliding (375 mm/s). The contamination was in the form of cement dust but the amount was not reported. Ten- to 15-fold increases in the sliding coefficient of friction were recorded.

Campbell and Fatemi (1989) and Campbell et al. (1993) reported the results of a systematic study of the effect of contamination on the friction of lubricated, dimpled PTFE bearings. Tests were conducted at an apparent pressure of 30 MPa, following load dwells of 12 hrs and by imposing motion at velocity of 1 mm/s. Contamination in the form of cement dust was introduced at various concentrations (reported in weight of

contaminant per unit area of interface) and results were obtained on the initial (static or breakaway) coefficient of friction and the sliding coefficient of friction for 200 cycles of movement. Substantial increases in friction were recorded for heavy contamination. For example, increases in the initial (breakaway) coefficient of friction of about 15 times were recorded with contamination of 0.239 mg/mm^2, which amounts to about 1 gram of cement dust for the 75-mm diameter specimens.

Campbell and Fatemi (1989) conducted tests with a contaminated stainless steel surface over the portion not in contact with PTFE, somewhat replicating in-service conditions. In these tests, the bearings were subjected to eccentric loading to facilitate infiltration of the contaminant. The contaminant was continuously replenished on the stainless steel surface during testing. These tests demonstrated little, if any, infiltration of the sliding interface by the contaminant and the coefficients of friction did not change.

It is clear that contamination, when artificially introduced in the sliding interface, has significant effects on friction. Although this effect has been measured for unlubricated bearings at very slow sliding velocities (conditions of breakaway), there is no doubt that large increases in the coefficient of friction will also occur at large velocities of sliding. Intuitively, we expect the increase in the high velocity coefficient of sliding friction of contaminated unlubricated PTFE-stainless steel interfaces to be less than the corresponding increase in the low velocity sliding friction because of the significance of the third body contribution to friction (see section 3.3) from contaminants is somewhat less at high velocities: due to the large third body contribution to friction from the agglomerates of PTFE debris. Nevertheless, the increase is expected to be more than any of the previously identified effects, including wear, temperature and corrosion.

Contamination of the sliding interface is possible if bearings are disassembled at the construction site. Sliding bearings should be delivered fully assembled, lightly pre-compressed and locked by side plates.

The results of Campbell and Fatemi (1989), Campbell et al. (1993) and previously by Long (1969) demonstrate that in-service contamination of the sliding interface of sliding bearings is unlikely, even in the presence of significant load eccentricity. Nevertheless it would be prudent to assume some small increase in friction due to in-service contamination that depends on the method of installation of the stainless steel surface. For example, if the stainless steel surface is installed facing up, it will likely collect debris over the years that might migrate into the sliding interface during movement of the bearing under service loads.

5.9 Effect of Lubrication

As discussed in Section 4, lubrication of the PTFE-stainless steel interface reduces the coefficient of friction. For a wide range of apparent pressures and velocities of sliding, the sliding coefficient of friction for highly polished stainless steel and for normal temperature is 0.02 or less. The lubricant, typically in the form of grease, is stored in dimples under hydrostatic pressure from where it is extruded to the sliding interface.

140

Dimpling is important for prolonging the effective life of the lubricant. Dimples cover approximately 30 percent of the apparent contact area. Grease consists of primarily oil or synthetic fluid (approximately 80 percent or more), a thickening agent (typically soap at approximately 10 percent) and additives (antioxidants, anticorrosion agents, etc. at less than 10 percent).

Campbell and Kong (1989), Campbell and Fatemi (1989) and Campbell et al. (1993) reported on the results obtained in the testing of lubricated, dimpled PTFE-stainless steel interfaces for a variety of conditions of temperature (20° and –25°C), surface roughness of stainless steel (0.03 and 0.04 µm R_a), apparent pressure (10 to 45 MPa) and velocity of sliding (up to 20 mm/s). The effects of contamination were studied as discussed previously. Selected results from these carefully conducted experiments are presented in Tables 5-7 and 5-8. A number of interesting observations can be made:

a) Friction is velocity dependent. At normal temperatures, fresh conditions (highly polished stainless steel) and a large velocity of sliding, the coefficient of sliding friction in the first cycle of movement is of the order of 0.02 (see Table 5-7). The reason for the observed substantial increase of friction with velocity, which is two-fold in the velocity range of 1 to 20 mm/s, is unclear. A likely explanation is that the increase is caused by third body effects (PTFE wear particles).

b) The coefficient of friction reduces to a very low value following some movement. As seen in Table 5-8 for normal temperature conditions and highly polished stainless steel, the coefficient of friction attains values of approximately 0.003 but it could be somewhat higher at velocities relevant to seismic motions. It might be assumed that such values would prevail for virgin conditions and following some small cumulative movement as a result of thermal and traffic effects. It is apparent that this reduction in the coefficient of friction after some small movement is the result of the spreading of lubricant from the dimples to the stainless steel plate.

c) There is a substantial effect of low temperature and of increased stainless steel surface roughness on the coefficient of friction. From the data in Tables 5-7 and 5-8 at the highest velocity, there is an increase of the coefficient of sliding friction of 5 to 8 for temperatures in the range of 20 to -25° C, and an increase of 3 to 8 for roughness in the range of 0.03 to 0.34 µm R_a.

For unfilled and unlubricated PTFE in contact with highly polished stainless steel, the increase in the sliding coefficient of friction is a factor of about 1.7 for the same temperature range (see Figure 5-15) and a sliding velocity of 20 mm/sec. The effect of surface roughness on the coefficient of sliding friction is very small (factor of 1.1) for the same range of roughness and velocities of motion (see Figure 5-23). The substantially greater effect of temperature on the coefficient of friction for lubricated rather than unlubricated PTFE bearings could be explained on the basis of frictional heating, which is much less in the lubricated bearings due to the very low friction. Importantly, the effect of stainless steel surface roughness could be explained on the basis of a change in the lubrication regime, which for the rougher surface is one with a smaller number of contact areas separated by a lubrication film.

TABLE 5-7 Coefficient of Sliding Friction of Lubricated Unfilled PTFE-Stainless Steel Interfaces (data from Campbell and Kong, 1989), Values of Friction are for First Cycle of Movement

Apparent Pressure (MPa)	Temperature 20° C		Temperature 25° C		Surface Roughness of Stainless Steel (μm R_a)
	v=1 mm/s	v=20 mm/s	v=1 mm/s	v=20 mm/s	
10	0.0068	0.0172	0.0251	0.0526	
15	0.0092	0.0258	0.0197	0.0673	
25	NA	0.0181	0.0420	0.0489	0.03
30	NA	0.0175	0.0139	0.0505	
45	0.0079	0.0160	0.0340	0.0395	
10	0.0132	0.0530	0.0528	0.0770	
15	0.0280	0.0381	0.0259	0.0559	
25	0.0118	0.0191	0.0307	0.0515	0.34
30	0.0095	0.0218	0.0166	0.0467	
45	0.0125	0.0185	0.0225	0.0595	

TABLE 5-8 Coefficient of Sliding Friction of Lubricated Unfilled PTFE-Stainless Steel Interfaces after 50 Cycles of Movement (2 m of travel) and Velocity of 20 mm/s (from Campbell and Kong, 1989)

Apparent Pressure (MPa)	Surface Roughness of Stainless Steel (μm R_a)	Coefficient of Sliding Friction	
		Temp. 20° C	Temp. -25° C
10		0.0064	0.0290
15		0.0028	0.0223
25	0.03	0.0035	0.0230
30		0.0044	0.0238
45		0.0030	0.0163
10		0.0310	0.0434
15		0.0233	0.0365
25	0.34	0.0136	0.0370
30		0.0107	0.0212
45		0.0078	0.0209

Despite the significant effects of low temperature and high roughness, the coefficient of sliding friction of lubricated PTFE bearings is low. As seen in Table 5-8, the values are generally less than 0.04 following small movement. If it were possible to maintain the lubricant in its original condition, the performance of lubricated PTFE bearings would likely be very good. However, the lubricants in PTFE bearings harden with time and replenishing the lubricant is extremely difficult (Campbell and Kong, 1987; Kauschke and Baigent, 1986). Kauschke and Baigent (1986) note, and the authors agree, that lubricated PTFE bearings have a limited lifetime and that provisions should be made to replace the PTFE sheets.

The results presented above are representative of the behavior of the tested interfaces, demonstrate the effects of the aforementioned parameters and they provide first-order data for use in research studies, preliminary designs and the development of specifications. The values assigned to the parameters should not be viewed as absolute.

Recently, Dolce et al. (2005) reported friction coefficient data for lubricated sliding bearings under the following conditions: apparent pressures of 9.4, 18.7 and 28.1MPa,, velocity of sliding in the range of 0 to 300 mm/sec, and temperatures (at start of experiment) of -10, 20 and 50°. Dolce's data show a small effect of velocity on the coefficient of friction. In general, the coefficient of friction was in the range of 0.005 to 0.018 at a temperature of 50° C, 0.01 to 0.025 at a temperature of 20° C and 0.015 to 0.030 at a temperature of -10° C.

Additional information on the low velocity frictional properties of lubricated PTFE-stainless steel interfaces can be found in Eggert and Kauschke (2002). Of particular interest are data on the coefficient of friction of lubricated interfaces at temperatures in the range of -35 to 20°C and for cumulative travel of up to 20 km: a significant increase in the coefficient of friction occurs at low temperatures after a travel of about 10 km, caused by loss of lubrication and contamination.

5.10 Wear

Wear is damage to the surface as a result of relative motion (Bayer, 1994). Section 5.5 presents the effect of cumulative motion on the frictional characteristics of sliding interfaces of interest in seismic isolation applications. One more effect of motion is wear in the form of loss of material from the sliding surface. Excessive wear or total loss of the PTFE or other mating material for stainless steel in seismic sliding bearings will result in substantial increase in friction and will render the bearings useless.

Seismic sliding bearings operate in two distinct regions of wear:

a) Service load conditions for which the velocity of sliding is extremely slow and wear is characterized as mild.
b) Seismic load conditions for which the velocity of sliding is large and wear is significant. The bearings operate well beyond the PV limit (see Bayer, 1994, for a

definition of this limit), but only for very short period of time (a few seconds) over the lifetime of the structure.

Prediction of wear under seismic conditions is practically impossible. High velocity testing as described in Section 4.8.3 is needed to predict wear. The presentation that follows concentrates on wear in the mild wear region for which some data are available and can be predicted by simple theories.

Data on wear of sliding seismic isolation bearings are limited to the results presented below. Only quantitative data are presented. It should be noted that some qualitative data were collected during the HITEC testing program. These data are not presented herein. The interested reader is referred to CERF (1998a) and CERF (1999).

One test of a Benicia-Martinez Type 1 FP bearing was the wear test that was developed to study the response of the FP bearings to service (non-seismic) loads (Imbsen, 2001). The bearing was subjected to 1520 m of travel: 10,000 cycles of sinusoidal loading at displacement amplitude of 38 mm at a peak velocity of 7.6 mm/sec. The apparent bearing pressure was 20 MPa. The composite liner used in the Type 1 FP bearing is typical of that used in bridge applications of FP bearings. The thickness of the composite liner, nominally 1.5 mm (59/1000 in) at the time of installation, was measured before and after the wear test by a Caltrans inspector. The results are presented in Figure 5-25. Before the test, the thickness of the liner ranged between 61/1000 and 75/1000 in (1.55 and 1.90 mm). The maximum loss of thickness due to wear, reported by Caltrans, was 0.03 mm: less than 2 percent of the nominal thickness.

Another testing program was a wear test of a FP bearing that was developed for a bridge application. The test was conducted by Earthquake Protection Systems, Inc., under the supervision of Caltrans. The test was a 20,000-cycle displacement history with 162 mm of travel per cycle. The key features of the tested bearing were:

- Overlay radius of curvature = 1880 mm (74 inches)
- Slider diameter = 222 mm (8.75 inches)
- Contact (bearing) pressure during testing = 104MPa (15 ksi)
- Maximum speed during testing = 7.6 mm (0.3 inches) per second
- Nominal thickness of liner = 0.89 mm (0.035 inch)
- Total travel = 3240 m

Test data are reproduced from EPS (2001) in Table 5-9. Note that the liner thickness of 0.89 mm used in this test is substantially less than that currently proposed for the bridge FP bearings (=1.5 mm); the speed of testing is orders of magnitude greater than that expected during thermal or traffic loading of bridge bearings; and the contact pressure of 104 MPa is much greater than that for the service (gravity) loading for typical sliding bridge bearings: usually less than about 35 MPa.

a. liner thickness in mils before test

b. liner thickness in mils after 1520 m of travel
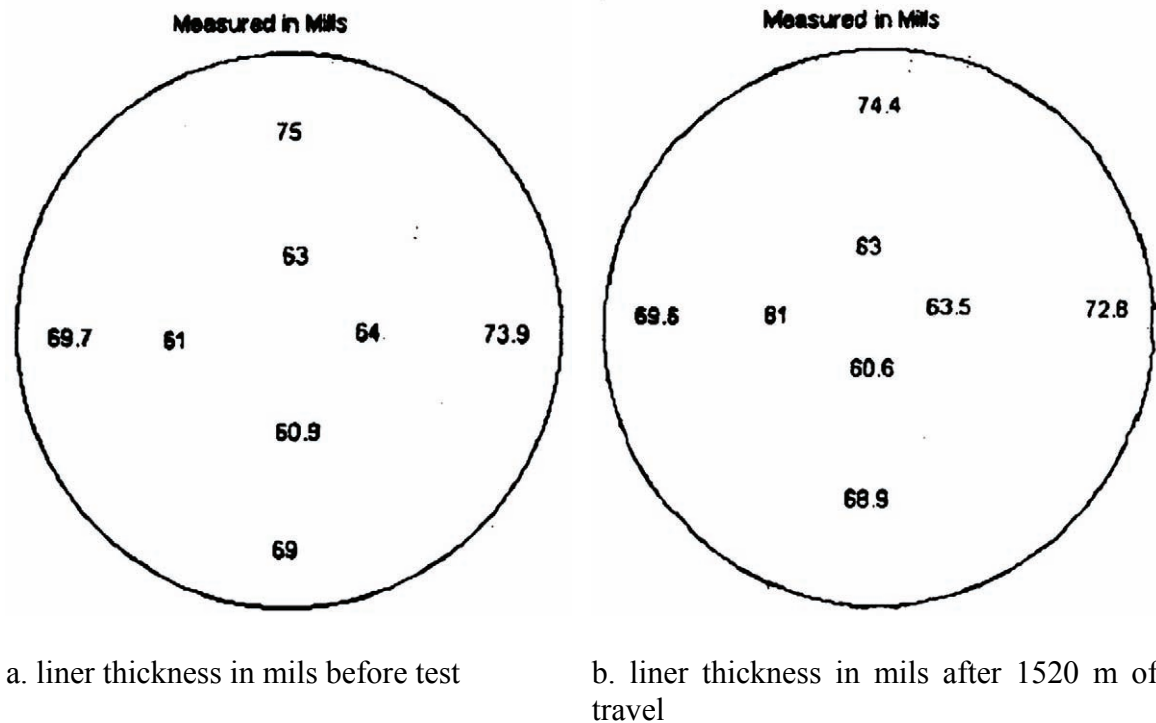
FIGURE 5-25 Wear Test Data for a Type 1 Benicia-Martinez FP Bearing

TABLE 5-9 Wear Data from Caltrans FP Bearing Test (adapted from EPS, 2001)

Cycle	Total Travel (m)	Liner Thickness (mm)	Wear (mm)	% Liner Thickness Remaining
0	0	0.89	0	100
6,500	1,053	0.79	0.10	89
10,000	1,620	0.74	0.15	83
15,000	2,430	0.71	0.18	80
20,000	3,240	0.71	0.18	80

Another testing program was a wear test of a FP bearing that was developed for an offshore platform application (Clarke et al., 2005). The test was conducted by Earthquake Protection Systems, Inc., under the supervision of the platform designer, AMEC, and the authors. The test was a 3,000-cycle displacement history with 1,062 mm of travel per cycle. The key features of the tested bearing were

- Overlay radius of curvature = 3960 mm (156 inches)
- Slider diameter = 535 mm (21.1 inches)
- Contact (bearing) pressure during testing = 31MPa (4.5ksi)
- Maximum speed during testing = 19 mm (0.75 inches) per second

145

- Nominal thickness of liner = 1.5 mm (0.059 inch)
- Total travel = 3048 m

The thickness of the bearing liner was measured at 10 locations (in a pattern similar to the pattern shown in Figure 5-25) before and at the conclusion of the wear test. Thickness data are presented in Table 5-10. The wear was insignificant. It should be noted that in some location the liner thickness actually increased as a result of transfer of debris from one area to another.

TABLE 5-10 Liner Thickness Data Before and After Wear Testing

Position	Thickness Before (mm)	Thickness After (mm)
1	1.96	1.93
2	1.93	1.95
3	1.88	1.88
4	1.83	1.95
5	1.91	1.91
6	1.85	1.83
7	1.85	1.81
8	1.91	1.90
9	1.91	1.85
10	1.83	1.80
Average	1.89	1.88

Prediction of wear (loss of thickness of bearing liner) is possible by making use of one of the simplest models for wear (Bayer, 1994). Specifically, wear in the FP bearings is of the abrasive type, in which the abrasive (stainless steel) is much harder than the abraded material (composite liner). Under these conditions, wear may be estimated as follows:

$$h = K \cdot p \cdot S \tag{5-5}$$

where h is the depth of wear, K is the wear coefficient, p is the bearing pressure and S is the distance traveled. The wear coefficient for the FP bearing sliding interface is about 5×10^{-10} MPa^{-1}. Using this value and (5-5), the following predictions can be made for the tested bearings:

Benicia-Martinez bearing
p = 20 MPa, velocity = 7.6 mm/sec, S = 1520m; liner thickness = 1.5 mm
$h = (5 \times 10^{-10})(20)(1520)(1000) = 0.0152$ mm.
Reported experimental value: $h = 0.03$mm.

146

Bearing tested under Caltrans supervision
p = 104 MPa, velocity = 7.6 mm/sec, S = 3240 m; liner thickness = 1.5 mm
h = $(5x10^{-10})(104)(3240)(1000)$ = 0.17 mm.
Reported experimental value: h = 0.18mm.

Offshore platform bearing
p = 31 MPa, velocity = 19 mm/sec, S = 3048 m; liner thickness = 1.9 mm
h = $(5x10^{-10})(31)(3048)(1000)$ = 0.048mm.
Reported experimental value: h=0.01mm.

These predictions of wear are reasonable and useful given the uncertainty of such calculations. It should be noted that wear in these three bearings is very small.

5.11 Sliding Interfaces with Chrome-Plated Carbon Steel

The sliding interface typically consists of stainless steel in contact with a softer material like PTFE or similar composites. Stainless steel offers substantial protection against corrosion and against the associated increase in friction at the interface over the lifetime of the seismically isolated structure. The AASHTO Specifications (AASHTO, 2002) specify stainless steel for use in flat sliding PTFE bearings. However, it permits the use of anodized aluminum for curved surfaces. The AASHTO Guide Specifications for Seismic Isolation Design (AASHTO, 1999) address the materials used in sliding bearing construction in the specification for system property modification factors for aging. The recommended values for un-lubricated bearings are in the range of 1.1 to 1.5 for interfaces consisting of stainless steel and PTFE. For interfaces consisting of chrome-plated carbon steel and PTFE, the recommended values of the aging factor are three times higher, that is, 3.3 to 4.5. Indirectly, the 1999 AASHTO excludes the use of chrome-plated surfaces. In contrast, the European Standard EN 1337 (European, 2004) allows the use of chrome-plated surfaces and is used in Europe particularly for spherical sliding surfaces. This is apparently needed because of the difficulty in using stainless steel overlays in spherically shaped bearings. Although it is difficult to shape the stainless steel overlays to the required shape, this practice has dominated in the United States out of concerns for the longevity of interfaces consisting of chrome-plated carbon steel. Evidence for the problems likely to occur in chrome-plated interfaces is provided in Figure 5-26 that presents data on friction obtained in the early 1990s by Oiles Corporation in Japan. The data presented in this figure were obtained from testing small specimens consisting of material Techmet-B of 60 mm diameter in contact with either stainless steel or chrome-plated carbon steel. Chrome was hard dense with thickness of 0.025 mm. Material Techmet-B is a composite used by the authors in bearings used in earthquake-simulator testing (Constantinou et al, 1990a). The specimens were subjected to an apparent pressure of 6.7 MPa (970 psi) and were tested using constant velocity motion of 10 mm/sec for 20 cycles. Tests were conducted prior to and after nine months of outdoor exposure while continuously loaded. There was a substantial increase in the first cycle coefficient of friction of the interface with the chrome-plated carbon steel as a result of increased roughness of the exposed chrome surface. Aging results in cracking of the chrome surface and corrosion of the supporting carbon steel. After many years of

service, the surface of chrome-plated steel will corrode, the extent of which depends on the thickness of the chrome, the conditions of the environment and the conditions of loading and motion during the lifetime of the structure. The EN 1337 (European, 2004) calls for minimum chrome thickness of 0.1 mm, which should improve the resistance to corrosion over the interface used in the tests of Figure 5-26. However, there is lack of data on the frictional properties of interfaces with chrome plated steel after long term aging. Based on the limited data provided in Figure 5-26, chrome-plated sliding interfaces should be penalized with a substantial aging factor.
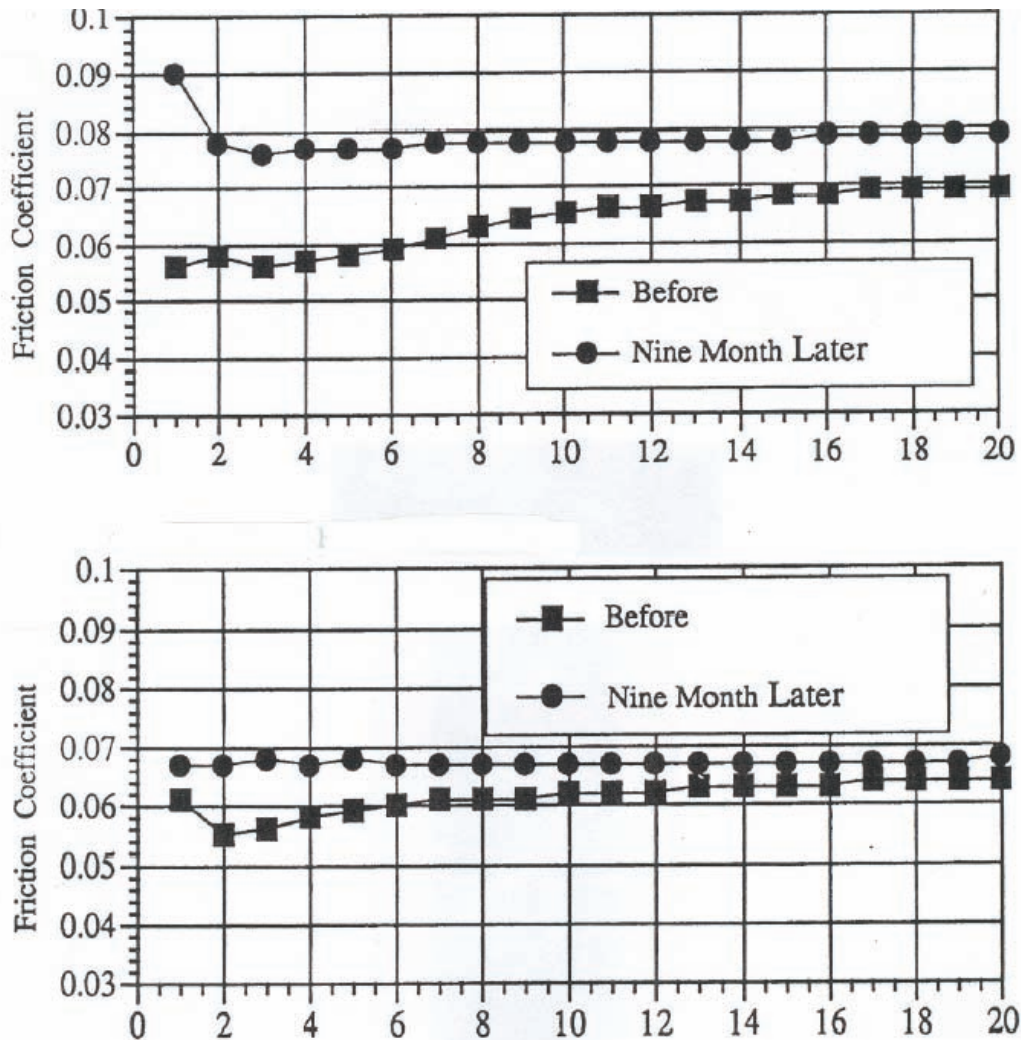
FIGURE 5-26 Effect of 9-Month Aging on Friction of Interface of Material Techmet-B in Contact with Chrome-Plated Carbon Steel (top) and with Stainless Steel (bottom)

148

5.12 Summary

Data on the frictional properties of interfaces consisting of PTFE or PTFE-based composites in contact with stainless steel and of certain bimetallic interfaces was presented and discussed in detail. Data on the effects of load dwell, apparent bearing pressure, velocity, temperature, cumulative movement (travel), roughness of stainless steel, corrosion of stainless steel, contamination and lubrication was described. Limited data on wear was presented. The longevity of chrome-plated sliding interfaces was discussed.

SECTION 6
ANALYSIS AND DESIGN OF SLIDING BEARINGS

6.1 Introduction

Contemporary sliding seismic isolation systems can take a variety of forms. Flat sliding bearings can be combined with elastomeric bearings to form hybrid isolation systems with a range of energy dissipation capabilities and stiffness. The basic types of flat sliding bearings are shown in Figure 6-1- pot, disk and spherical bearings. The three types differ in the construction of the rotational component of the bearing, with the spherical bearing having the least rotational resistance and hence the most favorable distribution of pressure on the sliding interfaces.

a. pot bearing   b. disc bearing

c. spherical bearing
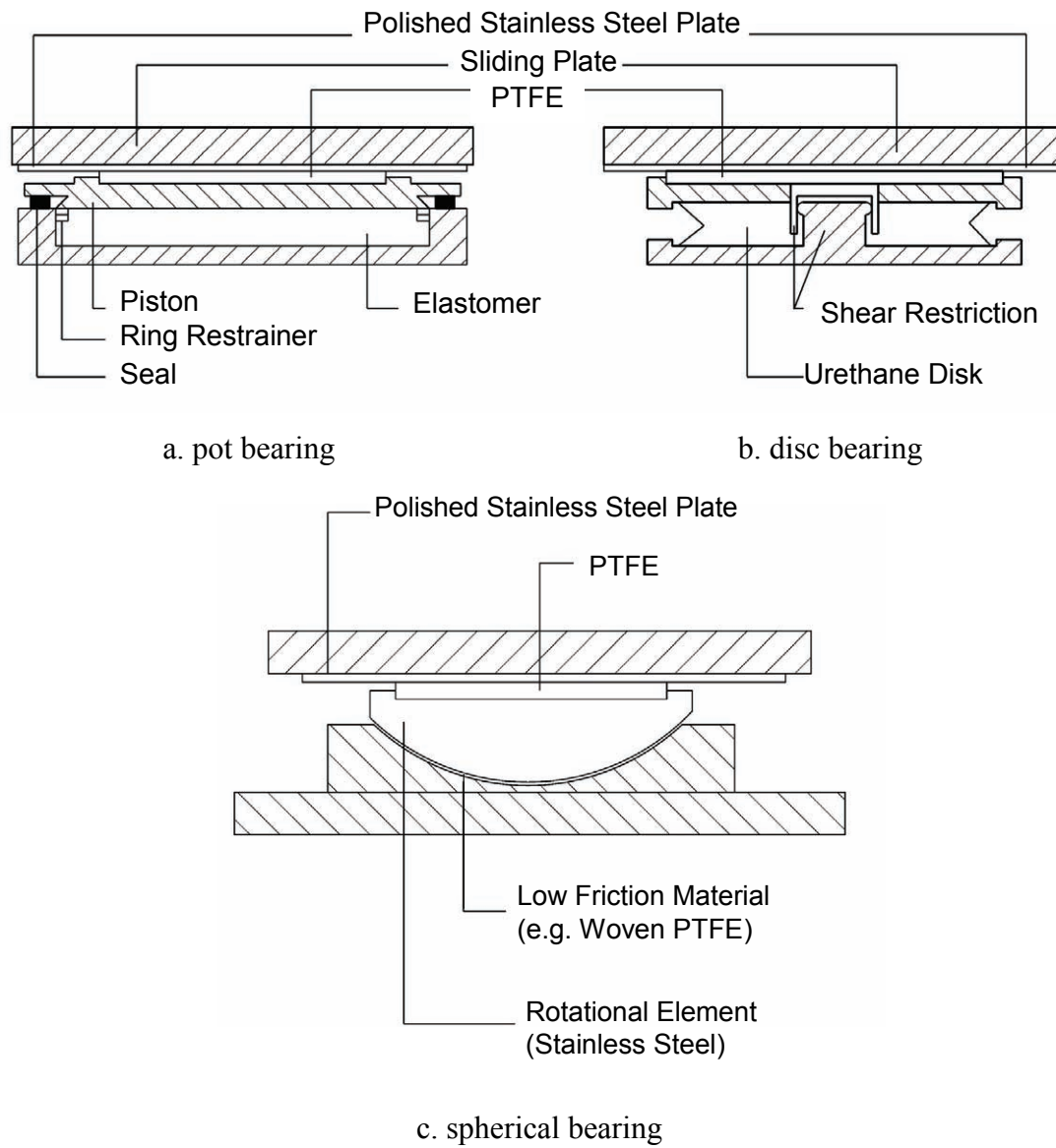
FIGURE 6-1 Flat Sliding Bearings

Materials used for the sliding interface of these bearings are typically austenitic stainless steel (either type 304 or preferably the most corrosion-resistant type 316 which contains molybdenum) in contact with unfilled PTFE. To achieve significant energy dissipation capability, the PTFE needs to be non-lubricated. Other materials have been used such as woven PTFE, PTFE-composites and bronze-lead composites, although bi-metallic interface are considered problematic (AASHTO, 1999; Constantinou et al., 1999).

Lubricated flat sliding bearings have been used in combination with yielding steel (elastoplastic) devices, such as that depicted in Figure 6-2 (Marioni, 1997), in bridge seismic isolation systems. In these systems, lock-up devices (or shock transmission units) are used to allow for unobstructed thermal movement of the bridge on the lubricated bearings. The devices lock-up in seismic excitation and engage the yielding steel devices, that dissipate energy and limit the seismic movement. However, such systems lack sufficient restoring force and might develop significant permanent displacements. The interested reader is referred to Tsopelas et al. (1997) and Roussis et al. (2003) for experimental and field observations on the behavior of elastoplastic isolation systems.
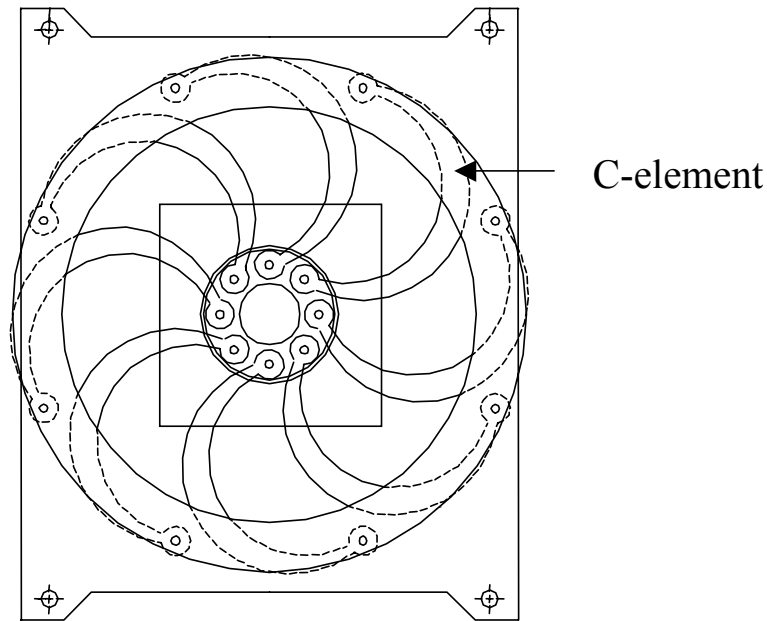
FIGURE 6-2   Elastoplastic Yielding Steel Device Used in Combination with Lubricated Sliding Bearings in Bridge Seismic Isolation

The single concave Friction Pendulum (FP) bearing (Figure 6-3) is a spherical bearing (for the rotational part) with a spherical sliding interface. It is similar to the spherical bearing of Figure 6-1(c) but has stiffness as a result of the curvature of the sliding interface. The lateral force, *F*, needed to impose a lateral displacement, *u*, of the FP bearing is given by (a more detailed description is provided in Section 6.3)

$$F = \frac{W}{R_E}u + \mu W \tag{6-1}$$

where W is the axial compressive load on the bearing, R_E is the effective radius of curvature of the sliding interface (the radius R minus the distance of the pivot point to the sliding surface), and μ is the coefficient of sliding friction. The FP bearing has found a number of applications in the seismic isolation of bridges, including the largest bearings in terms of seismic displacement capacity at the Benicia-Martinez Bridge and the largest in terms of load capacity at the I-40 Bridge (Imbsen, 2001). A variation on the single concave FP bearing is the Double Concave FP (DCFP) bearing, which is most suitable when compactness with large displacement capacity is desired. Since there is limited information on the DCFP bearing, Section 6.3 was developed to provide a general description of the bearing and present experimental results.
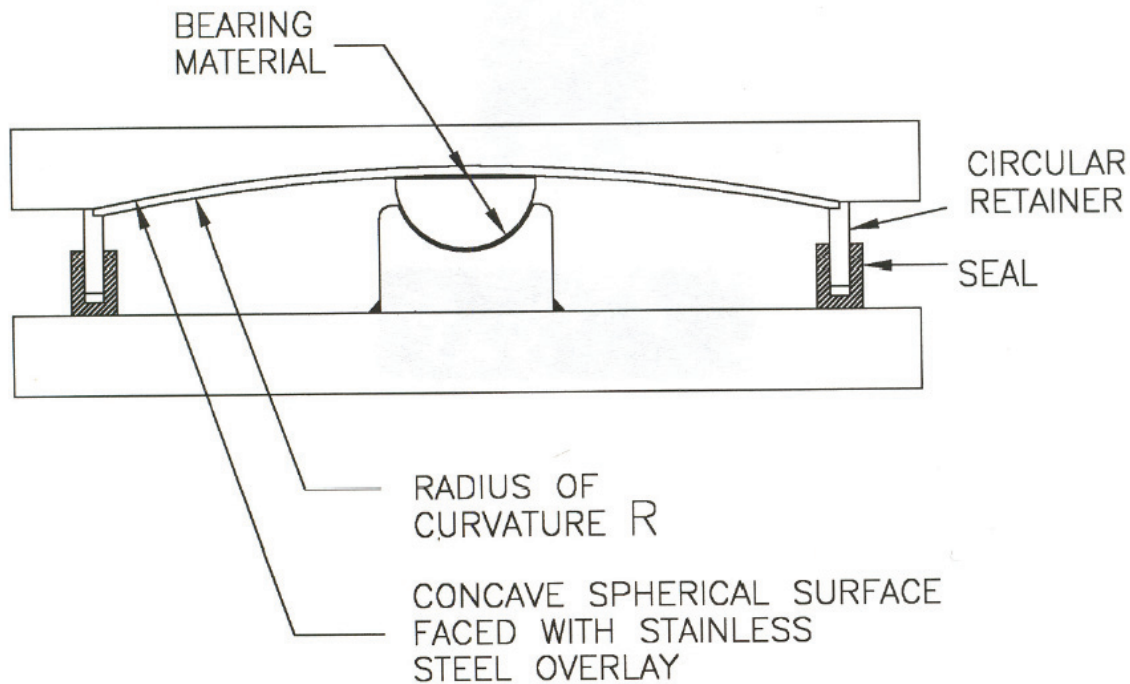
FIGURE 6-3 Friction Pendulum Bearing

Another sliding seismic isolation bearing is the Eradiquake bearing that is shown in Figure 6-4. It consists of a disc bearing with restoring force elements in the form of urethane springs. It is most suitable for small to moderate displacement demand and has found several applications in the Central and Eastern United States.
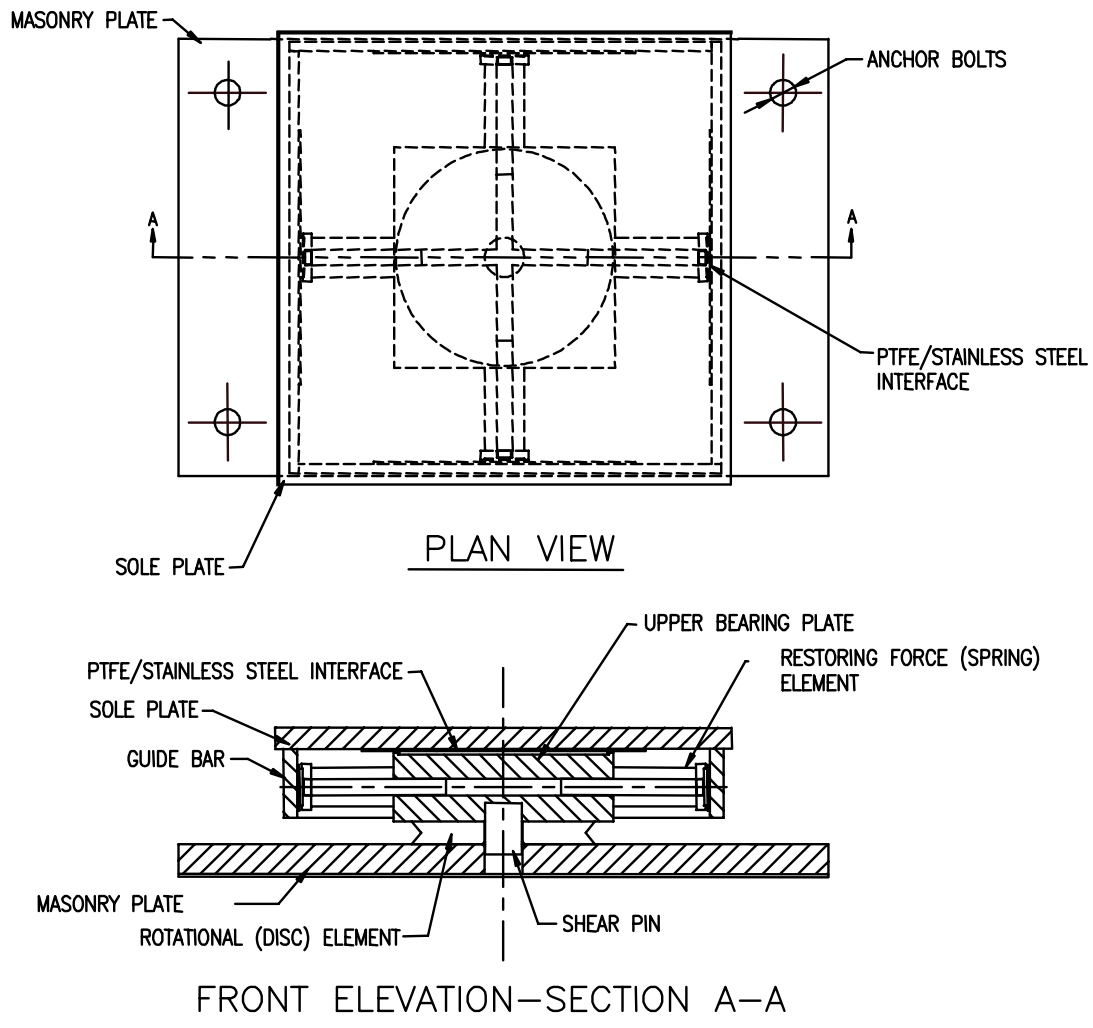
FIGURE 6-4 Eradiquake Isolation Bearing

6.2 Design of Sliding Bearings

The design of sliding bearings involves the following tasks:

a) Selection of materials for the sliding interface and the conditions of pressure to achieve the desired frictional characteristics.
b) Selection of the thickness of the stainless steel plate to avoid uplift or bow waves that may lead to rupture.
c) Selection of the PTFE thickness or other mating material to meet the desired wear characteristics for the application.
d) Selection of end-plate thickness to safely resist the applied loads and to provide sufficient stiffness to avoid distortion of the sliding surface.
e) Selection of the size and stiffness of the rotational to minimize edge stresses on the sliding interface and wear.

The following geometric and material specifications are recommended in AASHTO (1999) and should guide the design of sliding isolation bearings:

a) The useful thickness (thickness of the part projecting out of the recess or thickness of the part capable of wearing out) of sheet and woven PTFE should be at least 1.6 mm after compression. The European Standard EN 1337 (European, 2004) relates the useful thickness (or protrusion) to the dimensions of the sheet and requires a minimum thickness of 2.2 mm in the unloaded condition.

b) The useful thickness of other bearing liners should either be 1.6 mm or be determined on the basis of wear tests for the application. For bridge applications, wear due to bearing movement caused by traffic might dictate the selection of materials and their thickness.

c) The stainless steel sliding surface should be polished to a high degree of reflectivity. AASHTO (1999) recommends a finish with an arithmetic average (R_a) surface roughness of not more than 0.8 micrometers. The commercially available mirror finish will result in an arithmetic average surface roughness (R_a) of about 0.05 micrometers per ANSI/ASME B46.1-1985 (ASME, 1985).

d) The stainless steel should be austenitic and preferably of type 316 conforming to ASTM A240 (in the US) or type 5 CrNiMo conforming to DIN 17440 (in Germany) or equivalent. Austenitic 304 type is also acceptable although it has less corrosion resistance.

e) The thickness of the stainless steel sliding plate should be at least 1.5 mm for surfaces having a maximum dimension of less than 300 mm and at least 2.3 mm for surfaces having a maximum dimension of less than 900 mm. For larger dimensions, the thickness of the stainless steel plate should be verified by testing of full-size bearings at representative loads and velocities.

f) Materials other than corrosion-resistant austenitic stainless steel in contact with PTFE, woven PTFE, or other non-metallic liner materials are not recommended. In particular, chrome-plated carbon steel and bi-metallic interfaces are known to either corrode or undergo significant changes in the coefficient of friction (British Standards Institution, 1979; Constantinou et al., 1999).

g) Lubricated bearings should be of PTFE and dimpled. The diameter of the dimples should not exceed 8 mm and a depth less than 2 mm. The dimples should cover 20 to 30 percent of the PTFE surface. The lubricant should be silicone grease that is effective at very low temperatures.

Sliding bearings must have rotational capability in order to accommodate rotation resulting from loading, construction tolerances and thermal effects. Furthermore, the FP bearing needs to accommodate rotation, ϕ, resulting from lateral movement:

$$\phi = \sin^{-1}\left(\frac{u}{R}\right)$$ (6-2)

where u is the lateral movement and R is the radius of curvature. The ratio u/R is typically less than 0.2 and so the rotation is generally 0.2 rad or less.

The rotational resistance of sliding bearings is important for the calculation of the moment acting on the bearing and the associated edge stresses on the sliding interface. Roeder et al. (1995) presented experimental data on the rotational resistance of pot, disc and spherical bearings that can be used to guide the calculation of the rotational stiffness of sliding bearings.

6.3 Analysis of Double Concave Friction Pendulum Bearing

6.3.1 Introduction

The Double Concave Friction Pendulum (DCFP) bearing consists of two facing concave stainless steel surfaces. The upper and lower concave surfaces have radii of curvature R_1 and R_2 respectively, which can be different. The coefficients of friction of the concave surfaces are μ_1 and μ_2 respectively, which can also be different. An articulated slider faced with a non-metallic sliding material separates the two surfaces. The articulation is necessary for the appropriate distribution of pressure on the sliding interface and to accommodate differential movements along the top and bottom sliding surfaces.

The double concave bearing represents the first documented proposal for a seismic isolation system. Figure 6-5 shows the 1870 US patent of Jules Touaillon (1870) that describes a double concave rolling ball bearing. It took nearly 130 years to implement a double concave isolation system. Hyakuda et al. (2001) presented the description and observed response of a seismically isolated building in Japan which utilized DCFP bearings. The bearing used in Japan is similar to that shown in Figure 6-6(a) with equal radii concave surfaces but with a non-articulated slider. Articulation is needed to accommodate differential rotations of the slider top and bottom parts when friction is unequal on the two sliding interfaces and to evenly distribute load on the contact surface and avoid excessive wear. Tsai et al. (2005) described a DCFP bearing with articulated slider and presented experimental and analytical results on the behavior of the bearing for concave surfaces of equal radii and equal coefficients of friction at the top and bottom sliding surfaces.

The behavior of the DCFP bearing is described in this section. The presentation is different from those of prior studies and is based largely on the paper of Fenz and Constantinou (2006). The studies of Hyakuda et al. (2001) and Tsai et al. (2005) described the lateral force-displacement relationship of the bearing under conditions restricted to simultaneous sliding on both concave surfaces. A more general description of the behavior of the DCFP bearing is provided herein that accounts for (a) unequal radii of curvature of the two concave surfaces, (b) unequal coefficients of friction of the two sliding interfaces, (c) the effect of the height of the articulated slider on the lateral force-displacement relation, and (d) the effect of friction in the rotational part of the articulated slider on the lateral force-displacement relationship. Previous studies did not address these issues.

156
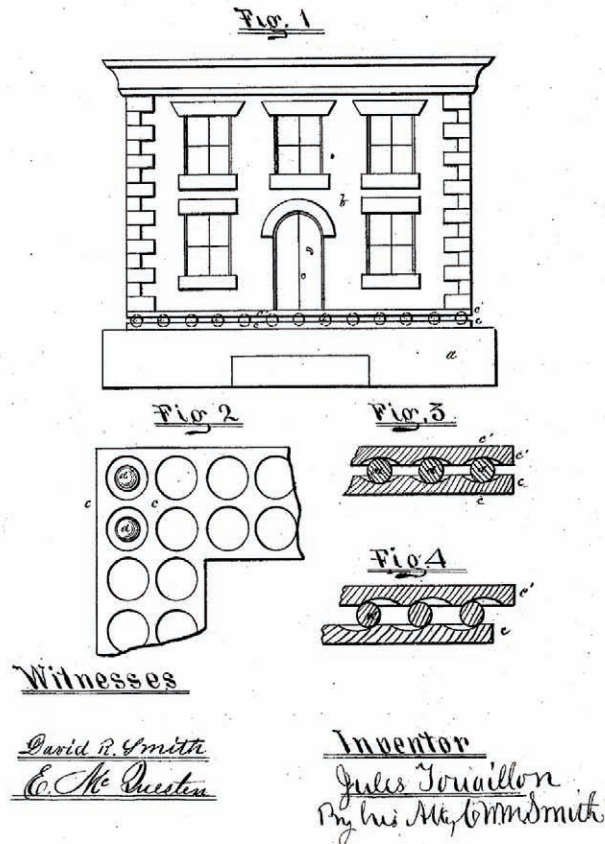
FIGURE 6-5 Jules Touaillon's Patent For Double Concave Ball Bearing

Moreover, experimental results on the behavior of model DCFP bearings are presented and compared to theoretical predictions. The experiments include four cases of bearing configuration, (a) equal radii and equal coefficients of friction, (b) equal radii and unequal coefficients of friction, (c) unequal radii and equal coefficients of friction and (d) unequal radii and unequal coefficients of friction. The presented results demonstrate a more complex behavior of DCFP bearing than previously thought. The lateral force-displacement relation of the bearing is shown to have a behavior ranging from rigid-linear hysteretic to rigid-bilinear hysteretic depending on the selection of the radii of curvature and the friction coefficients.

157

6.3.2 Force Displacement Relationship for the DCFP Bearing

Figure 6-6 presents cross sections through a DCFP bearing at various stages of displacement. Figure 6-6(a) shows a bearing at zero displacement and establishes the nomenclature used in this section. Figure 6-6(b) shows the bearing undergoing sliding on the lower concave surface only, a behavior that is possible when the coefficient of friction at the lower sliding interface is less than the coefficient of friction on the upper sliding interface. Movement such as that shown in Figure 6-6(b) requires rotation of the articulated slider. Given that friction cannot exactly be the same at the two sliding interfaces, there is always some rotation of the slider. This demonstrates the significance of articulation, without which, the slider would be subject to uneven wear. The maximum displacement capacity of the bearing is $2d$, where d is the maximum displacement capacity of a single concave surface, which is shown in Figure 6-6(c). Due to rigid body and relative rotation of the slider, the displacement capacity is actually slightly different than $2d$.
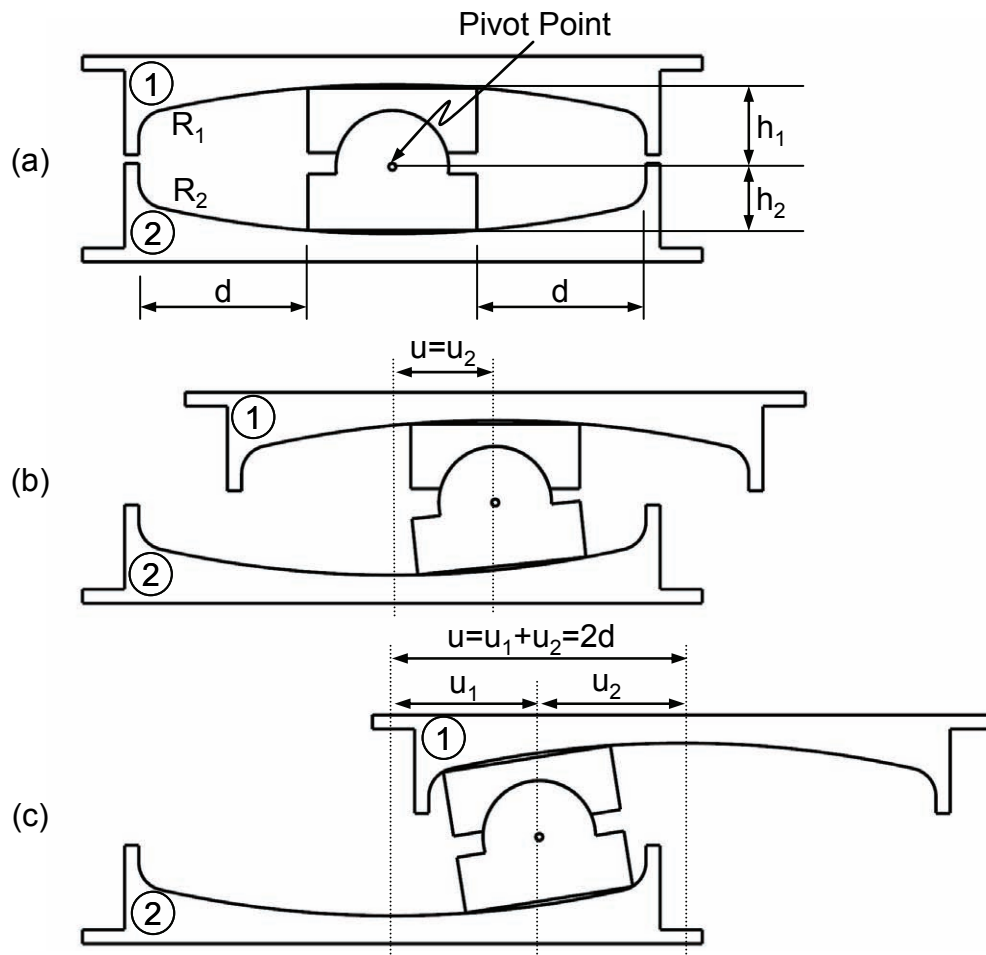
FIGURE 6-6 Section Through DCFP Bearing at Various Stages of Motion

158

To derive the force-displacement relationship for the DCFP bearing, the motions of the top and bottom surfaces are considered separately and then combined based on equilibrium and compatibility to produce the relationship for the entire bearing. Examining the free body diagram of the slider on the top concave surface in the deformed configuration as shown in Figure 6-7, the forces acting on the slider are:

a) The vertical load, W, acting at the pivot point.
b) The lateral force, F_1, transferred through the bottom part of the bearing and acting on the top part of the slider.
c) The friction force, F_1, acting along the sliding interface.
d) The resultant force of normal pressure acting on the sliding interface, S_1, which must be off center to satisfy moment equilibrium—demonstrating that the pressure distribution on the sliding interface is not uniform.
e) Friction tractions along the spherical surface of the articulated slider. These tractions cannot be directly measured in a test of a DCFP bearing. Rather, the effects of these tractions appear as part of the measured friction force. These tractions appear only when there is rotation of the articulated slider, which occurs only when the coefficient of friction is unequal on the two sliding interfaces, regardless of whether the two concave surfaces have equal or unequal radii of curvature.
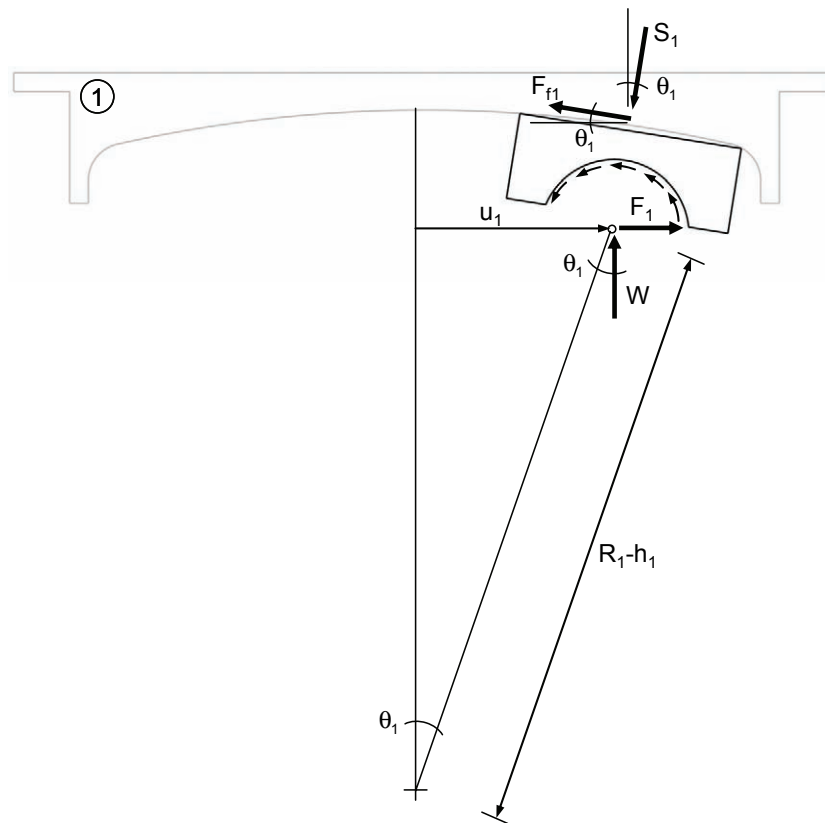
FIGURE 6-7 Free Body Diagram of Slider on Upper Concave Surface

159

Considering equilibrium in the horizontal and vertical directions, the following relationships are obtained:

$$F_1 - S_1 \sin\theta_1 - F_{f1}\cos\theta_1 = 0 \qquad (6\text{-}3)$$

$$W - S_1 \cos\theta_1 + F_{f1}\sin\theta_1 = 0 \qquad (6\text{-}4)$$

Note that in (6-3) and (6-4) the friction tractions do not appear; their effect is assumed to be part of the friction force F_{f1}.

From geometry, the displacement of the slider on the top concave surface, u_1 is:

$$u_1 = (R_1 - h_1)\sin\theta_1 \qquad (6\text{-}5)$$

where $R_1 - h_1$ is the distance from the center of the spherical surface to the pivot point of the articulated slider.

Combining (6-3) to (6-5), the force-displacement relationship that governs the motion on one concave sliding surface is the force-displacement relationship for the traditional FP bearing:

$$F_1 = \frac{W}{(R_1 - h_1)\cos\theta_1}u_1 + \frac{F_{f1}}{\cos\theta_1} \qquad (6\text{-}6)$$

A similar analysis of equilibrium for sliding on the bottom concave surface gives:

$$F_2 = \frac{W}{(R_2 - h_2)\cos\theta_2}u_2 + \frac{F_{f2}}{\cos\theta_2} \qquad (6\text{-}7)$$

where F_2 is the force transferred through the top part of the bearing and acting on the bottom slider, u_2 is the displacement of the slider along the bottom concave surface, F_{f2} is the friction force acting along the bottom sliding surface and θ_2 is the angle of rotation of the bottom part of the articulated slider.

Typically the radii of curvature are large compared to the displacements u_1 and u_2 such that angles θ_1 and θ_2 are small and the following simplifications can be made with negligible loss of accuracy:

$$\cos\theta_1 \approx \cos\theta_2 \approx 1 \qquad (6\text{-}8)$$

$$\sin\theta_1 \approx \theta_1 , \sin\theta_2 \approx \theta_2 \qquad (6\text{-}9)$$

Equations (6-6) and (6-7) can be simplified to:

$$F_1 = \frac{W}{R_1 - h_1} u_1 + F_{f1} \tag{6-10}$$

$$F_2 = \frac{W}{R_2 - h_2} u_2 + F_{f2} \tag{6-11}$$

Equations (6-10) and (6-11) govern the force-displacement relationship for the top and bottom sliding surfaces respectively. The significance of the height of the articulated slider becomes apparent in these equations. These equations also apply for the single concave FP bearing; FP bearings carrying large axial loads have substantial sliders, which influence their force-displacement behavior as noted above.

For the entire bearing, u, the total displacement (top plate relative to bottom plate) is the sum of the displacements on the top and bottom surfaces:

$$u = u_1 + u_2 \tag{6-12}$$

Furthermore, considering equilibrium of the slider in the horizontal direction (and excluding the insignificant inertia forces associated with the moving parts of the bearing):

$$F = F_1 = F_2 \tag{6-13}$$

Using (6-6) through (6-13), the force-displacement relationship for the bearing is:

$$F = \left(\frac{W}{R_1 + R_2 - h_1 - h_2} \right) u + \left(\frac{F_{f1}(R_1 - h_1) + F_{f2}(R_2 - h_2)}{R_1 + R_2 - h_1 - h_2} \right) \tag{6-14}$$

and the individual displacements on each sliding surface are:

$$u_1 = \left(\frac{F - F_{f1}}{W} \right)(R_1 - h_1) \tag{6-15}$$

$$u_2 = \left(\frac{F - F_{f2}}{W} \right)(R_2 - h_2) \tag{6-16}$$

Equation (6-14) is valid only when sliding is simultaneously occurring on both concave surfaces. Consider the case where friction at the sliding interfaces is unequal, for example, $F_{f1} < F_{f2}$. Upon application of lateral force, F, such that $F_{f1} < F < F_{f2}$, sliding will occur only on the surface of least friction. Motion will continue along only surface 1 ($u_1 = u, u_2 = 0$) until $F = F_{f2}$, when sliding will commence on both surfaces. This occurs at a displacement u^* given by:

$$u^* = (\mu_2 - \mu_1)(R_1 - h_1) \tag{6-17}$$

where $\mu_1 = F_{f1}/W$ and $\mu_2 = F_{f2}/W$ are the coefficients of friction ($\mu_1 \leq \mu_2$) at the two sliding interfaces. Therefore, (6-14) is valid only if $u \geq u^*$. If $u < u^*$, the force-displacement relationship is governed by (6-10) for $\mu_1 \leq \mu_2$ and (6-11) for $\mu_2 \leq \mu_1$. The generalized force-displacement behavior for the case $\mu_1 \leq \mu_2$ is presented in Figure 6-8.
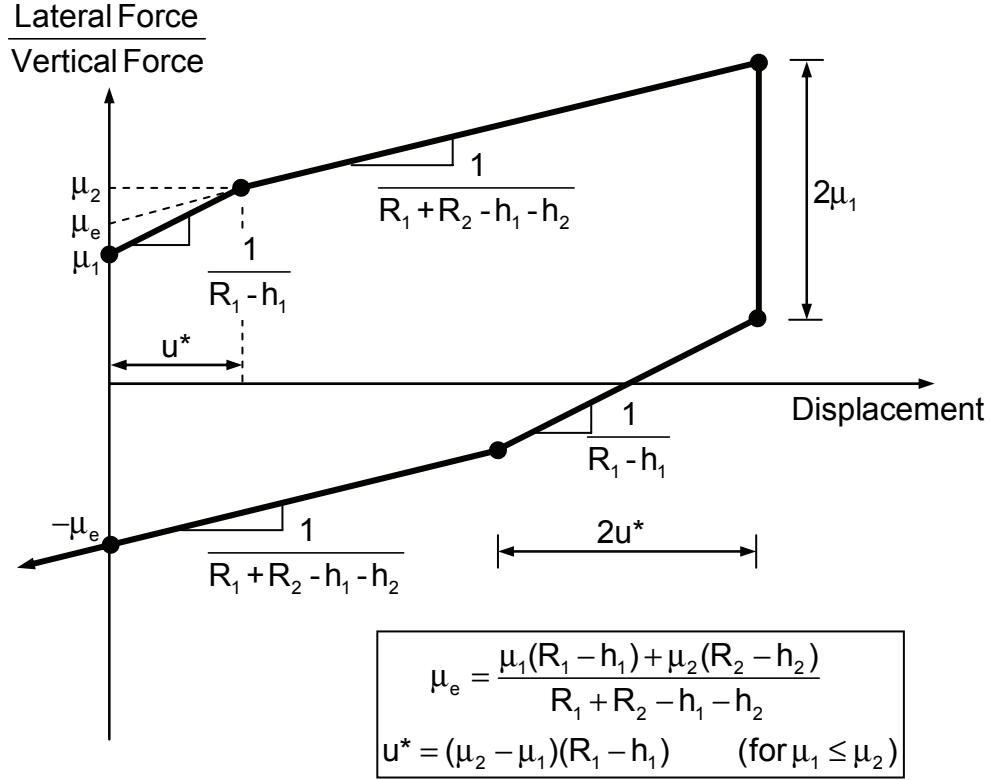
FIGURE 6-8 Force-displacement relationship for DCFP bearing with $\mu_1 \leq \mu_2$

Upon sliding on both concave surfaces, the characteristic strength of the bearing is equal to $\mu_e W$, where μ_e is the effective coefficient of friction. The effective coefficient of friction is derived from the second term of (6-14) by dividing by the vertical load, W.

$$\mu_e = \frac{\mu_1(R_1 - h_1) + \mu_2(R_2 - h_2)}{R_1 + R_2 - h_1 - h_2} \tag{6-18}$$

An interesting observation may be made by deriving expressions for the angles of rotation θ_1 and θ_2 (see Figure 6-7): the angles of rotation of the top and bottom parts of the articulated slider, respectively. If $\theta_1 = \theta_2$, the articulated slider moves as a rigid body without relative rotation. Based on the geometry presented in Figure 6-8 and (6-15), θ_1 is given by:

$$\theta_1 = \sin^{-1}\left(\frac{u_1}{R_1 - h_1}\right) = \sin^{-1}\left(\frac{F - F_{f1}}{W}\right) \tag{6-19}$$

162

Similarly, using (6-16), θ_2 is given by:

$$\theta_2 = \sin^{-1}\left(\frac{u_2}{R_2 - h_2}\right) = \sin^{-1}\left(\frac{F - F_{f2}}{W}\right) \tag{6-20}$$

Therefore, when the friction forces at the two sliding interfaces are equal, and irrespective of whether the two surfaces have equal or unequal radii, the angles of rotation are equal and the slider does not experience relative rotation.

When the normalized lateral force is plotted against the component of sliding displacement on each surface, the resulting hysteresis loop is that of a single concave FP bearing having the same radius of curvature and coefficient of friction. The overall force-displacement relationship for the DCFP bearing can be obtained by considering two single concave FP bearings acting in series. From equilibrium of the articulated slider, the horizontal forces F_1 and F_2 must be equal (except for the insignificant effect of the inertia force of the slider).

The behavior shown in Figure 6-8 assumes that the coefficient of friction at each sliding interface is constant. In reality, the coefficient of friction exhibits velocity dependence. Moreover, the magnitude of the friction force will be affected by contributions from friction tractions in the articulated slider as shown in Figure 6-7. These effects are apparent in the test results to be presented next.

6.3.3 Experimental Testing of DCFP

Testing of two DCFP bearings was performed using the single bearing test machine in the Structural Engineering and Earthquake Simulation Laboratory at the University at Buffalo (Kasalanati and Constantinou, 1999).

The first test specimen, shown in Figure 6-9, had two 229 mm diameter concave surfaces each with a radius of curvature of 474 mm. However, due to small differences in the height of the two parts of the slider (see Figure 6-9), the effective radii $R_1 - h_1$ and $R_2 - h_2$, were 438 and 442 mm respectively. The diameter of the articulated slider was 75 mm, yielding a total displacement capacity of 154 mm. The articulated slider was faced with a woven material similar to the PTFE Composite 1 in Section 5. To instrument the articulated slider and allow for observation during testing, the retainer ring was machined down.

Tests were conducted under a constant vertical load with three fully reversed cycles of sinusoidal motion at 100 mm amplitude and 0.10 Hz frequency, resulting in a peak velocity of 63 mm/sec: the velocity of the top part of the bearing with respect to the bottom part and not the peak sliding velocity. The peak sliding velocities were equal to or greater than 25 mm/sec (the composite material used in the bearing typically exhibits a peak coefficient of sliding friction at velocities exceeding 25 mm/sec).
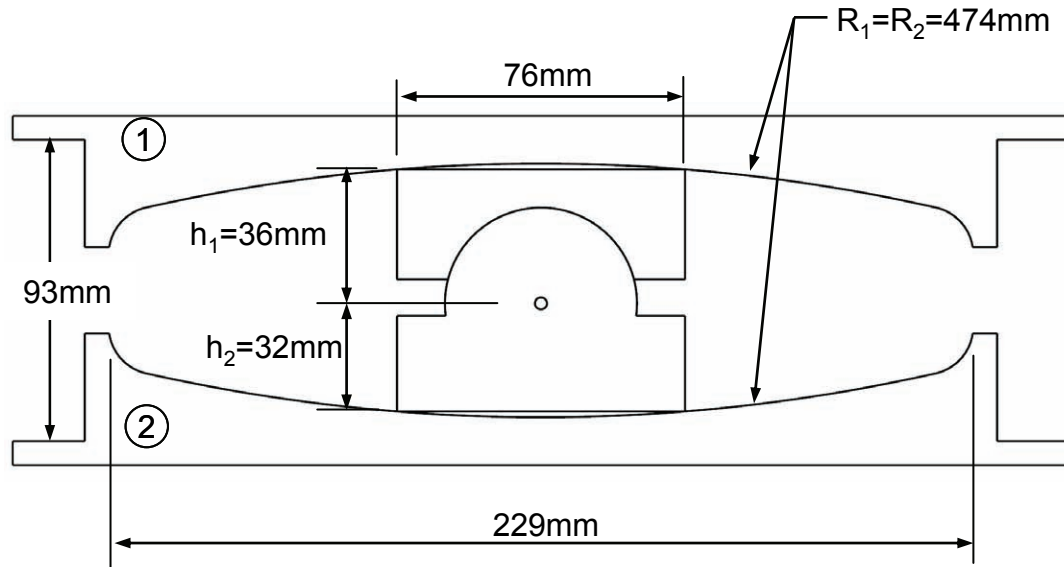
FIGURE 6-9 Tested DCFP Bearing with Concave Surfaces of Equal Radii

The frictional conditions were varied during the various tests. In one configuration, the bearing was tested with the two sliding interfaces having nearly identical frictional properties. In another configuration, the bottom surface of the articulated slider was coated with a silicone lubricant so that the two sliding surfaces had substantially different coefficients of friction. To achieve effective lubrication, the radius of curvature of the slider at its upper and lower surfaces was machined larger than the radius of the mating concave surface, which resulted in bearing over an annular area on the perimeter of the slider as shown approximately in Figure 6-9: the sliding interfaces contained a pocket of lubricant.

Figures 6-10 and 6-11 present the recorded hysteresis loops and histories of displacement and velocity for the cases where the two surfaces have nearly identical coefficients of sliding friction. In Figure 6-10 and figures that follow, both the overall and deconstructed hysteresis loops are presented. The values of the coefficient of friction shown in Figure 6-10 are those identified in the experiments. The velocity histories were obtained through numerical differentiation of the displacement data.

The analytical loops presented in Figure 6-10 were constructed using (6-10) to (6-18) and the measured values of $R_1 - h_1$, $R_2 - h_2, \mu_1$ and μ_2. The analytical and experimental results are in good agreement except that (a) the velocity dependence evident in the experimental hysteresis loops at maximum displacement are not incorporated in the analytical model, and (b) the displacements and velocities at the two sliding interfaces are slightly different from the theoretical predictions. The primary contribution to the

Equal Radii and Equal Friction Case
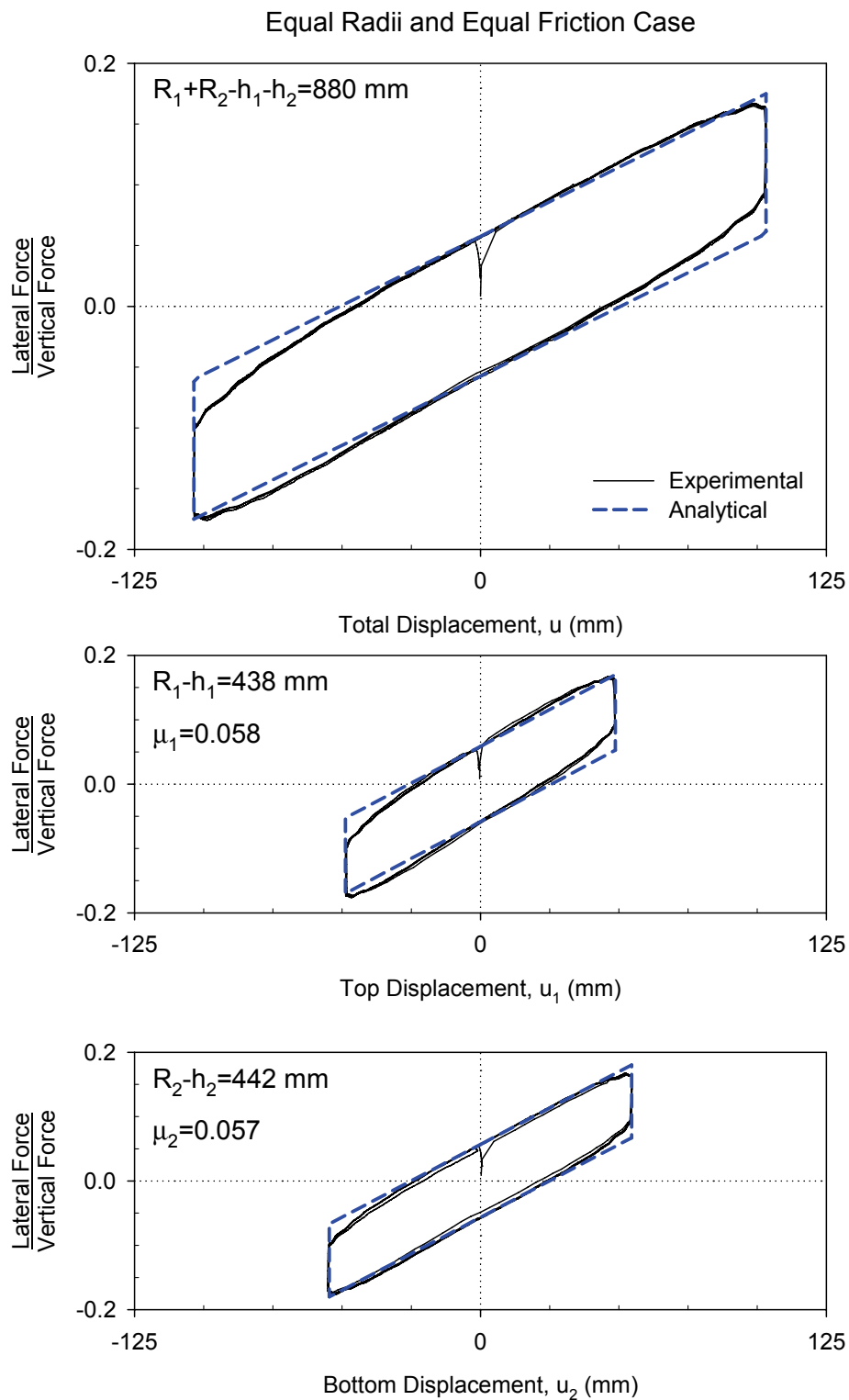
FIGURE 6-10 Comparison of Experimental and Analytical Results for the DCFP Bearing With Equal Radii and Equal Friction

165
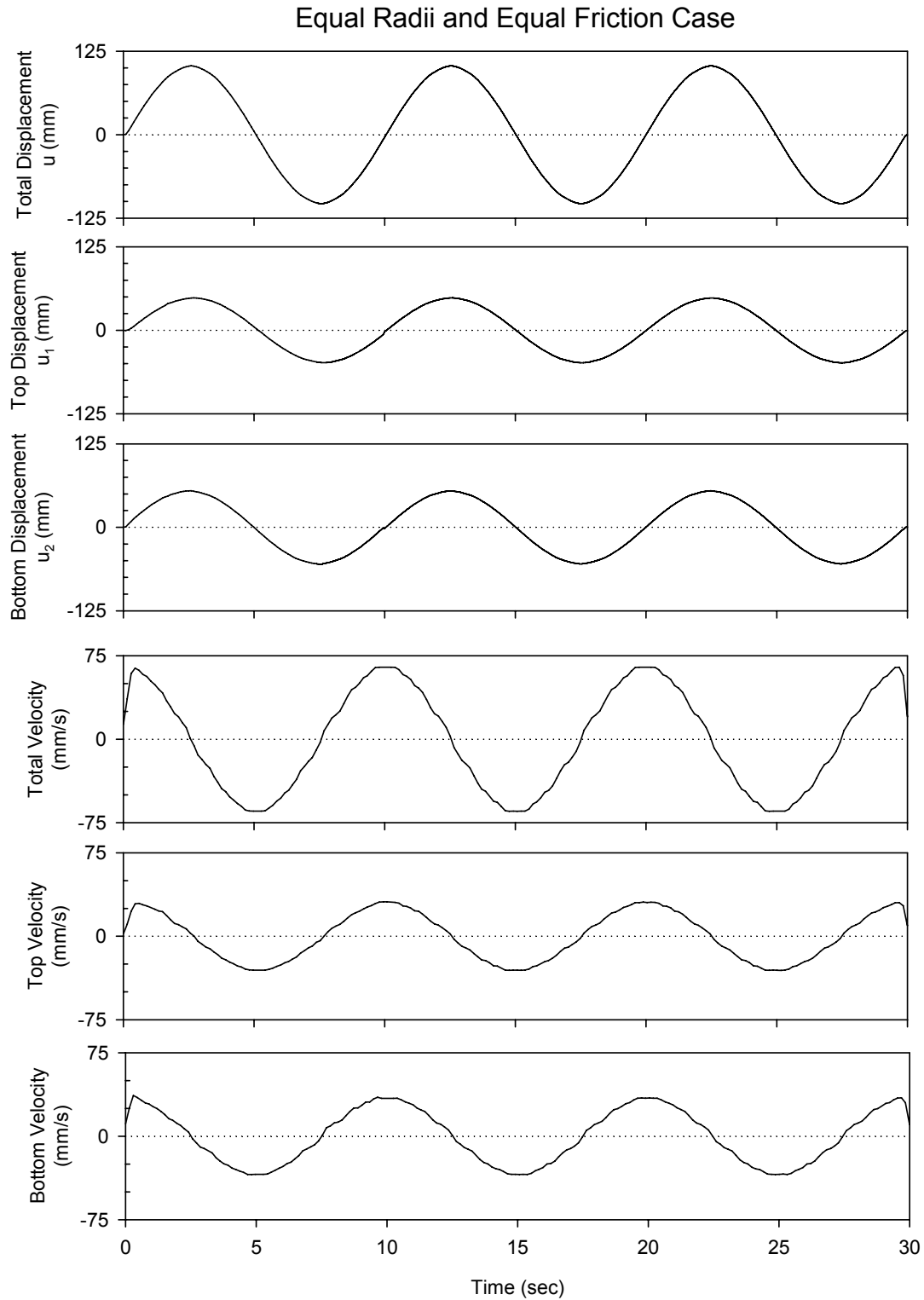
FIGURE 6-11 Recorded Histories of Displacement and Velocity for the DCFP Bearing With Equal Radii and Equal Friction

166
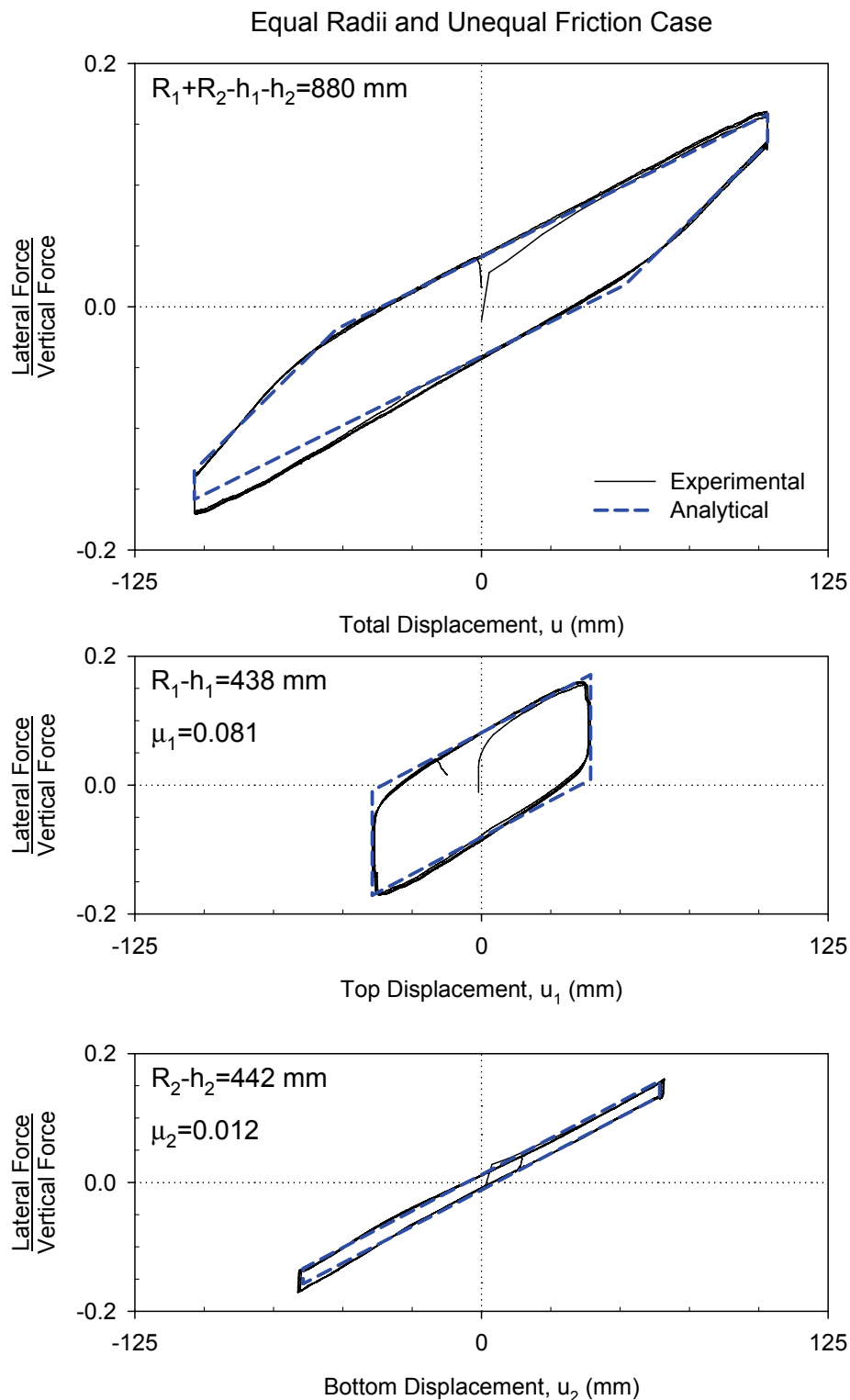
FIGURE 6-12 Comparison of Experimental and Analytical Results for the DCFP Bearing With Equal Radii and Unequal Friction.
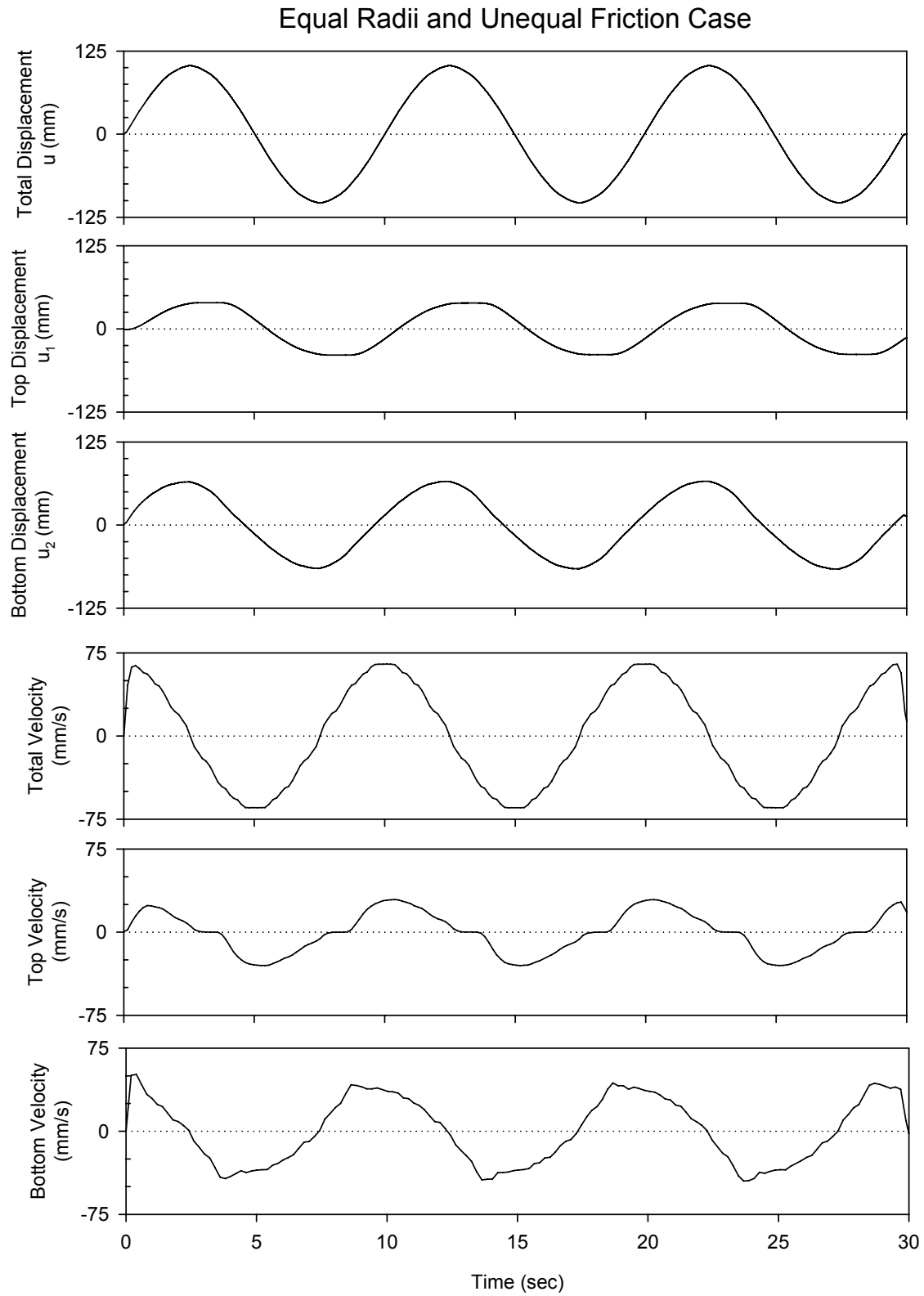
FIGURE 6-13   Recorded Histories of Displacement and Velocity for the DCFP Bearing With Equal Radii and Unequal Friction

difference is the effect of the rotation of the articulated slider on the measured displacement. The displacement of the slider should have been measured at the pivot point but this was not possible; the displacement transducer was placed slightly higher than the pivot point, resulting in a slight underestimation of u_1 and overestimation of u_2.

The behavior of the bearing is altered significantly when the coefficients of friction on each surface are different. In Figures 6-12 and 6-13, data is presented for a test performed with the bottom part of the slider lubricated as described previously. The analytical loops constructed using (6-10) through (6-18) using the experimentally measured values of friction $\mu_1 = 0.081$ and $\mu_2 = 0.012$ are also shown in Figure 6-12. The analytical loops are in good agreement with the experimental loops, except that the experimental force-displacement loops are asymmetric with more friction force measured when the displacement is negative. The experimental force-displacement loops for the lower interface show some asymmetry, so a contributor to the asymmetry in Figure 6-12 might have been actual asymmetry in the friction at the lower interface. The slight error in the displacement measurements also contributed to this asymmetry.

The histories of displacement and velocity show that upon reversal of motion, sliding only occurs on the surface of least friction. The velocity on the top surface is temporarily zero when the motion is reversed, as the coefficient of friction on the bottom surface is less.

The second configuration tested is shown in Figure 6-14 and had an upper concave surface with $R_1 = 762$ mm and a lower concave surface with $R_2 = 474$ mm. Three fully reversed cycles of sinusoidal motion with 100 mm amplitude and 0.10 Hz frequency were imposed under constant vertical load.
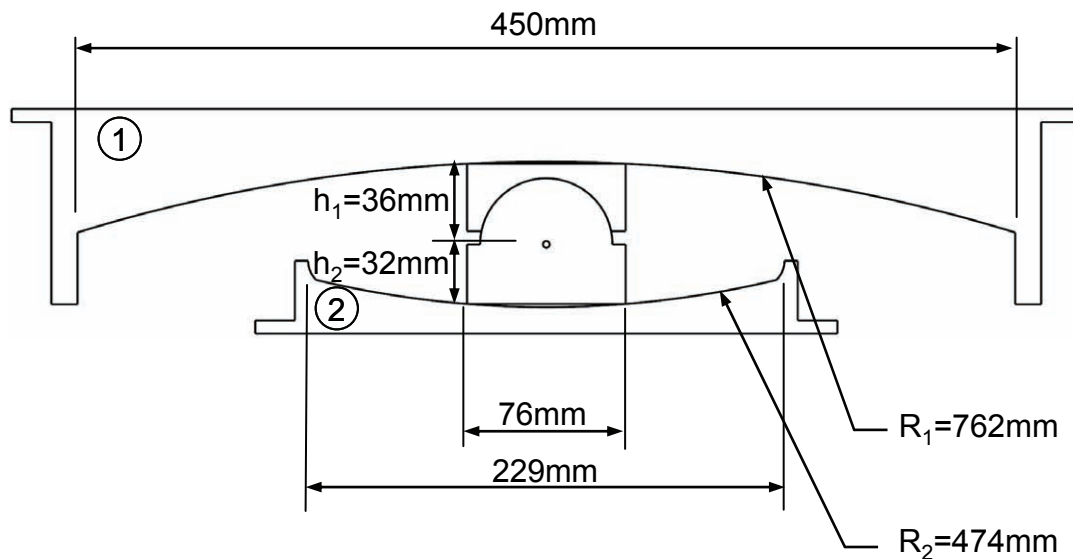
FIGURE 6-14 Tested Bearing with Concave Surfaces Having Unequal Radii of Curvature

When the coefficients of friction on each surface are equal, the behavior is rigid-linear hysteretic as shown in Figure 6-15, where again the experimentally obtained values of the coefficients of friction are indicated. Though there is simultaneous sliding on each surface over the full course of motion due to equal friction, the displacement amplitudes on each surface differ due to the different radii, as shown in Figure 6-16. The analytical loops, constructed using (6-10) through (6-18) and the experimentally determined values of μ_1 and μ_2 are in good agreement with the experimental loops.

Figure 6-17 presents force-displacement loops for the case when friction is unequal on each surface. The recorded histories of displacement and velocity are shown in Figure 6-18. The lower value of friction at the bottom sliding interface was achieved with lubrication as previously described. The analytical construction of the lateral force-displacement loops used (6-10) to (6-18) and the experimentally determined values of the coefficients of sliding friction: $\mu_1 = 0.038$ and $\mu_2 = 0.021$. The analytical loops are in good agreement with the experimental loops except for higher friction during sliding on one surface caused by rotation of the slider, which was not considered in the model.

In this test, the interface between the two parts of the articulated slider was cleaned of lubricant, which increased the friction tractions at this interface. The effect of these tractions may be seen in the deconstructed loop of the bottom part of the bearing in Figure 6-17. The coefficient of friction is greater than 0.021 during the intervals of motion over which sliding on the upper surface ceased (upon unloading over a total displacement interval equal to $2u^*$). During this time interval, the articulated slider underwent large relative rotation. When sliding starts at both surfaces, the relative rotation diminishes, resulting in a smaller friction-traction contribution to the total friction force. This interesting (albeit insignificant) behavior was observed only when the interior of the slider was free of lubrication.

6.3.4 Considerations for Analysis and Design of DCFP Bearings

DCFP bearings having concave surfaces of equal radii and equal friction were first applied in Japan on a small number of buildings (Hyakuda et al, 2001). To date, there have been no applications of DCFP bearings with different radii or different coefficients of friction. Some issues related to design and implementation of DCFP bearings are presented later in this report.

$P - \Delta$ Moment Transfer

In the single concave FP bearing, the $P - \Delta$ moment (moment resulting from vertical load P through the total bearing displacement Δ) is transferred to the structure or foundation on the side of the concave plate. For the DCFP bearing, this moment is divided between the two concave plates. The moment transferred to the top and bottom concave plates are Pu_1 and Pu_2, where u_1 and u_2 are the displacements on each surface given by (6-15) and (6-16). For bearings with $R_1 - h_1 = R_2 - h_2$ and $\mu_1 \approx \mu_2$, the displacements u_1 and u_2 are each equal to 0.5Δ and the moment transferred through each concave plate is therefore $0.5P\Delta$.

Unequal Radii and Equal Friction Case

$R_1+R_2-h_1-h_2=1168$ mm

$R_1-h_1=726$ mm

$\mu_1=0.029$

$R_2-h_2=442$ mm

$\mu_2=0.028$
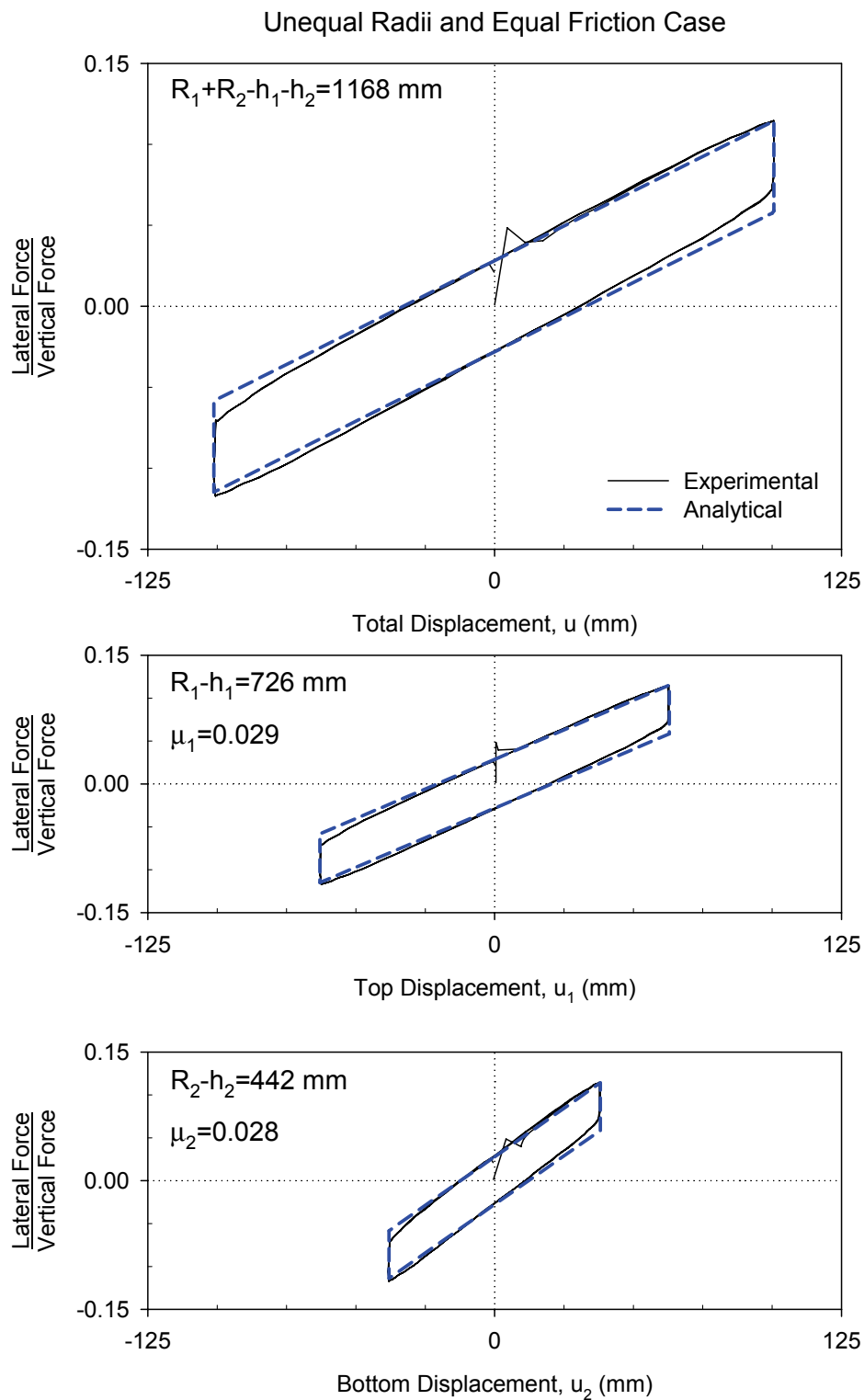
FIGURE 6-15   Comparison of Experimental and Analytical Results for DCFP Bearing With Unequal Radii and Equal Friction

171
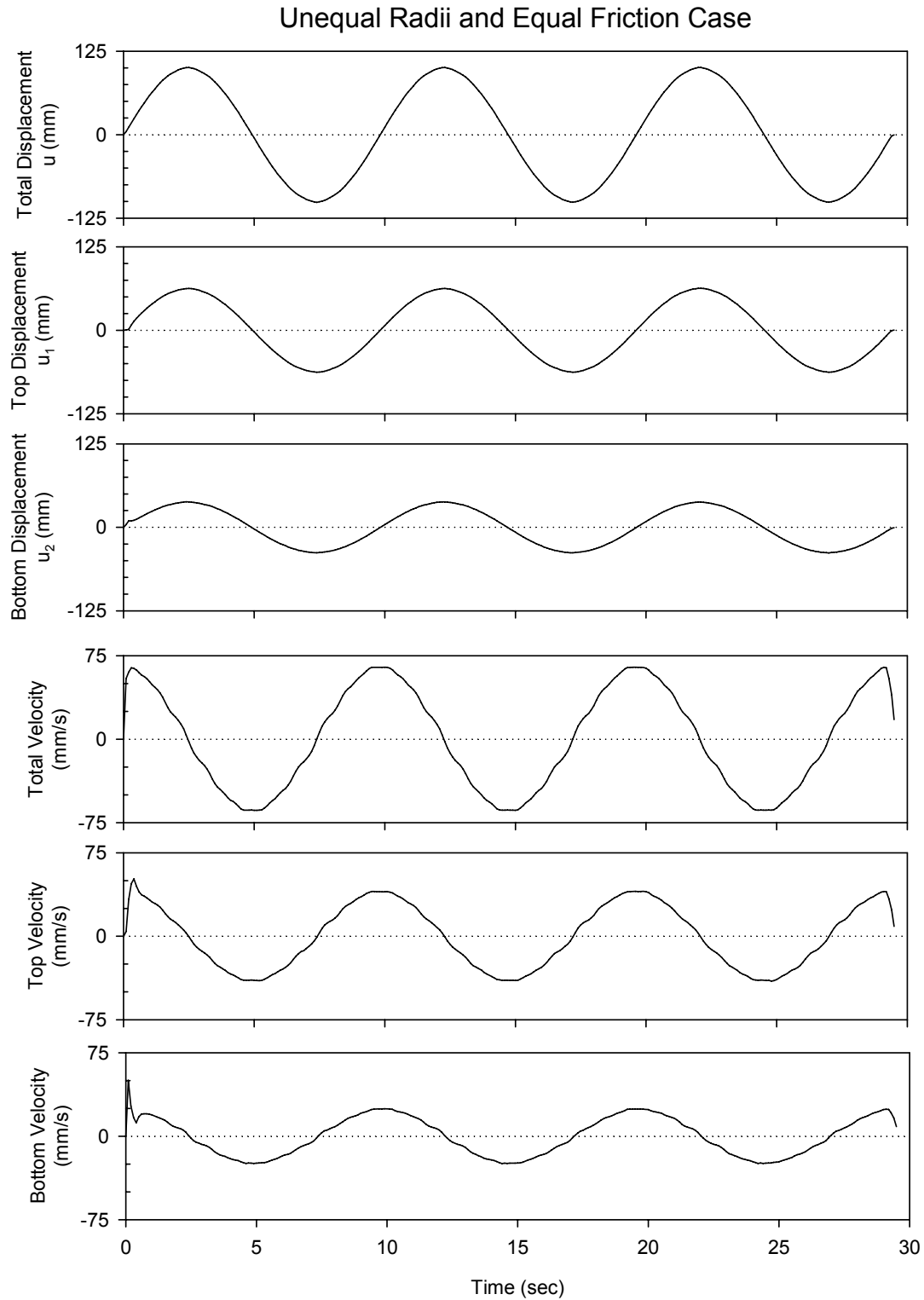
FIGURE 6-16 Recorded Histories of Displacement and Velocity for DCFP Bearing With Unequal Radii and Equal Friction

172
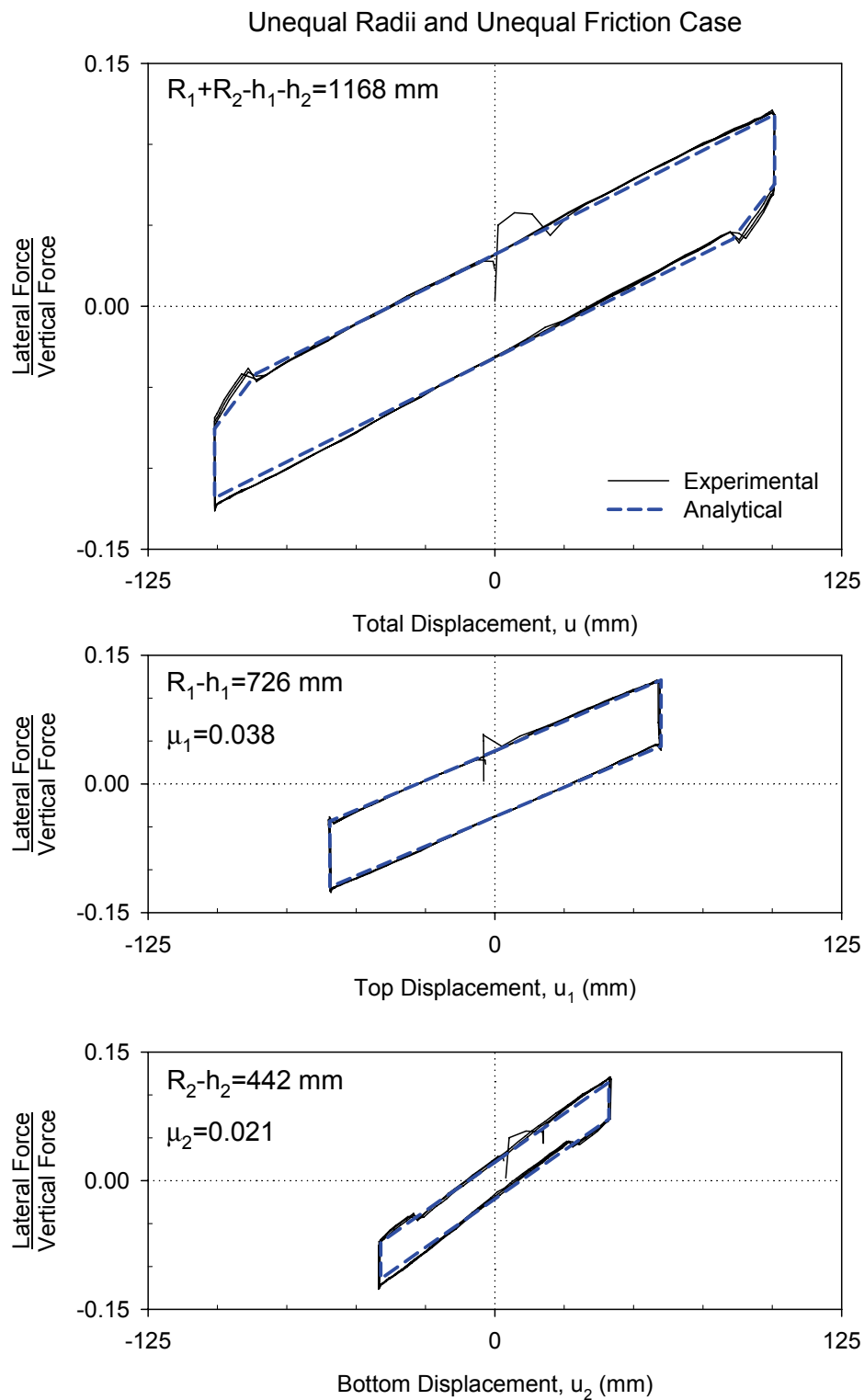
FIGURE 6-17 Comparison of Experimental and Analytical Results for DCFP Bearing With Unequal Radii and Unequal Friction
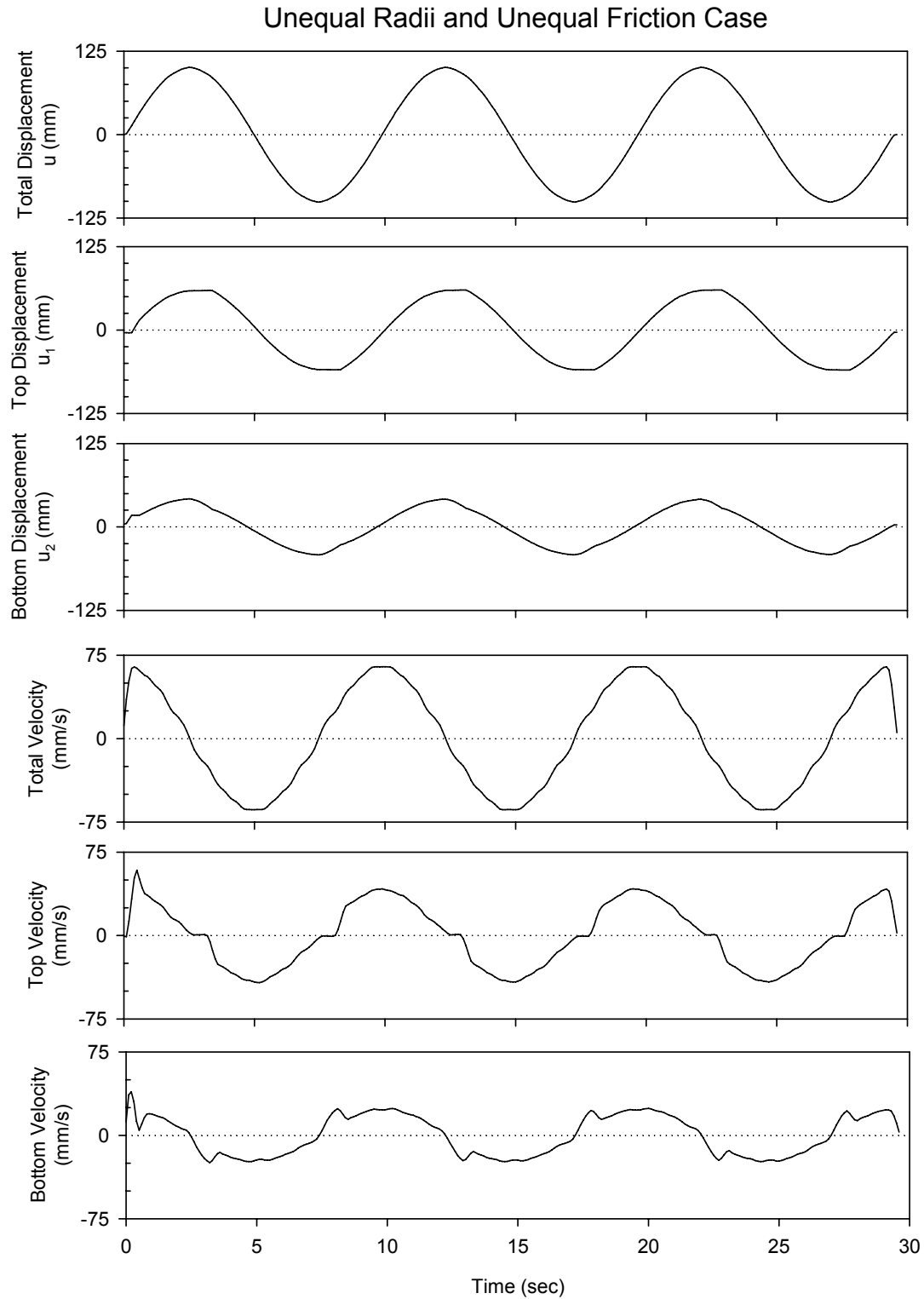
FIGURE 6-18 Recorded Histories of Displacement and Velocity for DCFP Bearing With Unequal Radii and Unequal Friction

174

Modeling for Dynamic Analysis

Various options exist for modeling of DCFP bearings in programs commonly used for response-history analysis of seismically isolated structures (i.e., SAP2000 and 3D-BASIS). For the simplest case of $R_1 - h_1 = R_2 - h_2$ and $\mu_1 \approx \mu_2$, the behavior of the bearing can be modeled as that of a traditional FP bearing with radius of curvature equal to $R_1 + R_2 - h_2 - h_1$ and coefficients of friction as determined by experimentation. The velocity dependence of the coefficient of friction is described by (5-1). At issue here is the value of parameter a that controls the transition from $f_{\min}$ to $f_{\max}$. Typically $f_{\max}$ is determined in a prototype bearing testing program and $f_{\min}$ and a are selected from available (and appropriate) experimental results.

The relevant velocities for the computation of these parameters are the sliding velocities on each concave surface and not the total velocity. For DCFP bearings of equal radii and coefficients of friction, the sliding velocities on each surface are equal and have magnitude equal to one half of the total velocity. Equation (5-1) applies but a value of $a/2$ must be specified. For example, a value of $a = 100$ sec/m is often used for modeling single concave FP bearings. To model a DCFP bearing with the same type of sliding interface, a value $a = 50$ sec/m should be specified in the analysis program.

For the general case of a DCFP bearing with unequal radii and unequal coefficients of friction, the behavior can be modeled using two traditional FP bearing elements in series. It was shown earlier that the overall force-displacement relationship can be deconstructed into the components on each sliding surface, yielding a hysteresis loop for each concave surface identical to that would be obtained for a traditional FP bearing with the same radius of curvature and coefficient of friction. Therefore, by defining two separate single concave FP elements with the radii of curvature and coefficients of friction of each concave surface and connecting them in series with a point mass representing the articulated slider, the overall behavior of the DCFP bearing is obtained. The velocity dependence of the coefficient of friction is still governed by (5-1), though the velocities of each isolator element represent the true sliding velocities on each surface. The rate parameter a need not be modified in this instance

Value of Property Modification Factor for Contamination

The concept of bounding analysis on the basis of system property modification factors or λ-factors is described herein in Section 12 and Constantinou et al. (1999). The concept is employed in the 1999 AASHTO Guide Specifications for Seismic Isolation Design and is a systematic procedure for calculating upper and lower bound values for the mechanical properties of seismic isolators to account for aging, contamination, history of loading, temperature and other effects.

For FP bearings, only the coefficient of friction is affected by the aforementioned effects. The system property modification factors for DCFP bearings are the same as those for traditional FP bearings except for the contamination factor. Separate factors should be considered for the upper and lower concave surfaces, respectively. Anticipating that DCFP bearings will be sealed (as unsealed bearings with a concave stainless steel surface facing up are not permitted in the 1999 AASHTO Guide Specifications), the

contamination factors will be $\lambda_{c1} = 1.0$ for the upper (downward facing) surface and $\lambda_{c2} = 1.1$ for the lower (upward facing) surface. The contamination factor for the entire bearing is then given by

$$\lambda_c = \frac{\lambda_{c1}\mu_1(R_1 - h_1) + \lambda_{c2}\mu_2(R_2 - h_2)}{\mu_1(R_1 - h_1) + \mu_2(R_2 - h_2)} \tag{6-21}$$

This expression was derived on the basis of (6-18) that combines the contributions of the frictional forces from the two sliding interfaces. Therefore, for the typical case of DCFP bearings with equal radii and friction, $\lambda_c = (\lambda_{c1} + \lambda_{c2})/2 = 1.05$.

Slider Offset and Permanent Displacements
In displacement-controlled tests in which the coefficients of friction on the top and bottom surfaces are unequal, the articulated slider will offset inside the bearing. This is evident in Figure 6-13 where it can be seen that there are equal and opposite displacements, denoted $\bar{u}$, on the top and bottom surfaces even though the total bearing displacement is zero. That is, $u = 0, u_1 = -u_2 = \pm\bar{u}$.

The magnitude of $\bar{u}$ can be calculated readily and expressed in a number of ways. By setting $u_1 = \bar{u}$ and $u_2 = -\bar{u}$ in (6-10) and (6-11), respectively, and using (6-13):

$$|\bar{u}| = \frac{|\mu_1 - \mu_2|}{\dfrac{1}{R_1 - h_1} + \dfrac{1}{R_2 - h_2}} \tag{6-22}$$

Considering the decomposed force-displacement loops, it is clear that $\bar{u}$ is the distance the slider must move as the normalized lateral force changes from μ_e to μ_1 or μ_2. Since the force-displacement relationship is linear with a known slope, $\bar{u}$ can be alternatively expressed in terms of the effective coefficient of friction as:

$$\bar{u} = (\mu_e - \mu_1)(R_1 - h_1) \tag{6-23}$$

$$\bar{u} = (\mu_e - \mu_2)(R_2 - h_2) \tag{6-24}$$

Equations (6-23) and (6-24) establish the convention of positive $\bar{u}$ on the surface of least friction. The slider advances more on the surface of least friction and lags on the surface of higher friction.

The slider offset does not accumulate from cycle to cycle with continuous cyclic motion. After *n* cycles of motion, the slider offset is $\bar{u}$ and not $n\bar{u}$. This is corroborated by the records of displacement presented in Figures 6-13 and 6-18. The value of $\bar{u}$ computed using (6-22) and the experimentally measured values of the coefficient of friction are 15.2 mm for the case of equal radii and unequal friction and 4.7 mm for the case of unequal radii and unequal friction. The values extracted from the displacement histories of these tests are typically within 1 mm of the theoretical value. Furthermore, the

176

experimental values of $\bar{u}$ are constant from cycle to cycle, indicating that the offset does not grow with repeated cycling.

A second issue related to design of the DCFP bearing is the permanent bearing displacement, u_p, after earthquake excitation. The bearing can exist in an equilibrium position of nonzero displacement in which the static friction force balances the restoring force, $F_f = F_r$. For the DCFP bearing, it is possible to have permanent displacements on both sliding surfaces, given by:

$$u_{p1} = \mu_{\min,1}(R_1 - h_1) \tag{6-25}$$

$$u_{p2} = \mu_{\min,2}(R_2 - h_2) \tag{6-26}$$

where $\mu_{\min,1}$ and $\mu_{\min,2}$ are the coefficients of friction of each sliding surface at very small velocity. These displacements add to give the total possible permanent displacement of the top plate relative to the bottom plate:

$$u_p = \mu_{\min,1}(R_1 - h_1) + \mu_{\min,2}(R_2 - h_2) \tag{6-27}$$

Comparing (6-23) and (6-24) with (6-25) and (6-26) it is evident that in all cases, the permanent displacement possible on an individual sliding surface is larger than the offset displacement. Furthermore, the issue of permanent displacements is more critical for DCFP bearings than for traditional (single concave) FP bearings since there are two sliding surfaces on which the permanent displacements occur.

The value of u_p given by (6-27) represents the maximum possible permanent displacement. The coda segments of typical earthquake ground motions are of moderate to low level excitation that tends to re-center seismically isolated structures. Earthquake-simulator tests of structures isolated with traditional Friction Pendulum bearings have shown that the permanent displacement after excitation is small and approximately an order of magnitude less than the maximum possible permanent displacement (Tsopelas et al., 1996; Mosqueda et al., 2004). Similar results were recorded by the authors in simulator tests of a quarter-scale six-story structure isolated with DCFP bearings. The isolation system of that study consisted of four equal radii, equal friction DCFP bearings with $R_1 + R_2 - h_1 - h_2 = 3520$ mm and $\mu_{\min,1} \approx \mu_{\min,2} \approx 0.02$ at the prototype scale. Figure 6-19 shows the measured permanent displacements of the isolation system after unidirectional tests consisting of various historical earthquake records. The median value of permanent displacement at the prototype scale for these 19 tests was 6 mm; the value predicted by (6-27) is 70 mm, which is an order of magnitude greater than the measured result and consistent with the results of previous studies.
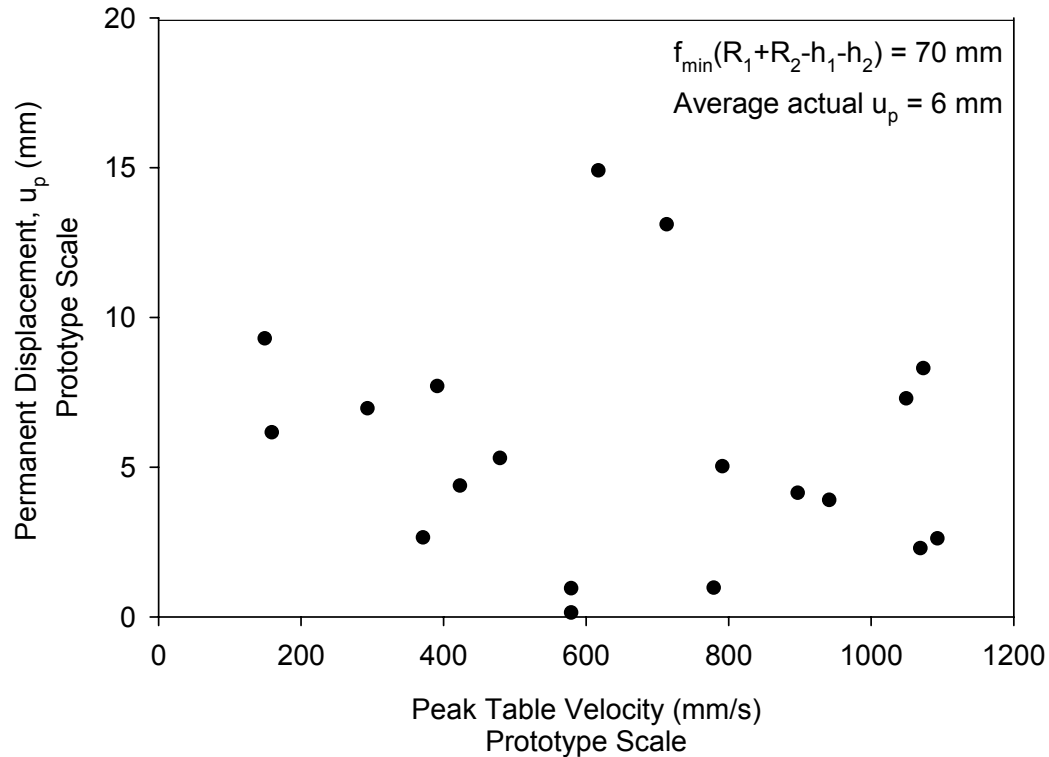
FIGURE 6-19   Actual Permanent Displacements (in prototype scale) of DCFP Bearings Measured after Nineteen Unidirectional Earthquake Simulator Tests

6.4 Procedure for Design of End Plates of Sliding Bearings

The end plates of sliding bearings can be designed as column end plates (e.g., see DeWolf and Ricker, 2000). A procedure is illustrated for the Friction Pendulum bearing of Figure 6-3 and the DCFP bearing shown in Figure 6-20. The procedure followed herein for the capacity check of the end plates follows principles similar to those used in the safety check of end plates of elastomeric bearings presented in Section 9.12. For Friction Pendulum bearings, the overturning moment can be neglected and the axial load can be considered to be concentrically transferred at the location of the articulated slider: the contribution to the overturning moment of $P\Delta$ is set aside when the bearing is analyzed in the deformed position. This is equivalent to the treatment of elastomeric bearings by use of the reduced area procedure as described in Section 9.12.

Analysis and safety checks of the end plates must be performed for service loads, for load combinations involving design basis earthquake (DBE) and maximum considered earthquake (MCE) shaking. In all three checks, end plates should not be subjected to significant inelastic action that might compromise the function of the bearing, where significant inelastic action is prevented as follows:

178

a) For service and for DBE shaking load effects, the end plates shall meet the Load and Resistance Factor Design (LRFD) requirements of the 13th Edition of the Steel Construction Manual (AISC, 2006) using the minimum specified material strengths and resistance, ϕ, factors.[1]

b) For MCE shaking load effects, the end plates shall meet the Load and Resistance Factor Design (LRFD) requirements of the 13th Edition of the Steel Construction Manual (AISC, 2006) using the expected material strengths and resistance factors set equal to 1.0. Expected material strengths can be established using Table I-6-1 of the AISC Seismic Provisions for Structural Steel Buildings (AISC, 2005; also in FEMA 356, Federal Emergency Management Agency, 2000) or from tests data. In the event that an expected material strength cannot be established, the minimum specified value should be used.

The axial load P is the factored load equal to

- Service load effects: $1.25D + 1.75L$ for bridges and $1.2D + 1.6L$ for buildings
- DBE and MCE shaking effects: $1.25D + L + E$ for bridges and $1.2D + L + E$, for buildings

where D is the dead load effect, L is the live load effect and E is the earthquake load effect, where the load factors are based on the 2004 AASHTO LRFD Bridge Design Specifications (AASHTO, 2004) and ASCE-7-05 Minimum Design Loads for Buildings and Other Structures (ASCE, 2005). The following steps should be followed given factored load P, bearing displacement Δ and bearing geometry per Figure 6-20:

a) Calculate the concrete bearing strength:

$$f_b = \phi_c (0.85 f_c') \sqrt{\frac{A_2}{A_1}} \le \phi_c 1.7 f_c' \qquad (6\text{-}28)$$

In (6-28), f_c' is the specified compressive strength, A_1 is the loaded area, A_2 is area of the lower base of the largest frustum of a pyramid, cone or tapered wedge contained wholly within the support and having for its upper base the loaded area. Escobar et al. (2006) give additional information on the bearing strength of concrete.

b) Calculate the diameter b_1 of the loaded area:

$$b_1 = \sqrt{\frac{4P}{\pi f_b}} \qquad (6\text{-}29)$$

---

[1] The procedure presented here is strictly applicable to FP and DCFP bearings constructed with housing and concave plates of structural steel. These components of FP and DCFP bearings can also be constructed with ductile cast iron. In this case, the mechanical properties of the appropriate cast iron requirements should be used for safety checking instead of values set forth in the AISC Steel Manual and the AISC Seismic Provisions for Structural Steel Buildings.
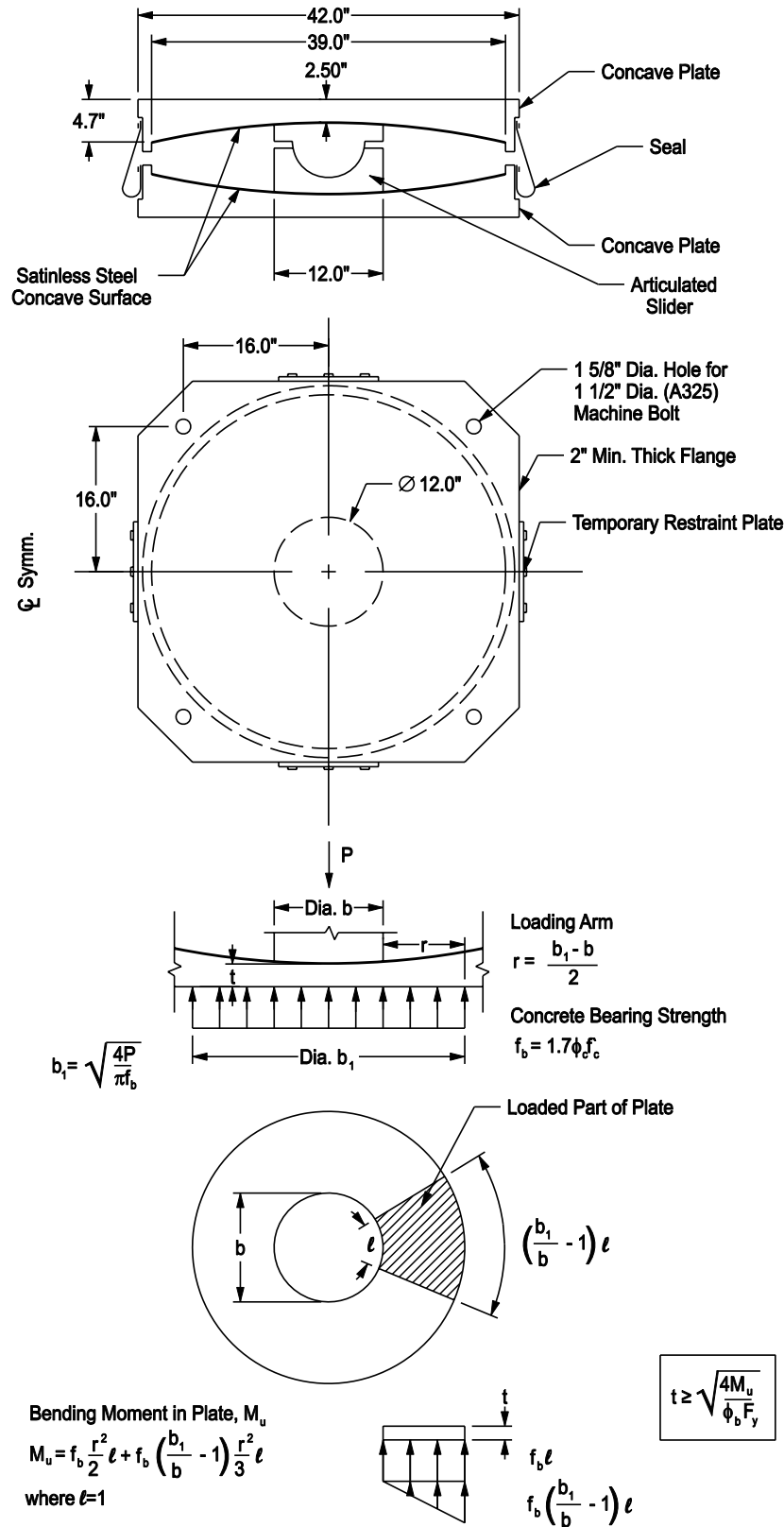
FIGURE 6-20 DCFP Bearing and the Procedure for End Plate Design

180

c) Calculate the loading arm:

$$r = \frac{b_1 - b}{2} \tag{6-30}$$

d) Calculate the required plate bending strength for unit plate length:

$$M_{u,s} = f_b \frac{r^2}{2} + f_b \left(\frac{b_1}{b} - 1 \right) \frac{r^2}{3} \tag{6-31}$$

where f_b is the concrete bearing strength and all other terms are defined above. Equation (6-31) accounts for the circular shape of the loaded area as illustrated in Figure 6-20. However, (6-31) is based on a simplified representation of plate bending that is valid for small values of ratio of the arm r to slider diameter b. An exact solution was obtained for the bending moment under elastic conditions (Roark, 1954), which is based on the representation shown in Figure 6-21 of a circular plate built-in along the inner edge and uniformly loaded. The moment per unit length at the built end is

$$M_{u,e} = f_b b_1^2 \left(\frac{(1+\nu)\ln\frac{b_1}{b} - \frac{1+3\nu}{4} + \frac{1-\nu}{4}\left(\frac{b}{b_1}\right)^4 + \nu\left(\frac{b}{b_1}\right)^2}{8(1+\nu) + 8(1-\nu)\left(\frac{b}{b_1}\right)^2} \right) \tag{6-32}$$

where ν is Poisson's ratio and all other terms are defined above. Figure 6-21 presents values of the moment normalized by the product $f_b b_1^2$ as calculated by the simplified [equation (6-31)] and the exact [equation (6-32)] procedure for $\nu = 0.3$. The results agree well for values of b/b_1 that approach unity. The correction factor shown in Figure 6-21 is the ratio of the moment calculated by the exact and the simplified procedures. The factor can be used to calculate the exact moment by multiplying the correction factor by the result of (6-31)—alternately, (6-32) can be used directly.

e) Calculate the required plate thickness:

$$t \geq \sqrt{\frac{4M_u}{\phi_b F_y}} \tag{6-33}$$

where F_y is the yield stress (minimum specified or expected) of the steel end plate.

Parameters ϕ_c (bearing) and ϕ_b (bending) are equal to 0.65 and 0.9, respectively, for service load and DBE load effects conditions and are each equal to 1.0 for MCE computations. The thickness calculated using (6-31) or (6-32) is compared with the available thickness that for concave plates is dependent on the position of the slider. For

181

service loading conditions and for building applications, the slider is assumed to be centered in the bearing and the thickness for safety checking is the plate thickness at the edge of the slider (see the third panel in Figure 6-20); for bridge applications it is appropriate to consider that the slider is off-center (due to thermal and live-load displacements) and that the plate thickness for safety checking is the value around the perimeter of the off-center slider. If the service-load displacement is larger than one half of the slider diameter, the thickness for safety checking should be taken as the minimum value (at the center of the bearing). For DBE and MCE checking, the plate can be checked in the offset position. Note that for bearing installations that involve significant bearing axial forces due to vertical shaking and/or overturning moments, maximum axial forces might develop at displacements less than the maximum values computed for DBE and MCE shaking.

The procedure outlined above may be modified as follows:

a) For cases with additional plates backing the bearing plate, the required bending strength must be partitioned to the plates in proportion to their plastic strength, that is, in proportion to $F_y t^2$ for each plate. Equation (6-32) can then be used with for each plate together with its corresponding moment.

b) The effect of the lateral force acting at the slider-to-concave plate interface might be incorporated by the procedures outlines in DeWolf and Ricker (2000) for the case of combined axial force and moment. This moment, which typically does not include any $P\Delta$ component, is small for the concave plate bearings (the loading arm is the thickness of the plate, which is small) and so it can be neglected. However, the moment might be important for checking the safety of the housing plate of single concave bearings for cases where the slider is at some significant distance from the plate-to-concrete interface.

Consider the bearing of Figure 6-20. Assume that the specified strength of the concrete $f_c' = 27.6\,\text{MPa} = 4\,\text{ksi}$ and the factored load for service load conditions is 6942 kN = 1560 kip. The plate material is cast ductile iron ASTM A536, grade 65-45-12 with a minimum yield strength $F_y = 311\,\text{MPa} = 45\,\text{ksi}$. Assume that the bearing is to be installed in a bridge for which $\Delta = 150\,\text{mm} = 6\,\text{in}$ and that the minimum concave plate thickness is 63.5 mm = 2.5 in. Equation (6-28) gives a bearing pressure $f_b = 30.5\,\text{MPa} = 4.42\,\text{ksi}$, and (6-29) and (6-30) give $b_1 = 538\,\text{mm} = 21.2\,\text{in}$ and $r = 117\,\text{mm} = 4.6\,\text{in}$ for a slider diameter equal to 305 mm = 12 in. The correction factor for $b/b_1 = 12/21.2 = 0.57$ from Figure 6-21 is 0.87. The required flexural strength is calculated from (6-30) using the correction factor of factor 0.87 as $M_u = 70.66 \times 0.87 = 61.5\,\text{k-in/in} = 273.2\,\text{kN-mm/mm}$. The required thickness of the concave plate from (6-33) is $t = 62.6\,\text{mm} = 2.46\,\text{in}\,[1]$, which is less than the assumed thickness of 63.5 mm or 2.5 in. The 63.5-mm thick plate is this safe for service-load conditions.

---

[1] The high level of precision presented in the text is intended solely to help the reader follow the computation.

The above procedure for designing end plates of sliding bearing is based on strength and does not consider any requirements for stiffness. A minimum stiffness might be required to prevent distortion of a bearing that will impair its proper function. For example, AASHTO (2002) requires a certain minimum thickness for base plates of pot bearings to counteract uneven bearing that might result from the inability of the elastomer in the pot to fill the space of the deformed bearing. The problem appears to be specific to pot bearings. The European Standard for Structural Bearings EN1337 (European, 2004) has more specific requirements that seek to prevent distortion of the sliding surface (a) as a result of short-term and long-term deformation in the concrete, and (b) during transport and installation. Permanent deformations of the end plates are associated with comparable deformations of the sliding surface that will result in increased wear.
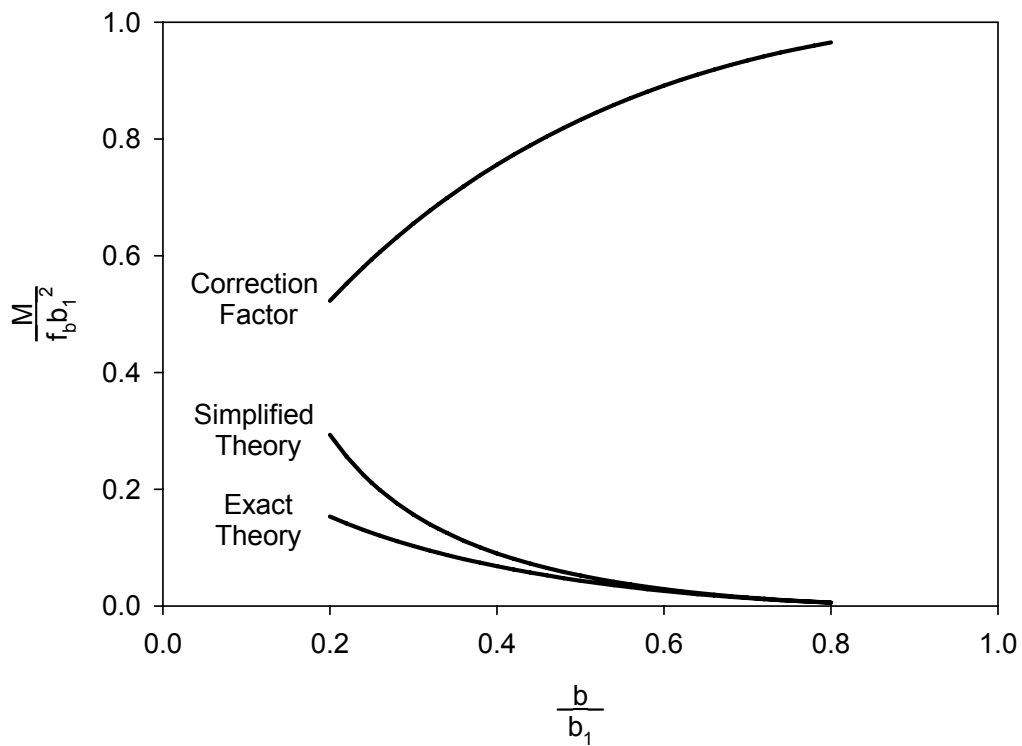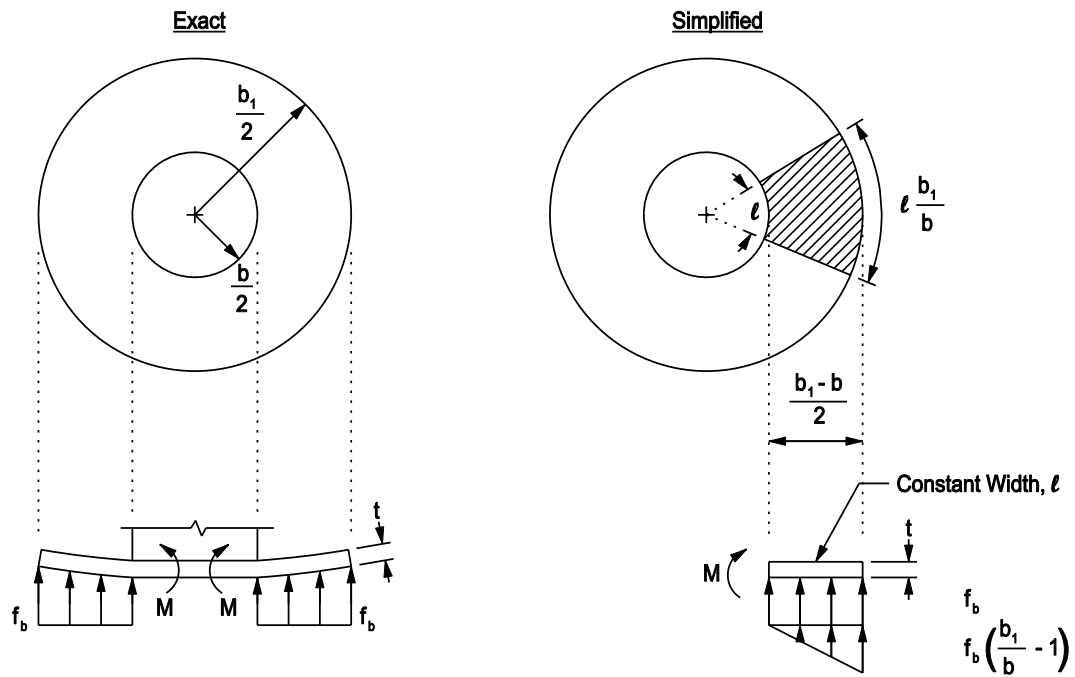
FIGURE 6-21 Comparison of Moment in End Plate Calculated by Exact and by Simplified Theories and Correction Factor for $\nu=0.3$

SECTION 7
MECHANICAL PROPERTIES OF ELASTOMERIC BEARINGS

7.1 Introduction

Elastomeric bearings for seismic isolation applications are typically made of natural rubber with reinforcing steel plates as described in Section 2. Rubber is a cross-linked polymer that can be produced in numerous compounds with different properties. It differs substantially from other materials: it has high elastic deformation, a very large elongation at break (it is the most deformable material known) and it is virtually incompressible. This section provides an overview of the mechanical properties of rubber and describes the basic properties of elastomeric bearings.

7.2 Vulcanization

Vulcanization or curing is the conversion of raw rubber by means of chemical cross-linking from a plastic state to an essentially elastic state (Hills, 1971). The treatment or processing of raw rubber defines its strength, elasticity, resistance to solvents and relative insensitivity to temperature changes.

The discovery of vulcanization by Charles Goodyear in 1839 provides the foundation of the modern rubber industry. Goodyear discovered that raw rubber heated with sulfur gave a product with high elasticity and insensitivity to temperature change. Nowadays, vulcanization of rubber bearings is accomplished by use of sulfur, peroxide or urethane, and the application of heat and pressure. Other additives in rubber produce a variety of effects. Accelerators are used to shorten the duration of heating or lower the heat necessary for vulcanization. Fillers are used to modify the mechanical properties of the final product. The most commonly used filler is carbon black, which modifies the hardness, stiffness, elongation at break, creep and relaxation characteristics and the fatigue life of the rubber. Anti-ozonants are used to protect the product from cracking due to ozone attack. Anti-oxidants delay degradation due to exposure to oxygen and reduce aging effects.

7.3 Basic Mechanical Properties of Natural Rubber

Vulcanized natural rubber is characterized by low shear modulus, low modulus of elasticity, nearly incompressible behavior and extremely high elongation at break. It is effectively nonlinear viscoelastic at low levels of strain and transforms to nonlinear hysteretic at large strains. It's behavior is such that it does not retrace the same path on reloading but it slowly returns to the original shape when loading is removed (Stanton and Roeder, 1982).

When subjected to uniaxial tensile stress without restraint in the transverse direction, rubber exhibits the type of behavior shown in Figure 7-1 (Brown, 1996). The behavior is characterized by high modulus of elasticity at small strains, followed by reduced modulus at larger strains and then increased modulus at even higher strains. The same behavior is

observed when rubber is tested in pure shear with a specimen that has large area and small thickness. For example, the shear modulus might be 3.0 MPa for strains below 20%, approximately 0.7 MPa for strains of 50 to 200% and more than 2.0 MPa for strains larger than 300%. These values may be controlled by special compounding and treatment of the rubber during vulcanization.

Rubber is nearly incompressible material with Poisson's ratio very close to 0.5 (between 0.498 and 0.499). It is better to describe the bulk behavior of rubber with the bulk modulus rather than Poisson's ratio. The bulk modulus is large and very difficult to measure. A commonly used value for bulk modulus, K, in the analysis of elastomeric bearings is $K = 2000$ MPa (300 ksi). The ratio of bulk modulus to shear modulus of rubber is of the order of 2000 to 3000.
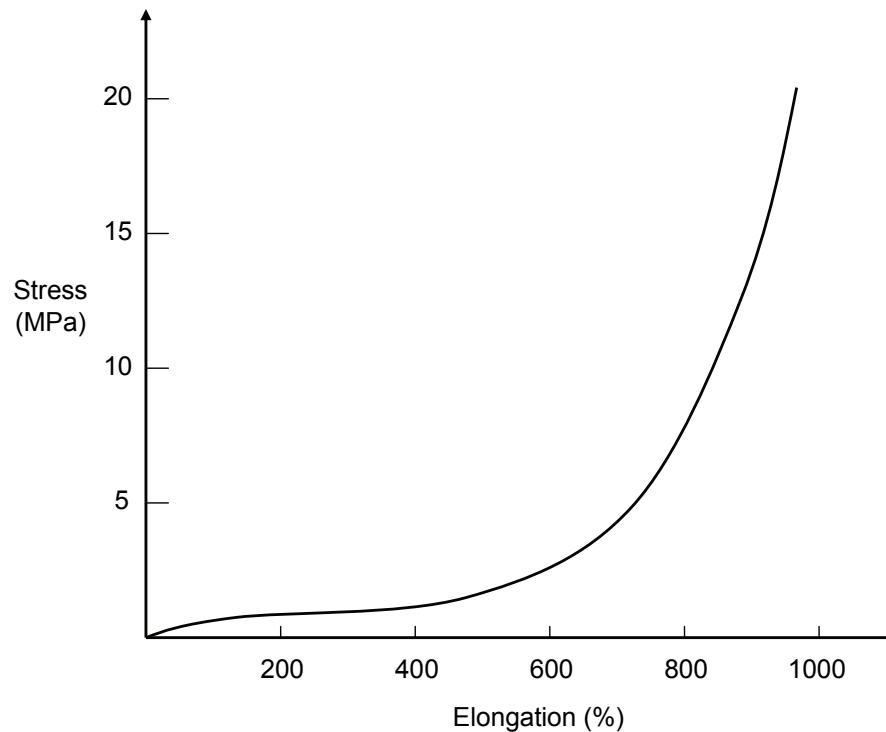
FIGURE 7-1 Example of Uniaxial Tensile Stress-Strain Curve for Rubber

Rubber is often characterized by the shear modulus determined in accordance with ASTM Standard D4014 (American Society for Testing and Materials, 1988). The test is conducted under quasi-static conditions and the shear modulus is determined as the tangent modulus in the 6th cycle of loading at a shear strain of 50%. The test specimen is a quadruple stack of small square rubber blocks with each block having identical dimensions so that the total length is 25 mm and the thickness is 6 mm. The shape factor S for these specimens, defined as the area loaded divided by area free to bulge under compressive loading is approximately 1. By comparison, elastomeric bearings in seismic isolation applications have shape factors larger than 10. For a small shape factor, the specimen is subjected to combined shear and bending so that the measured shear modulus G_a is less than the shear modulus G obtained from specimens with large shape factors or

186

from combined compression and shear testing of elastomeric bearings. This often leads to confusion since engineers often use G_a for calculations of stiffness, thus underestimating the stiffness (and thus overestimating the effective period) of an isolated structure. In general, $G \approx G_a$ if the shape factor is greater than 3.

Another property used to characterize a rubber is hardness. In the US, hardness is typically measured as Durometer Hardness Type Shore A per ASTM Standard D2240 (American Society for Testing and Materials, 1988). Hardness is a measure of indentation imposed using an instrument called a durometer. The British Standard BS5400 (British Standards Institution, 1983) uses a different hardness measure called International Rubber Hardness Degrees or IRHD to characterize rubber (also, described in ASTM Standard D1415). IRHD and Durometer A hardness are nearly identical (with IRHD being slightly less than Shore A) for the hardness range of 40 to 70 that is typical of the rubbers used for seismic isolation applications (Brown, 1966).

The behavior of rubber in compression is markedly affected by the shape factor of the specimen. This behavior is described in Section 9 where the analysis of elastomeric bearings is presented.

The behavior of rubber in shear under dynamic conditions is complex. Since this behavior is affected by the shape factor, it is best to describe the behavior of rubber in shear in terms of the horizontal force-displacement relations of elastomeric bearings under the action of vertical load. This is presented in Section 7.5.

7.4 Construction and Manufacture of Elastomeric Bearings

Elastomeric bearings consist of bonded alternating layers of rubber and steel shims as shown in Figure 7-2. This figure shows two alternate ways of connecting the bearing to the superstructure above and substructure below. Dowels are used when tension in the bearing must be avoided. Bolted bearings are typically used nowadays because well-fabricated elastomeric bearings have significant tensile strain capacity. Connection details other than those shown in Figure 7-2 have also been used in practice, including keeper plates that enable a bearing to respond as if it were doweled.

Large elastomeric bearings are often manufactured with a central hole to allow for more uniform heating of the rubber during the vulcanization process. Figure 7-3 shows the internal construction of a rubber bearing that was cut in half; the central hole is visible in this photograph. This high damping rubber bearing was used in the Foothills Communities Law and Justice Center in California (Naeim and Kelly, 1999). Dowels were used in this bearing to connect it to the structure.

Typically the shape factor of elastomeric bearings used for seismic isolation applications is greater than 10 and often substantially greater than 10. Large shape factors are needed to minimize shear stresses due to compression and to increase the buckling load capacity of the bearing.

The process by which large-size elastomeric bearings are made is presented in Table 7-1. Smaller bearings can also be made by injection molding. In this case a mold is made to support the steel plates in precise positions. Heated mixed rubber is then injected from the perimeter into the mold and kept under pressure during the curing process. This process is potentially problematic because the rubber moves from the exterior towards the interior during injection and can partially remove the adhesive. Bearings made by injection molding can have inferior rubber-to-steel bond strength.
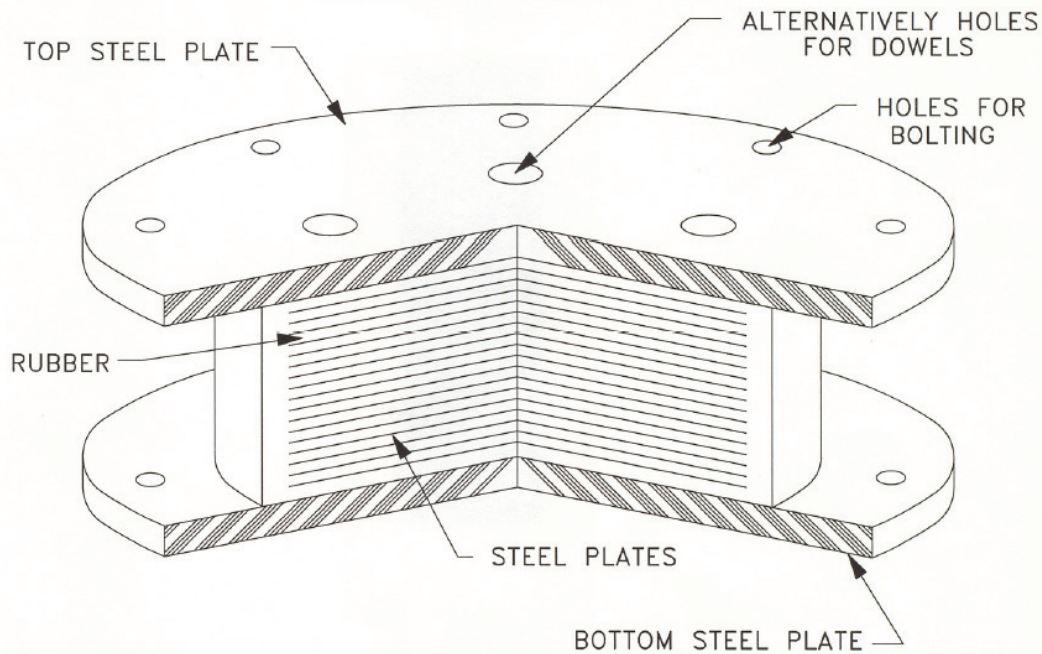
FIGURE 7-2 Construction of an Elastomeric Bearing

FIGURE 7-3 Section Through a Rubber Bearing to Show Internal Construction

188

TABLE 7-1 Production of Elastomeric Bearings

Process	Description
Mixing of rubber	Raw rubber, carbon black, sulfur and other additives are mixed
Sheeting (calendaring) of rubber	The mixed product is passed through rollers to create sheets of rubber of the specified thickness
Cutting of rubber	Rubber is cut into the desired shapes (circular, annular)
Cutting of steel plate	End plates and shim plates of the required thickness are cut into the desired shapes
Steel plate surface treatment	End plates and shim plates are sand-blasted
Application of adhesives	End plates and shim plates are coated with (proprietary) adhesives
Forming (lay-up) of bearing	End plates, shim plates and rubber sheets are assembled; Cover rubber is placed on the outside of the bearing
Curing (vulcanization)	The formed bearing is set in a mold and cured under pressure and heat: rubber is vulcanized and bonded to the steel
Finishing	End plates are painted; The lead plug is inserted in for lead-rubber bearings

7.5 Basic Mechanical Properties of Natural Rubber Bearings

Rubber bearings can be broadly placed into two categories: low damping and high damping. For both categories, the behavior in shear under the action of compressive load is most interesting and is discussed first. Herein, low damping rubber bearings have effective damping less than 10 percent and generally less than 5 percent, whereas high damping rubber bearings exhibit effective damping of 10 percent and higher.

Consider the bearing shown in Figure 7-4. It is a rubber bearing tested at the University at Buffalo, without and with a lead core. The results presented below are for the bearing constructed without a lead core, in which case the bearing did not have a hole in its center (results for the companion lead-rubber bearing are presented in Section 8). The rubber is of the low damping type and designated as natural rubber, Grade 3 per standard ASTM D4014 (American Society for Testing and Materials, 1988). The bearing was tested under average conditions of bearing pressure (vertical load divided by bonded rubber area) equal to 6.9 MPa (1000 psi) and lateral sinusoidal motion of amplitude equal to 113 mm and frequency in the range of 0.035 to 0.35 Hz, so that the peak velocity was in the range of 25 to 250 mm/sec. The shape factor of the bearing was $S = 10.7$. The bearing was tested first after conditioning for 48 hours at a temperature of $49^{o}C$, then at $20^{o}C$ and then again after conditioning for 48 hours at the temperature of $-26^{o}C$. Four fully reversed cycles of motion were imposed on the test specimen.
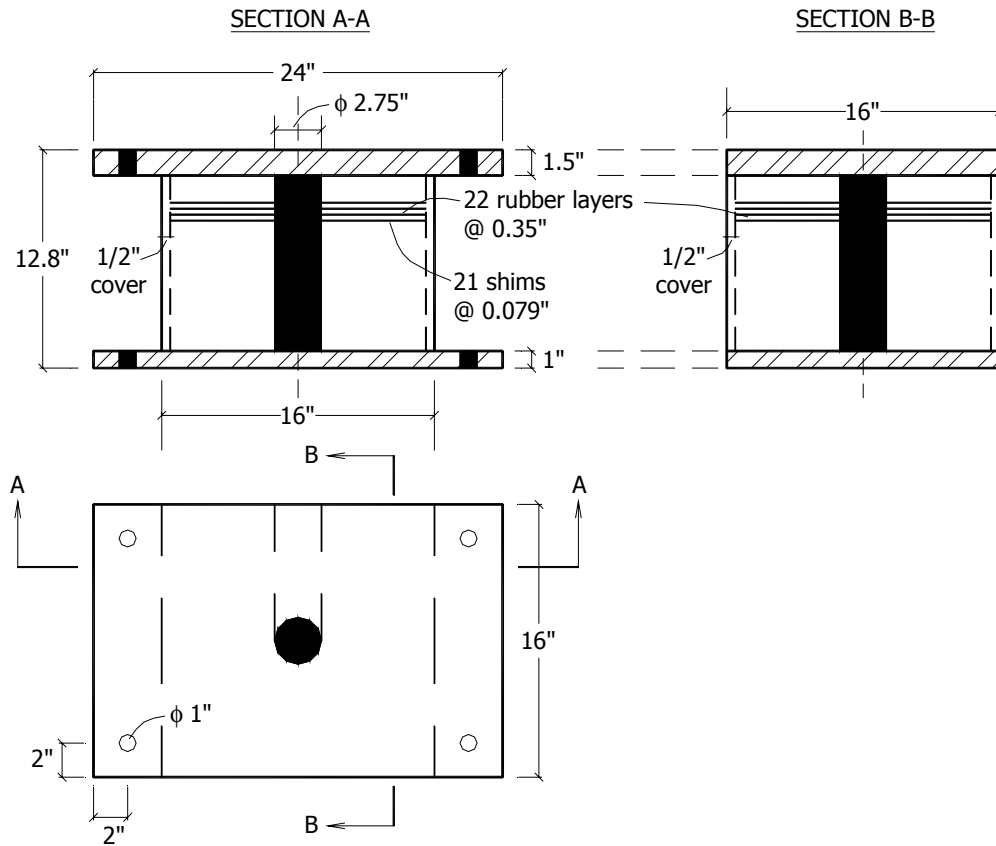
FIGURE 7-4 Tested Bearing with and without Lead Core (1 inch=25.4mm)

The recorded lateral force-displacement loops for temperatures of 20°C and -26°C and for frequency of 0.35 Hz are shown in Figure 7-5. Low temperature has a significant effect on the stiffness and energy dissipated per cycle. The behavior of the bearing could be described as approximately hysteretic at 20°C but as viscoelastic at -26°C. The mechanical properties of this bearing were extracted for the recorded loops are presented in Table 7-2. These mechanical properties are (AASHTO, 1999; Constantinou et al, 1998):

Effective stiffness

$$K_{eff} = \frac{\left|F^{+}\right| + \left|F^{-}\right|}{\left|\Delta^{+}\right| + \left|\Delta^{-}\right|} \qquad (7-1)$$

where Δ^{+} and Δ^{-} are the maximum positive and minimum negative displacements amplitudes and F^{+} and F^{-} are the forces corresponding to Δ^{+} and Δ^{-}, respectively. For pure hysteretic behavior, F^{+} and F^{-} are the maximum positive and minimum negative forces as illustrated in Figure 7-6.

190
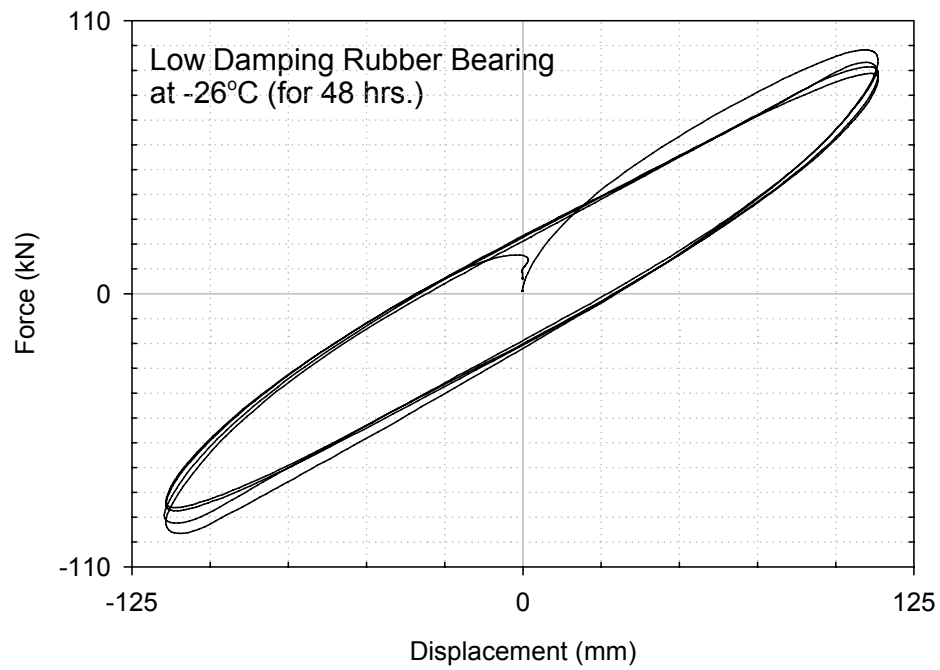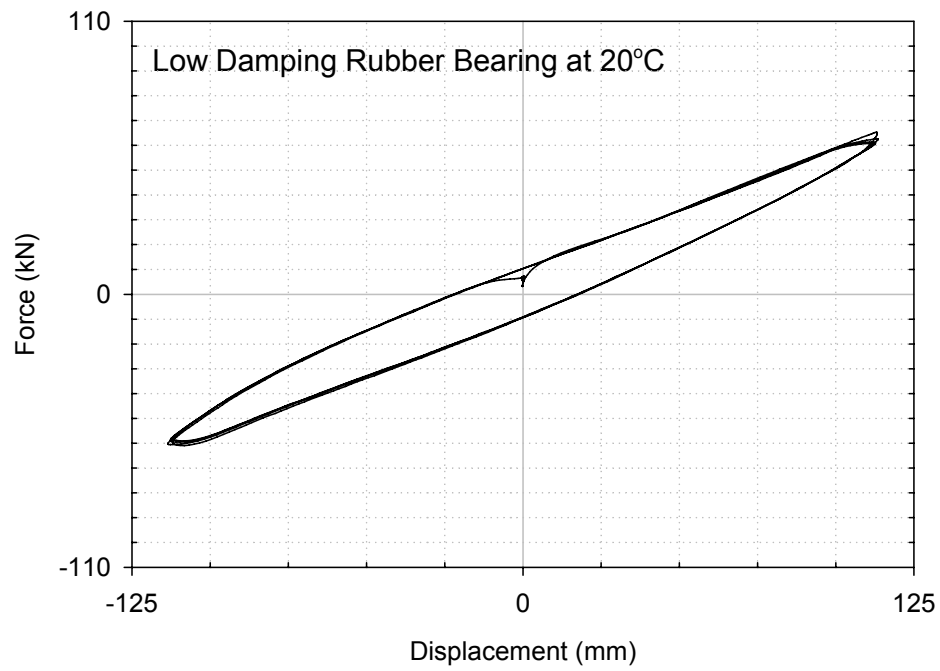
FIGURE 7-5 Lateral Force-Displacement Loops of a Low Damping Rubber Bearing

Viscoelastic behavior   Hysteretic behavior
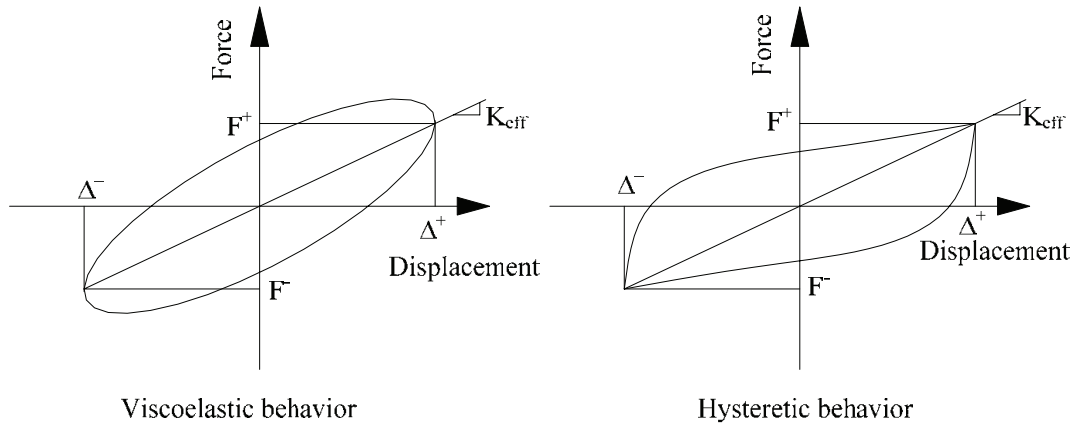
FIGURE 7-6 Definition of Effective Stiffness

Effective shear modulus

$$G_{eff} = \frac{K_{eff} T_r}{A_r} \tag{7-2}$$

where T_r is the total rubber thickness (=196 mm for this bearing) and A_r is the bonded rubber area (= 145,161 mm^2 for this bearing). The effective shear modulus is regarded as a mechanical property of the rubber under the tested conditions and the can be used to calculate the effective stiffness of bearings of other geometries.

Effective damping

$$\beta_{eff} = \frac{2}{\pi} \left[\frac{EDC}{K_{eff} \left(\left| \Delta^+ \right| + \left| \Delta^- \right| \right)^2} \right] \tag{7-3}$$

where EDC is the area enclosed by the hysteresis loop and all other terms have been defined previously.

The data of Table 7-2 illustrate the dependence of mechanical properties of low damping rubber bearings on temperature, cycling and frequency of loading, which can be summarized as follows:

a) Low temperature has a substantial effect on both stiffness and damping, resulting in increases in both quantities of about 50 to 60 percent from 20°C to -26°C. The percent increase will be greater when the exposure to low temperature is longer (see Section 7.7 below).

b) High temperature has an insignificant effect on stiffness and damping, with small reductions in stiffness and damping.

192

c) The influence of the number of cycles of loading is insignificant with only minor changes observed at the lowest temperature tested—due to an increase in temperature caused by hysteretic and/or viscous energy dissipation. The increase in temperature is small (see Section 7.6) and approximately $1^{\circ}C$ per cycle.

d) There are no scragging effects.

e) The frequency of motion (or the velocity of motion) has insignificant effect on the mechanical properties; the behavior can be assumed to be rate-independent.

These characteristics are typical for low damping rubber compounds (effective shear modulus at 50 percent strain of about 0.7 MPa).

TABLE 7-2 Mechanical Properties of a Low Damping Rubber Bearing (Bearing Pressure of 6.9 MPa and Rubber Shear Strain of 0.58)

Condition at Test	Freq. (Hz)	Peak Velocity (mm/sec)	Cycle-	EDC (kNmm)	Effective Stiffness (kN/mm)	Effective Damping (%)	Effective Shear Modulus (MPa)
At 49°C for 48 hrs	0.35	250	1	2701	0.49	0.07	0.66
	0.35	250	2	2600	0.49	0.07	0.66
	0.35	250	3	2588	0.49	0.07	0.66
	0.35	250	4	2622	0.49	0.07	0.66
At 20°C for 48 hrs	0.35	250	1	3436	0.56	0.08	0.75
	0.35	250	2	3391	0.54	0.08	0.73
	0.35	250	3	3312	0.53	0.08	0.71
	0.35	250	4	3278	0.53	0.08	0.71
At 20°C for 48 hrs	0.175	125	1	2939	0.53	0.07	0.71
	0.175	125	2	3018	0.53	0.07	0.71
	0.175	125	3	3007	0.53	0.07	0.71
	0.175	125	4	2973	0.53	0.07	0.71
At 20°C for 48 hrs	0.035	25	1	3007	0.49	0.08	0.66
	0.035	25	2	2826	0.49	0.07	0.66
	0.035	25	3	2769	0.49	0.07	0.66
	0.035	25	4	2735	0.49	0.07	0.66
At -26°C for 48 hrs	0.35	250	1	8862	0.82	0.14	1.10
	0.35	250	2	7833	0.79	0.13	1.06
	0.35	250	3	8251	0.77	0.13	1.04
	0.35	250	4	8025	0.75	0.13	1.01

Figure 7-7 is a drawing of a low damping rubber bearing tested at large shear strains at the University at Buffalo. The bearing had a bonded rubber area $A_r = 49,087 \text{ mm}^2$, a total rubber thickness $T_r = 82.5 \text{ mm}$ and a shape factor $S = 9.8$. The bearing was used as part of a tuned mass damper in which 144 identical bearings were used to construct four multi-stage rubber bearings that support a weight of 1000 kN. Figure 7-8 is a photograph of the bearing during testing at large lateral deformation; Figure 7-9 presents representative force-displacement loops at shear strains of 75 and 175 percent. The frequency of testing was 1 Hz, temperature was 20°C and the axial load was 28 kN. Scragging is evident in the large strain test (right hand panel) and modest hysteresis is apparent at large strains. The effective damping for this bearing is less than 5 percent; the effective shear modulus is about 0.65 MPa.
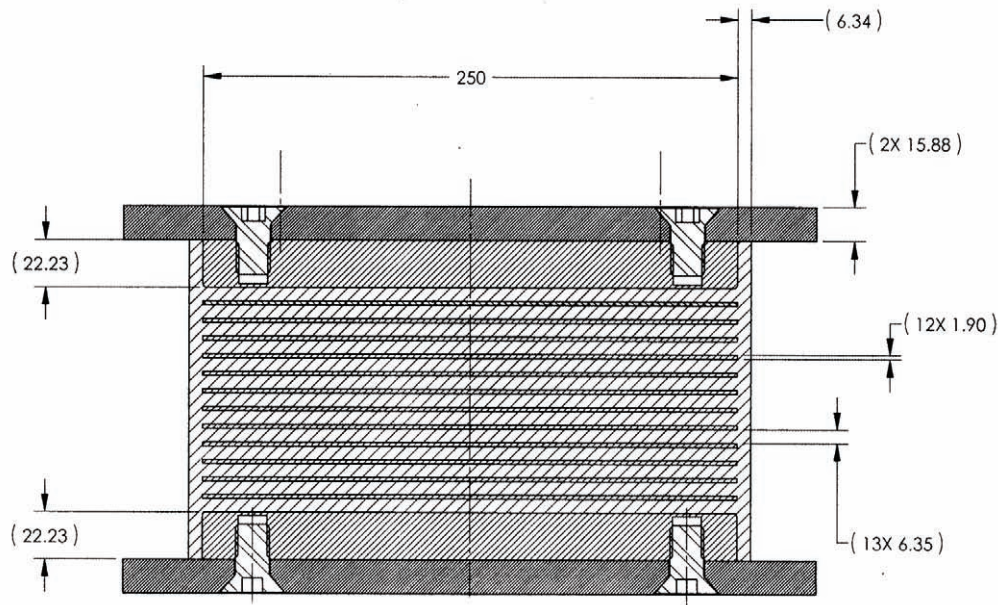
FIGURE 7-7 Low Damping Rubber Bearing Tested at Large Shear Strains

The force-displacement response of *high damping* rubber bearings is similar to that shown in Figure 7-9 but with larger energy dissipated per cycle—see Figure 7-10. Information on high damping rubber bearings can be found in Kelly (1991), CERF (1998b) and CERF (1999). The mechanical properties of the bearing of Figure 7-10 are presented in Figure 7-11 in terms of effective shear modulus and damping ratio. This bearing was tested at the University of California at Berkeley: bonded rubber area $A_r = 52,258 \text{ mm}^2$, rubber thickness $T_r = 82.5 \text{ mm}$ and shape factor $S = 9$. The data presented in Figures 7-10 and 7-11 are for scragged conditions and shear strains up to 180%. At shear strains greater than 180%, the effective stiffness of this bearing increased, which is a common characteristic of high damping rubber bearings. The threshold strain at stiffening depends on the compounding of the rubber; for example, the threshold strain for the Bridgestone bearings tested by Kelly (1991) was approximately 250%.

194

FIGURE 7-8 View of Bearing of Figure 7-7 during Large Lateral Deformation Test
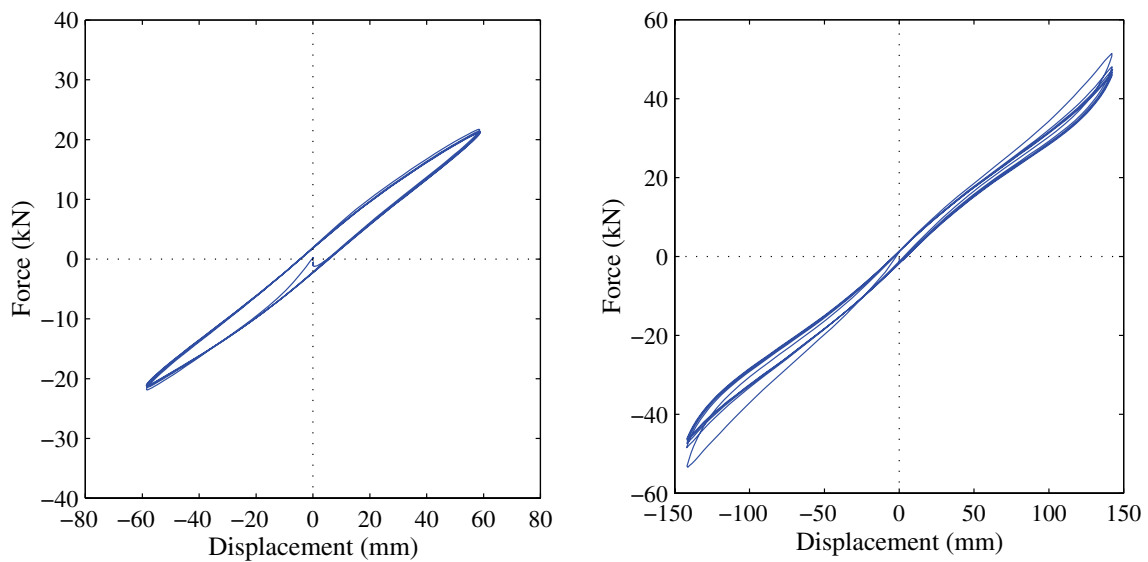
FIGURE 7-9 Force-Displacement Loops at Shear Strains of 75 percent and 175 percent

195
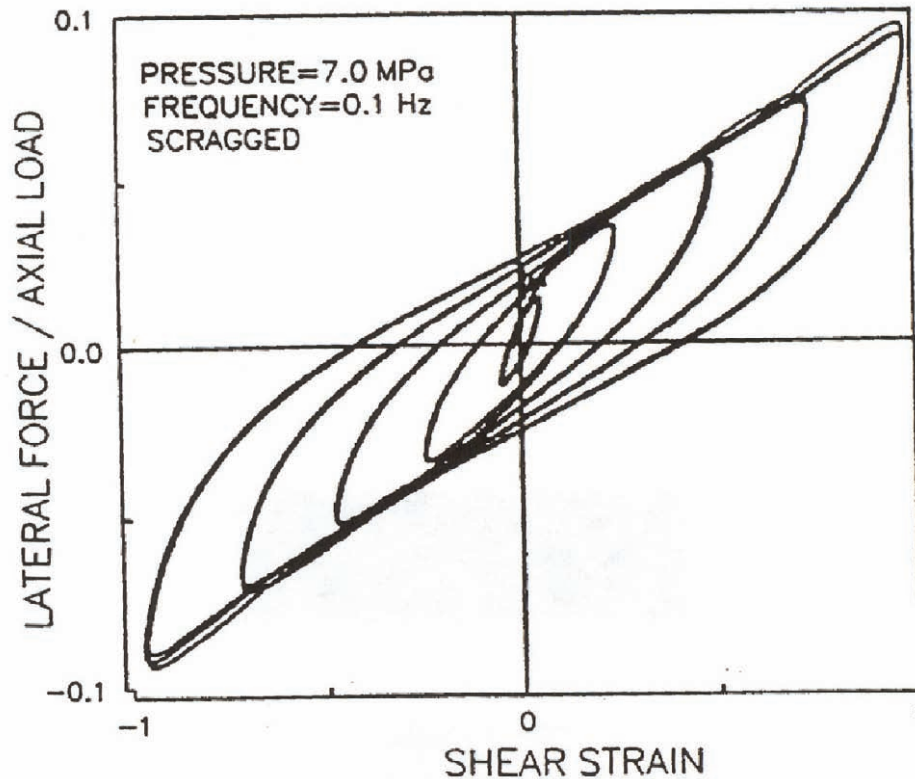
FIGURE 7-10 Lateral Force-Displacement Loops for a Typical High Damping Rubber Bearing

The following common characteristics of high damping rubber bearings can be gleaned from Figure 7-11:

The following common characteristics of high damping rubber bearings can be gleaned from Figure 7-11:

a) Increasing axial pressure results reduces the effective stiffness and increases the effective damping.
b) Increasing the frequency of excitation results in modest increases in effective stiffness and damping.
c) The effective stiffness at small strains is relatively large: a desirable characteristic for resisting wind loadings without significant lateral deformation. However, for bridges, in which large service loads can be imposed on bearings due to braking, etc., the initial stiffness of high-damping rubber bearings is often considered to be too low.

Under compressive loading, elastomeric bearings exhibit vertical high stiffness as a result of the confined conditions of stress and the near incompressibility of rubber. Section 9 provides the theoretical background for the calculation of vertical stiffness. Figure 7-12 presents a typical vertical force-vertical displacement relationship for a rubber bearing in compression. The bearing is a lead-rubber bearing tested at the University at Buffalo.

196

Herein it is assumed that the lead core does not affect the vertical stiffness so that the behavior seen in this figure is considered representative of all rubber bearings. At small axial deformations, the bearing exhibits very low axial stiffness as a result of internal imperfections such as non parallel end plates. The compression stiffness is typically obtained from the ascending branch of this loop, as shown in the figure, for an axial load equal to the in-service or gravity load.
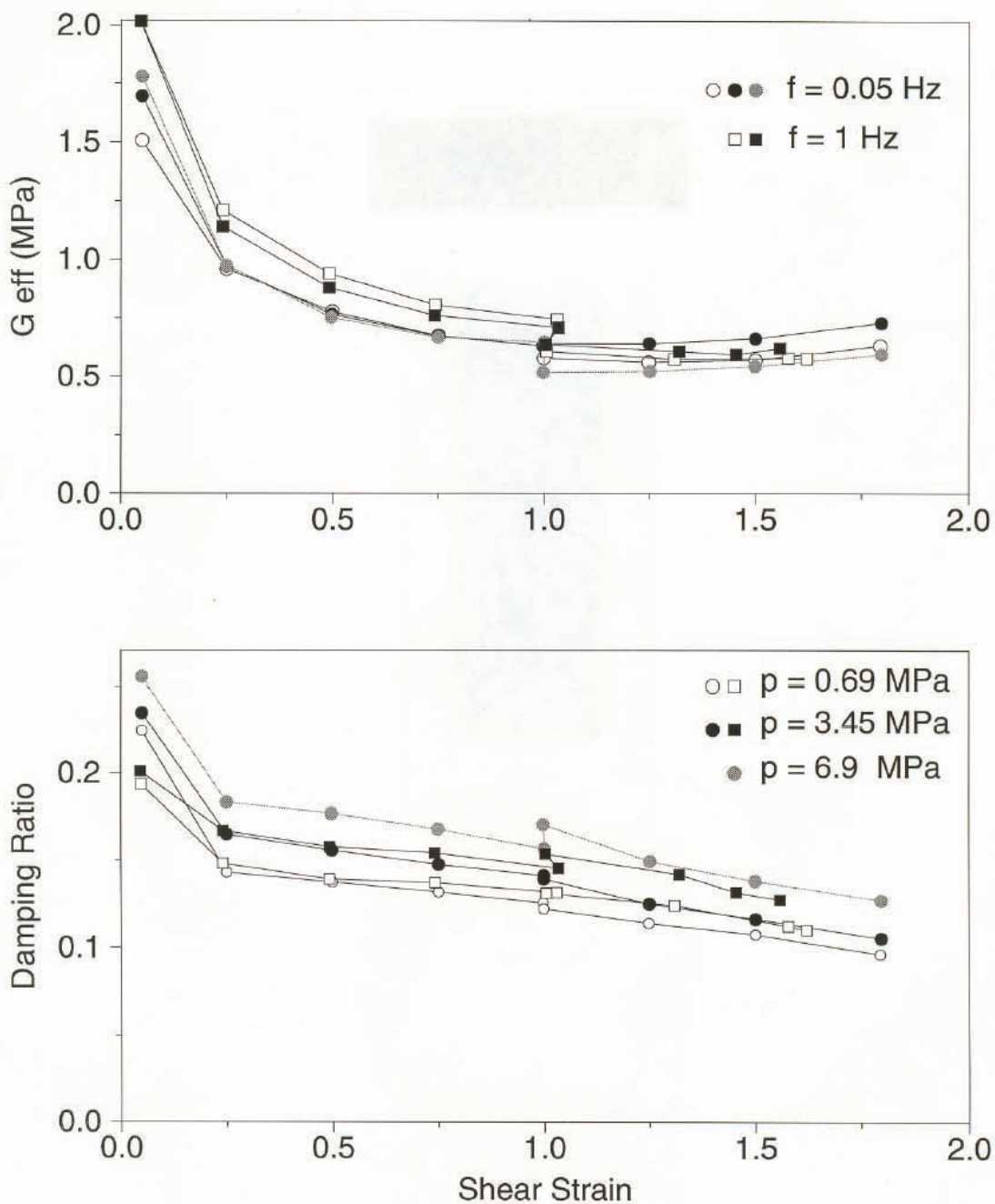
FIGURE 7-11   Typical mechanical properties of a High Damping Rubber Bearing

197
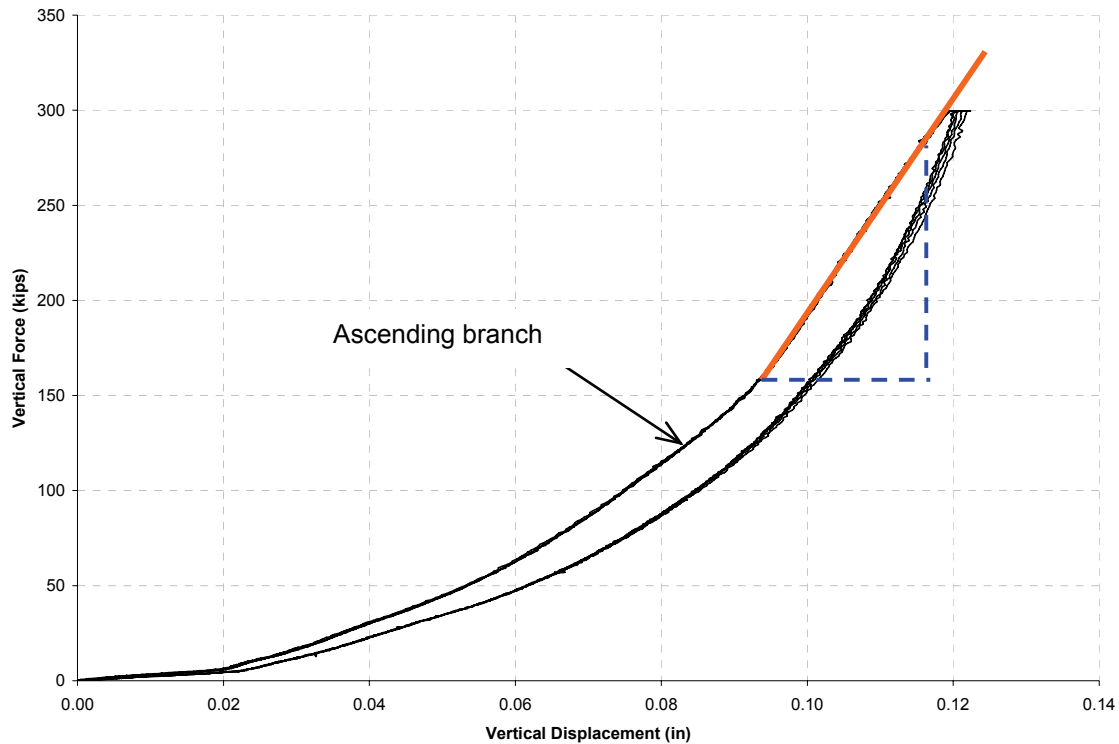
FIGURE 7-12   Representative Vertical Load-Displacement Relation of Rubber Bearing in Compression (1 kip = 4.45 kN, 1 inch = 25.4mm)

The behavior of rubber bearings in tension is illustrated in Figure 7-13 for the bearing of Figure 7-7. Figure 7-14 shows the deformed bearing at a displacement equal to 60 % of the rubber thickness. For small tensile loads, the bearing exhibits a stiffness that is comparable to the compression stiffness. At a level of load or axial pressure that is dependent on the rubber compound (typically 1.5 to 2.5 MPa) the bearing cavitates (see Gent, 1990, 2001), namely, small cracks develop in the volume of the rubber. As a result, confinement is lost[1] and the stiffness drops by a substantial amount. Section 9 provides the theoretical basis for the reduction in stiffness that is of the order of S^2, where S is the shape factor. For the bearing of Figure 7-7, $S = 9.8$ and the reduction in vertical stiffness following cavitation is of the order of 100.

---

[1] In the limit, the triaxial stress state in the volume of the elastomer prior to cavitation is essentially replaced by a uniaxial stress state in columns of elastomer, formed by the cracking, whose aggregate are equals the bonded area.
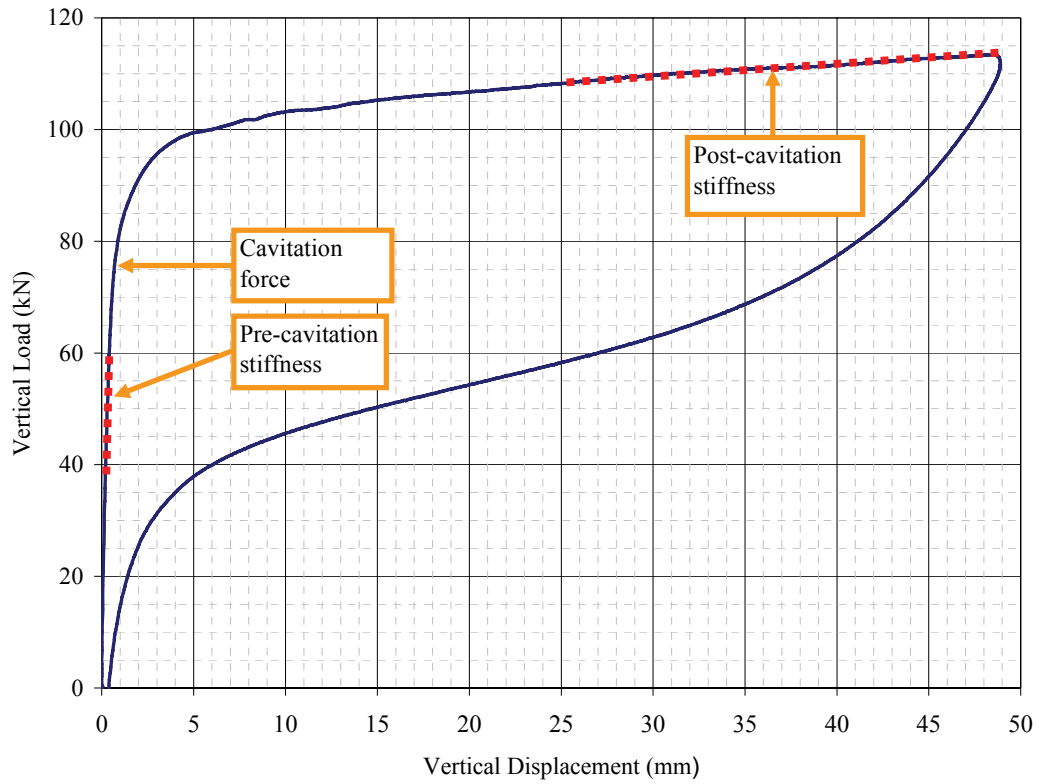
FIGURE 7-13   Representative Vertical Load-Displacement Relationship for a Rubber Bearing in Tension

FIGURE 7-14 Rubber Bearing at Tensile Deformation of 60% of the Total Rubber Thickness

199

7.6 Heating of Elastomeric Bearings

When elastomeric rubber bearings are subjected to motion, heat is generated in the rubber. The heat generation is mechanical in origin and likely based on viscous action and friction between cross-linked rubber molecules and molecular chains. When heat is generated in the solid, the equations of heat conduction are (Carslaw and Jaeger, 1959)

$$\frac{\partial^2 T}{\partial x^2} + \frac{\partial^2 T}{\partial y^2} + \frac{\partial^2 T}{\partial z^2} - \frac{1}{D}\frac{\partial T}{\partial t} = -\frac{A}{k} \tag{7-4}$$

where T is the temperature rise, k is the thermal conductivity of rubber, D is the thermal diffusivity of rubber and A is the rate of heat production per unit volume per unit time.

The generated heat is practically independent of the space variables (x, y and z) since it is primarily dependent on the shear strain, which is essentially constant through the entire volume of the rubber. Moreover, if we neglect heat radiation and heat conduction through the end plates of the bearings, we conclude that the temperature is independent of the space variables. The rate of heat production per unit volume per unit time is given by

$$A = \tau \frac{d\gamma}{dt} \tag{7-5}$$

where τ is the shear stress in the rubber and γ is the shear strain in rubber. Equation (7-4) reduces to

$$\frac{dT}{dt} = \frac{D}{k}\tau\frac{d\gamma}{dt} \tag{7-6}$$

or

$$\rho c \frac{dT}{dt} = \tau\frac{d\gamma}{dt} \tag{7-7}$$

in which the ratio k/D has been replaced by its equivalent ρc, where ρ is the mass density of rubber and c is the specific heat of rubber. Integration yields

$$T(t) = \frac{1}{\rho c}\int_o^t \tau\, d\gamma \tag{7-8}$$

or

$$T(t) = \frac{1}{\rho c V}\int_o^t F\, du \tag{7-9}$$

200

where V is the volume of rubber, F is the lateral force on the bearing and u is the lateral displacement of the bearing.

The integral in (7-9) is the area enclosed by the lateral force - lateral displacement loop of a bearing. The temperature rise is dependent only on frequency through its effect on the lateral force. This effect is typically small and testing at reduced frequencies should not affect the quality of the test results at low temperatures.

We proceed with calculating estimates of the temperature rise during testing. Consider cyclic motion at amplitude u_{max}. For the idealized bilinear hysteresis shown in Figure 3-1, the temperature rise per cycle calculated using (7-9) is

$$T_c = \frac{4Q_d(u_{max} - u_y)}{\rho c A_r T_r} \tag{7-10}$$

where u_y is the yield displacement, A_r is the bonded rubber area and T_r is the total rubber thickness. Equation (7-10) can be rewritten as

$$T_c = \frac{4p(\gamma_{max} - \gamma_{y)}}{\rho c}\left(\frac{Q_d}{N}\right) \tag{7-11}$$

where p is the average bearing pressure, N is the vertical load on the bearing, γ_{max} is the rubber shear strain at u_{max} and γ_y is the rubber shear strain at the yield displacement.

Consider now typical values of these variables for high damping rubber bearings: $p = 7$ MPa, $\gamma_{max} = 1.5$, $\gamma_y = 0.07$, $Q_d / N = 0.05$, and $\rho c = 2\times10^6 \text{ N}/(\text{m}^2\,^{\circ}\text{C})$. For these values of the variables, the temperature rise per cycle calculated using (7-11) is less than 1°C, which is insignificant. For the hysteresis loop of Figure 7-10, in which $Q_d / N = 0.02$, the temperature rise per cycle would be much less than 1°C, a result that agrees with the observation of Nakano et al. (1993) who reported a temperature rise of about 0.6°C per cycle during a 50-cycle test. On the basis of these results, we conclude that the temperature rise during dynamic tests of high damping rubber bearings is too small to warrant consideration in design.

7.7 Effect of Temperature on Mechanical Properties

It is well known that low temperatures increase both the stiffness and strength of elastomeric bearings. The results of Figure 7-5 and Table 7-2 provide evidence for this behavior. Roeder et al. (1987) presented a comprehensive review of the influence of temperature on the mechanical properties of elastomeric bearings. In general, the effect of low temperature consists of an instantaneous thermal stiffening, which is achieved within the time needed for thermal equilibrium, and crystallization stiffening, which is time-dependent. Figure 7-15 illustrates the typical low-temperature behavior of elastomeric bearings. Time t_1 depends on the size of the bearing and particularly its height. On the basis of the results of Roeder et al. (1987), t_1 can be of the order of 12 to 24 hours for large-size elastomeric bearings such as those used in seismic isolation applications. Time

t_2 is dependent on the rubber compound and temperature and is relatively short–of the order of a few hours. When crystallization stiffening begins, the rubber stiffens because of reorientation of its molecular structure. Crystallization is reversed when the temperature is increased.
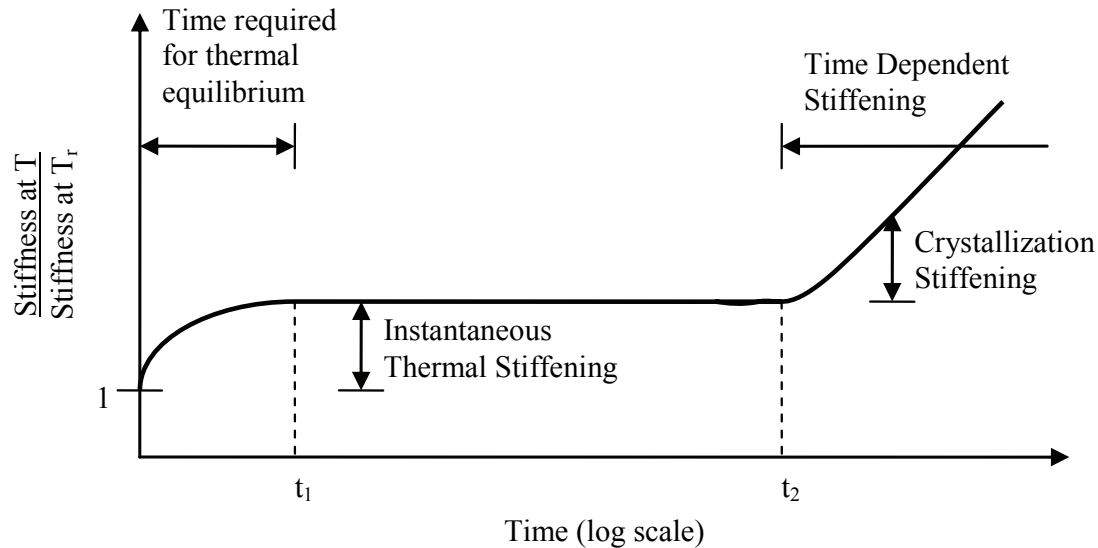
NOTE: T_r = reference temperature (typ. 20°C), $T<<T_r$

FIGURE 7-15   Time-dependent Low Temperature Behavior of Elastomeric Bearings

When the temperature falls below the *glass transition* temperature, which is compound dependent,, the elastomer becomes brittle and many of its mechanical and physical properties undergo significant and rapid changes. Natural rubber has a glass transition temperature of about -55°C.

Roeder et al. (1987) concluded that thermal stiffening in elastomeric bearings is likely to be a serious problem in Alaska, limited parts of the continental United States, and much of Canada and that crystallization is a problem when temperature drops below 0°C.

It is clear that the mechanical properties of elastomeric bearings are affected by low temperatures and the duration of exposure to these temperatures. It is unfortunate that most of the studies on the effect of low temperature on the properties of elastomeric seismic isolation bearings, with the exception of the study of Yakut and Yura (2002), which is discussed later in this report, have neglected the significance of duration of exposure. Some of the studies neglect to report the duration of exposure, whereas others report a single approximate exposure time.

Skinner et al. (1993) report on the effect of low temperature on the properties of a lead-rubber bearing tested in New Zealand. The exposure time is not reported. The peak force and displacement is reported from which only the effective stiffness can be calculated.

For a strain of 0.5 and a test frequency of 0.9 Hz, the effective stiffness increased by factors of 1.4 and 1.2 at temperatures of -35 and -15°C, respectively, with respect to the stiffness at the reference temperature of 18°C. At a temperature of 45°C the factor was 0.9.

Nakano et al. (1993) reported data on the effective stiffness and damping of one lead-rubber and one high damping rubber bearing that were cooled to a temperature of about -18°C and then tested. Measurements were made at various temperatures up to 5°C as the bearings warmed up during testing. The exposure time for each reported temperature was extremely short (presumed to be of the order of a few minutes). Nevertheless, these data are useful and used herein to establish property modification factors for high damping rubber bearings.

Kim et al. (1996) reported the low temperature properties of one lead-rubber and one low damping rubber bearing. The bearings were cooled to -60°C for at least three days and then tested. Force-displacements loops and values of characteristic strength and post-yield stiffness are reported for various temperatures. Testing was conducted over a range of rubber shear strains at a frequency of 0.1 Hz. This is a well documented set of results, which is used herein to establish property modification factors for temperature effects on lead-rubber bearings. However, the reader is cautioned that the results might have been affected by the history of cooling (a lengthy exposure at a very low temperature and then a quick warming up to the temperatures identified for testing).

Yakut and Yura (2002) investigated parameters affecting the low temperature performance of elastomers. They tested small-size neoprene and natural rubber bearings for a range of temperatures and exposure times and measured the shear modulus of the elastomers at shear strains of less than 30%. A representative result from this study is presented in Figure 7-16, which shows the ratio of the shear modulus at low temperature to the shear modulus at room temperature (assumed 20°C) as a function of temperature and duration of exposure for four materials. NR denotes low damping natural rubber and NEO neoprene in this figure. The 100 and 150 following NR or NEO denotes the room temperature shear modulus of the material in psi. Material NR100 is typically used in lead-rubber seismic isolation bearings. The data indicate the following:

a) Natural rubber shows superior behavior to neoprene at low temperatures, as measured by smaller percentage increases in shear modulus.
b) For NR100, exposure at temperature of -20°C (-30°C) and for up to 10 (3) days has little time-dependent effect on the shear modulus.
c) Time-dependent low temperature stiffening is more pronounced for rubbers with larger shear moduli.
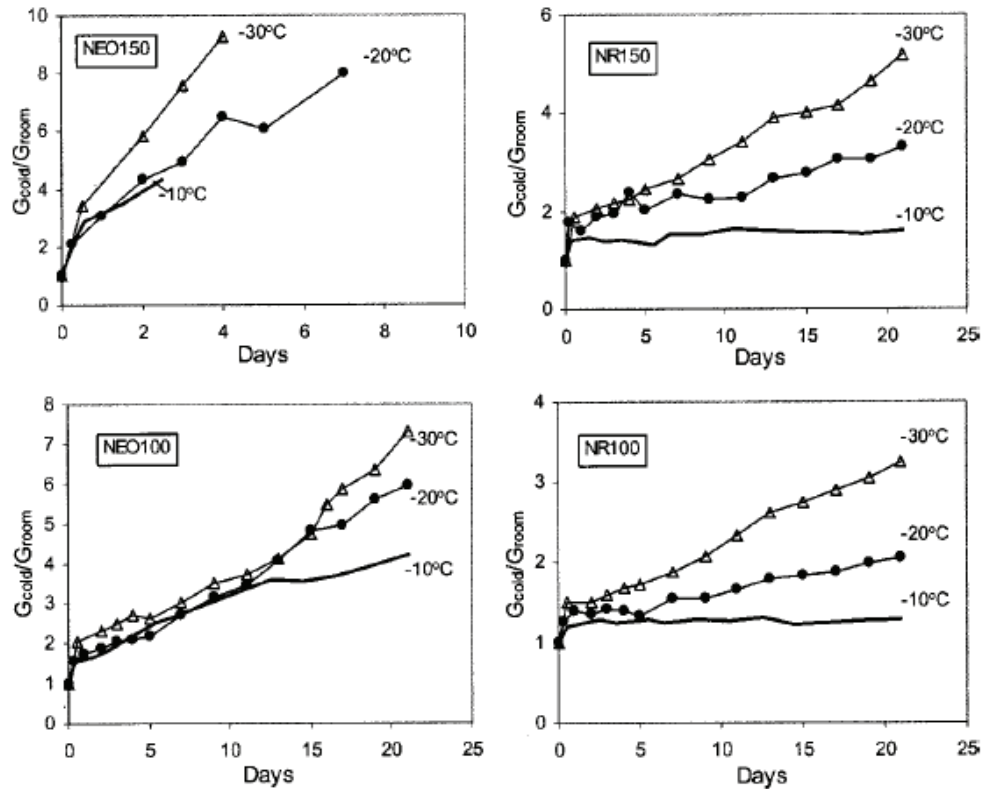
FIGURE 7-16 Low Temperature and Duration of Exposure Effects on Elastomers (Yakut and Yura, 2002)

7.8 Scragging and Recovery of Elastomeric Bearings

Elastomeric bearings typically exhibit higher characteristic strength and stiffness when tested for the first time. The properties under these conditions are termed *virgin* or *unscragged*. Subsequent testing under the same conditions results in stable but lower values of strength and stiffness, which are termed herein as *scragged* properties. Figure 7-17 presents force-displacement loops from the testing of a small-scale high damping elastomeric bearing (Kasalanati and Constantinou, 1999). Figure 7-18 presents loops for a moderate-scale high damping rubber bearing tested by Thompson et al. (2000).

Thompson et al. (2000) tested 23 moderate-scale rubber bearings with effective damping in the range of 0.05 to 0.17 and established that the extent of scragging increases as the shear modulus of rubber decreases and the effective damping increases. Data are presented in Figure 7-19, where the third-cycle effective shear modulus at 100% shear strain was used as the point of reference because it is often used by manufacturers to characterize the lateral stiffness of rubber bearings. In this figure, the effective damping was computed per (7-3) using the effective shear stiffness at 100% shear strain. They found that the ratio of effective stiffness in the 1st cycle (virgin condition) to the effective stiffness in the 3rd cycle (scragged condition) varied between about 1.4 and 2.1 as the effective shear modulus of rubber decreased from about 2.4 MPa (350 psi) to about 0.24

MPa (35 psi). The ratio of effective stiffness in the first cycle (virgin conditions) to the effective stiffness in the stable cycle (scragged conditions) is defined herein to be the property modification factor for scragging or the scragging factor. Figure 7-19 presents values of the scragging factor as determined by Thompson et al. (2000).
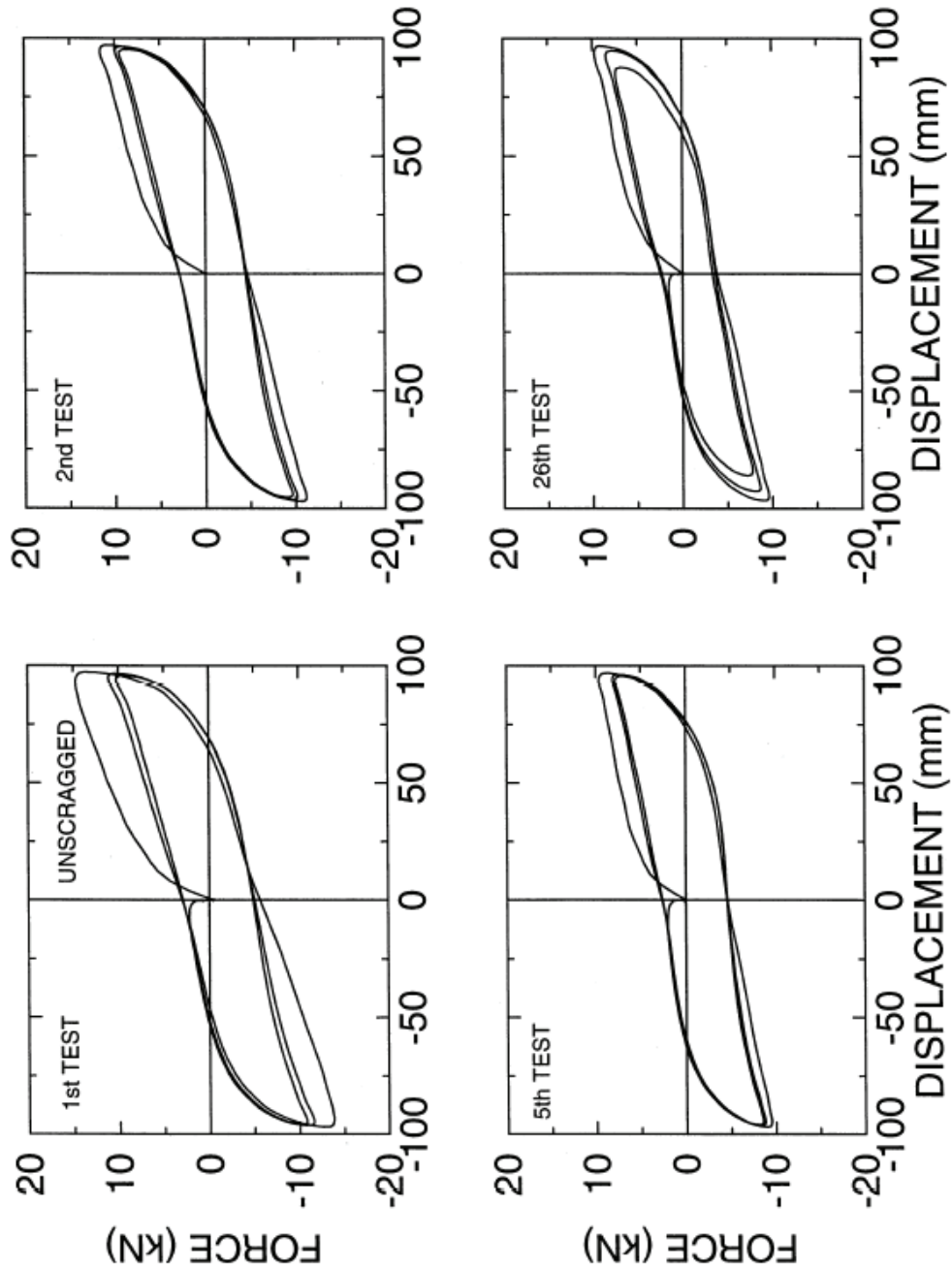
FIGURE 7-17 Lateral Force-Lateral Displacement Loops of a Small-Scale High Damping Elastomeric Bearing Demonstrating Effects of Scragging (tests at frequency of 1.0 Hz) (Kasalanati and Constantinou, 1999)

205
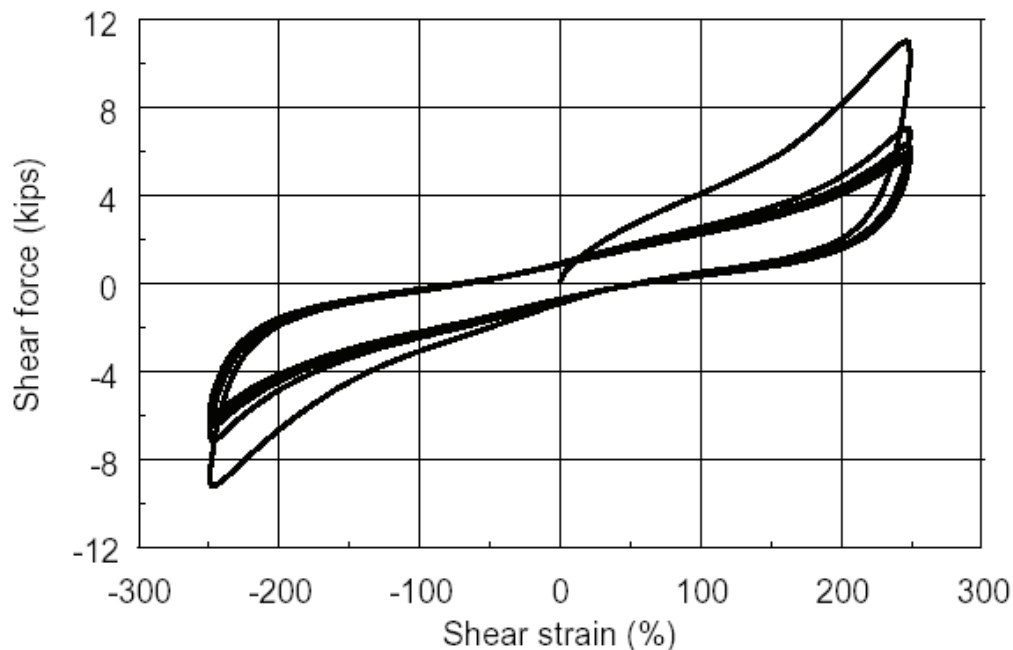
FIGURE 7-18 Effects of Scragging in a Rubber Bearing (Thompson et al., 2000)
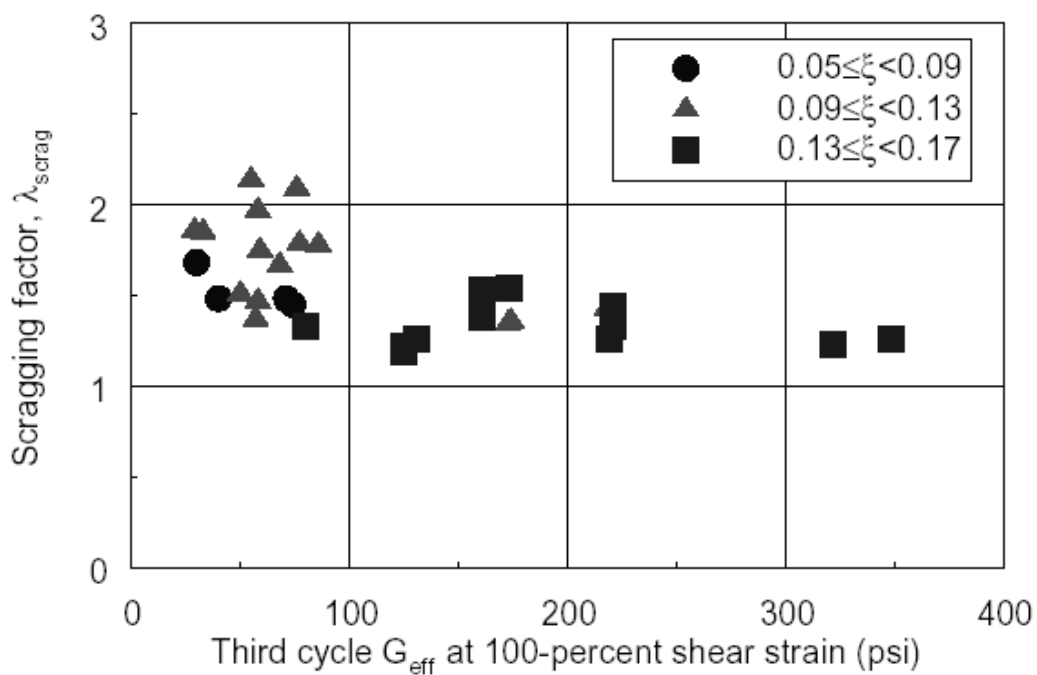
FIGURE 7-19 Values of Scragging Factor for High Damping Elastomeric Bearings (100 psi=0.69MPa) (Thompson et al., 2000)

Morgan et al. (2001) extended the study of Thompson et al. and presented results from tests of 45 moderate-scale rubber bearings fabricated by six manufacturers using a total

206

of 12 compounds. The results are most similar to those presented in Figure 7-19, namely, that the percentage reduction in the effective modulus from the first to third cycle depends on the formulation of the rubber compound, the vulcanization profile used to fabricate the isolator and the imposed strain history.

Filler materials such as carbon black, synthetic elastomers, oils and resins are routinely added to natural rubber to reduce the modulus and/or increase the damping of high damping rubber bearings. The addition of carbon black to natural rubber tends to increase the damping and shear modulus; other fillers are then added to the compound to reduce the shear modulus. The data of Thompson et al. (2000) and Morgan et al. (2001) suggest that the greater the volume of filler (maximized by high damping and low shear modulus), the greater the likely scragging effect. Low modulus (0.45 MPa or 65 psi), low damping rubber can employed in lead-rubber bearings and such an elastomer might be compounded by reducing the percentage of carbon black by comparison with that in a natural rubber bearing (shear modulus of approximately 0.69 MPa or 100 psi)—scragging effects are likely small in such compounds.

Production isolators are often scragged as part of the manufacturer's quality control program. Such scragging generally involves unidirectional shearing of the isolator to a level of shear strain that is less than the maximum design strain. Morgan et al. (2001) conducted bi-directional tests of two types of seismic isolation bearing to determine whether testing a bearing along one axis served to scrag the bearing along the perpendicular horizontal axis. The tests involved one fully reversed cycle to 250% shear strain followed by one fully reversed cycle to 250% shear strain in the orthogonal horizontal direction. The results of these tests indicated that scragging along one axis significantly influences response on the perpendicular axis. Data from the cruciform-orbit tests of another low-modulus, high-damping rubber bearing from another manufacturer support this observation, but the degree of interaction appears to be compound dependent. For many years it was assumed that the molecular structure of rubber was damaged by testing and that scragged properties were permanent. Nowadays, it is widely accepted that rubber bearings recover their virgin properties. Mullins (1969) observed that rubber samples that softened over numerous cycles of stretching recovered their initial mechanical properties over time and noted that recovery of stiffness was accelerated and more complete at high temperatures. Data reported in Cho and Retamal (1993), Murota et al. (1994), Kulak et al. (1998) and Thompson et al. (2000) demonstrate that significant recovery occurs within a short period of time following testing. Kulak reported recovery data from large-strain tests of high-modulus, high damping elastomers and concluded that elastomers do recover stiffness and that scragging of a bearing prior to installation is not important (other than as a quality-control check). Morgan et al. (2001) analyzed data from tests of four high-damping rubber bearings (one high-modulus and two low-modulus compounds) that were not axially loaded between tests. For one high-modulus and one low-modulus compound, 100-percent recovery was observed in a five-year period; more than 65% of the recovery in the low-modulus compound was observed in the first 12 month period. For the remaining low-modulus compound, 60% recovery was observed in one month.

The process of recovery (and aging as noted in Section 7.9) suggests that chemical processes continue in a bearing following vulcanization. It is highly likely that full recovery of virgin properties occurs with time, with the time to full recovery being dependent on the rubber compound, the extent of its curing, and the ambient temperature. The available data suggest that full recovery of first cycle properties should be assumed for analysis and design of seismic isolation systems. The virgin and scragged mechanical properties of a bearing can then be captured by testing by analysis of the first and third cycles of response, respectively—see Figures 7-17 and 7-18 for sample data.

7.9 Aging of Elastomeric Bearings

7.9.1 Introduction

Long-term changes in the mechanical properties of elastomers can result from stiffening (hardening) due to continued vulcanization of the elastomer and degradation of the elastomer due to exposure to oxygen and ozone (Morgan et al., 2001). Protection against ozone and oxygen-related degradation can be achieved by including various waxes and chemical anti-oxidants in the rubber matrix (Roberts, 1988). Although bulk components such as seismic isolation bearings are generally not significantly affected by ozone and oxygen, elastomeric bearings are normally fabricated with a layer of cover rubber that includes these anti-oxidants to protect the core of the bearing from significant infiltration by oxygen and ozone. Age-related stiffening or hardening due to continued vulcanization of an elastomer can lead to an increase in the effective shear modulus with time. The percentage increase in effective modulus will vary depending on a number of factors including the completeness of the initial vulcanization (consumption of free sulfur) and temperature (Thompson et al., 2000; Morgan et al. 2001).

There are several reports on the in-service performance of elastomeric bearings used in non-seismic bridge applications. These reports provide little information on the aging characteristics of the bearings. Some of the reports describe bearing failures (e.g., Stanton and Roeder, 1982; Manning and Bassi, 1986; and Taylor et al., 1992). The failures are attributed to elastomer debonding, bearing misalignment, excessive creep, surface cracking, and inappropriate installation. Excluding failures that can be attributed to poor fabrication quality, which can be prevented with a rigorous quality control and inspection program, the in-service history of elastomeric bridge bearings is very good.

There are few reports that contain information that provide insight into the in-service performance of rubber bearings. Malik (1991) described the condition of 20-year-old natural rubber bearings that were removed from a bridge in New York State. The mechanical properties of the bearings at the time of installation weren't measured or reported but the bearings were subjected to and passed the standard physical tests except those for compression (per ASTM D395, American Society for Testing and Materials, 1988). Malik reported that some of the bearings removed from the bridge had developed significant cracks such that the steel reinforcement was exposed. Similar problems were reported in Ontario, Canada, by Manning and Bassi (1986). In both cases, the authors reported that the bearings could resist safely the imposed loads and thermal

displacements. If these bearings had been seismic isolators, the cracks would have represented significant defects had the bearings been subjected to large earthquake-induced displacements. However, it is likely that these (older) bearings had insufficient anti-oxidant in the rubber compound, which led to the observed cracking. Parenthetically, modern elastomers are typically compounded with sufficient anti-oxidant to prevent such cracking.

Stevenson and Price (1986) reported a study on 20-year-old natural rubber bearings that were removed from a bridge in England. The bearings were in good condition and their physical properties were found to meet the requirements for new bridge bearings. Data on the lateral stiffness of the bearings at the time of installation was not available but the design documents called for a lateral stiffness in the range of 1.36 to 2.04 kN/mm (or 1.7 kN/mm ± 20%). These bearings were subjected to combined compression and shear tests. The measured value of the lateral stiffness of one pair the bearings was reported to be 1.8 kN/mm: the lateral stiffness might have increased by as much as 32%, decreased by as much as 12% with respect to the bounding design values, or not changed at all.

7.9.2 High-damping rubber bearings

Important information on the effect of aging on the mechanical properties of prototype seismic isolation bearings was reported by Clark et al. (1996). Lead-rubber and high-damping rubber bearings that were tested in 1982 in conjunction with the construction of the Foothill Communities Law and Justice Center in California were retested in early 1994 and early 1995, 12 and 13 years after initial testing. Moreover, a pair of high-damping rubber bearings were removed from the building and retested after 12 years of service. The 1983-vintage tests and the 1995-vintage tests involved different test-machine configurations and likely different rates of loading and so a direct comparison of results is not possible. Further, data were not recorded for the virgin bearings and the virgin (1983-vintage) test data were not available in digitized form.

Morgan et al. (2001) report the results of aging-related tests conducted at the University of California, Berkeley. The subject bearings were retested in late 1994 and early 1995 by Clark et al. (1996), as noted above, and tested again by Morgan et al. (2001) in June 1999 using identical strain histories to those used by Clark et al. so that changes in effective modulus could be detected independent of strain-history effects. Third-cycle shear moduli were reported to exclude the effects of scragging and recovery. The effective stiffness of the bearings increased with time, between 10% and 32%, but the dependence of the increase on shear strain was weak. This percentage increase in stiffness, although quantifiable for five-year aging studies, cannot be linearly extrapolated to estimate increases in stiffness over longer periods of time—due in part to nature of age stiffening in elastomers. The ongoing vulcanization of the rubber matrix occurs more rapidly in the first few years after the rubber is compounded, but slows over time as the free sulfur is consumed. For this reason, the effective shear modulus will likely reach a limiting value, which can only be evaluated, for a given compound and vulcanization profile by long-term aging studies.

Data on the aging characteristics of elastomeric bearings with effective damping exceeding 15% do not exist. High damping can be achieved by incomplete curing but such bearings will generally exhibit large differences between the virgin and scragged properties. The virgin properties will likely be recovered in a relatively short time and then exceeded with time as a result of on-going consumption of the sulfur left following the initial curing of the bearing.

7.9.3 Lead-rubber bearings

The data on the testing of lead-rubber bearings show an insignificant change in the characteristic strength and some minor increase in the effective stiffness of the bearings. The characteristic strength of a lead-rubber bearing is dictated by the yield strength of the lead core—properties that will not change with time. Age-related changes in the post-yield stiffness are those of the elastomer. If fully cured natural (low damping) rubber is used in the bearing, the age-stiffening of the bearing will be small. If filled elastomers are used in the bearing, the data of Section 7.9.2 can be used to estimate the likely increase in post-yield stiffness with time.

7.9.4 Accelerated aging tests

Some manufacturers of high damping rubber bearings have claimed insignificant changes in mechanical properties of such bearings with time. Kojima and Fukahori (1989) presented data for high damping rubber bearings that suggest changes of less than 10% over a period of 60 years.

These data are based on accelerated aging tests of rubber specimens at high temperature - tests that utilize the Arrhenius method. Accelerated aging of rubber is based on exposure of rubber samples (typically, dumbbell specimens per ASTM Standard D412, American Society for Testing and Materials, 1988) to high temperatures (typically in the range of 60° to 80°C) in a vacuum for relatively short periods of time, up to 30 days. The procedure utilizes the known degradation of rubber at high temperatures to indirectly produce data on the effect of the passage of time on the properties of rubber. We believe that the results of such tests cannot provide any useful information on the long-term properties of elastomeric bearings for the following reasons:

  a) The relationship between short-term accelerated testing of small specimens and the long-term in-situ performance of elastomeric bearings is not understood.
  b) Such tests cannot reveal the effect of creep deflections, static loading, and history of motion and loading on the long-term properties of elastomeric bearings.
  c) There is virtually no data on the aged properties of in-service high damping rubber bearings and validation of the results of the aging tests is not possible.

The Arrhenius method explores the degradation of rubber at high temperatures. Tests on small rubber specimens are conducted after exposure to at least three high temperatures. Information is obtained on the time required for a particular event to occur at each temperature (e.g., failure, increase of shear modulus by 15%, reduction of the elongation

210

at break by 15%). This information is then used to estimate the time required for the same event to occur at operating temperature of the bearing.

The Arrhenius method cannot provide conclusive evidence on the long-term properties of in-situ aged elastomeric bearings for the reasons stated above. However, the method is used, inappropriately, to provide information on *life expectancy*. The Arrhenius rate law (Nelson, 1990) is used for these calculations as described below.

According to the Arrhenius rate law, the rate of a simple, first order chemical reaction is related to the Kelvin temperature, *T,* as follows

$$(rate) = A' \exp\left[-\frac{E}{kT}\right] \tag{7-12}$$

where A' is a constant that is characteristic of test conditions and of the failure or degradation mechanism of the specimen, E is the activation energy and k is Boltzmann's constant.

Based on the view that rubber degradation is a simple, first order chemical reaction, one might assume that the specimen has degraded when some critical amount of the material has reacted or

$$(\text{critical amount}) = (rate) \times (\text{time to specific degradation}) \tag{7-13}$$

From (7-13) one can express the time to specific degradation, τ, as

$$\tau = \frac{(\text{critical amount})}{(rate)} \tag{7-14}$$

and using (7-12)

$$\tau = A \exp\left[\frac{E}{kT}\right] \tag{7-15}$$

where A is a constant depending on the specimen geometry, size and test method. Equation (7-15) is known as the Arrhenius life relationship. The logarithm (base 10) of (7-15) is

$$\log(\tau) = a_0 + \frac{a_1}{T} \tag{7-16}$$

and $\log(\tau)$ is linearly dependent on the inverse of the Kelvin temperature.

As an example, the Arrhenius method is used to predict the time to degradation of the shear modulus of a particular high-damping rubber compound. In this case, degradation is defined as a 15% increase in the shear modulus. Specimens of the subject rubber were

211

maintained in vacuum at temperatures of 60°, 70° and 80°C and periodically tested to measure the shear modulus. The times were determined by interpolation to be 45, 13.5 and 4.5 days, respectively, for the three temperatures. Figure 7-20 shows the Arrhenius plot for this example. Extrapolation determines the expected time to a 15% increase in the modulus at an operating temperature of 15°C: 29,000 days or 79.5 years. This is a problematic prediction because it extrapolates 45-day data to a time period that is 650 times greater. Even more ridiculous is the prediction of a life expectancy of 160,500 days or 440 years if the bearing was to be kept at temperature of 5°C. Apparently, confirmation of such predictions is impossible.

The Arrhenius method is useful in the evaluation of materials on a laboratory basis (such as in the comparison of various rubber compounds). However, its use for the prediction of life expectancy of elastomeric bearings is highly problematic for the reasons stated above.
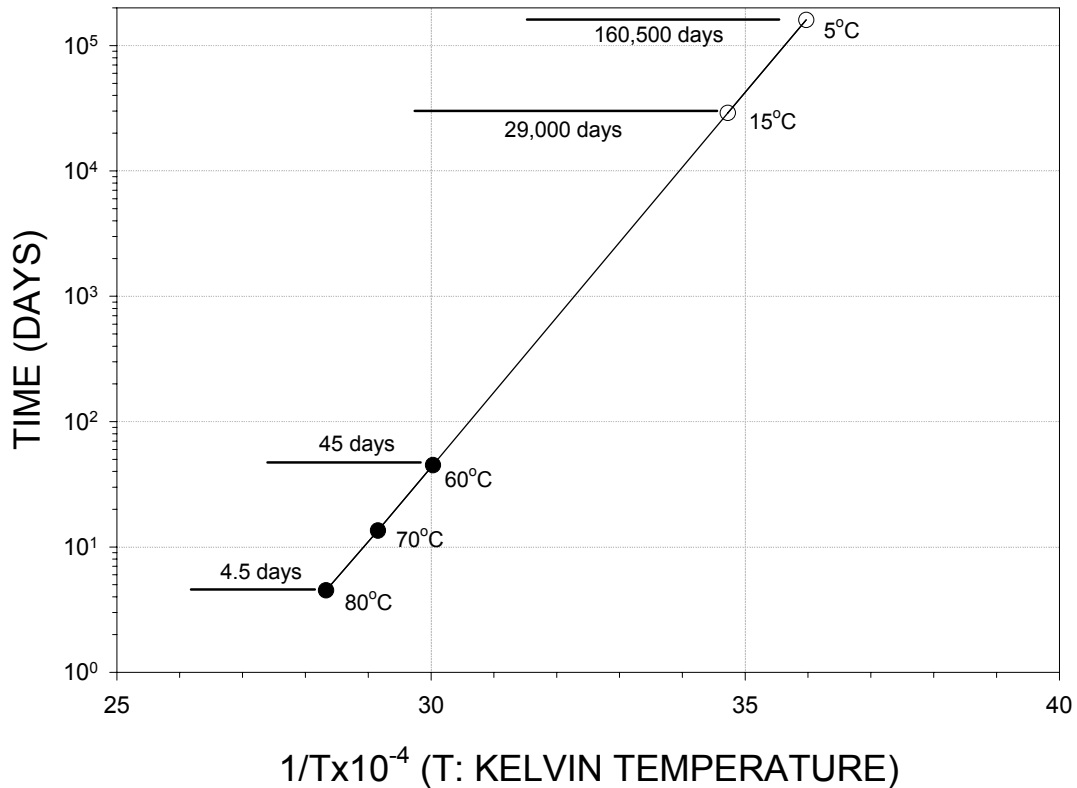
FIGURE 7-20 Arrhenius Plot for Time to Increase the Shear Modulus by 15%

SECTION 8
MECHANICAL PROPERTIES OF LEAD-RUBBER BEARINGS

8.1 Introduction

Lead-rubber bearings have found widespread application in the seismic isolation of bridges and buildings. They are typically constructed using low damping natural rubber and so Section 7 herein should be read by those interested in lead-rubber bearings. The unique feature of lead-rubber bearings is the addition of a cylinder of lead in the core of the bearing to enhance energy dissipation. Lead contributes also to the stiffness of the bearing, although that contribution is relatively minor.

8.2 Construction of Lead-Rubber Bearings

A lead-rubber bearing typically consists of a natural rubber bearing such as that shown in Figure 7-2 with a central core of lead. Figure 7-4 illustrates the construction of a lead-rubber bearing that was tested at the University at Buffalo. Figure 8-1 is a photograph of a lead-rubber bearing that was cut to reveal its internal construction. Note that the top and bottom (flange) plates of the bearing are connected to the end plates of the rubber bearing through countersunk bolts. This type of construction allows for confinement of the lead plug at the core of the bearing. The plug is typically cut longer than the height of the rubber bearing (by an amount less than 5%) so the core is compressed upon bolting the flange plates to the end plates. The lead core expands laterally and wedges into the rubber layers between the shim plates. Under such (confined) conditions, the lead core provides excellent energy dissipation capacity (with a magnitude dependant on the diameter of the lead plug or cylinder).
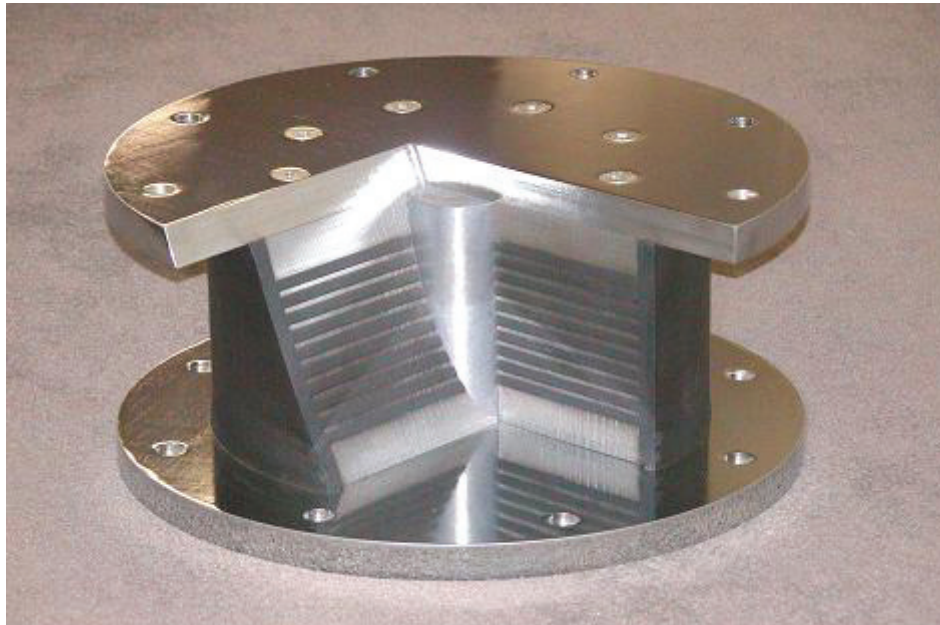
FIGURE 8-1 Internal Construction of a Lead-Rubber Bearing (Courtesy of DIS)

213

Lead-rubber bearings have also been constructed using multiple lead cores. There are a few applications of multiple core lead-rubber bearings in Japan and one in California, all in bridges. Figure 8-2 is a schematic of a multiple core lead-rubber bearing used for bridge applications in Japan. The figure also shows lateral restrainers that were employed in Japan for the seismic isolation of bridges, where bridges were isolated only in the longitudinal direction - a practice not used in the United States.
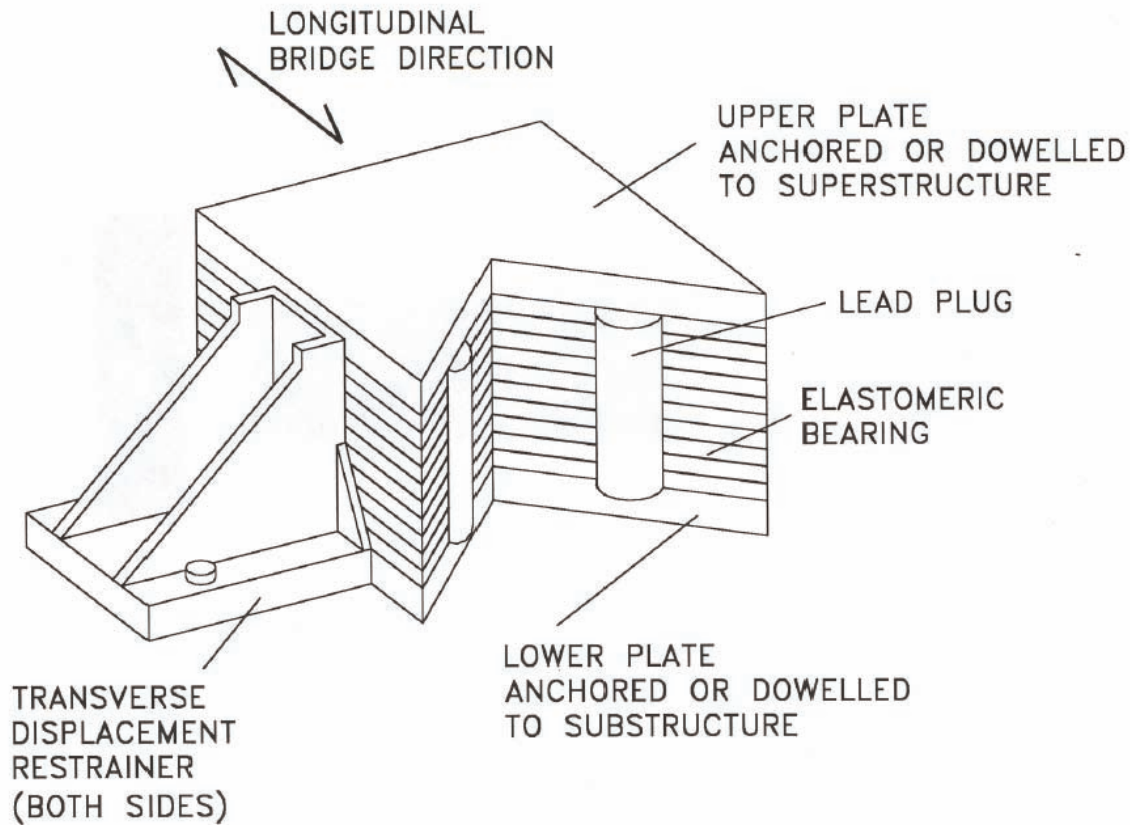
FIGURE 8-2 Multiple-Core Lead-Rubber Bearing Used in Japan

There is very little information on the behavior of multiple-core lead-rubber bearings. These bearing do not necessarily behave as a single, large-diameter-core lead-rubber bearing. Given that applications of the multiple core lead-rubber bearings are limited in number, these bearings are not discussed further.

8.3 Mechanical Properties of Lead-Rubber Bearings

8.3.1 Introduction

The basic mechanical properties of lead-rubber bearings are presented in this and following sections using results of tests of several different bearings. Consider first a small scale lead-rubber bearing that was tested extensively at the University at Buffalo. Data from tests of this bearing are used to demonstrate overall behavior. Second, results of tests of a large-scale bearing are used to address the issue of heating of lead-rubber

214

bearings; see Section 8.8. Third, results of tests of two moderate-scale bearings are used to address the effect of loading history - see Section 8.5. Tests of the moderate-scale bearing of Figure 7-4 are used to demonstrate the effects of low temperature and velocity. Finally, test results from a second large scale bearing are used to demonstrate the effects of velocity.

8.3.2 Small-Scale Bearing

Figure 8-3 presents drawings of two small bearings tested at the University at Buffalo. The first is a low damping natural rubber bearing with rubber designated as Durometer Shore A Hardness 50, Grade 5. The second is a lead-rubber bearing made of exactly the same rubber where the ratio of lead-core diameter to bonded rubber diameter was 0.21 (=1.5/7.0). The first specimen served as the control specimen to identify the effect of the lead core. Note that the two specimens have identical construction except for the hole in the center of the bearing.

The rubber bearing of Figure 8-3a was tested at a normal pressure of 6.9 MPa (1000 psi), a frequency of 0.5 Hz and lateral displacement so that the rubber shear strain ranged between 37% and 187%. The bearing exhibited very low damping. The effective stiffness and shear modulus were determined per Section 7. Results are presented in Table 8-1.

TABLE 8-1 Properties of the Low Damping Rubber Bearing

Pressure (MPa)	Frequency (Hz)	Rubber Shear Strain	Effective Shear Modulus (MPa)
6.9	0.5	0.37	0.46
6.9	0.5	0.74	0.40
6.9	0.5	1.14	0.36
6.9	0.5	1.50	0.35
6.9	0.5	1.87	0.36

The lead-rubber bearing was tested extensively using the test parameters and sequence presented in Table 8-2. All tests were conducted at a constant axial load except for one that was conducted under variable axial load. The idle time between experiments is reported so that the effects of heating of the lead core can be assessed.

Representative lateral force-displacement loops are presented in Figure 8-4. All are presented for a normal pressure of 6.9 MPa (1000psi) and frequency of 0.5 Hz. The shear strains are 150%, 250% and 300%. Figure 8-5 presents the loops recorded in a test with 25 continuous cycles at pressure of 6.9 MPa, frequency of 0.5 Hz and shear strain of 150%. The excellent energy dissipation characteristics of the bearing are evident in these two figures. The results of the 25-cycle test show stable behavior after a number of cycles, which indicates that the temperature of the lead core stabilized.

215
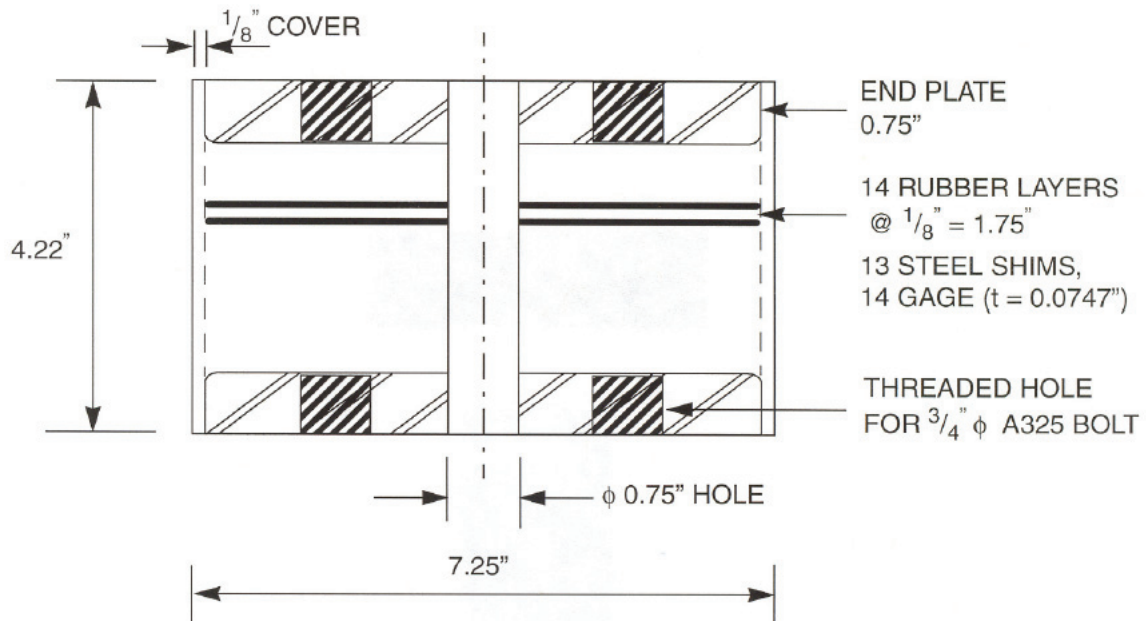
a. low-damping rubber bearing
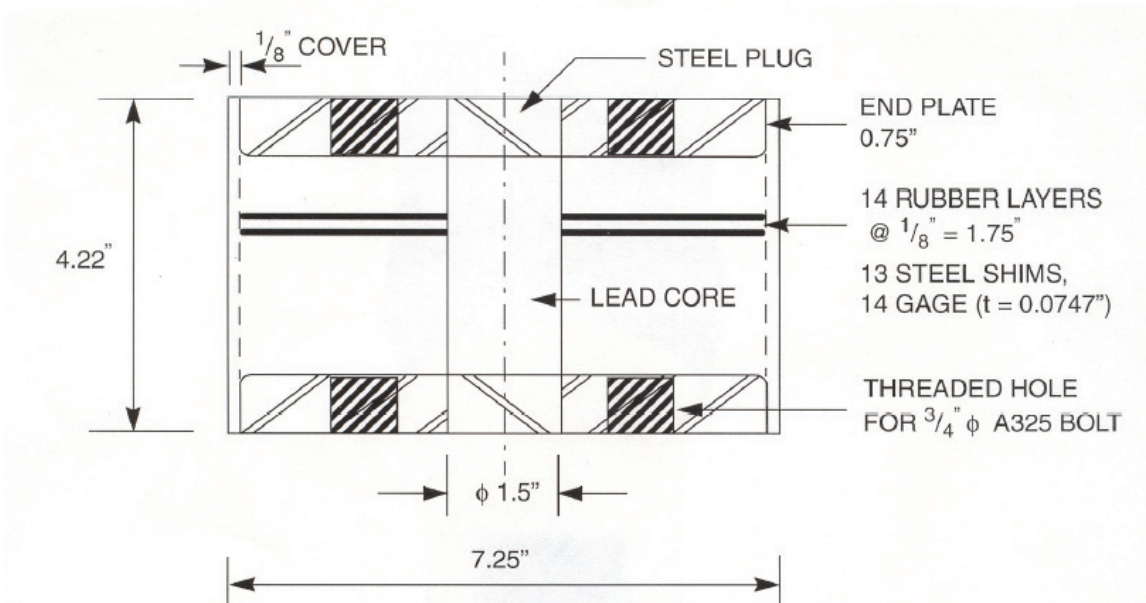
b. lead-rubber bearing

FIGURE 8-3 Construction of Small-Scale Bearings (1 inch=25.4mm)

216

TABLE 8-2 Test Parameters and Sequence of Testing for Lead-Rubber Bearing

Test No.	Pressure (MPa)	Frequency (Hz)	Amplitude (mm)	Shear Strain (%)	No. Cycles	Idle Time to Previous Test (min.)
E2001.001	6.9	0.5	67	150	3	-
E2001.002	6.9	0.5	17	37	3	4
E2001.003	6.9	0.5	33	74	3	2
E2001.004	6.9	0.5	51	114	3	2
E2001.005	6.9	0.5	67	150	3	2
E2001.006	6.9	0.5	83	187	3	2
E2001.007	6.9	0.5	67	150	25	2
E2002.001	3.5	0.5	67	150	3	110
E2002.002	3.5	0.5	17	37	3	1
E2002.003	3.5	0.5	33	74	3	0.5
E2002.004	3.5	0.5	51	114	3	0.5
E2002.005	3.5	0.5	67	150	3	0.5
E2002.006	3.5	0.5	83	187	3	1
E2003.001	6.9	0.1	67	150	3	4
E2003.002	6.9	0.1	17	37	3	2
E2003.003	6.9	0.1	33	74	3	1
E2003.004	6.9	0.1	51	114	3	1
E2003.005	6.9	0.1	67	150	3	0.5
E2003.006	6.9	0.1	83	187	3	1
E2004.001	6.9	0.5	67	150	3	4
E2005.001	6.9	1.0	67	150	3	0.5
E2005.002	6.9	1.0	17	37	3	0.3
E2005.003	6.9	1.0	33	74	3	0.3
E2005.004	6.9	1.0	51	114	3	0.3
E2005.005	6.9	1.0	67	150	3	0.2
E2005.006	6.9	1.0	83	187	3	1.5
E2006.000	0.5 to 6.9	0.5	67	150	3	8
E2007.000	6.9	0.5	111	250	3	3.5
E2007.001	6.9	0.5	133	300	3	2
E2008.000	6.9	0.5	67	150	3	1087
E2009.000	6.9	0.1	67	150	3	1.5
E2010.000	6.9	1.0	67	150	3	2
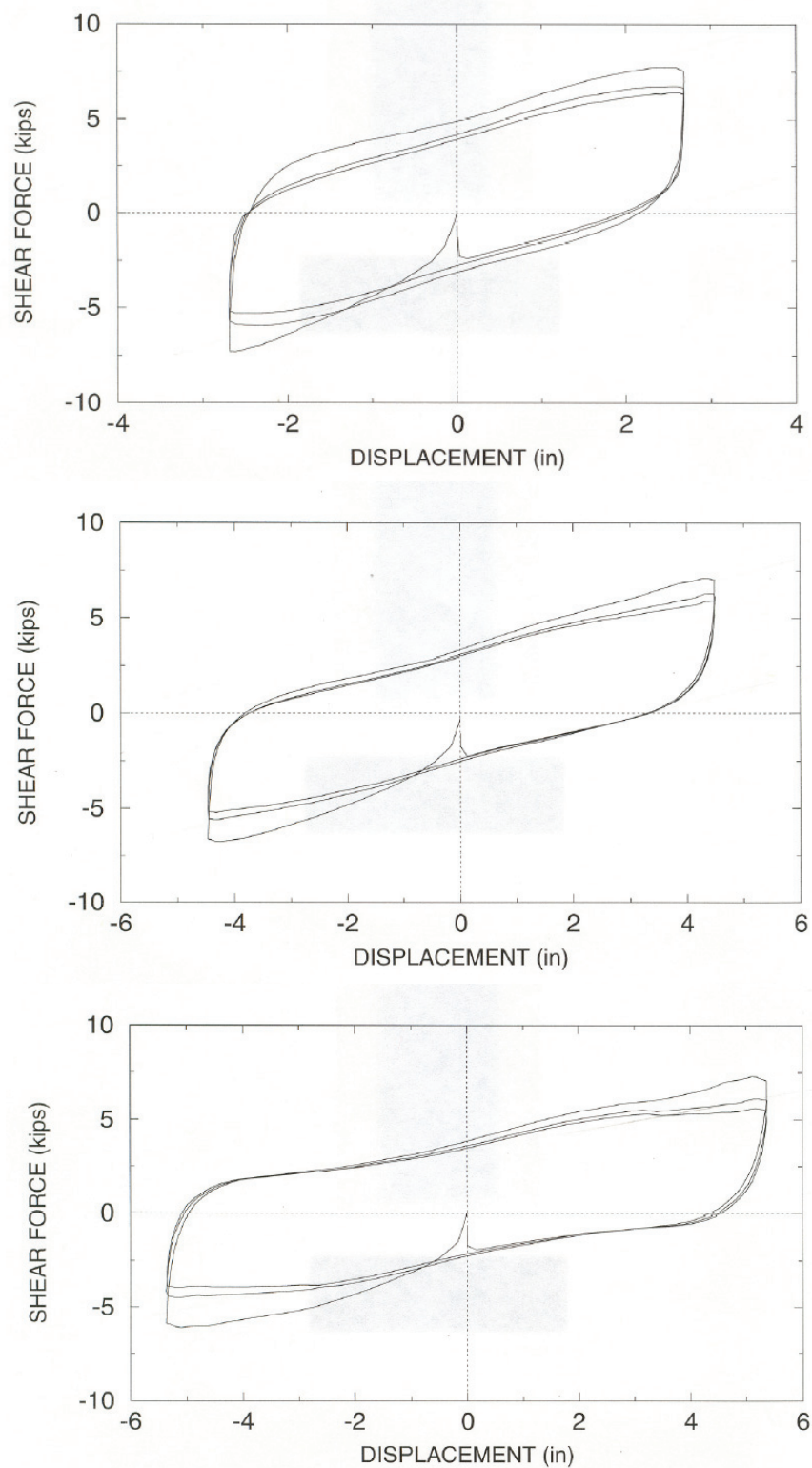
FIGURE 8-4 Recorded Force-Displacement Loops of Lead-Rubber Bearing in Tests with Pressure of 6.9MPa and Frequency of 0.5Hz, Shear Strains of 150%, 250% and 300%, (1 kip=4.45 kN, 1 inch=25.4 mm)

218
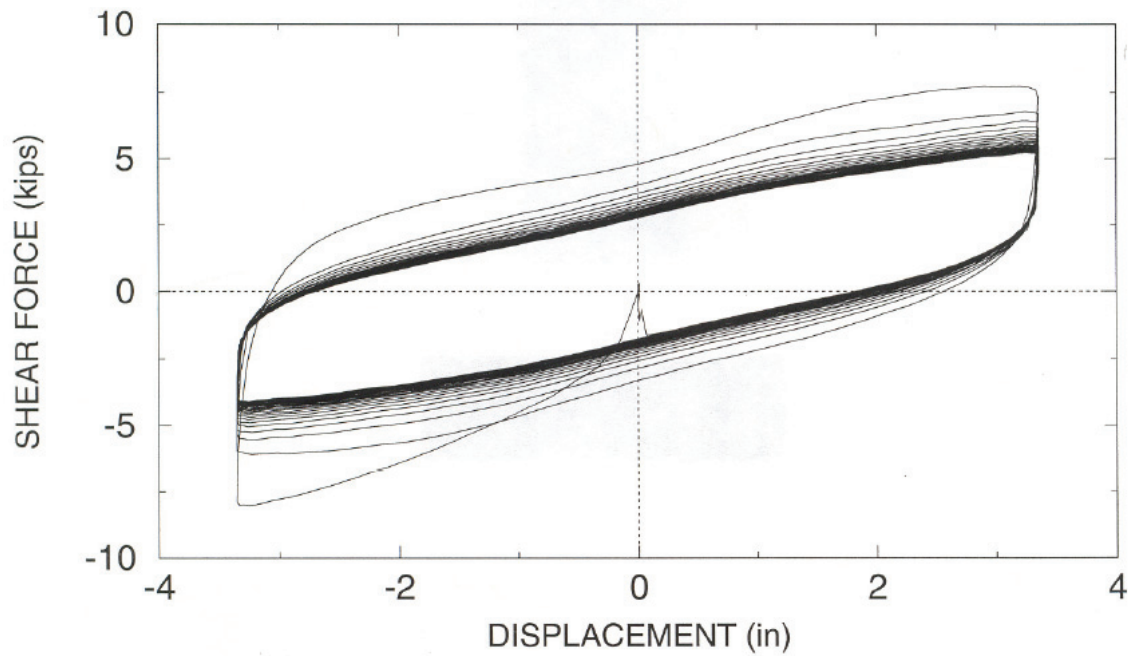
FIGURE 8-5 Force-Displacement Loops of Lead-Rubber Bearing in Test with 25 Cycles, Frequency=0.5 Hz, Pressure=6.9 MPa and Shear Strain=150% (1 kip=4.45 kN, 1 inch=25.4 mm)

Figure 8-6 presents the recorded histories of load and the loops in the test in which the axial load was varied so that the pressure ranged between 0.48 and 6.9 MPa (70 to 1000 psi). The distortion of the loops as a result of the varying axial load is evident, although the effect is not significant enough to warrant consideration in analysis.

The mechanical properties of the bearings were established on the basis of the following assumptions and equations. The bearing was assumed to have the idealized behavior of Figure 3-1. The critical parameters are the characteristic strength Q_d and the post-elastic stiffness K_d. These two parameters are related to the geometric and material properties of the bearing as follows:

$$Q_d = A_L \sigma_L \tag{8-1}$$

$$K_d = f_L \frac{GA_r}{T_r} \tag{8-2}$$

where f_L is a parameter that accounts for the effect of the lead core on the post-elastic stiffness (expected to be close to unity), G is the effective shear modulus of rubber, σ_L is the effective yield strength of lead, T_r is the total rubber thickness, A_r is the bonded rubber area, and A_L is the area of the lead core.

219
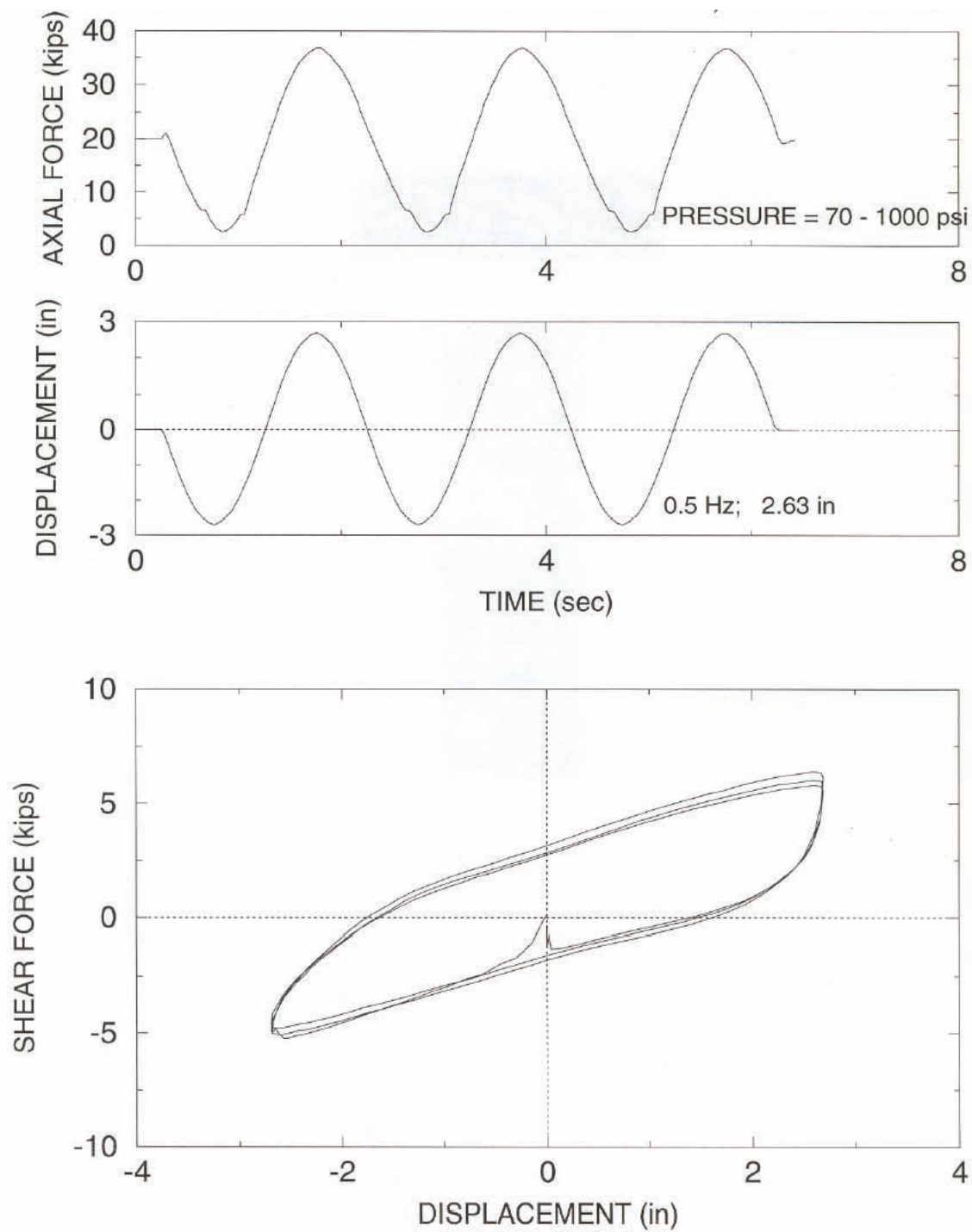
FIGURE 8-6 Force-Displacement Loops and Histories of Load of Lead-Rubber Bearing Subjected to Variable Axial Load. Frequency=0.5Hz, Shear Strain=150%, (1000 psi=6.9 MPa, 1 kip=4.45 kN, 1 inch=25.4 mm)

220

Values for f_L and σ_L were determined using equations (8-1) and (8-2) and the measured values of Q_d, K_d and G—the latter being established from the results of tests of the control specimen. Results are presented in Table 8-3. It can be observed that

a) There is a complex relationship between the test parameters and the mechanical properties of the bearing.

b) The value of f_L ranges between a lower bound of 1.0 after repeated cycling and a reasonable upper bound of 1.2. The value depends on the size of lead plug and the degree of confinement of the lead and cannot be determined from testing of a *representative* bearing. Rather, in the absence of test data for the bearing to be used, the parameter assumed for preliminary analysis should be in the range of 1.0 to 1.2. It must be recognized that these values were based on stiffness data from two different bearings, assuming that the shear modulus was the same for both. These properties can vary, even in nominally identical bearings, as shown later in this report.

c) The effective yield stress of lead is primarily affected by the cycle number, which indirectly reflects the effect of heating of the lead core. Figure 8-7 presents a summary of the effective yield stress for the case of normal pressure equal to 6.9 MPa (1000 psi) and a frequency of 0.5 Hz. The drop in the effective yield stress over 3 cycles of testing is modest for this bearing and appears to be independent of the rubber shear strain.

d) There is permanent drop in the effective yield strength after repeated testing that likely is the result of fracture of the lead core. At the conclusion of the testing, the bearing was cut and indeed the lead core was fractured in three pieces. Nonetheless, the bearing maintained substantial capacity to dissipate energy.

The values of the effective yield stress for lead presented in Table 8-3 and Figure 8-7 should be viewed as representative values that depend on the size of the bearing, the geometry of the bearing and the degree of confinement of the lead. Additional data to be presented next demonstrate that for large bearings, the value of the effective yield stress is less than the values presented in this table and figure. The effect of the hysteresis in the rubber has not been removed from the measured characteristic strength (see equation 8-1) prior to division by the lead core area to calculate the effective yield stress of the lead. This likely leads to some of the observed differences in the effective yield stress of lead for various bearing sizes. Nevertheless, the correction was not made due to (a) uncertainties in the procedure to make the correction in the absence of control specimens without a lead core, (b) complexities in adding the effect of rubber hysteresis on the characteristic strength when analysis is performed, and (c) the errors are relatively small and can be accounted for in the analysis by incorporating uncertainty in the nominal values of the strength and then using bounding methods of analysis. However, the effect of rubber hysteresis will be accounted for when calculations of lead core temperature are made in Section 8.8.

TABLE 8-3 Mechanical Properties of a Small Scale Lead-Rubber Bearing

Test No.	Pressure (MPa)	Frequency (Hz)	Shear Strain (%)	Post-Elastic Stiffness K_d (kN/mm)	Characteristic Strength Q_d (kN)		Lead Effective Yield Stress, σ_{YL} (MPa)		f_L
					First	Last	First	Last	
E2001.001	6.9	0.5	150	0.224	20.0	14.5	17.5	12.7	1.22
E2001.002	6.9	0.5	37	NA	13.1	13.1	11.5	11.5	NA
E2001.003	6.9	0.5	74	0.264	15.7	13.9	13.8	12.2	1.24
E2001.004	6.9	0.5	114	0.256	17.3	13.9	15.1	12.2	1.34
E2001.005	6.9	0.5	150	0.228	17.8	14.5	15.6	12.7	1.24
E2001.006	6.9	0.5	187	0.214	18.1	13.9	15.8	12.2	1.12
E2001.007	6.9	0.5	150	0.193*	18.1	10.0	15.8	8.8	1.05*
E2002.001	3.5	0.5	150	0.219	17.8	12.2	15.6	10.7	NA
E2002.002	3.5	0.5	37	NA	8.9	8.9	7.8	7.8	NA
E2002.003	3.5	0.5	74	0.313	12.0	10.9	10.5	9.5	NA
E2002.004	3.5	0.5	114	0.294	13.9	11.1	12.2	9.7	NA
E2002.005	3.5	0.5	150	0.235	13.6	10.9	11.9	9.5	NA
E2002.006	3.5	0.5	187	0.228	13.6	10.8	11.9	9.4	NA
E2003.001	6.9	0.1	150	0.198	13.6	12.2	11.9	10.7	NA
E2003.002	6.9	0.1	37	NA	9.7	9.7	8.5	8.5	NA
E2003.003	6.9	0.1	74	0.219	11.7	10.6	10.2	9.3	NA
E2003.004	6.9	0.1	114	0.207	12.2	10.9	10.7	9.5	NA
E2003.005	6.9	0.1	150	0.198	12.2	11.3	10.7	9.9	NA
E2003.006	6.9	0.1	187	0.180	12.5	11.4	11.0	10.0	NA
E2004.001	6.9	0.5	150	0.198	13.1	10.8	11.5	9.5	1.08
E2005.001	6.9	1.0	150	0.214	13.3	10.8	11.7	9.5	NA
E2005.002	6.9	1.0	37	NA	7.3	7.3	6.4	6.4	NA
E2005.003	6.9	1.0	74	0.271	9.7	8.6	8.9	7.5	NA
E2005.004	6.9	1.0	114	0.233	11.8	10.0	10.3	8.8	NA
E2005.005	6.9	1.0	150	0.212	12.0	10.0	10.5	8.8	NA
E2005.006	6.9	1.0	187	0.198	12.8	10.0	11.2	8.8	NA
E2006.000	0.5 to 6.9	0.5	150	NA	11.1	9.3	9.7	8.2	NA
E2007.000	6.9	0.5	250	0.147	12.8	11.7	11.2	10.3	NA
E2007.001	6.9	0.5	300	0.095	13.3	12.2	11.7	10.7	NA
E2008.000	6.9	0.5	150	0.191	13.3	10.9	11.7	9.5	1.04
E2009.000	6.9	0.1	150	0.165	12.2	10.9	10.7	9.6	NA
E2010.000	6.9	1.0	150	0.186	13.2	10.6	11.5	9.3	NA

1. Last cycle is cycle 3, except for test E2001.007 for which the last cycle is cycle 25
2. NA means that value could not be determined.
3. * reported value is for first cycle; value of K_d for cycle 25 was 0.16 kN/mm.

222
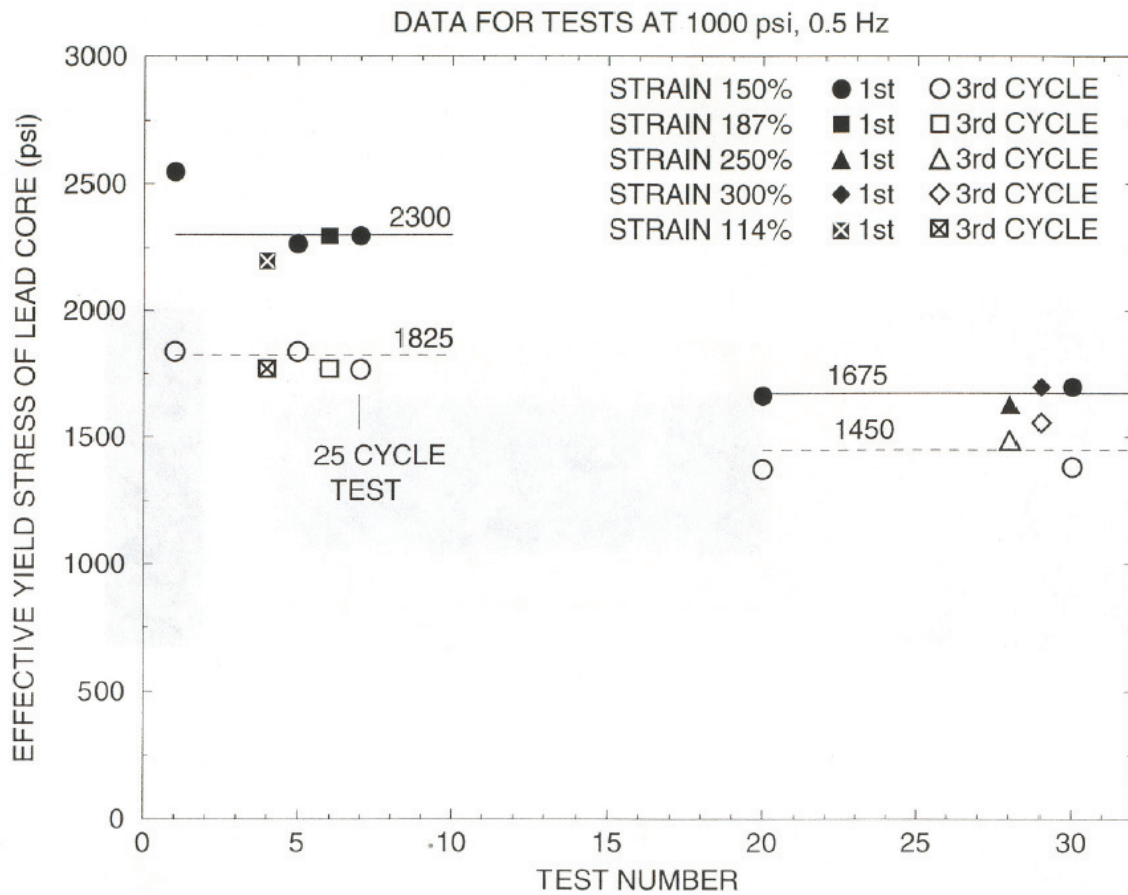
FIGURE 8-7 Effective Yield Stress of Lead as a Function of Test Number (1000 psi = 6.9 MPa)

8.3.3 Moderate Scale Bearings

Two bearings (numbered 1 and 2) of the geometry shown in Figure 7-4 were tested at the University at Buffalo in the prototype testing of isolators for a bridge application in New York State. The rubber was low damping and designated as natural rubber, Grade 3 per ASTM D4014 (American Society for Testing and Materials, 1988). The total rubber thickness T_r was 195.6 mm, the bonded rubber area A_r was $141,329 \, mm^2$, the lead area A_L was $3,832 \, mm^2$ and the shape factor was 10.4. The ratio of lead-core diameter to bonded diameter was 0.17 (=2.75/15.0). The bearings were tested under an average bearing pressure (vertical load divided by bonded rubber area) of 6.7 MPa (975 psi) and lateral sinusoidal motion of amplitude equal to 113 mm (peak shear strain of 58%) and frequency in the range of 0.035 to 0.35 Hz so that peak velocity was in the range of approximately 25 to 250mm/sec. Figure 8-8 presents a sample of recorded loops of lateral force-displacement for bearing No. 2 at temperature of 20^oC and -26^oC. The frequency of testing was 0.35 Hz so that the peak velocity was 250 mm/sec. Table 8-4 presents the mechanical properties of the bearings.

223
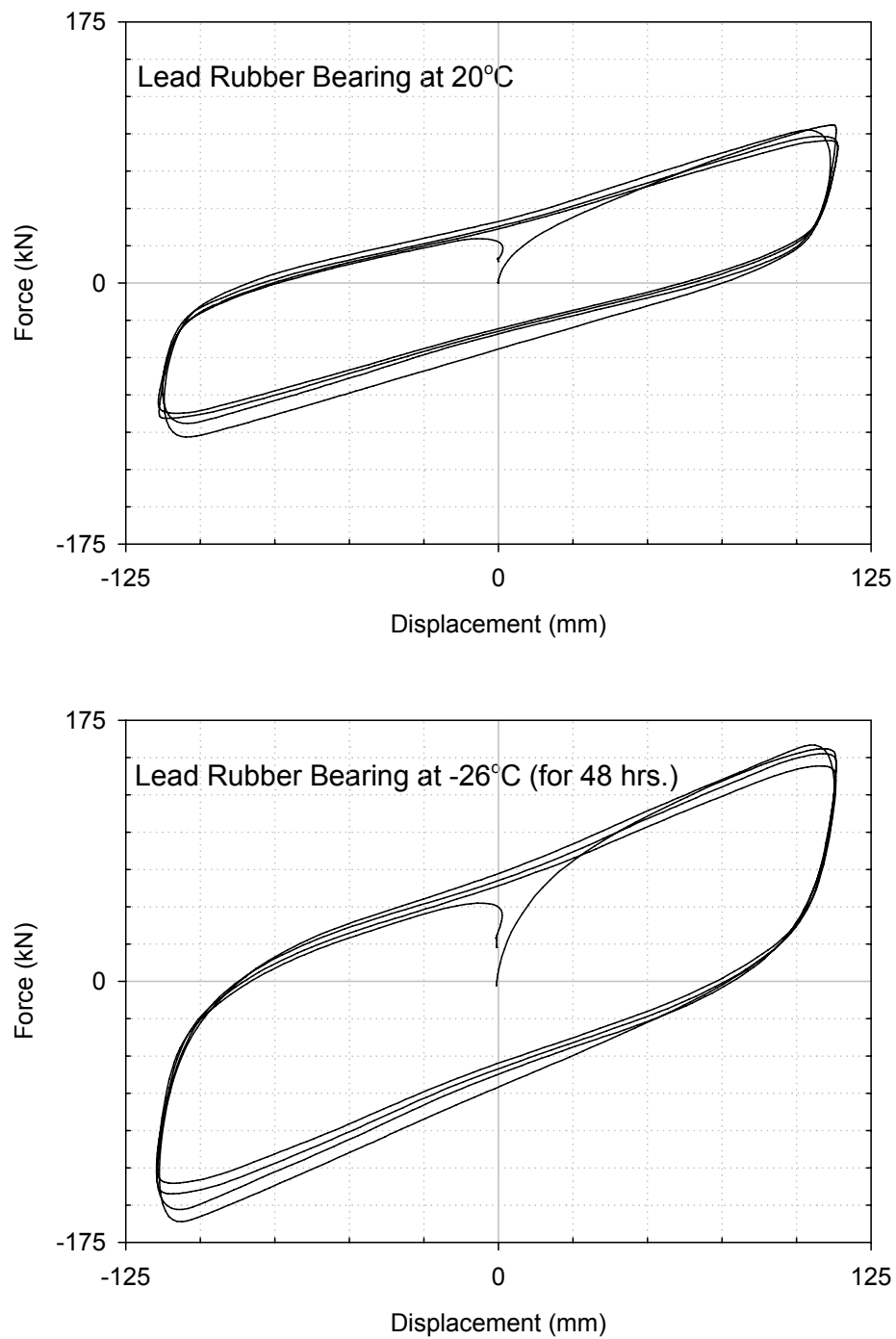
FIGURE 8-8 Recorded Force-Displacement Loops of the Lead-Rubber Bearing of Figure 7-4 (Pressure=6.7 MPa, Shear Strain=58%, Velocity = 250 mm/sec)

TABLE 8-4 Mechanical Properties of Moderate Scale Lead-Rubber Bearings (Tested at an Amplitude of 113 mm and a Shear Strain of 58%)

Bearing	Condition of Test	Peak Vel. (mm/s)	Cycle	EDC (kN-mm)	Effective Stiffness (kN/mm)	Post-elastic Stiffness (kN/mm)	Effective Damping	Lead Yield Stress (MPa)
1	at 20°C for 48 hrs	250	1.	17441	0.88	0.50	0.25	11.2
			2.	17361	0.86	0.48	0.25	11.1
			3.	15971	0.81	0.46	0.25	10.3
			4.	15135	0.79	0.46	0.24	9.7
2	at 20°C for 48 hrs	250	1.	18367	0.93	0.53	0.25	11.8
			2.	17260	0.89	0.51	0.24	11.1
			3.	16062	0.84	0.49	0.24	10.3
			4.	15259	0.81	0.48	0.23	9.8
1	at -26°C for 48 hrs	250	1.	25635	1.19	0.63	0.27	16.5
			2.	25274	1.17	0.62	0.27	16.2
			3.	24030	1.09	0.57	0.27	15.4
			4.	22889	1.05	0.55	0.27	14.7
2	at -26°C for 48 hrs	250	1.	30269	1.45	0.79	0.26	19.4
			2.	29942	1.33	0.68	0.28	19.2
			3.	28099	1.28	0.67	0.27	18.0
			4.	26212	1.19	0.62	0.27	16.8
2	at 49°C for 48 hrs	250	1.	15225	0.82	0.49	0.23	9.8
			2.	14863	0.79	0.47	0.23	9.5
			3.	14027	0.75	0.44	0.23	9.0
			4.	13496	0.74	0.44	0.23	8.7
1	at 49°C for 48 hrs	250	1.	14954	0.77	0.44	0.24	9.6
			2.	14490	0.74	0.42	0.24	9.3
			3.	13643	0.70	0.41	0.24	8.8
			4.	13145	0.70	0.41	0.23	8.4
1	at 20°C for 48 hrs	25	1.	15282	0.70	0.37	0.27	9.8
			2.	15203	0.65	0.32	0.29	9.8
			3.	14954	0.65	0.32	0.29	9.6
			4.	14796	0.65	0.32	0.28	9.5
1	at 20°C for 48 hrs	125	1.	17689	0.81	0.42	0.27	11.4
			2.	16988	0.74	0.37	0.29	10.9
			3.	16152	0.72	0.37	0.28	10.4
			4.	15621	0.72	0.37	0.27	10.0

The energy dissipated per cycle (EDC) was computed using the force and displacement histories, the effective stiffness was calculated using equation (7-1) and the effective damping was calculated using equation (7-3). The effective yield stress of lead was calculated using equation (8-1) with Q_D per equation (3-8) with yield displacement Y equal to 12 mm. The post-elastic stiffness, K_D, was calculated using equation (3-6).

The results presented in Table 8-4 demonstrate the following:

a) Bearings that are nominally identical can have substantially different mechanical properties. In the two bearings described herein, properties differed by between 5% and 20%. Differences can result from variations in both mixing and curing of the rubber and manufacturing (e.g., insertion and confinement of the lead core). The degree of variation will be dependent on the experience of the manufacturer and the size of the bearing because large bearings might require several batches of rubber, each of which might have different properties.

b) Temperature has a substantial effect on the stiffness and energy dissipated per cycle. Changes in the value of the effective yield stress of lead (computed using the procedures described herein) at low temperatures are due to changes in the properties of both the rubber and the lead core.

c) The average first-cycle value of the effective yield stress of lead was 11.5 MPa at the highest velocity and at a temperature of 20^oC. This value is consistent with that reduced from the data reported for a lead-rubber bearing produced by both Dynamic Isolation Systems and Skellerup and tested by CERF (1998c, 1998d). The reduction in yield stress with an increasing number of cycles depends on the heat generated in the lead core and cannot be determined from testing of a single geometry of bearing. Therefore theoretical treatment, such as provided in Section 8.8, is required.

d) The velocity of motion has a significant effect on the mechanical properties of lead-rubber bearings. For velocities between 25 and 250 mm/sec, the post-elastic stiffness increased by about 35% and the effective yield stress by about 15%. The change is primarily a result of viscoelastic behavior of the rubber.

e) Values of f_L could not be determined accurately due to variability in the properties of the rubber. Values of the effective stiffness without the lead core are required for this calculation but since the bearing-to-bearing variability is in the range of 20%, it was not possible to compute the value of f_L.

8.3.4 Large Scale Bearings

Figure 8-9 shows a large scale lead-rubber bearing designed by the authors for a bridge application. The bearing had a total rubber thickness $T_r = 254$ mm, a bonded rubber area $A_r = 650,232$ mm^2, a lead-core area $A_L = 24,829$ mm^2 and a shape factor $S = 22.6$. Six identical bearings were tested at an axial load of 3695 kN and a displacement of 305 mm, with a peak shear strain of 120%. The tests were conducted at a slow speed with a peak velocity slightly less than 25 mm/sec.
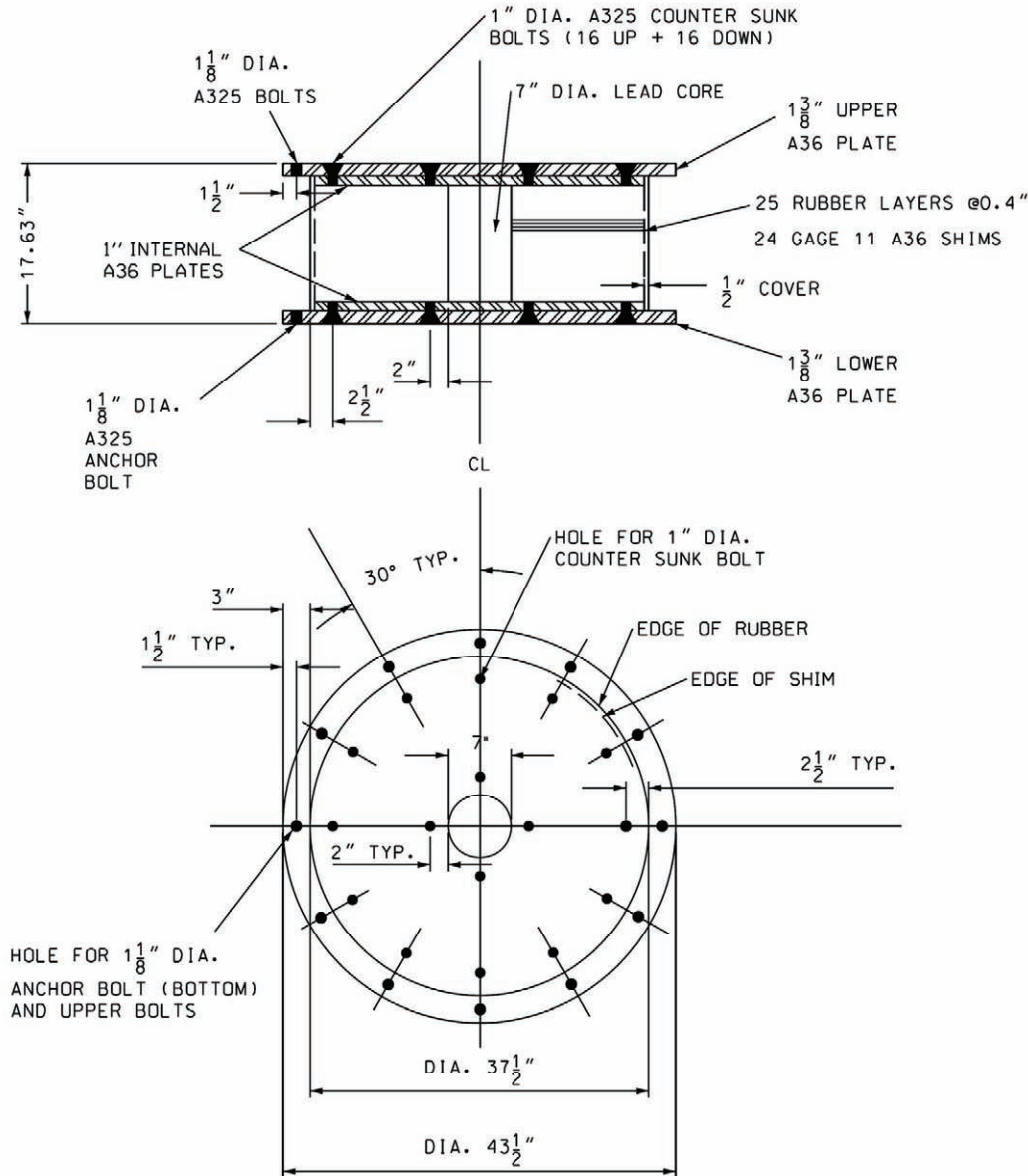
FIGURE 8-9 Large Scale Lead Rubber Bearing 1 (1 inch=25.4 mm)

Figure 8-10 presents the recorded lateral force-displacement loops for one of the bearings: No. 13429. The properties of the other five bearings, measured here in terms of effective stiffness and energy dissipated per cycle, varied by less than 5%. Table 8-5 summarizes the mechanical properties of the bearing for each of the five test cycles. A comparison of the results presented in this table with those of Table 8-4 shows a much larger reduction in energy dissipated per cycle and effective yield stress of lead with increasing number of cycles due to heating of the lead core. Note that the first cycle value of the effective yield stress of 12.2 MPa is within 5% of the value obtained from the testing of the moderate scale bearing (see Section 8.3.2) and the values presented in CERF (1998c and 1998d).

227
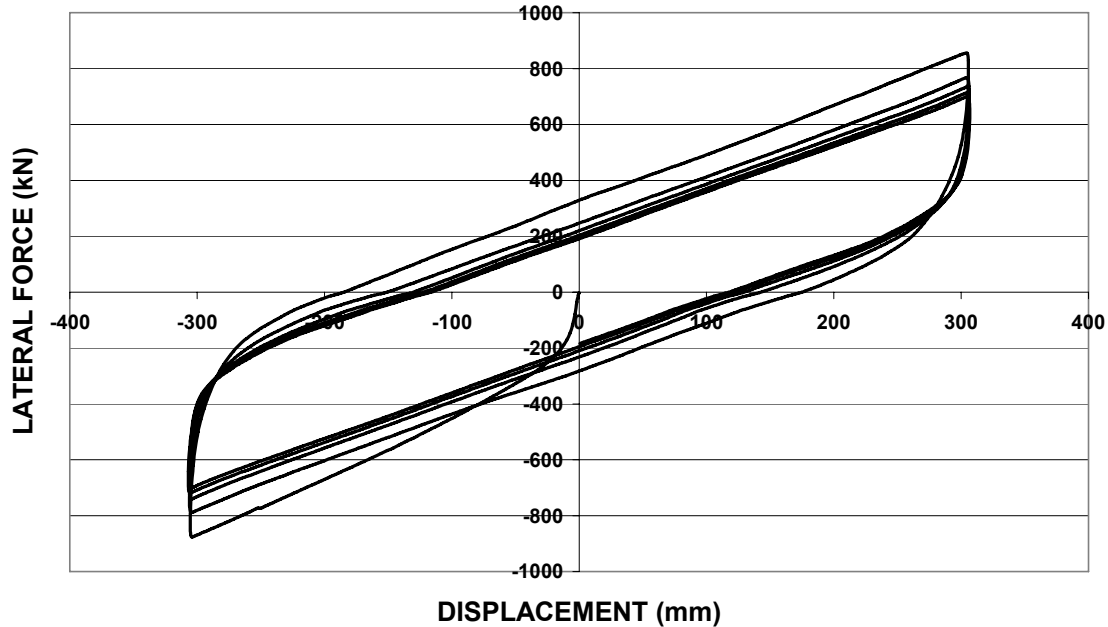
FIGURE 8-10 Force-Displacement Loops of a Large Scale Lead-Rubber Bearing 1 at 120% Shear Strain (1 kip=4.45 kN, 1 inch=25.4 mm)

TABLE 8-5 Mechanical Properties of Large Scale Lead-Rubber Bearing 1 (Tested at an Amplitude of 305 mm, a Shear Strain of 120% and a Peak Velocity of 25 mm/sec)

Cycle	Effective Stiffness (kN/mm)	Energy Dissipated Per Cycle (kN-mm)	Effective Damping	Effective Yield Stress of Lead (MPa)
1	2.83	358825	0.22	12.2
2	2.54	298218	0.20	9.6
3	2.41	263190	0.19	9.2
4	2.33	245162	0.18	7.9
5	2.28	232491	0.17	7.2

Figure 8-11 shows another large scale lead-rubber bearing designed by the authors for a building application. Low and high speed test data are available for this bearing. The bearing had a total rubber thickness $T_r = 208$ mm, a bonded rubber area $A_r = 906,871$ mm^2, a lead-core area $A_L = 73,062$ mm^2 mm^2 and a shape factor $S = 32.3$. The ratio of lead-core diameter to bonded diameter was 0.28. Two identical bearings were tested under an nominal axial load of 10,266 kN and a displacement of 483 mm, resulting in a peak shear strain of 232%. (The axial load varied during dynamic testing

228

from 9,300 to 11,400 kN.) The tests were conducted at high speed with a peak velocity of 1000 mm/sec and again at a slow speed of 25 mm/sec.

Figure 8-12 presents the recorded lateral force-displacement loops for one of the bearings for the high and low speed tests. The mechanical properties of the other bearing were nearly identical. Table 8-6 summarizes the mechanical properties for each of the three cycles of testing. The characteristic strength of the bearing in each cycle was obtained using (3-8) with a yield displacement Y assumed to be equal 25 mm. The effective yield stress of lead was calculated using (8-1). Table 8-6 shows a large reduction in energy dissipated per cycle and the effective yield stress of lead with an increasing number of cycles as a result of heating of the lead core. Note that the lead core in this bearing has a diameter equal to 28% of the bonded diameter and larger than any other lead-rubber bearing discussed previously in this report. The temperature rise of the lead core is dependent on the volume of the lead. The effective yield stress of the lead is higher than that computed for other bearings, likely as a result of the contribution from the rubber, which is strain rate dependent. The reduction in energy dissipated per cycle and effective yield stress of lead with increasing cycles demonstrates the effect of the speed of testing, which are moderate for the three cycles of testing. The speed of testing affects the temperature of the lead core and the effects become important if the cycle count is high.
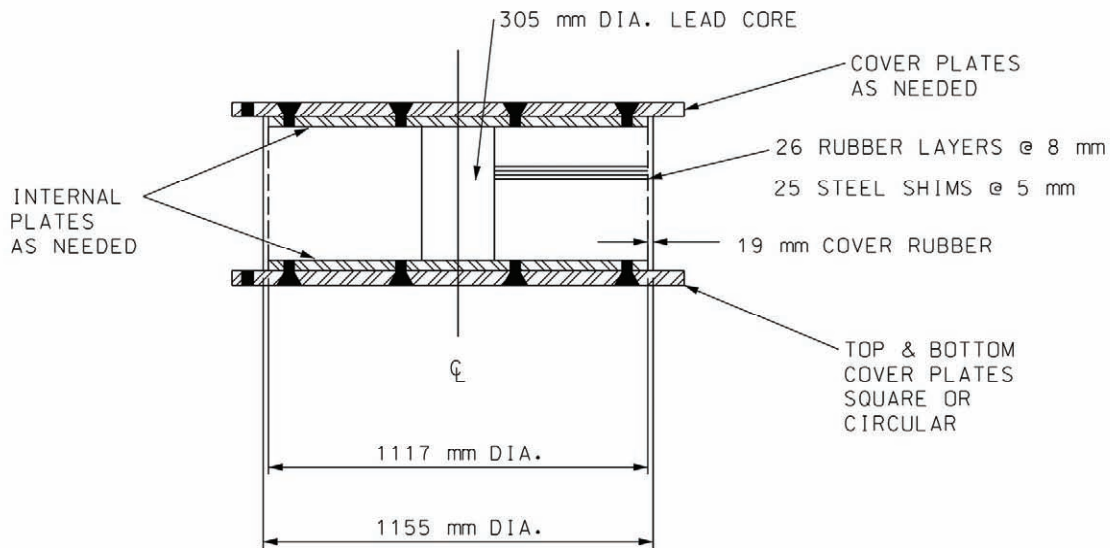
FIGURE 8-11 Large Scale Lead Rubber Bearing 2
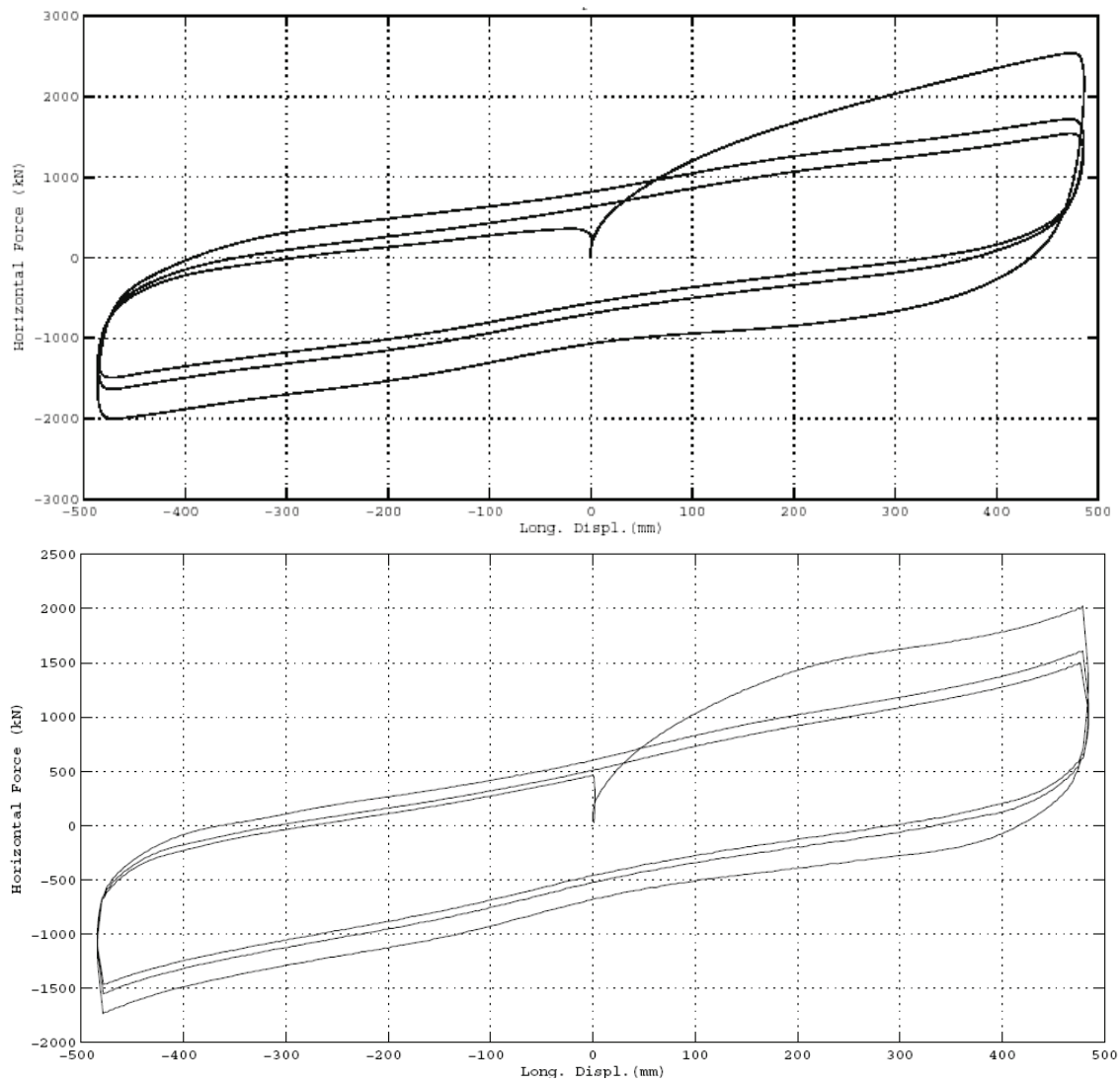
FIGURE 8-12 Force-Displacement Loops of Large Scale Lead-Rubber Bearing 2 at 232% Shear Strain, Axial Load of 10266 kN and Peak Velocity of 1 m/sec (top panel) and 25 mm/sec (bottom panel)

230

TABLE 8-6 Mechanical Properties of Large Scale Lead-Rubber Bearing 2 (Tested at an Amplitude of 483 mm and Shear Strain of 232%)

Cycle	Peak Velocity (mm/s)	Effective Stiffness (kN-mm)	EDC (kN-m)	Effective Damping	Effective Yield Stress of Lead (MPa)
1	1000	4.67	2059.1	0.30	15.4
2	1000	3.45	1389.8	0.27	10.4
3	1000	3.12	1117.1	0.24	8.4
1	25	3.89	1471.7	0.26	11.0
2	25	3.27	1109.6	0.23	8.3
3	25	3.07	973.2	0.22	7.3

8.4 Aging of Lead-Rubber Bearings

Lead-rubber bearings are typically manufactured with low damping natural rubber. The aging characteristics of this type of elastomer were described in Section 7.9. Moreover, the mechanical properties of lead are not expected to change during the lifetime of a typical structure.

8.5 Effect of Load History on the Mechanical Properties of Lead-Rubber Bearings

Bearings in bridges are subjected to continuous movement due to traffic and temperature effects. The result of this cumulative movement on sliding bearings is wear, which has been described in Section 5.10. There is very little data on the effect of cumulative movement on the mechanical properties of elastomeric bearings.

Two lead-rubber bearings were tested at the University at Buffalo under slow speeds that are representative of service loading (thermal expansion and contraction) and high speeds representative of seismic loading prior to and following a cumulative slow speed test of 1.6 km (1 mile).

Figure 8-13 presents drawings of the bearings; the ratio of the lead-core diameter to the bonded diameter was 0.29. The bearings were tested individually as shown in Figure 8-14 to obtain their mechanical properties under thermal and dynamic loads and as a pair in the slow speed, 1.6 km cumulative movement test-see Figure 8-15.

Figure 8-16 presents the recorded lateral force-displacement loops for lead-rubber bearing No. 2 for a dynamic sinusoidal test (peak velocity of 250 mm/sec) and a thermal loading test (constant velocity of 0.15 mm/sec) prior to the 1.6 km cumulative travel test. The axial load on the bearing was 1362 kN in the dynamic test (average pressure on rubber equal to 8.1 MPa) and was 1802 kN in the slow test (average pressure on rubber equal to 10.8 MPa). The significant increase (factor of 2.5) in the effective yield stress of lead due to dynamic loading is clearly seen in this figure.

After these tests the two bearings were subjected to an axial load of 1825 kN (average rubber pressure equal to 10.9 MPa) and 15,840 cycles of lateral movement with amplitude of 25 mm and constant velocity of 3.4 mm/sec. The total travel was 1584 m. The movement was intended to represent the effect of traffic loading-and the velocity of motion was larger than that expected under thermal loading. Ideally the velocity should have been about 1 mm/sec (see Section 5.5) but time constraints required the use of a higher speed. The testing was conducted over a period of 19 days with 8-10 hours of testing per day. The bearings were cooled during testing with large fans that maintained a temperature on the central moving steel plate of 29^0C after stabilization (at the start of test the temperature was 23^0C). The internal temperature in the lead core was not recorded. Figure 8-17 presents the recorded loops (the force is from two specimens tested as a pair) in the first 5 cycles (1 to 5) and cycles 15,823 to 15,828. There is little difference in the behavior of the bearings at the start of testing and end of the test. There is a change in the hysteresis-loop dimensions in the first five cycles due to an increase in the temperature of the lead core. Once the temperature of the lead core stabilizes, the loop shape does not change.
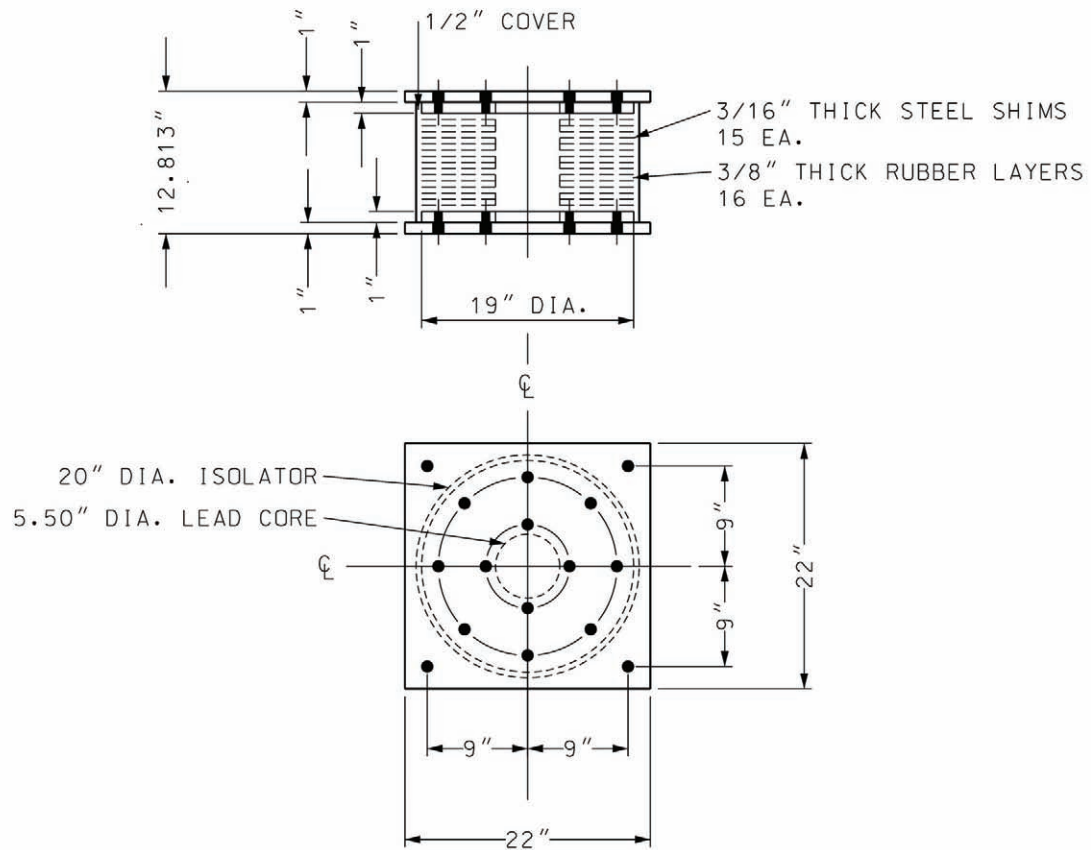
FIGURE 8-13 Large Scale Lead Rubber Bearing Tested for 1.6 km of Cumulative Travel (1 inch=25.4 mm)

FIGURE 8-14 Lead-Rubber Bearing During High Speed Testing

FIGURE 8-15   Lead-Rubber Bearings Tested in Pairs in the 1.6km Cumulative Travel Test

BEARING No. 2, BEFORE 1.6km CUMULATIVE TRAVEL TEST
(5 cycles, shear strain 75%, peak velocity 250mm/sec)

DISPLACEMENT (mm)
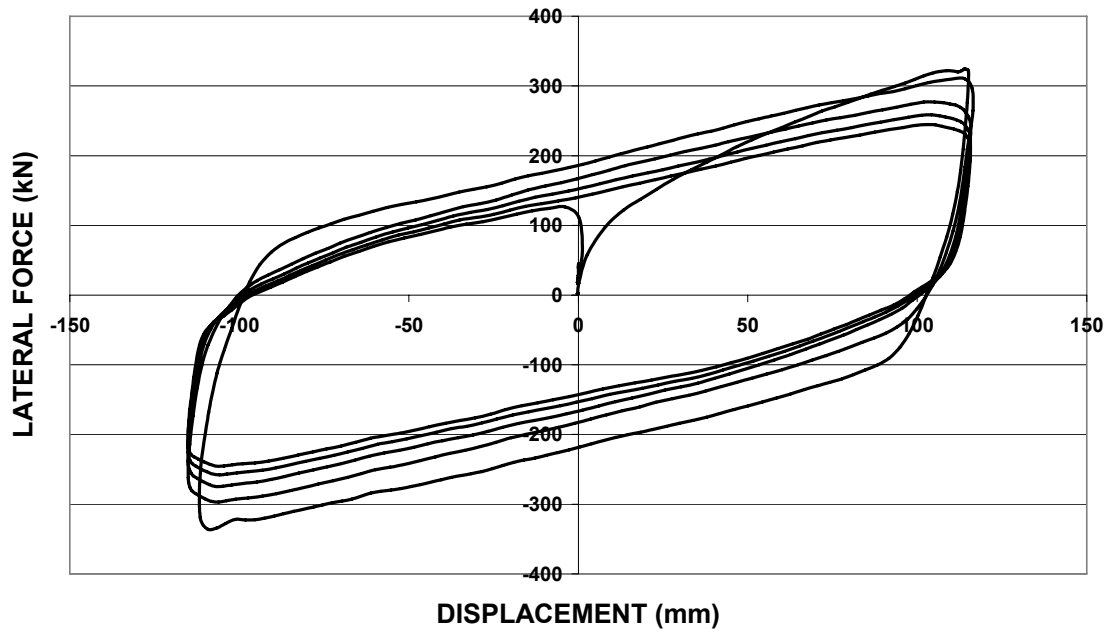
BEARING No. 2, BEFORE 1.6km CUMULATIVE TRAVEL TEST
(3 cycles, constant velocity 0.15 mm/sec)
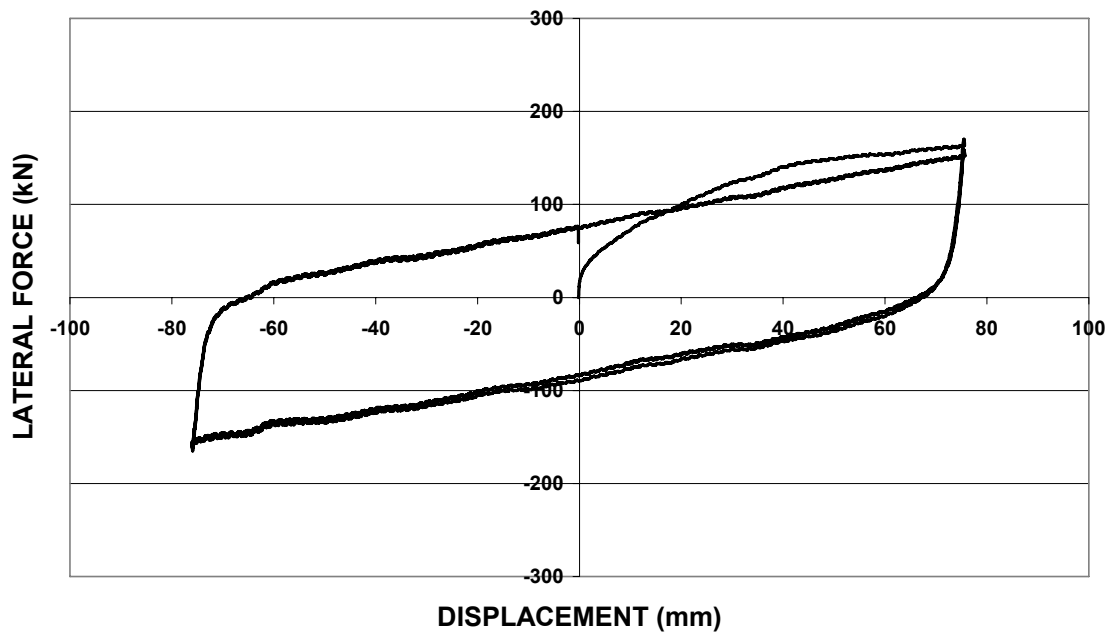
DISPLACEMENT (mm)

FIGURE 8-16   Force-Displacement Loops of Lead-Rubber Bearing No.2 Under Seismic and Service Load Conditions Prior to the Cumulative Travel Test

235

**CUMULATIVE TRAVEL TEST
CYCLES 1 to 5**

**CUMULATIVE TRAVEL TEST
CYCLES 15823 to 15828**
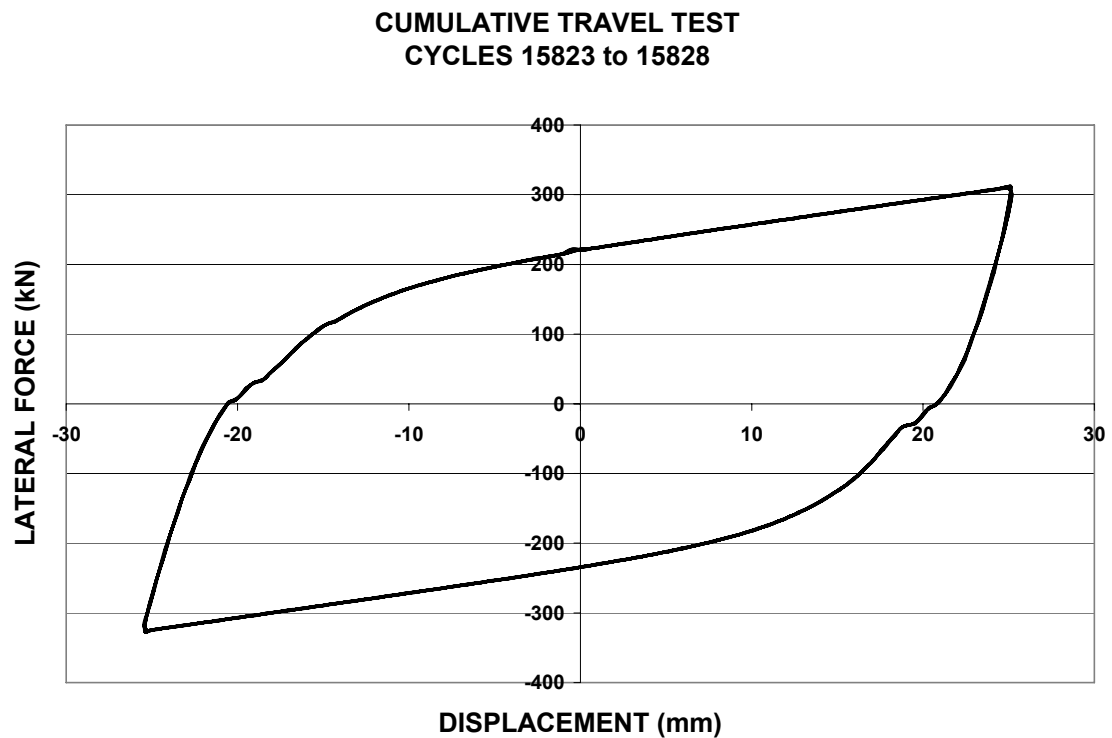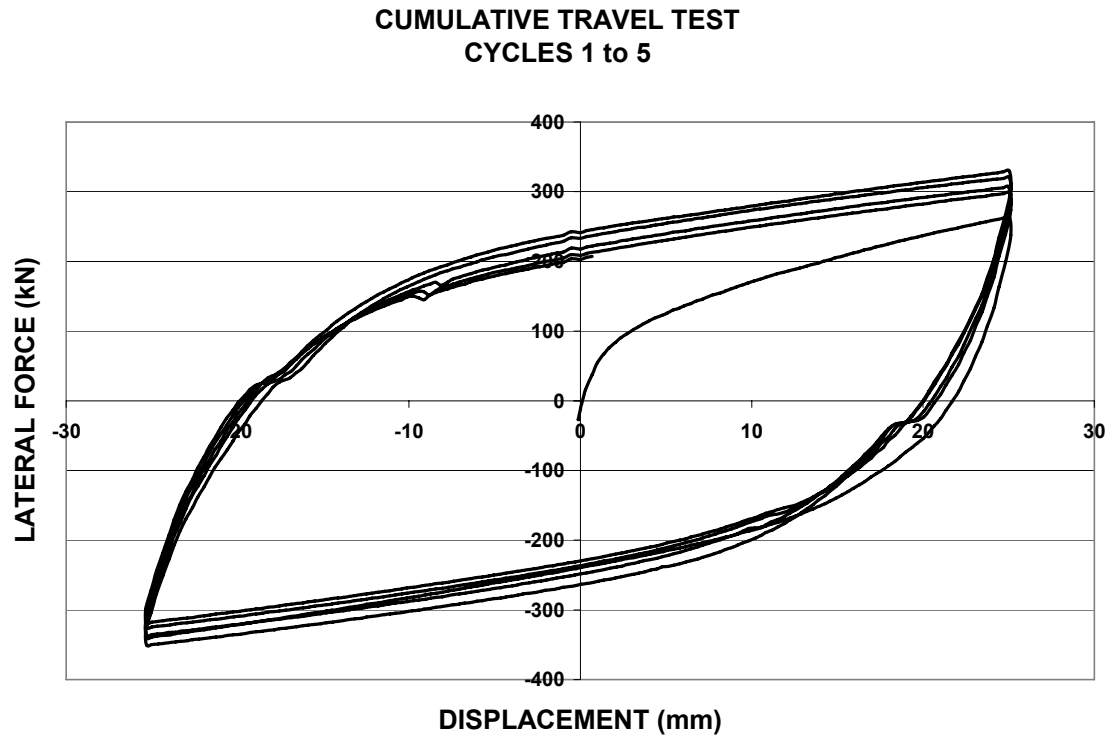
FIGURE 8-17 Force-Displacement Loops of the Pair of Lead-Rubber Bearings In the Cumulative Travel Test

236

Figure 8-18 presents the recorded lateral force-displacement loops for lead-rubber bearing No. 2 for a dynamic sinusoidal test (peak velocity of 250 mm/sec) and a thermal loading test (constant velocity of 0.15 mm/sec), which was conducted after the 1.6 km cumulative travel test. The axial load on the bearing was 1807 kN for the dynamic test (average rubber pressure equal to 10.8 MPa) and 1802 kN for the slow speed test (average rubber pressure equal to 10.8 MPa). The increase in axial load on the bearing in the dynamic test compared with the test conducted prior to the cumulative travel test (1807 kN versus 1362 kN) was the result of test error.

A comparison of the results in Figures 8-16 (prior to the cumulative travel test) and 8-18 (after the cumulative travel test) reveal a minor increase in the characteristic strength in the dynamic test and a major increase in the characteristic strength in the service load test. The increase in the characteristic strength is by a factor of approximately 1.75. Such change is substantial and warrants consideration in analysis and design. This change was observed in both bearings.

Bearing No.2 was also subjected to two slower tests after the cumulative travel test. The bearing was subjected to axial loads of 1807 kN and 1931 kN, respectively, in the two tests (average rubber pressure of 10.8 and 11.5 MPa, respectively), and one cycle of lateral movement at a constant velocity of 0.05 mm/sec and 0.00353 mm/sec, respectively. Figures 8-19 and 8-20 present the recorded force-displacement loops. There is an insignificant change in characteristic strength as the velocity reduces from 0.15 mm/sec (Figure 8-18) to 0.05 mm/sec and then to 0.00353 mm/sec. The duration of one-cycle motion was 0.6, 1.8 hours and 24 hours, respectively, in these tests—velocities representative of thermal loading.

Two possible mechanisms that contributed to the observed increase in strength of the lead-rubber bearings were considered:

a) The origin is due to increased confinement of lead, possibly due to the elevated temperature in the cumulative travel testing. It should be noted that the testing was conducted accelerated both in the speed of motion and in the continuity of the motion. Actual conditions involve slower speeds and interrupted motion so that temperature in the lead core is unlikely to change.
b) The origin is due to strain hardening effects induced by repeated plastic deformation (Van Vlack 1980). In this case the elevated temperature of the test would have accelerated the process of recrystallization and subsequent grain growth which would have actually reduced the strain hardening effect. That is, had the cumulative travel test been conducted at speeds that do not cause heating of lead, the increase in strength would have been larger. Conversely, the imposed 25 mm amplitude of deformation (much larger than that expected in service – about 1 mm) could have magnified the strain hardening effect.

To investigate the origin of the observed increase in strength, the two bearings were kept unloaded (so that any confinement effects relax) for a period of nearly 3.5 years and re-tested in April 2007 in high speed and low speed motions – conditions identical to those

237

in the tests prior to the cumulative travel test. Results from these tests are shown in Figure 8-21. The average normal load in the dynamic test was 1442 kN and in the slow speed test it was 1905 kN. Comparison of the results in Figures 8-18 and 8-21 demonstrate no change in the strength of the bearings. Therefore, a mechanical origin for the effect (increased confinement) is not likely. Rather, most likely explanation for the observed increase in strength is strain hardening due to plastic deformation with a likely reduction of the effects due to accelerated recrystallization of lead resulting from the increased temperature.

We conclude that cumulative travel causes substantial increase in the strength of lead-rubber bearings under conditions of very low speeds caused by service loading. Moreover, accelerated testing for cumulative travel effects likely eases these effects due to heating of lead. However, the extent of imposed inelastic action in cumulative inelastic action may have also magnified the increase in strength. Therefore, this issue warrants further investigation.

BEARING No. 2 AFTER 1.6km CUMULATIVE TRAVEL TEST
(5 cycles, shear strain 75%, peak velocity 250mm/sec)
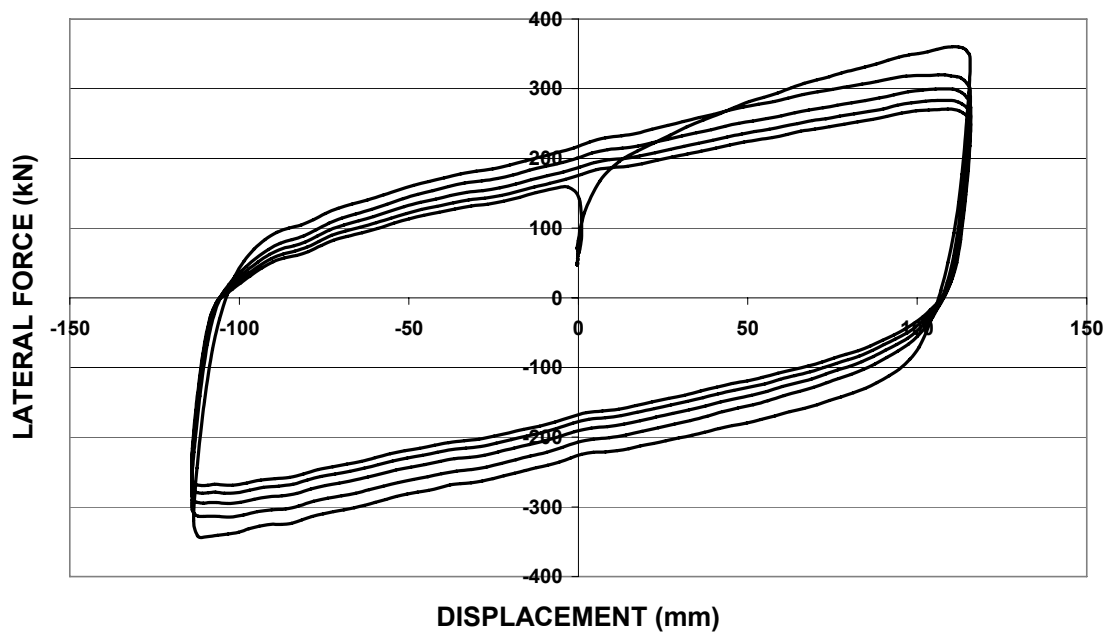
BEARING No. 2 AFTER 1.6km CUMULATIVE TRAVEL TEST
(3 cycles, constant velocity 0.15mm/sec)
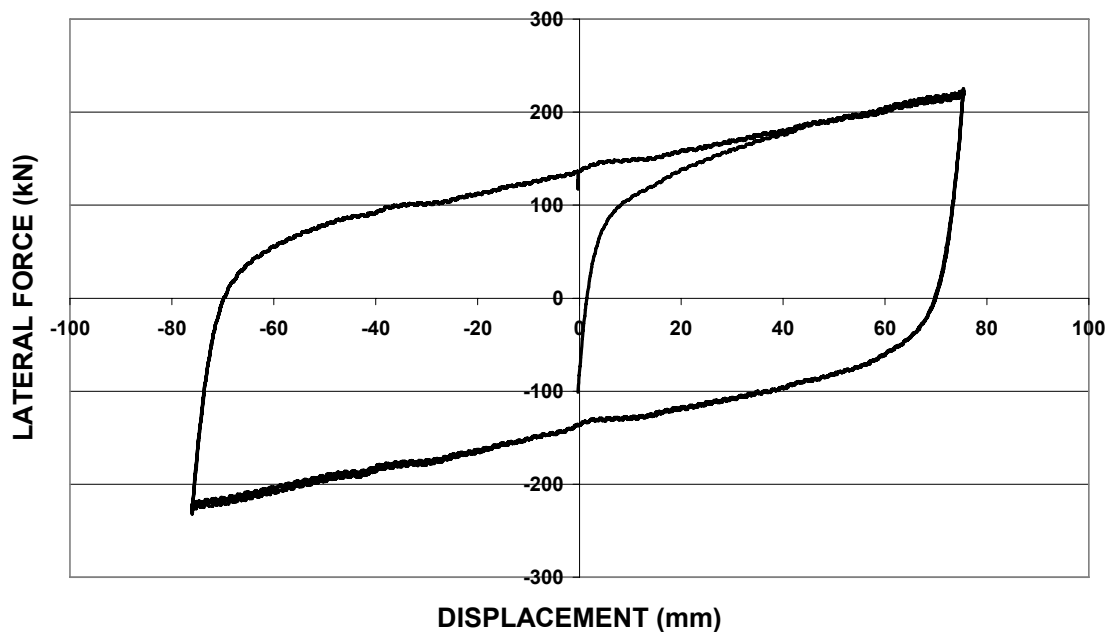
FIGURE 8-18   Force-Displacement Loops of Lead-Rubber Bearing No. 2 Under Seismic and Thermal Load Conditions After the Cumulative Travel Test

239

BEARING No. 2 AFTER 1.6 km CUMULATIVE TRAVEL TEST
(1 cycle, constant velocity 0.05mm/sec)
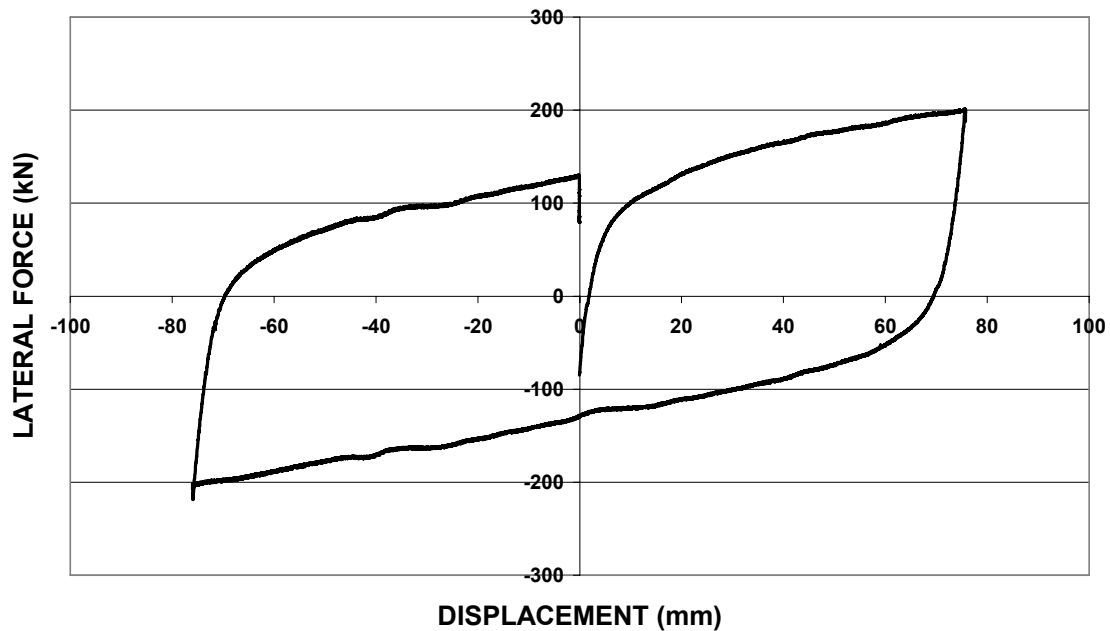
FIGURE 8-19   Force-Displacement Loops of Lead-Rubber Bearing No.2 Under Thermal Load Conditions After the Cumulative Travel Test

BEARING No. 2 AFTER 1.6 km CUMULATIVE TRAVEL TEST
(1 cycle, constant velocity 0.00353mm/sec)
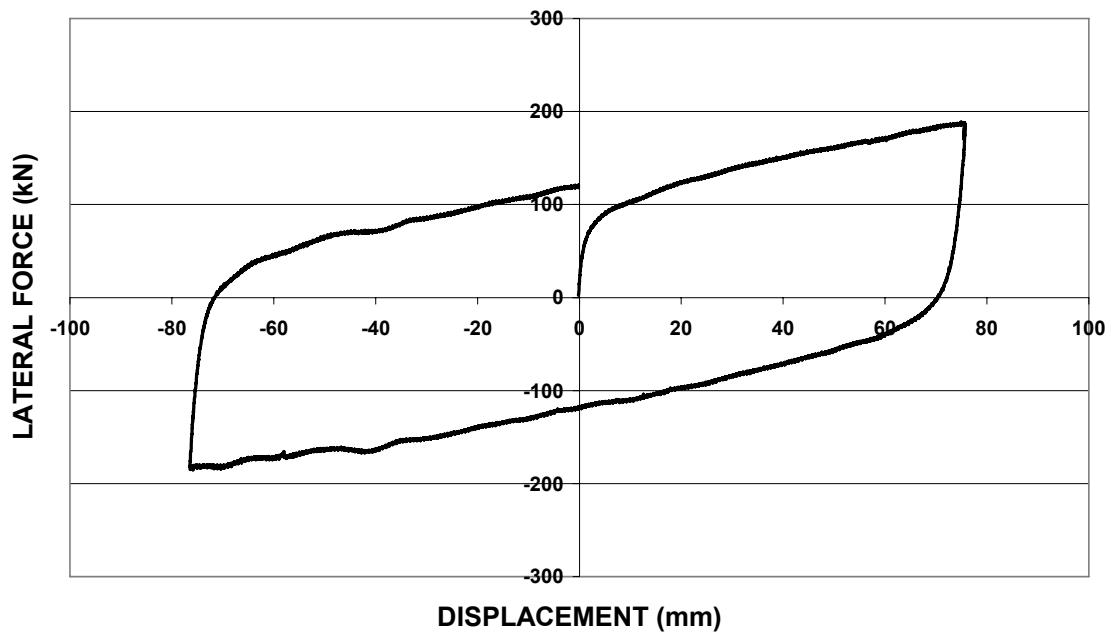
FIGURE 8-20   Force-Displacement Loops of Lead-Rubber Bearing No.2 Under Extremely Slow Thermal Load Conditions After the Cumulative Travel Test

240

BEARING No. 2, 3.5 YRS AFTER 1.6 km CUMULATIVE TRAVEL TEST
(5 cycles, shear strain 75%, peak velocity 250mm/sec)
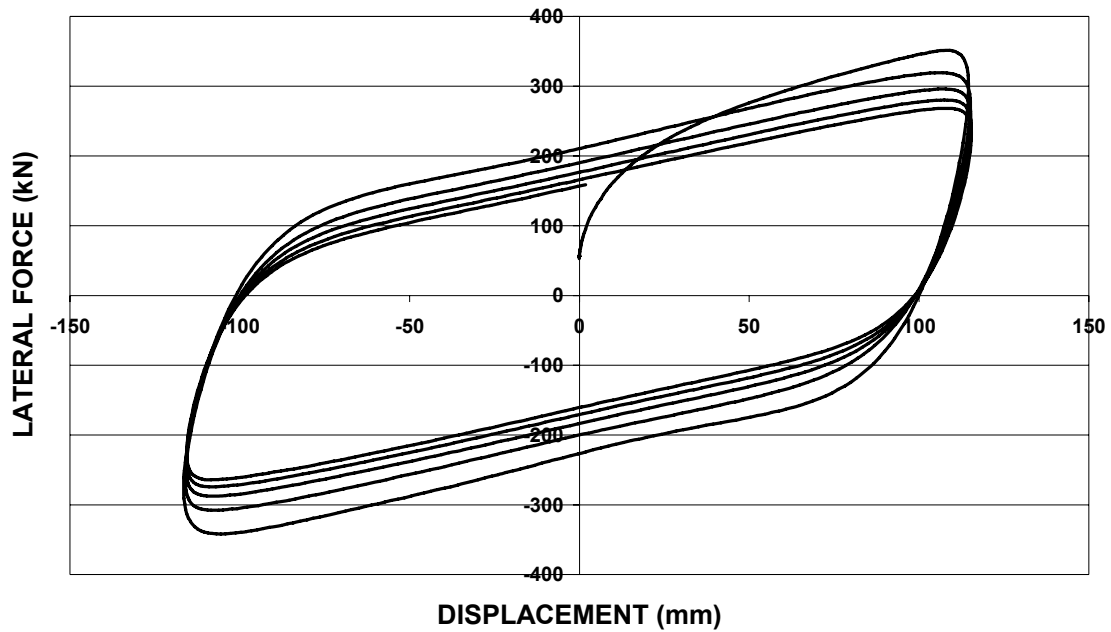
BEARING No. 2, 3.5 YRS AFTER 1.6 km CUMULATIVE TRAVEL TEST
(3 cycles, constant velocity 0.15mm/sec)
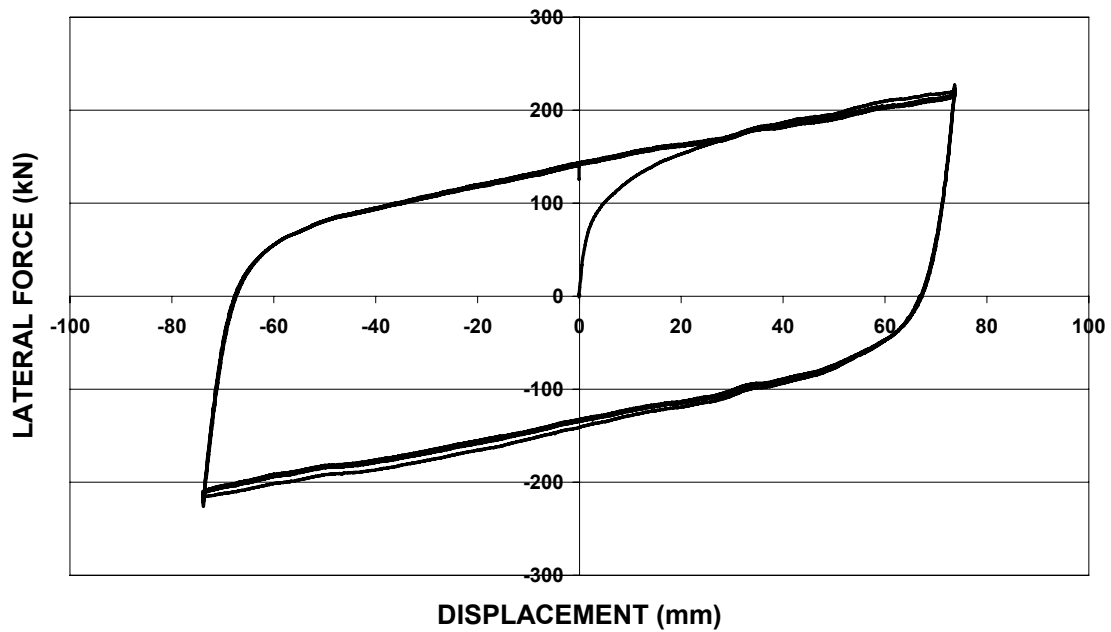
FIGURE 8-21 Force-Displacement Loops of Lead-Rubber Bearing No. 2 Under Seismic and Thermal Load Conditions 3.5 Years After the Cumulative Travel Test

241

8.6 Effect of Velocity on the Characteristic Strength of Lead Rubber Bearings

The results presented in Figures 8-16 through 8-20 demonstrate that the velocity of motion has a significant effect on the characteristic strength of lead rubber bearings. Table 8-7 presents information on the characteristic strength and effective yield stress of lead (per equation 8-1) for the tests described in Section 8.5. The table identifies the shear strain rate, calculated as the peak velocity of testing divided by the total rubber thickness of 6 in. (152.4 mm).

TABLE 8-7 Effect of Velocity on Characteristic Strength of a Lead Rubber Bearing

Condition	Cycle	Peak Velocity (mm/sec)	Shear Strain Rate (sec^{-1})	Strength (kN)	Effective Yield Stress (MPa)
Before cumulative travel test	1	0.15	984x10^{-6}	78.0	5.1
Before cumulative travel test	1	254	1.67	201.7	13.1
	2			174.4	11.4
	3			160.0	10.5
	4			147.0	9.7
	5			136.7	8.9
After cumulative travel test	1	0.00353	23×10^{-6}	118.2	7.8
After cumulative travel test	1	0.05	328×10^{-6}	122.3	8.0
After cumulative travel test	1	0.15	984×10^{-6}	136.0	8.9
After cumulative travel test	1	254	1.67	223.0	14.5
	2			204.0	13.3
	3			189.0	12.4
	4			177.0	11.6
	5			163.0	10.6

The data collected after the cumulative travel test is relevant to bridge applications. The effective yield stress of lead after the cumulative travel test is plotted in Figure 8-22 as a function of the shear strain rate. The graph indicates that the effective yield stress follows the relation

242

$$\sigma_L = a\dot{\gamma}^b \tag{8-3}$$

with $a = 14.06$ and $b = 0.067$ for strain rates greater than 3×10^{-4} sec^{-1} and $a = 8.74$ and $b = 0.011$ for strain rates less than 3×10^{-4} sec^{-1}. These results are somewhat at odds with those reported in Skinner et al. (1993), who report that equation (8-3) applies with $b = 0.035$ for a strain rate greater than 3×10^{-4} sec^{-1} and $b = 0.15$ for smaller strain rates. The results presented in Skinner et al (1993) are based on specimens not previously subjected to large cumulative travel. Using (8-3) and the limited data available for the bearing prior to the cumulative travel test, $a = 12.26$ and $b = 0.126$, which are valid for strain rates greater than 1×10^{-3} sec^{-1}. This value of b is similar to the value reported by Skinner et al (1993). It is noteworthy that the strain rate threshold of 3×10^{-4} sec^{-1} is observed in both the tests of Skinner et al. and of the authors and it appears to be valid regardless of whether the bearings have been subjected to large cumulative travel.
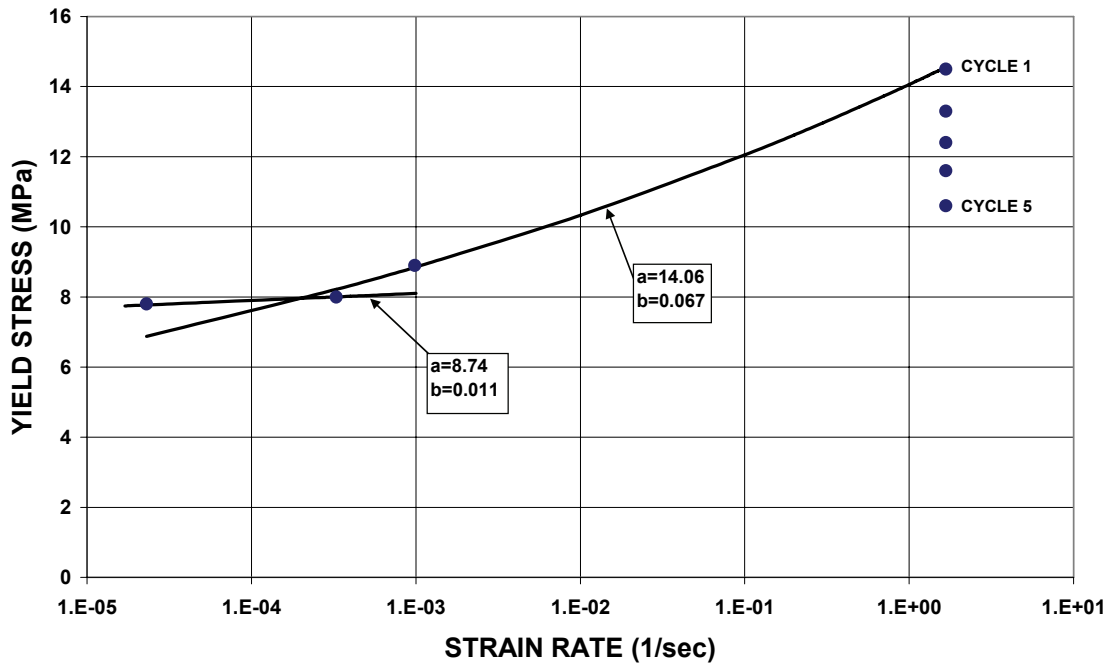
FIGURE 8-22 Effective Yield Stress of Lead as Function of Shear Strain Rate

Lead is the only common metal for which the processes of recovery, re-crystallization and grain growth occur simultaneously at room temperature so that it can forever recover its original mechanical properties following inelastic action (Skinner et al, 1993). The dependency of the effective yield stress of lead on the history of motion is interesting. Two possible reasons for the change in behavior are (1) geometric changes in the lead core, leading to an increase in the confinement of the lead during large cumulative movement, and (2) altered mechanical properties. The phenomenon is sufficiently important to warrant further investigation.

8.7 Relaxation in Lead Rubber Bearings

The results presented in Section 8.5 suggest that following large cumulative travel, lead rubber bearings exhibit a marked change in the rate of reduction of the effective yield stress of lead with decreasing rate of shear strain. Equation (8-3) with $a = 8.74$ and $b = 0.011$ for strain rates below 3×10^{-4} sec^{-1} predicts the yield stress of lead under slow thermal loading conditions to be about 60% of the value under dynamic seismic conditions, computed using $a = 14.06$, $b = 0.067$ and strain rates larger than 2.0 - an important implication for the design of bridges supported by lead rubber bearings.

However, temperature changes in bridges result in motion of variable speed that includes intervals in which the bearings do not move. Under such conditions, lead rubber bearings relax and the characteristic strength drops exponentially with time. Figure 8-23 presents results of relaxation testing of one of the lead rubber bearings of Figure 8-13 following the 1.6 km cumulative travel test. The bearing was subjected to one and one-quarter cycles of large velocity motion and the residual displacement of 75 mm was then maintained for a period of 30 minutes as shown in the figure. The displacement was then returned to zero under dynamic conditions and the force required to maintain the zero displacement was recorded for a period of eight minutes.

The recorded force at zero displacement in the 8-minute relaxation test provides useful information on the characteristic strength of the bearing. At zero displacement, the recorded force is the characteristic strength of the bearing. The force was corrected in Figures 8-23 and 8-24 for bias at the start of the experiment so that the loop in the first cycle has equal positive and negative strength. As seen in Figure 8-23, the characteristic strength of the bearing drops from 182 kN under dynamic conditions to 62 kN in eight minutes, namely, a drop to one-third of the dynamic value.

Additional information can be obtained from the force history at 75 mm displacement after subtracting the force contributed by the rubber - accomplished by measuring the restoring force from the recorded loop and subtracting it from the total force. This is shown in Figure 8-24. The characteristic strength drops to one-third of the dynamic value as was observed in the test at zero lateral displacement. The characteristic strength drops to about one-fourth of the dynamic value after 30 minutes of relaxation.

BEARING NO. 1 AFTER 1.6km CUMULATIVE TRAVEL TEST
RELAXATION TEST
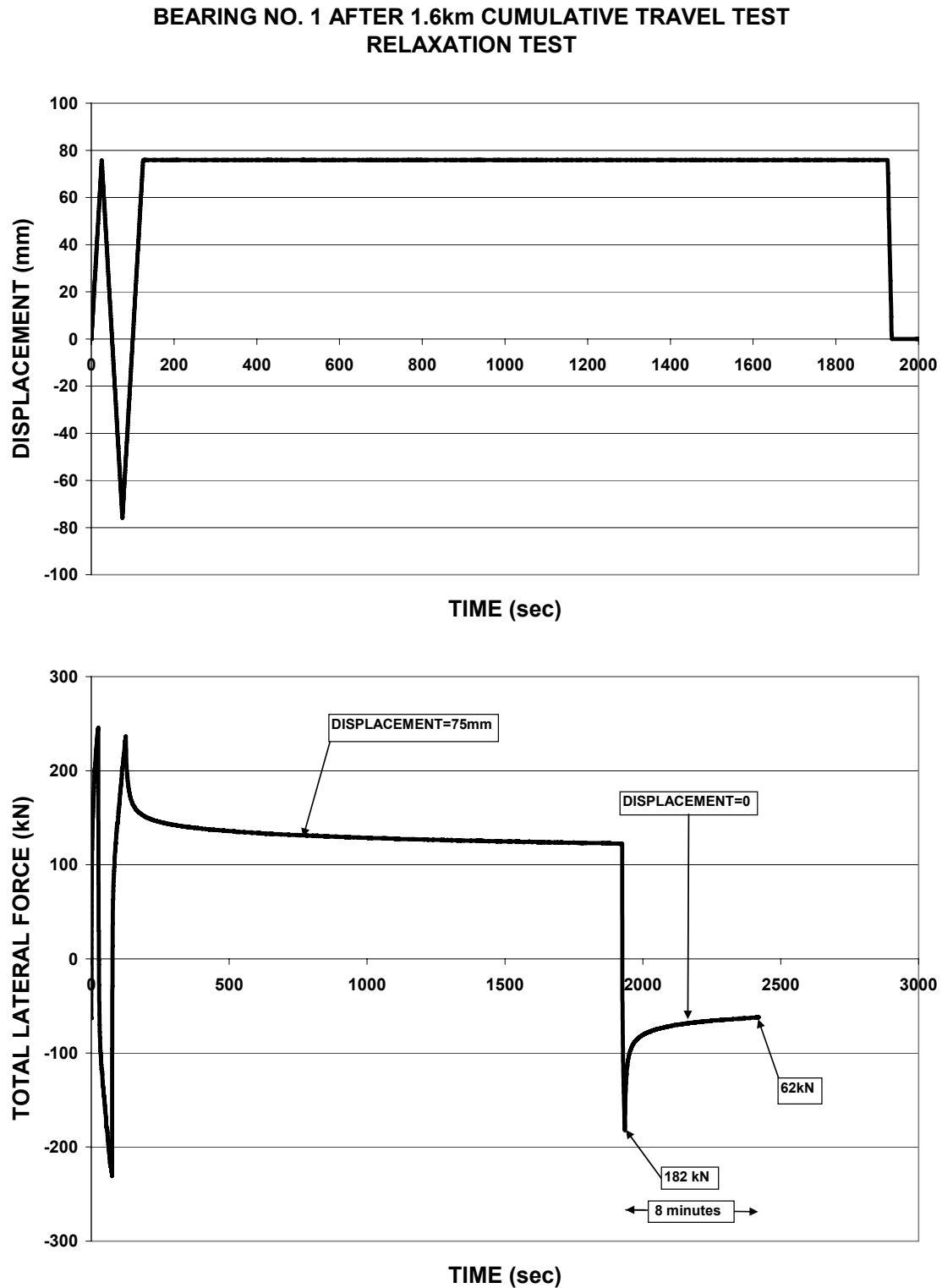
FIGURE 8-23 Imposed Displacement History and Recorded Lateral Force in Relaxation Test

BEARING No. 1 AFTER 1.6 km CUMULATIVE TRAVEL TEST
RELAXATION TEST
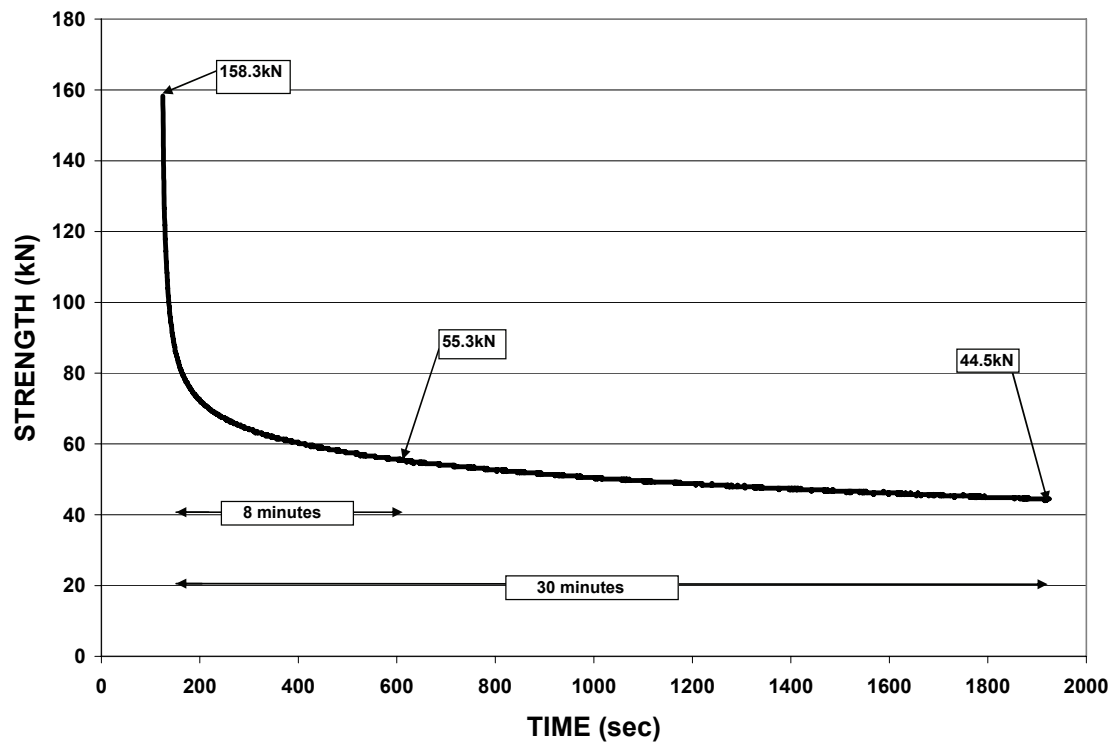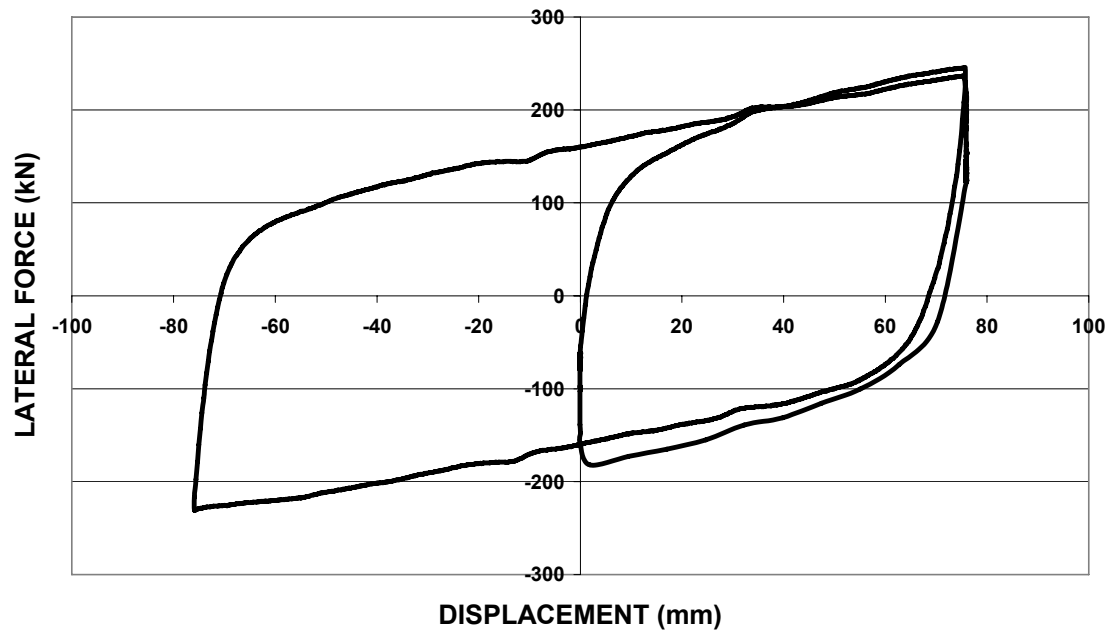
FIGURE 8-24   Recorded Lateral Force-Displacement Loop and Characteristic Strength of Bearing during a 30-minute Relaxation Test at 75 mm Displacement

246

8.8 Heating of Lead Rubber Bearings

8.8.1 Introduction

This section discusses the prediction of the temperature rise and reduction in characteristic strength of lead-rubber bearings under repeated cycling. In lead-rubber bearings under cyclic loading, heat is generated primarily in the lead core from where it flows vertically and radially into the steel end and shim plates. Heat is generated in the rubber but this is typically small (see Section 7.6) and can be ignored.

It is well established that the energy dissipated per cycle and the characteristic strength of lead-rubber bearings reduce with an increasing number of cycles. The reduction is substantial in the first few cycles if the motion is of high speed. For example, Figure 8-25 presents the energy dissipated per cycle from the testing of the large size lead-rubber bearing of Figure 8-9. The testing was conducted under dynamic conditions with a peak velocity of nearly 1 m/sec. Figure 8-25 shows both the measured dissipated energy and the estimated contribution to the dissipated energy by the lead core. For this calculation, it was assumed that the rubber contributes to the equivalent viscous damping ratio or effective damping of the bearing by 0.04.

It is clear from this figure that there is a substantial reduction in energy dissipation per cycle in the initial cycles after which the energy dissipated per cycle tends to stabilize. A brief interruption of the testing and a restart, results in an almost complete recovery of the original energy dissipation per cycle. These observations clearly demonstrate that the reduction in the energy dissipation per cycle is the result of heating of the lead core. The core will reach a near constant temperature after a number of cycles when the rate of heat generation is equal to the rate of heat lost by conduction through the steel plates. The near complete recovery after the 2-minute interruption in the testing clearly demonstrates the significance of heat conduction.

The thermal properties of lead, rubber and steel are given in Table 8-8, which presents data obtained from several sources (American Society of Metals, 1991; American Society of Metals, 1992; Lide, 1993; Hofmann, 1970 and Guruswamy, 2000). Note that thermal properties of lead are practically unaffected by temperature up to the melting point. Another important observation is that rubber has a much lower thermal conductivity and thermal diffusivity than either lead or steel. Accordingly, it may be assumed that heat conducts entirely through the steel shim plates and the steel end plates of the bearing.
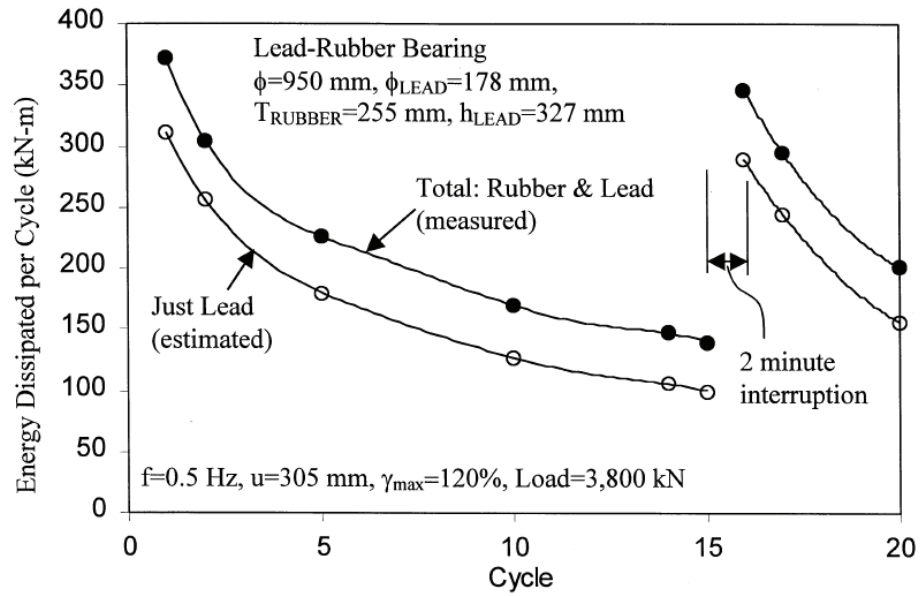
FIGURE 8-25   Energy Dissipation per Cycle in the Lead-Rubber Bearing of Figure 8-9

TABLE 8-8 Thermal and Other Properties of Lead, Steel and Rubber

Temperature (^{o}C)	-25	25	75	125	225	327[1]
Thermal Conductivity, k (W/(m^{o}C))						
Lead[2]	36.0	35.3	34.7	34.0	32.8	31.4
Rubber	-	0.16	-	-	-	-
Carbon Steel[3]	-	54.0	53.0	51.0	47.0	44.0
Thermal Diffusivity, α (m^2/s)						
Lead[2]	-	2.42×10^{-5}	2.34×10^{-5}	2.29×10^{-5}	2.14×10^{-5}	2.00×10^{-5}
Rubber	-	7.24×10^{-8}	-	-	-	-
Carbon Steel[3]	-	1.48×10^{-5}	-	-	-	-
Specific Heat, c (J/(g^{o}C))						
Lead[2]	0.127	0.129	0.131	0.132	0.137	0.142
Rubber	-	1.7	-	-	-	-
Carbon Steel[3]	-	0.45	-	-	-	-
Density, ρ (g/cm^3)						
Lead[2]	-	11.36	11.30	11.24	11.17	11.00
Rubber	-	1.3	-	-	-	-
Carbon Steel[3]	-	7.9	-	-	-	-

1. Temperature just prior to melting of lead

2. 99.99% pure lead

3. Less than 0.5% carbon

8.8.2 Dependence of Effective Yield Stress on Temperature

The reduction in the energy dissipation per cycle is the result of the reduction in the effective yield stress of lead with increasing temperature. The yield stress of lead cannot be accurately measured due to the tendency of the material to creep. However, the ultimate strength (which should be somehow related to the effective yield stress) can be measured and representative data are shown in Figure 8-26. The data were obtained from published sources (Hofmann 1970 and American Society for Metals – ASM – 1979) and from tests conducted by the authors. Standard specimens of lead of 99.99% purity were used in these tests which were conducted at two different rates of strain and at various temperatures including one test at -30^{0}C. The specimens had a 0.5in nominal diameter

and a 4in reduced section length (see ASTM International, Annual Book of ASTM Standards (2005), Vol. 03.01, Designation E8-04, p. 68, Specimen 3).
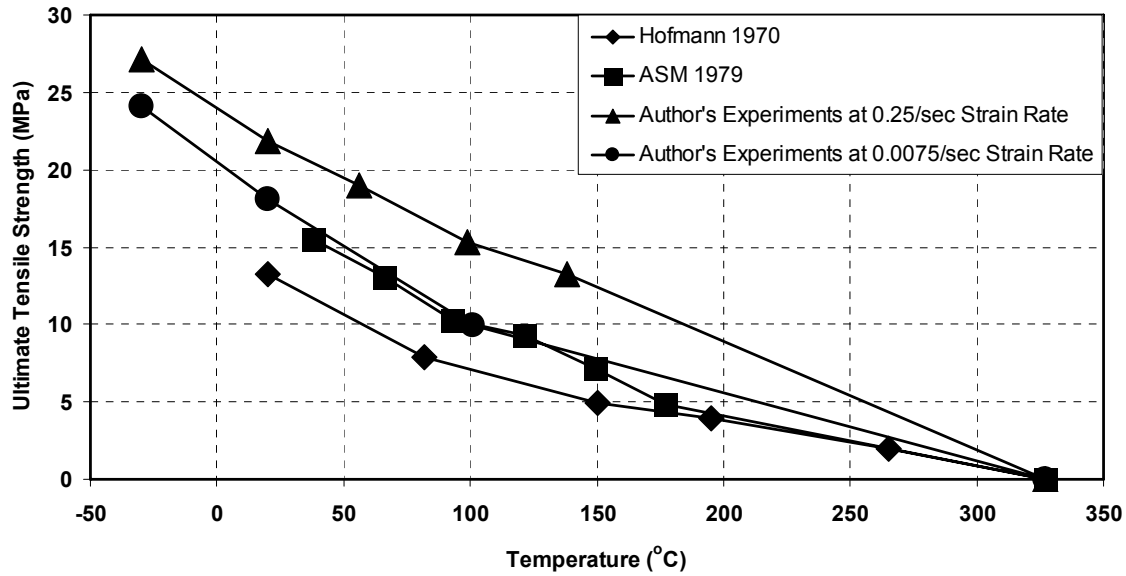
FIGURE 8-26 Experimental Values of Ultimate Tensile Strength of Lead

The lead core absorbs energy by resisting motion, so the heat produced within the lead core is in fact the work of the resisting force in the core. This force is the product of the effective yield stress and the cross-sectional area of the lead core. The experimental results shown in Figure 8-25 show a gradually decreasing energy dissipated per cycle (EDC), thus implying that the effective yield stress σ_{YL} drops as the temperature of the lead plug increases. There are no direct data for such a relationship between σ_{YL} and temperature. A reasonable assumption would be to consider that the ratio of the effective yield stress of lead σ_{YL} to the ultimate stress of lead σ_{ult} is constant at all temperatures.

That is, assuming that σ_{ult} is a function $f(T_{Lt})$, then

$$\frac{\sigma_{YL}}{\sigma_{YL0}} = \frac{f(T_{Lt})}{f(T_{L0})} \tag{8-4}$$

where σ_{YL} is the effective yield stress at temperature of lead T_{Lt} and σ_{YL0} is the initial effective yield stress, defined as the effective yield stress at the initial (or starting) temperature T_{L0}. The ratio σ_{YL}/σ_{YL0} in equation (8-4) will be referred to as the normalized effective yield stress. In order to establish a relation between σ_{YL} and temperature, one should determine a relationship between σ_{ult} and temperature and have an estimate of the initial effective yield stress σ_{YL0}.

There are four sets of experimental data on the ultimate tensile strength in Figure 8-26. On the basis of these data, the relationship between σ_{ult} and the temperature of lead, T_{Lt}, could be either logarithmic or linear as described by equations (8-5) and (8-6):

$$\sigma_{ult} = C_1 \cdot \ln(T_{Lt}) + C_2 \qquad (8\text{-}5)$$

$$\sigma_{ult} = L_1 \cdot T_{Lt} + L_2 \qquad (8\text{-}6)$$

The parameters in (8-5) and (8-6) were determined by best fitting the available data on σ_{ult} and temperature. Table 8-9 summarizes information on the best fitting curves for the four sets of data and Figures 8-27 to 8-30 compare prediction by (8-5) and (8-6) to the test data. As will be shown, linear/bilinear equations allow for closed-form solution of the problem of prediction of the reduction of strength of lead-rubber bearings in cyclic motion. For this reason, as well as because they are valid for negative temperatures and are simpler to deal with in dimensional analyses (parameters L_1 and L_2 have well defined units), the linear/bilinear relations are preferable to the logarithmic ones.

TABLE 8-9 Information on Best Fitting Curves for the Four Sets of Experimental Data on Ultimate Tensile Strength of Lead (Temperature in ^{0}C, Stress in MPa)

Case	Curve	Parameter
Hofmann 1970	Logarithmic I	C_1=-4.55, C_2=27.35
ASM 1979	Logarithmic II	C_1=-7.33, C_2=43.29
Author's at Strain Rate=0.25/sec	Linear	L_1=-7.39E-02, L_2=23.61
Author's at Strain Rate=0.0075/sec	Bilinear	L_1=-1.08E-01, L_2=20.64 for T_{Lt}<100^{0}C L_1=-4.38E-02, L_2=14.32 for T_{Lt}>100^{0}C
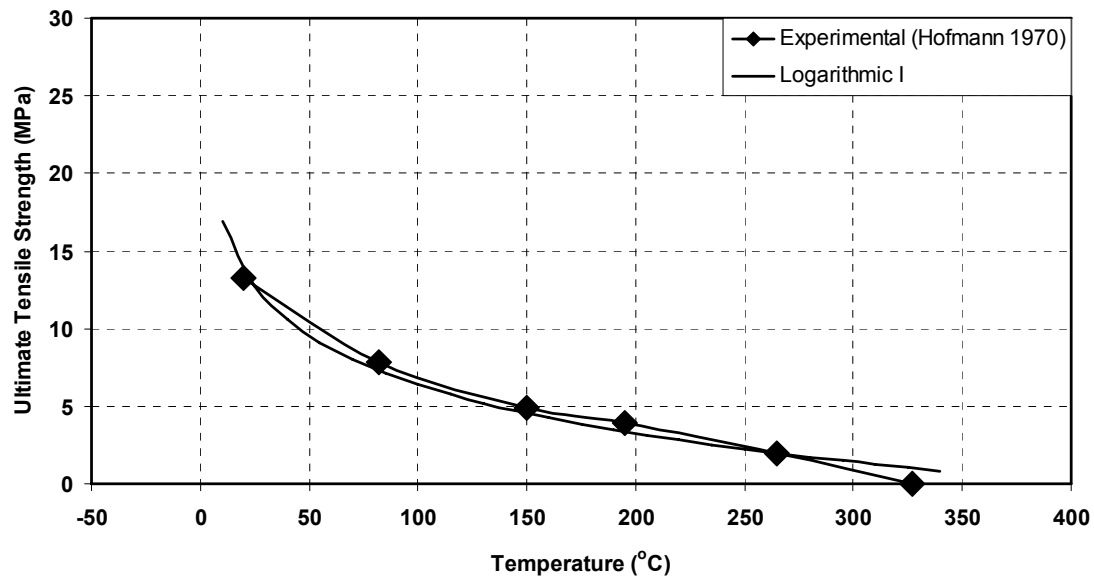
FIGURE 8-27 **Relation Between Ultimate Tensile Strength of Lead and Temperature Based on Data of Hofmann 1970**
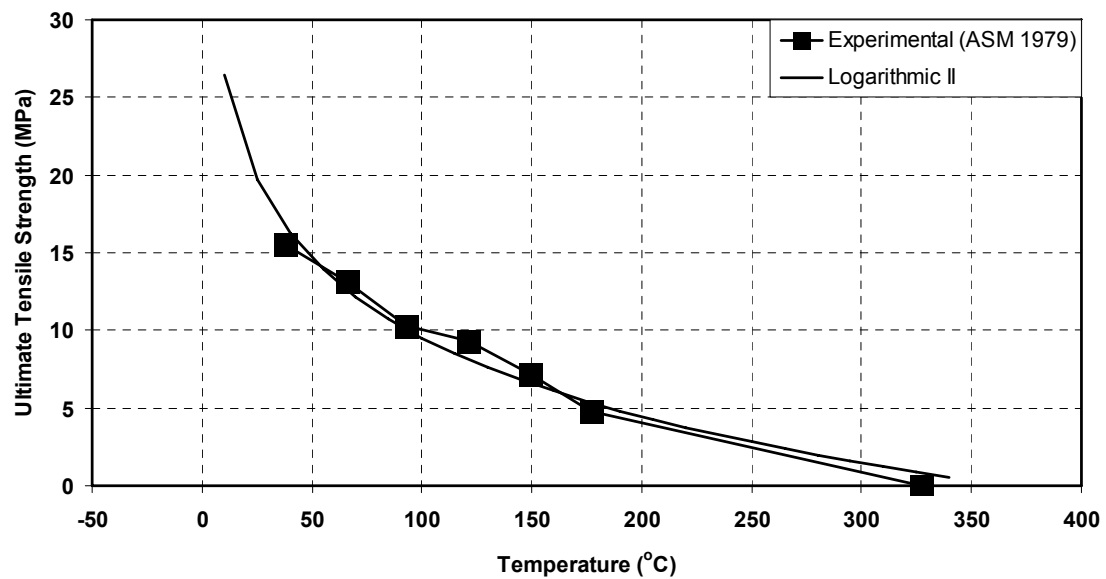
FIGURE 8-28 **Relation Between Ultimate Tensile Strength of Lead and Temperature Based on Data of ASM 1979**
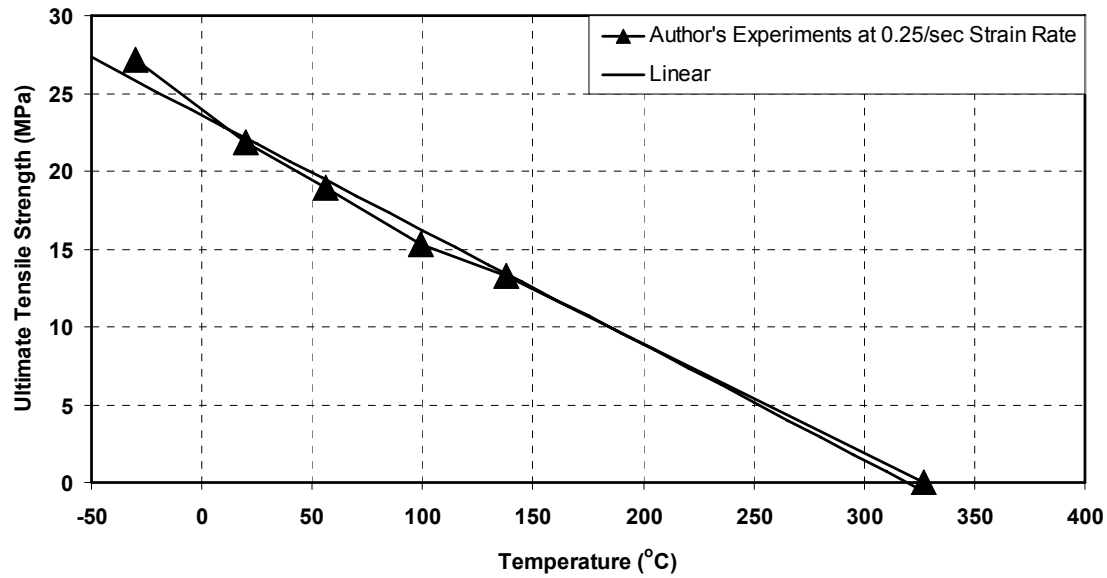
FIGURE 8-29 Relation Between Ultimate Tensile Strength of Lead and Temperature Based on Author's Experiments at 0.25/sec Strain Rate
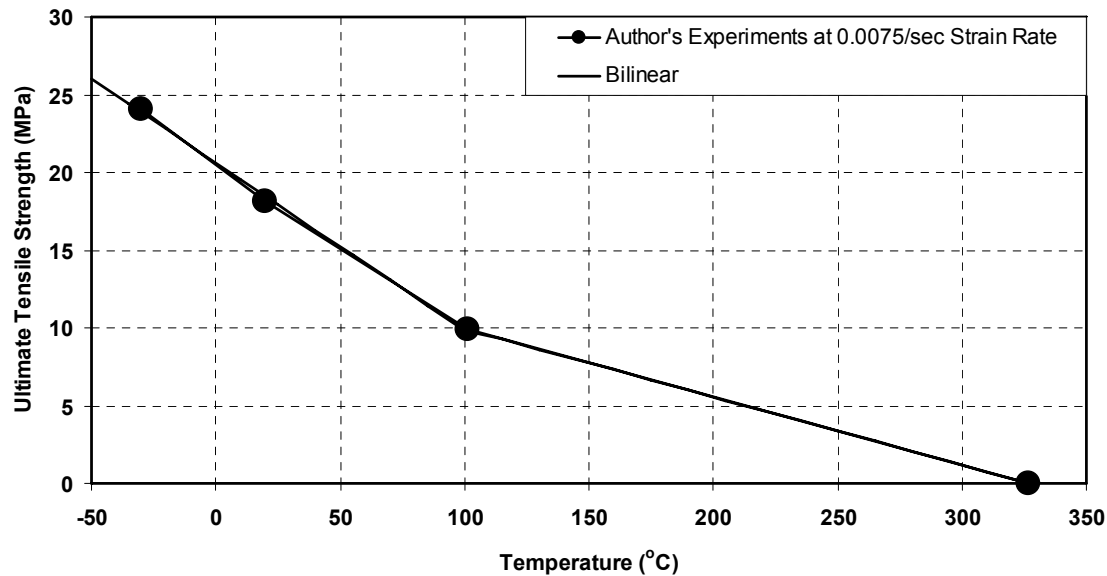
FIGURE 8-30 Relation Between Ultimate Tensile Strength of Lead and Temperature Based on Author's Experiments at 0.0075/sec Strain Rate

The reference (i.e. initial/at ambient temperature) effective yield stress σ_{YL0} in equation (8-4) cannot be directly obtained in testing. For example consider the bearing of Figure 8-9 and assume that the experiment started when the temperature of the bearing was 20^0C. When the measurement of the energy dissipated per cycle (EDC) was first made after one cycle, the temperature was certainly higher than 20^0C. Therefore, the data at the first

253

cycle cannot be used to estimate σ_{YL0}. However, extrapolation of the EDC data to the hypothetical value of zero cycles provides a useful estimate of σ_{YL0}. From Figure 8-25, the value is EDC=375 kN-m. Using equations (8-1) and (3-8) with an assumed yield displacement $Y = 12mm$, a value of $\sigma_{YL,0} = 12.8MPa$ for the hypothetical "0$^{\text{th}}$" cycle is obtained for the bearing of Figure 8-9 and the testing speed and amplitude given in Figure 8-25. This value corresponds to the "average" value of σ_{YL} during the "0$^{\text{th}}$" cycle while with a similar process we may calculate the "average" value of σ_{YL} during the 1$^{\text{st}}$ cycle of motion, $\sigma_{YL,1}$. The sought value of σ_{YL0} at the beginning of testing (end of "0$^{\text{th}}$" cycle and start of 1$^{\text{st}}$ cycle) may then be estimated by averaging $\sigma_{YL,0}$ and $\sigma_{YL,1}$.

8.8.3 Modeling and Analytical Solution

We seek either a closed-form solution or explicit formulations that can be numerically solved to compute the temperature rise in a lead core and the reduction in characteristic strength of lead-rubber bearings under cyclic loadings. Solutions are presented in this section.

Analysis of the problem of the temperature rise in lead-rubber bearings requires the solution of the problem of conduction of heat in a composite cylinder. Consider a lead-rubber bearing with bonded rubber radius R, lead core radius a, end plate thickness t_p and total shim plate thickness t_s. An appropriate model would be the one shown in Figure 8-31 with zero initial increase in temperature (i.e., initial temperature equal to the initial temperature, T_{L0}). Heat is generated inside the lead core at a rate of $q'''(t)$ (heat production rate per unit volume of lead) and is conducted outward through the end plates (of thickness t_p each) and the shim plates (of total thickness t_s). Let q_1 be the amount of heat flowing per unit time through one of the end plates and q_2 be the amount of heat flowing per unit time through the shim plates (note that the shims are treated as a unity, being modeled as a hollow cylinder with inner radius equal to a, outer radius equal to R and thickness equal to the combined thickness of all shims, t_s).

254
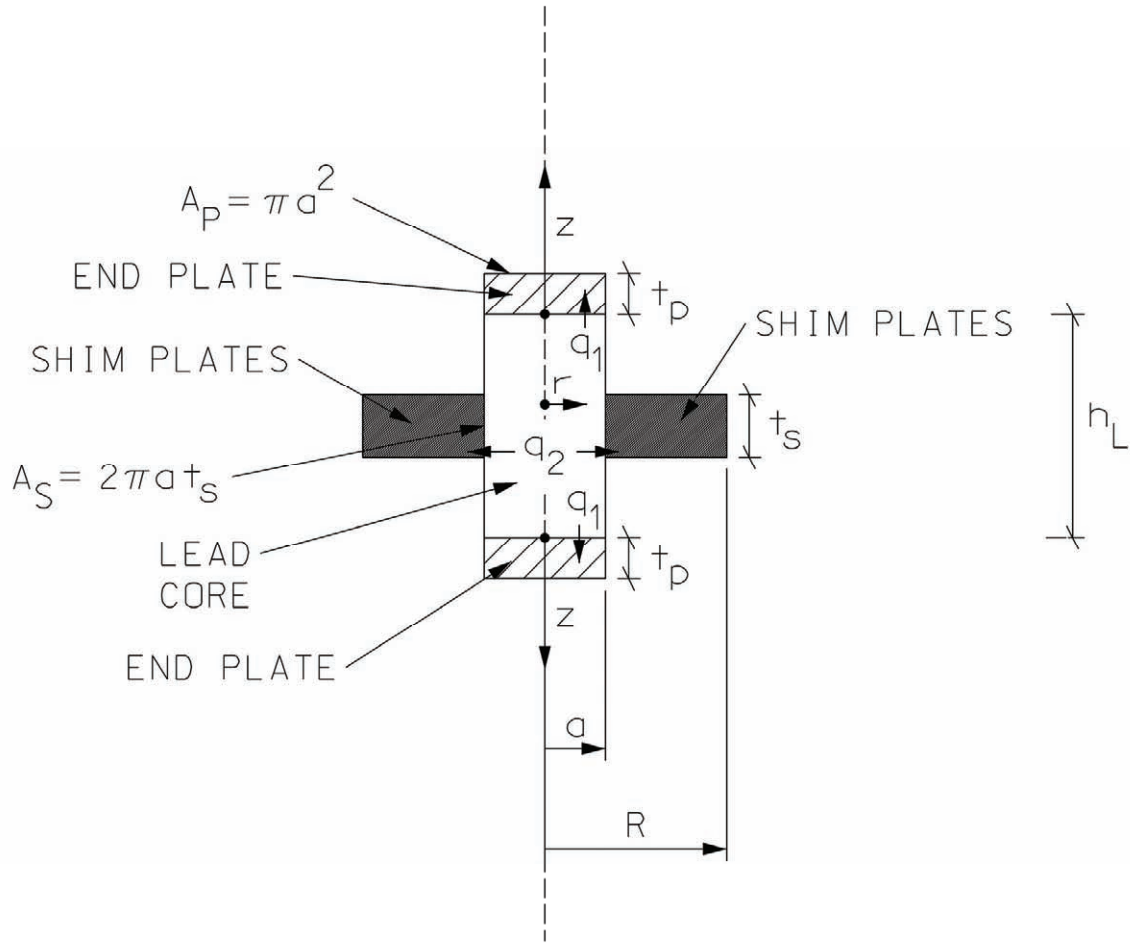
FIGURE 8-31 Model for the Simplified Analysis of Heat Conduction in Lead-Rubber Bearings

Considering harmonic motion of the bearing, the heat production rate $q'''(t)$ is given by

$$q'''(t) = \frac{\left| \sigma_{YL} \cdot A_L \cdot \dfrac{du}{dt} \right|}{V_L} = \frac{\sigma_{YL} \cdot \left| \dfrac{du}{dt} \right|}{h_L} = \frac{\sigma_{YL} \cdot \omega \cdot u_0 \cdot |\cos \omega t|}{h_L} \qquad (8\text{-}7)$$

where h_L is the height of the lead core, u_0 is the amplitude of motion, ω is the circular frequency of motion and the other terms have already been defined.

The following basic assumptions are made:

a) The increase in the temperature of lead T_L (measured with respect to the initial temperature) is only a function of time (that is, there is no space variability) with the exception of two small transition layers at the end plates-lead core interface and shim plates-lead core interface.

b) Convection and radiation at the free boundaries are neglected.

255

c) There is perfect contact between the lead core and the steel plates at their interface; that is, the increase in temperature of the lead core is equal to the increase in temperature of the end plates, T_P, and shim plates, T_S, at their points of contact. This increase in interface temperature is half of the increase in the temperature of lead T_L.

d) Conduction is the major mechanism of heat transfer and the solid is treated as stationary with a heat production rate within the lead core equal to the rate of energy dissipation within the lead core given by (8-7). Heat conduction is through the end plates (one-dimensional in the vertical direction) and shim plates (one-dimensional in the radial direction).

e) There is no conduction of heat through the rubber layers. This is a reasonable assumption given that rubber has a thermal conductivity much lower than that of steel.

f) Both the top and bottom end plates of the bearing are considered to be in contact with a large volume of steel as was, in fact, the case for all the experimental results presented later on. The case of end plates being in contact with concrete needs separate treatment considering different boundary conditions (e.g., insulated outer ends of end plates).

g) The following two types of solutions are considered:
   i. There is no heat conduction through the steel plates, i.e. all the heat which is dissipated by the lead core is consumed in elevating its temperature.
   ii. There is conduction through the steel plates, however there is unlimited volume of steel for the "heat front" to expand in both the end and the shim plates. In the following, the quantities t_{pf} and R_f represent the distance of the "heat front" in the end plates from the lead core and in the shim plates from the center of the bearing, respectively.

The thermal equation for the lead core is

$$\rho_L \cdot c_L \cdot V_L \frac{dT_L}{dt} = q'''(t) \cdot V_L - 2 \cdot q_1(t) - q_2(t) \tag{8-8}$$

where V_L is the volume of the lead core, ρ_L is the density of lead and c_L is the specific heat of lead. It is important to note that the density and the specific heat of lead are practically unaffected by the temperature (see Table 8-8). While volume V_L of the lead core slightly increases as the lead core is heated, we assume in the analysis that it remains constant.

Heat flux q_1 is given by

$$q_1(t) = -k_S \cdot A_P \cdot \frac{\partial T_P}{\partial z}\bigg|_{z=0} \tag{8-9}$$

Heat flux q_2 is given by

$$q_2(t) = -k_S \cdot A_S \cdot \left. \frac{\partial T_S}{\partial r} \right|_{r=a} \tag{8-10}$$

In the above equations, $A_p \left(= \pi a^2\right)$ is the area of the end plate in contact with the lead plug and $A_s \left(= 2\pi a t_s\right)$ is the inside area of the shim plates imaginary hollow cylinder (see Figure 8-31). Solution of equation (8-8) for the lead core temperature rise T_L requires first that the heat fluxes q_1 and q_2 be obtained by solving the individual problems for the end plates and the shim plates.

The thermal equation for the end plates is

$$\frac{\partial^2 T_P}{\partial z^2} = \frac{1}{\alpha_S} \frac{\partial T_P}{\partial t} \tag{8-11}$$

where $T_P(z,t)$ is the increase in temperature of the end plates and α_S is the thermal diffusivity of the end plate material (steel).

The thermal equation for the shim plates is

$$\frac{\partial^2 T_S}{\partial r^2} + \frac{1}{r} \frac{\partial T_S}{\partial r} = \frac{1}{\alpha_S} \frac{\partial T_S}{\partial t} \tag{8-12}$$

where $T_S(r,t)$ is the increase in temperature of the shim plates and α_S is the thermal diffusivity of the shim plate material (steel).

Ozisik (1989, 1993) presented solutions to the general problems of the one-dimensional heat conduction through a slab and the one-dimensional heat conduction through a hollow cylinder for all possible combinations of boundary conditions. In both cases the solution may be separated into two parts, a steady-state part and a transient part that decays exponentially with time. Ignoring the transient parts in all cases, we may assume a logarithmic distribution of temperature inside the shim plates and a linear distribution inside the end plates. Also the following boundary and initial conditions are assumed. It should be noted that these conditions imply a non-uniform distribution of temperature in the lead core that is consistent with observations in finite element analyses.

$$T_P(0,t) = \frac{T_L(t)}{2} \tag{8-13}$$

$$T_P(t_{pf},t) = 0 \tag{8-14}$$

$$T_P(z,0) = 0 \tag{8-15}$$

$$T_S(a,t) = \frac{T_L(t)}{2} \tag{8-16}$$

257

$$T_S(R_f, t) = 0 \tag{8-17}$$

$$T_S(r, 0) = 0 \tag{8-18}$$

where, as already discussed, $t_{pf}(t)$ and $R_f(t)$ are time-dependent variables controlling the location of the heat front in the end and shim plates respectively.

That is,

$$T_P(z, t) = \left(1 - \frac{z}{t_{pf}(t)}\right) \cdot \frac{T_L(t)}{2} \tag{8-19}$$

$$T_S(r, t) = \left(\frac{\ln(r / R_f(t))}{\ln(a / R_f(t))}\right) \cdot \frac{T_L(t)}{2} \tag{8-20}$$

The thermal energy stored inside each of the end plates, E_1 is

$$E_1 = \int_0^{t_{pf}(t)} \rho_S \cdot c_S \cdot A_P \cdot T_P(z, t) \cdot dz \tag{8-21}$$

and the energy stored in the shim plates, E_2, is

$$E_2 = \int_a^{R_f(t)} \rho_S \cdot c_S \cdot t_s \cdot T_S(r, t) \cdot 2\pi r dr \tag{8-22}$$

The assumption is made that the ratio of the heat fluxes is equal to the ratio of the stored energies:

$$\frac{q_1}{q_2} = \frac{E_1}{E_2} \tag{8-23}$$

Combining (8-9), (8-10), (8-19), (8-20), (8-21), (8-22) and (8-23), a relationship connecting the "heat front" parameters $t_{pf}(t)$ and $R_f(t)$ can be evaluated as

$$2 \cdot \left(\frac{t_{pf}}{a}\right)^2 = \left(\frac{R_f}{a}\right)^2 - 1 - 2 \cdot \ln\left(\frac{R_f}{a}\right) \tag{8-24}$$

Equation (8-24) is essentially a linear relationship between R_f / a and t_{pf} / a when the latter is in the range of nearly zero to 4. For simplicity, (8-24) is approximated by the simpler expression

$$\left(\frac{R_f}{a}\right) = 1 + 1.2\left(\frac{t_{pf}}{a}\right) \tag{8-25}$$

258

which compares very well with (8-24) as seen in Figure 8-32 particularly for the typical range of 0 to 2 for t_{pf}/a.
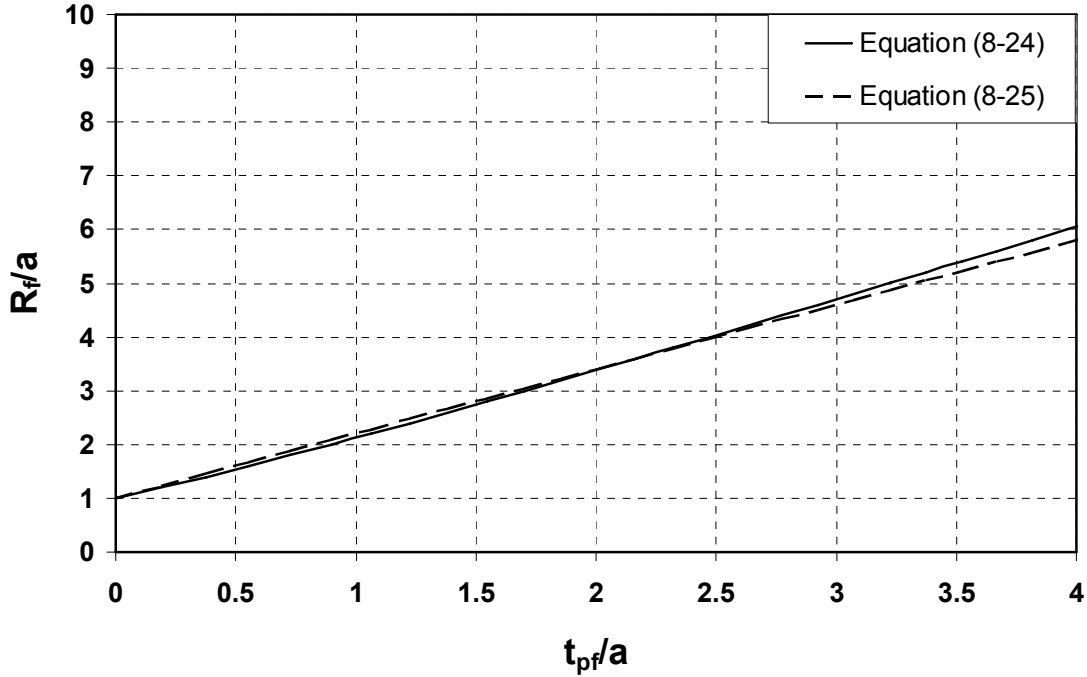
FIGURE 8-32 Relationships Between Heat Front Parameters

An energy balance condition is used for calculating the distance $t_{pf}(t)$ of the heat front in the end plates from the lead core. The thermal energy generated inside the lead core is equal to the sum of the thermal energies stored in the lead core and the steel plates. More specifically, we have

$$\int_0^t \sigma_{YL} \cdot A_L \cdot |v(\tau)| \cdot d\tau = T_L \rho_L c_L V_L + 2 \cdot \int_0^{t_{pf}(t)} \rho_S c_S A_P T_P(z,t)dz + \int_a^{R_f(t)} \rho_S c_S t_s T_S(r,t)2\pi r dr \quad (8\text{-}26)$$

which, in turn, due to Equations (8-19), (8-20), (8-21), (8-22), (8-24) and (8-25) gives

$$\int_0^t \sigma_{YL}|v(\tau)|d\tau = T_L \left\{ \rho_L c_L h_L + \frac{\rho_S c_S}{2}\left(t_{pf}(t) + t_s \frac{\left(\dfrac{t_{pf}(t)}{a}\right)^2}{\ln\left(1+1.2\dfrac{t_{pf}(t)}{a}\right)} \right) \right\} \quad (8\text{-}27)$$

where $v(t)$ is the time history of the velocity and $|v(t)|$ represents its magnitude.

Equation (8-8) combined with (8-7), (8-9), (8-10), (8-19), (8-20) and (8-25) gives

259

$$(\rho_L \cdot c_L \cdot h_L) \cdot \frac{dT_L}{dt} = \sigma_{YL} \cdot |v(t)| - \frac{k_S \cdot T_L(t)}{t_{pf}(t)} \cdot \left(1 + \left(\frac{t_s}{a}\right) \cdot \frac{\dfrac{t_{pf}(t)}{a}}{\ln\left(1 + 1.2\dfrac{t_{pf}(t)}{a}\right)}\right) \qquad (8\text{-}28)$$

Considering that t_{pf}/a ranges between 0 and 2, (8-27) and (8-28) may be further simplified as follows:

$$\int_0^t \sigma_{YL} |v(\tau)| d\tau = T_L \left\{ \rho_L c_L h_L + \frac{\rho_S c_S}{2} t_{pf}(t) \left(1 + 1.47\left(\frac{t_s}{a}\right)\right) \right\} \qquad (8\text{-}29)$$

$$(\rho_L \cdot c_L \cdot h_L) \cdot \frac{dT_L}{dt} = \sigma_{YL} \cdot |v(t)| - \frac{k_S \cdot T_L(t)}{t_{pf}(t)} \cdot \left(1 + \left(\frac{t_s}{a}\right) \cdot \left(0.83 + 0.41\frac{t_{pf}(t)}{a}\right)\right) \qquad (8\text{-}30)$$

The simplification is based on the function $y = x^2 / \ln(1 + 1.2 \cdot x)$ being approximately equal to $y = 1.47x$ for x between 0 and 2 (see Figure 8-33). Also, function $y = x / \ln(1 + 1.2x)$ is approximately equal to $y = 0.83 + 0.41x$ for the same range of x (see Figure (8-34).
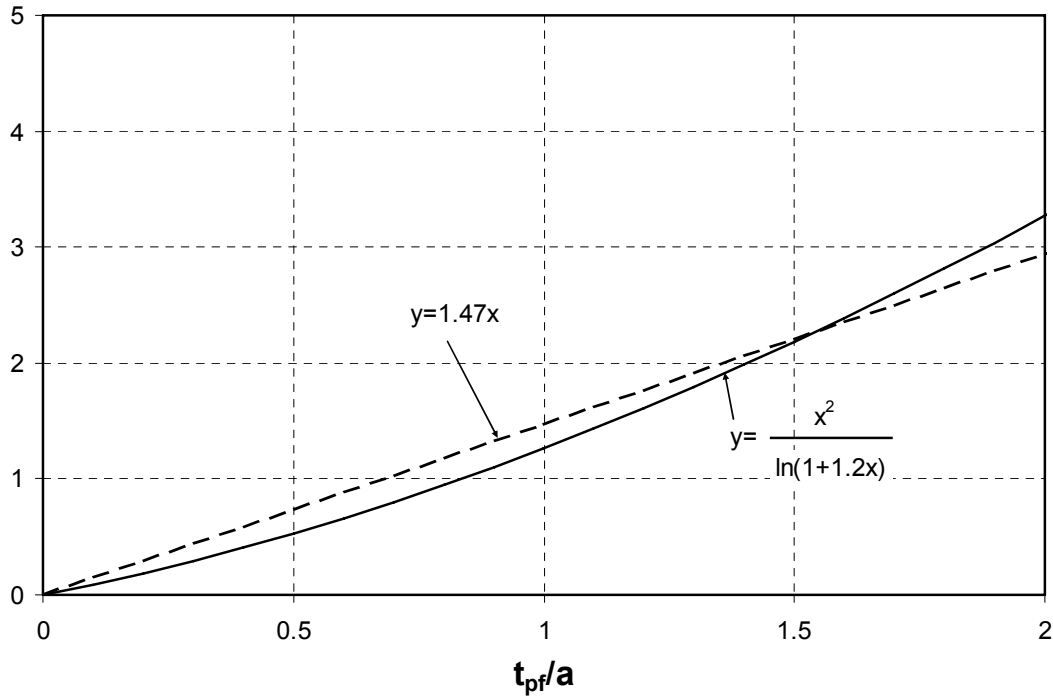
FIGURE 8-33 Simplification Used in Equation (8-27)
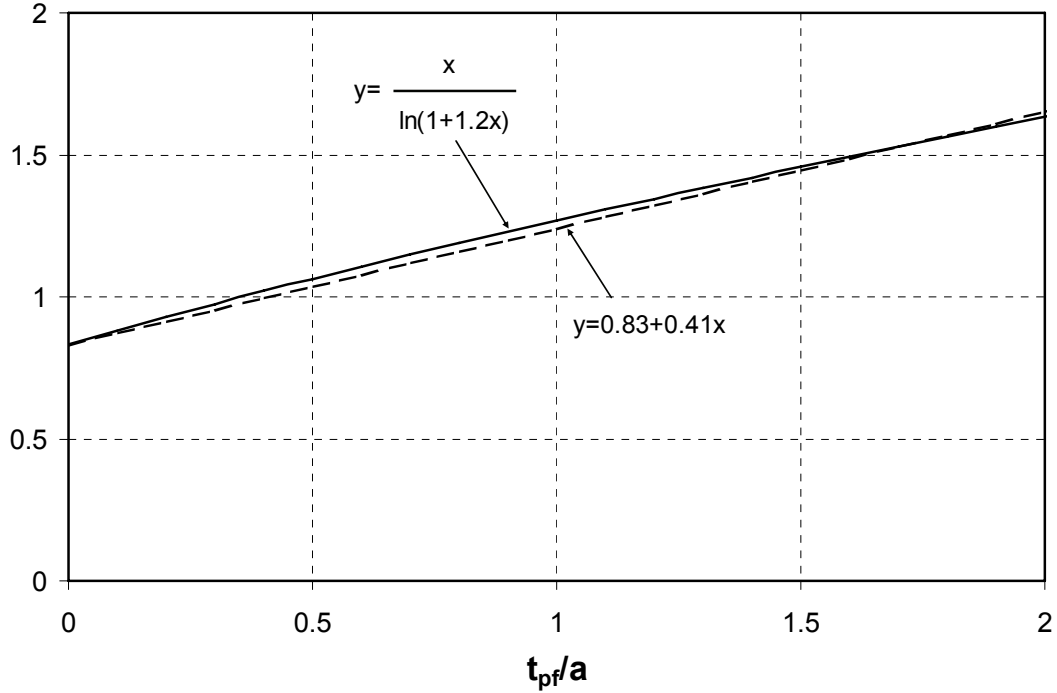
FIGURE 8-34 Simplification Used in Equation (8-28)

Equations (8-29) and (8-30) may be used to numerically evaluate the temperature and the strength of the lead core when the lead-rubber bearing undergoes repeated cycling with a velocity time history $v(t)$. Equations (8-29) and (8-30) also apply for the case of bidirectional motion if one interprets $v(t)$ as the resultant velocity. This is because the yield stress of lead theoretically remains parallel to the instantaneous velocity throughout the cyclic motion of a lead-rubber bearing. The presented theory implies that lead essentially behaves as a rigid-plastic material, i.e. it yields at a very small deformation and the portion of the recoverable elastic energy upon motion reversal is small. Therefore, it is not applicable for very low strains, i.e. when the amplitude is not much larger than the yield displacement of the bearing.

Solution of (8-29) and (8-30) starts with the assumption of an initial small value for the parameter t_{pf}. Equation (8-30) is then used to determine the temperature of the lead core for the next two time steps. Thereafter, at the beginning of each time step the parameter t_{pf} is calculated using (8-29) and then used in (8-30) to calculate the temperature at the end of the step.

For $\Delta t =$ time step, $T_{Lt}(i) =$ temperature of lead, $T_L(i) =$ rise in temperature of lead with respect to the initial temperature T_{L0}, $\sigma_{YL}(i) =$ effective yield stress, $v(i) =$ velocity of motion and $t_{pf}(i) =$ value of the heat front parameter t_{pf}, time $t = (i-1)\cdot \Delta t$ and $i =$ time step, the algorithm proceeds as follows:

a) Assume a small initial value of t_{pf}, say $t_{pf0} = 0.01m$.

b)
$$T_L(1) = 0 \tag{8-31}$$

261

c) $\quad T_L(2)=T_L(1)+\left\{\sigma_{YL}(1)\cdot v(1)-\left(\dfrac{k_S\cdot T_L(1)}{t_{pf0}}\right)\left(1+\left(\dfrac{t_s}{a}\right)\cdot\left(0.83+0.41\cdot\dfrac{t_{pf0}}{a}\right)\right)\right\}\cdot\dfrac{\Delta t}{\rho_L c_L h_L}$ (8-32)

d) $\quad T_L(3)=T_L(2)+\left\{\sigma_{YL}(2)\cdot v(2)-\left(\dfrac{k_S\cdot T_L(2)}{t_{pf0}}\right)\left(1+\left(\dfrac{t_s}{a}\right)\cdot\left(0.83+0.41\cdot\dfrac{t_{pf0}}{a}\right)\right)\right\}\cdot\dfrac{\Delta t}{\rho_L c_L h_L}$ (8-33)

e) $\quad t_{pf}(i)=\dfrac{\dfrac{\sum\limits_{j=1}^{i-1}\sigma_{YL}(i)\cdot v(i)\cdot dt}{T_L(i)}-\rho_L c_L h_L}{0.5\rho_S c_S\left(1+1.47\left(\dfrac{t_s}{a}\right)\right)}\,,\ i\geq 3$ (8-34)

f) $\quad T_L(i+1)=T_L(i)+\left\{\sigma_{YL}(i)\cdot v(i)-\left(\dfrac{k_S\cdot T_L(i)}{t_{pf}(i)}\right)\left(1+\left(\dfrac{t_s}{a}\right)\cdot\left(0.83+0.41\cdot\dfrac{t_{pf}(i)}{a}\right)\right)\right\}\cdot\dfrac{\Delta t}{\rho_L c_L h_L}$ (8-35)

where $\sigma_{YL}(i)$ is a function of temperature $T_{Lt}(i)$ (per Equation 8-5 or 8-6) and

$$T_{Lt}(i)=T_{L0}+T_L(i)$$ (8-36)

The process described above may be used for any bidirectional input motion as long as the amplitude is much larger than the yield displacement of the bearing.

8.8.4 Simplified Solution

It is reasonable to assume that for a short time interval after the start of an experiment, heat conduction through the steel shim plates and the steel end plates is negligible. Accordingly, the heat generated in the lead core is entirely consumed for the rise of its own temperature. That is, fluxes q_1 and q_2 are zero. In that case, (8-30) becomes for harmonic motion of amplitude u_0 and circular frequency ω:

$$\left(\rho_L\cdot c_L\cdot h_L\right)\cdot\dfrac{dT_L}{dt}=\sigma_{YL}\cdot\omega\cdot u_0\cdot\left|\cos\omega t\right|$$ (8-37)

On the basis of this assumption, and furthermore utilizing the linear relationship between effective yield stress of lead and temperature (combining Equations (8-4) and (8-6)), (8-37) becomes:

$$\rho_L\cdot c_L\cdot h_L\dfrac{dT_{Lt}}{dt}=\left(\dfrac{\sigma_{YL0}}{f(T_{L0})}\right)\cdot\left[L_1\cdot T_{Lt}+L_2\right]\cdot\omega\cdot u_0\cdot\left|\cos\omega t\right|$$ (8-38)

This equation integrated from the beginning to the end of half-cycle "k" results in

$$T_{Lt}^{(k)} = \left(T_{Lt}^{(k-1)} + \frac{L_2}{L_1} \right) \cdot \exp\left(\frac{2 \cdot \sigma_{YL0} \cdot L_1 \cdot u_0}{f(T_{L0}) \cdot (\rho_L \cdot c_L \cdot h_L)} \right) - \frac{L_2}{L_1} \qquad (8\text{-}39)$$

Equation (8-39) provides the absolute temperature at the end of any half-cycle "k" when knowing the absolute temperature at the end of the previous half-cycle "k-1". It is evident that, for no conduction through the steel plates, the frequency has no effect on the calculated temperature. The most significant parameter is the ratio of displacement amplitude to lead core height, or shear strain in the lead core u_0 / h_L. It will be shown that this simplified solution provides a good approximation in many cases of harmonic motion, especially at high speeds, for large-size bearings and for a small number of cycles.

8.8.5 Finite Element Analysis

Numerical solutions using finite element modeling are complex and time consuming but very useful in verifying the assumptions made in the presented solutions and investigating the accuracy of the derived analytical solutions. Particularly, a finite element solution is useful for (a) investigating the significance of the transient terms in the temperature histories of the steel plates and (b) investigating the validity of the assumption of constant temperature distribution within the lead plug. Accordingly, a finite element model was developed with the intention of investigating the aforementioned items (a) and (b) above and also the accuracy and validity of the derived analytical solutions.

A finite element model was developed for analyzing many different bearing geometries. The model was developed in computer code ABAQUS (Hibbitt, Karlsson & Sorensen, 2004) with all elements being of the type: axisymmetric, 4-node linear diffusive heat transfer element DCAX4 (see Figure 8-35). All free boundaries were modeled as heat-insulated. This means that (a) radiation effects at the free rubber and steel shim ends are neglected, and (b) the steel structures above and below the bearing represent the conditions of the actual bearing installation (in a massive test machine or in structure) where the temperature rise is zero at some distance t_p from the lead core. For the analysis, the heat generation within the lead core was defined as a property of the material. The heat generation rate within the core (thermal energy per time per volume) is given by Equation (8-8). The initial temperature was assumed to be equal to 20^0C unless otherwise specified.

263
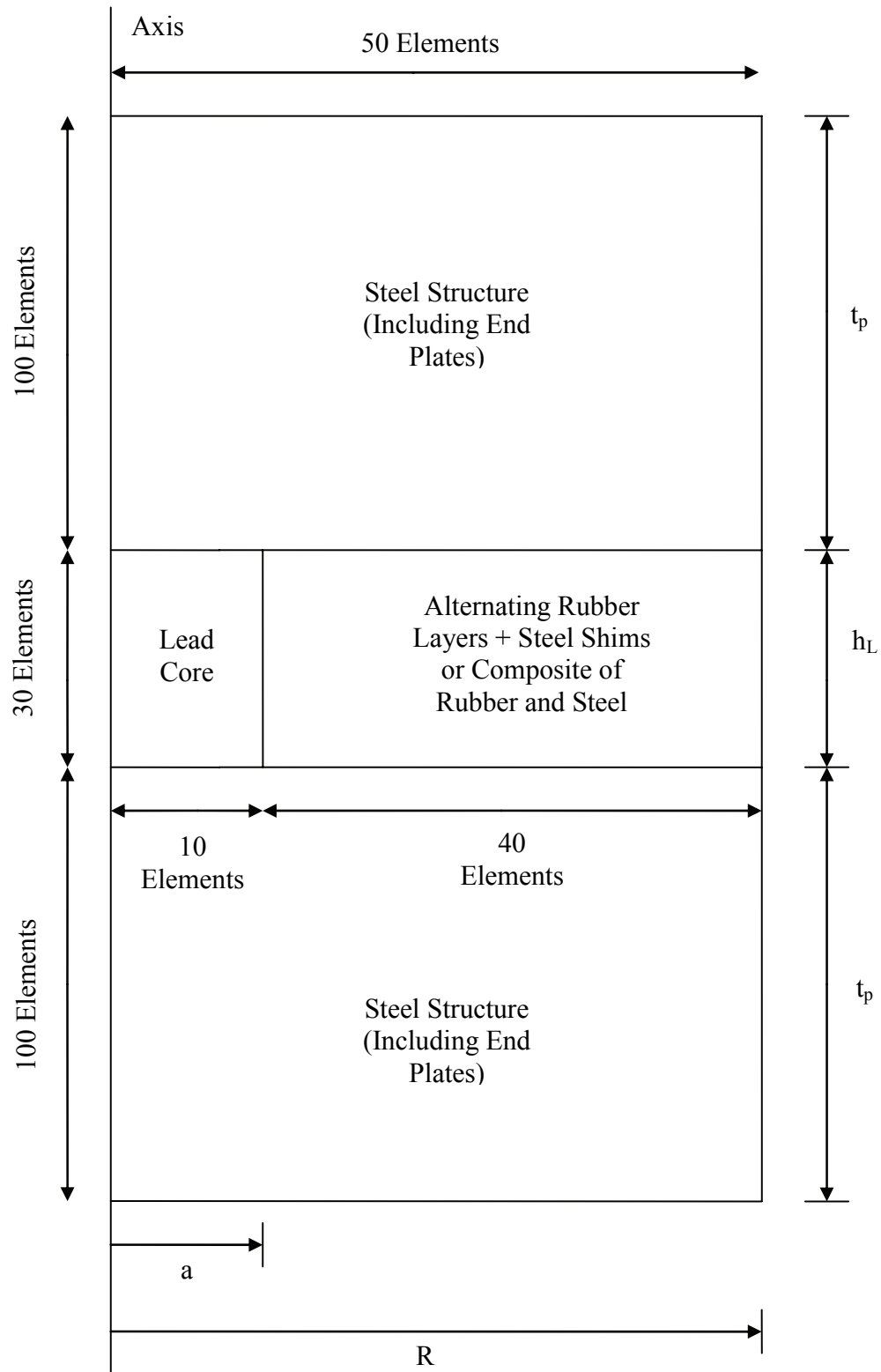
FIGURE 8-35 Axisymmetric Finite Element Model for Lead Rubber Bearing Heating

Table 8-10 presents the material properties used for the steel end and shim plates, the lead core and the rubber layers. Note that in the finite element model the rubber is not assumed to be a perfect thermal insulator but is rather modeled as a material with a low thermal conductivity. Moreover, in one analysis the alternate layers of rubber and shim plates were directly modeled whereas in the other examples they were modeled as anisotropic composite material with two values of thermal conductivity, one radial and one vertical. Salazar (2003) states that for this composite the effective heat capacity is

$$\rho c = v_1 (\rho_1 c_1) + v_2 (\rho_2 c_2) \tag{8-40}$$

where v_i is the volume fraction of component i. Also, the effective thermal conductivity parallel to the layers ($k_{eff,radial}$) and that perpendicular to the layers ($k_{eff,vert}$) are given by

$$k_{eff,radial} = v_1 k_1 + v_2 k_2 \tag{8-41}$$

$$\frac{1}{k_{eff,vert}} = \frac{v_1}{k_1} + \frac{v_2}{k_2} \tag{8-42}$$

For a lead-rubber bearing with a total shim plate thickness t_s and lead core height h_L, the volume fractions for steel and rubber in the composite region are given by

$$v_{steel} = \frac{t_s}{h_L} \tag{8-43}$$

$$v_{rubber} = 1 - \frac{t_s}{h_L} \tag{8-44}$$

TABLE 8-10 Material Parameters Used in Finite Element Analysis

Parameter	End and Shim Plates (Steel)	Rubber Layers (Rubber)	Lead Core (Lead)
Density, $\rho \left(\frac{kg}{m^3}\right)$	7900	1300	11200
Conductivity, k $\left(\frac{W}{m \cdot {}^o C}\right)$	50	0.16	34
Specific Heat, c $\left(\frac{J}{kg \cdot {}^o C}\right)$	450	1700	130

8.8.6 Examples

A number of examples are presented in which experimental data on the energy dissipated per cycle, which is directly proportional to the characteristic strength, of lead rubber bearings over several cycles are compared to (a) predictions of finite element analysis, (b) predictions of the analytical solution obtained by numerical solution of equations (8-29) and (8-30) in which various relations between σ_{YL} and temperature were used, and (c) predictions of the simplified solution of equation (8-39) in which the bilinear relation (see Table 8-9) was used.

The experimental values of energy dissipated per cycle include both the part associated with energy dissipation in the lead core and the part associated with energy dissipation in the rubber. Therefore, before using the experimental data to obtain the initial effective yield stress σ_{YL0} through the process described in Section 8.8.2, the portion of the energy dissipated by the rubber should be estimated and then subtracted from the total energy dissipated per cycle. This estimation requires testing of control specimens without lead core. In the absence of such experimental results, the rubber contribution to the energy dissipated per cycle may be estimated by assuming that rubber contributes to the effective damping a specific amount.

The theoretically predicted energy dissipated per cycle is calculated as follows:

a) The temperature of the lead core in the middle of the first cycle is obtained by analysis (analytic or numerical – FEM).
b) Combined use of (8-4) and (8-5) (or (8-6)) gives the effective yield stress of lead for the first cycle while (8-1) combined with (3-8) gives the energy dissipated in the lead core during the first cycle.
c) The estimated energy dissipated in the rubber is added to the energy dissipated in the lead core, giving the total theoretically predicted dissipated energy to be compared against its experimentally determined value for the first cycle.
d) The previous steps are repeated for each next cycle of motion.

8.8.6.1 Example 1

Consider the bearing of Figure 8-9 with energy dissipated per cycle data from its testing shown in Figure 8-25. Figure 8-36 shows the force-displacement loop recorded in that experiment. Figure 8-37 shows the finite element model used for the analysis.
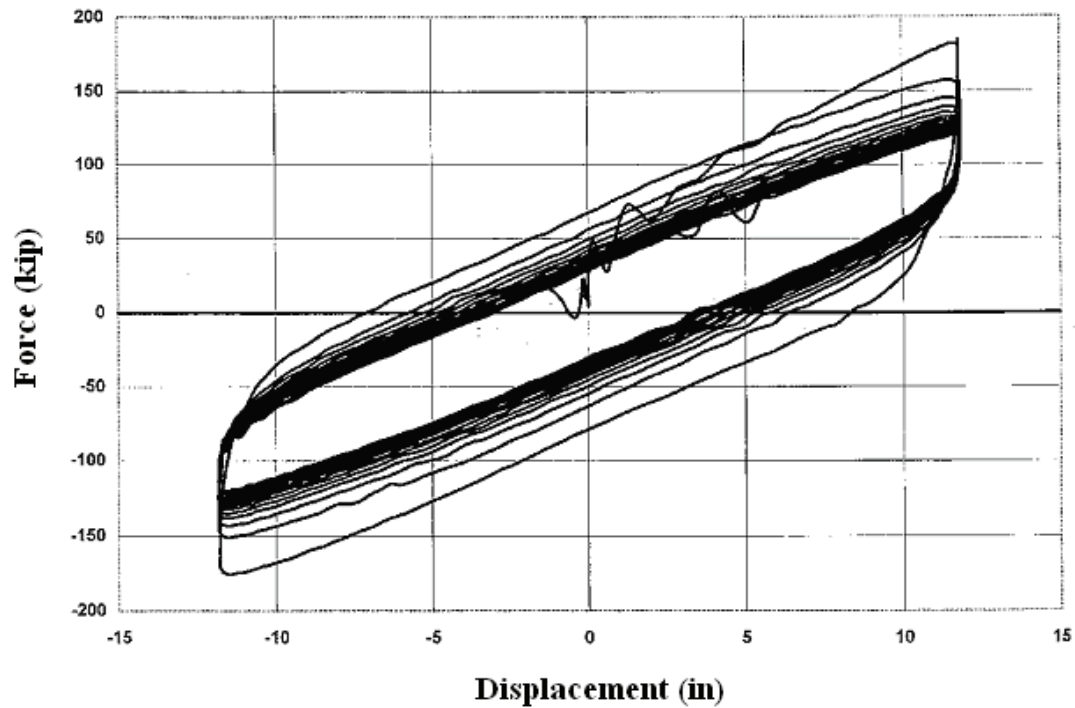
FIGURE 8-36 Force-Displacement Loop of Bearing of Figure 8-9 Load=850kip (3783kN), Displacement Amplitude=12in (305mm) and Frequency=0.5Hz (Peak Velocity=37.7in/s=958mm/s)

267
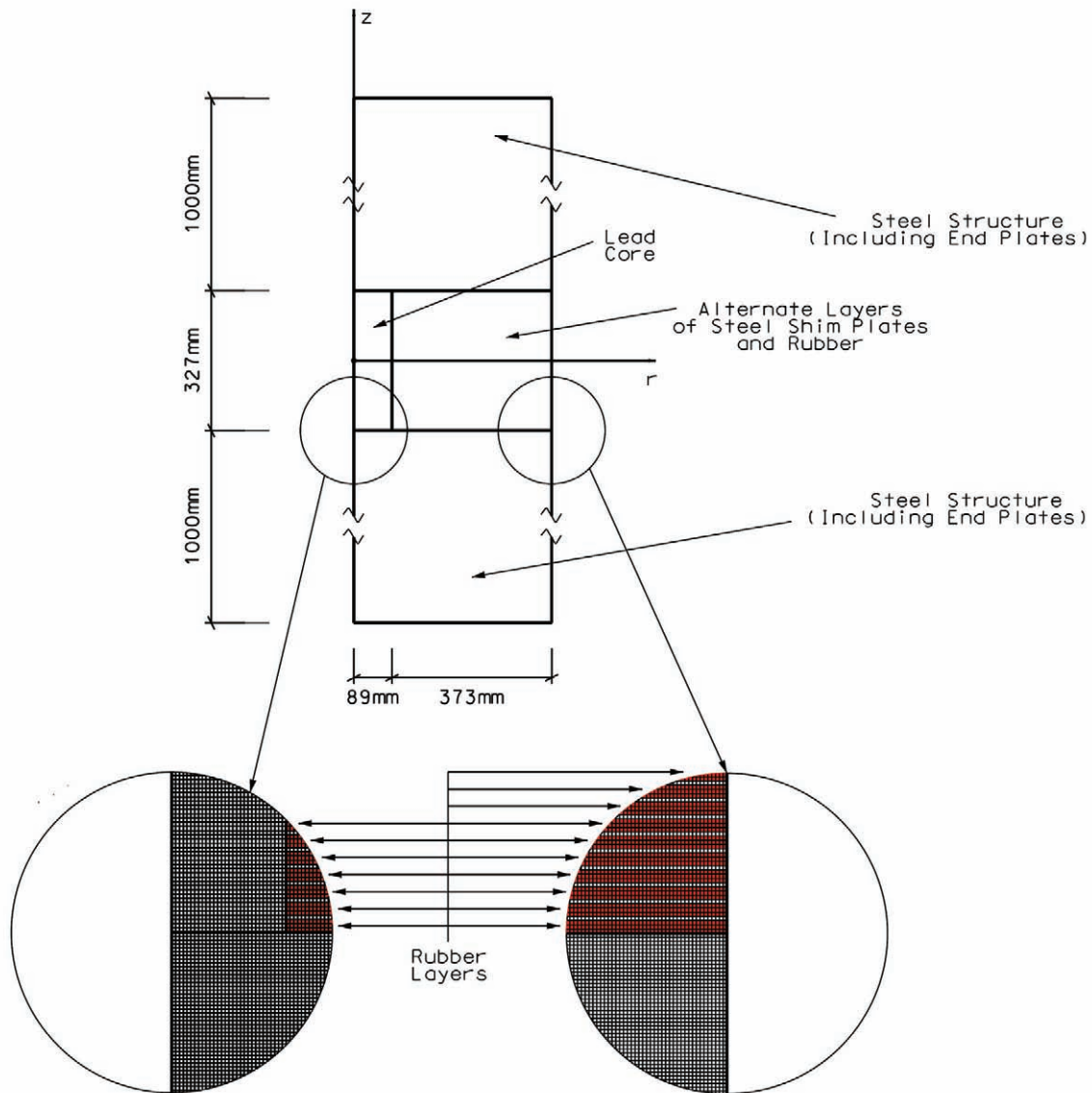
FIGURE 8-37 Explicit Finite Element Model for the Analysis of Temperature Rise in the Bearing of Figure 8-9

This explicit, finely meshed finite element model will only be used in this example. Table 8-11 provides the data used in the analysis. Figure 8-38 presents the calculated histories of temperature and energy dissipated per cycle, and Figures 8-39 and 8-40 present temperature profiles in the lead core obtained in the finite element analysis.

The results in Figure 8-38 demonstrate good agreement between experimental results and results of finite element analysis and of the simplified solution. The latter two solutions appear to be nearly identical, an indication that in this case heat conduction through the steel plates is insignificant. This is due to the high speed of testing. Interestingly, the analytical solution tends to underpredict the temperature and overpredict the strength. The fact that even the simplified solution, which neglects heat losses, also slightly underpredicts the temperature by comparison to the explicit finite element solution, suggests that the rubber contribution to the dissipated energy has been overestimated.

268

TABLE 8-11 Data Used in Analysis of Example 1

Amplitude of Sinusoidal Motion, u_0	305 mm	
Period of Sinusoidal Motion, T	2.0 sec	
Peak Velocity of Sinusoidal Motion, v_{max}	958 mm/s	
Initial (Reference) Lead Effective Yield Stress (σ_{YL0})	11.6 MPa	
Initial Temperature, T_{L0}	20^0C	
Parameters of Bilinear Relation of σ_{YL} vs. Temperature	L_1=-1.08E-01, L_2=20.64 for $T_{Lt}<100^0$C L_1=-4.38E-02, L_2=14.32 for $T_{Lt}>100^0$C	
Equiv. Damp. Ratio for Estimating Rubber Contribution to EDC (β)	0.05	
Yield Displacement (Y)	12 mm	
Thermal Properties of Rubber, Steel and Lead	Per Table 8-10	
Thermal Properties of Rubber Layer and Steel Shim Composite	Heat Capacity, $\rho c\ (\dfrac{J}{m^{3\cdot 0}C})$	2510260
	Radial Conductivity, $k_{eff,radial}$ $(\dfrac{W}{m\cdot^0 C})$	11.3
	Vertical Conductivity, $k_{eff,vert}$ $(\dfrac{W}{m\cdot^0 C})$	0.21
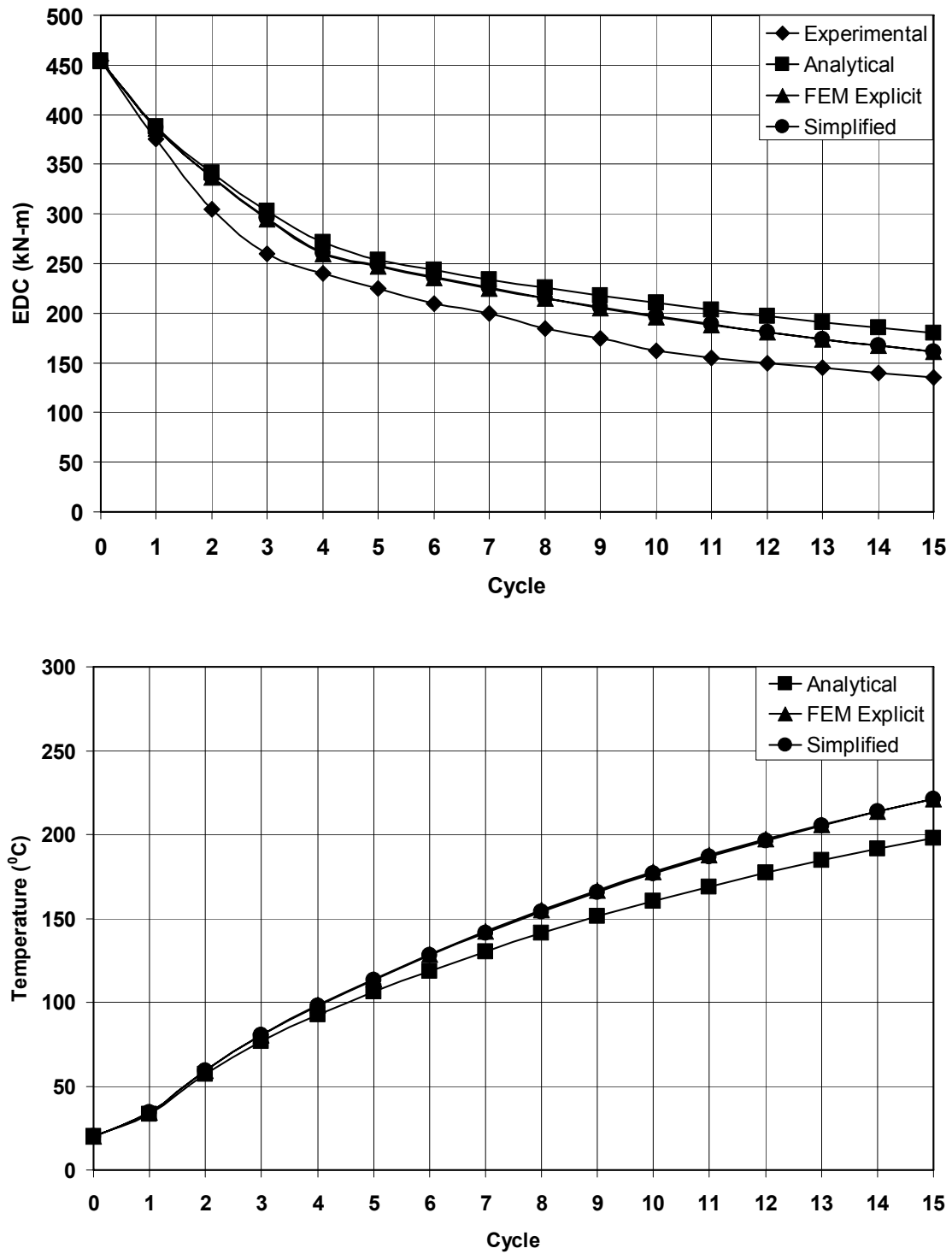
FIGURE 8-38 Temperature and Energy Dissipated per Cycle Histories for Example 1

270
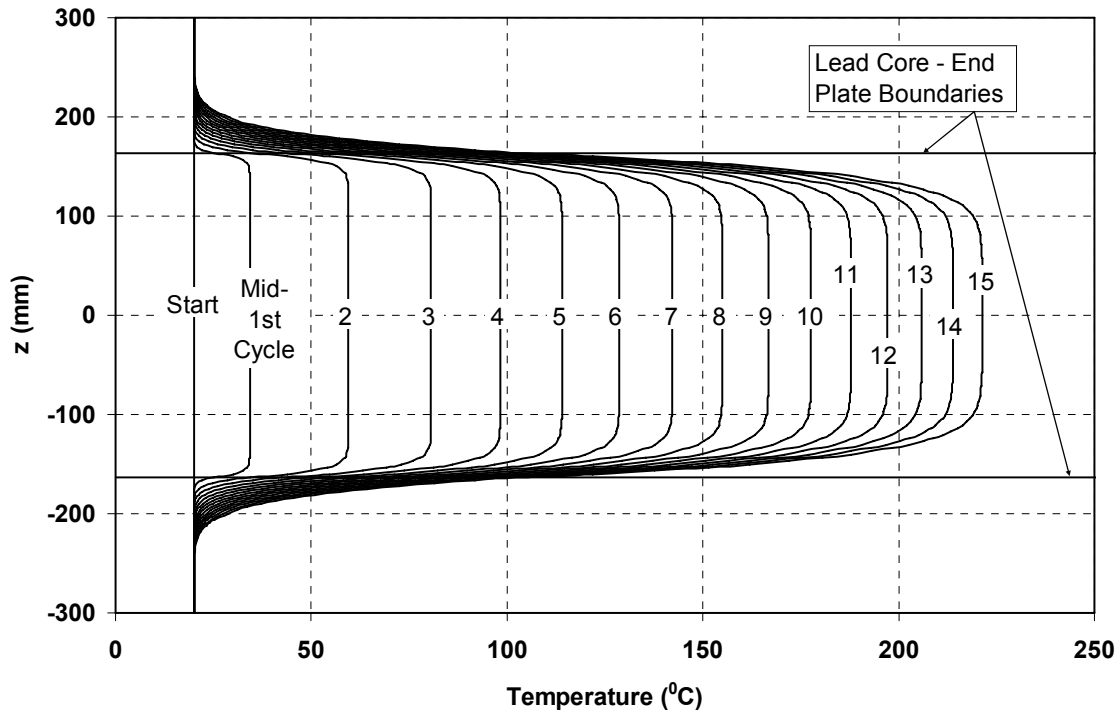
FIGURE 8-39   Vertical Temperature Distribution at the Center of the Bearing (r=0) of Figure 8-9 Obtained in Explicit Finite Element Analysis
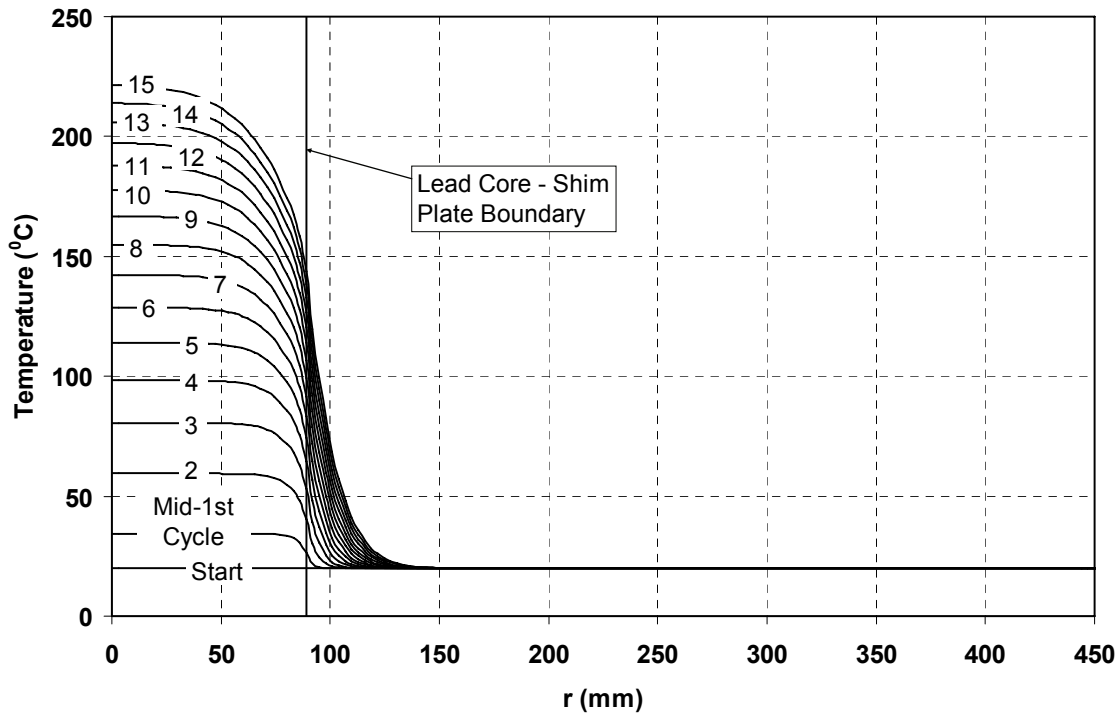
FIGURE 8-40   Horizontal Temperature Distribution (at z=7mm) of the Bearing of Figure 8-9 Obtained in Explicit Finite Element Analysis

271

The finite element analysis results in Figures 8-39 and 8-40 demonstrate uniform lead core temperature over height and minimal extent of temperature increase in the steel shims. The first observation confirms the assumptions made in the analytical solution and the second observation indicates insignificant heat conduction through the steel shims. This explains the success of the simplified solution in better predicting the history of characteristic strength than the analytical solution. Note that the latter exploits heat conduction through the steel plates and should overestimate the strength in situations where heat conduction is insignificant (such as in high speed motion and small number of cycles).

In a further study the results of the explicit finite element model of Figure 8-37 are compared to the results of the simpler finite element model in which the rubber layers and steel shims were replaced with a continuous anisotropic medium (termed composite finite element analysis). Results on the predictions of the two finite element models are presented in Figure 8-41. Evidently, the two models predict identical results. This observation indicates that the simple finite element model is reliable for use in such analyses.
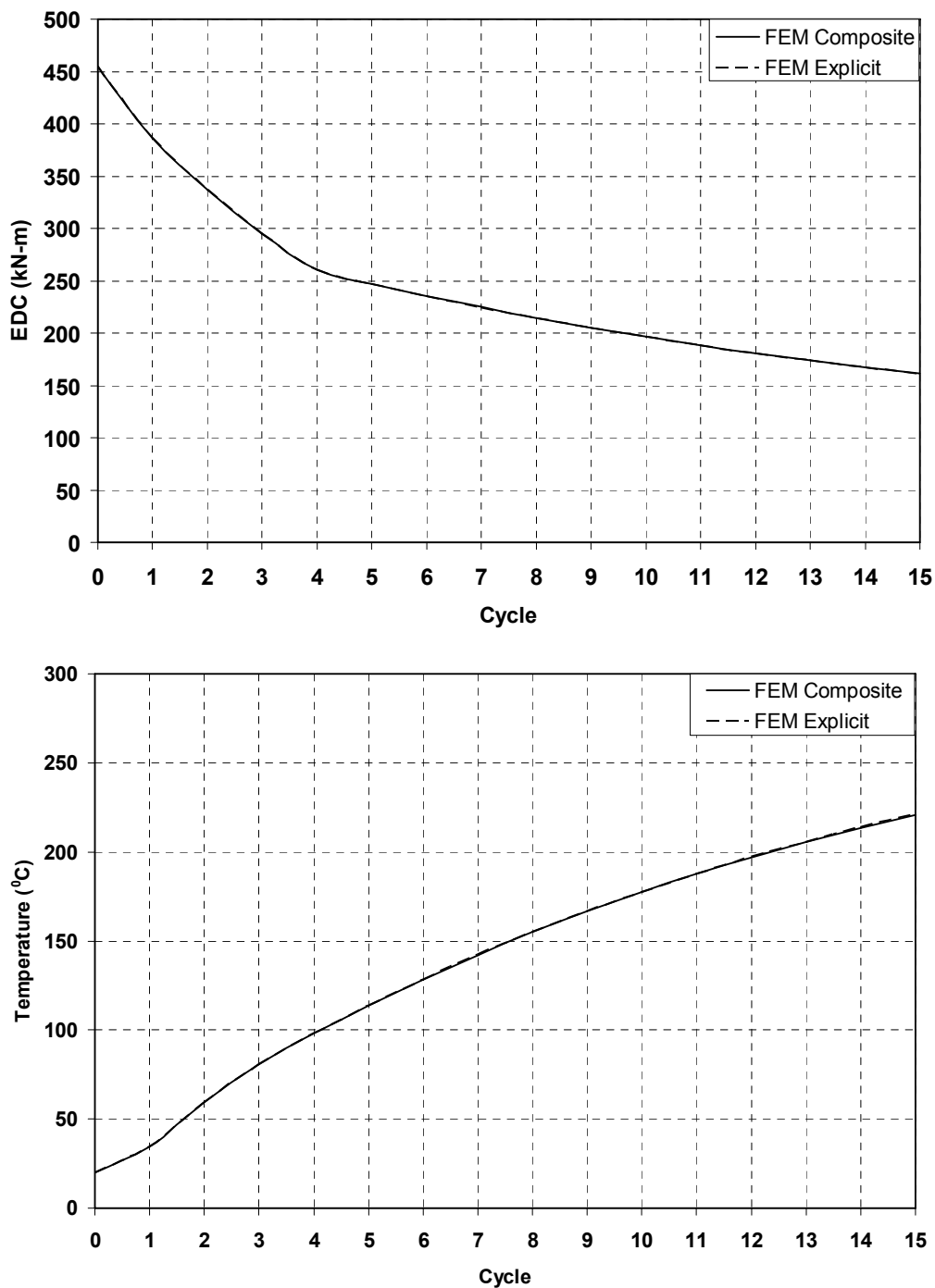
FIGURE 8-41 Comparison of Temperature and Energy Dissipated per Cycle Histories for the Bearing of Figure 8-9 Subjected to a Harmonic Motion with 305mm Amplitude and 2.0sec Period as Calculated by FE Model with Explicit and Composite Representation of the Rubber and Steel

273

The difference between the finite element and the analytical solutions may be attributed to the fact that the FEM-obtained temperature values are collected from the center of the lead core where heat losses are relatively small. By contrast, the analytically obtained values have the physical meaning of average lead core temperature rather than any local value. It should also be noted that the assumption incorporated in the analytical model that the steel-lead interface temperature increase is equal to half the temperature increase in the lead core seems to be realistic (see Figures 8-39 and 8-40).

8.8.6.2 Example 2

Example 2 is the bearing of Figure 7-4 and with test data presented in Figures 7-5 and 8-8 and Tables 7-2 and 8-4. In this case, a control specimen without lead core was also tested so that it was possible to directly determine the contributions of lead and rubber to the energy dissipated per cycle. Moreover, this bearing was tested at low, normal and high starting temperatures.

Example 2 concentrates on the test at start temperature of 20^0C and peak velocity of 250mm/sec. The data used in the analysis are presented in Table 8-12. Note that the finite element analysis was based on the simpler composite model.

Temperature and energy dissipated per cycle (EDC) histories are presented in Figure 8-42 and compared to experimental results. Predictions of EDC by all methods of analysis, including the simplified method, compare very well to experimental results over the four cycles of testing.

TABLE 8-12 Data Used in Analysis of Example 2

Amplitude of Sinusoidal Motion, u_0	113 mm
Period of Sinusoidal Motion, T	2.84 sec
Peak Velocity of Sinusoidal Motion, v_{max}	250 mm/s
Initial (Reference) Lead Effective Yield Stress (σ_{YL0})	9.4 MPa
Initial Temperature, T_{L0}	20^0C
Parameters of Bilinear Relation of σ_{YL} vs. Temperature	L_1=-1.08E-01, L_2=20.64 for $T_{Lt}<100^0$C L_1=-4.38E-02, L_2=14.32 for $T_{Lt}>100^0$C
Equiv. Damp. Ratio for Estimating Rubber Contribution to EDC (β)	NA
Yield Displacement (Y)	12 mm
Thermal Properties of Rubber, Steel and Lead	Per Table 8-10

Thermal Properties of Rubber Layer and Steel Shim Composite	Heat Capacity, ρc $(\dfrac{J}{m^{3}\cdot^0 C})$	2447353
	Radial Conductivity, $k_{eff,radial}$ $(\dfrac{W}{m\cdot^0 C})$	9.0
	Vertical Conductivity, $k_{eff,vert}$ $(\dfrac{W}{m\cdot^0 C})$	0.19

FIGURE 8-42 Temperature and Energy Dissipated per Cycle Histories for Example 2

276

8.8.6.3 Example 3

Example 3 is the same as example 2 (bearing of Figure 7-4, peak velocity of 250mm/sec) but with a start temperature of -26^0C. Data used for analysis are presented in Table 8-13 and the calculated histories of temperature and EDC are presented in Figure 8-43. The composite finite element model was used for analysis. The predictions of the theory, including the simplified solution, are in good agreement with the experimental results.

TABLE 8-13 Data Used in Analysis of Example 3

Amplitude of Sinusoidal Motion, u_0	113 mm	
Period of Sinusoidal Motion, T	2.84 sec	
Peak Velocity of Sinusoidal Motion, v_{max}	250 mm/s	
Initial (Reference) Lead Effective Yield Stress (σ_{YL0})	11.2 MPa	
Initial Temperature, T_{L0}	-26^0C	
Parameters of Bilinear Relation of σ_{YL} vs. Temperature	L_1=-1.08E-01, L_2=20.64 for $T_{Lt}<100^0$C L_1=-4.38E-02, L_2=14.32 for $T_{Lt}>100^0$C	
Equiv. Damp. Ratio for Estimating Rubber Contribution to EDC (β)	NA	
Yield Displacement (Y)	12 mm	
Thermal Properties of Rubber, Steel and Lead	Per Table 8-10	
Thermal Properties of Rubber Layer and Steel Shim Composite	Heat Capacity, ρc $(\frac{J}{m^{3.0}C})$	2447353
	Radial Conductivity, $k_{eff,radial}$ $(\frac{W}{m \cdot ^0 C})$	9.0
	Vertical Conductivity, $k_{eff,vert}$ $(\frac{W}{m \cdot ^0 C})$	0.19

FIGURE 8-43 Temperature and Energy Dissipated per Cycle Histories for Example 3

279

8.8.6.4 Example 4

Example 4 is the same as example 2 (bearing of Figure 7-4, peak velocity of 250mm/sec) but with a start temperature of 49^0C. Data used for analysis are presented in Table 8-14 and the calculated histories of temperature and EDC are presented in Figure 8-44. The composite finite element model was used for analysis. The predictions of the theory, including the simplified solution, are in good agreement with the experimental results.

TABLE 8-14 Data Used in Analysis of Example 4

Amplitude of Sinusoidal Motion, u_0	113 mm	
Period of Sinusoidal Motion, T	2.84 sec	
Peak Velocity of Sinusoidal Motion, v_{max}	250 mm/s	
Initial (Reference) Lead Effective Yield Stress (σ_{YL0})	8.2 MPa	
Initial Temperature, T_{L0}	49^0C	
Parameters of Bilinear Relation of σ_{YL} vs. Temperature	L_1=-1.08E-01, L_2=20.64 for $T_{Lt}<100^0C$ L_1=-4.38E-02, L_2=14.32 for $T_{Lt}>100^0C$	
Equiv. Damp. Ratio for Estimating Rubber Contribution to EDC (β)	NA	
Yield Displacement (Y)	12 mm	
Thermal Properties of Rubber, Steel and Lead	Per Table 8-10	
Thermal Properties of Rubber Layer and Steel Shim Composite	Heat Capacity, ρc $(\frac{J}{m^{3\cdot0}C})$	2447353
	Radial Conductivity, $k_{eff,radial}$ $(\frac{W}{m\cdot^0C})$	9.0
	Vertical Conductivity, $k_{eff,vert}$ $(\frac{W}{m\cdot^0C})$	0.19

281

FIGURE 8-44 Temperature and Energy Dissipated per Cycle Histories for Example 4

282

8.8.6.5 Example 5

Example 5 is the same as example 2 (bearing of Figure 7-4, start temperature of 20^0C) but with peak velocity of 25mm/sec rather than 250mm/sec. Note that velocities of 25mm/sec or less are typically used in production testing of isolators. Data used for analysis are presented in Table 8-15 and the calculated histories of temperature and EDC are presented in Figure 8-45. The composite finite element model was used for analysis. Also, the linear yield stress to temperature relation was used.

The predictions of the finite element and the analytical solutions on EDC are in very good agreement with the experimental values. The underprediction of EDC (although small in four cycles) and overprediction of temperature by the simplified method of analysis is the result of neglect of heat conduction through the shim and end plates in this slow test. Nevertheless, the prediction of EDC history by the simplified method is good for the four cycles of the test.

TABLE 8-15 Data Used in Analysis of Example 5

Amplitude of Sinusoidal Motion, u_0	113 mm
Period of Sinusoidal Motion, T	28.4 sec
Peak Velocity of Sinusoidal Motion, v_{max}	25 mm/s
Initial (Reference) Lead Effective Yield Stress (σ_{YL0})	7.9 MPa
Initial Temperature, T_{L0}	20^0C
Parameters of Bilinear Relation of σ_{YL} vs. Temperature	L_1=-1.08E-01, L_2=20.64 for $T_{Lt}<100^0$C L_1=-4.38E-02, L_2=14.32 for $T_{Lt}>100^0$C
Equiv. Damp. Ratio for Estimating Rubber Contribution to EDC (β)	NA
Yield Displacement (Y)	12 mm
Thermal Properties of Rubber, Steel and Lead	Per Table 8-10

Thermal Properties of Rubber Layer and Steel Shim Composite	Heat Capacity, ρc $(\dfrac{J}{m^{3 \cdot 0}C})$	2447353
	Radial Conductivity, $k_{eff,radial}$ $(\dfrac{W}{m \cdot ^0 C})$	9.0
	Vertical Conductivity, $k_{eff,vert}$ $(\dfrac{W}{m \cdot ^0 C})$	0.19

FIGURE 8-45 Temperature and Energy Dissipated per Cycle Histories for Example 5

8.8.6.6 Example 6

Example 6 is the bearing of Figure 8-11 for which recorded loops in testing are shown in Figure 8-12. Mechanical properties of the bearing obtained in testing are presented in Table 8-6. The data used for analysis are presented in Table 8-16.

Figure 8-46 presents histories of temperature and EDC predicted by analysis and compares those to experimental results. The prediction of EDC history is very good by all methods of analysis including the simplified method. This is due to the high speed of testing for which heat conduction effects are not significant for the first few cycles of motion.

TABLE 8-16 Data Used in Analysis of Example 6

Amplitude of Sinusoidal Motion, u_0	483 mm	
Period of Sinusoidal Motion, T	3.0 sec	
Peak Velocity of Sinusoidal Motion, v_{max}	1012 mm/s	
Initial (Reference) Lead Effective Yield Stress (σ_{YL0})	16.7 MPa	
Initial Temperature, T_{L0}	20^0C	
Parameters of Bilinear Relation of σ_{YL} vs. Temperature	L_1=-1.08E-01, L_2=20.64 for T_{Lt}<100^0C L_1=-4.38E-02, L_2=14.32 for T_{Lt}>100^0C	
Equiv. Damp. Ratio for Estimating Rubber Contribution to EDC (β)	0.03	
Yield Displacement (Y)	30 mm	
Thermal Properties of Rubber, Steel and Lead	Per Table 8-10	
Thermal Properties of Rubber Layer and Steel Shim Composite	Heat Capacity, ρc ($\frac{J}{m^{3} \cdot {}^{0}C}$)	2714880
	Radial Conductivity, $k_{eff,radial}$ ($\frac{W}{m \cdot {}^{0}C}$)	18.9
	Vertical Conductivity, $k_{eff,vert}$ ($\frac{W}{m \cdot {}^{0}C}$)	0.26
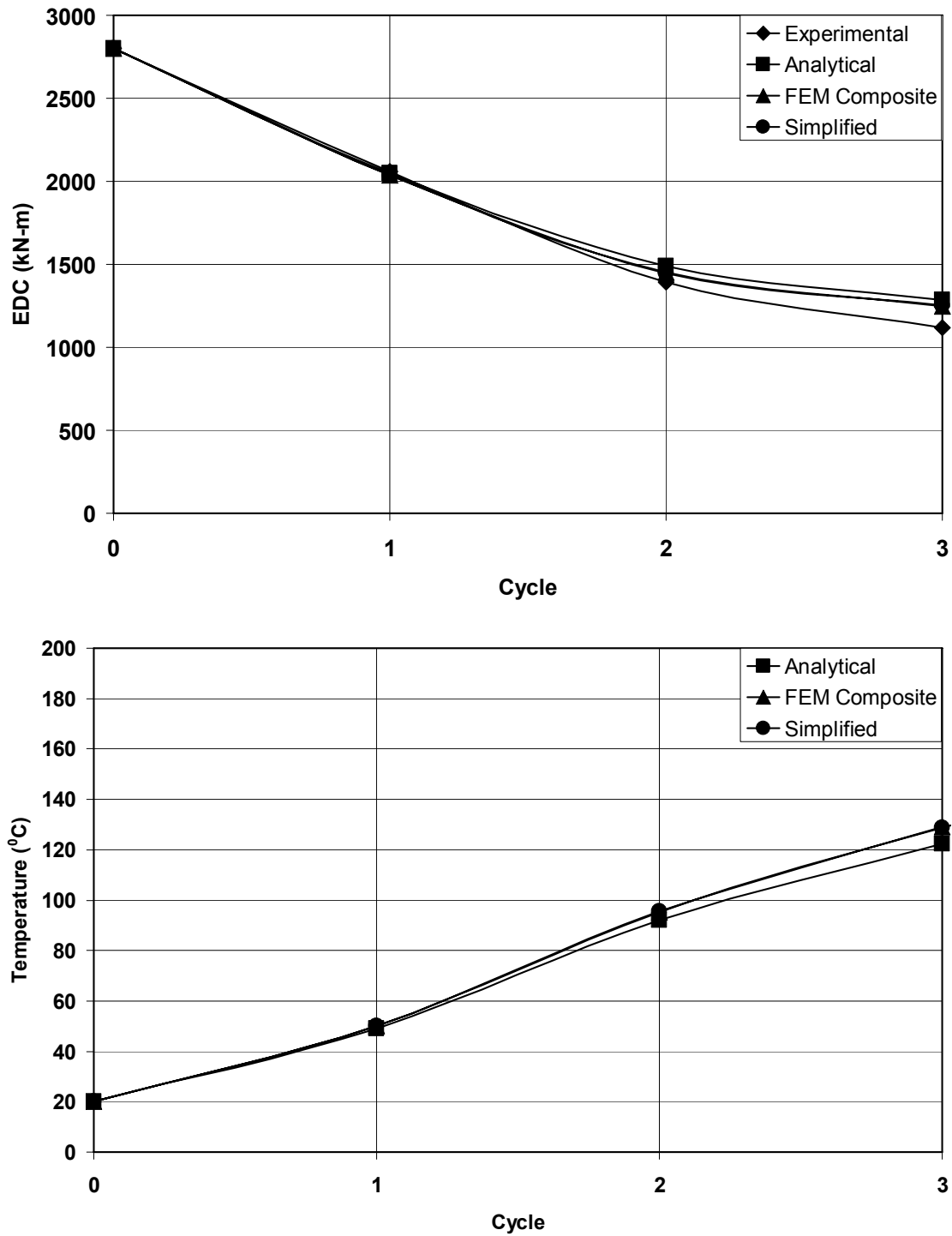
FIGURE 8-46 Temperature and Energy Dissipated per Cycle Histories for Example 6

288

8.8.7 Example 7

Example 7 is the small scale bearing of Figure 8-47. The bearing was tested under compressive load of 68kN and 10 cycles of lateral harmonic motion of 57mm displacement amplitude (rubber shear strain of 100%) at frequency of 1.0Hz. Data used for analysis are presented in Table 8-17. The calculated histories of temperature and EDC are presented in Figure 8-48 where the EDC is also compared to the experimental results. Evidently, the analytical and finite element predictions are very good, whereas the prediction of EDC by the simplified method deteriorates as the number of cycle increases due to overprediction of temperature as a result of neglect of heat conduction.
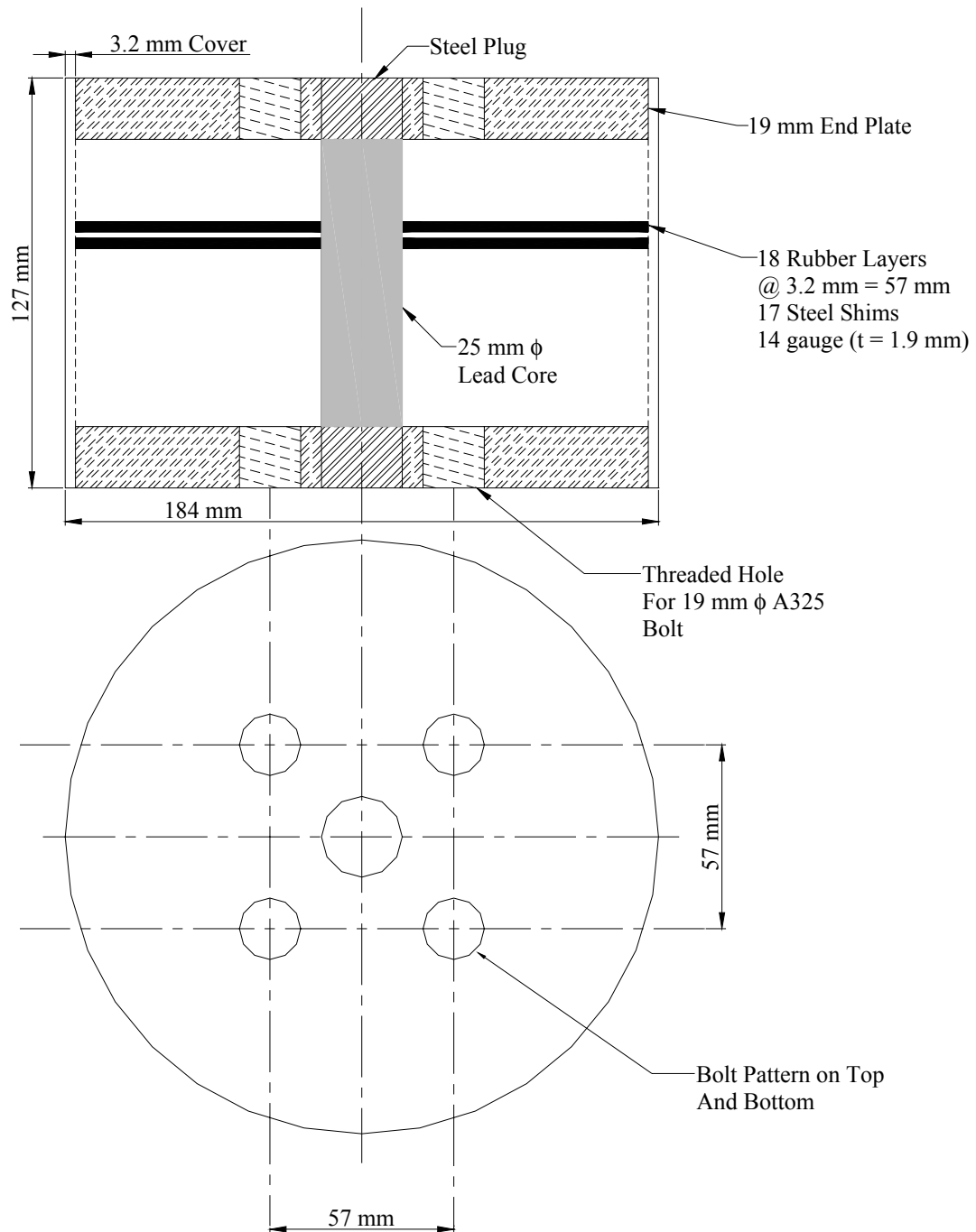
FIGURE 8-47 Tested Small Scale Lead-Rubber Bearing

TABLE 8-17 Data Used in Analysis of Example 7

Amplitude of Sinusoidal Motion, u_0	57 mm	
Period of Sinusoidal Motion, T	1.0 sec	
Peak Velocity of Sinusoidal Motion, v_{max}	358 mm/s	
Initial (Reference) Lead Effective Yield Stress (σ_{YL0})	13.3 MPa	
Initial Temperature, T_{L0}	20^0C	
Parameters of Bilinear Relation of σ_{YL} vs. Temperature	L_1=-1.08E-01, L_2=20.64 for T_{Lt}<100^{0}C L_1=-4.38E-02, L_2=14.32 for T_{Lt}>100^{0}C	
Equiv. Damp. Ratio for Estimating Rubber Contribution to EDC (β)	0.05	
Yield Displacement (Y)	5 mm	
Thermal Properties of Rubber, Steel and Lead	Per Table 8-10	
Thermal Properties of Rubber Layer and Steel Shim Composite	Heat Capacity, ρc ($\frac{J}{m^{3} \cdot {}^0 C}$)	2693596
	Radial Conductivity, $k_{eff,radial}$ ($\frac{W}{m \cdot {}^0 C}$)	18.1
	Vertical Conductivity, $k_{eff,vert}$ ($\frac{W}{m \cdot {}^0 C}$)	0.25

FIGURE 8-48 Temperature and Energy Dissipated per Cycle Histories for Example 7

8.8.6.8 Example 8

Example 8 is the small scale bearing of Figure 8-47 that was used for example 7. For example 8 the bearing was tested at the same compressive load of 68 kN as example 7 and for 10 cycles of 114mm displacement amplitude (rubber shear strain of 200%) at 0.5 Hz frequency. While the peak velocity (358mm/sec) is the same in examples 7 and 8, theory predicts more temperature increase in the larger amplitude test.

Data used in the analysis are presented in Table 8-18 and Figure 8-49 presents the calculated histories of temperature and EDC. The comparison of results demonstrates very good prediction of EDC history by the analytical and finite element methods but substantial underprediction of EDC by the simplified method.

TABLE 8-18 Data Used in Analysis of Example 8

Amplitude of Sinusoidal Motion, u_0	114 mm	
Period of Sinusoidal Motion, T	2.0 sec	
Peak Velocity of Sinusoidal Motion, v_{max}	358 mm/s	
Initial (Reference) Lead Effective Yield Stress (σ_{YL0})	13.5 MPa	
Initial Temperature, T_{L0}	20^0C	
Parameters of Bilinear Relation of σ_{YL} vs. Temperature	L_1=-1.08E-01, L_2=20.64 for T_{Lt}<100^{0}C L_1=-4.38E-02, L_2=14.32 for T_{Lt}>100^{0}C	
Equiv. Damp. Ratio for Estimating Rubber Contribution to EDC (β)	0.05	
Yield Displacement (Y)	5 mm	
Thermal Properties of Rubber, Steel and Lead	Per Table 8-10	
Thermal Properties of Rubber Layer and Steel Shim Composite	Heat Capacity, ρc ($\frac{J}{m^{3} \cdot ^0 C}$)	2693596
	Radial Conductivity, $k_{eff,radial}$ ($\frac{W}{m \cdot ^0 C}$)	18.1
	Vertical Conductivity, $k_{eff,vert}$ ($\frac{W}{m \cdot ^0 C}$)	0.25

FIGURE 8-49 Temperature and Energy Dissipated per Cycle Histories for Example 8

8.8.7 Concluding Remarks on Heating of Lead Rubber Bearings

A theory has been presented that is capable of predicting the temperature rise of the lead core and the associated reduction in characteristic strength and energy dissipation per cycle (EDC) of lead-rubber bearings. The theory includes a simplified case in which an explicit closed-form solution was derived. The closed-form solution is useful in engineering calculations. It is accurate when testing is at realistic high speed motion and provided the number of cycles is less than about 10. The analytic solution developed can also be applied in cases of random bidirectional motion, provided that the amplitude is much larger than the yield displacement of the bearing.

The validity of the theory and its basic assumptions have been confirmed by limited finite element analyses. Both the analytic solution (including the simplified, closed-form solution) and the finite element analysis predicted well the energy dissipated per cycle in most cases where experimental results were available. On the basis of the presented analysis results, it is concluded that testing at quasi-static conditions (as often done due to limited availability of high speed testing machines), results in a lesser increase in the lead core temperature and in a lesser reduction of EDC.

SECTION 9
ANALYSIS AND DESIGN OF ELASTOMERIC BEARINGS

9.1 Introduction

Elastomeric bearings consist of alternate layers of rubber and steel shims so that the composite unit exhibits large vertical stiffness and low horizontal stiffness. Figure 9-1 illustrates this characteristic of elastomeric bearings. The large vertical stiffness prevents undesirable rocking response of an isolated structure, reduces shear strain in the rubber, reduces creep deformations in the rubber and increases the capacity of the bearings to carry axial load at large displacements.
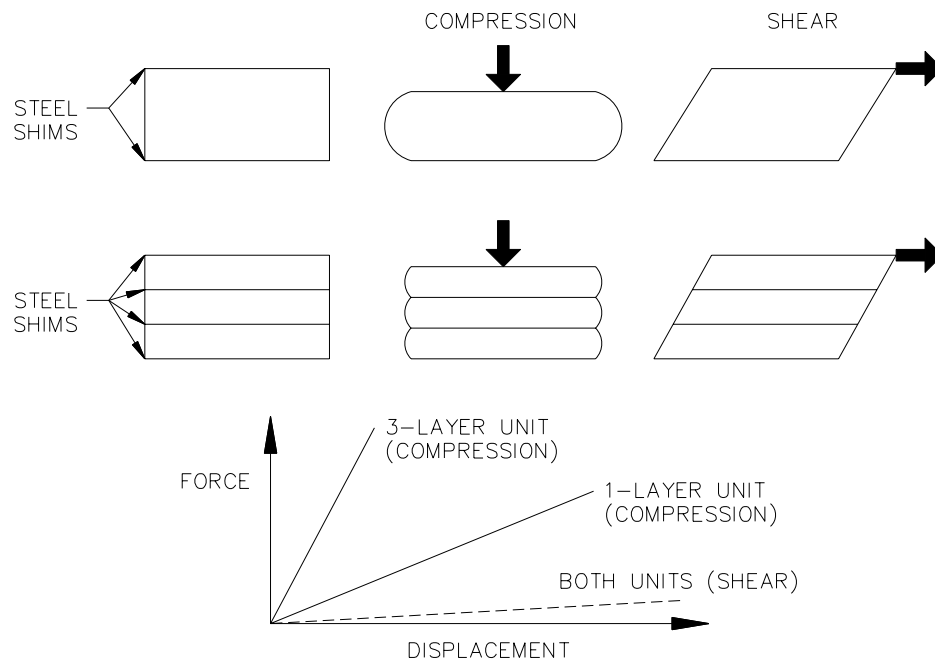
FIGURE 9-1 Behavior of Elastomeric Bearings in Compression and Shear

This section of the report presents a summary of the analysis and design of elastomeric bearings. Two excellent sources of information on the mechanics of elastomeric bearings are Stanton and Roeder (1982) and Kelly (1993).

9.2 Analysis of Compression of Elastomeric Bearings

Elastomeric bearings subjected to compression exhibit nonlinear stiffening behavior as shown in Figure 7-12. An analytical description of this behavior is very complex and not amenable to closed form solution that is useful for engineering calculations. Solutions were developed assuming linear elastic behavior and infinitesimal strains. Only one exact solution is known under these conditions, which applies to cylindrical bonded rubber

297

layers (Moghe and Neft, 1971). The solution for the compression stiffness of the cylinder is presented in terms of an infinite series of Bessel functions.

Approximate solutions were developed that assume either incompressible or nearly incompressible material behavior. Although approximate, these solutions are simple enough for use in engineering calculations and provide insight into the behavior of elastomeric bearings. The basic problem treated in these solutions is the compression of a single bonded rubber layer. Figure 9-2 shows the geometry of bonded layers of various shapes and the notation for dimensions used in these solutions. The dimensions shown this figure are bonded dimensions. Actual elastomeric bearings have cover rubber that has a small effect on the behavior, which is neglected in the solutions presented herein. Also, the hollow cylindrical bearing represents a case in which rubber is allowed to bulge freely on the inside and outside surfaces. It applies to bearings that have a central hole used in the manufacturing process to allow for uniform heating but does not apply to lead-rubber bearings in which the central hole is filled with lead. Figure 9-3 illustrates the compression of a single constrained rubber layer by load P and the resulting distributions of shear strain and compressive stress along a cross-section at mid-height of the layer. The layer deforms vertically by an amount Δ_c and bulges by u_0. The distribution of shear strain is nearly linear with the theory predicting a linear distribution with a maximum value of γ_c. The compressive stress distribution is nearly parabolic with a maximum value of p_{max}.
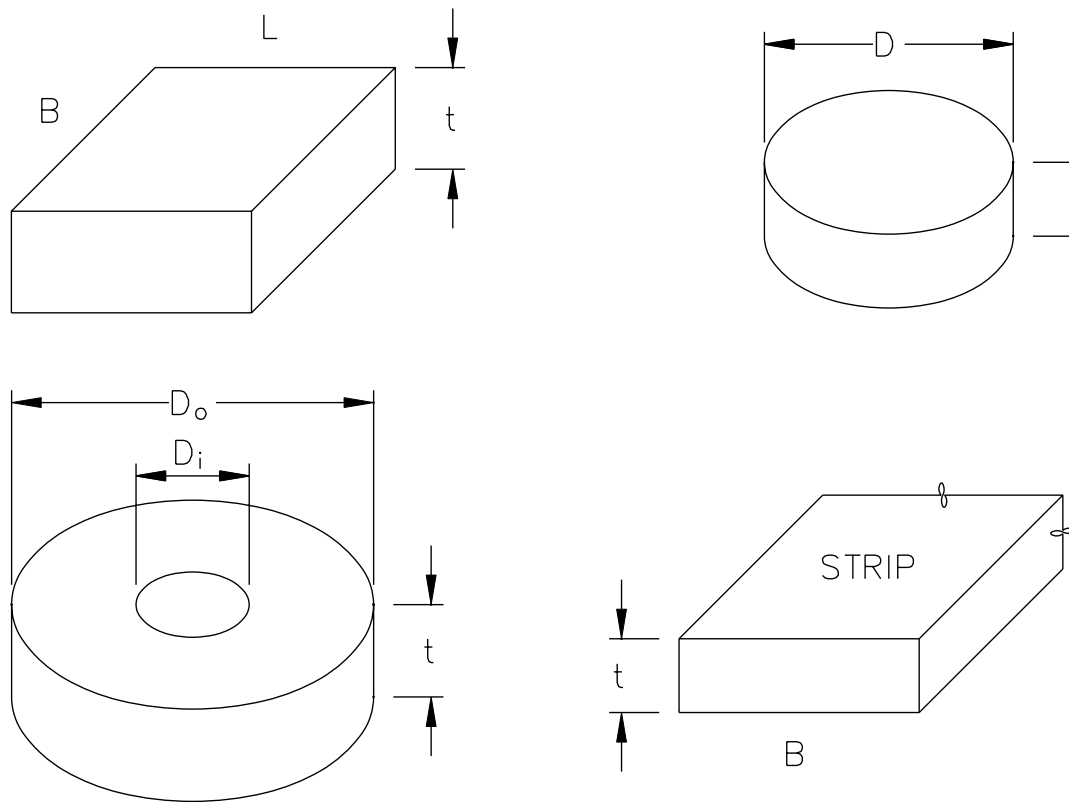
FIGURE 9-2 Dimensions of Single Rubber Layers
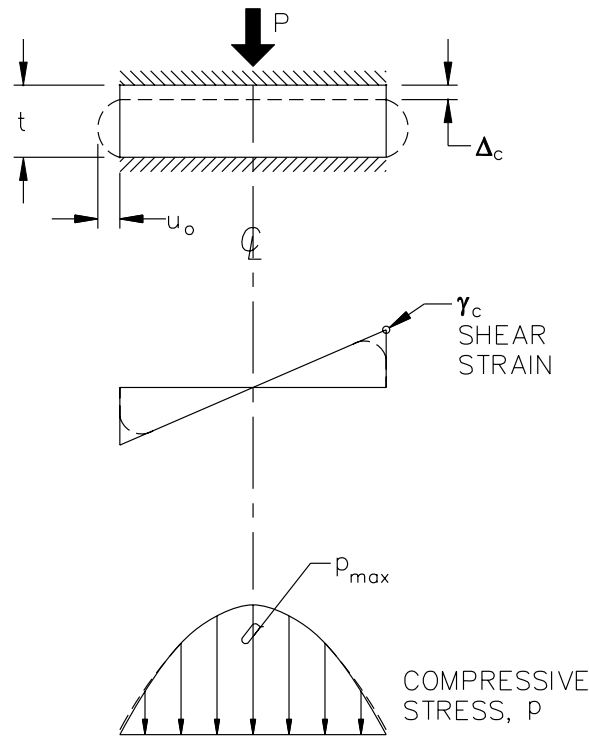
FIGURE 9-3 Compression of a Single Constrained Rubber Layer

Two approximate solutions have been developed for compression of elastomeric bearings. The first solution, developed by Gent and Lindley (1959), assumes

a) rubber is incompressible
b) the rubber layer is unconstrained (contact at top and bottom surfaces is frictionless) so that on compression by load P it uniformly deforms vertically and expands laterally
c) the top and bottom surfaces are subjected to shear tractions and additional vertical load so that the lateral deformations at the top and bottom surfaces are zero and the vertical displacement remains the same as in (b)
d) compressibility of rubber is accounted for in an empirical way by introducing the bulk modulus, K, and a correction factor, $\bar{k}$, based on experimental results

The second solution is based on the seminal work of Conversy (1967), which was developed further for different shapes (Chalhoub and Kelly, 1990; Constantinou et al., 1992), and assumes

a) all normal stresses are equal at any point within the constrained layer (thus the solution is often termed the *pressure solution*)
b) shear stresses in the horizontal plane are zero ($\tau_{xy} = 0$ where z is the vertical axis)
c) all normal stresses are equal to zero on the free lateral surfaces

299

d) points lying on a vertical line in the unstrained material lie on a parabola after deformation

These assumptions lead to solutions that involve only the shear modulus, G, and bulk modulus, K, and the geometric properties of the layer. The shape factor, S, is a geometric parameter that is very important and is defined as the area of rubber that is loaded, divided by the area of rubber that is free to bulge. For the shapes shown in Figure 9-2, the shape factor is given by the following equations:

Rectangular bearing

$$S = \frac{BL}{2(B+L)t} \tag{9-1}$$

Square bearing

$$S = \frac{B}{4t} \tag{9-2}$$

Strip bearing

$$S = \frac{B}{2t} \tag{9-3}$$

Circular bearing

$$S = \frac{D}{4t} \tag{9-4}$$

Circular hollow bearing

$$S = \frac{D_o - D_i}{4t} \tag{9-5}$$

Table 9-1 presents results for the parameters of maximum shear strain, γ_c, maximum compressive strain, p_{max}, and the compression modulus E_c, which is used to calculate the vertical stiffness and is given by

$$E_c = \frac{Pt}{A\Delta_c} \tag{9-6}$$

where A is the bonded rubber area, t is the rubber layer thickness and Δ_c is the vertical displacement of the layer. Another parameter in these solutions is the imposed vertical strain ε_c given by (9-7).

$$\varepsilon_c = \frac{\Delta_c}{t} \qquad (9\text{-}7)$$

TABLE 9-1   Expressions for Compression Modulus, Shear Strain and Maximum Compressive Stress in a Constrained Rubber Layer in Compression

Parameter	Compression Modulus for Incompress. Material E_c	Compression Modulus for Compressible Material $E_c^{'}$	Compression Modulus for Compressible Material and Large Bulk Modulus $E_c^{'}$	Shear Strain for Incompress. Material γ_c	Maximum Compressive Stress for Incompress. Material p_{max}
Strip bearing, pressure solution[1]	$4GS^2$	Infinite series solution (see Stanton and Roeder, 1982; Kartoum, 1987)	NA	$4.5S\varepsilon_c =$ $1.1\dfrac{P}{AGS}$	$1.5\dfrac{P}{A}$
Square bearing, pressure solution	$6.75GS^2$	Infinite series solution (see Stanton and Roeder, 1982; Kartoum, 1987)	NA	$5.1S\varepsilon_c =$ $0.76\dfrac{P}{AGS}$	$2.1\dfrac{P}{A}$
Circular bearing, pressure solution	$6GS^2$	Bessel function solution (see Chalhoub and Kelly, 1990; Constantinou et al., 1992)	$\left(\dfrac{1}{6GS^2}+\dfrac{4}{3K}\right)^{-1}$	$6S\varepsilon_c =$ $\dfrac{P}{AGS}$	$2\dfrac{P}{A}$
Circular hollow bearing, pressure solution[2]	$6GS^2F$	Bessel function solution (see Constantinou et al., 1992)	$\left(\dfrac{1}{6GS^2F}+\dfrac{4}{3K}\right)^{-1}$	$6S\varepsilon_c f$	NA
Strip bearing, Gent/Lindley Solution	$\dfrac{4}{3}E(1+\bar{k}S^2)$	NA	$\left(\dfrac{3}{4E(1+\bar{k}S^2)}+\dfrac{1}{K}\right)^{-1}$	$6S\varepsilon_c$	$1.5\dfrac{P}{A}$
Circular bearing, Gent/Lindley solution	$E(1+2\bar{k}S^2)$	NA	$\left(\dfrac{1}{E(1+2\bar{k}S^2)}+\dfrac{1}{K}\right)^{-1}$	$6S\varepsilon_c$	$2\dfrac{P}{A}$

1. $\varepsilon_c = \dfrac{P}{AE_c}$, 2. $F = \dfrac{(\frac{D_o}{D_i})^2+1}{(\frac{D_o}{D_i}-1)^2}+\dfrac{1+\frac{D_o}{D_i}}{(1-\frac{D_o}{D_i})\ln(\frac{D_o}{D_i})}$, 3. $f = \dfrac{(\frac{D_o}{D_i})^2-\ln(\frac{D_o}{D_i})^2-1}{(\frac{D_o}{D_i}-1)\ln(\frac{D_o}{D_i})^2} \approx 1.0+0.13(\dfrac{D_o}{D_i})$,

Note that the pressure and Gent/Lindley solutions result in expressions for the compression modulus that include the shear modulus, G, and the modulus of elasticity, E. For elastic, isotropic material that is nearly incompressible (as assumed for this analysis), $E = 3G$. However, measurements of the two moduli indicate deviation from isotropy so that for the common rubber materials used in elastomeric bearings, $E \approx 4G$.

The expressions for the compression modulus when accounting for compressibility, E_c', is useful in calculating the vertical stiffness of elastomeric bearings. The correction for compressibility is actually very important for this calculation. The correction for compressibility introduced in the Gent/Lindley solution is arbitrary and not based on rational mechanics. This required correction using factor $\bar{k}$ that originally appeared in the British BE 1/76 (United Kingdom Highways Directorate, 1976) and is still used in the AASHTO Guide Specifications for Seismic Isolation Design (AASHTO, 1999). All reference to this factor has been removed from the AASHTO Standard Specifications and AASHTO LRFD Specifications (AASHTO, 2002; 2004). Values of the factor depend on the rubber hardness and are presented in Table 9-2. The correction for compressibility introduced through the pressure solution is mathematically rigorous and its accuracy has been confirmed by comparison to experimental results (e.g., Kasalanati and Constantinou, 1999 and 2005; Chalhoub and Kelly, 1990).

TABLE 9-2 Values of Correction Factor $\bar{k}$

Rubber Hardness (Shore A)	50	60	70
$\bar{k}$	0.75	0.6	0.55

The solutions for the maximum shear strain and the maximum compressive stress are valid for an incompressible material. Although solutions exist for compressible materials, the solutions for incompressible materials are always conservative (see Constantinou et al., 1992) and are significantly simpler for use in engineering calculations.

9.3 Analysis of Rotation of Elastomeric Bearings

Similar to the analysis of compression, approximate analysis of rotation of elastomeric bearings on the basis of the pressure solution and the Gent/Meinecke solution (see Gent and Meinecke, 1970 for application of the Gent/Lindley approach to the problem of rotation) has been performed (e.g., Stanton and Roeder, 1982; Kartoum, 1987; Chalhoub and Kelly, 1990). Figure 9-4 shows a constrained layer of rubber subjected to rotation due to moment M. The resulting shear strains at mid-height and the vertical stress distribution are shown in the figure. Of interest in the analysis of rotation is the calculation of the maximum shear strain γ_r and rotation modulus E_r, which is defined as follows:

$$E_r = \frac{Mt}{I\theta} \tag{9-8}$$

where θ is the angle of rotation and I is the moment of inertia about the axis of rotation. Knowledge of the rotation modulus allows for calculation of the rotational stiffness of a layer which is needed in the analysis of stability of elastomeric bearings.
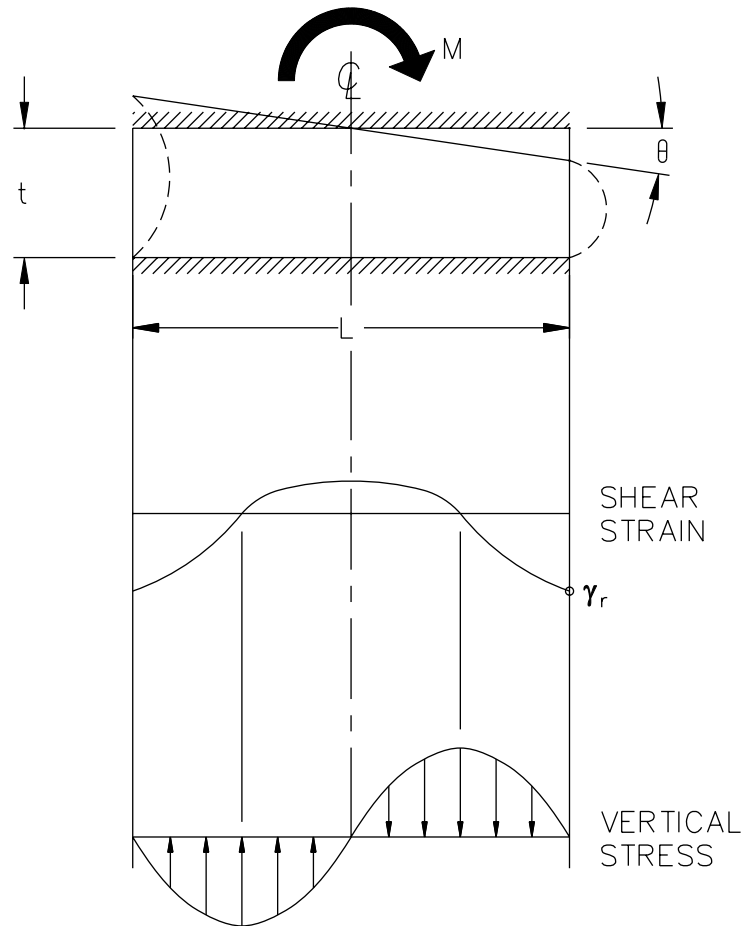
FIGURE 9-4 Rotation of Single Constrained Rubber Layer

Table 9-3 presents results for the parameters of maximum shear strain γ_r and the rotation modulus E_r derived on the basis of the two approximate analysis approaches. It is of interest to compare the results in Tables 9-1 and 9-3 for the compression and rotation moduli for an incompressible material of circular and square bearings (the typical cases in seismic isolation) for which

$$E_r = \frac{E_c}{3} \qquad (9\text{-}9)$$

9.4 Analysis of Shear of Elastomeric Bearings

Elastomeric seismic isolation bearings are typically constructed with large shape factor (i.e., 10 or larger) so that on lateral deformation, the rubber is subjected to primarily shear in its bulk. Accordingly, the shear strain in the rubber, γ_s, is calculated as

$$\gamma_s = \frac{\Delta_s}{t} \tag{9-10}$$

where Δ_s is the lateral deformation of the rubber layer of thickness t.

TABLE 9-3 Expressions for Rotation Modulus and Shear Strain in Constrained Rubber Layer in Rotation

Parameter	Rotation Modulus for Incompressible Material E_r	Rotation Modulus for Compressible Material E_r'	Shear Strain for Incompressible Material γ_r
Strip bearing, pressure solution	$0.8GS^2$	Infinite series solution (see Stanton and Roeder, 1982; Kartoum, 1987)	$2S^2\theta = \frac{L^2\theta}{2t^2}$
Square bearing, pressure solution	$2.23GS^2$	Infinite series solution (see Stanton and Roeder, 1982; Kartoum, 1987)	$7.6S^2\theta = \frac{0.474L^2\theta}{t^2}$
Circular bearing, pressure solution	$2GS^2$	Bessel function solution (see Chalhoub and Kelly, 1990)	NA
Strip bearing, Gent/Meinecke solution	$E(\frac{4}{3}+\frac{S^2}{4})$	NA	NA
Square bearing, Gent/Meinecke solution	$E(1+0.742S^2)$	NA	NA
Circular bearing, Gent/Meinecke solution	$E(1+\frac{2}{3}S^2)$	NA	NA

9.5 Torsion of Elastomeric Bearings

Torsional rotations are typically very small and can be estimated using the simplified procedures set forth in specifications such as the California Building Code (California Buildings Standards Commission, 2001):

$$\phi \approx \frac{12eD}{b^2 + d^2} \tag{9-11}$$

where e is eccentricity between the center of resistance of the isolation system and the center of mass, D is the displacement of the isolation system at its center of resistance and b and d are the plan dimensions of the structure. On the basis of (9-11), rotations are of the order of 0.01 rad. The maximum shear strain in a circular bearings is

$$\gamma = \phi \cdot \frac{r}{h} \tag{9-12}$$

where r is the radius of bearing and h is the height of bearing. Since r is typically equal to or just greater than h, the maximum shear strain is of the order of 0.01 and thus insignificant. In general, the torsional resistance of individual bearings and the stresses and strains resulting from torsion are insignificant and can be neglected in analysis.

9.6 Analysis of Multilayer Elastomeric Bearings

The analysis of elastomeric bearings presented in Sections 9.2 to 9.4 applies to single layers of constrained rubber. Multilayer rubber bearings consist of many layers of alternating rubber and steel. Figure 9-5 illustrates the deformation of multilayer elastomeric bearings in the three basic modes of deformation: compression, shear and rotation.
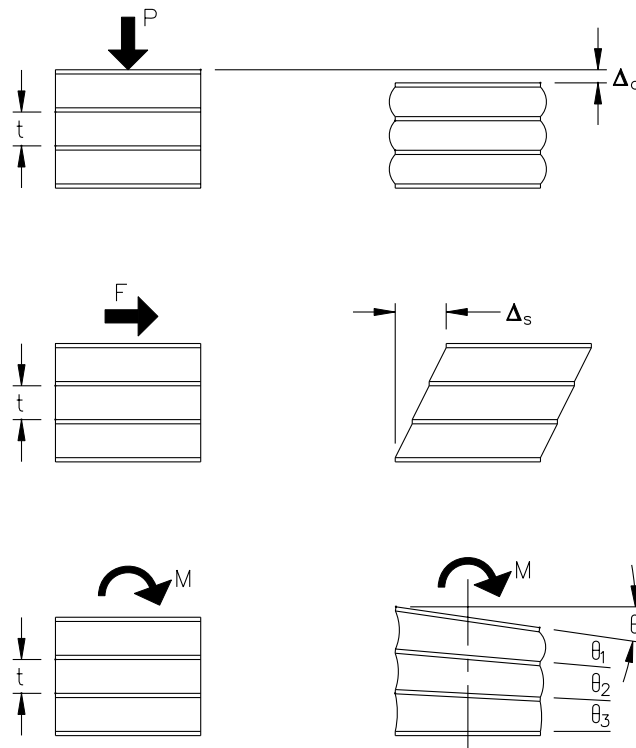
FIGURE 9-5 Deformation of Multilayer Elastomeric Bearings

305

The deformations induced in each layer of rubber are additive so that the total deformation is the sum of the deformations in each layer (i.e., $\theta = \theta_1 + \theta_2 + \theta_3$). The equations presented in Tables 9-1 and 9-3 for shear strain due to compression and rotation are valid for multilayered bearings. They are presented below following manipulation for incompressible material behavior–which leads to conservative (large) estimates of strains.

For compression of circular and square bearings:

$$\gamma_c = \frac{P}{AGS} \tag{9-13}$$

This equation applies to circular bearings and is slightly conservative for square bearings.

For compression of circular hollow bearings:

$$\gamma_c = \frac{P}{AGS}\left(\frac{f}{F}\right) \tag{9-14}$$

where f and F are defined in the footer to Table 9-1.

For rotation of circular and square bearings:

$$\gamma_r = \frac{B^2\theta}{2tT_r} \tag{9-15}$$

where T_r is the total rubber thickness (sum of thicknesses of rubber layers). Note that equation (9-15) applies to square bearings but is generally used for all bearing shapes.

The equation for the shear strain due to lateral deformation needs to be modified to:

$$\gamma_s = \frac{\Delta_s}{T_r} \tag{9-16}$$

The vertical stiffness of multilayer bearings in compression is given by

$$K_v = A\left\{\sum_i t_i\left[\frac{1}{E_{ci}} + \frac{4}{3K}\right]\right\}^{-1} \tag{9-17}$$

In this equation, t_i is the thickness and E_{ci} is the compression modulus for incompressible material behavior of the ith rubber layer. The summation in (9-17) extends over all rubber layers. We prefer the compressibility correction based on the pressure approach. The bulk modulus in (9-17) is typically assumed to be $K = 2000$ MPa (290 ksi).

306

9.7 Stability of Elastomeric Bearings

Elastomeric bearings must be checked for instability in both the undeformed and deformed configurations.

Elastomeric bearings can be installed either a) dowelled or recessed in keeper plates or b) bolted. Figure 9-6 shows construction details and deformational characteristics of the two installations. In the undeformed state, when loaded only by vertical force, the buckling load of bearings installed in either configuration is theoretically the same. Under combined vertical load and lateral deformation, the two bearings have different instability limits.
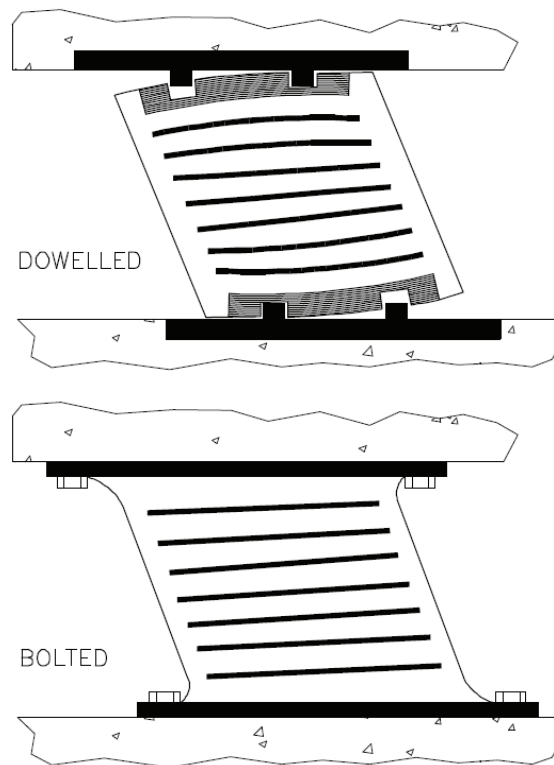
FIGURE 9-6 Characteristics of Dowelled and Bolted Elastomeric Bearings

Elastomeric bearings are treated as slender columns with shear flexibility for the calculation of the buckling load. Timoshenko and Gere (1961) presented a well documented theory of buckling of columns accounting for shear deformations. However, the original treatment of this problem was presented in Haringx (1948). The first treatment of the effect of shear deformations on buckling of columns appears to have been derived by F. Engesser (1891). Gent (1964) was the first to recognize the application of the Haringx theory to reinforced elastomeric bearings. Stanton and Roeder (1982), Roeder et al. (1987), Kelly (1993) and Naiem and Kelly (1999) also presented this theory with the key product being the buckling load of a column

307

$$P_{cr} = \frac{\sqrt{G^2 A_s^2 + 4GA_s P_E} - GA_s}{2} \tag{9-18}$$

where P_E is the Euler buckling load, G is the shear modulus and A_s is the shear area. The Euler load for a column with fixed ends that is allowed to translate is

$$P_E = \frac{\pi^2 E I_s}{h^2} \tag{9-19}$$

where E is the modulus of elasticity, I_s is the moment of inertia about the axis of buckling and h is the length of the column. The application of (9-18) and (9-19) to elastomeric bearings requires interpretation of the various parameters in these equations. Kelly (1993) suggests the following:

(a) Elastomeric bearings are composites of rubber and steel, in which the steel shims do not deform in shear but their height contributes to the slenderness of the bearing. To account for this, the length h must the total height of rubber and steel shims and the area and moment of inertia must be modified as follows:

$$A_s = A \frac{h}{T_r} \tag{9-20}$$

$$I_s = I \frac{h}{T_r} \tag{9-21}$$

where A and I are the area and moment of inertia of the bonded rubber area, T_r is the total rubber thickness and h is the bearing height, including the rubber and the shims but excluding the end plates.

(b) The modulus of elasticity must be interpreted as the rotation modulus,

$$E = E_r \tag{9-22}$$

For large shape factors ($S \geq 5$), $P_E \gg GA_s$ and (9-18) simplifies to

$$P_{cr} = \sqrt{P_E GA_s} = \pi \sqrt{E_r GIA} / T_r \tag{9-23}$$

On the basis of this theory, the following simplified equations may be used to calculate the critical load P_{cr} in the undeformed state. For *circular* bearings of diameter, B, rubber layer thickness, t and total rubber thickness, T_r, the buckling load is :

$$P_{cr} = 0.218 \frac{GB^4}{tT_r} \tag{9-24}$$

where $E_r = 2GS^2$ was used. For *square* bearings of plan dimensions B by B, the buckling load is

$$P_{cr} = 0.340 \frac{GB^4}{tT_r} \qquad (9\text{-}25)$$

where $E_r = 2.25GS^2$ was used. During large lateral deformation, dowelled bearings and bearings recessed in keeper plates experience partial uplift. At some critical lateral displacement, D_{cr}, the bearings roll-over or overturn. Roll-over is illustrated in Figure 9-7. At the initiation of overturning, the point of application of the vertical load P reaches the edge of the bearing. The figure also shows the bearing lateral force-displacement relationships that are used to calculate the critical displacement. The first is linear elastic that is commonly used to represent the behavior of bearings in terms of the effective stiffness K_{eff}. The second is bilinear hysteretic with stiffening at large displacements.
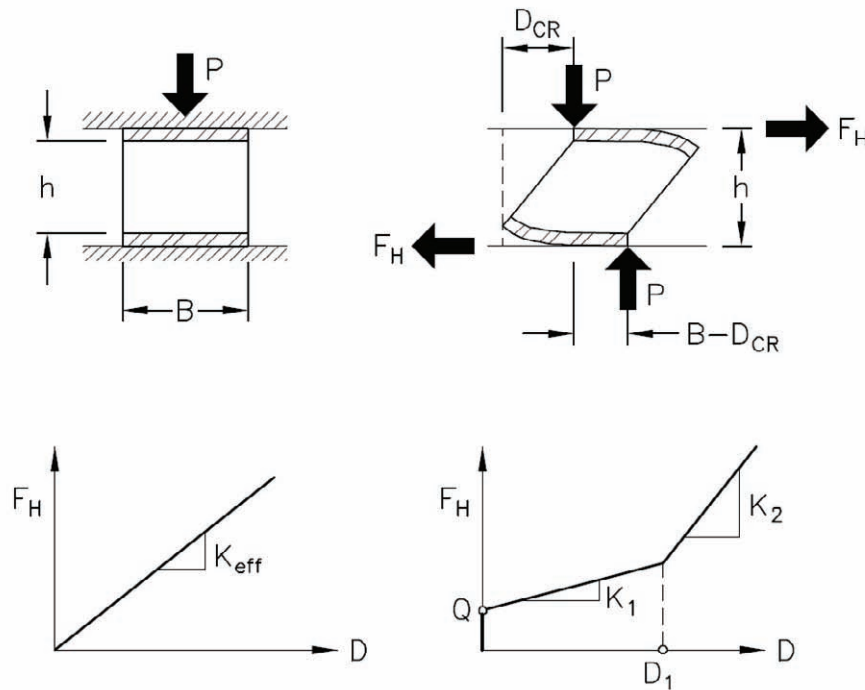
FIGURE 9-7 Overturning of Dowelled Bearing and Lateral Force-Displacement Relationships

The critical displacement is calculated from equilibrium:

$$F_H h = P(B - D_{cr}) \qquad (9\text{-}26)$$

where F_H is the lateral force acting on the bearing, P is the axial load on the bearing and B is the plan dimension (e.g., diameter or square bearing dimension). For the linear force-displacement relationship of Figure 9-7:

309

$$F_H = K_{eff}D \tag{9-27}$$

and

$$D_{cr} = \frac{PB}{K_{eff}h + P} \tag{9-28}$$

For the bilinear hysteretic representation in which the bearing is characterized by the characteristic strength Q and the post-elastic stiffness K_1,

$$F_H = Q + K_1 D \tag{9-29}$$

and

$$D_{cr} = \frac{PB - Qh}{K_1 h + P} \tag{9-30}$$

For the bilinear hysteretic representation with stiffening in which the bearing is characterized by the characteristic strength Q, the post-elastic stiffness K_1 and stiffness K_2 at displacements greater than D_1,

$$F_H = Q + K_1 D_1 + K_2(D - D_1) \text{ for } D \geq D_1 \tag{9-31}$$

and

$$D_{cr} = \frac{PB - Qh + (K_2 - K_1)D_1 h}{K_2 h + P} \tag{9-32}$$

Equation (9-32) is valid when the critical displacement is larger than the limit, else (9-30) must be used.

There is no satisfactory simple rational theory to predict the behavior of bolted elastomeric bearings at large lateral deformations. However, the following equation has been shown to produce conservative results (Buckle and Liu, 1994; Buckle et al., 2002; Warn, 2006) :

$$P'_{cr} = P_{cr} \frac{A_r}{A} \tag{9-33}$$

where P'_{cr} is the buckling load in deformed state, A is the bonded area and A_r is the reduced bonded area defined as the overlap between the top and bottom bonded elastomer areas of the deformed bearing. Buckle et al. (1994, 2002) and Warn (2006) have shown that (9-33) under-predicts the buckling load for values of $A_r / A \leq 0.2$ for which experiments showed bearings maintaining a significant capacity to resist axial load with increasing lateral deformation. Nagarajaiah and Ferrell (1999) produced analytical

310

results based on nonlinear material behavior that better approximated the experimental results.

Figure 9-8 illustrates the reduced (overlap) area for rectangular and circular bearings. The reduced area for lateral bearing displacement D is given by the following equations: For rectangular bearings of bonded rubber dimensions B_1 by B_2:

$$A_r = B_2(B_1 - D) \tag{9-34}$$

For circular bearings of diameter B:

$$A_r = \frac{B^2}{4}(\delta - \sin\delta) \tag{9-35}$$

where

$$\delta = 2\cos^{-1}(\frac{D}{B}) \tag{9-36}$$
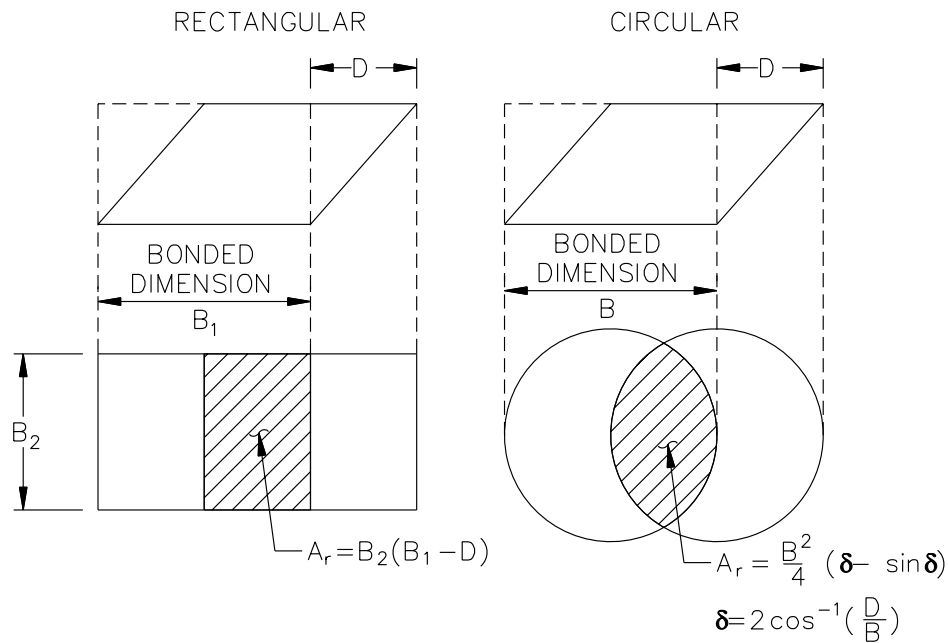
FIGURE 9-8 Reduced Area of Elastomeric Bearings

9.8 Reduction of Height upon Lateral Displacement and Effect on Vertical and Lateral Stiffness

Upon lateral displacement, elastomeric bearings shorten. Although the reduction in height is small, it can be important if the isolation system is composed of bearings with varying vertical stiffness, for example, in a hybrid elastomeric-sliding isolation system.

311

Koh and Kelly (1987) and Kelly (1993) present both a simple physical model and an exact solution that describes the reduction in height of an elastomeric bearing upon lateral displacement. The physical model provides information on the post-buckling behavior of a bearing and the effect of axial load on mechanical damping.

The physical model of Koh and Kelly is presented in Figure 9-9. It consists of a rigid column of height h that equals to the height of the bearing (the total thickness of the rubber and the steel shims). The column a rotational spring of constant K_1 at its base and a shear spring of constant K_2. Constant K_2 is established by assuming that K_1 equals infinity so that the bearing has only shear stiffness:

$$K_2 = \frac{GA}{T_r} = \frac{GA_s}{h} \tag{9-37}$$

where A_s is given by (9-20). If K_1 equals infinity, the buckling load of the column with the rotational spring only is K_1/h so that constant K_1 is given by

$$K_1 = P_E h \tag{9-38}$$

where P_E is the Euler buckling load given by (9-19).

Equilibrium of forces in the direction of displacement s and of moments about point O in Figure 9-9, for small values of rotation θ, gives

$$P\theta + F_H - K_2 s = 0 \tag{9-39}$$

$$P(s + \theta h) + F_H h - K_1 \theta = 0 \tag{9-40}$$

Solution of these equations results in expressions for the rotation θ and shear deformation, s as follows:

$$\theta = \frac{F_H}{GA_s} \frac{GA_s + P}{P_E - P(1 + \frac{P}{GA_s})} \tag{9-41}$$

$$\frac{s}{h} = \frac{F_H}{GA_s} \frac{P_E}{P_E - P(1 + \frac{P}{GA_s})} \tag{9-42}$$

The horizontal stiffness of the bearing including the effect of the vertical load, K_H^*, and the vertical displacement of the bearing, v, are:

$$K_H^* = \frac{F_H}{u} = \frac{F_H}{s + \theta h} \tag{9-43}$$

312

$$v = s\theta + h\frac{\theta^2}{2} \tag{9-44}$$

where u is the lateral displacement of the bearing.
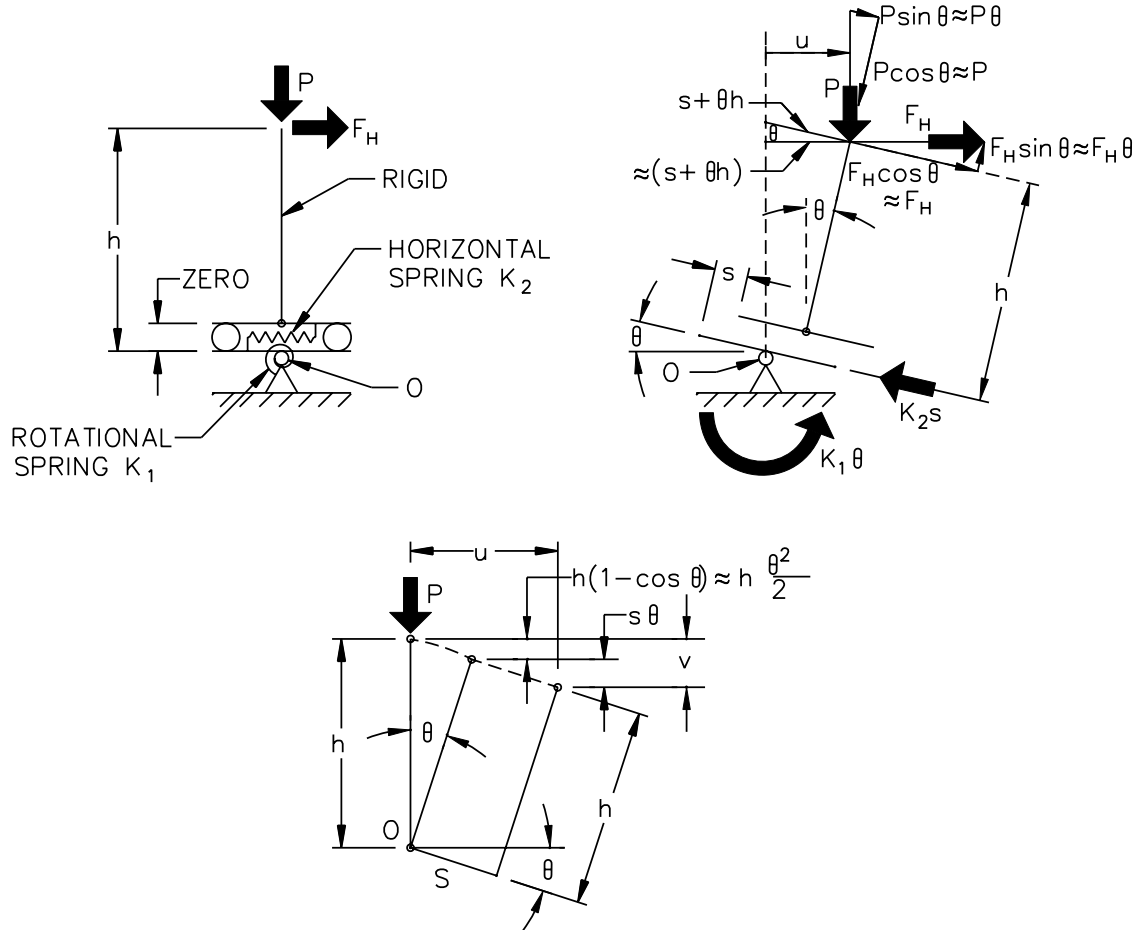
FIGURE 9-9 Simple Physical Model of Elastomeric Bearing and Equilibrium and Geometry in Deformed State

Assuming that $P_E \gg P$ and $P_E \gg GA_s$ and dropping higher order terms,

$$K_H^* = \frac{GA}{T_r}(1 - \frac{P^2}{P_{cr}^2}) \tag{9-45}$$

$$v = \frac{(GAh + PT_r)u^2}{\pi^2 E_r I} \tag{9-46}$$

where P_{cr} is given by (9-23). The total vertical displacement v^t consists of a component due to lateral displacement given by (9-46) and a component due to the compressive load P given by $PT_r / E_c A$. After replacing E_r by $E_c / 3$

313

$$v^t = \frac{PT_r}{E_c A}\left[1 + \frac{3A(GAh + PT_r)u^2}{\pi^2 PIT_r}\right]$$ (9-47)

Equation (9-47) can be used to calculate the vertical stiffness K_v as the ratio of P/v^t,

$$K_v = \frac{E_c A}{T_r}\left[\frac{1}{1 + (\frac{3GA^2 h}{\pi^2 PIT_r} + \frac{3A}{\pi^2 I})u^2}\right]$$ (9-48)

Equation (9-48) can be further simplified by assuming that $h \approx T_r$ and $P \gg GA$, resulting in

$$K_v = \frac{E_c A}{T_r}\left[\frac{1}{1 + \frac{3}{\pi^2}\left(\frac{u}{r}\right)^2}\right] = K_{vo}\left[\frac{1}{1 + \frac{3}{\pi^2}\left(\frac{u}{r}\right)^2}\right]$$ (9-49)

where r is the radius of gyration of the bonded rubber area and K_{vo} is the vertical stiffness at zero lateral displacement.

$$r = \sqrt{\frac{I}{A}}$$ (9-50)

Warn and Whittaker (2006) investigated the accuracy of (9-49) by testing two small scale low damping elastomeric bearings (LDR) and two small scale lead-rubber bearings (LR) of the geometry shown in Figure 9-10. The vertical stiffness was obtained at three nominal levels of axial load (about which the vertical load was varied) at lateral displacements ranging from zero up to the bearing diameter.

Results are presented in Figures 9-11 and 9-12 where the ratio of the vertical stiffness to the vertical stiffness at zero displacement ($K_{vo} = E_c A/T_r$) is plotted versus the ratio of lateral displacement Δ to the radius R of the bearing. The results in these figures demonstrate that (9-49) provides a good representation of the vertical stiffness. It should be noted that measurement of the vertical stiffness is difficult given the small displacements involved, the effect of rotations of the loading apparatus and the nonlinear behavior of the bearing in compression. Moreover, the large thickness of the rubber cover contributed to deviations of theoretical and experimental results.

314
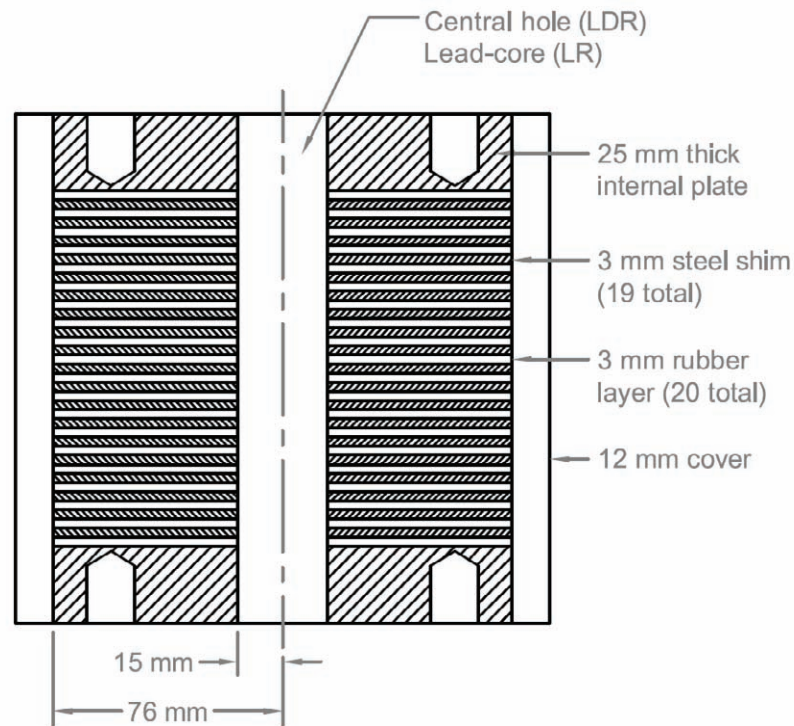
FIGURE 9-10 Elastomeric Bearings Tested by Warn and Whittaker (2006)
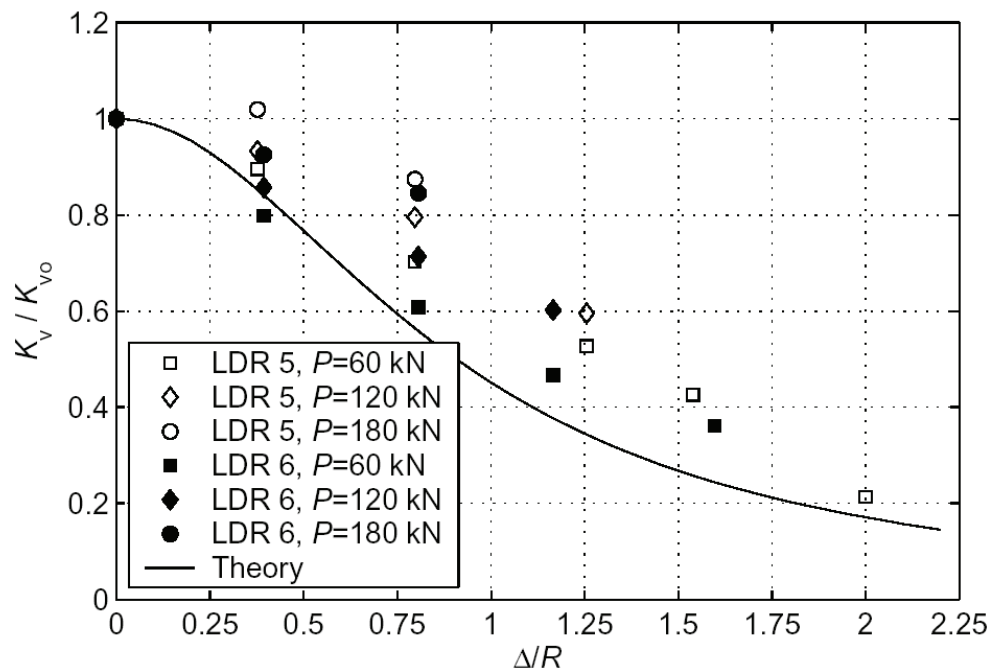
FIGURE 9-11   Comparison of Theoretical and Experimental Values of Vertical Stiffness of Elastomeric Bearings Subject to Lateral Deformation (Warn and Whittaker, 2006)

315
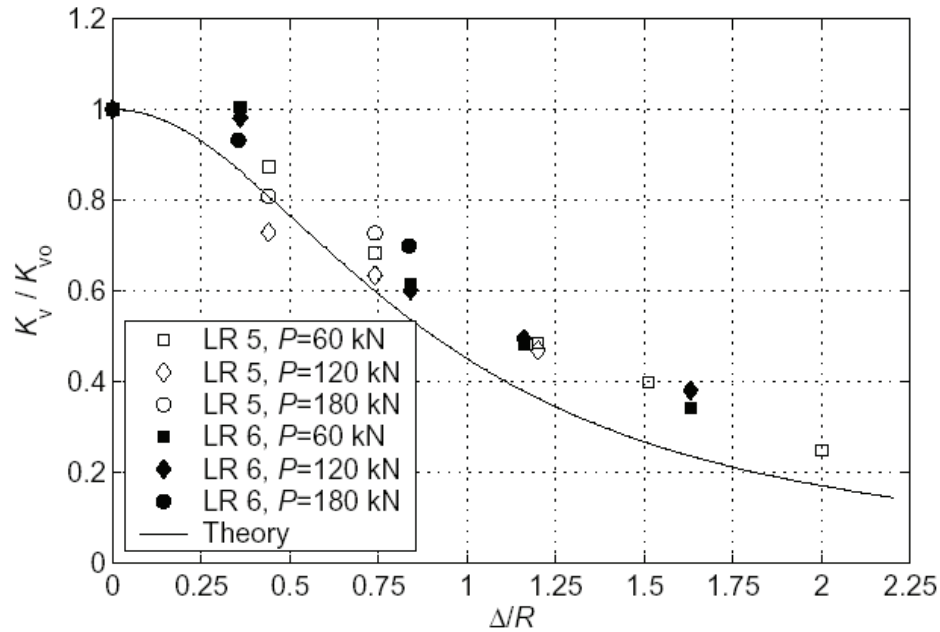
FIGURE 9-12 Comparison of Theoretical and Experimental Values of Vertical Stiffness of Lead-Rubber Bearings Subject to Lateral Deformation (Warn and Whittaker, 2006)

9.9 Behavior in Tension

Tension in elastomeric bearings has traditionally been avoided because it can result in failure in poor quality bearings and of difficulties associated with testing bearings in tension. However, high quality elastomeric bearings can sustain substantial tensile deformation and this characteristic can be utilized if tension is unavoidable. A sample application involved the use of the bearing shown in Figure 7-7 in a 100-ton tuned mass damper for the seismic protection of a drilling derrick on an offshore platform. This section briefly discusses the behavior of elastomeric bearings in tension and provides a procedure to compute the vertical stiffness of a bearing in tension.

The behavior of elastomeric bearings in tension has been discussed in Section 7. In general, elastomeric bearings exhibit the same stiffness in tension and compression up to a level of negative pressure that produces cavitation in the rubber. Cavitation is the formation of microscopic cracks. At negative pressure greater than those required to produce cavitation, the tensile stiffness drops dramatically. Figure 7-13 illustrates this behavior for the bearing of Figure 7-7. Cavitation occurs at a negative pressure of about $3G$ where G is the shear modulus of rubber (Gent, 1990). For the bearing of Figure 7-7, which was composed of rubber with $G = 0.6\,\text{MPa}$, the negative pressure at cavitation was 1.7 MPa.

316

Prior to cavitation, the rubber under tensile load is in a state of near hydrostatic tension with superimposed shear (see the pressure theory assumption in Section 9.2). The tensile stiffness is given by

$$K_{vt} = \frac{E_t A}{T_r}$$

(9-51)

where E_t is the tension modulus that prior to cavitation is equal to the compression modulus E_c. Following cavitation, the state of stress in the rubber reduces to one of uniaxial tension. The tensile stiffness is still given by (9-51) but with $E_t = E$. Herein we assume that the area of the bearing remains the same after cavitation despite the formation of cracks. The ratio of the vertical stiffness prior to and after cavitation is E_c / E. Given that $E \approx 4G$ (Gent, 2001) for the elastomers used in seismic isolation applications and using the equation for the compression modulus for cylindrical bearings,

$$\frac{K_{vt,\text{pre-cavitation}}}{K_{vt,\text{post-cavitation}}} \approx \frac{E_c}{E} \approx \frac{1}{\dfrac{2}{3S^2} + \dfrac{16G}{3K}}$$

(9-52)

Considering a representative value for the ratio $G/K \approx 0.75/2000$ and values of the shape factor in the range of 10 to 20 that is typical of seismic isolation bearings, the ratio of the pre-cavitation to post-cavitation tensile stiffness is in the range of about 100 to 500. This ratio is so large that, in tension, elastomeric bearings can be assumed to have zero post-cavitation stiffness. A model of behavior in the vertical direction that is appropriate for elastomeric bearings is presented in Figure 9-13. The proposed behavior is elastic with limit on capacity in tension equal to $3GA$ (the cavitation force) and in compression equal to the buckling load P_{cr}' given by (9-33), which depends on the lateral displacement u. The stiffness in compression is given by (9-49), which accounts for the effect of lateral deformation u. This model presumes that the possible but unusual phenomenon of tensile buckling (Kelly, 2003) does not occur. A simplified version of this model that can be readily implemented in currently available computer software is based on removing the dependency on lateral deformation by evaluating P_{cr}' and the compression stiffness at a representative lateral displacement. It should be noted that the model of Figure 9-13 is valid for the following conditions:

  a) In tension, is valid only for the initial loading and on unloading to zero. When reloading the cavitation force substantially reduces and could be taken as zero.
  b) In compression, is valid up to the critical load and is not valid on unloading if the critical load has been reached.

Use of a relationship such as that shown in Figure 9-13 allows for a realistic calculation of the distribution of axial load on bearings as either cavitation occurs or buckling is imminent. Moreover, it allows for calculation of the tensile displacement demand on bearings, where the tensile displacement prior to cavitation is likely very small and after cavitation very large with a magnitude that is dependent on the duration of loading and the speed of vertical motion.
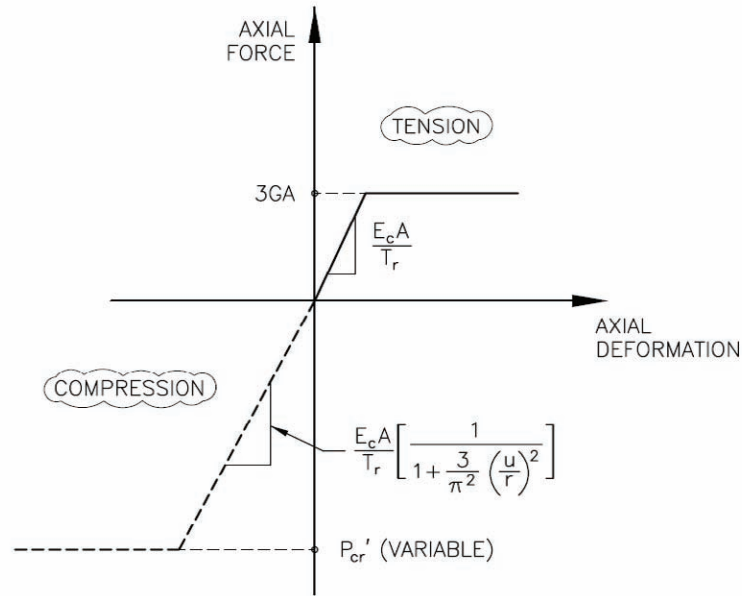
FIGURE 9-13 Vertical Stiffness Model for Elastomeric Bearing

9.10 Analysis and Design of Reinforcing Shims

Specifications for the design of elastomeric bearings such as the AASHTO Standard and the AASHTO LRFD Specifications (AASHTO, 2002; AASHTO, 2004) present equations for determining the thickness of shim reinforcing plates that are based on the illustrations of Figure 9-14. The figure shows a portion of a rectangular bearing of width B cut at the centerline and at the mid height of two adjacent rubber layers that contain a single reinforcing steel shim. The bearing is loaded by an unfactored compressive load P. The thickness of the shim is t_s and the thickness of each rubber layer is t. The stresses acting on this portion of the bearing are shown, consisting of a compressive stress p that has parabolic distribution over the width of the bearing with max value p_{max}, the shear stresses acting at the mid-height of the rubber layers and the stress in the shim σ_s. Neglecting the effect of the shear stresses and conservatively assuming that pressure $p = p_{max} = 2P/A$ (see Table 9-1 for the case of square and circular bearings), the tensile stress in the shim is calculated from equilibrium as

$$\sigma_s = 2\frac{t}{t_s}\frac{P}{A} \tag{9-53}$$

Procedures for shim plate design are presented in an allowable stress design (ASD) format (see AASHTO, 2002, 2004); the tensile stress is limited to $2F_y/3$, where F_y is the yield stress of the shim material. The required shim plate thickness is given by

$$t_s \geq \frac{3tP}{AF_y} \tag{9-54}$$

318
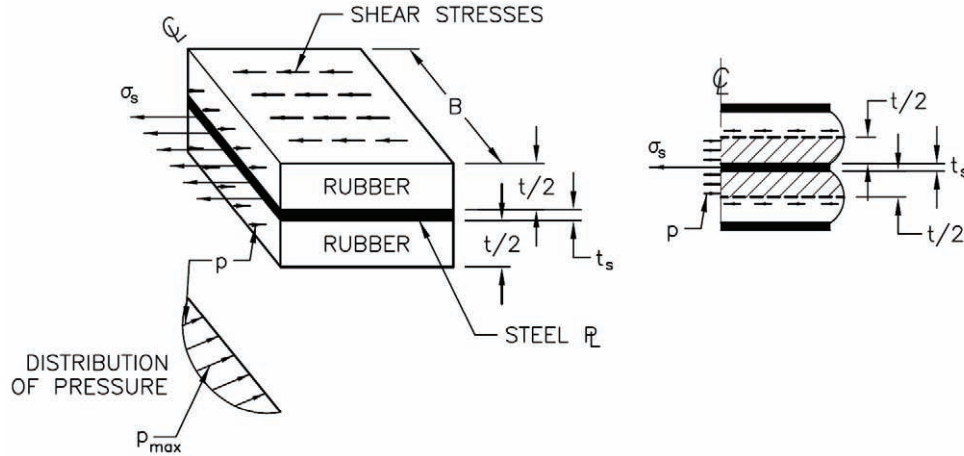
FIGURE 9-14 Bearing Section Used to Calculate Stresses in Reinforcing Shims

The AASHTO procedure assumes $p_{max} = 1.5P/A$ and restricts the stress to $F_y/2$, producing the same result as (9-54). The above equation applies to shims without holes. AASHTO (2002, 2004) requires approximately twice the thickness calculated by (9-54) if holes are present.

Equation (9-54) can be written in a Load and Resistance Factor Design (LRFD) format as follows:

$$t_s \geq \frac{2tP_u}{A(\phi_t F_y)} \tag{9-55}$$

where P_u is the factored load, ϕ_t is the strength reduction factor in tension, and all other terms have been defined previously.

Roeder et al. (1987) presented an improved theory for calculating the stresses in reinforcing shims. The theory recognizes that the state of stress in the shims of circular bearings is one of radial and hoop tension caused by the shear stresses acting at the interface of rubber and shim and of compression in the vertical direction caused by the vertical pressure. This stress state is illustrated in Figure 9-15. The distribution of the shear tractions is linear with the radial dimension. The axial pressure is maximized at the center of the shim (Roeder at al, 1987) where

$$\sigma_z = -2\frac{P}{A} \tag{9-56}$$

$$\sigma_r = \sigma_\theta = \frac{t}{t_s}\frac{P}{A}\left(\frac{3+\nu}{2}\right) = 1.65\frac{t}{t_s}\frac{P}{A} \tag{9-57}$$

where ν is Poisson's ratio of the shim material that herein is taken as 0.3 for steel. The minus sign in (9-56) denotes compression.

319
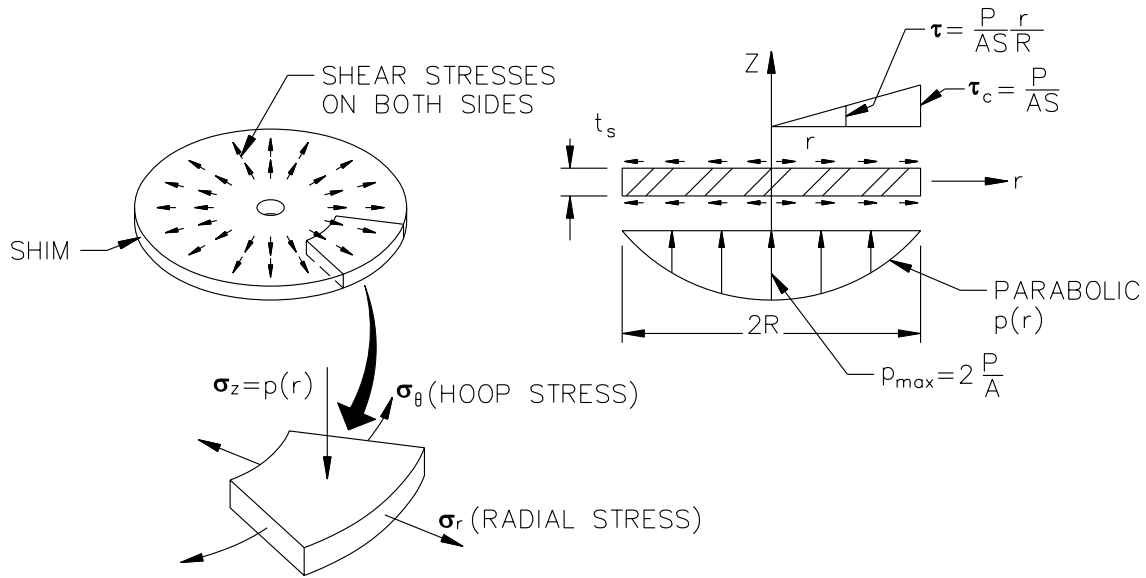
FIGURE 9-15 Tractions Acting on Circular Shim and Resulting Stresses

For design, the Tresca yield criterion can be used to limit the maximum shear stress, τ_{max}, where the maximum shear stress is given by

$$\tau_{max} = \frac{\sigma_r - \sigma_z}{2} = \frac{P}{2A}\left(1.65\frac{t}{t_s} + 2\right)$$ (9-58)

If ASD is used to size the shims, $\tau_{max} = 0.4F_y$ and

$$t_s \geq \frac{1.65t}{0.8F_y\dfrac{A}{P} - 2}$$ (9-59)

If LRFD is used to size the shims, $\tau_{max} = \phi(0.6F_y) = 0.54F_y$ and

$$t_s \geq \frac{1.65t}{1.08F_y\dfrac{A}{P_u} - 2}$$ (9-60)

The factor of 1.65 applies to the case of shims without holes. If holes are present in the shims, the factor must be increased and 3.0 is recommended to be consistent with the AASHTO Specifications (2002, 2004) and the recommendations of Roeder et al. (1987). These equations apply to both elastomeric and lead-rubber bearings. It should be noted that the LRFD version of the equations to size the shims is based on theory that does not consider the ultimate conditions of the shim but rather considers only initiation of yield. An appropriate theory needs to be developed.

320

9.11 Assessment of Safety of Elastomeric Bearings

Analysis of a seismically isolated structure will result in load and displacement demands. Herein it is assumed that the seismically isolated structure is analyzed for service (gravity) conditions and under seismic conditions for a design basis earthquake (DBE) and a maximum considered earthquake (MCE). Analysis is performed for upper and lower bound properties of the isolation system so that two sets of response parameters are calculated for each loading case. The safety checks described herein should be performed for the loads and displacement demands calculated for each set of response parameters. Safety assessment of elastomeric bearings can be based on either ASD or LRFD checks. Pairs of equations (a. and b.) are presented below for the checks; the first equation in a pair uses the ASD format and represents the state-of-practice AASHTO Guide Specification for Seismic Isolation Design (AASHTO, 1999); the second equation in a pair uses the LRFD format and represents a proposal by the authors based on the nominal yield strength of the shim plate steel and an ultimate shear strain in the elastomer of 700% - a shear strain that requires high quality control on both the elastomer and the bearing construction. The checks for Maximum Considered Earthquake shaking will generally be more critical than those for the Design Basis Earthquake shaking. Design equations for bearings subjected to tensile loads in Design Basis and/or Maximum Considered Earthquake Shaking are not provided.

9.11.1 Service Load Checking

The assumed axial loads and lateral displacements for the service-level checks are

- Dead load, D: P_D
- Live load, L: P_L
- Factored axial load, P_u, where the load factors are given by the appropriate code or guideline
- Non-seismic lateral displacement: Δ_S
- Non-seismic bearing rotation: θ_S

The rotation includes the effects of dead, live and construction loadings. The shear strains in the rubber are calculated using these loads and displacements and the equations of Section 9.6 that are presented below for circular and square bearings. The bonded dimension of the bearing (diameter or square side) is B, the total rubber thickness is T_r, the individual rubber thickness is t, and the individual steel shim thickness is t_s.

Shear strain due to compression

$$\gamma_{C_S} = \frac{P_D + P_L}{A_r GS} \qquad \text{ASD (9-61a)}$$

$$\gamma_{Cs}^u = \frac{P_u}{A_r GS} \qquad \text{LRFD (9-61b)}$$

where G is the shear modulus, S is the shape factor, A_r is the reduced bonded rubber area given by (9-34) through (9-36) for displacement $D = \Delta_S$ (for both ASD and LRFD calculations) and all other terms are defined above

Shear strain due to lateral displacement

$$\gamma_{S_s} = \frac{\Delta_S}{T_r}$$
ASD (9-62a)

$$\gamma_{S_s}^u = \frac{\Delta_S}{T_r}$$
LRFD (9-62b)

Shear strain due to rotation

$$\gamma_{r_s} = \frac{B^2\theta_S}{2tT_r}$$
ASD (9-63a)

$$\gamma_{r_s}^u = \frac{B^2\theta_S}{2tT_r}$$
LRFD (9-63b)

Buckling load at service displacement Δ_S

$$P_{cr_s}' = P_{cr}\frac{A_r}{A}$$
ASD and LRFD (9-64)

where P_{cr} is calculated using (9-24) or (9-25).

A bearing design may be considered acceptable if

$$\gamma_{C_s} \leq 2.5$$
ASD (9-65a)

$$\gamma_{C_s}^u \leq 3.5$$
LRFD (9-65b)

$$\gamma_{C_s} + \gamma_{S_s} + \gamma_{r_s} \leq 5.0$$
ASD (9-66a)

$$\gamma_{C_s}^u + \gamma_{S_s}^u + \gamma_{r_s}^u \leq 7.0$$
LRFD (9-66b)

$$t_s \geq \frac{\alpha t}{0.8F_y\frac{A_r}{(P_D+P_L)}-2} \geq 1.5 \text{ mm}$$
ASD (9-67a)

$$t_s \geq \frac{\alpha t}{1.08 F_y \dfrac{A_r}{P_u} - 2} \geq 1.5 \text{ mm} \qquad \text{LRFD (9-67b)}$$

$$\frac{P'_{cr_s}}{P_D + P_L} \geq 3.0 \qquad \text{ASD (9-68a)}$$

$$\frac{P'_{cr_s}}{P_u} \geq 1.33 \qquad \text{LRFD (9-68b)}$$

In these equations $\alpha = 1.65$ for shim plates without holes and 3.0 otherwise, and all other terms have been defined previously Equations (9-65a) and (9-66a) are taken from the 1999 AASHTO Guide Specification for Seismic Isolation Design (AASHTO, 1999); (9-68a) is an industry-standard check, albeit conservative. The LRFD equations presented above are preliminary and mutable; (9-68b) imposes an indirect strength reduction factor (or ϕ in the LRFD format) of 0.75 on the buckling calculation.

LRFD equation (9-67b) (and equations 9-72b and 9-77b that follow) is based on elastic stress distribution and does not consider the ultimate state of stress in the shim plate. An appropriate theory needs to be developed, otherwise the presented LRFD formulation is likely conservative.

9.11.2 Design Basis Earthquake Checking

The assumed axial loads and lateral displacements for the Design Basis Earthquake (DBE) checks are

- Dead load, D: P_D
- Seismic live load, SL: P_{SL}
- Earthquake axial load due to DBE shaking, E: $P_{E_{DBE}}$, where earthquake-induced axial loads can result from both overturning moments in the superstructure and vertical earthquake shaking
- Factored axial load: P_u, including dead, live and DBE earthquake effects, where the load factors are given by the appropriate code or guideline
- Non-seismic bearing rotation: θ_S
- Seismic lateral displacement: $\Delta_{E_{DBE}}$.

Bearing rotation due to earthquake effects are neglected for this check. The seismic live load is the point-in-time live load acting at the time of the earthquake; a value of $0.5 P_L$ is generally used for buildings but a smaller value might be justified for bridges carrying large live loads. Regardless, the requirements of the applicable codes and guidelines should be followed for the live load calculation.

323

Shear strain due to compression

$$\gamma_{C_{DBE}} = \frac{(P_D + P_{SL} + P_{E_{DBE}})}{A_r GS}$$

ASD (9-69a)

$$\gamma^{u}_{C_{DBE}} = \frac{P_u}{A_r GS}$$

LRFD (9-69b)

where the reduced bonded rubber area is given by (9-34) through (9-36) for a displacement $D = \Delta_{E_{DBE}}$.

Shear strain due to lateral displacement

$$\gamma_{S_{DBE}} = \frac{\Delta_{E_{DBE}}}{T_r}$$

ASD (9-70a)

$$\gamma^{u}_{S_{DBE}} = \frac{\Delta_{E_{DBE}}}{T_r}$$

LRFD (9-70b)

A bearing design is considered acceptable if

$$\gamma_{C_{DBE}} + \gamma_{S_{DBE}} + 0.5\gamma_{r_S} \leq 5.5$$

ASD (9-71a)

$$\gamma^{u}_{C_{DBE}} + \gamma^{u}_{S_{DBE}} + 0.5\gamma_{r_S} \leq 7.0$$

LRFD (9-71b)

$$t_s \geq \frac{1.65t}{0.8F_y \dfrac{A_r}{(P_D + P_{SL_{DBE}} + P_{E_{DBE}})} - 2} \geq 1.5 \text{ mm}$$

ASD (9-72a)

$$t_s \geq \frac{1.65t}{1.08F_y \dfrac{A_r}{P_u} - 2} \geq 1.5 \text{ mm}$$

LRFD (9-72b)

In (9-70), the factor α is set equal to 1.65 on the basis that the reduced or overlapping bonded rubber area does not include the central hole. Equation (9-71a) is taken directly from AASHTO (1999).

324

9.11.3 Maximum Considered Earthquake Checking

The assumed axial loads and lateral displacements for the Maximum Considered Earthquake (MCE) checks are

- Dead load, D: P_D
- Seismic live load, SL: P_{SL}
- Earthquake axial load due to MCE shaking, E: $P_{E_{MCE}}$, where earthquake-induced axial loads can result from both overturning moments in the superstructure and vertical earthquake shaking
- Factored axial load: P_u, including dead, live and MCE earthquake effects, where the load factors are given by the appropriate code or guideline
- Non-seismic bearing rotation: θ_S
- Seismic lateral displacement: $\Delta_{E_{MCE}}$.

Bearing rotation due to earthquake effects are neglected for this check. The engineer-of-record might assume a point-in-time seismic live load for the MCE check that is smaller than that for the DBE check because the mean annual frequency of MCE shaking is less, and sometimes much less, than that of DBE shaking. Regardless, the requirements of appropriate codes and guidelines must be followed. Shear strains in the rubber and the buckling load (if bolted) and rollover displacement (if dowelled) are calculated using the procedures and equations set forth in Section 9-7.

Shear strain due to compression

$$\gamma_{C_{MCE}} = \frac{(P_D + P_{SL_{MCE}} + P_{E_{MCE}})}{A_r GS} \qquad \text{ASD (9-73a)}$$

$$\gamma_{C_{MCE}}^u = \frac{P_u}{A_r GS} \qquad \text{LRFD (9-73b)}$$

where the reduced bonded rubber area is given by (9-34) through (9-36) for a displacement $D = \Delta_{E_{MCE}}$.

Shear strain due to lateral displacement

$$\gamma_{S_{MCE}} = \frac{\Delta_{E_{MCE}}}{T_r} \qquad \text{ASD (9-74a)}$$

$$\gamma_{S_{MCE}}^u = \frac{\Delta_{E_{MCE}}}{T_r} \qquad \text{LRFD (9-74b)}$$

Buckling load at MCE displacement

$$P'_{cr_{MCE}} = P_{cr} \frac{A_r}{A} \geq 0.15 P_{cr} \qquad (9\text{-}75)$$

where P_{cr} is calculated using either (9-24) or (9-25) and the reduced bonded area is computed for the MCE displacement, $\Delta_{E_{MCE}}$. Equation (9-75) is based on (9-33) but with an adjustment to address the conservatism of that equation.

Rollover displacement for ASD computations with $P = P_D + P_{SL_{MCE}} + P_{E_{MCE}}$ used to compute D_{cr} or $P = P_u$ to compute D^u_{cr} for LRFD computations, using (9-30) or (9-32). A bearing design is considered acceptable if

$$\gamma_{C_{MCE}} + \gamma_{S_{MCE}} + 0.5\gamma_{r_S} \leq 5.5 \qquad \text{ASD (9-76a)}$$

$$\gamma^u_{C_{MCE}} + \gamma^u_{S_{MCE}} + 0.5\gamma_{r_S} \leq 7.0 \qquad \text{LRFD (9-76b)}$$

$$t_s \geq \frac{1.65t}{0.8F_y \dfrac{A_{rs}}{(P_D + P_{SL_{MCE}} + P_{E_{MCE}})} - 2} \geq 1.5 \text{ mm} \qquad \text{ASD (9-77a)}$$

$$t_s \geq \frac{1.65t}{1.08F_y \dfrac{A_{rs}}{P_u} - 2} \geq 1.5 \text{ mm} \qquad \text{LRFD (9-77b)}$$

$$\frac{P'_{cr_{MCE}}}{(P_D + P_{SL_{MCE}} + P_{E_{MCE}})} \geq 1.2 \qquad \text{ASD (9-78a)}$$

$$\frac{P'_{cr_{MCE}}}{P_u} \geq 1.0 \qquad \text{LRFD (9-78b)}$$

$$\frac{D_{cr}}{\Delta_{E_{MCE}}} \geq 1.2 \qquad \text{ASD (9-79a)}$$

$$\frac{D^u_{cr}}{\Delta_{E_{MCE}}} \geq 1.0 \qquad \text{LRFD (9-79b)}$$

In (9-77), the factor α is set equal to 1.65 on the basis that the reduced or overlapping bonded rubber area does not include the central hole.

The design equations presented in this section can be used to size components of elastomeric bearings. Final sizes of rubber layers and shim plates should be developed by experienced isolator suppliers, however deviation from the requirements of these design

326

equations should not be accepted without theoretical and experimental validation. Slow (service loadings) and high-speed (seismic loadings) testing under combined compression and shear (and tension if imposed) should be performed to confirm the safety of each type of bearing.

9.12 Design of End Plates of Elastomeric Bearings

9.12.1 Introduction

An LRFD-based design procedure for end plates of elastomeric bearings is presented herein based on treating end plates as column base plates. The procedure is similar to the one employed in the design of sliding bearings (Section 6) but more detailed because of the potential for tensile forces in one or more bolts.

We consider the elastomeric bearing of Figure 9-16 with an imposed axial load P and lateral displacement u. End moments M develop as a result of equilibrium in the deformed configuration. The two alternative approaches for the analysis and design of the end plates:

a) The axial load P is carried through the reduced bonded area, which is defined as the overlapping area of the bonded rubber areas at the top and bottom of the bearing. The reduced bonded area is given by (9-34) through (9-36).
b) The axial load P and overturning moment M act at the centroid of the end plates.

Analysis and design of the end plates must be performed for the effects of DBE and MCE shaking. The MCE check will generally be critical because the reduced bonded area is smaller and the magnitude of the axial loads, compressive or tensile, larger. The DBE check is for elastic response and uses minimum specified material strengths and strength reduction factors. The MCE check is for *essentially* elastic response and uses expected material strengths and no strength reduction factors ($\phi = 1.0$).

The axial load P is a factored load including dead load, live load and earthquake effects; the load factors are typically specified in the code or guideline that forms the basis for the design . The moment M is given by

$$M = \frac{F_H h^{'}}{2} + \frac{Pu}{2} \tag{9-80}$$

where F_H is the bearing shear force and h' is the overall height of the bearing.

TOP VERTICAL STRESS

EFFECTIVE AREA

BEARING EQUILIBRIUM

$$M_o = \frac{F_H h'}{2} + P\left(a + \frac{u}{2} - \frac{B}{2}\right)$$

EFFECTIVE AREA

$$M = M_o + P \cdot \left(\frac{B}{2} - a\right)$$

OR

$$M = \frac{F_H h'}{2} + \frac{P \cdot u}{2}$$

BOTTOM VERTICAL STRESS

EFFECTIVE AREA
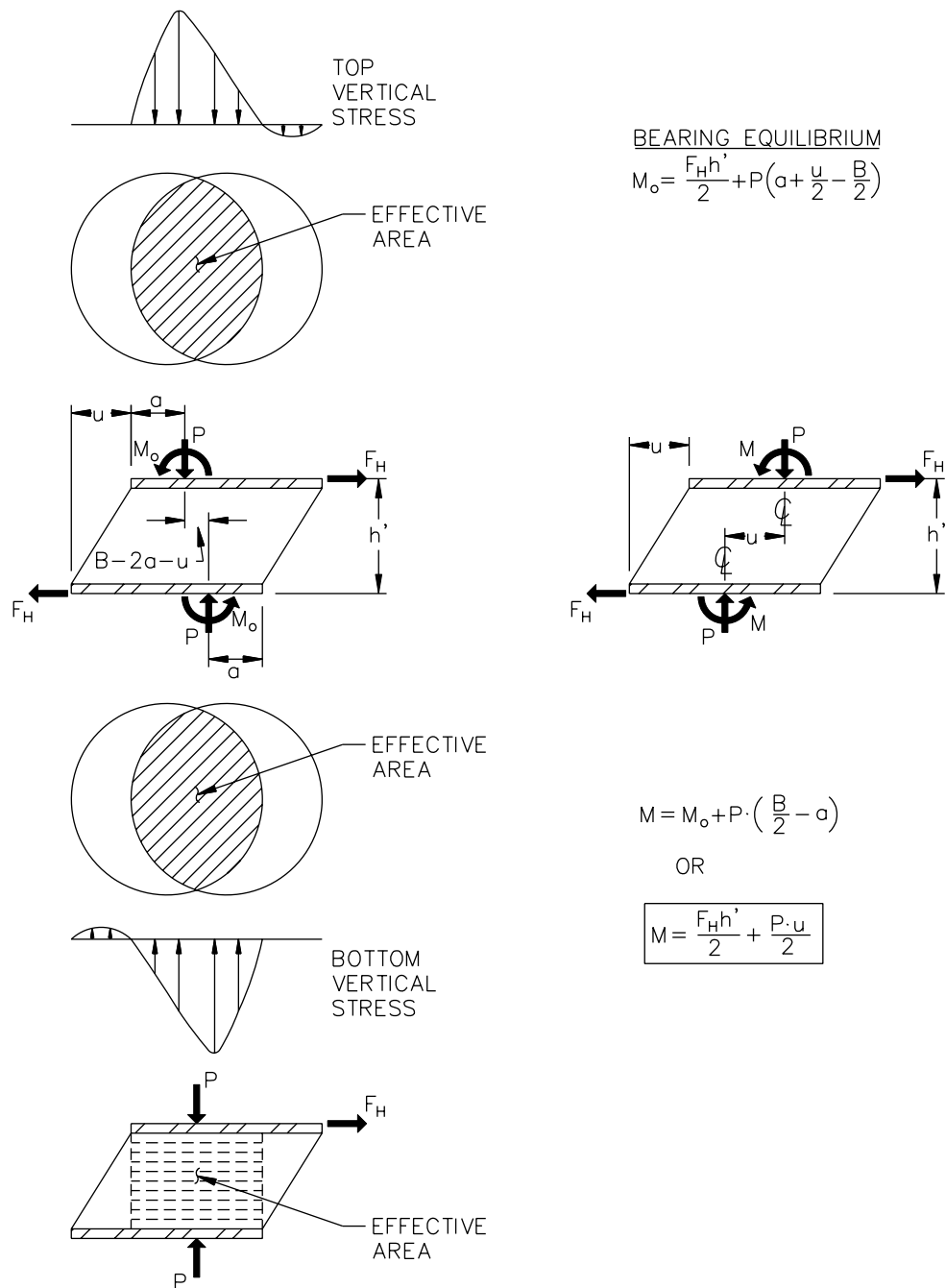
FIGURE 9-16 Deformed Bearing and Forces Acting on End Plates

9.12.2 Reduced Area Procedure

Figure 9-17 shows the construction of a typical elastomeric bearing (a lead-rubber bearing in this instance). Each end plate consists of an internal plate and a mounting plate joined using countersunk bolts. Due to the large number of bolts used to connect the two plates, the bolts will typically have sufficient strength so that the two plates can be

328

considered to be integral with a thickness equal to the sum of the individual plate thickness (= 70 mm in this example).
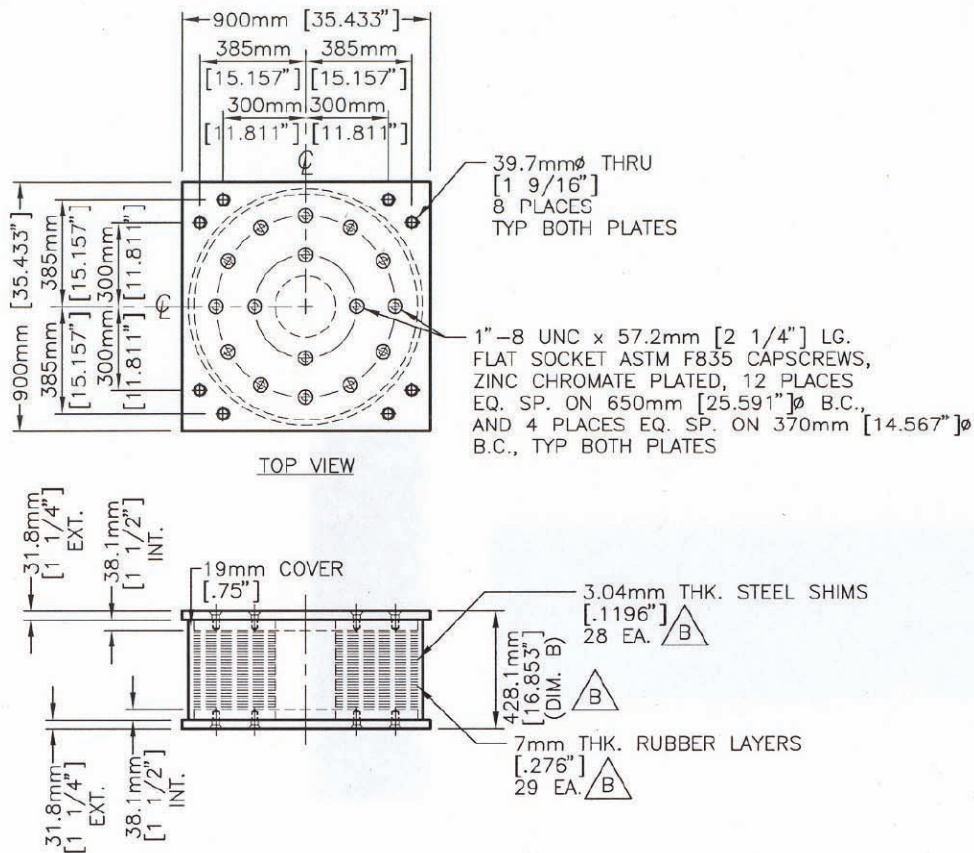
FIGURE 9-17 Typical Construction of a Lead-Rubber Bearing

Figure 9-18 shows the internal construction of an elastomeric bearing. The key design variables are

- Top mounting plate thickness, t_{tp}
- Bottom mounting plate thickness, t_{bp}
- Internal plate thickness, t_{ip}
- Bonded rubber diameter, $L = D - 2c_s$, where c_s is the rubber cover thickness and D is the overall diameter of the bearing
- Thickness of grout below and above the bearing, t_g

For end-plate design using the reduced-area procedure (left-hand panels of Figure 9-16), the factored axial load P is transferred through the reduced bonded area and the LRFD procedure for concentrically loaded plates is used. For the purpose of calculation, the reduced bonded area is assumed to be rectangular with dimensions $0.75L \times b$, where L is the bonded rubber diameter.

329
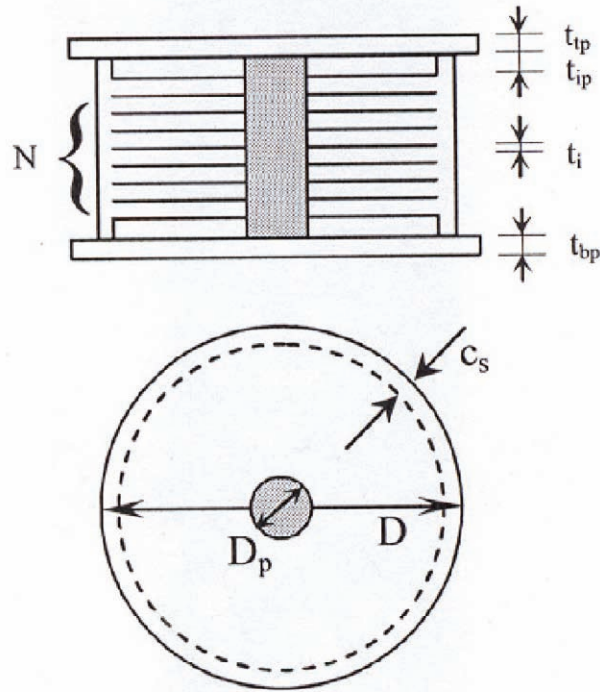
FIGURE 9-18 Internal Construction of an Elastomeric Bearing

Figure 9-19 illustrates the procedure for checking the end plate thickness for a factored axial load P, displacement u and the bearing geometry of Figure 9-18:

a) Calculate the reduced bonded rubber area A_r; include the lead core (if a lead-rubber bearing) in the calculation of A_r if the reduced area includes the core.

b) Calculate the dimension b of the equivalent rectangular reduced bonded area:

$$b = \frac{A_r}{0.75L} \tag{9-81}$$

c) Calculate the design concrete bearing strength:

$$f_b = 1.7\phi_c f_c' \tag{9-82}$$

In (9-82), the use of 1.7 requires that the concrete (grout) be confined by an area of concrete at least twice the reduced bonded rubber area.

d) Calculate the dimension b_1 of the concrete bearing area carrying the axial load:

$$b_1 = \frac{P}{0.75L f_b} \tag{9-83}$$

This calculation assumes, per standard practice, that the bearing pressure is uniform beneath the assumed rectangular bearing area. Escobar et al. (2006) provide updated information on bearing stress distributions beneath concentrically loaded steel plates bearing on plain concrete.

e) Calculate the cantilever length associated with the assumed bearing area:

$$r = \frac{b_1 - b}{2} \tag{9-84}$$

f) Calculate the required bending strength per unit length of the plate:

$$M_u = \frac{f_b r^2}{2} \tag{9-85}$$

g) Calculate the required thickness of the end plate:

$$t \geq \sqrt{\frac{4M_u}{\phi_b F_y}} \tag{9-86}$$

where F_y is the minimum specified yield stress for the DBE check and the expected yield stress ($= R_y F_y$) for the MCE check [$R_y = 1.3$ for ASTM A36 plate and $R_y = 1.1$ for ASTM A572 Grade 50 plate per Table I-6-1 of the AISC Seismic Provisions, (AISC, 2005)]; and ϕ_c and ϕ_b are equal to 0.65 and 0.9, respectively, for the DBE check, and 1.0 and 1.0, respectively, for the MCE check.

The anchor bolts and the concrete must also be checked for tension and bearing, respectively. The forces in the anchor bolt s will be computed and the adequacy of the bolts established using the load-moment procedure presented in Section 9.12.3. The concrete bearing stress resulting from the transfer of the axial load through the reduced bonded area must be less than the concrete bearing design strength. For this check, the critical bearing area is equal to that of a truncated 45-degree pyramid with an upper face area equal to the equivalent reduced area ($0.75Lb$ and a height equal to the thickness of the steel end plates and the grout. (The grout must also be checked for adequate bearing strength). The concrete bearing area (at the base of the truncated pyramid) is

$$A_c = (0.75L + 2t_{ip} + 2t_{bp} + 2t_g)(b + 2t_{ip} + 2t_{bp} + 2t_g) \tag{9-87}$$

where the t_{ip} is the thickness of the internal plate (see Figure 9-18), t_{bp} is the thickness of the bottom (top) mounting plate (See Figure 9-18), and t_g is the thickness of the grout. The bearing stress is acceptable if the factored load is

$$P_u \leq f_b A_c \tag{9-88}$$

where the concrete bearing strength is given by (9-82).
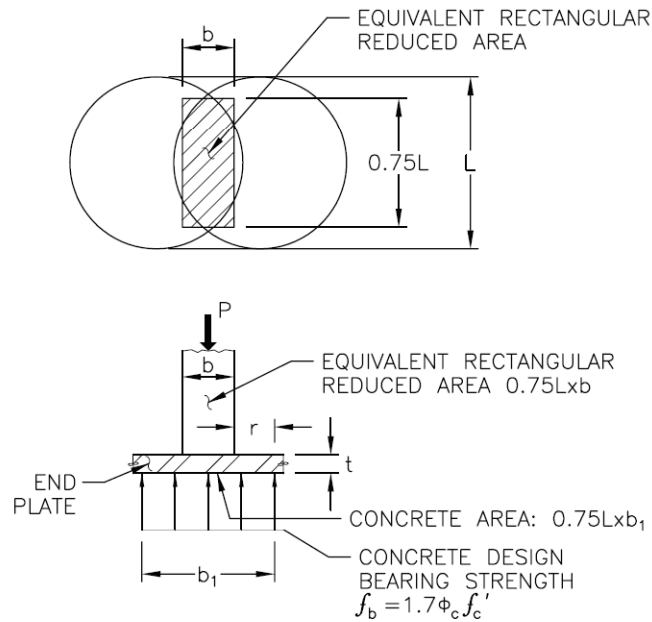
BENDING MOMENT IN END PLATE: $M_u = \dfrac{f_b \cdot r^2}{2}$

REQUIRED END PLATE THICKNESS: $t \geqslant \sqrt{\dfrac{4M_u}{\phi_b F_y}}$

CALCULATION OF DIMENSION b_1:

$\dfrac{P}{0.75L \cdot b_1} = f_b \rightarrow b_1 = \dfrac{P}{0.75L f_b}$

CALCULATION OF ARM r: $r = \dfrac{b_1 - b}{2}$

FIGURE 9-19 End Plate Design Using Reduced Area Procedure

9.12.3 Load-Moment Procedure

In the load-moment procedure the distribution of the concrete bearing stress on the mounting plate and anchor bolt forces are determined. The design procedure follows that for a column base plate with an imposed axial load and moment..

We start assuming no bolt is in tension. Figure 9-20 presents a free body diagram of the bearing. The mounting plate is square with plan dimension *B*. Equilibrium in the vertical direction and of moments about point O results in the following equations for dimension *A* and stress f_1:

332

$$A = \frac{3}{2}B - 3\frac{M}{P} \tag{9-89}$$

$$f_1 = \frac{2P}{AB} \le f_b \tag{9-90}$$
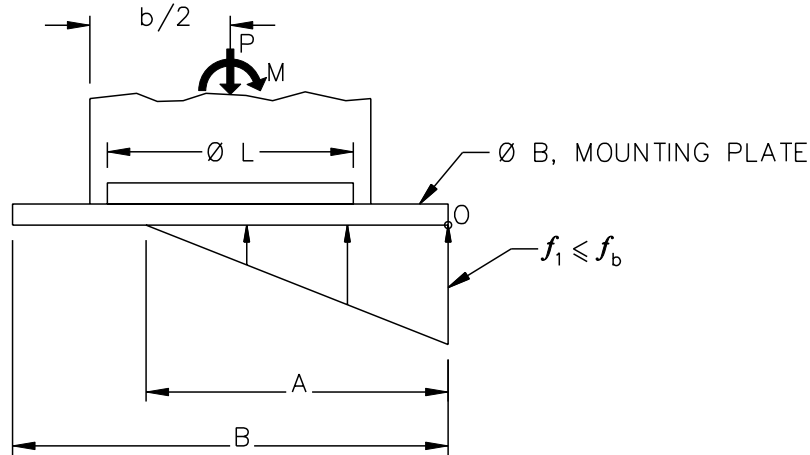
$P - B \times A \times f_1 / 2 = 0 \quad\Big\} \quad A = \frac{3}{2}B - 3\frac{M}{P}$

$M - \frac{PB}{2} + \frac{PA}{3} = 0 \quad\Big\} \quad f_1 = \frac{2P}{AB} \le f_b$

FIGURE 9-20 Free Body Diagram of End Plate without Bolt Tension

Equations (9-87) and (9-88) are valid provided that f_1 is less than or equal to the concrete design bearing strength given by (9-82). If dimension A is larger than B, the assumed stress distribution is incorrect and the calculations must be repeated by assuming a trapezoidal distribution of stress over the entire area of the plate—the case of a small ratio of M to P for which there is no bolt tension.

If f_1 is larger than f_b, tensile forces will develop in the bolts—see Figure 9-21. The maximum concrete stress is f_b. Equilibrium in the vertical direction and of moments about point O' results in the following equations for dimension A and bolt tension T:

$$A^2\left(\frac{Bf_b}{6}\right) - A\left(\frac{f_b BC}{2}\right) + \left(M - PC - \frac{PB}{2}\right) = 0 \tag{9-91}$$

$$T = \frac{f_b AB}{2} - P \tag{9-92}$$

333
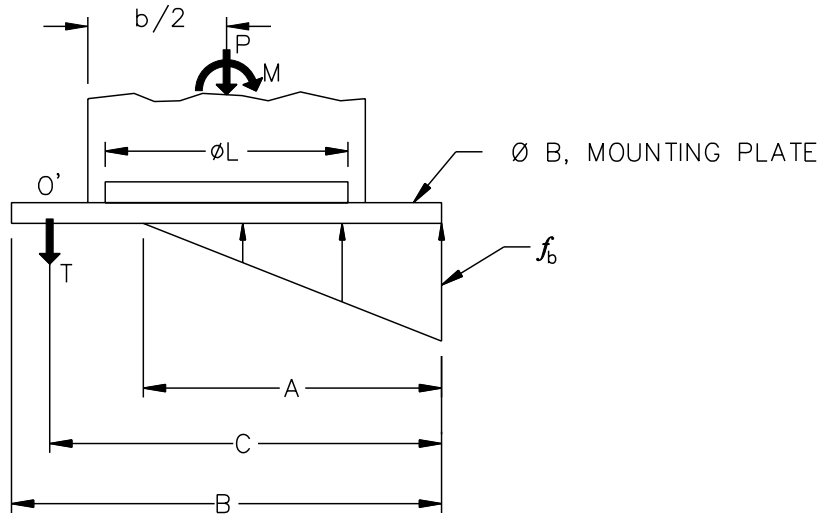
$$P + T - f_b \frac{AB}{2} = 0$$

$$f_b \frac{AB}{2}\left(C - \frac{A}{3}\right) - M - P\left(C - \frac{B}{2}\right) = 0$$

$$A^2\left(\frac{Bf_b}{6}\right) - A\left(\frac{f_b B\ C}{2}\right) + \left(M - PC - \frac{PB}{2}\right) = 0$$

$$T = \frac{f_b AB}{2} - P$$

FIGURE 9-21 Free Body Diagram of End Plate with Bolt Tension

Equation (9-89) is solved first for *A*, which is used in (9-92) to calculate the tension in the bolts. Herein, the bolt tensile force *T* represents the tensile force in a number of bolts at distance *C* from the edge of the mounting plate. If several rows of bolts are present,, a distribution of bolt tension must be assumed.

This analysis produces a concrete bearing stress distribution that can be used to check the adequacy of the mounting plate. In the event of bolt tension, the mounting plate is typically bent about a section at the junction of the mounting and internal plates. Given that the mounting plate is typically square and the internal plate circular, the bending stress calculation for the mounting plate is not straightforward. The preferred method uses yield line theory to check the adequacy of the mounting plate. An alternate, albeit conservative method, replaces the circular internal plate with an equivalent square plate; the bending moment in the mounting plate is then calculated using the difference between the dimensions of the mounting plate and the equivalent square internal plate as the lever arm, *r* - see Figure 9-22. Given the sensitivity of the calculation to the length of the lever arm and the inherent conservatism in the calculation, it is appropriate to consider an equivalent square dimension *b* per Figure 9-22, which is slightly larger than that given by the equal area rule $(= \sqrt{\pi}L/2)$, say $b = 0.93L$.

334

For circular mounting plates, the procedure must be modified to calculate the pressure beneath (above) the bottom (top) plate and the bending moment. For the bending moment calculation, the procedure of Section 6.4 can be used.

EQUIVALENT SQUARE INTERNAL PLATE

$$\pi L^2/4 = b^2 \Rightarrow b = \frac{\sqrt{\pi}}{2}L \text{ or } b \approx 0.93L$$

$$r = C - \frac{b}{2} - \frac{B}{2}$$

$$(B-b)/2 = r$$

$$M_u = f_1 \frac{r^2}{2} \text{ or } T \times r$$

$$t_{bp} \geq \sqrt{\frac{4M_u}{F_b F_y}}$$
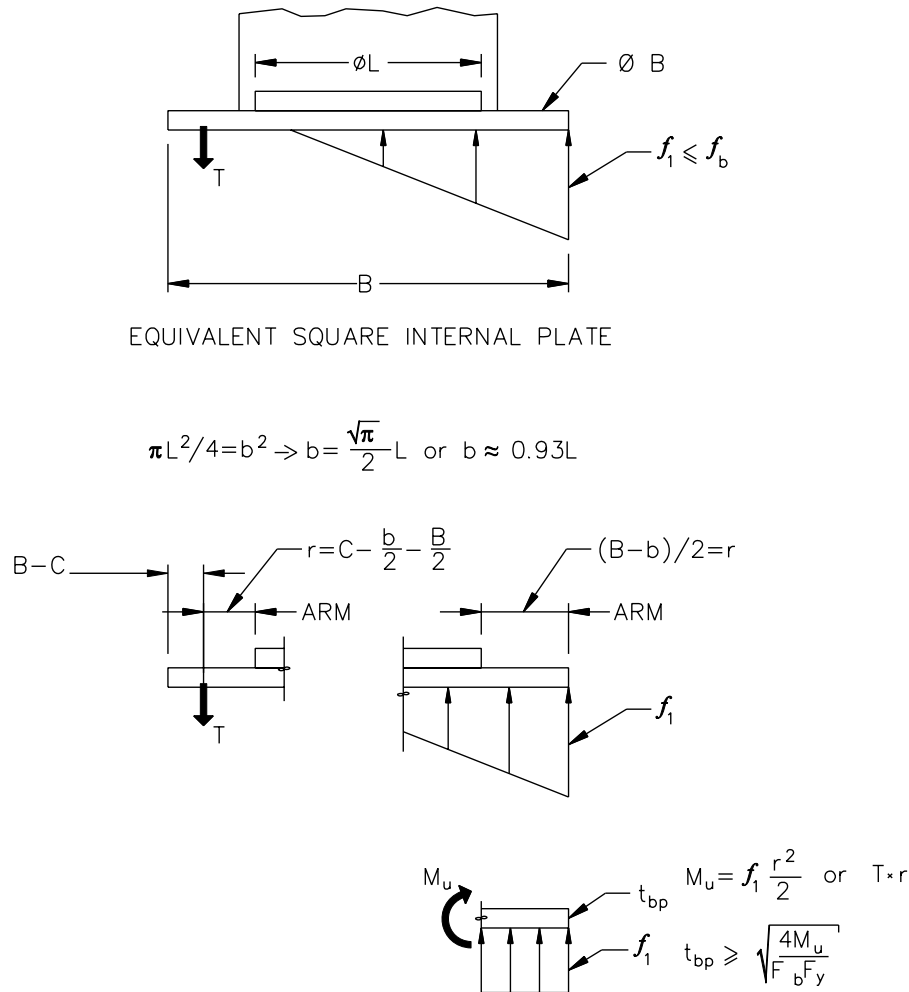
FIGURE 9-22 Simplified Procedure for Checking a Mounting Plate

9.12.4 Design Example

This section presents a simple design example that uses the analysis and design procedures set forth in this section of the report. For the example, a large number of significant figures have been used to simplify the presentation for the reader—a smaller number are warranted in design practice.

Consider the bearing of Figure 9-17. For MCE shaking, the factored load $P_u = 6000 \text{ kN}$, the displacement $u = 555 \text{ mm}$ and the moment $M_u = 1900 \text{ kNm}$ The specified compressive strength of the concrete is $f_c' = 27.6 \text{ MPa}$ and is considered confined for this problem. The steel is ASTM A36 with expected value of yield stress

335

$F_y = 1.3 \times 36 = 46.8 \text{ ksi}$ (= 320 MPa). The geometry of the bearing is given by $B = 900 \text{ mm}$, $L = 813 \text{ mm}$ $t_{ip} = t_{bp} = 31.8 \text{ mm}$ and $t_g \geq 25 \text{ mm}$.

The design calculations proceed as follows:

For the reduced bonded rubber area—use (9-35) and (9-36)

$$\delta = 2\cos^{-1}\left(\frac{u}{L}\right) = 2\cos^{-1}\left(\frac{555}{813}\right) = 1.64$$

$$A_r = \frac{L^2}{4}(\delta - \sin\delta) = 105940 \text{ mm}^2$$

Equation (9-79) is used to compute dimension b:

$$b = \frac{A_r}{0.75L} = \frac{105940}{0.75 \times 813} = 174 \text{ mm}$$

The concrete bearing strength is given by (9-82):

$$f_b = 1.7\phi_c f_c' = 1.7 \times 1 \times 27.6 = 46.9 \text{ MPa}$$

Equations (9-83), (9-84), (9-85) and (9-86) are used to check the adequacy of the plates:

$$b_1 = \frac{P_u}{0.75Lf_b} = \frac{6000000}{0.75 \times 813 \times 46.9} = 210 \text{ mm}$$

$$r = \frac{b_1 - b}{2} = \frac{210 - 174}{2} = 18 \text{ mm}$$

$$M_u = \frac{f_b r^2}{2} = \frac{46.9 \times 18^2}{2} = 7598 \text{ Nmm/mm width}$$

$$t \geq \sqrt{\frac{4M_u}{\phi_b F_y^{\exp}}} = \sqrt{\frac{4 \times 7598}{1 \times 320}} = 10 \text{ mm} \leq (t_{ip} + t_{bp}) = (38.1 + 31.8) = 69.9 \text{ mm}$$

The internal and mounting plates (in total, the end plates) are therefore adequate.

Equations (9-87) and (9-88) are used to check the bearing stress on the concrete as follows:

$$\begin{aligned} A_c &= (0.75L + 2t_{ip} + 2t_{bp} + 2t_g)(b + 2t_{ip} + 2t_{bp} + 2t_g) \\ &= (0.75 \times 813 + 2 \times 38.1 + 2 \times 31.8 + 2 \times 25)(174 + 2 \times 38.1 + 2 \times 31.8 + 2 \times 25) \\ &= 290900 \text{ mm}^2 \end{aligned}$$

$$\frac{P_u}{A_c} = \frac{6000000}{290900} = 20.6 \text{ MPa} \leq f_b = 46.9 \text{ MPa} \text{ and the concrete is adequate}.$$

Equations (9-89) and (9-90) are used to compute bolt tensile forces. For the first iteration, assume no bolt tension but then check the assumption.

$$A = \frac{3}{2}B - 3\frac{M}{P} = 1.5 \times 900 - 3 \times \frac{1900x10^6}{6000000} = 400 \text{ mm}$$

$$f_1 = \frac{2P}{AB} = \frac{2 \times 6000000}{400 \times 900} = 33.3 \text{ MPa} \leq f_b = 46.9 \text{ MPa} \rightarrow \text{ there is no tension in the bolts}$$

The mounting plate is checked using the procedure of Figure 9-22.

$$b \approx 0.93L = 0.93 \times 813 = 756 \text{ mm}$$

$$r = \frac{B-b}{2} = \frac{900-756}{2} = 72 \text{ mm}$$

$$M_u = \frac{f_1 r^2}{2} = \frac{33.3 \times 72^2}{2} = 86313 \text{ Nmm/mm}$$

$$t_{bp} \geq \sqrt{\frac{4M_u}{\phi_b F_y}} = \sqrt{\frac{4 \times 86313}{1 \times 320}} = 32.8 \text{ mm} > 31.8 \text{ mm NG}$$

Therefore, a thicker plate is required.

SECTION 10
MECHANICAL PROPERTIES OF PASSIVE DAMPING DEVICES

10.1 Introduction

Passive energy dissipation devices (widely known as dampers) can be used to absorb and dissipate earthquake-and wind-induced energy in bridges. Such dampers can be implemented in conventional and seismically isolated bridges and require that relative displacement be developed across the damper to dissipate energy.

This chapter introduces displacement-dependant and velocity-dependant dampers in Section 10.2. Fluid viscous dampers are one type of velocity-dependant damper. Since only fluid viscous dampers have been implemented in bridges in the United States at the time of this writing, emphasis is placed on such dampers in this chapter.

The physical construction of fluid viscous dampers is introduced in Section 10.3. The mechanical behavior of linear and nonlinear fluid viscous dampers is described in Section 10.4. The influence of service and earthquake loadings on the force response of fluid viscous dampers is described in Section 10.5. Shock transmission units are introduced in Section 10.6. Restoring force and damping devices are introduced in Section 10.7. A discussion on the aging and failure of fluid viscous dampers is presented in Section 10.8.

10.2 Passive Energy Dissipation Hardware

10.2.1 Displacement and Velocity-Dependent Energy Dissipation Devices

Passive energy dissipation (damping) hardware is generally divided into three categories (Whittaker and Constantinou, 2004): displacement-dependent, velocity-dependent, and other. Examples of displacement-dependent or hysteretic systems include devices based on yielding of metal and friction. Figure 2-14a presents sample force-displacement loops for hysteretic dampers. Examples of velocity-dependent systems include dampers consisting of viscoelastic solid materials, dampers operating by deformation of viscoelastic fluids (e.g., viscous shear walls), and dampers operating by forcing fluid through an orifice (e.g., viscous fluid dampers). Figure 2-14b illustrates the behavior of these velocity-dependent systems. Other systems have characteristics that cannot be classified by one of the basic types depicted in Figures 2-14a or 2-14b. Examples are dampers made of shape memory alloys, frictional-spring assemblies with re-centering capabilities, and fluid restoring force/damping dampers. For information on these dampers, the reader is referred to ATC (1993), Constantinou et al. (1998), EERI (1993), Soong and Constantinou (1994), Soong and Dargush (1997) and Hanson and Soong (2001).

The dominant type of damper in use at this time for earthquake and wind applications is the fluid viscous damper. The fluid viscous damper is discussed in detail in the following sections of this chapter. One hysteretic damper that could be implemented in braced towers or piers of bridges is the buckling restrained brace (BRB). The construction and

mechanical properties of the BRB are discussed in Subsection 10.2.2. Buckling restrained braces could replace conventional concentric braces to improve the hysteretic response of piers.

10.2.2 Construction and Mechanical Properties of Buckling Restrained Braces

The buckling restrained brace (BRB) was developed in Japan in the mid-1980s (Watanabe et al., 1988) and has been used on a significant number of building projects in the United States. The schematic of Figure 2-15 illustrates the key components of the BRB constructed by a Japanese manufacturer, namely, a cruciform cross section of welded steel plate, often of low-yield steel, that is designed to yield in both tension and compression, and an exterior steel tube of circular or rectangular cross section that is selected such that the buckling capacity of the tube exceeds the squash load of the internal cross section. The space between the internal cross section and the steel tube is filled with a concrete-like material to delay local buckling of the cruciform cross section outstands. Proprietary materials are used to de-bond the internal cross section from the concrete-like material. The BRB is designed to have approximately equal strength in tension and compression, and is conceptually superior to the concentrically braced frame because the beam at the intersection point of the chevron braces does not have to be designed for large out-of-balance vertical forces. Figure 10-1 presents a photograph of a BRB frame tested at Berkeley (Mahin, 2006) and the force-displacement relationship for a BRB, also tested at Berkeley (Black et al., 2002).

a. BRB test frame (Mahin, 2006)
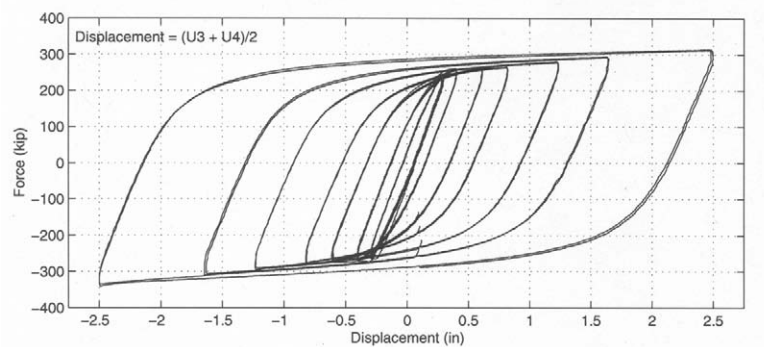
b. BRB response (Black et al,. 2002)

FIGURE 10-1 Buckling-Restrained Braces and Frames

340

10.3 Construction of Fluid Viscous Dampers

Figure 10-2 is a cross section through fluid viscous dampers in two alternate constructions. The key mechanical components of the dampers are the piston rod, piston head, damper casing (cylinder), seals and a silicone-based fluid.
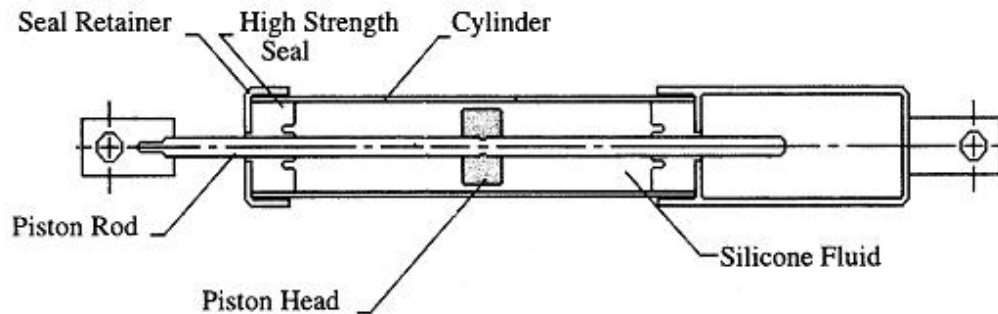
a) damper construction with run-through piston rod
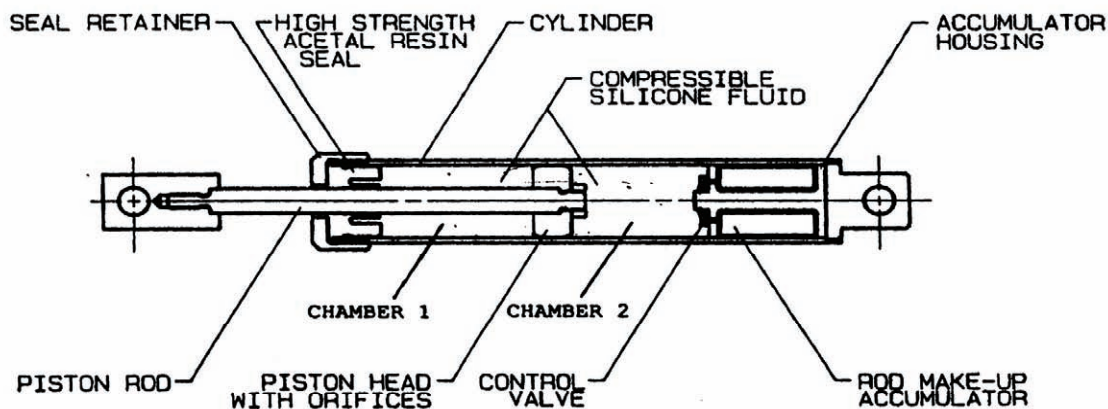
b) damper construction with an accumulator

FIGURE 10-2 Construction of a Fluid Viscous Damper

Accumulators are provided in some dampers to replace lost fluid in the body of the damper (chambers 1 and 2 in Figure 10-2b) due to seal weepage and to accommodate changes in internal damper pressure due to fluctuations in fluid temperature (Penton, 2004) and/or the use of single-acting dampers in which the piston rod is located on one side of the piston head only. The use of an accumulator in a damper can result in the development of restoring force (Constantinou and Symans, 1992) but such an effect can only be assessed by full-scale dynamic testing. Moreover, accumulators may have negative impact on the longevity and reliability of dampers which cannot be easily assessed other than by long term field observations. The damper shown in Figure 10-2b was originally used in testing at the University at Buffalo (Constantinou and Symans, 1992) but not implemented to the knowledge of the authors.

The construction of dampers with run-through piston rod as shown in Figure 10-2a is typical of what is used today in applications of seismic isolation and damping systems. The use of this construction ensures that the damper does not exhibit any undesirable stiffness as a result of compression of the fluid in the damper. Fluidic devices that are capable of providing restoring force in a variety of forms are discussed in Section 10.7.

Manufacturers of fluid viscous dampers use a variety of materials for the piston rod, piston head, damper casing and seals. For optimal corrosion resistance (a significant concern for dampers installed in bridges), stainless steels should used for the cylinder and rod. Alternate materials are plated steels but the corrosion resistance will depend on the quality and coverage of the material used for plating. Piston rods must typically be highly polished to optimize the function of the damper, maximize the life of the seals and minimize the frictional resistance of the damper; polishing should be parallel to the axis of the piston rod and a maximum piston-rod surface roughness should be specified. It is best for longevity and reliability that the piston rods are made of highly polished stainless steel.

OSHA-approved silicone based oils are typically used for the fluid in viscous dampers. The selection of oil type by the damper vendor is based on the required mechanical properties of the damper, including temperature dependence on viscosity and compressibility.

Pure viscous behavior can be produced by forcing fluid through an orifice (Constantinou and Symans, 1993; Soong and Constantinou, 1994; Soong and Dargush, 1997), which can be installed inside a piston head or be formed by a gap between the piston head and the cylinder. Figure 10-3 is a cross-section through a piston head in a fluid viscous damper – fluid flows from chamber to chamber in this instance through and around the piston head. Standard through-piston-head orifices with specific flow characteristics can be purchased from hydraulics-related suppliers. Custom-designed orifices have also been used for selected applications. Fluid flow around the piston head is controlled by shaping the edges of the piston head and maintaining a specific clearance between the piston head and the cylinder, which can require the use of specialized metals on the perimeter of the piston head to provide thermal compensation so that piston head and cylinder expand under repeated cycling but maintain the specified clearance–the design of such piston heads is generally project specific and proprietary to the supplier. Some types of fluid viscous dampers utilize external piping to move the fluid from chamber to chamber via valves installed on the cylinder on either side of the piston head. In general, the use of valves reduces the reliability and longevity of the devices.

Seals in fluid viscous dampers vary by damper supplier and function across a wide range of pressures, from low (0-20 psi, 0 – 0.14 MPa) to high (5000+ psi, 34+ MPa). High strength acetal resin seals are shown in Figure 10-2–these seals utilize the high static and dynamic internal fluid pressure to press the seal onto the piston rod and prevent leakage.
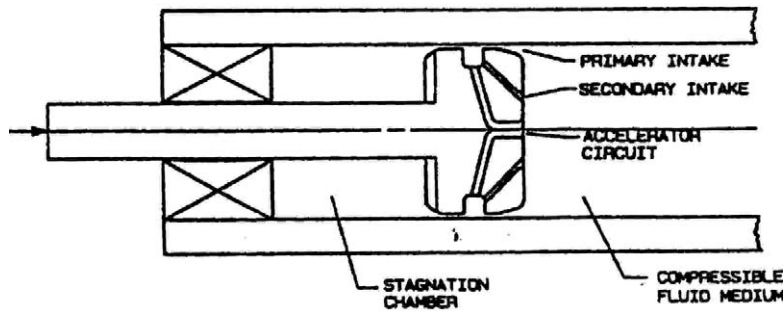
FIGURE 10-3 Piston-head Orifices

Each end of a damper should be articulated to permit rotation in the plane of the axis of the damper and perpendicular to that plane. Such articulation is generally using spherical bearing that allow multi-axis rotation of the damper. Bearings are often constructed from stainless steel or plated steel.

10.4 Mechanical properties of fluid viscous dampers

Axial force is developed in a damper due to a difference in fluid pressure across the piston head; the force output of a damper is given by

$$F = A_1 p_1 - A_2 p_2 \tag{10-1}$$

where A_1 and A_2 are the areas of the piston head exposed to fluid in chambers 1 and 2 (see Figure 10-2b), respectively, and p_1 and p_2 are the fluid pressures in chambers 1 and 2, respectively. For the single-acting damper of Figure 10-2b (rod on one side of the piston head only), the difference between A_1 and A_2 is the area of the piston rod: the difference in the piston-face areas can produce asymmetric force-displacement loops. For double-acting or through-rod dampers (rod on both sides of the piston head as shown in Figure 10-2a), A_1 is equal to A_2 and equation (10-1) reduces to

$$F = A_1 \Delta p \tag{10-2}$$

where Δp is the pressure drop across the piston head. The relationship between Δp and the velocity of the piston head with respect to the cylinder, $\dot{\Delta}$, is defined by the passage of fluid through and/or around the piston head.

The force output of a viscous damper is generally specified as follows:

$$F = C \left| \dot{\Delta} \right|^{\alpha} \operatorname{sgn}(\dot{\Delta}) \tag{10-3}$$

where C is a damping constant that is dependant on the area of the piston head, $\dot{\Delta}$ is defined above, α is an exponent in the range of 0.1 to 2.0, and sgn is the signum function. The simplest form is the linear fluid viscous damper for which the exponent is equal to 1.0. Nonlinear fluid viscous dampers, with exponents in the range of 0.3 to 0.5 are often used to limit the force output of the damper for velocities in excess of the design velocity and to maximize the energy dissipated per cycle to a given peak velocity and

343

peak displacement. Figure 10-4 below presents the experimentally measured force-displacement response for a nonlinear viscous damper rated for a force output of 667 kN (150 kips) at a velocity of 1 m/second; the amplitude of the test displacement was 177 mm (7 inches).
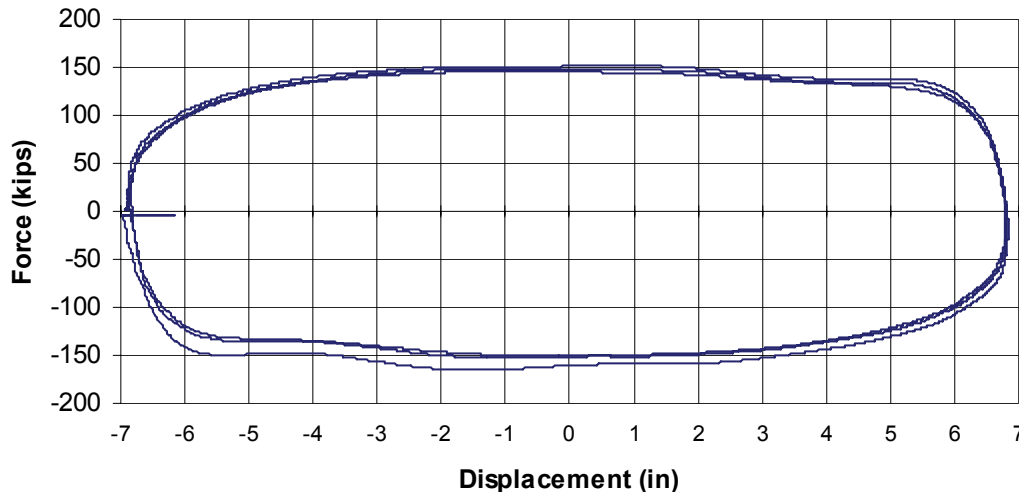
FIGURE 10-4 Force-Displacement Response of a Nonlinear Fluid Viscous Damper (1 kip = 4.44kN, 1 inch = 25.4 mm)

Figure 10-5 enables a comparison of the force-velocity relationships for two fluid viscous dampers, each designed to produce a force output of 2223 kN (500 kips) at a velocity of 635 mm (25 inches) per second: a linear damper for which $F = 20v$, where F is the force in kips and v is the relative velocity in inches/sec and a nonlinear damper with an exponent of 0.3 for which $F = 190.4v^{0.3}$. For velocities of less than 635 mm (25 inches) per second, the force output of the nonlinear damper is greater than that of the linear damper. Importantly, for velocities greater than the target value of 635 mm (25 inches) per second, the force output of the nonlinear damper increases only modestly by comparison with that of the linear damper—a design attribute because the damper framing must be designed for forces in excess of those associated with the target velocity to account for the uncertainties in the earthquake ground motions and the response predictions. Differences in the velocity exponent for the damping device are realized by (a) modification of the orifices, either annular or through-piston head and (b) by use of relief valves and accumulators. The latter method typically affects the reliability and longevity of the device.

The use of highly nonlinear viscous damping devices (particularly those with a very low velocity exponent) can negatively impact the performance of nonstructural components (Wolff and Constantinou, 2004; Pavlou and Constantinou, 2006)—an issue for buildings but not bridges.
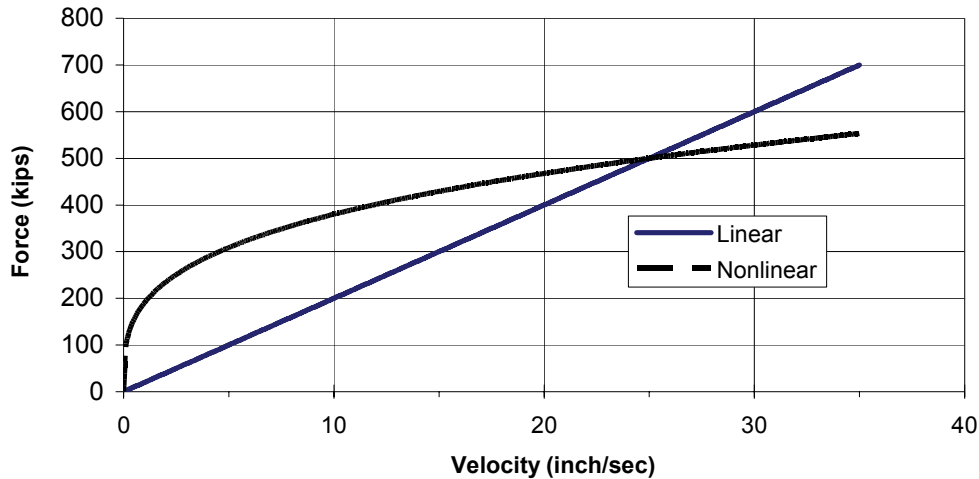
FIGURE 10-5   Force-Velocity Responses of Linear and Nonlinear Fluid Viscous Dampers (1 kip = 4.44kN, 1 inch = 25.4 mm)

10.5 Effect of Temperature Increase on the Response of Fluid Viscous Dampers

An increase in the operating temperature of the damper fluid can have two key effects on the force-velocity-displacement response of a fluid viscous damper, namely, (a) a reduction in the viscosity of the fluid that effectively leads to a reduction in the effective damper constant, C, and the force output of the damper; and (b) failure of the seals that retain the fluid in the damper. Figure 10-6 illustrates the influence of temperature rise on the hysteretic response of two 1067 kN (240 kip) fluid viscous dampers subjected to sinusoidal displacement histories with a frequency of 0.5 Hz and a displacement of ± 304 mm (12 inches). The force output in both fluid viscous dampers decreases with repeated cycling, with a larger percentage drop in damper type 1.

The operating temperature of the silicone fluid in a damper can increase or decrease due to fluctuations in ambient temperature and will increase as a result of energy input due to service wind loadings (small amplitude displacements, long duration) and earthquake shaking (large amplitude shaking, short duration). Fluid viscous dampers dissipate energy via heat, some of which is lost to the atmosphere though conduction and convection but most of which is retained in the fluid (for the earthquake shaking condition). Makris (1998) and Makris et al. (1998) developed closed form solutions to compute the temperature rise in fluid viscous dampers for small amplitude (wind) motions and large-amplitude (earthquake) motions, respectively. For the heating of the viscous fluid under small amplitude motions, Makris demonstrated that the temperature rise is proportional to the pressure drop across the piston head (Δp) and the piston velocity relative to the casing (v): the smaller the pressure drop (and thus smaller force output at a given velocity) the smaller the steady state temperature. Moreover, Makris demonstrated that small amplitude cycling about the neutral position resulted in the greatest steady state temperature increase on the piston head but that the steady-state temperature attenuates

345

rapidly with distance from the piston head. For large amplitude motions that stroke the damper from end to end and thus force most of the damper fluid through the orifices, Makris et al. showed that the fluid temperature at every point in the damper is by-and-large constant, that the temperature rise is proportional to the pressure drop across the piston head and independent of the relative velocity of the damper with respect to the cylinder. Closed form solutions were developed for idealized loading histories (harmonic wave motion and triangular wave motion).
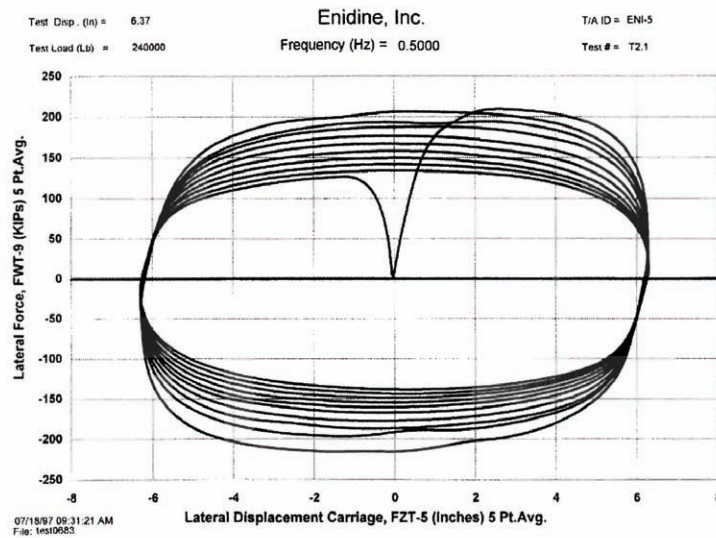
a. damper type 1 (CERF, 1999b)
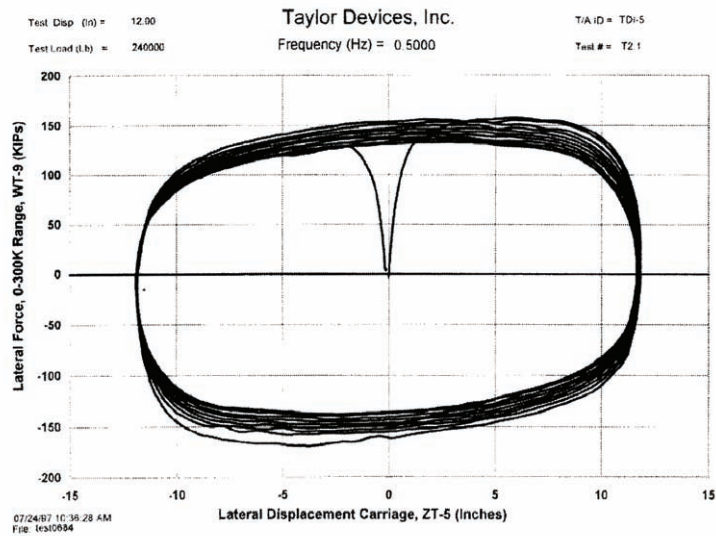
b. Damper type 2 (CERF, 1999c)

FIGURE 10-6 Effect of Temperature Rise on Hysteretic Response of Fluid Viscous Dampers (1 kip = 4.44kN, 1 inch = 25.4 mm)

346

Taylor (2006) observed that no closed form solution of the type proposed by Makris has been validated in prototype dampers and that the localized heating of the fluid and of the material that is used to construct the orifices makes the development of a closed form solution intractable. Taylor noted that the damper manufacturer must address thermal effects and their influence on hysteretic response through selection of fluid (boiling point, flashpoint and viscosity-temperature response), seals, fluid pressure, overall damper geometry, thermal mass of fluid and metal, and the size and locations of the orifices.

For implementation in bridges, each damper should be tested using loading environments consistent with those that will likely be experienced over the design life of the damper because a) closed form solutions are unavailable for complex loading environments, and b) the assumptions made in derived the equations might be invalid for selected damping devices. For prototype and production testing and performance evaluation, full-scale dynamic tests should be undertaken to characterize the change in hysteresis (force-displacement response) with repeated cycling – although the increase in temperature with repeated cycling is an academic curiosity, it is the change in hysteresis (loss of energy dissipation or damping) that the bridge engineer is most interested in. Information on testing dampers is presented in Section 13.

10.6 Shock Transmission Units

Shock transmission units (also termed lock-up devices) are variants on fluid viscous dampers, allowing near-unrestricted motion at low (thermal) velocities and near-rigid behavior at high (earthquake) velocities. Shock transmission units are used to link (or lock) together segments of a bridge (e.g., a series of simply supported spans) to form an integral unit that transfers service loads (e.g. due to vehicle braking) and extreme loads (e.g., earthquake-induced) along the axis of the bridge into the substructure in a predetermined manner. Figure 10-7 (adapted from Taylor, 2000) provides a conceptual application of shock transmission unites with the objective of linking rigidly the three segments of the bridge to the abutments and the piers. Units range in size from tens to thousands of kips.

Figure 10-8 provides a conceptual longitudinal section through a double-acting shock-transmission unit (Taylor, 2000). The construction is virtually identical to that of a fluid viscous damper, with the key difference being the orifices through the piston head. Construction materials are identical to that of fluid viscous dampers except for the operating medium, which might be a putty-type material rather than silicone oil. Shock transmission units are generally compact because the required displacement capacity (stroke) is small. The operation of the unit is identical to that of the fluid damper, namely, relative motion between the piston head and the cylinder forces fluid (or a putty-type material) from one chamber to the other through orifices in the piston head. The orifices are generally small with a large ratio of length to diameter - providing high flow resistance at low velocities.

347
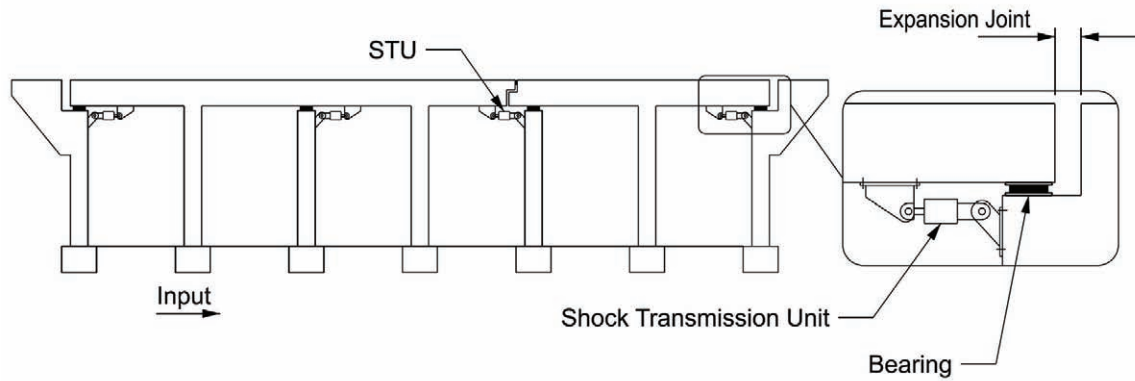
FIGURE 10-7 Shock Transmission Unit Conceptual Application (adapted from Taylor, 2000)
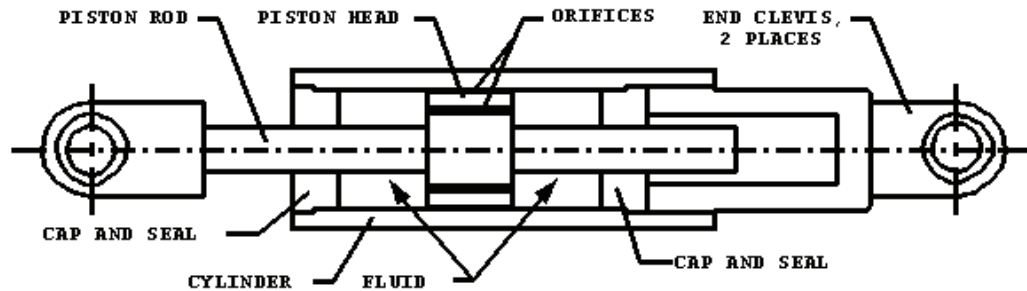
FIGURE 10-8 Shock Transmission Unit Construction Details (Taylor, 2000)

The force output of a shock transmission unit can be expressed using (10-3). The velocity exponent of a shock transmission unit is normally one or greater, with unit output force of less than 10% of the rated (force) capacity of the unit at velocities associated with thermal expansion (e.g., of the order of 0.0025 mm/sec) and development of the rated force of the unit at velocities of the order of 1 to 10% of the expected velocity in the design event (e.g., velocity due to earthquake, wind, braking). The energy dissipated by a shock transmission unit is generally small and is ignored for the purpose of analysis and design. Using the example of Figure 10-5, for which $F = 20v$ and $F = 190.4v^{0.3}$ (units of kips and inches/second) for the linear and nonlinear fluid viscous dampers, respectively, with a target velocity of 635 mm (25 inches) per second, the force-velocity relationship for a 2220 kN (500)-kip shock transmission unit could be $F = 2000v$ in units of kips and inches/second, where the force output at 127 mm (0.005 inch) per second is 89 kN (20 kips) (4% of the rated capacity) and 2220 kN (500 kips) at 6.3 mm (0.25 inch) per second (1% of the target velocity).

348

10.7 Restoring Force and Damping Devices

Tsopelas and Constantinou (1994), Soong and Dargush (1996) and Constantinou et al. (1998) describe the behavior of fluidic restoring force and damping devices. Such devices can be designed to be rigid under service loading and to provide a restoring force and damping under earthquake loadings. They can be used in road and railway bridges where high stiffness is needed for gravity, traffic, wind and centrifugal forces.

Figure 10-9 presents a force-displacement loop of one such device used in the earthquake-simulator testing of a bridge model (Tsopelas and Constantinou, 1994). The device is a compressible fluid spring that is pressurized to develop a preload. Orifices were used to produce a viscous damping force. The principles of operation are illustrated in Figure 10-10: a hydraulic cylinder is completely filled with fluid; a rod of area A_r is forced into the cylinder so that the volume of the fluid is reduced by an amount $A_r u$, where u is the imposed rod displacement. The overpressure p in the cylinder is

$$p = \frac{F}{A_r} \qquad (10\text{-}4)$$

where F is the imposed force.
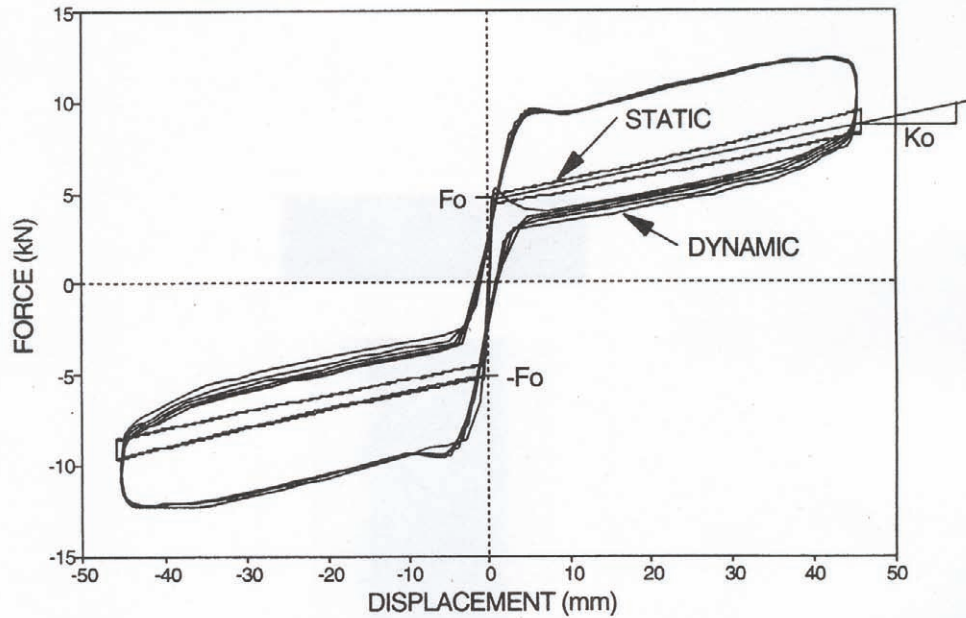
FIGURE 10-9 Sample Force-Displacement Loops of Small-Scale Restoring Force/Damping Device

The overpressure is related to the change of volume of the fluid $\Delta V = A_r u$

$$p = K \frac{\Delta V}{V} \qquad (10\text{-}5)$$

349
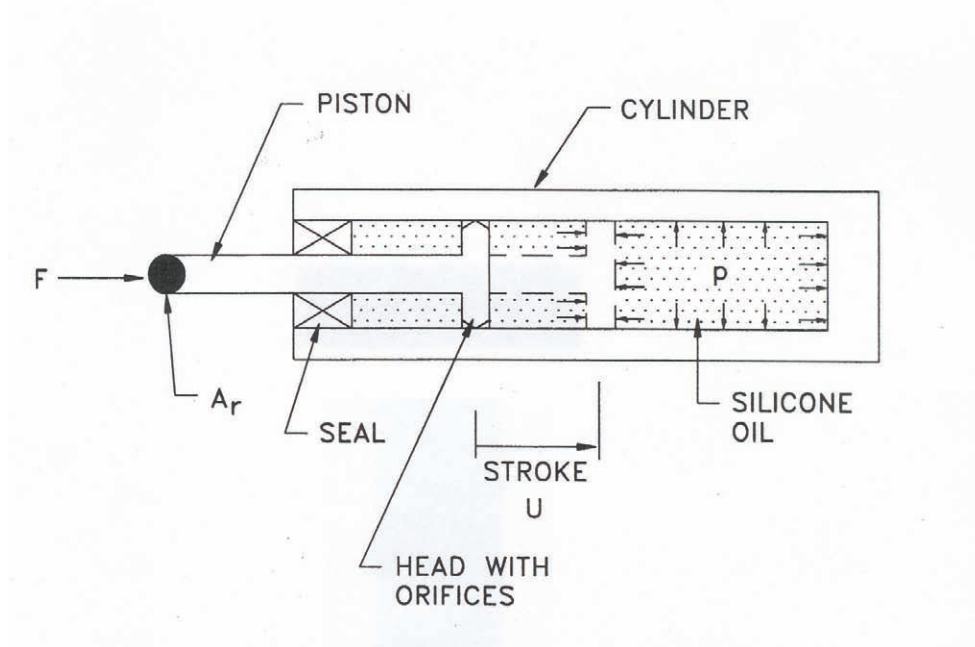
FIGURE 10-10 Operation of Restoring Force/Damping Device

where V is the fluid volume and K is the bulk modulus of the fluid. Equations (10-4) and (10-5) give the following expression for the force F

$$F = \frac{KA_r^2}{V}u \qquad (10\text{-}6)$$

This relationship is shown in Figure 10-11a. The force-displacement relationship is stiffening-nonlinear because the volume of the fluid is reduced as the displacement u increases.

Friction in the seal alters the force-displacement relationship as shown in Figure 10-11b. By pressurizing the device to an initial pressure of p_o, a preload F_o develops, where

$$F_o = A_r p_o \qquad (10\text{-}7)$$

The preload must be exceeded for the rod to initiate motion. The force-displacement relationship with preload is shown in Figure 10-11c. Fluid passage through orifices in the piston head produces a viscous force and the force-displacement relationship takes the form shown in Figure 10-11d. The damping force in Figure 10-11d is intentionally shown to be different in one direction than the other (these also the loops of the tested device presented in Figure 10.9.) This behavior is achieved by additional orifice area in one direction only. This behavior might be desirable if greater damping is required for large stroke (e.g., to reduce the displacement demand) and less damping is required for small stroke (e.g., to enable re-centering).

350
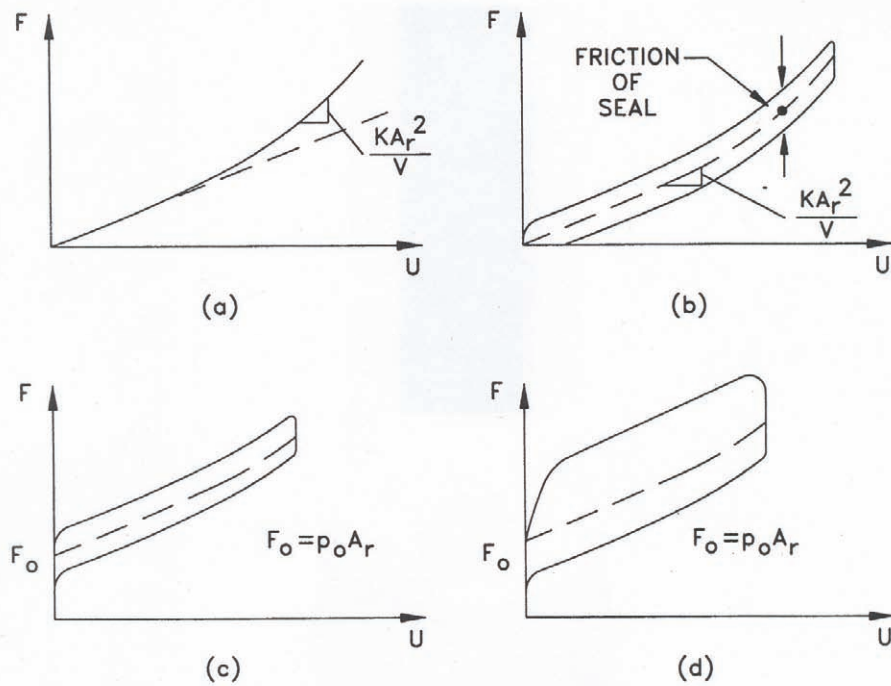
FIGURE 10-11 Components of Force in Restoring Force/Damping Device

Compression-only restoring force and damping devices can be used independently or combined in devices that function in both compression and tension. Figure 10-12 shows the construction of the device tested by Tsopelas and Constantinou (1994). Such devices, with force outputs of up to 1500 kN, have used for defense applications since the early 1970s.
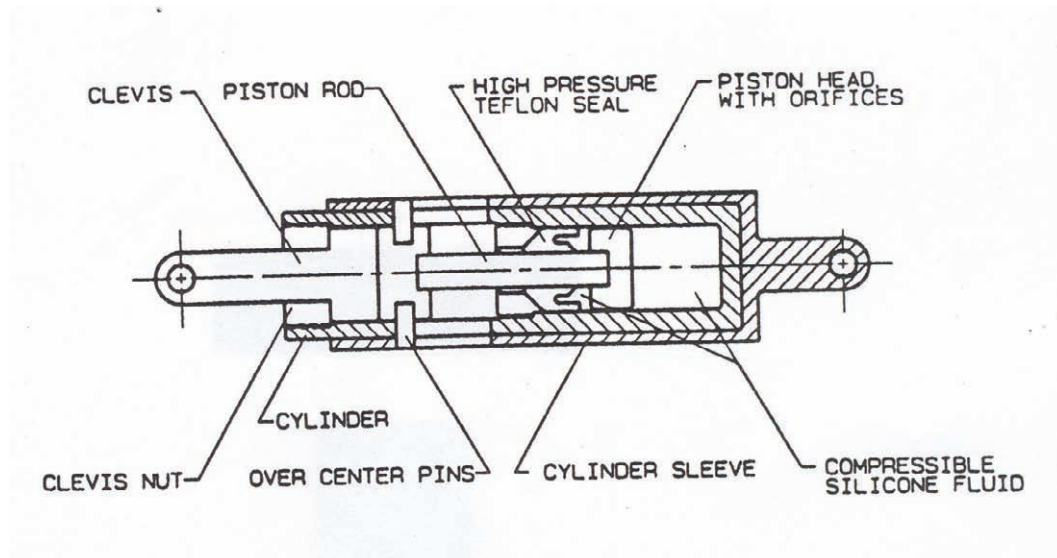
FIGURE 10-12 Construction of Double Acting Restoring Force/Damping Device

351

10.8 Service Life of Fluid Viscous Dampers

The service life of a fluid viscous damper (and shock transmission unit) can be limited by corrosion of metallic components, failure of the seals and aging of the operating medium (silicone-based oil for fluid dampers and silicone-based oil or putty for shock transmission units).

Corrosion of metal parts can lead to direct loss of fluid from the cylinder or loss of fluid due to seal failure (corroded piston rod moving over the seals). Appropriate specification of metallic components can mitigate possible corrosion, with stainless steels generally providing a longer service life than plated steels. Accelerated corrosion testing can be performed in a salt spray chamber using ASTM Standard B117, which provides a controlled corrosive environment that is intended to represent accelerated marine-type atmospheric conditions. Specimen type, length of exposure in the chamber and acceptance criteria must be specified by the engineer. However, as discussed in Section 4.10 such accelerated aging tests do not truly simulate the conditions of a device subjected to continuous movement over 30 to 50 years in a corrosive environment. Best practice is to require highly polished stainless steel piston rod and avoid the use of plated steel.

The failure of the seals in a fluid viscous damper or shock transmission unit can be considered catastrophic. Fluid dampers and shock transmission units are cycled daily in bridge structures due to thermal expansion and contraction of the bridge deck, braking loads and traffic-induced vibration: 20,000+ service-level cycles in a 50-year period. Importantly, the seals have to function properly under conditions of extreme loading at any time over the design life of the damper or unit, which can exceed 50 years. Seal quality is of the utmost importance; special attention to seal design must be emphasized and a prototype testing program must address pressure and movement demands on seals. Modifications to the size of the orifices in a shock transmission unit might be needed to permit service-level testing at velocities greater than that associated with thermal cycling of a bridge.

Aging of the silicone-base oils over the design life of a damper or shock transmission unit is not considered to be of concern. Changes in mechanical properties due to cyclic loading, although considered negligible, can be evaluated by testing of full-scale units. The change in mechanical properties of the putty used in selected shock transmission units should be evaluated by accelerated aging tests, although the results of such tests should be interpreted with care. Changes in mechanical properties of the putty due to cyclic loading should be evaluated by testing of full-scale units.

The likely changes of properties of fluid dampers and shock transmission devices over the lifetime of the structure cannot be currently predicted. Considering that catastrophic failures of seals can be prevented by proper design and use of appropriate materials, the range of property values to be considered in analysis and design could be that due to inherent variability of properties. Typically, a range of ±15% of the nominal value is considered acceptable and should be used in upper and lower bound analysis.

SECTION 11
CONFIGURATIONS OF DAMPING SYSTEMS

11.1 Introduction

Passive energy dissipation devices and shock transmission units have been installed in bridges in a number of configurations. Optimal configurations maximize the supplemental damping per unit cost. All configurations require relative displacement between the ends of the dampers to dissipate energy and all must accommodate thermal cycling of the bridge but develop only small forces.

Substantial relative horizontal displacements of between ±50 mm and ±200 mm can develop in conventional (non-isolated) bridges due to thermal expansion and contraction. This occurs across expansion joints between segments of a bridge superstructure and between piers/abutments and segments of a bridge superstructure (the locations are indicated in Figure 10-7). Fluid viscous dampers and shock transmission units could be installed in these locations. Fluid viscous dampers and buckling restrained braces could be installed in bridge piers such as those shown in Figure 11-1.

11.2 In-line-brace and Diagonal-brace Configurations

The traditional damper configurations are termed herein *in-line* and *diagonal*. The *in-line* configuration is shown in Figure 10-7 where the relative displacement between the ends of the damping device is equal to the relative displacement of the adjacent bridge segments. An example of a *diagonal* (or angled) configuration would be a knee-brace installation between the vertical face of an abutment and the underside of a segment of bridge deck: in this configuration, the extension and contraction of the damper is less than the relative horizontal displacement between the ends of the damper.

For the *in-line* configurations of Figure 10-7 and the *diagonal* installation described in the preceding paragraph, only the fluid viscous damper (or shock transmission unit) can be deployed because a buckling restrained brace would develop large axial forces under thermal cycling of the bridge.

Passive energy dissipation devices could be installed in tall bridge piers to mitigate the response of the pier and the supported superstructure. If displacement-dependent dampers (e.g., buckling restrained brace) are to be installed in these piers, the cost-effective solution is to install the braces either diagonally across the panel (per Figure 11-1) or in a chevron configuration (braces meeting at the midpoint of a beam spanning the dimension of the pier (see Figure 11-2 for a chevron-brace installation of buckling restrained braces in a building).

Fluid viscous dampers could be installed in parallel with a braced framing system (either new or existing) in a bridge pier but the relative horizontal displacements between the ends of the damper will generally be small. Large damper forces are then needed to develop moderate levels of supplemental damping. Damper displacements in

353

conventionally configured systems will be less than or equal to the relative horizontal displacement of the panel of framing in which the damper is installed. For a small-stroke fluid viscous damper, special details would be required that will substantially increase the volume and cost of the damper.

FIGURE 11-1 Braced Steel Piers

FIGURE 11-2 Chevron Brace Installation of Buckling Restrained Braces

Research projects at the University at Buffalo (e.g., Constantinou and Sigaher, 2000; Constantinou et al., 2001; Sigaher and Constantinou, 2003) expanded the utility of fluid viscous damping devices to stiff structural systems and small displacement applications through the use of mechanisms that magnify the damper displacement. Such magnification permits the use of dampers with smaller force outputs (smaller damper

volume), larger strokes, and reduced cost. Two configurations are the toggle-brace and the scissor-jack, each of which is discussed below.

11.3 Alternate Damper Configurations

The toggle-brace configuration is shown in Figures 11-3 and 11-4a below. The supplemental framing consists of toggles AB and BC that are configured as a shallow truss. The damper is placed perpendicular to toggle AB. If the damper is sited at location 1, the configuration is termed lower-toggle; the damper is sited at location 2 in the upper-toggle configuration. The most effective configuration is the upper toggle. In each configuration, displacement of point C with respect to point A, equal to panel drift u, causes toggle AB to rotate. The resulting changes in distance between points B and D, and B and E are the damper displacements u_{D1} and u_{D2}, respectively. These displacements are related to the panel drift, u, through simple equations.
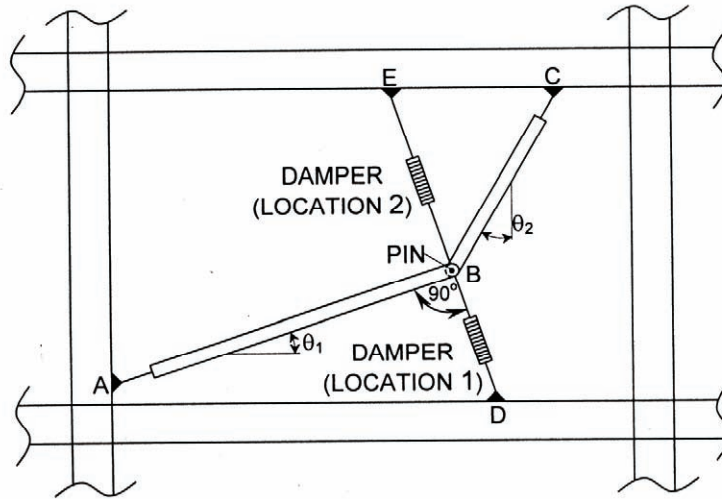
FIGURE 11-3 Toggle-brace Assembly

Damping forces in the toggle-brace system are small but are magnified in the shallow truss and delivered to the framing system by axial forces in the braces. The absence of flexure in the toggle-brace assembly facilitates the use of small structural sections and standard connection details. The assembly is compact and can be installed in a square space with a side length equal to the column height-the dimensions of a panel in a bridge pier. For small rotations and damper location number 1, the damper displacement is related to the interstory drift, u, as follows:

$$u_D = fu \qquad (11\text{-}1)$$

For damper location 2, the relation is:

$$u_D = (f + \sin\theta_1)u = f_u u \qquad (11\text{-}2)$$

355

a. upper toggle-brace   b. scissor jack

FIGURE 11-4 Toggle-brace and Scissor-jack Damper Assemblies on the Buffalo Simulator

where,

$$f = \frac{\sin\theta_2}{\cos(\theta_1 + \theta_2)}$$
(11-3)

The displacement magnification factors f and f_u depend only on the inclination of the toggle braces. High displacement magnifications can be achieved although values are sensitive to small changes in θ_1 and θ_2. Magnification factors of between 2 and 3 can be easily achieved and are insensitive to small variations in changes in θ_1 and θ_2. For small rotations and location 1, the relation between the damper force, F, and the force exerted by the toggle-brace assembly on the structural frame, F_F, is

$$F_F = f F$$
(11-4)

For location 2,

$$F_F = f_u F$$
(11-5)

Equations (11-1) through (11-5) have the same form as those equations written for dampers installed in diagonal or in-line braces and dampers atop chevron braces.

356

The reverse toggle and the scissor-jack assemblies of Figures 11-4b and 11-5 are variants of the toggle-brace assembly. Equations similar to those presented above for the toggle-brace assemblies have been developed for the reverse toggle and the scissor-jack systems; details are provided in Figure 11-5.

To illustrate the effectiveness of the toggle-brace and scissor-jack assemblies for stiff framing systems, consider the six damper configurations and simple single-panel framing system presented in Figure 11-5. The diagonal and the in-line installations represent conventional damper configurations. For the purpose of comparison, assume that the single-panel structure has a fundamental period of 0.3 second, a linear fluid viscous damper with a damping constant, C, equal to 160 kNs/m, a frame weight of 1370 kN, and angles, θ, θ_1, θ_2, θ_3 and ψ as shown in Figure 11-5.

The force output of the damper, F, is given by:

$$F = C\dot{u}_D \tag{11-6}$$

where $\dot{u}_D$ is the relative velocity between the ends of the damper along the axis of the damper. The damping force exerted on the frame by the damper assembly, F_F, is given by

$$F_F = Cf^2\dot{u} \tag{11-7}$$

where $\dot{u}$ is the relative velocity over the height of the panel and f is equal to f_u if the damper is placed in location 2 of the toggle brace in Figure 11-3. The damping ratio of the panel of Figure 11-5, with weight, $\bar{W}_1$, and fundamental period, T_1, is:

$$\beta_{v1} = \frac{Cf^2 g T_1}{4\pi \bar{W}_1} \tag{11-8}$$

Figure 11-5 provides a comparison of the various damper configurations in a simple structure that is not intended to represent a bridge. The damping ratios for the conventional diagonal and in-line configurations are less than 5% of critical and greater than 23% for the toggle-brace and scissor-jack assemblies. The displacement magnification factors for the toggle-brace and scissor-jack assemblies exceed 2.1.

Although these alternate damper configurations have not yet been employed in bridges, there are four applications to buildings, one in region of high seismic hazard: the 37-story Yerba Buena Tower in San Francisco that incorporates fluid viscous dampers in the reverse-toggle configuration. This configuration, in which the toggles and dampers connect directly to the beam-to-column joints, eliminates additional bending in the beams and provides for easy and reliable calculation of the magnification factor. Figure 11-6 presents a photograph of one of the toggle-brace assemblies in the Yerba Buena tower. Also, Figure 11-7 presents a photograph of one scissor-jack assembly at the Olympic Committee Building in Cyprus.

Diagonal		$f = cos\,\theta$	$\theta = 37^{o}$ $f = 0.799$ $\beta = 0.032$
In-line		$f = 1.00$	$f = 1.00$ $\beta = 0.05$
Lower Toggle		$f = \dfrac{sin\,\theta_2}{cos(\theta_1 + \theta_2)}$	$\theta_1 = 31.9^{o}, \theta_2 = 43.2^{o}$ $f = 2.662$ $\beta = 0.344$
Upper Toggle		$f = \dfrac{sin\,\theta_2}{cos(\theta_1 + \theta_2)} + sin\,\theta_1$	$\theta_1 = 31.9^{o}, \theta_2 = 43.2^{o}$ $f = 3.191$ $\beta = 0.509$
Reverse Toggle		$f = \dfrac{\alpha\,cos\,\theta_1}{cos(\theta_1 + \theta_2)} - cos\,\theta_2$	$\theta_1 = 30^{o}, \theta_2 = 49^{o}, \alpha = 0.7$ $f = 2.521$ $\beta = 0.318$
Scissor-Jack		$f = \dfrac{cos\,\psi}{tan\,\theta_3}$	$\theta_3 = 9^{o}, \psi = 70^{o}$ $f = 2.159$ $\beta = 0.233$

FIGURE 11-5 Effectiveness of Damper Configurations

358

FIGURE 11-6 Reverse-toggle Brace Installation

FIGURE 11-7 Scissor-jack Assembly Installation

The integrity and performance of these alternately configured fluid viscous damping systems will be dependant on the environmental protection provided to the toggle braces and connections of the dampers and braces to the bridge superstructure/substructure. The protection afforded to the toggle braces and connections must be similar to that for the fluid viscous dampers.

SECTION 12
SYSTEM PROPERTY MODIFICATION FACTORS

12.1 Introduction

The properties of seismic isolation bearings vary due to the effects of wear, aging, temperature, environmental exposure and history of loading. Although the exact state of a bearing at the time of seismic excitation will be unknown, it is possible to establish probable maximum and minimum values of its key mechanical properties over the its lifetime of use. Analysis can then be conducted with both the minimum and maximum values to envelope the likely response of the isolated structure.

The probable maximum and minimum values of key mechanical properties could be established by statistical analysis of the distribution of the properties and consideration of the likelihood of occurrence of relevant events, including the design seismic event. However, it is simpler to assess the impact of a particular effect on the properties of a bearing by either testing (e.g., effect of temperature on the coefficient of friction in sliding bearings) or a combination of testing, rational analysis and engineering judgment. This section of the report addresses methods for computing the likely variations in material properties of sliding and elastomeric bearings and the influence of these variations in component properties on the seismic response of the isolated structure.

Default maximum and minimum values of key mechanical properties are presented in this section. These values can be updated with appropriate test data. Manufacturers are encouraged to develop composite- and elastomer-specific values for all system property modification factors.

12.2 System Property Modification Factors

Consider that a nominal value of a mechanical property of an isolation bearing is known either on the basis of past experience or from prototype testing. The nominal value typically applies for a fresh and scragged bearing (that is, the bearing has been tested to remove virgin effects), a temperature of $20^{\circ}C$ and specific values of vertical load, frequency (or velocity) and strain (or displacement). Let this value be H_n. We note that the nominal value will generally have a range of values. For example, a nominal value of the coefficient of friction might be specified deterministically as 0.05 but in reality will vary as a function of bearing size, axial loading, speed of motion, and amplitude of motion. For the coefficient of friction for the sliding bearing, the range might be between 0.04 and 0.06.. For the purpose of this discussion, assume that the lower and upper bounds on the nominal value are H_{nL} and H_{nU}.

A manufacturer will generally agree on ranges of values for mechanical properties that will be part of the isolator specification and the contract for the manufacture, supply and performance of the bearings. The ranges must be sufficient to avoid delays due to an inability to manufacture the bearings to overly tight tolerances and experimentation with

unreliable manufacturing methods and curing processes to meet an overly restrictive specification.

The minimum and maximum values of this property, $H_{\max}$ and $H_{\min}$ respectively, are defined as the product of lower and upper bounds on the nominal value and a series of *System Property Modification Factors*, or λ factors, as follows:

$$H_{\max} = \lambda_{\max} H_{nL} \tag{12-1}$$

$$H_{\min} = \lambda_{\min} H_{nU} \tag{12-2}$$

where

$$\lambda_{\max} = \lambda_{\max,1} \times \lambda_{\max,2} \times \ldots \lambda_{\max,n} \tag{12-3}$$

$$\lambda_{\min} = \lambda_{\min,1} \times \lambda_{\min,2} \times \ldots \lambda_{\min,n} \tag{12-4}$$

Each of the individual values of $\lambda_{\max,i}$ (i = 1 to n), is greater than or equal to 1.0, whereas each of the individual values of $\lambda_{\min,i}$, is less than or equal to 1.0. Moreover, individual value of λ is associated with a different effect, such as wear, contamination, aging, history of loading, temperature and environmental exposure.

For example, consider the effect of temperature on the coefficient of friction of a sliding bearing. The range of temperature over the lifetime of the structure must be established for site or geographic region of the project. This range need not be that of extreme (lowest and highest) temperatures. Assume that the temperature range is -10$^{\mathrm{o}}$C to 50$^{\mathrm{o}}$C. Testing could be performed at these limiting temperatures and the values of λ established as the ratio of the coefficient of friction at the test temperature to the coefficient of friction at the reference temperature (say 20$^{\mathrm{o}}$C). For this example, $\lambda_{\min,t}$ will be based on the test data for the highest temperature (50$^{\mathrm{o}}$C) and $\lambda_{\max,t}$ will be based on the test data for the lowest temperature (-10$^{\mathrm{o}}$C).

As another example, consider the effect of wear on the coefficient of friction. The cumulative travel can be determined per Section 5.5 on the basis of the geometric characteristics of the bridge (span, girder depth, etc.), average vehicle crossing rate and lifetime of the bridge.. Tests can then be performed to establish the corresponding values for λ. The factor $\lambda_{\max,tr}$ will typically be the ratio of the coefficients of friction determined from high velocity testing following and prior to a sustained test at the appropriate velocity (~1 mm/s) for a total movement equal to the calculated cumulative travel. The value of $\lambda_{\min,tr}$ will be determined in a similar manner but at a total movement less than the cumulative travel at which the coefficient of friction is minimized.

Warn and Whittaker (2006) present sample results from an analytical study investigating how changes in the mechanical properties of individual seismic isolators in isolated bridge structures affect system response. The results of response-history analysis considering a simple seismically isolated bridge model, twenty nominal isolation systems

and a range of modification factors were used to quantify the change in system response: maximum displacement and maximum shear force. The range of λ values selected and used for response-history analysis was based an investigation of those values presented in the 1999 AASHTO Guide Specifications for Seismic Isolation Design for typical bridge isolation systems. System response data, more specifically the change in maximum shear force data, was translated into threshold values of λ for different percentage increases in maximum shear force. These threshold values were intended to provide design engineers with a tool to evaluate design alternatives prior to performing bounding analysis. The reader is referred to Warn and Whittaker (2006a, 2006c) for much additional information.

12.3 System Adjustment Factors

The system property modification factors are computed using (12-3) and (12-4). Although each one of the individual factors describes the impact of a specific effect (e.g., wear) on the mechanical properties of a bearing, the simple multiplication of maximum and minimum values per (12-3) and (12-4) might result in a system factor that is very conservative: the probability that several additive effects (e.g., lowest temperature, maximum travel and maximum corrosion) occur simultaneously with the maximum considered earthquake is very small.

A system property modification factor can be adjusted to reflect the required degree of conservatism. This adjustment should be based on a statistical analysis of the variations in mechanical properties with time, the probability of occurrence of joint events and the significance of the structure. A simple procedure for adjusting λ_{max} and λ_{max} is also required for routine implementation.

Such a procedure is described in Constantinou et al (1999) and implemented in the AASHTO Guide Specification for Seismic Isolation Design (AASHTO, 1999). The procedure uses an adjustment factor, a, as follows

$$\overline{\lambda}_{max} = 1 + (\lambda_{max} - 1)a \tag{12-5}$$

$$\overline{\lambda}_{min} = 1 + (1 - \lambda_{min})a \tag{12-6}$$

where $\overline{\lambda}_{max}$ and $\overline{\lambda}_{min}$ are the adjusted maximum and minimum system property modification factors, respectively. A value of a equal to 1.0 results in no adjustment, that is, the maximum variations have already taken place at the time of the design earthquake.

The AASHTO Guide Specification for Seismic Isolation Design proposes the following adjustment factors for bridges: 1.0 for critical bridges, 0.75 for essential bridges and 0.66 for all other bridge - values based on engineering judgment and a desire to employ a conservative approach for mission-critical bridges. Alternate values of parameter a should be developed after years of observation of the performance of seismically isolated bridges and other structures. Equations (12-5) and (12-6) should be modified to reflect the time required for maximum and minimum values of λ to be realized. For example, the effects of aging will likely be realized in a few years after the fabrication of the

363

bearings and no downwards adjustment of $\lambda_{\max}$ should be permitted in the calculation of $\bar{\lambda}_{\max}$.

12.4 Property Modification Factors for Sliding Bearings

12.4.1 Introduction

The property modification factors proposed in this subsection have been established on the basis of the test data of Section 5 and interpretation of the nature of friction presented in Section 4. The factors should be applied to the nominal value of the coefficient of friction under conditions consistent with design-event shaking, namely, high velocity motions. The proposed values are presented in tables for a range of effects and address the influence of service conditions, installation details and materials.

Three sliding interfaces are identified in these tables:

a) Unlubricated PTFE**:** Includes unlubricated interfaces consisting of highly polished austenitic stainless steel in contact with PTFE or similar composite materials (such as those used in FP bearings).

b) Lubricated PTFE: Includes lubricated interfaces consisting of highly polished austenitic stainless steel in contact with unfilled PTFE; lubrication is provided by grease stored in dimples.

c) Bimetallic interfaces**:** Includes interfaces consisting of stainless steel in contact with bronze (or similar metals and alloys) and without or with solid lubricants such as graphite, lead, PTFE, etc; the basic feature of this interface is bimetallic contact that might be significantly affected by load dwell; this interface does not include dissimilar metals (e.g., carbon and low alloy steels in contact with copper alloys), which should be avoided.

12.4.2 Effect of Aging, ($\lambda_{\max,a}$, $\lambda_{\min,a}$)

For stainless steel-PTFE interfaces, the proposed values are based on the effect of surface roughness on the coefficient of friction—data that are reported in Section 5. Where data were unavailable, values have been based on engineering judgment. For bimetallic interfaces, the proposed values are based on the effect of load dwell reported in Section 4.7 after adjustment for the likely effects of corrosion.

Table 12-1 presents values for $\lambda_{\max,a}$; values for $\lambda_{\min,a}$ are set equal to 1.0. The proposed values are based on the following assumptions: a) exposure time of 30 years; b) for PTFE interfaces, the stainless steel is austenitic of type 304—lower values might be justified for type 316 stainless steel as discussed in Section 5.7; c) unsealed bearings are prone to exposure to water and salt, each of which promotes corrosion; and d) the three installation types and four environmental conditions of Table 5-6 can be distilled to two installation types (sealed and unsealed) and two environmental conditions: normal (rural and urban) and severe (marine and industrial).

TABLE 12-1 System Property Modification Factor for Effects of Aging, $\lambda_{max,a}$, on the Coefficient of Friction of Sliding Bearings

Interface	Unlubricated PTFE		Lubricated PTFE		Bimetallic interface	
Installation	sealed	unsealed	sealed	unsealed	sealed	unsealed
Normal environment	1.1	1.2	1.3	1.4	2.0	2.2
Severe environment	1.2	1.5	1.4	1.8	2.2	2.5

12.4.3 Effect of Contamination, ($\lambda_{max,c}$, $\lambda_{min,c}$)

Values for $\lambda_{max,c}$ are proposed in Table 12-2 for the effect of contamination; $\lambda_{min,c}$ should be set equal to 1.0. The values for $\lambda_{max,c}$ are based on the data presented in Section 5.8. Contamination is considered only for in-service bearings; contamination due to disassembly of the bearings at the construction site is not considered. Unsealed bearings installed with the stainless steel surface facing upward are considered to be highly susceptible to contamination and this installation method is not considered here. It is the opinion of the authors that such an installation is inappropriate.

For other installations, the effect of contamination is expected to be modest and $\lambda_{max,c}$ for contamination should be in the range of 1.0 to 1.1, with exception of unsealed lubricated PTFE bearings. For this bearing, contamination is likely to cause hardening of the lubricant and a significant increase in the coefficient of sliding friction; $\lambda_{max,c} = 3.0$ reflects this observation and the use of unsealed lubricated PTFE bearings is discouraged. In Table 12-2, $\lambda_{max,c} = 1.1$ is proposed for sealed bearings with the stainless steel facing upward for which it is presumed that some contamination is likely from falling rust or paint particles from the carbon steel plate of the bearing above the stainless steel surface. If this plate is protected against corrosion by galvanizing or painting for 30-year lifetime, $\lambda_{max,c}$ can be taken as 1.0.

12.4.4 Effect of Cumulative Movement or Travel, ($\lambda_{max,tr}$, $\lambda_{min,tr}$)

The proposed factors for the effect of cumulative movement (or travel) are based on the data presented in Section 5.5, which indicate that the coefficient of friction reduces following small cumulative movement but increases following larger movement. The percentage increase depends on the roughness of the stainless steel and the composition of the sliding interface.

365

TABLE 12-2 System Property Modification Factor for Effects of Contamination, $\lambda_{max,c}$, on the Coefficient of Friction of Sliding Bearings

Installation Method	Unlubricated PTFE	Lubricated PTFE	Bimetallic interfaces
Sealed with stainless steel surface facing downward	1.0	1.0	1.0
Sealed with stainless steel surface facing upward, bearing galvanized/painted for 30 year life	1.0	1.0	1.0
Sealed with stainless steel surface facing upward	1.1	1.1	1.1
Unsealed with stainless steel surface facing downward	1.1	3.0	1.1
Unsealed with stainless steel surface facing upward	discouraged	discouraged	discouraged

The proposed factors for cumulative travel are based on data for unfilled PTFE in contact with highly polished stainless steel. These data show trends that are similar to those observed for the tested PTFE composite material (see Figures 5-19 and 5-20). There are limited or no data on the effect of cumulative motion for the commonly used sliding interfaces for cumulative travel in excess of 2 km. Accordingly, the proposed values are limited to travel of 2 km. The manufacturers of sliding bearings are encouraged to establish values of $\lambda_{max,tr}$ and $\lambda_{min,tr}$ as a function of the thickness of the composite material, roughness of stainless steel and apparent bearing pressure.

The 1999 AASHTO Guide Specifications for Seismic Isolation Design (AASHTO, 1999) specify $\lambda_{max,tr} = 1.0$. The minimum value, after significant travel is likely 0.8 to 0.9 for unlubricated PTFE bearings and 1.0 for lubricated PTFE bearings. There is no data upon which to base values for bimetallic interfaces. Table 12-3 presents values for $\lambda_{max,tr}$. The lack of numerical entries in the table reflects the lack of test data.

TABLE 12-3 System Property Modification Factor for Effects of Travel, $\lambda_{max,tr}$, on the Coefficient of Friction of Sliding Bearings

Cumulative travel (m)	Unfilled PTFE	Lubricated PTFE	Bimetallic interface
1000	1.0	1.0	NA
2000	1.2	1.0	NA
>2000	NA	NA	NA

12.4.5 Effect of Temperature ($\lambda_{\max,t}$, $\lambda_{\min,t}$)

The test results presented in Sections 5.4 and 5.9 demonstrate the effect of temperature on the coefficient of friction. In general, the coefficient of friction increases with a reduction in temperature of the sliding interface. The increase in friction is dependent on the frictional heating during the interval between the start of the experiment and the time at which the measurement is made.

The proposed values for $\lambda_{\max,t}$ that are presented in Table 12-4 for unfilled PTFE interfaces are based on the test results of Section 5.4. These values are also likely appropriate for the PTFE-composite interface under the test conditions described in Section 5.4 although those results show a smaller effect of temperature on the frictional properties of this interface. The proposed values for lubricated bearings are based on the data presented in Section 5.9 (from Campbell and Kong, 1989) and Tables 5-7 and 5-8.

Table 12-4 presents values for $\lambda_{\max,t}$ at a reference temperature of 20°C. For unlubricated and lubricated PTFE interfaces, appropriate values for $\lambda_{\min,t}$ are 0.9 and 0.8, respectively, at 50°C.

TABLE 12-4   System Property Modification Factor for Effects of Temperature, $\lambda_{\max,t}$, on the Coefficient of Friction of Sliding Bearings

Temp. (^{O}C)	Unlubricated PTFE	Lubricated PTFE	Bimetallic interfaces
20	1.0	1.0	NA
0	1.1	1.3	NA
20	1.0	1.0	NA
0	1.1	1.3	NA
-10	1.2	1.5	NA
-30	1.5	3.0	NA
-40	1.7	NA	NA
-50	2.0	NA	NA

12.5 System Property Modification Factors for Elastomeric Isolation Systems

12.5.1 Introduction

System property modification factors for the effects of aging, temperature, travel and scragging in elastomeric isolation systems are presented herein.

Elastomeric bearings are produced in a variety of compounds and values for λ will vary as a function of compound. The values presented in the 1999 AASHTO Guide Specifications for Seismic Isolation Design were based primarily on the studies described

in Section 7.9. The values for λ presented below are based on the Guide Specification and the studies reported in Thompson et al. (2000) and Morgan et al. (2001).

12.5.2 Effect of Aging ($\lambda_{\max,a}$, $\lambda_{\min,a}$)

Age hardening of elastomers due to continued vulcanization of the rubber matrix causes an increase in both the post-yielding stiffness and the characteristic strength (or effective stiffness) of elastomeric bearings. If the free sulfur in the rubber is consumed during the curing process, the increase in stiffness with age is likely small to zero. Large differences between unscragged and scragged properties (and recovery of these properties) suggest that vulcanization continues following curing and a potential for age hardening.

Table 12-5 lists values for $\lambda_{\max,a}$ for low and high damping rubber bearings. Herein, we relate the effects of aging to the difference between the unscragged and scragged stiffness at 150-percent shear strain for elastomeric bearings with greater than 5% damping—see the footnote to the table. The values of 1.1 and 1.2 presented in the table are based on the data reviewed in Section 7.9 and the studies of Thompson et al. (2000) and Morgan et al. (2001); the value of 1.3 is based on results reported by Morgan et al. (2001).

TABLE 12-5 System Property Modification Factor for Effects of Aging, $\lambda_{\max,a}$, for Elastomeric Bearings

Rubber Compound	Post-Yield Stiffness, K_d	Characteristic Strength, Q_d
Low damping	1.1	1.1
High damping-1	1.2	1.2
High damping-2	1.3	1.3

1. Low damping defined as less than or equal to 5% of critical.

2. High damping-1 represents rubber compounds with a ratio of unscragged (1st half cycle) to scragged (3rd cycle) effective stiffness at 150% shear strain of 1.25 or less; all other high damping rubbers are defined as high damping-2.

12.5.3 Effect of Scragging ($\lambda_{\max,sc}$, $\lambda_{\min,sc}$)

The effects of scragging in elastomeric bearings were described in Section 7.7. If the nominal properties of an elastomeric isolation system are based on scragged properties, the system property modification factors can be used to estimate the full recovery to virgin properties. Alternately, the ratio of 1st (virgin) to 3rd cycle properties at the appropriate conditions of axial load and shear strain can be used to estimate $\lambda_{\max,sc}$.

Table 12-6 presents values for $\lambda_{\max,sc}$ that are based on the data presented in Section 7.7; $\lambda_{\min,sc}$ can be set equal to 1.0. Values for $\lambda_{\max,sc}$ are presented as a function of effective shear modulus and effective damping at 100% shear strain. (Recent tests of a low-damping, low modulus elastomer, used in lead-rubber bearings by some manufacturers,

368

show little-to-no scragging.) Note that the proposed values are defaults and should only be used in the absence of scragging data for the compound under consideration.

TABLE 12-6 System Property Modification Factor for Effects of Scragging-Recovery, $\lambda_{\max,sc}$, on the Properties of Elastomeric Bearings

Effective Shear Modulus at 100% Shear Strain (MPa)	Effective Damping at 100% Shear Strain	Post-Yield Stiffness, K_d	Characteristic Strength, Q_d
≤0.45	>0.10	2.0	2.0
≤0.45	≤0.10	1.5	1.5
≥0.45	>0.10	1.5	1.5
≥0.45	≤0.10	1.2	1.2

12.5.4 Effect of Temperature, ($\lambda_{\max,t}$, $\lambda_{\min,t}$)

The mechanical properties of elastomeric bearings are affected by low temperatures and the length of exposure to low temperatures. Table 12-7 presents values for $\lambda_{\max,t}$ that are based on the data presented in Sections 7.6 and 8.3. The lead-rubber and low-damping rubber bearing data are for grade 3 natural rubber; the data for high damping rubber are for elastomers described as high-damping-1 per Table 12-5.

TABLE 12-7 System Property Modification Factors for Effects of Temperature, $\lambda_{\max,t}$, on the Properties of Elastomeric Bearings

Temp. (^{o}C)	Post-Yield Stiffness, K_d		Characteristic Strength, Q_d	
	LDRB, LRB	HDRB	LDRB, LRB	HDRB
20	1.0	1.0	1.0	1.0
0	1.1	1.2	1.2	1.2
-10	1.1	1.4	1.4	1.4
-30	1.3	2.0	1.8	2.3

1. LDRB = low damping rubber bearing; LRB = lead-rubber bearing

2. HDRB = high damping rubber bearing

SECTION 13
TESTING OF SEISMIC ISOLATION AND DAMPING HARDWARE

13.1 Introduction

Current seismic codes and guidelines in the United States related to the analysis, design and implementation of seismic isolation and passive damping systems (e.g., 1999 AASHTO; 2001 California Building Code; ASCE Standard 7-05) mandate prototype and production testing of protective hardware. Such testing is required because of the importance of the protective hardware in reducing the seismic response of the structure; most isolators and dampers are custom designed and constructed; non-traditional civil engineering materials (e.g., composites, elastomers and fluids) are used for construction; and some hardware involve moving parts (i.e., mechanical systems). The testing protocols (sequences and cycles) presented in these current documents can be traced, by-and-large, back to SEAONC (1986) and AASHTO (1991).

Prototype seismic isolators and dampers should be full-scale manufactured products that meet the geometric, material and performance requirements of the construction documents and the specifications. Prototype hardware should be tested and accepted for construction before production hardware is ordered. Prototype hardware is tested rigorously to ensure that the proposed production hardware will meet the requirements of the construction documents and specifications for service (e.g., gravity, traffic, wind, braking) and extreme (e.g., earthquake) loadings. Prototype testing should not be waived unless the vendor of the protective hardware can provide data from tests of identical or similar bearings (dampers) under identical or more rigorous force and displacement (shear strain) demands to those proposed.

The definition of similar is dependant upon the type and construction of the bearing or damper. For a Friction Pendulum bearing, the general construction and geometry, low-friction high-load composite, composite bonding process, stainless steel overlay, and composite-stainless steel contact pressure should be nearly identical. For a lead-rubber bearing, the general construction and geometry (including lead plug diameter, ratio of plug diameter to bonded diameter and shape factor), vulcanization process (and thermal profile) and axial pressure should be nearly identical. For a fluid viscous damper, the general construction materials and geometry, internal fluid pressure, orifices and seals should be nearly identical. Much of this information is considered proprietary by the hardware manufacturers and it might be difficult or impossible to establish similarity.

Production isolators and dampers should be constructed identically to the prototype bearings (dampers) using the same materials and processes to ensure that the mechanical properties of the prototype and production bearings are most similar. Production isolators are tested for the dual reasons of quality control (ensuring that bearings of a given type and size have near-identical properties) and checking mechanical properties (ensuring that the properties meet the intent of the specification). The 1999 AASHTO Guide Specification for Seismic Isolation Design (AASHTO, 1999) describes production bearing tests as quality control tests.

371

13.2 Testing for Service-Load Conditions

13.2.1 Background

Seismic isolation bearings should be tested for longevity and robustness under service loadings due to a) cycling of the bridge deck and substructure due to thermal and live load, b) braking, and c) live-load induced rotations of the superstructure. AASHTO (1999) writes that tests be performed to account for movements associated with thermal displacements and live load rotations for no less than 30 years. If the design life of the bridge exceeds 30 years, the expected design-life movements should be imposed on the bearings.

Daily heating and cooling of a bridge will produce thermally-induced displacements and rotations in the superstructure and the substructure. Both the longitudinal displacements and girder rotations produce travel in the bearings. In elastomeric bearings, the travel produces small amplitude shear strains in the elastomer and could lead to a high-cycle fatigue failure of the bearing. In sliding bearings, the travel produces movement over the sliding surface, perhaps leading to a fatigue-type failure of component(s) of the bearing and excessive wear of materials at the sliding interface.

The magnitude of the displacements and rotations can be estimated by gathering information on the expected daily fluctuations in temperature at the site of the bridge (often expressed as monthly maxima and minima), the exposure of the bridge to direct sunlight (which will effect the temperature fluctuations in the bridge), the span lengths, the coefficients of thermal expansion of the construction materials used in the bridge, and the expected maximum deflection of the bridge due to live loads (including lateral distribution and impact). For bridges in the United States, Section 3.12.2.2 of the AASHTO LRFD Specifications (AASHTO, 2004) provides information on the temperature range to be considered.

Section 5.5 notes that displacements and rotations due to live loading on a typical bridge are orders of magnitude greater than those due to daily fluctuations in temperature. For the sample simply supported steel bridge of that section spanning 100 feet, span-to-depth ratio of 30, daily temperature fluctuation of $20°F$, average traffic speed of 60 km/hr, 10 crossings per hour and a 30 year service life, the cumulative movements are

1) 90 m due to thermal loading (measured at the mid-depth of the steel girders)
2) 5300 m due to live (vehicular) loading (at the top or bottom of the steel girders)

The velocity of movement, v, associated with the vehicular loading is of the order of 1 mm/second.

The cumulative movement produces lateral displacements and rotations in elastomeric bearings, both of which produce shear strain. The imposed displacement and rotation in each cycle, u and θ, respectively, produce shear strain as follows:

$$\gamma_s = \frac{u}{T_r} \tag{13-1}$$

and

$$\gamma_\theta = \frac{B^2 \theta}{2t T_r} \tag{13-2}$$

where T_r is the total thickness of rubber, B is the diameter (side dimension) of a circular (square) bearing, and t is the thickness of one rubber layer. The shear strain due to displacement u is essentially constant across the diameter of the bearing; the shear strain due to rotation θ is varies linearly across the diameter of the bearing with peak values near the edges of the bearing. In Friction Pendulum bearings, the displacement u produces sliding of the articulated slider across the stainless steel overlay; the rotation θ is accommodated by rotation of the articulated slider within the socket in the housing plate.

The 1999 AASHTO Guide Specification requires a minimum value of 1600 m (1 mile) be used as the basis of a travel (wear) test. If the service (cumulative) displacement u^T exceeds the minimum value, the service displacement must be used for testing. Support rotation is not addressed explicitly in the Guide Specification although such rotations can introduce peak shear strains in elastomeric bearings that exceed those due to displacement u. Support rotation θ can be incorporated into a travel test for an elastomeric bearing as follows:

a) Introduce a steel wedge of included angle α between the top of the bearing and the loading platen of the test machine to impose (support) rotation on the bearing. Subject the bearing to the computed cumulative travel (at displacement amplitude u) under an appropriate thermal profile. (Angle α can be taken as 0.5θ because the shear strain due to support rotation varies linearly across the diameter of the bearing.)

b) Add the shear strain associated with 0.5θ (because the shear strain due to support rotation varies linearly across the diameter of the bearing) to the shear strain associated with displacement u to compute the displacement amplitude u^* for the travel test. Subject the bearing to n cycles of loading at amplitude u^*, where n is the service cumulative displacement u^T divided by $4u$.

Consider the sample steel bridge from Section 5.5 for which u equals 1 mm and θ equals 0.002 rad. Assume that the bridge is supported by elastomeric bearings with a diameter of 600 mm, total rubber thickness of 250 mm and a rubber layer thickness of 10 mm. The shear strain due to displacement u is 0.4%. The peak shear strain due to rotation θ is 1.4%: more than 3 times the strain due to displacement.

Travel tests should be performed on a prototype bearing unless a similar (see definition in Section 13.1) bearing has been subjected to an identical or more rigorous travel test, measured here in terms of cumulative displacement u^T, rate of load application and

pressure. As a practical matter, the displacement should be imposed at as high a rate as possible (to reduce the duration of the test) but not less than 60 mm per minute (approximately 2.4 inches per minute)—all without producing excessive rate-dependent temperature increase or wear in the bearing. Testing should be performed at room temperature, which is defined as $20 \pm 8°C (68 \pm 15°F)$ (e.g., 1999 AASHTO Guide Specification) and at the expected in-service average pressure (gravity load divided by either bonded rubber area (elastomeric bearing) or slider area (FP bearing)).

The effects of travel on a bridge bearing are likely exacerbated at low temperatures. If bearings are to be installed in a bridge at a site designated as a low-temperature area, either a) some percentage of the travel test should be performed at an appropriately low temperature, or b) the specified travel distance should be increased. The 1999 AASHTO Guide Specification recommends that either a) 10% of the travel test be performed at the lower temperature (and provides guidance on the temperature as a function of low-temperature area), or b) for a room temperature test, the cumulative travel distance be increased to twice the service displacement but not less than 3200 m. Also, the European Standard EN1337 (European, 2004) has recommended elaborate profiles of temperature in the range of -50°C to 35°C together with a movement history that totals 20km. The EN1337 specification applies to sliding bearings, which are described only as lubricated, and the test is to be conducted on small specimens of apparent contact diameter 3in (75 mm) without any imposed rotation.

13.2.2 Seismic Isolator Test Matrix, Test Description and Acceptance Criteria

Seismic isolators (bearings) will generally not be subjected to cumulative movement tests as part of a prototype testing program. Rather, it is expected that these tests will be performed on representative sizes (geometry) of isolators to provide project-independent information on a) the changes in seismic performance, if any, due to the in-service loading, and b) the service-life response of the isolators (bearings). A matrix for service-life tests of seismic isolators is presented in Table 13-1 below. The tests should be conducted in the order shown in the table.

Service-life testing of seismic isolators will require the specification of gravity load, velocity and displacements and frequencies of testing. Since service-life testing will generally be performed on a project-independent basis and not as part of a prototype testing program, values must be assumed for the gravity load, velocity, displacements and loading frequency. A seismic isolator manufacturer, knowing the likely applications of their product(s), should develop conservative (large) values of gravity load (GL), velocity (v), travel (displacement) amplitude (u), service (cumulative) displacement (u^T) and frequency for testing so as to maximize the utility of the testing program. Given that live load rotations and displacements are computed based on 100% of the live load, full gravity load should be applied to the test isolator(s), namely, GL = $1.0D + 1.0L$, where D and L are representative values of dead load and live load for the isolator, respectively.

The service-life testing program described below involves two seismic characterization tests, one before and one after the service-life test. The seismic isolator manufacturer

374

must select representative values of design-event isolator displacement (d) and frequency (f_1) for the seismic tests. The design-event isolator displacement should be that associated with a Maximum Considered Earthquake (MCE).

A detailed description of each test listed in Table 13-1 is presented in this section. Each test is identified by its ID number, its purpose is described, a procedure is proposed and commentary is provided.

Acceptance criteria are not provided herein for the service-life tests. The results of the tests described in this section, including changes in mechanical properties for service and seismic loadings must be factored into the engineer's assessment of the prototype test results. Changes in mechanical properties due to service-life testing of seismic isolation bearings should not be used to adjust non-compliant results of prototype tests to demonstrate compliance with a specification because the design earthquake can strike at any time over the service life of the bridge.

TABLE 13-1 Matrix of Service-Life Tests for Isolation Bearings[1]

Test ID	Description	Axial load[2]	Temp (°C)	Cycles[3]	Displacement[4]	Frequency (Hz)
ST1	Baseline characterization test	GL	20 ± 8	3	d	f_1
ST2	Service-life test[5]	GL	20 ± 8	NA	u	NA
ST3	Seismic characterization test	GL	20 ± 8	3	d	f_1

1. See Section 13.2.2 for a detailed description of each test

2. $GL = 1.0D + 1.0L$ for the service-life tests, where D is the maximum dead load and L is the maximum live load.

3. Cycles of sinusoidal loading at the effective frequency of the isolated structure, f_1.

4. Displacement amplitude of sinusoidal loading: d = amplitude of test displacement (= peak design-event displacement, excluding the effects of torsion); u (or u^*) = displacement due to live-loading of the bridge

5. Fully reversed cycles of sinusoidal (or constant velocity) motion of amplitude u (or u^*) to a total lateral displacement equal to the cumulative movement u^T.

Test ST1: Baseline Characterization Test

Purpose: To provide reference information on the dynamic response of the isolator (bearing).

Procedure: Supply a virgin (unscragged) isolator to the test facility and install it in the test machine. Apply an axial compressive load equal to 100 percent of the gravity load (= GL). Test at an ambient and bearing temperature of $20 \pm 8°C$. Apply three (3) cycles of sinusoidal loading to a lateral displacement amplitude d, at a loading frequency of f_1, where f_1 is the calculated effective frequency (inverse of effective period) of the isolated bridge. The displacement amplitude should be the calculated displacement in the maximum earthquake without the effect of torsion (D_M). Continuously record and report the vertical and lateral force and displacement histories for the duration of the test. Plot the lateral-force-versus lateral displacement relationship for the test. Record and report the ambient temperature at the start of the test.

Commentary: This test provides benchmark data on the force-displacement response of the virgin seismic isolator. The test article must not have been tested previously by the manufacturer regardless of whether it is the practice of the manufacturer to conduct such tests as part of a quality control program. If the test is project independent, representative values of d and f_1 for the isolator being tested should be used. Three cycles of displacement are specified based on the studies of Warn and Whittaker (2004), who demonstrated that less than three fully-reversed cycles at the maximum displacement are expected for isolation systems with strength-to-supported weight ratio (Q_d / W) of 0.06 or larger and period based on a post-elastic stiffness associated with a period of 2.5 seconds or greater.

Test ST2: Service-Life (Travel) Test

Purpose: To simulate the effects of service-life movement on the seismic isolator.

Procedure: Apply an axial compressive load equal to 100 percent of the gravity load (= GL). Test at an ambient and bearing temperature of $20 \pm 8°C$. Apply sinusoidal or sawtooth loading of user-specified amplitude u for n cycles where n is equal to the computed cumulative travel u^T divided by $4u$. The testing frequency should not exceed 0.1 Hz. The average speed shall be the greater of the user-specified velocity v or 60 mm per minute. Continuously record and report the vertical and lateral force and displacement histories for the duration of the test. Plot the lateral force-versus displacement relationship for three cycles of loading at a minimum of 10 equally spaced displacement intervals over the course of the test. Record and report the ambient temperature every hour for the duration of the test. Report and numerically characterize wear in all components of the seismic isolator.

If the isolator is to be simultaneously subjected to a rotation (between the end plates) of θ and lateral displacement u, either a) install a wedge with an included angle of between 0.5θ and θ between the top of the bearing and the loading platen, or b) increase the amplitude of the displacement history from u to u^* as described in Section 13.2.1.

If isolation bearings of the type being tested are to be installed in low-temperature areas (designated by AASHTO as temperature zones A, B, C and D[1], the 1999 AASHTO Guide Specification writes that either a) 10 percent of the service-life test be performed at the 20, 5, -5 and -25°F (-7, -15, -21 and -26°C), for temperature zones A, B, C and D, respectively, or b) the cumulative travel be doubled to $2u^T$ and the test performed at $20 \pm 8°C$ for all temperature zones. The European Standard EN1337 Part 2 (European, 2004) presents a temperature profile for a long-term sliding test in which most of the test is performed at a constant $20°C$ but the test involves steps from $35°C$ to $-50°C$. If tests are conducted at temperatures below $20°C$, the entire bearing must be cooled to the target temperature and the target temperature must be maintained for a minimum of one hour before the service-life test can recommence. Calibrated thermocouples shall be used to monitor the interior and exterior temperature of the bearing. However, it should be recognized that internal thermocouples are difficult to install and maintain during such prolonged tests.

Commentary: The purpose of this test is to provide information on the service-life response of the seismic isolator. Such information is most important because the seismic isolator must function as a conventional bridge bearing and accommodate the daily live load and thermal cycling of the bridge superstructure. An upper limit on the test frequency of 0.1 Hz is suggested to avoid excessive energy input to the isolator per unit time - energy that would not be input to the isolator under in-service conditions. The loading frequency should be established using the average speed v and the live-load induced bearing (sliding) displacement amplitude u. (In the event that the thermally-induced displacement exceeds u, it will be conservative to service-test the bearing using the thermally-induced displacement amplitude and the average speed v from live loading of the bridge.

Installation of a wedge-shaped plate is the simplest and most widely used method for imposing rotation on a seismic isolation bearing. A minimum included angle of 0.5θ is specified because the rotation induced shear strain varies from 0 to θ over the course of one cycle of live-load induced rotation.

Testing of seismic isolation bearings at temperatures other than room temperature is challenging because seismic isolators are typically large in size with significant thermal mass (i.e., it takes a long time to cool the core of a large elastomeric or steel-based sliding bearing to temperatures much below freezing). Not only is it difficult to uniformly cool an isolation bearing to temperatures below freezing but the temperature of the bearing must be maintained at the low temperature(s) for a significant period while testing and the temperature of the core of the bearing must be monitored. Modifications to a standard test machine will likely be needed to accommodate the equipment required for low-temperature testing of seismic isolation bearings.

Damage to or wear of sliding and elastomeric isolation bearings in the service-life test will typically be observed through changes in the hysteretic response to cyclic loading.

---

[1] The AASHTO LRFD Specification (AASHTO, 2004) characterizes low temperature zones A, B, C, D and E by 50-year low temperatures of 0, -20, -30, -45 and less than $-45°F$, respectively.

Regardless, sliding and/or rotating surfaces should be inspected for wear following the service-life test. Wear should be documented using thickness measurements and photographs taken before and after the service-life test. The lateral force-versus displacement relationships produced at the minimum of 10 equally spaced displacement intervals over the course of the test should be compared to characterize the change in mechanical properties of the isolation bearing with service-life travel.

Test ST3: Characterization Test

Purpose: To provide reference information on the dynamic response of the isolator (bearing).

Procedure: Apply an axial compressive load equal to 100 percent of the gravity load (= GL). Test at an ambient and bearing temperature of $20 \pm 8°C$. Apply three cycles of sinusoidal loading to a lateral displacement of amplitude d, at a loading frequency of f_1, where f_1 is the calculated effective frequency of the isolated bridge. Continuously record and report the vertical and lateral force and displacement histories for the duration of the test. Plot the lateral-force-versus lateral displacement relationship for the test. Record and report the ambient temperature at the start of the test. Compare the lateral-force-versus lateral displacement relationships from tests ST1 and ST3.

Commentary: This test serves to characterize the effect of rotation and cumulative displacement on the properties of the isolator relevant to earthquake loadings. Changes in the seismic properties of the isolator (bearing) can be assessed by comparing the results of tests ST1 and ST3. A technical basis for the changes in mechanical properties, if any, should be prepared and documented to permit the project-independent results to be used in conjunction with project-specific prototype testing.

13.2.3 Fluid Viscous Dampers

Fluid viscous dampers should be tested for longevity and robustness under service loadings producing displacements and rotations in the superstructure. Identical to seismic isolation bearings, tests should be performed to account for movements associated with thermal displacements and live load rotations of the bridge for the design life of the bridge but no less than 30 years. The service displacement of the damper will depend on its location with respect to the neutral axis of the superstructure: no travel due to end rotation will occur if the damper is located at the neutral axis of the superstructure; other points of attachment, distant from the neutral axis will result in end-rotation-induced displacement in the damper. Travel in a fluid viscous damper could result in seal damage (and thus damper failure) due to excessive movement of the piston rod over the seals. Testing is undertaken in a manner similar to that described above for seismic isolation bearings. However, such tests cannot capture the effects of piston-rod bearing on the seals that over time can produce permanent deformation in the seals and fluid loss resulting from piston-rod movement over deformed seals. Piston-rod bearing stresses on seals, caused potentially by the damper spanning between its points of support (generally

378

its ends to which articulated bearings are attached), can be mitigated or eliminated through appropriate design, including provision of bearings or an external sleeve.

The 1999 AASHTO Guide Specification requires a minimum value of 1600 m (1 mile) to be used as the basis of a travel (wear) test if the damper is located at the neutral axis of the superstructure. If the calculated service displacement exceeds the minimum value, the computed displacement should be used for testing. If the damper is located at soffit of the superstructure (or isolation bearing), the minimum test displacement is doubled to 3200 m. Travel tests should be performed on a prototype damper unless a similar (see footnote above) damper has been subjected to an identical or more rigorous travel test, measured here in terms of total imposed displacement, rate of load application and contact pressure. For the reasons given above, the displacement should be imposed at as high a rate as possible (to reduce the duration of the test) but not less than 60 mm per minute (approximately 2.4 inches per minute)—all without producing an excessive temperature increase in the damper fluid or wear in the seals of the damper. Testing should be performed at room temperature ($20 \pm 8°C$) and the damper should be supported for testing in the same configuration as the proposed in-service condition (to avoid reducing artificially the piston-rod-induced bearing stresses on the seals).

The effects of service loading on a bridge damper are likely exacerbated at low temperatures with changes in fluid viscosity and seal properties. If dampers are to be installed in a bridge at a site designated as a low-temperature area, then, identical to seismic isolation bearings, either a) some percentage of the travel test should be performed at an appropriately low temperature, or b) the specified travel distance should be increased. The 1999 AASHTO Guide Specification recommends that either a) 10% of the travel test be performed at the lower temperature (and provides guidance on the temperature as a function of low-temperature area), or b) for a room temperature test, the cumulative travel distance be increased to twice the assumed service displacement but not less than 3200 m.

One possible service-load test that is not included below involves high cycle testing of the piston rod-to-seal interface and the spherical bearings in a plane perpendicular to the axis of the piston rod. Consider the installation of fluid viscous dampers across an expansion joint in a bridge remote from a support. The passage of vehicular traffic across the expansion joint might produce millions of cycles of relative vertical displacements between the ends of the dampers, a) generating rotations in the spherical bearings at each end of the damper, and b) impressing the piston-rod into the damper seals, which might result in high-cycle failure of the spherical bearings and fluid leakage from the damper, respectively. These effects should be mitigated through structural detailing, to provide adequate gravity support to the damper and appropriate internal construction details. If such detailing is not possible, a service-life test should be devised (likely on a project-specific basis) to interrogate the fatigue life of the spherical bearings and damper seals.

13.2.4 Fluid Damper Test Matrix, Test Description and Acceptance Criteria

Fluid viscous dampers, like seismic isolators, will generally not be subjected to cumulative movement tests as part of a prototype testing program. Rather, these tests will generally be performed on representative sizes (geometry) of dampers to provide project-independent information on a) the changes in seismic performance, if any, due to the in-service loading, and b) the service-life response of the dampers. A matrix for service-life tests of dampers is presented in Table 13-2 below. The tests should be conducted in the order shown in the table.

Service-life testing of fluid viscous will require the specification of velocity, displacements and frequency of testing. Since service-life testing will generally be performed on a project-independent basis and not as part of a prototype testing program, values for velocity, displacements and loading frequency must be assumed. A damper manufacturer, knowing the likely applications of their product(s), should develop conservative (large) values of velocity v, travel (displacement) amplitude u, service (cumulative) displacement u^T and frequency for testing so as to maximize the utility of the testing program.

The service-life testing program described below involves two seismic characterization tests, one before and one after the service-life test. The damper manufacturer must select representative values of design-event isolator displacement d and effective frequency f_1 for the seismic tests. It is recommended that the design-event displacement is selected to be the displacement in the MCE.

A detailed description of each test listed in Table 13-2 is presented in this section. Each test is identified by its ID number, its purpose is described, a procedure is proposed and commentary is provided.

TABLE 13-2 Matrix of Service-Life Tests for Fluid Viscous Dampers[1]

Test ID	Description	Temp (°C)	Cycles[2]	Displacement[3]	Frequency (Hz)
ST1	Baseline characterization test	20 ± 8	3	d	f_1
ST2	Service-life test[4]	20 ± 8	NA	u	NA
ST3	Seismic characterization test	20 ± 8	3	d	f_1

1. See Section 13.2.2 for a detailed description of each test
2. Cycles of sinusoidal loading at the effective frequency of the isolated structure, f_1.
3. Displacement amplitude of sinusoidal loading: d = amplitude of test displacement (= peak design-event displacement, excluding the effects of torsion); u (or u^*) = displacement due to live-loading of the bridge
4. Fully reversed cycles of sinusoidal loading of amplitude u (or u^*) to a total lateral displacement equal to the cumulative movement u^T.

Acceptance criteria are not provided herein for the service-life tests. The results of the tests described in this section, including changes in mechanical properties for service and seismic loadings must be factored into the engineer's assessment of the prototype test results. Changes in mechanical properties due to service-life testing of fluid viscous dampers should not be used to adjust non-compliant results of prototype tests to demonstrate compliance with a specification because the design earthquake can strike at any time over the service life of the bridge.

Test ST1: Baseline Characterization Test

Purpose: To provide reference information on the dynamic response of the fluid viscous damper

Procedure: Supply a damper to the test facility and install it in the test machine in its intended in-service configuration. Test at an ambient and damper temperature of $20 \pm 8°C$. Apply three (3) cycles of sinusoidal loading to a lateral displacement amplitude d, at a loading frequency of f_1, where f_1 is the calculated effective frequency (inverse of effective period) of the isolated bridge. The displacement amplitude should be taken as the calculated displacement in the Maximum Considered Earthquake without the effect of torsion (D_M). Continuously record and report the vertical and lateral force and displacement histories for the duration of the test. Plot the lateral-force-versus lateral displacement relationship for the test. Record and report the ambient temperature at the start of the test.

Commentary: This test provides benchmark data on the force-displacement response of the fluid viscous damper. The test article must not have been tested previously by the manufacturer regardless of whether it is the practice of the manufacturer to conduct such tests as part of a quality control program. If the test is project independent, representative values of d and f_1 for the damper being tested should be used.

Test ST2: Service-Life (Travel) Test

Purpose: To simulate the effects of service-life movement on the fluid viscous damper.
Procedure: Install the damper in the test machine in its intended in-service configuration. Test at an ambient and damper temperature of $20 \pm 8°C$. Apply sinusoidal or sawtooth loading of user-specified amplitude u for n cycles where n is equal to the computed cumulative travel u^T divided by $4u$. The testing frequency should not exceed 0.1 Hz. The average speed shall be the greater of the user-specified velocity v or 60 mm per minute. Continuously record and report the axial force and displacement histories for the duration of the test. Plot the axial force-versus axial displacement relationship for three cycles of loading at a minimum of 10 equally spaced displacement intervals over the course of the test. Record and report the ambient temperature every hour for the duration of the test. Wear in all components of the damper must b reported.

If dampers of the type being tested are to be installed in low-temperature areas (designated temperature zones A, B, C and D by AASHTO), the AASHTO Guide

381

Specification writes that either a) 10 percent of the service-life test be performed at the 20, 5, -5 and -15°F (-7, -15, -21 and -26°C), for temperature zones A, B, C and D, respectively, or b) the cumulative travel be doubled to $2u^T$ and the test performed at $20 \pm 8°C$ for all temperature zones. The European Standard EN1337 Part 2 (European, 2004) presents a thermal profile for a long-term sliding test of bridge bearings in which most of the test is performed at a constant 20°C but the initial and final phases of the test involved a stepped thermal profile that steps down from 20°C to -50°C and back to 20°C. If tests are conducted at temperatures below 20°C, the entire damper must be cooled to the target temperature and the target temperature must be maintained for a minimum of 15 minutes before the service-life test can recommence. Calibrated thermocouples shall be used to monitor the temperature of the damper (this is typically done on the exterior of the damper at various locations in the vicinity of the neutral piston head position).

Commentary: The purpose of this test is to provide information on the service-life response of the fluid viscous damper. Such information is most important because the damper must accommodate the daily live load and thermal cycling of the bridge superstructure. An upper limit on the test frequency of 0.1 Hz is suggested to avoid excessive energy input to the damper per unit time—energy that would not be input to the damper under in-service conditions. The loading frequency should be established using the average speed *v* and the live-load induced displacement amplitude *u*. In the event that the thermally-induced displacement exceeds *u*, it would be conservative to service-test the damper using the thermally-induced displacement amplitude and the average speed *v* from live loading of the bridge.

Damage to or wear in fluid viscous dampers in the service-life test will typically be observed through changes in the hysteretic response to cyclic loading. Regardless, sliding and/or rotating surfaces should be inspected for wear following the service-life test. Wear should be documented using photographs taken before and after the service-life test. The axial force versus axial displacement relationships produced at the minimum of 10 equally spaced displacement intervals over the course of the test should be compared to characterize the change in mechanical properties of the fluid viscous damper with service-life travel.

Test ST3: Characterization Test

Purpose: To provide reference information on the dynamic response of the fluid viscous damper.

Procedure: Install the damper in the test machine in its intended in-service configuration. Test at an ambient and damper temperature of $20 \pm 8°C$. Apply three cycles of sinusoidal loading to a lateral displacement of amplitude d, at a loading frequency of f_1, where f_1 is the calculated effective frequency of the isolated bridge. Continuously record and report the vertical and lateral force and displacement histories for the duration of the test. Plot the lateral-force-versus lateral displacement relationship

for the test. Record and report the ambient temperature at the start of the test. Compare the lateral-force-versus lateral displacement relationships from tests ST1 and ST3.

Commentary: This test serves to characterize the effect of cumulative displacement on the properties of the damper relevant to earthquake loadings. Changes in the seismic properties of the damper can be assessed by comparing the results of tests ST1 and ST3. A technical basis for the changes in mechanical properties, if any, should be prepared and documented to permit the project-independent results to be used in conjunction with project-specific prototype testing.

13.3 Testing for Extreme Seismic Conditions

13.3.1 Extreme (Severe) Earthquake Shaking

The robust performance of seismic isolation bearings and/or fluid viscous dampers is key to the survival of a structure subjected to severe earthquake shaking—providing gravity-load support to the superstructure (bearings only) and dissipating earthquake-induced energy (bearings and dampers). High confidence in the response of isolators and dampers subjected to severe excitations is achieved through prototype and production testing.

The earthquake shaking of a superstructure supported by seismic isolation bearings will produce shear and axial forces and deformations in the bearings. Shear forces and deformations will be produced simultaneously along the transverse and longitudinal axes of the superstructure, with the magnitudes along each axis being determined by the characteristics of the earthquake ground motion (beyond the scope of this report) and the mechanical properties of the bearing. Earthquake shaking of a structure equipped with fluid viscous dampers should only produce axial forces in the dampers and inertial loadings parallel to the longitudinal axis of the damper.

The definition of severe earthquake shaking varies by code and regulatory authority. Importantly, severe is a relative measure—severe shaking in the Central and Eastern United States might be represented by peak accelerations of the order of 0.2 g whereas west of the Rocky Mountains, acceleration greater than 0.4 g might not qualify as severe. For analysis and design of isolated bridges, buildings and infrastructure, severe shaking is generally associated with median or mean ground motion with a low probability of exceedance. For example, isolated buildings are checked for mean ground motions with a 2% probability of exceedance in 50 years (mean recurrence interval of 2475 years). Some mission-critical structures are checked for ground motions with much longer mean recurrence intervals—100,000 years is the definition of the recurrence interval for safe shutdown earthquake shaking for nuclear structures.

The reader must note that mean ground motions for maximum considered earthquake shaking do not represent maximum shaking and will not produce maximum possible displacements in seismic isolators or dampers. For a given recurrence interval, earthquake shaking appreciably greater than mean earthquake shaking is possible.

Further, increasing the recurrence interval or return period (i.e., reducing the probability of exceedance in a given time period) will increase the mean level of ground shaking. The AASHTO Guide Specification for Seismic Isolation Design (AASHTO, 1999) specifies maximum shaking as ground motion (represented using an acceleration response spectrum) with a 10% probability of exceedance in 50 years (mean recurrence interval or return period of 475 years). AASHTO describes this ground motion representation as a design event and isolators and dampers are sized on the basis of analysis and design for design-event shaking. Importantly, the commentary to the Guide Specification notes that shaking more severe than the design event should be acknowledged. For information, other codes and specifications for seismic isolator and damper design (for non-bridge structures) typically require functionality of the hardware for ground motion demands associated with a 2% probability of exceedance in 50 years (mean recurrence interval or return period of 2475 years).

13.3.2 Variables for Prototype and Production Testing

Prototype and production testing of seismic isolators and dampers typically require the specification of the loads, velocities and displacements, in addition to the effective frequency of the isolated structure in design-event shaking, f_1.

- Vertical dead load (D) and live load (L) due to gravity—isolators only
- Axial earthquake-induced load (E)—isolators (vertical) and dampers (horizontal)
- Braking-induced loads (B)—isolators and dampers
- Wind-induced loads (WL)-isolators and dampers
- Earthquake-induced velocities (v)—isolators and dampers
- Earthquake-induced displacements (d)—isolators and dampers

Peak earthquake-induced velocities in the design event should be computed for the purpose of dynamic testing of isolators and dampers.

13.4 Prototype Testing of Seismic Isolators and Dampers

13.4.1 Seismic Isolator Test Matrix

A number of codes and guidelines, including AASHTO (1999), HITEC (2002) and ASCE (2005), present a plan for prototype testing of seismic isolators. The matrix of tests presented in Table 13-3 below is based in large part on these documents. The test plan, its sequence, and the number of cycles of loading for each test were chosen a) because only two prototype isolators will generally be available for testing for each proposed isolator size, and b) to facilitate a direct comparison of responses (e.g., dynamic response characteristics versus static response characteristics).

The test plan of Table 13-3 assumes that the isolation bearing has mechanical properties that are independent of the direction of loading (e.g., elastomeric bearings are circular and not square) and that the isolators are not equipped with sacrificial restraints. If such conditions are not satisfied, the reader is directed to Section 2.4 of HITEC (2002) for

additional tests that will address the characterization of the mechanical properties of isolation bearings and sacrificial restraints.

The prototype bearing test matrix includes core and supplemental tests. Core tests for isolators, denoted herein as IC*, should be performed for each project (unless identical or more rigorous tests have been performed on similar bearings.) Supplemental tests for isolators, denoted herein as IS*, need only be performed if the in-service isolators are subjected to either low temperatures per the AASHTO LRFD Specification (AASHTO, 2004) and/or tensile axial forces in design-event shaking.

Prototype tests will generally be project-specific for which loads, velocities, displacements and frequencies will be computed for design-event shaking. The prototype isolator tests involve three levels of axial load, namely, a) maximum plausible compressive load to characterize individual isolator stability, b) maximum plausible tensile load (if any) to characterize individual isolator integrity, and c) point-in-time gravity loads to characterize isolation system response. These axial loads should be calculated as follows:

- Maximum compressive axial load (MCL): $1.2D + SLL + |E|$
- Maximum tensile axial load (MTL): $0.9D - |E|$
- Point-in-time compressive axial load (GL): $D + SLL$

where D, SLL and E are dead, seismic live and design-event earthquake effects, respectively. The seismic live load is the portion of live load considered acting during the design–event earthquake. These loads should be computed for each size/type of prototype isolator. The dead load and live load should be mean (expected) values for the size/type of isolator. The design-event earthquake effect, E, should be taken as the value predicted for design-event shaking for the size/type of isolator, including the effects of vertical earthquake shaking.

Displacement d should be selected to be the displacement in the MCE, which is typically designated as the Maximum Displacement, D_M. Displacement d^* should be taken as the MCE displacement, including the effects of torsion: typically designated as the Total Maximum Displacement, D_{TM}.

13.4.2 Seismic Isolator Test Description

A detailed description of each test listed in Table 13-3 is presented herein, organized by core (IC) and supplemental (IS) tests. Each test is identified by its ID number, its purpose is described, and a procedure is proposed. Commentary is provided.

Test IC1: Service-Level Test—Wind and Braking loads

Purpose: To simulate the effect of service-level loads on the seismic isolator.

Procedure: Supply a virgin (unscragged) isolator to the test facility and install it in the test machine. Apply an axial compressive load equal to the best estimate, in-service gravity load (= GL). Test at an ambient and bearing temperature of $20 \pm 8°C$. Apply a static lateral load equal to *F*/2, where *F* is equal to the greater of the design wind load and design braking load. Apply 1000 fully reversed lateral load cycles of force amplitude *F*/2 at a testing frequency larger than or equal to 0.5 Hz. Following cyclic testing, maintain the lateral load at *F*/2 for 10 minutes. Remove the lateral load and monitor the movement of the isolation bearing for at least another 10 minutes. Continuously record and report the vertical and lateral force and displacement histories for the duration of the test, including the 10+ minute period following removal of the lateral load. Record and report the ambient temperature at the start of the test. Report the residual displacement.

TABLE 13-3 Matrix of Prototype Tests for Isolation Bearings[1]

Test ID	Description	Axial load[2]	Temp ^{0}C	Cycles[3]	Displacement[4]	Frequency (Hz)
IC1	Service-level test—wind and braking loads	*GL*	20 ± 8	1000	NA	≥ 0.5
IC2	Dynamic test	*GL*	20 ± 8	3	*d*	f_1
IS1	Temperature test	*MCL*	T[5]	3	*d*	f_1
IC3	Stability test	*MCL*	20 ± 8	1	d^*	f_1
IS2	Tension test	*MTL*	20 ± 8	2	*d*	f_1

1. See Section 13.4.2 for a detailed description of each test

2. See text in Section 13.4.1 for definitions of axial load.

3. Cycles of sinusoidal loading at the effective frequency of the isolated structure, f_1.

4. Displacement amplitude of sinusoidal loading: *d* = peak design-event displacement, excluding the effects of torsion, d^* = peak design-event displacement, including the effects of torsion.

5. Temperature to be defined by the engineer-of-record as appropriate for the site of the isolated bridge.

Commentary: The purpose of the test is to confirm the resistance of the isolation bearing in shear to braking loads and wind loads. The lateral load is maintained for 10 minutes to judge the performance of the isolator under sustained wind loading. The displacement response of the isolator should be monitored for at least 10 minutes after the test to observe if the isolator re-centers.

Test IC2: Dynamic Test

Purpose: To provide information on the dynamic response of the isolator for design-event shaking.

Procedure: Apply an axial compressive load equal to the best estimate, in-service gravity load (= GL). Test at an ambient and bearing temperature of $20 \pm 8°C$. Apply three cycles of sinusoidal loading to a lateral displacement equal to the total design displacement, d, at a loading frequency of f_1, where f_1 is the calculated effective frequency (inverse of effective period) of the isolated structure. Continuously record and report the vertical and lateral force and displacement histories for the duration of the test. Plot the lateral-force versus lateral displacement relationship for all cycles. Record and report the ambient temperature at the start of the test.

Commentary: This test provides data on the dynamic response of the seismic isolator for design-event shaking. The three cycles of loading is based on energy considerations as developed by Warn and Whittaker (2004). Measured responses should be checked against the limiting values set forth in the project specification.

Test IC3: Stability Test

Purpose: To provide information on the dynamic response of the isolator for displacements in excess of the total design displacement in maximum considered earthquake.

Procedure: Apply an axial compressive load equal to the maximum compressive load, including design-event earthquake shaking effects (= MCL). Test at an ambient and bearing temperature of $20 \pm 8°C$. Apply one cycle of sinusoidal loading to a lateral displacement equal to the total maximum displacement, d^*, at a loading frequency of f_1, where f_1 is the effective frequency of the isolated structure. Continuously record and report the vertical and lateral force and displacement histories for the duration of the test. Plot the lateral-force versus lateral displacement relationship. Record and report the ambient temperature at the start of the test.

Commentary: This test provides data on the dynamic response of the seismic isolator for the maximum displacement calculated in the MCE and under a factored vertical load. Given that the vertical load MCL is a factored load of very short duration, one cycle of motion is sufficient to assess the stability of the bearing.

Test IS1: Temperature Test

Purpose: To provide information on the dynamic response of the isolator at a temperature below $20°C$.

Procedure: Condition the seismic isolator so that the temperature throughout the isolator is uniform at T. For an elastomeric bearing (or a bearing containing elastomeric

components), maintain the bearing temperature at T for not less than the maximum number of consecutive days below freezing specified in the AASHTO LRFD Specification (AASHTO, 2004). For an all-metal sliding bearing (e.g., the Friction Pendulum bearing), maintain the bearing temperature at T for not less than 12 hours. Use thermocouples to monitor the temperature in the core of an elastomeric bearing or near the sliding interface of a sliding bearing. Apply an axial compressive load equal to the best estimate, in-service gravity load (= GL). Apply three cycles of sinusoidal loading to a lateral displacement equal to the total design displacement, d, at a loading frequency of f_1, where f_1 is the calculated effective frequency of the isolated structure. Continuously record and report the vertical and lateral force and displacement histories for the duration of the test. Record and report the ambient temperature at the start of the test.

Commentary: The temperature characterization test provides data on the dynamic response of the seismic isolator for design-event shaking at an ambient temperature far below $20°C$. Measured responses should be checked against the limiting values set forth in the specification and can be used to establish system property modification factors for the effects of temperature.

The AASHTO LRFD Specification (AASHTO, 2004) identifies temperature zones A, B, C, D and E based on 50-year low temperatures. The AASHTO Guide Specification recommends that isolators planned for installation in low temperature areas be tested for dynamic response at temperatures of -7, -15, -21, and -26°C for zones A, B, C and D, respectively. These temperatures should be used as default values for T.

Prototype testing of seismic isolation bearings at temperatures other than room temperature is challenging because seismic isolators are typically large in size with significant thermal mass The bearing must first be cooled and its temperature then maintained at T for a significant period (measured in days for an elastomeric bearing). Importantly, the temperature of the bearing must be maintained at T up to the point of testing, which might prove difficult if the bearing is cooled away from the test machine.

Test IS2: Tension Test

Purpose: To provide information on the response of the seismic isolator to tensile forces at the total design displacement in design-event shaking.

Procedure: Apply an axial tensile load equal to the maximum tensile load, including design-event earthquake shaking effects (= MTL). Test at an ambient and bearing temperature of $20 \pm 8°C$. Apply two cycles of sinusoidal loading to a lateral displacement equal to the total design displacement in design-event shaking, d, at a loading frequency of f_1, where f_1 is the calculated effective frequency of the isolated structure. Continuously record and report the vertical and lateral force and displacement histories for the duration of the test. Plot the lateral-force versus lateral displacement relationship for all cycles. Record and report the ambient temperature at the start of the test.

Commentary: Seismic isolation bearings can be subjected to net tensile forces due to overturning moments and/or the effects of vertical earthquake shaking. This test is used to characterize the force-displacement response and stability of the isolator subjected to combined tension and shear. Although the axial load on the seismic isolator can change from compression to tension (and vice-versa) over the course of the horizontal displacement excursions from $-d$ to $+d$, the axial load is kept constant at MTL to simplify the execution of the test. The tension test should be conducted only when $|E|$ is larger than $0.9D$ and the bearing is designed to sustain tension. For sliding bearings that experience uplift, the test should not be conducted.

13.4.3 Seismic Isolator Prototype Testing Acceptance Criteria

Prototype isolator acceptance criteria should be developed on a project-specific basis and be consistent with the bounding shear force-lateral displacement relationships assumed for analysis and design of the isolation system, as adjusted for variations in material properties that cannot be characterized by prototype testing. Figure 13-1 presents sample limits for a seismic isolator with a bilinear shear force-lateral displacement relationship. The area shown shaded represents acceptable response for the prototype isolator. Note that two bounding shear force-lateral displacement responses might be required to define acceptable behaviors under service and extreme earthquake loadings. Default acceptance criteria are provided below.

Test IC1: Service-Level Test - Wind and Braking Loads

Acceptance criteria: 1) Non-negative tangent lateral stiffness computed using the measured shear force-lateral displacement relationship. 2) Displacement due to the application of the dynamic load F less than the value specified by the engineer-of-record. 3) Displacement due to the 10-minute application of the design wind load less than the value specified by the engineer-of-record. 4) Residual displacement recorded after the removal of the design wind load less than the value specified by the engineer-of-record. 5) No structural damage to the seismic isolator, including, elastomer or sliding material delamination and cracks in the cover rubber wider than 5 mm.

Test IC2: Dynamic Test

Acceptance criteria: 1) Non-negative tangent lateral stiffness computed using the measured shear force-lateral displacement relationship. 2) Measured shear force-lateral displacement response that lies between the limits set forth by the engineer-of-record (i.e., the shaded region contained by the sample shear force-lateral displacement loops of Figure 13-1, as adjusted for the project-specific application) for the specified cycles of dynamic loading. 3) No structural damage to the seismic isolator, including, elastomer or sliding material delamination and cracks in the cover rubber wider than 5 mm.

389

Test IC3: Stability Test

Acceptance criteria: 1) Non-negative tangent lateral stiffness computed using the measured shear force-lateral displacement relationship. 2) No structural damage to the seismic isolator, including, elastomer or sliding material delamination and cracks in the cover rubber wider than 5 mm.

Test IS1: Temperature Test

Acceptance criteria: 1) Non-negative tangent lateral stiffness computed using the measured shear force-lateral displacement relationship. 2) Measured shear force-lateral displacement response that lies between the limits set forth by the engineer-of-record (i.e., the shaded region contained by the sample shear force-lateral displacement loops of Figure 13-1, as adjusted for the project-specific application) for the specified cycles of dynamic loading. 3) No structural damage to the seismic isolator, including, elastomer or sliding material delamination and cracks in the cover rubber wider than 5 mm.
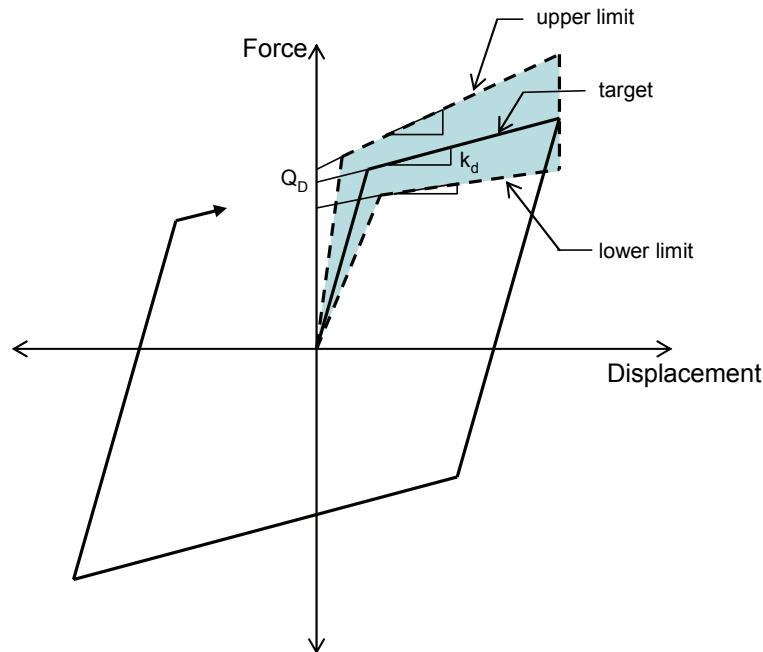
FIGURE 13-1   Sample Limits on Isolator Force-Displacement Response for Prototype Testing

Test IS2: Tension Test

Acceptance criteria: 1) Non-negative tangent lateral stiffness computed using the measured shear force-lateral displacement relationship. 2) Measured shear force-lateral displacement response that lies between the limits set forth by the engineer-of-record (i.e., the shaded region contained by the sample shear force-lateral displacement loops of Figure 13-1, as adjusted for the project-specific application) for specified cycles of dynamic loading. 3) No structural damage to the seismic isolator, including, elastomer or sliding material delamination and cracks in the cover rubber wider than 5 mm.

13.4.4 Fluid Viscous Damper Test Matrix

Among other seismic codes and guidelines, HITEC (2002) and ASCE (2005) present a plan for prototype testing of fluid viscous dampers. The test matrix that is presented in Table 13-4 below is based in large part on these documents; the matrix is similar in content and focus to that presented in Table 13-3 for seismic isolators. The tests should be conducted in the order shown in the table. If a test is omitted for any reason, the sequence should be resumed immediately following the omitted test.

The numbers of cycles of loading presented in the table below are based on the assumption that the dampers are to be installed in parallel with a seismic isolation system. If the fluid viscous dampers are to be installed elsewhere in a structure, the numbers of cycles should be adjusted upwards based on energy considerations as described in Warn and Whittaker (2004).

The prototype bearing test matrix includes core and supplemental tests, following the terminology presented in the CERF report on testing large-size seismic isolators and dampers. Core tests for dampers, denoted herein as DC*, should be performed for each project (unless identical or more rigorous tests have been performed on similar dampers.) Supplemental tests for dampers, denoted herein as DS*, need only be performed if the in-service dampers are subjected to low temperatures per the AASHTO LRFD Specification (AASHTO, 2004).

Prototype damper tests will generally be project-specific for which a peak load, peak velocity v, peak displacement d and isolated effective frequency f_1 will be computed for design-event shaking. Recognizing that the seismic response of in-service dampers is not harmonic and that the cycles in which the peak velocity v and peak displacement d are reached will not be the same, the frequency of loading for the prototype (sinusoidal) tests is defined based on v and d and not f_1.

Displacement d should be selected to be the displacement in the MCE, which is typically designated as the Maximum Displacement, D_M. Displacement d^* should be taken as the MCE displacement, including the effects of torsion: typically designated as the Total Maximum Displacement, D_{TM}.

13.4.5 Fluid Viscous Damper Test Description

A detailed description of each test listed in Table 13.4 is presented herein, organized by core (DC) and supplemental (DS) tests. Each test is identified by its ID number, its purpose is described, and a procedure is proposed. Commentary is provided.

Test DC1: Dynamic Test

Purpose: To provide information on the dynamic response of the damper for design-event shaking.

391

Procedure: Install the prototype damper in a test fixture that replicates the in-service condition. Test at an ambient and damper temperature of $20\pm8°C$. Apply a uniformly distributed static load to the damper, equal to 150% of the weight of the damper. Apply three cycles of sinusoidal loading to a lateral displacement equal to displacement d at a loading frequency of $v/(2\pi d)$, where v is the peak relative velocity between the ends of the damper in the design event. Continuously record and report the axial force, velocity and displacement histories for the duration of the test. Plot the axial force versus axial displacement relationship for all cycles. Plot the axial force versus velocity relationship for all cycles. Record and report the ambient temperature at the start of the test. Report any loss of fluid from the damper. Allow the damper to cool prior to the following test such that the internal temperature of the damper is $20\pm8°C$.

TABLE 13-4 Matrix of Prototype Tests for Fluid Viscous Dampers[1]

Test ID	Description	Temp ^{0}C	Cycles[2]	Velocity[3]	Displacement[4]	Frequency (Hz)
DC1	Dynamic test	20 ± 8	3	v	d	$v/(2\pi d)$
DS1	Temperature test	T[5]	3	v	d	$v/(2\pi d)$
DC2	Robustness test	20 ± 8	3	$1.2v$	d^*	$1.2v/(2\pi d)$

1. See Section 13.4.5 for a detailed description of each test

2. Cycles of sinusoidal loading at a frequency defined by the peak velocity v and displacement d.

3. Peak velocity of sinusoidal loading: v = peak design-event velocity.

4. Displacement amplitude of sinusoidal loading: d = peak design-event displacement, excluding the effects of torsion, d^* = peak design-event displacement, including the effects of torsion.

5. Temperature to be defined by the engineer-of-record as appropriate for the site of the damped bridge.

Commentary: This test provides data on the dynamic response of the fluid viscous damper for design-event shaking. The end conditions and supports for the prototype damper should be identical to those proposed for the in-service condition. The application of additional gravity load to the damper (equal to 50% of the weight of the damper), which is assumed to be installed horizontally, is intended to account for vertical dynamic response of the damper during design event shaking. The 50% increase is a default value. If dynamic analysis of the structure indicates that a larger increment in load is warranted, the larger increment in load must be applied to the damper during testing.

Measured force-displacement and force-velocity responses should be checked against the limiting values and bounds set forth in the project specification.

Test DC2: Robustness Test

Purpose: To provide information on the dynamic response of the fluid viscous damper for velocities in excess of the peak velocity in design-event shaking.

Procedure: Install the prototype damper in a test fixture that replicates the in-service condition. Test at an ambient and damper temperature of $20 \pm 8°C$. Apply a uniformly distributed static load to the damper, equal to 150% of the weight of the damper. Apply three cycles of sinusoidal loading to a lateral displacement equal to displacement d^* at a loading frequency of $1.2v/(2\pi d^*)$, where v is the peak relative velocity between the ends of the damper for design-event shaking. Continuously record and report the axial force, velocity and displacement histories for the duration of the test. Plot the axial force versus axial displacement relationship for all cycles. Plot the axial force versus velocity relationship for all cycles. Record and report the ambient temperature at the start of the test. Report any loss of fluid from the damper. Allow the damper to cool prior to the following test such that the internal temperature of the damper is $20 \pm 8°C$.

Commentary: This test provides data on the dynamic response of the fluid viscous damper for the maximum displacement calculated in the MCE and for a factored velocity.

Test DS1: Temperature Test

Purpose: To provide information on the dynamic response of the fluid viscous damper at a temperature below $20°C$.

Procedure: Cool the damper so that the external (and internal) temperature is uniform at T. Maintain the damper temperature at T for not less than 12 hours. Use thermocouples to monitor the temperature on the casing of the damper. Apply a uniformly distributed static load to the damper, equal to 150% of the weight of the damper. Apply three cycles of sinusoidal loading to a lateral displacement equal to the total design displacement, d, at a loading frequency of $v/(2\pi d)$, where v is the peak relative velocity between the ends of the damper in the design event. Continuously record and report the axial force, velocity and displacement histories for the duration of the test. Plot the axial force versus axial displacement relationship for all cycles. Plot the axial force versus velocity relationship for all cycles. Record and report the ambient temperature at the start of the test. Report any loss of fluid from the damper.

Commentary: The temperature test provides data on the dynamic response of the fluid viscous damper for design-event shaking at an ambient temperature far below $20°C$. Measured responses should be checked against the limiting values set forth in the specification.

The AASHTO LRFD Specification (AASHTO, 2004) identifies temperature zones A, B, C, D and E based on 50-year low temperatures. The AASHTO Guide Specification recommends that dampers planned for installation in low temperature areas be tested for

dynamic response at temperatures of -7, -15, -21, and -26°C for zones A, B, C and D, respectively. These temperatures should be used as default values for T.

13.4.6 Fluid Viscous Damper Acceptance Criteria

Prototype damper acceptance criteria should be developed on a project-specific basis and be consistent with the bounding shear force-lateral displacement relationships assumed for analysis and design, as adjusted for variations in material properties that cannot be characterized by prototype testing. Figure 13-2 presents sample limits for a fluid viscous damper with a linear force-velocity relationship. The area shown shaded represents acceptable response for the prototype damper. Note that two bounding shear force-lateral displacement responses might be required to define acceptable behaviors under service and extreme earthquake loadings. Default acceptance criteria are provided below.

The orifices in fluid viscous dampers are designed and manufactured to provide the required force-velocity relationship over a wide range of velocities, up to and including the peak velocity in design-event shaking. It will be difficult or impossible to design and manufacture an orifice to provide the same force-velocity relationship at the peak velocity (say 1000 mm/sec) and one-quarter of the peak velocity (250 mm/sec). Consideration should be given to specifying the desired force-velocity relationship over a velocity range from 25% to 100% of the peak velocity and limiting the force output of the damper to the value at 25% of the peak velocity for all velocities less than 25% of the peak value.

Test DC1: Dynamic Test

Acceptance criteria: 1) Measured shear force-lateral displacement response that lies between the limits set forth by the engineer-of-record (i.e., the shaded region contained by the sample shear force-lateral displacement loops of Figure 13-2, as adjusted for the project-specific application) for the specified cycles of dynamic loading. 2) No leakage of fluid. (Minute amounts of fluid leakage may be acceptable as specified by the engineer). 3) No structural damage to any component of the damper.

Test DC2: Robustness Test

Acceptance criteria: 1) No leakage of fluid. (Minute amounts of fluid leakage may be acceptable as specified by the engineer). 2) No structural damage to any component of the damper.

Test DS1: Temperature Test

Acceptance criteria: 1) Measured shear force-lateral displacement response that lies between the limits set forth by the engineer-of-record for all cycles of dynamic loading. 2) No leakage of fluid. (Minute amounts of fluid leakage may be acceptable as specified by the engineer). 3) No visible damage to any component of the damper.
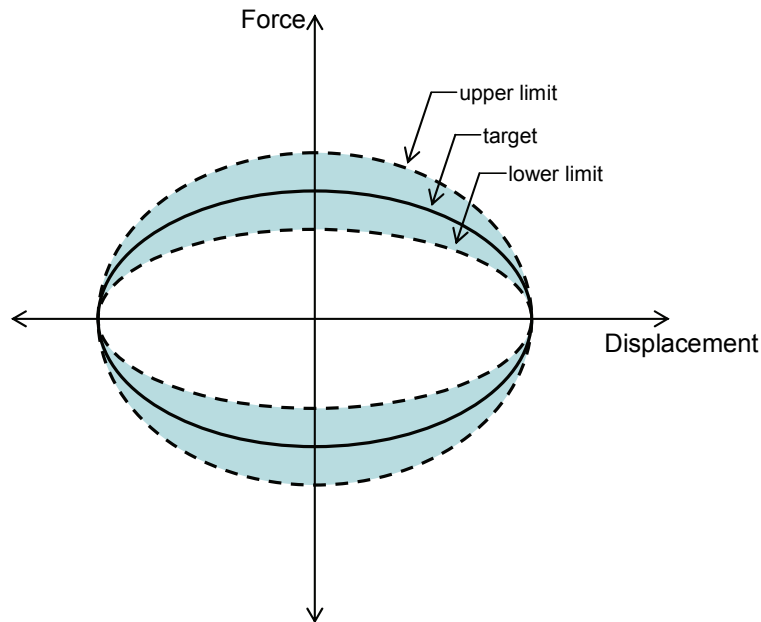
FIGURE 13-2   Sample Limits on Damper Force-Displacement Response for Prototype Testing

13.5 Production (Quality Control) Testing of Seismic Isolators and Dampers

A seismic quality control test should be performed on each isolator or damper before it is shipped from the manufacturing facility. Other quality control tests not related to seismic performance might be required but such tests are not described here.

Test QCI should be performed on each isolator and Test QCD should be performed on each damper. The purpose of the quality control test is to verify that the isolator/damper meets the requirements of the specification for seismic performance. A summary description of and acceptance criteria for the quality control tests are presented below.

Test QCI: Dynamic Isolator Test

Purpose: A quality control test to ensure that the isolator performance meets the requirements of the specification for design-event shaking.

Procedure: Apply an axial compressive load equal to the best estimate, in-service gravity load (= GL). Test at an ambient and bearing temperature of $20 \pm 8°C$. Apply three cycles of sinusoidal loading to a lateral displacement equal to d at a loading frequency of f_1, where f_1 is the calculated effective frequency of the isolated structure. Displacement d should be taken as the Maximum (MCE) Displacement, D_M. Continuously record and report the vertical and lateral force and displacement histories for the duration of the test. Plot the lateral-force versus lateral displacement relationship for all cycles. Record and report the ambient temperature at the start of the test.

Acceptance criteria: 1) Measured shear force-lateral displacement response that lies between the limits set forth by the engineer-of-record for the specified cycles of dynamic loading. 2) No structural damage.

Test QCD: Dynamic Damper Test

Purpose: A quality control test to ensure that the damper performance meets the requirements of the specification for design-event shaking.

Procedure: Install the prototype damper in a test fixture that replicates the in-service condition. Test at an ambient and damper temperature of $20 \pm 8°C$. Apply three cycles of sinusoidal loading to a lateral displacement equal to *d* at a loading frequency of $v/(2\pi d)$, where *v* is the peak relative velocity between the ends of the damper in the design event. Displacement *d* should be taken as the Maximum (MCE) Displacement, D_M. Continuously record and report the axial force, velocity and displacement histories for the duration of the test. Plot the axial force versus axial displacement relationship for all cycles. Plot the axial force versus velocity relationship for all cycles. Record and report the ambient temperature at the start of the test. Report any loss of fluid from the damper.

Acceptance criteria: 1) Measured force-lateral displacement response that lies between the limits set forth by the engineer-of-record for the specified cycles of dynamic loading. 2) No leakage of fluid. (Minute amounts of fluid leakage may be acceptable as specified by the engineer). 3) No structural damage to any component of the damper.

SECTION 14

SUMMARY AND CONCLUSIONS

This report presents state-of-the-art knowledge on the behavior of contemporary seismic isolators (elastomeric and lead-rubber bearings; sliding isolators) and hydraulic dampers under service and seismic loadings. The effects of temperature, loading history, wear, corrosion, contamination, lubrication and aging are considered to enable reliable predictions of the seismic response of seismically protected structures.

The study reported herein identified a number of substantial gaps in the understanding of isolator and damper behavior under service and seismic loads, including:

1. Aging can influence substantially the mechanical properties of seismic isolators. Field and laboratory data that address aging are most limited. The basic science of aging is not well understood. The utility of accelerated aging tests will be most limited until the mechanics and chemistry are understood.

2. A systematic study of the effects of low temperature and duration of exposure to low temperature on all types of isolators is required.

3. Our knowledge of the lifetime behavior of seismic protective system hardware is incomplete and limited to selected components rather than complete systems. There is almost complete lack of knowledge on the lifetime behavior of evolving systems (such as adaptive, semi-active, smart materials, etc.).

4. Friction is not well understood at the atomic/nano level. Improved understanding of friction could lead to the development of alternate sliding interfaces.

5. The mechanical properties of confined and unconfined lead under static and dynamic loadings are inadequately characterized. Materials science and engineering studies are required to better characterize the behavior of lead.

6. Principles and procedures for designing and testing reduced-scale prototype bearings must be developed to a) replace dynamic tests of prototype bearings where such tests are not physically possible, and b) enable engineers to evaluate new sizes of bearings based on data collected from dynamic tests of *similar* bearings.

7. The effects of loading history (e.g., travel) are significant for certain types of seismic isolation bearings. The behavior of all types of seismic isolators prior to and after significant cumulative movement should be studied in more detail.

8. There is a need to develop a systematic approach for accounting for the effects of the history of loading, aging and environment on the behavior of hardware in the analysis and design of bridge with seismic protective systems. This should be in the form of rationally established system property adjustment factors for the

397

combination of the aforementioned effects of history of loading, etc.   The approach should parallel the development of load combination factors in LRFD procedures. The system property adjustment factors that are currently in use have been assigned values on the basis of "engineering judgment" with minimal scientific basis, resulting, most likely, to very conservative combinations of the effects of extreme events on the behavior of the hardware.

9. There is need to advance from the mere collection of experimental data to fundamental understanding of phenomena so that predictions of lifetime behavior can be made and then verified by experiments and observation.

SECTION 15
REFERENCES

(1)   Al-Hussaini, T. M., Zayas, V. A. and Constantinou, M. C. (1994), Seismic Isolation of Multistory Frame Structures Using Spherical Sliding Isolation Systems", Report NCEER-94-0007, National Center for Earthquake Engineering Research, Buffalo, NY.

(2)   American Association of State Highway and Transportation Officials (1991), "Guide Specifications for Seismic Isolation Design", Washington, D.C.

(3)   American Association of State Highway and Transportation Officials (1999), "Guide Specifications for Seismic Isolation Design", Washington, D.C.

(4)   American Association of State Highway and Transportation Officials (2002), "Standard Specifications for Highway Bridges", 17th Edition, Washington, D.C.

(5)   American Association of State Highway and Transportation Officials (2004), "AASHTO LRFD Bridge Design Specifications", Washington, D.C.

(6)   American Institute of Steel Construction-AISC (2006), "Manual for Steel Construction, "Load and Resistance Factor Design, 13th Edition, Chicago, Illinois.

(7)   American Institute of Steel Construction-AISC (2005), "Seismic Design Manual," Chicago, Illinois

(8)   American Society of Civil Engineers (2005), "Minimum Design Loads for Buildings and Other Structures,' Standard ASCE/SEI 7-05.

(9)   American Society for Metals (1979), Metals Handbook, 9th Edition, Vol. 2, *Properties and Selection: Nonferrous Alloys and Pure Metals*, American Society for Metals, Metals Park, Ohio.

(10)   American Society for Metals (1992), *Friction, Lubrication, and Wear Technology*, ASM Handbook, Vol. 18, Metals Park, Ohio.

(11)   American Society of Mechanical Engineers (1985), "Surface Texture (Surface Roughness, Waviness, and Lay)", Standard ANSI/ASME B46.1-1985, New York, NY.

(12)   American Society for Testing and Materials (1988), "Rubber", Section 9, Philadelphia, PA.

(13)   Applied Technology Council (ATC) (1997), "NEHRP Guidelines for the Seismic Rehabilitation of Buildings and NEHRP Commentary on the Guidelines for the Seismic Rehabilitation of Buildings," Report Nos. FEMA 273 and 274, prepared

for the Building Seismic Safety Council and published by the Federal Emergency Management Agency, Washington, DC.

(14) Applied Technology Council (1993), "Proceedings of Seminar on Seismic Isolation, Passive Energy Dissipation, and Active Control," Report No. ATC-17-1, Redwood City, CA, March.

(15) Applied Technology Council (2005), "Improvement of Nonlinear Static Seismic Analysis Procedures," Report Federal Emergency Management Agency-FEMA 440, Washington, D.C.

(16) ASTM International. *Annual Book of ASTM Standards*. Vol. 03.01. ASTM International: West Conshohocken, PA, 2005.

(17) Bayer, R.G. (1994), *Mechanical Wear Prediction and Prevention,* Marcel Dekker, Inc., New York, NY.

(18) Benzoni, G. and Seible, F. (1999), "Design of the Caltrans Seismic Response Modification Device (SRMD) Test Facility", Proceedings of U.S.-Italy Workshop on Seismic Protective Systems for Bridges, Multidisciplinary Center for Earthquake Engineering Research, Buffalo, NY.

(19) Black, C., Makris, N. and Aiken, I. D. (2000), "Component Testing, Stability Analysis and Characterization of Buckling Restrained Unbonded Braces," Report No. PEER 2002/08, Pacific Earthquake Engineering Research Center, University of California, Berkeley, CA.

(20) Bondonet, G. and Filiatrault, A. (1997), "Frictional Response of PTFE Sliding Bearings at High Frequencies", J. Bridge Engng., ASCE, Vol. 2, No. 4, 139-148.

(21) Bowden, F. P. and Tabor, D. (1950), *The Friction and Lubrication of Solids: Part I*, Oxford University Press, Oxford, UK.

(22) Bowden, F. P. and Tabor, D. (1964), *The Friction and Lubrication of Solids: Part II*, Oxford University Press, Oxford, UK.

(23) Bowden, F. P. and Tabor, D. (1973), *Friction; an Introduction to Tribology*, Heinemann, UK.

(24) Buckle, I.G. and Liu, H. (1994), "Critical Loads of Elastomeric Isolators at High Shear Strain", Proc. 3rd US-Japan Workshop on Earthquake Protective Systems for Bridges", Report NCEER-94-0009, National Center for Earthquake Engineering Research, Buffalo, NY.

(25) Buckle, I., Nagarajaiah, S., and Ferrell, K. (2002). "Stability of Elastomeric Isolation Bearings: Experimental Study." Journal of Structural Engineering-ASCE, Vol. 128, No.1, 3-11.

(26) British Standards Institution (1983), "Commentary on Corrosion at Bimetallic Contacts and its Alleviation", PD 6484:1979, London, UK.

(27) British Standards Institution (1990), "Steel, Concrete and Composite Bridges. Part 9. Bridge Bearings, Section 9.1 Code of Practice for Design of Bridge Bearings, "BS5400: Section 9.1:1983, London, UK.

(28) Brown, R. (1996), *Physical Testing of Rubber*, 3rd Edition, Chapman and Hall, London.

(29) Building Seismic Safety Council (BSSC) (2003), "NEHRP Recommended Provisions for Seismic Regulations for New Buildings and Other Structures," 2003 Edition. Report Nos. FEMA 450, Federal Emergency Management Agency, Washington, DC.

(30) California Buildings Standards Commission (2001) "California Building Code," Sacramento, California.

(31) Campbell, T. I. and Fatemi, M. J. (1989), "Further Laboratory Studies of Friction in TFE Slide Surface of a Bridge Bearing", Report ME-89-06, Ministry of Transportation and Communications, Ontario, Canada.

(32) Campbell, T. I. and Kong, W. L. (1987),"TFE Sliding Surfaces in Bridge Bearings, Report ME-87-06, Ministry of Transportation and Communications, Ontario, Canada.

(33) Campbell, T. I. and Kong, W. L. (1989), "Laboratory Studies of Friction in TFE Slide Surfaces of Bridge Bearings", Report ME-89-04, Ministry of Transportation and Communications, Ontario, Canada.

(34) Campbell, T. I., Pucchio, J. B., Roeder, C. W. and Stanton, J. F. (1991), "Frictional Characteristics of PTFE Used in Slide Surfaces of Bridge Bearings", Proc. 3rd World Congress on Joint Sealing and Bearing Systems for Concrete Structures, Toronto, Ontario, Canada, Vol. 2 of Preprints (published by the National Center for Earthquake Engineering Research, Buffalo, NY), 847-870.

(35) Carslaw, H. S. and Jaeger, J. C. (1959), *Conduction of Heat in Solids*, 2nd Edition, Oxford University Press, London, UK.

(36) CERF (1998a), "Evaluation Findings for Earthquake Protection Systems, Inc. Friction Pendulum Bearings," CERF Report #40370, Civil Engineering Research Foundation, Washington, D.C.

(37)   CERF (1998b), "Evaluation Findings for Scougal Rubber Corporation High Damping Rubber Bearings," CERF Report #40373, Civil Engineering Research Foundation, Washington, D.C.

(38)   CERF (1998c), "Evaluation Findings for Dynamic Isolation Systems, Inc. Elastomeric Bearings," CERF Report #40369, Civil Engineering Research Foundation, Washington, D.C.

(39)   CERF (1998d), "Evaluation Findings for Skellerup Base Isolation Elastomeric Bearings," CERF Report #40376, Civil Engineering Research Foundation, Washington, D.C.

(40)   CERF (1999a), "Summary of Evaluation Findings for the Testing of Seismic Isolation and Energy Dissipating Devices," CERF Report #40404, Civil Engineering Research Foundation, Washington, D.C.

(41)   CERF (1999b), "Evaluation Findings for Enidine, Inc. Viscous Damper," Technical Evaluation Report HITEC 99-02, Civil Engineering Research Foundation, American Society of Civil Engineers, Reston, VA.

(42)   CERF (1999c), "Evaluation Findings for Taylor Devices Fluid Viscous Damper," Technical Evaluation Report HITEC 99-03, Civil Engineering Research Foundation, American Society of Civil Engineers, Reston, VA.

(43)   Chalhoub, M.S. and Kelly, J.M. (1990), "Effect of Compressibility on the Stiffness of Cylindrical Base Isolation Bearings, " International Journal of Solids and Structures, Vol. 26, No. 7, 743-760.

(44)   Cho, D.M. and Retamal, E. (1993). "The Los Angeles County Emergency Operations Center on High Damping Rubber Bearings to Withstand an Earthquake Bigger than the Big One." Proc. ATC-17-1 Seminar on Seismic Isolation, Passive Energy Dissipation, and Active Control, March, San Francisco, CA, Applied Technology Council, Redwood City, CA.

(45)   Clark, P. W., Kelly, J. M. and Aiken, I. D. (1996), "Aging Studies of High-Damping Rubber and Lead-Rubber Seismic Isolators", Proc. 4th U.S.-Japan Workshop on Earthquake Protective Systems for Bridges, published by the Public Works Research Institute, Ministry of Construction, Japan as Technical Memorandum No. 3480, 75-89.

(46)   Clarke, C.S.J., Buchanan, R. and Efthymiou, M. (2005), "Structural Platform Solution for Seismic Arctic Environments-Sakhalin II Offshore Facilities," Offshore Technology Conference, Paper OTC-17378-PP, Houston.

(47)   Constantinou, M. C. (1998), "Application of Seismic Isolation Systems in Greece", Proc. Structural Engineers World Congress, San Francisco, CA, July.

(48)   Constantinou, M.C., Kartoum, A. And Kelly, J.M. (1992), "Analysis of Compression of Hollow Circular Elastomeric Bearings," Engineering Structures, Vol. 14, No. 2, 103-111.

(49)   Constantinou, M. C., Mokha, A. S. and Reinhorn, A. M. (1990a), "Experimental and Analytical Study of a Combined Sliding Disc Bearing and Helical Steel Spring Isolation System", Report NCEER-90-0019, National Center for Earthquake Engineering Research, Buffalo, NY.

(50)   Constantinou, M., Mokha, A. and Reinhorn, A. (1990b), "Teflon Bearings in Base Isolation. II: Modeling", J. Structural Engng., ASCE, Vol. 116, No. 2, 455-474.

(51)   Constantinou, M.C. and Quarshie, J.K. (1998), "Response Modification Factors For Seismically Isolated Bridges", Report No. MCEER-98-0014, Multidisciplinary Center for Earthquake Engineering Research, University at Buffalo, State University of New York, Buffalo, NY.

(52)   Constantinou, M.C. and Sigaher, N. (2000), "Energy Dissipation System Configurations for Improved Performance", Proc. 2000 Structures Congress, ASCE, Philadelphia, PA, May.

(53)   Constantinou, M. C., Soong, T. T. and Dargush, G. F. (1998), *Passive Energy Dissipation Systems for Structural Design and Retrofit*, Monograph, National Center for Earthquake Engineering Research, Buffalo, NY.

(54)   Constantinou, M. C. and M. D. Symans (1992). "Experimental and Analytical Investigation of Seismic Response of Buildings with Supplemental Fluid Viscous Dampers," Report NCEER-92-0032, National Center for Earthquake Engineering Research, Buffalo, NY.

(55)   Constantinou, M.C., Tsopelas, P., Hammel, W. and Sigaher, A.N. (2001), "Toggle-Brace-Damper Seismic Energy Dissipation Systems", Journal of Structural Engineering, ASCE, Vol. 127, No. 2, Feb.,105-112.

(56)   Constantinou, M.C., Tsopelas, P., Kasalanati, A. and Wolff, E.D. (1999), "Property Modification Factors for Seismic Isolation Bearings", Report No. MCEER-99-0012, Multidisciplinary Center for Earthquake Engineering Research, Buffalo, NY.

(57)   Constantinou, M. C., Tsopelas, P., Kim, Y-S. and Okamoto, S. (1993), " NCEER-Taisei Corporation Research Program on Sliding Seismic Isolation Systems for Bridges: Experimental and Analytical Study of a Friction Pendulum System (FPS),

Report NCEER-93-0020, National Center for Earthquake Engineering Research, Buffalo, NY.

(58) Conversy, F. (1967), "Appareils d'Appui en Caoutchouc Frette,' Annales des Ponts et Chaussies, Vol. VI, Nov.-Dec.

(59) CSI (2002), "SAP2000 Analysis Reference Manual," Computers and Structures Inc., Berkeley, CA.

(60) Davison, R. W., DeBold, T. and Johnson, M. J. (1987), "Corrosion of Stainless Steels", in Metals Handbook, 9th Edition, Vol. 13, *Corrosion*, American Society for Metals, Metals Park, Ohio.

(61) Den Hartog, J. P. (1931), "Forced Vibrations with Combined Coulomb and Viscous Friction", Trans. ASME, Vol. 53 (APM-53-9), 107-115.

(62) DeWolf, J.T. and Ricker, D.T. (1990), *Column Base Plates*, Steel Design Guide Series 1, American Institute of Steel Construction, Chicago, Illinois.

(63) Dolce, M, Cardone, D. and Croatto, F. (2005), "Frictional Behavior of Steel-PTFE Interfaces for Seismic Isolation," Bulletin of Earthquake Engineering, Vol.3, No. 1, 75-99.

(64) Du Pont (1981), "Teflon-Mechanical Design Data", E. I. du Pont de Nemours & Co., Polymer Products Department, Wilmington, Delaware.

(65) EERI (1993), "Theme Issue: Passive Energy Dissipation," Earthquake Spectra, Vol. 9, pp. 319-636.

(66) Eggert, H. and Kauschke, W (2002), *Structural Bearings*, Ernst & Sohn, Berlin, Germany.

(67) Engesser, F. (1891), Zentr. Bauverwaltung, Vol. II, 483.

(68) EPS (2001), "Composite Bearing Liner Materials in Friction Pendulum Bearings," Technical Report, Earthquake Protection Systems, Richmond, CA.

(69) European Committee for Standardization (2004), "Structural Bearings", European Standard EN 1337, Brussels.

(70) European Committee for Standardization (2005), "Design of Structures for Earthquake Resistance. Part 2: Bridges," Eurocode 8, EN1998-2, draft, August.

(71) Federal Emergency Management Agency (2000), "Prestandard and Commentary for the Seismic Rehabilitation of Buildings," FEMA 356, Washington, D.C.

(72) Fenz, D. and Constantinou, M.C. (2006), "Behavior of Double Concave Friction Pendulum Bearing," Earthquake Engineering and Structural Dynamics, Vol. 35, No.11, 1403-1424.

(73) Garlock Bearings, Inc. (1987), " DU Self-Lubricating Bearings", Catalog 781-C, Thorofare, New Jersey.

(74) Gent, A.N. (1964), "Elastic Stability of Rubber Compression Springs," Journal of Mechanical Engineering Science, Vol.6, No.4, 318-326.

(75) Gent, A.N.(1990), "Cavitation in Rubber: a Cautionary Tale", Charles Goodyear Medal Address, 137th Meeting, Rubber Division, American Chemical Society, Washington, D.C., G49-G53.

(76) Gent, A.N. (2001), *Engineering with Rubber*, Hanser Publishers.

(77) Gent, A.N. and Lindley, P.B. (1959), "The Compression of Bonded Rubber Blocks", Proc. Institution of Mechanical Engineers, Vol. 173, 111-222.

(78) Gent, A.N. and Meinecke, E.A. (1970), "Compression, Bending and Shear of Bonded Rubber Blocks," Polymer Engineering and Science, Vol. 10, No. 1, 48-53.

(79) Grigorian, C. E. and Popov, E. P. (1993), "Slotted Bolted Connections for Energy Dissipation", Proc. Seminar on Seismic Isolation, Passive Energy Dissipation, and Active Control, ATC-17-1, Applied Technology Council, Redwood City, CA, Vol. 2, 545-556.

(80) Guruswamy, S. (2000), *Engineering Properties and Applications of Lead Alloys*, Marcel Dekker, Inc., New York.

(81) Hamburger, R. O., Rojahn, C., Moehle, J. P., Bachman, R., Comartin, C. D. and Whittaker, A. S. (2004). "Development of Next-generation Performance-based Earthquake Engineering Design Criteria for Buildings", Proceedings, 13th World Conference on Earthquake Engineering, Paper 1819, Vancouver, B.C., Canada.

(82) Haringx, J.A.(1948), "On Highly Compressible Helical Springs and Rubber Rods, and Their Application for Vibration-free Mountings,", Philips Research Reports, Parts I, II and III.

(83) Heaton, H. T., Hall, J. F., Wald, D. J. and Halling, M. W. (1995), "Response of High-rise and Base-isolated Buildings to a Hypothetical Mw 7.0 Blind Thrust Earthquake," Science, Vol. 267, 206-211.

(84) Hibbitt, Karlsson and Sorensen, Inc. (2004), "ABAQUS Analysis User's Manual," Version 6.4, Pawtucket, Rhode Island.

(85)   Hills, D.A. (1971), *Heat Transfer and Vulcanization of Rubber*, Elsevier Pub. Co.

(86)   HITEC-Highway Innovative Technology Evaluation Center (1996), "Guidelines for the Testing of Seismic Isolation and Energy Dissipation Devices," CERF Report HITEC 96-02.

(87)   HITEC-Highway Innovative Technology Evaluation Center (2002), "Guidelines for Testing Large Seismic Isolation and Energy Dissipation Devices," CERF Report 40600.

(88)   Hwang, J. S., Chang, K. C. and Lee, G. C. (1990), "Quasi-Static and Dynamic Sliding Characteristics of Teflon-Stainless Steel Interfaces", J. Structural Engineering, ASCE, Vol. 116, No. 10, 2747-2762.

(89)   Hyakuda, T., Saito, K., Matsushita, T., Tanaka, N., Yoneki, S., Yasuda, M., Miyazaki, M., Suzuki, A. and Sawada T.(2001), "The Structural Design and Earthquake Observation of a Seismic Isolation Building Using Friction Pendulum System, Proceedings, 7th International Seminar on Seismic Isolation, Passive Energy Dissipation and Active Control of Vibrations of Structures, Assisi, Italy.

(90)   Imbsen, R.A. (2001), "Use of Isolation for Seismic Retrofitting Bridges," J. Bridge Engineering, ASCE, Vol.6, No.6, 425-438.

(91)   International Nickel Company (1970), "Corrosion Resistance of the Austenitic Chromium-Nickel Stainless Steels in Atmospheric Environments", Chromium-Nickel Stainless Steel Data, Section III, Bulletin B, Suffern, NY.

(92)   Jacobsen, F. K. (1977), "TFE Expansion Bearings for Highway Bridges", Report FHWA-IL-PR-71, Illinois Department of Transportation, Springfield, Illinois, April.

(93)   Kani, N., Takayama, M. and Wada, A. (2006), "Performance of Seismically Isolated Buildings in Japan", Paper 2181, Proceedings, 8th Natioanal Conference on Earthquake Engineering, San Francisco, CA.

(94)   Kartoum, A., (1987), "A Contribution to the Analysis of Elastomeric Bearings," M.S. Thesis, Department of Civil Engineering, Drexel University, Philadelphia, PA.

(95)   Kasalanati, A. and Constantinou, M.C. (1999), "Experimental Study of Bridge Elastomeric and Other Isolation and Energy Dissipation Systems With Emphasis on Uplift Prevention and High Velocity Near Source Seismic Excitation," Technical Report MCEER-99-0004, Multidisciplinary Center for Earthquake Engineering Research, State University of New York at Buffalo, Buffalo, NY.

(96) Kasalanati, A. and Constantinou, M.C. (2005), "Testing and Modeling of Prestressed Isolators", Journal of Structural Engineering, ASCE, Vol. 131, No.6, 857-866.

(97) Katsaras, C.P., Panagiotakos, T.B. and Kolias, B., (2006), "Evaluation of Current Code Requirements for Displacement Restoring Force Capability of Seismic Isolation Systems and Proposals for Revision", DENKO Consultants, Greece, *Deliverable 74*, LESSLOSS European Integrated Project.

(98) Kauschke, W. and Baigent, M. (1986), "Improvements in the Long Term Durability of Bearings in Bridges, Especially of PTFE Slide Bearings", Proc. 2nd World Congress on Joint Sealing and Bearing Systems for Concrete Structures, American Concrete Institute, Detroit, Michigan, Publication SP-94, Vol. 2, 577-612.

(99) Kim, D.K., Mander, J.B. and Chen, S.S. (1996)," Temperature and Strain Effects on the Seismic Performance of Elastomeric and Lead-rubber Bearings," Proc. 4th World Congress on Joint Sealing and Bearing Systems for Concrete Structures, American Concrete Institute, Farmington Hills, Michigan, Publication SP-164, Vol. 1, 309-322.

(100) Kelly, J.M. (1991), "Dynamic and Failure Characteristics of Bridgestone Isolation Bearings," Report No. UCB/EERC-91/04, Earthquake Engineering Research Center, University of California, Berkeley.

(101) Kelly, J.M. (1993), *Earthquake-Resistant Design with Rubber*, Springer-Verlag, London.

(102) Kelly, J.M. (2003), "Tension Buckling in Multilayer Elastomeric Bearings," J. Engineering Mechanics, ASCE, Vol. 129, No. 12, 1363-1368.

(103) Koh, C.G. and Kelly, J.M. (1987), "Effects of Axial Load on Elastomeric Bearings", Report No. UCB/EERC-86/12, Earthquake Engineering Research Center, University of California, Berkeley.

(104) Kojima, H. and Fukahori, Y. (1989), "Performance and Durability of High Damping Rubber Bearings for Earthquake Protection", distributed by Bridgestone Corp., Japan with other documentation on its seismic isolation products.

(105) Kulak, R. F., Coveney, V. A. and Jamil, S., (1998), "Recovery Characteristics of High-Damping Elastomers Used in Seismic Isolation Bearings", Seismic, Shock and Vibration Isolation—1998, ASME Publications PVP Vol. 379, American Society of Mechanical Engineers, Washington, D.C.

(106) Krim, J. (1996), "Friction at the Atomic Scale", Scientific American, Vol. 275, No. 4, 74-80, October.

(107) Lee, D. E. (1993), The Base Isolation of Koeberg Nuclear Power Station 14 Years after Installation", Proc. Post-SMiRT Conference Seminar on Isolation, Energy Dissipation and Control of Vibrations of Structures, Capri, Italy, August.

(108) Lee, D. J. (1981), "Recent Experience in the Specification, Design, Installation, and Maintenance of Bridge Bearings", Proc. World Congress on Joint Sealing and Bearing Systems for Concrete Structures, American Concrete Institute, Detroit, Michigan, Publication SP-70, Vol. 1, 161-175.

(109) Lide, D. R. (1993), editor, *Handbook of Chemistry and Physics*, 74th Edition, CRC Press, Boca Raton, Florida.

(110) Lin, Y.Y., Miranda, E. And Chang, K.C. (2005), "Evaluation of Damping Factors for Estimating Elastic Response of Structures with High Damping," Earthquake Engineering and Structural Dynamics, Vol. 34, No. 11, 1427-1443.

(111) Long, J. E. (1969), "The Performance of PTFE in Bridge Bearings", Civil Engineering and Public Works Review, UK, May, 459-462.

(112) Long, J. E. (1974), *Bearings in Structural Engineering*, J. Wiley & Sons, New York.

(113) Makison, K. R. and Tabor, D. (1964), "The Friction and Transfer of Polytetrafluoroethylene", Proc. Royal Society A, Vol. 281, 49-61.

(114) Mahin, S. A. (2006), personal communication.

(115) Makris, N. (1998), "Viscous Heating of Fluid Dampers. I: Small-amplitude Motions," Journal of Engineering Mechanics, Vol. 124, No. 11, pp 1210-1216.

(116) Makris, N., Roussos, Y., Whittaker, A. S., and Kelly, J. M. (1998), "Viscous Heating of Fluid Dampers. I: Large-amplitude Motions," Journal of Engineering Mechanics, Vol. 124, No. 11, pp 1217-1223.

(117) Makris, N. and Constantinou, M. C. (1991), "Analysis of Motion Resisted by Friction: II. Velocity-Dependent Friction", Mech. Struct. & Mach., Vol. 19(4), 501-526.

(118) Malik, A. H. (1991), "Replacement of Twenty-Year Old Elastomeric Bearings", Proc. 3rd World Congress on Joint Sealing and Bearing Systems for Concrete Structures, Toronto, Ontario, Canada, Vol. 2 of Preprints (published by the National Center for Earthquake Engineering Research, Buffalo, NY), 1109-1120.

(119) Manning, D. and Bassi, K. (1986), "Bridge Bearing Performance in Ontario", Proc. 2nd World Congress on Joint Sealing and Bearing Systems for Concrete

Structures, American Concrete Institute, Detroit, Michigan, Publication SP-94, Vol. 2, 1017-1050.

(120) Marioni, A. (1997), "Development of a New Type of Hysteretic Damper for the Seismic Protection of Bridges," Proc. Fourth World Congress on Joint Sealants and Bearing Systems for Concrete Structures, SP-1-164, Vol. 2, American Concrete Institute, 955-976.

(121) Mayrbaurl, R. M. (1986), "High Cycle Bearing Tests for the Manhattan Bridge", Proc. 2nd World Congress on Joint Sealing and Bearing Systems for Concrete Structures, American Concrete Institute, Detroit, Michigan, Publication SP-94, Vol. 1, 343-370.

(122) Mellon, D. and Post, T. (1999), "Caltrans Bridge Research and Applications of New Technologies", Proceedings of U.S.-Italy Workshop on Seismic Protective Systems for Bridges, Multidisciplinary Center for Earthquake Engineering Research, Buffalo, NY.

(123) Military Standards (1976), "Dissimilar Metals", MIL-STD-889B, July, Department of Defense.

(124) Moehle, J. P. (2003). "A Framework for Performance-based Earthquake Engineering", Proceedings, Tenth U.S.-Japan Workshop on Improvement of Building Seismic Design and Construction Practices, Report ATC-15-9, Applied Technology Council, Redwood City, California.

(125) Moghe, S.R. and Neft, H.F. (1971), "Elastic Deformations of Constrained Cylinders," J. Applied Mechanics, ASME, Vol. 38, 393-399.

(126) Mokha, A. S. , Constantinou, M. C. and Reinhorn, A. M. (1990a), "Experimental Study and Analytical Prediction of Earthquake Response of a Sliding Isolation System with a Spherical Surface", Report NCEER-90-0020, National Center for Earthquake Engineering Research, Buffalo, NY.

(127) Mokha, A., Constantinou, M. and Reinhorn, A. (1990b), "Teflon Bearings in Base Isolation. I: Testing", J. Structural Engng., ASCE, Vol. 116, No. 2, 438-454.

(128) Mokha, A., Constantinou, M. C. and Reinhorn, A. M. (1988), "Teflon Bearings in Aseismic Base Isolation: Experimental Studies and Mathematical Modeling", Report NCEER-88-0038, National Center for Earthquake Engineering Research, Buffalo, NY.

(129) Mokha, A., Constantinou, M. C. and Reinhorn, A. M. (1991), "Further Results on Frictional Properties of Teflon Bearings", J. Structural Engineering, ASCE, Vol. 117, No. 2, 622-626.

(130) Morgan, T., Whittaker, A. S. and Thompson, A., (2001), "Cyclic Behavior of High-Damping Rubber Bearings", *Proceedings*, 5th World Congress on Joints, Bearings and Seismic Systems for Concrete Structures, American Concrete Institute, Rome, Italy, October.

(131) Mosqueda, G., A. S. Whittaker, and G. L. Fenves (2004), "Characterization and Modeling of Friction Pendulum Bearings Subjected to Multiple Components of Excitation," *Journal of Structural Engineering*, ASCE, Vol. 130, No.3, 433-442.

(132) Muller-Rochholz, J. F. W., Fiebrich, M. and Breitbach, M. (1986a), "Measurement of Horizontal Bridge Movements due to Temperature, Wind and Traffic", Proc. 2nd World Congress on Joint Sealing and Bearing Systems for Concrete Structures, American Concrete Institute, Detroit, Michigan, Publication SP-94, Vol. 1, 409-418.

(133) Muller-Rochholz, J. F. W., Fiebrich, M. and Breitbach, M. (1986b), "Short Time Field Measurements on Bearings of a Steel Bridge", Proc. 2nd World Congress on Joint Sealing and Bearing Systems for Concrete Structures, American Concrete Institute, Detroit, Michigan, Publication SP-94, Vol. 1, 453-464.

(134) Mullins, L., (1969), "Softening of Rubber by Deformation", Rubber Chemistry and Technology, Vol. 42, No. 1, February.

(135) Murota, N., Goda, K., Suzuki, S., Sudo, C. and Suizu, Y. (1994), "Recovery Characteristics of Dynamic Properties of High Damping Rubber Bearings." Proc. 3rd U.S.-Japan Workshop on Earthquake Protective Systems for Bridges, January, Berkeley, CA, Report No. NCEER-94-0009, National Center for Earthquake Engineering Research, Buffalo, NY.

(136) Naeim, F. and Kelly, J.M. (1999), *Design of Seismic Isolated Structures*, J. Wiley & Sons, New York.

(137) Nagarajaiah, S. and Sun, X. (2000), "Response of Base-isolated USC Hospital Building in Northridge Earthquake," Journal of Structural Engineering-ASCE, Vol. 126, No.10, 1177-1186.

(138) Nagarajaiah, S. and Ferrell, K. (1999), "Stability of Elastomeric Seismic Isolation Bearings," Journal of Structural Engineering-ASCE, Vol. 125, No.9, 946-954.

(139) Nagarajaiah, S., Reinhorn, A.M., and Constantinou, M.C. (1989), "Nonlinear Dynamic Analysis of Three Dimensional Base Isolated Structures (3D-BASIS)," Technical Report NCEER-89-0019, National Center for Earthquake Engineering Research, State University of New York at Buffalo, Buffalo, NY.

(140) Nakano, O., Nishi, H., Shirono, T. and Kumagai, K. (1993), "Temperature-Dependence of Base-Isolation Bearings", Proc. 2nd U.S.-Japan Workshop on

Earthquake Protective Systems for Bridges, Technical Memorandum No. 3196 , Public Works Research Institute, Tsukuba Science City, Japan.

(141) Nelson, W. (1990), *Accelerated Testing*, J. Wiley & Sons, New York.

(142) Ozisik, M. N. (1989), *Boundary Value Problems of Heat Conduction*, Dover Publications, Inc., New York.

(143) Ozisik, M. N. (1993), *Heat Conduction*, 2nd Edition, John Wiley and Sons, Inc., New York.

(144) Pavlou, E. and Constantinou, M.C. (2004), "Response of Elastic and Inelastic Structures with Damping Systems to Near-Field and Soft-Soil Ground Motions," Engineering Structures, Vol. 26, 1217-1230.

(145) Pavlou, E. and Constantinou, M.C. (2006), "Response of Nonstructural Components in Structures with Damping Systems, "Journal of Structural Engineering, ASCE, Vol. 132, No. 7, 1108-1117..

(146) Pavot, B. and Polust E. (1979), "Aseismic Bearing Pads", Tribology International, Vol. 13, No. 3, 107-111.

(147) Paynter, F. R. (1973), "Investigation of Friction in PTFE Bridge Bearings", The Civil Engineer in South Africa, August, 209-217.

(148) Pekcan, G., Mander J. B., and Chen S. S. (1999) "Design and Retrofit Methodology for Buildings Structures with Supplemental Energy Dissipating Systems," Technical Report MCEER-99-0021, Multidisciplinary Center for Earthquake Engineering Research, University at Buffalo, State University of New York, Buffalo, NY.

(149) Penton (2004), Fluid *Power Handbook & Directory,* 2004-2005 Edition, Penton Media Inc.

(150) Predicting Bearing Wear (1968), Reprint No. 34, The Journal of Teflon, E. I. du Pont de Nemours and Company, Wilmington, Delaware.

(151) Rabinowicz, E. (1995), *Friction and Wear of Materials*, J. Wiley & Sons, Inc., New York.

(152) Ramirez, O. M., M. C. Constantinou, C. A. Kircher, A. Whittaker, M. Johnson, J. D. Gomez and C. Z. Chrysostomou (2001), "Development and Evaluation of Simplified Procedures of Analysis and Design for Structures with Passive Energy Dissipation Systems," Technical Report MCEER-00-0010, Revision 1, Multidisciplinary Center for Earthquake Engineering Research, University of Buffalo, State University of New York, Buffalo, NY.

(153) Roark, R.J. (1954), *Formulas for Stress and Strain*, McGraw-Hill Book Co., New York.

(154) Roeder, C.W., Stanton, J.F. and Taylor, A.W. (1987), "Performance of Elastomeric Bearings", Report No. 298, National Cooperative Highway Research Program, Transportation Research Board, Washington, D.C.

(155) Roeder, C.W., Stanton, J.F. and Campbell, T.I. (1995), "Rotation of High Load Multirotational Bridge Bearings", Journal of Structural Engineering, ASCE, Vol. 121, No. 4, 746-756.

(156) Romanoff, M. (1957), "Underground Corrosion", National Bureau of Standards, Circular 579, Department of Commerce, Washington, DC.

(157) Roussis, P.C., Constantinou, M.C., Erdik, M., Durukal, E.and Dicleli, M. (2003), "Assessment of Performance of Seismic Isolation System of Bolu Viaduct," Journal of Bridge Engineering, ASCE, Vol. 8, No.4, 182-190.

(158) Salazar, A. (2003), "On Thermal Diffusivity", European Journal of Physics, Vol. 24, p. 351-358.

(159) Sarkar, A. D. (1980), *Friction and Wear*, Academic Press, London, UK.

(160) Sato, M, Nishi, H., Kawashima, K. And Unjoh, S. (1994), "Response of On-Netoh Bridge during Kushiro-Oki Earthquake of January 1993," Proceedings, 3rd U.S.-Japan Workshop on Earthquake Protective Systems for Bridges," Report NCEER-94-0009, National Center for Earthquake Engineering Research, Buffalo, NY.

(161) Shames, I. H. and Cozzarelli, F. A. (1992), *Elastic and Inelastic Stress Analysis*, Prentice Hall, Englewoods Cliffs, New Jersey.

(162) Sigaher, A.N. and Constantinou, M.C. (2003), "Scissor-Jack-Damper Energy Dissipation System", Earthquake Spectra, Vol.19, No.1, Feb.,133-158.

(163) Skinner, R.I., Robinson, W.H. and McVerry, G.H. (1993), *An Introduction to Seismic Isolation,* John Wiley and Sons, Chichester, UK.

(164) Soong, T. T. and Constantinou, M. C. (editors) (1994), *Passive and Active Structural Vibration Control in Civil Engineering*, CISM Course and Lectures No. 345, Springer-Verlag, Wien- New York.

(165) Soong, T. T. and Dargush, G. F. (1997), *Passive Energy Dissipation Systems in Structural Engineering*, J. Wiley & Sons, London, UK.

(166) Stanton, J. F. and Roeder, C. W. (1982), "Elastomeric Bearings Design, Construction, and Materials", NCHRCP Report 248, Transportation Research Board, Washington, D.C.

(167) Stevenson, A. and Price, A. R. (1986), "A Case Study of Elastomeric Bridge Bearings After 20 Years Service", Proc. 2nd World Congress on Joint Sealing and Bearing Systems for Concrete Structures, American Concrete Institute, Detroit, Michigan, Publication SP-94, Vol. 1, 113-136.

(168) Steward, J.P., Conte, J.P and Aiken, I.D. (1999), "Observed Behavior of Seismically Isolated Buildings," Journal of Structural Engineering-ASCE, Vol. 125, No. 9, 955-964.

(169) Structural Engineers Association of Northern California-SEAONC (1986), "Tentative Seismic Isolation Design Requirements," San Francisco, CA.

(170) Swanson Analysis Systems, Inc. (1996), "ANSYS User's Manual", Version 5.3. Houston, PA.

(171) Tabor, D. (1981), "Friction-The Present State of Our Understanding", J. Lubrication Techn., ASME, Vol. 103, 169-178.

(172) Taylor, D. (2000), "Fluid lock-up devices - a Robust Means to Control Multiple Mass Structural Systems Subjected to Seismic or Wind Inputs," Proceedings, 71st SAVIAC Shock and Vibration Symposium, Arlington, VA.

(173) Taylor, D. (2006), personal communication.

(174) Taylor, A. W., Lin, A. N. and Martin, J. W. (1992), "Performance of Elastomers in Isolation Bearings: A Literature Review", Earthquake Spectra, Earthquake Engineering Research Institute, Oakland, CA, Vol. 8, No. 2, 279-303.

(175) Taylor, M. E. (1972), "PTFE in Highway Bridge Bearings", Report LR 491, Transport and Road Research Laboratory, Department of the Environment, UK.

(176) Thompson, J. B., Turrell, G. C. and Sandt B. W. (1955), "The Sliding Friction of Teflon", SPE Journal, Vol. 11(4), 13-14.

(177) Thompson, A.C.T., Whittaker, A.S., Fenves, G.L. and Mahin S.A. (2000), "Property Modification Factors for Elastomeric Seismic Isolation Bearings," Proceedings, 12th World Congress in Earthquake Engineering, New Zealand.

(178) Timoshenko, S.P. and Gere, J.M. (1961), *Theory of Elastic Stability*, McGraw-Hill, New York.

(179) Transportation Research Board (1977), "Bridge Bearings", NCHRP Report 41, Washington, DC.

(180) Transportation Research Board (1989), "Pot Bearings and PTFE Surfaces", Research Results Digest, No. 171, Washington, DC, September.

(181) Tsai, C.S., Chiang, T.C. and Chen, B.J. (2005), "Experimental Evaluation of Piecewise Exact Solution for Predicting Seismic Responses of Spherical Sliding Type Isolated Structures," Earthquake Engineering and Structural Dynamics, Vol. 34, No. 9, 1027-1046.

(182) Tsopelas, P. Okamoto, S., Constantinou, M. C., Ozaki, D. and Fujii, S. (1994), "NCEER-Taisei Corporation Research Program on Sliding Seismic Isolation Systems for Bridges: Experimental and Analytical Study of a System Consisting of Sliding Bearings, Rubber Restoring Force Devices and Fluid Dampers", Report NCEER-94-0002, National Center for Earthquake Engineering Research, Buffalo, NY.

(183) Tsopelas, P. and Constantinou, M. C. (1994), "NCEER-Taisei Corporation Research Program on Sliding Seismic Isolation Systems for Bridges: Experimental and Analytical Study of a System Consisting of Sliding Bearings and Fluid Restoring Force/Damping Devices", Report NCEER-94-0014, National Center for Earthquake Engineering Research, Buffalo, NY.

(184) Tsopelas, P. and Constantinou, M.C., (1997), "Study of Elastoplastic Bridge Seismic Isolation System", Journal of Structural Engineering, ASCE, Vol. 123, No. 4, pp. 489-498.

(185) Tsopelas, P., Constantinou, M. C., Kim, Y-S. and Okamoto, S. (1996), "Experimental Study of FPS System in Bridge Seismic Isolation", Earthquake Engineering and Structural Dynamics, Vol. 25, 65-78.

(186) Tsopelas, P., Constantinou, M.C., Kircher, C.A. and Whittaker, A.S. (1997), "Evaluation of Simplified Methods of Analysis For Yielding Structures," Report No. NCEER-97-0012, National Center for Earthquake Engineering Research, State University of New York, Buffalo, NY.

(187) Tsopelas, P., Constantinou, M. C., Okamoto, S., Fujii, S. and Ozaki, D. (1996), "Experimental Study of Bridge Seismic Sliding Isolation Systems", Engineering Structures, Vol. 18, No. 4, 301-310.

(188) Tsopelas, P., Okamoto, S., Constantinou, M. C., Ozaki, D. and Fujii, S. (1994), " NCEER-Taisei Corporation Research Program on Sliding Seismic Isolation Systems for Bridges: Experimental and Analytical Study of Systems Consisting of Sliding Bearings, Rubber Restoring Force Devices and Fluid Dampers", Report NCEER-94-0002, National Center for Earthquake Engineering Research, Buffalo, NY.

(189) Tsopelas, P.C., Roussis, P.C., Constantinou, M.C, Buchanan, R. and Reinhorn, A.M. (2005), "3D-BASIS-ME-MB: Computer Program For Nonlinear Dynamic Analysis of Seismically Isolated Structures", Report No. MCEER-05-0009, Multidisciplinary Center for Earthquake Engineering Research, Buffalo, NY.

(190) Touaillon, J. (1870), "Improvement in Buildings", United States Patent Office, Letters Patent No. 99,973, February 15.

(191) Tyler, R. G. (1977), "Dynamic Tests on PTFE Sliding Layers under Earthquake Conditions", Bulletin of the New Zealand National Society for Earthquake Engineering, Vol. 10, No. 3, September, 129-138.

(192) Uang, C. M. and Bertero, V. V. (1988), "Implications of Recorded Earthquake Ground Motions on Seismic Design of Building Structures", Report No. UCB/EERC-88/13, Earthquake Engineering Research Center, University of California, Berkeley.

(193) United Kingdom Highways Directorate (1976), "Design Requirements for Elastomeric Bridge Bearings," Technical Memorandum BE 1/76, Department of Environment.

(194) Van Vlack, L. H. (1980), *Elements of Materials Science & Engineering*, 4th Edition, Addison-Wesley Publishing Company.

(195) Warn, G.P. and Whittaker, A.S. (2004), "Performance Estimates in Seismically Isolated Bridge Structures", Engineering Structures, Vol. 26, 1261-1278.

(196) Warn, G. P., and Whittaker, A. S. (2006), "Property Modification Factors for Seismically Isolated Bridges." *Journal of Bridge Engineering*, ASCE, Vol. 11, No. 3, 371-378.

(197) Watanabe, A., Y. Hitomi, E. Saeki. A. Wada, and M. Fujimoto (1988), "Properties of Brace Encased in Buckling Restrained Concrete and Steel Tube," *Proceedings*, Ninth World Conference on Earthquake Engineering, vol. 4, 719-723, Tokyo, Japan.

(198) Whittaker, A.S., Aiken, I., Bergman, D., Clark, P., Cohen, J., Kelly, J. and Scholl, R. (1993), "Code Requirements for the Design and Implementation of Passive Energy Dissipation Devices", Proceedings of Seminar on Seismic Isolation, Passive Energy Dissipation, and Active Control, Report No. ATC-17-1, Redwood City, CA, March.

(199) Whittaker, A.S., C.M. Uang and V.V. Bertero (1988), "Implications of Recent Research on Current Seismic Regulations Pertaining to Steel Dual Systems,"

Proceedings, Conference on Tall Buildings in Seismic Regions, Council for Tall Buildings and Urban Habitat, Los Angeles, CA, February.

(200) Winters, C.W. and Constantinou, M. (1993), "Evaluation of Static and Response Spectrum Analysis Procedures of SEAOC/UBC for Seismic Isolated Structures," Report No. NCEER-93-0004, National Center for Earthquake Engineering Research, State University of New York, Buffalo, N.Y.

(201) Wolff, E.D. (1999), "Frictional Heating in Sliding Bearings and an Experimental Study of High Friction Materials," M.S. Thesis, University at Buffalo, Buffalo, NY.

(202) Wolff, E.D. and Constantinou, M.C. (2004), "Experimental Study of Seismic Isolation Systems with Emphasis on Secondary System Response and Verification of Accuracy of Dynamic Response History Analysis Methods", Report No. MCEER-04-0001, Multidisciplinary Center for Earthquake Engineering Research, Buffalo, NY.

(203) Xanthakos, P. P. (1994), *Theory and Design of Bridges*, John Wiley & Sons, New York.

(204) Yakut, A. and Yura, J.A. (2002), "Parameters Influencing Performance of Elastomeric Bearings at Low Temperatures," Journal of Structural Engineering, ASCE, Vol. 128, No. 8, pp. 986-994.

(205) Yoshizawa, H. and Israelachvilli, J. (1993), "Fundamental Mechanisms of Interfacial Friction. 2. Stick-Slip Friction of Spherical and Chain Molecules", J. Phys. Chem., Vol. 97, 11300-11313.

MCEER Technical Reports

MCEER publishes technical reports on a variety of subjects written by authors funded through MCEER. These reports are available from both MCEER Publications and the National Technical Information Service (NTIS). Requests for reports should be directed to MCEER Publications, MCEER, University at Buffalo, State University of New York, Red Jacket Quadrangle, Buffalo, New York 14261. Reports can also be requested through NTIS, 5285 Port Royal Road, Springfield, Virginia 22161. NTIS accession numbers are shown in parenthesis, if available.

NCEER-87-0001 "First-Year Program in Research, Education and Technology Transfer," 3/5/87, (PB88-134275, A04, MF-A01).

NCEER-87-0002 "Experimental Evaluation of Instantaneous Optimal Algorithms for Structural Control," by R.C. Lin, T.T. Soong and A.M. Reinhorn, 4/20/87, (PB88-134341, A04, MF-A01).

NCEER-87-0003 "Experimentation Using the Earthquake Simulation Facilities at University at Buffalo," by A.M. Reinhorn and R.L. Ketter, to be published.

NCEER-87-0004 "The System Characteristics and Performance of a Shaking Table," by J.S. Hwang, K.C. Chang and G.C. Lee, 6/1/87, (PB88-134259, A03, MF-A01). This report is available only through NTIS (see address given above).

NCEER-87-0005 "A Finite Element Formulation for Nonlinear Viscoplastic Material Using a Q Model," by O. Gyebi and G. Dasgupta, 11/2/87, (PB88-213764, A08, MF-A01).

NCEER-87-0006 "Symbolic Manipulation Program (SMP) - Algebraic Codes for Two and Three Dimensional Finite Element Formulations," by X. Lee and G. Dasgupta, 11/9/87, (PB88-218522, A05, MF-A01).

NCEER-87-0007 "Instantaneous Optimal Control Laws for Tall Buildings Under Seismic Excitations," by J.N. Yang, A. Akbarpour and P. Ghaemmaghami, 6/10/87, (PB88-134333, A06, MF-A01). This report is only available through NTIS (see address given above).

NCEER-87-0008 "IDARC: Inelastic Damage Analysis of Reinforced Concrete Frame - Shear-Wall Structures," by Y.J. Park, A.M. Reinhorn and S.K. Kunnath, 7/20/87, (PB88-134325, A09, MF-A01). This report is only available through NTIS (see address given above).

NCEER-87-0009 "Liquefaction Potential for New York State: A Preliminary Report on Sites in Manhattan and Buffalo," by M. Budhu, V. Vijayakumar, R.F. Giese and L. Baumgras, 8/31/87, (PB88-163704, A03, MF-A01). This report is available only through NTIS (see address given above).

NCEER-87-0010 "Vertical and Torsional Vibration of Foundations in Inhomogeneous Media," by A.S. Veletsos and K.W. Dotson, 6/1/87, (PB88-134291, A03, MF-A01). This report is only available through NTIS (see address given above).

NCEER-87-0011 "Seismic Probabilistic Risk Assessment and Seismic Margins Studies for Nuclear Power Plants," by Howard H.M. Hwang, 6/15/87, (PB88-134267, A03, MF-A01). This report is only available through NTIS (see address given above).

NCEER-87-0012 "Parametric Studies of Frequency Response of Secondary Systems Under Ground-Acceleration Excitations," by Y. Yong and Y.K. Lin, 6/10/87, (PB88-134309, A03, MF-A01). This report is only available through NTIS (see address given above).

NCEER-87-0013 "Frequency Response of Secondary Systems Under Seismic Excitation," by J.A. HoLung, J. Cai and Y.K. Lin, 7/31/87, (PB88-134317, A05, MF-A01). This report is only available through NTIS (see address given above).

NCEER-87-0014 "Modelling Earthquake Ground Motions in Seismically Active Regions Using Parametric Time Series Methods," by G.W. Ellis and A.S. Cakmak, 8/25/87, (PB88-134283, A08, MF-A01). This report is only available through NTIS (see address given above).

NCEER-87-0015 "Detection and Assessment of Seismic Structural Damage," by E. DiPasquale and A.S. Cakmak, 8/25/87, (PB88-163712, A05, MF-A01). This report is only available through NTIS (see address given above).

NCEER-87-0016   "Pipeline Experiment at Parkfield, California," by J. Isenberg and E. Richardson, 9/15/87, (PB88-163720, A03, MF-A01). This report is available only through NTIS (see address given above).

NCEER-87-0017   "Digital Simulation of Seismic Ground Motion," by M. Shinozuka, G. Deodatis and T. Harada, 8/31/87, (PB88-155197, A04, MF-A01). This report is available only through NTIS (see address given above).

NCEER-87-0018   "Practical Considerations for Structural Control: System Uncertainty, System Time Delay and Truncation of Small Control Forces," J.N. Yang and A. Akbarpour, 8/10/87, (PB88-163738, A08, MF-A01). This report is only available through NTIS (see address given above).

NCEER-87-0019   "Modal Analysis of Nonclassically Damped Structural Systems Using Canonical Transformation," by J.N. Yang, S. Sarkani and F.X. Long, 9/27/87, (PB88-187851, A04, MF-A01).

NCEER-87-0020   "A Nonstationary Solution in Random Vibration Theory," by J.R. Red-Horse and P.D. Spanos, 11/3/87, (PB88-163746, A03, MF-A01).

NCEER-87-0021   "Horizontal Impedances for Radially Inhomogeneous Viscoelastic Soil Layers," by A.S. Veletsos and K.W. Dotson, 10/15/87, (PB88-150859, A04, MF-A01).

NCEER-87-0022   "Seismic Damage Assessment of Reinforced Concrete Members," by Y.S. Chung, C. Meyer and M. Shinozuka, 10/9/87, (PB88-150867, A05, MF-A01). This report is available only through NTIS (see address given above).

NCEER-87-0023   "Active Structural Control in Civil Engineering," by T.T. Soong, 11/11/87, (PB88-187778, A03, MF-A01).

NCEER-87-0024   "Vertical and Torsional Impedances for Radially Inhomogeneous Viscoelastic Soil Layers," by K.W. Dotson and A.S. Veletsos, 12/87, (PB88-187786, A03, MF-A01).

NCEER-87-0025   "Proceedings from the Symposium on Seismic Hazards, Ground Motions, Soil-Liquefaction and Engineering Practice in Eastern North America," October 20-22, 1987, edited by K.H. Jacob, 12/87, (PB88-188115, A23, MF-A01). This report is available only through NTIS (see address given above).

NCEER-87-0026   "Report on the Whittier-Narrows, California, Earthquake of October 1, 1987," by J. Pantelic and A. Reinhorn, 11/87, (PB88-187752, A03, MF-A01). This report is available only through NTIS (see address given above).

NCEER-87-0027   "Design of a Modular Program for Transient Nonlinear Analysis of Large 3-D Building Structures," by S. Srivastav and J.F. Abel, 12/30/87, (PB88-187950, A05, MF-A01). This report is only available through NTIS (see address given above).

NCEER-87-0028   "Second-Year Program in Research, Education and Technology Transfer," 3/8/88, (PB88-219480, A04, MF-A01).

NCEER-88-0001   "Workshop on Seismic Computer Analysis and Design of Buildings With Interactive Graphics," by W. McGuire, J.F. Abel and C.H. Conley, 1/18/88, (PB88-187760, A03, MF-A01). This report is only available through NTIS (see address given above).

NCEER-88-0002   "Optimal Control of Nonlinear Flexible Structures," by J.N. Yang, F.X. Long and D. Wong, 1/22/88, (PB88-213772, A06, MF-A01).

NCEER-88-0003   "Substructuring Techniques in the Time Domain for Primary-Secondary Structural Systems," by G.D. Manolis and G. Juhn, 2/10/88, (PB88-213780, A04, MF-A01).

NCEER-88-0004   "Iterative Seismic Analysis of Primary-Secondary Systems," by A. Singhal, L.D. Lutes and P.D. Spanos, 2/23/88, (PB88-213798, A04, MF-A01).

NCEER-88-0005   "Stochastic Finite Element Expansion for Random Media," by P.D. Spanos and R. Ghanem, 3/14/88, (PB88-213806, A03, MF-A01).

NCEER-88-0006   "Combining Structural Optimization and Structural Control," by F.Y. Cheng and C.P. Pantelides, 1/10/88, (PB88-213814, A05, MF-A01).

NCEER-88-0007   "Seismic Performance Assessment of Code-Designed Structures," by H.H-M. Hwang, J-W. Jaw and H-J. Shau, 3/20/88, (PB88-219423, A04, MF-A01). This report is only available through NTIS (see address given above).

NCEER-88-0008   "Reliability Analysis of Code-Designed Structures Under Natural Hazards," by H.H-M. Hwang, H. Ushiba and M. Shinozuka, 2/29/88, (PB88-229471, A07, MF-A01). This report is only available through NTIS (see address given above).

NCEER-88-0009   "Seismic Fragility Analysis of Shear Wall Structures," by J-W Jaw and H.H-M. Hwang, 4/30/88, (PB89-102867, A04, MF-A01).

NCEER-88-0010   "Base Isolation of a Multi-Story Building Under a Harmonic Ground Motion - A Comparison of Performances of Various Systems," by F-G Fan, G. Ahmadi and I.G. Tadjbakhsh, 5/18/88, (PB89-122238, A06, MF-A01). This report is only available through NTIS (see address given above).

NCEER-88-0011   "Seismic Floor Response Spectra for a Combined System by Green's Functions," by F.M. Lavelle, L.A. Bergman and P.D. Spanos, 5/1/88, (PB89-102875, A03, MF-A01).

NCEER-88-0012   "A New Solution Technique for Randomly Excited Hysteretic Structures," by G.Q. Cai and Y.K. Lin, 5/16/88, (PB89-102883, A03, MF-A01).

NCEER-88-0013   "A Study of Radiation Damping and Soil-Structure Interaction Effects in the Centrifuge," by K. Weissman, supervised by J.H. Prevost, 5/24/88, (PB89-144703, A06, MF-A01).

NCEER-88-0014   "Parameter Identification and Implementation of a Kinematic Plasticity Model for Frictional Soils," by J.H. Prevost and D.V. Griffiths, to be published.

NCEER-88-0015   "Two- and Three- Dimensional Dynamic Finite Element Analyses of the Long Valley Dam," by D.V. Griffiths and J.H. Prevost, 6/17/88, (PB89-144711, A04, MF-A01).

NCEER-88-0016   "Damage Assessment of Reinforced Concrete Structures in Eastern United States," by A.M. Reinhorn, M.J. Seidel, S.K. Kunnath and Y.J. Park, 6/15/88, (PB89-122220, A04, MF-A01). This report is only available through NTIS (see address given above).

NCEER-88-0017   "Dynamic Compliance of Vertically Loaded Strip Foundations in Multilayered Viscoelastic Soils," by S. Ahmad and A.S.M. Israil, 6/17/88, (PB89-102891, A04, MF-A01).

NCEER-88-0018   "An Experimental Study of Seismic Structural Response With Added Viscoelastic Dampers," by R.C. Lin, Z. Liang, T.T. Soong and R.H. Zhang, 6/30/88, (PB89-122212, A05, MF-A01). This report is available only through NTIS (see address given above).

NCEER-88-0019   "Experimental Investigation of Primary - Secondary System Interaction," by G.D. Manolis, G. Juhn and A.M. Reinhorn, 5/27/88, (PB89-122204, A04, MF-A01).

NCEER-88-0020   "A Response Spectrum Approach For Analysis of Nonclassically Damped Structures," by J.N. Yang, S. Sarkani and F.X. Long, 4/22/88, (PB89-102909, A04, MF-A01).

NCEER-88-0021   "Seismic Interaction of Structures and Soils: Stochastic Approach," by A.S. Veletsos and A.M. Prasad, 7/21/88, (PB89-122196, A04, MF-A01). This report is only available through NTIS (see address given above).

NCEER-88-0022   "Identification of the Serviceability Limit State and Detection of Seismic Structural Damage," by E. DiPasquale and A.S. Cakmak, 6/15/88, (PB89-122188, A05, MF-A01). This report is available only through NTIS (see address given above).

NCEER-88-0023   "Multi-Hazard Risk Analysis: Case of a Simple Offshore Structure," by B.K. Bhartia and E.H. Vanmarcke, 7/21/88, (PB89-145213, A05, MF-A01).

NCEER-88-0024   "Automated Seismic Design of Reinforced Concrete Buildings," by Y.S. Chung, C. Meyer and M. Shinozuka, 7/5/88, (PB89-122170, A06, MF-A01). This report is available only through NTIS (see address given above).

NCEER-88-0025   "Experimental Study of Active Control of MDOF Structures Under Seismic Excitations," by L.L. Chung, R.C. Lin, T.T. Soong and A.M. Reinhorn, 7/10/88, (PB89-122600, A04, MF-A01).

NCEER-88-0026   "Earthquake Simulation Tests of a Low-Rise Metal Structure," by J.S. Hwang, K.C. Chang, G.C. Lee and R.L. Ketter, 8/1/88, (PB89-102917, A04, MF-A01).

NCEER-88-0027   "Systems Study of Urban Response and Reconstruction Due to Catastrophic Earthquakes," by F. Kozin and H.K. Zhou, 9/22/88, (PB90-162348, A04, MF-A01).

NCEER-88-0028   "Seismic Fragility Analysis of Plane Frame Structures," by H.H-M. Hwang and Y.K. Low, 7/31/88, (PB89-131445, A06, MF-A01).

NCEER-88-0029   "Response Analysis of Stochastic Structures," by A. Kardara, C. Bucher and M. Shinozuka, 9/22/88, (PB89-174429, A04, MF-A01).

NCEER-88-0030   "Nonnormal Accelerations Due to Yielding in a Primary Structure," by D.C.K. Chen and L.D. Lutes, 9/19/88, (PB89-131437, A04, MF-A01).

NCEER-88-0031   "Design Approaches for Soil-Structure Interaction," by A.S. Veletsos, A.M. Prasad and Y. Tang, 12/30/88, (PB89-174437, A03, MF-A01). This report is available only through NTIS (see address given above).

NCEER-88-0032   "A Re-evaluation of Design Spectra for Seismic Damage Control," by C.J. Turkstra and A.G. Tallin, 11/7/88, (PB89-145221, A05, MF-A01).

NCEER-88-0033   "The Behavior and Design of Noncontact Lap Splices Subjected to Repeated Inelastic Tensile Loading," by V.E. Sagan, P. Gergely and R.N. White, 12/8/88, (PB89-163737, A08, MF-A01).

NCEER-88-0034   "Seismic Response of Pile Foundations," by S.M. Mamoon, P.K. Banerjee and S. Ahmad, 11/1/88, (PB89-145239, A04, MF-A01).

NCEER-88-0035   "Modeling of R/C Building Structures With Flexible Floor Diaphragms (IDARC2)," by A.M. Reinhorn, S.K. Kunnath and N. Panahshahi, 9/7/88, (PB89-207153, A07, MF-A01).

NCEER-88-0036   "Solution of the Dam-Reservoir Interaction Problem Using a Combination of FEM, BEM with Particular Integrals, Modal Analysis, and Substructuring," by C-S. Tsai, G.C. Lee and R.L. Ketter, 12/31/88, (PB89-207146, A04, MF-A01).

NCEER-88-0037   "Optimal Placement of Actuators for Structural Control," by F.Y. Cheng and C.P. Pantelides, 8/15/88, (PB89-162846, A05, MF-A01).

NCEER-88-0038   "Teflon Bearings in Aseismic Base Isolation: Experimental Studies and Mathematical Modeling," by A. Mokha, M.C. Constantinou and A.M. Reinhorn, 12/5/88, (PB89-218457, A10, MF-A01). This report is available only through NTIS (see address given above).

NCEER-88-0039   "Seismic Behavior of Flat Slab High-Rise Buildings in the New York City Area," by P. Weidlinger and M. Ettouney, 10/15/88, (PB90-145681, A04, MF-A01).

NCEER-88-0040   "Evaluation of the Earthquake Resistance of Existing Buildings in New York City," by P. Weidlinger and M. Ettouney, 10/15/88, to be published.

NCEER-88-0041   "Small-Scale Modeling Techniques for Reinforced Concrete Structures Subjected to Seismic Loads," by W. Kim, A. El-Attar and R.N. White, 11/22/88, (PB89-189625, A05, MF-A01).

NCEER-88-0042   "Modeling Strong Ground Motion from Multiple Event Earthquakes," by G.W. Ellis and A.S. Cakmak, 10/15/88, (PB89-174445, A03, MF-A01).

NCEER-88-0043   "Nonstationary Models of Seismic Ground Acceleration," by M. Grigoriu, S.E. Ruiz and E. Rosenblueth, 7/15/88, (PB89-189617, A04, MF-A01).

NCEER-88-0044   "SARCF User's Guide: Seismic Analysis of Reinforced Concrete Frames," by Y.S. Chung, C. Meyer and M. Shinozuka, 11/9/88, (PB89-174452, A08, MF-A01).

NCEER-88-0045   "First Expert Panel Meeting on Disaster Research and Planning," edited by J. Pantelic and J. Stoyle, 9/15/88, (PB89-174460, A05, MF-A01).

NCEER-88-0046   "Preliminary Studies of the Effect of Degrading Infill Walls on the Nonlinear Seismic Response of Steel Frames," by C.Z. Chrysostomou, P. Gergely and J.F. Abel, 12/19/88, (PB89-208383, A05, MF-A01).

NCEER-88-0047   "Reinforced Concrete Frame Component Testing Facility - Design, Construction, Instrumentation and Operation," by S.P. Pessiki, C. Conley, T. Bond, P. Gergely and R.N. White, 12/16/88, (PB89-174478, A04, MF-A01).

NCEER-89-0001   "Effects of Protective Cushion and Soil Compliancy on the Response of Equipment Within a Seismically Excited Building," by J.A. HoLung, 2/16/89, (PB89-207179, A04, MF-A01).

NCEER-89-0002   "Statistical Evaluation of Response Modification Factors for Reinforced Concrete Structures," by H.H-M. Hwang and J-W. Jaw, 2/17/89, (PB89-207187, A05, MF-A01).

NCEER-89-0003   "Hysteretic Columns Under Random Excitation," by G-Q. Cai and Y.K. Lin, 1/9/89, (PB89-196513, A03, MF-A01).

NCEER-89-0004   "Experimental Study of `Elephant Foot Bulge' Instability of Thin-Walled Metal Tanks," by Z-H. Jia and R.L. Ketter, 2/22/89, (PB89-207195, A03, MF-A01).

NCEER-89-0005   "Experiment on Performance of Buried Pipelines Across San Andreas Fault," by J. Isenberg, E. Richardson and T.D. O'Rourke, 3/10/89, (PB89-218440, A04, MF-A01). This report is available only through NTIS (see address given above).

NCEER-89-0006   "A Knowledge-Based Approach to Structural Design of Earthquake-Resistant Buildings," by M. Subramani, P. Gergely, C.H. Conley, J.F. Abel and A.H. Zaghw, 1/15/89, (PB89-218465, A06, MF-A01).

NCEER-89-0007   "Liquefaction Hazards and Their Effects on Buried Pipelines," by T.D. O'Rourke and P.A. Lane, 2/1/89, (PB89-218481, A09, MF-A01).

NCEER-89-0008   "Fundamentals of System Identification in Structural Dynamics," by H. Imai, C-B. Yun, O. Maruyama and M. Shinozuka, 1/26/89, (PB89-207211, A04, MF-A01).

NCEER-89-0009   "Effects of the 1985 Michoacan Earthquake on Water Systems and Other Buried Lifelines in Mexico," by A.G. Ayala and M.J. O'Rourke, 3/8/89, (PB89-207229, A06, MF-A01).

NCEER-89-R010   "NCEER Bibliography of Earthquake Education Materials," by K.E.K. Ross, Second Revision, 9/1/89, (PB90-125352, A05, MF-A01). This report is replaced by NCEER-92-0018.

NCEER-89-0011   "Inelastic Three-Dimensional Response Analysis of Reinforced Concrete Building Structures (IDARC-3D), Part I - Modeling," by S.K. Kunnath and A.M. Reinhorn, 4/17/89, (PB90-114612, A07, MF-A01). This report is available only through NTIS (see address given above).

NCEER-89-0012   "Recommended Modifications to ATC-14," by C.D. Poland and J.O. Malley, 4/12/89, (PB90-108648, A15, MF-A01).

NCEER-89-0013   "Repair and Strengthening of Beam-to-Column Connections Subjected to Earthquake Loading," by M. Corazao and A.J. Durrani, 2/28/89, (PB90-109885, A06, MF-A01).

NCEER-89-0014   "Program EXKAL2 for Identification of Structural Dynamic Systems," by O. Maruyama, C-B. Yun, M. Hoshiya and M. Shinozuka, 5/19/89, (PB90-109877, A09, MF-A01).

NCEER-89-0015   "Response of Frames With Bolted Semi-Rigid Connections, Part I - Experimental Study and Analytical Predictions," by P.J. DiCorso, A.M. Reinhorn, J.R. Dickerson, J.B. Radziminski and W.L. Harper, 6/1/89, to be published.

NCEER-89-0016   "ARMA Monte Carlo Simulation in Probabilistic Structural Analysis," by P.D. Spanos and M.P. Mignolet, 7/10/89, (PB90-109893, A03, MF-A01).

NCEER-89-P017   "Preliminary Proceedings from the Conference on Disaster Preparedness - The Place of Earthquake Education in Our Schools," Edited by K.E.K. Ross, 6/23/89, (PB90-108606, A03, MF-A01).

NCEER-89-0017   "Proceedings from the Conference on Disaster Preparedness - The Place of Earthquake Education in Our Schools," Edited by K.E.K. Ross, 12/31/89, (PB90-207895, A012, MF-A02). This report is available only through NTIS (see address given above).

NCEER-89-0018   "Multidimensional Models of Hysteretic Material Behavior for Vibration Analysis of Shape Memory Energy Absorbing Devices, by E.J. Graesser and F.A. Cozzarelli, 6/7/89, (PB90-164146, A04, MF-A01).

NCEER-89-0019   "Nonlinear Dynamic Analysis of Three-Dimensional Base Isolated Structures (3D-BASIS)," by S. Nagarajaiah, A.M. Reinhorn and M.C. Constantinou, 8/3/89, (PB90-161936, A06, MF-A01). This report has been replaced by NCEER-93-0011.

NCEER-89-0020   "Structural Control Considering Time-Rate of Control Forces and Control Rate Constraints," by F.Y. Cheng and C.P. Pantelides, 8/3/89, (PB90-120445, A04, MF-A01).

NCEER-89-0021   "Subsurface Conditions of Memphis and Shelby County," by K.W. Ng, T-S. Chang and H-H.M. Hwang, 7/26/89, (PB90-120437, A03, MF-A01).

NCEER-89-0022   "Seismic Wave Propagation Effects on Straight Jointed Buried Pipelines," by K. Elhmadi and M.J. O'Rourke, 8/24/89, (PB90-162322, A10, MF-A02).

NCEER-89-0023   "Workshop on Serviceability Analysis of Water Delivery Systems," edited by M. Grigoriu, 3/6/89, (PB90-127424, A03, MF-A01).

NCEER-89-0024   "Shaking Table Study of a 1/5 Scale Steel Frame Composed of Tapered Members," by K.C. Chang, J.S. Hwang and G.C. Lee, 9/18/89, (PB90-160169, A04, MF-A01).

NCEER-89-0025   "DYNA1D: A Computer Program for Nonlinear Seismic Site Response Analysis - Technical Documentation," by Jean H. Prevost, 9/14/89, (PB90-161944, A07, MF-A01). This report is available only through NTIS (see address given above).

NCEER-89-0026   "1:4 Scale Model Studies of Active Tendon Systems and Active Mass Dampers for Aseismic Protection," by A.M. Reinhorn, T.T. Soong, R.C. Lin, Y.P. Yang, Y. Fukao, H. Abe and M. Nakai, 9/15/89, (PB90-173246, A10, MF-A02). This report is available only through NTIS (see address given above).

NCEER-89-0027   "Scattering of Waves by Inclusions in a Nonhomogeneous Elastic Half Space Solved by Boundary Element Methods," by P.K. Hadley, A. Askar and A.S. Cakmak, 6/15/89, (PB90-145699, A07, MF-A01).

NCEER-89-0028   "Statistical Evaluation of Deflection Amplification Factors for Reinforced Concrete Structures," by H.H.M. Hwang, J-W. Jaw and A.L. Ch'ng, 8/31/89, (PB90-164633, A05, MF-A01).

NCEER-89-0029   "Bedrock Accelerations in Memphis Area Due to Large New Madrid Earthquakes," by H.H.M. Hwang, C.H.S. Chen and G. Yu, 11/7/89, (PB90-162330, A04, MF-A01).

NCEER-89-0030   "Seismic Behavior and Response Sensitivity of Secondary Structural Systems," by Y.Q. Chen and T.T. Soong, 10/23/89, (PB90-164658, A08, MF-A01).

NCEER-89-0031   "Random Vibration and Reliability Analysis of Primary-Secondary Structural Systems," by Y. Ibrahim, M. Grigoriu and T.T. Soong, 11/10/89, (PB90-161951, A04, MF-A01).

NCEER-89-0032   "Proceedings from the Second U.S. - Japan Workshop on Liquefaction, Large Ground Deformation and Their Effects on Lifelines, September 26-29, 1989," Edited by T.D. O'Rourke and M. Hamada, 12/1/89, (PB90-209388, A22, MF-A03).

NCEER-89-0033   "Deterministic Model for Seismic Damage Evaluation of Reinforced Concrete Structures," by J.M. Bracci, A.M. Reinhorn, J.B. Mander and S.K. Kunnath, 9/27/89, (PB91-108803, A06, MF-A01).

NCEER-89-0034   "On the Relation Between Local and Global Damage Indices," by E. DiPasquale and A.S. Cakmak, 8/15/89, (PB90-173865, A05, MF-A01).

NCEER-89-0035   "Cyclic Undrained Behavior of Nonplastic and Low Plasticity Silts," by A.J. Walker and H.E. Stewart, 7/26/89, (PB90-183518, A10, MF-A01).

NCEER-89-0036   "Liquefaction Potential of Surficial Deposits in the City of Buffalo, New York," by M. Budhu, R. Giese and L. Baumgrass, 1/17/89, (PB90-208455, A04, MF-A01).

NCEER-89-0037   "A Deterministic Assessment of Effects of Ground Motion Incoherence," by A.S. Veletsos and Y. Tang, 7/15/89, (PB90-164294, A03, MF-A01).

NCEER-89-0038   "Workshop on Ground Motion Parameters for Seismic Hazard Mapping," July 17-18, 1989, edited by R.V. Whitman, 12/1/89, (PB90-173923, A04, MF-A01).

NCEER-89-0039   "Seismic Effects on Elevated Transit Lines of the New York City Transit Authority," by C.J. Costantino, C.A. Miller and E. Heymsfield, 12/26/89, (PB90-207887, A06, MF-A01).

NCEER-89-0040   "Centrifugal Modeling of Dynamic Soil-Structure Interaction," by K. Weissman, Supervised by J.H. Prevost, 5/10/89, (PB90-207879, A07, MF-A01).

NCEER-89-0041   "Linearized Identification of Buildings With Cores for Seismic Vulnerability Assessment," by I-K. Ho and A.E. Aktan, 11/1/89, (PB90-251943, A07, MF-A01).

NCEER-90-0001   "Geotechnical and Lifeline Aspects of the October 17, 1989 Loma Prieta Earthquake in San Francisco," by T.D. O'Rourke, H.E. Stewart, F.T. Blackburn and T.S. Dickerman, 1/90, (PB90-208596, A05, MF-A01).

NCEER-90-0002   "Nonnormal Secondary Response Due to Yielding in a Primary Structure," by D.C.K. Chen and L.D. Lutes, 2/28/90, (PB90-251976, A07, MF-A01).

NCEER-90-0003   "Earthquake Education Materials for Grades K-12," by K.E.K. Ross, 4/16/90, (PB91-251984, A05, MF-A05). This report has been replaced by NCEER-92-0018.

NCEER-90-0004   "Catalog of Strong Motion Stations in Eastern North America," by R.W. Busby, 4/3/90, (PB90-251984, A05, MF-A01).

NCEER-90-0005   "NCEER Strong-Motion Data Base: A User Manual for the GeoBase Release (Version 1.0 for the Sun3)," by P. Friberg and K. Jacob, 3/31/90 (PB90-258062, A04, MF-A01).

NCEER-90-0006   "Seismic Hazard Along a Crude Oil Pipeline in the Event of an 1811-1812 Type New Madrid Earthquake," by H.H.M. Hwang and C-H.S. Chen, 4/16/90, (PB90-258054, A04, MF-A01).

NCEER-90-0007   "Site-Specific Response Spectra for Memphis Sheahan Pumping Station," by H.H.M. Hwang and C.S. Lee, 5/15/90, (PB91-108811, A05, MF-A01).

NCEER-90-0008   "Pilot Study on Seismic Vulnerability of Crude Oil Transmission Systems," by T. Ariman, R. Dobry, M. Grigoriu, F. Kozin, M. O'Rourke, T. O'Rourke and M. Shinozuka, 5/25/90, (PB91-108837, A06, MF-A01).

NCEER-90-0009   "A Program to Generate Site Dependent Time Histories: EQGEN," by G.W. Ellis, M. Srinivasan and A.S. Cakmak, 1/30/90, (PB91-108829, A04, MF-A01).

NCEER-90-0010   "Active Isolation for Seismic Protection of Operating Rooms," by M.E. Talbott, Supervised by M. Shinozuka, 6/8/9, (PB91-110205, A05, MF-A01).

NCEER-90-0011   "Program LINEARID for Identification of Linear Structural Dynamic Systems," by C-B. Yun and M. Shinozuka, 6/25/90, (PB91-110312, A08, MF-A01).

NCEER-90-0012   "Two-Dimensional Two-Phase Elasto-Plastic Seismic Response of Earth Dams," by A.N. Yiagos, Supervised by J.H. Prevost, 6/20/90, (PB91-110197, A13, MF-A02).

NCEER-90-0013   "Secondary Systems in Base-Isolated Structures: Experimental Investigation, Stochastic Response and Stochastic Sensitivity," by G.D. Manolis, G. Juhn, M.C. Constantinou and A.M. Reinhorn, 7/1/90, (PB91-110320, A08, MF-A01).

NCEER-90-0014   "Seismic Behavior of Lightly-Reinforced Concrete Column and Beam-Column Joint Details," by S.P. Pessiki, C.H. Conley, P. Gergely and R.N. White, 8/22/90, (PB91-108795, A11, MF-A02).

NCEER-90-0015   "Two Hybrid Control Systems for Building Structures Under Strong Earthquakes," by J.N. Yang and A. Danielians, 6/29/90, (PB91-125393, A04, MF-A01).

NCEER-90-0016   "Instantaneous Optimal Control with Acceleration and Velocity Feedback," by J.N. Yang and Z. Li, 6/29/90, (PB91-125401, A03, MF-A01).

NCEER-90-0017   "Reconnaissance Report on the Northern Iran Earthquake of June 21, 1990," by M. Mehrain, 10/4/90, (PB91-125377, A03, MF-A01).

NCEER-90-0018   "Evaluation of Liquefaction Potential in Memphis and Shelby County," by T.S. Chang, P.S. Tang, C.S. Lee and H. Hwang, 8/10/90, (PB91-125427, A09, MF-A01).

NCEER-90-0019   "Experimental and Analytical Study of a Combined Sliding Disc Bearing and Helical Steel Spring Isolation System," by M.C. Constantinou, A.S. Mokha and A.M. Reinhorn, 10/4/90, (PB91-125385, A06, MF-A01). This report is available only through NTIS (see address given above).

NCEER-90-0020   "Experimental Study and Analytical Prediction of Earthquake Response of a Sliding Isolation System with a Spherical Surface," by A.S. Mokha, M.C. Constantinou and A.M. Reinhorn, 10/11/90, (PB91-125419, A05, MF-A01).

NCEER-90-0021   "Dynamic Interaction Factors for Floating Pile Groups," by G. Gazetas, K. Fan, A. Kaynia and E. Kausel, 9/10/90, (PB91-170381, A05, MF-A01).

NCEER-90-0022   "Evaluation of Seismic Damage Indices for Reinforced Concrete Structures," by S. Rodriguez-Gomez and A.S. Cakmak, 9/30/90, PB91-171322, A06, MF-A01).

NCEER-90-0023   "Study of Site Response at a Selected Memphis Site," by H. Desai, S. Ahmad, E.S. Gazetas and M.R. Oh, 10/11/90, (PB91-196857, A03, MF-A01).

NCEER-90-0024   "A User's Guide to Strongmo: Version 1.0 of NCEER's Strong-Motion Data Access Tool for PCs and Terminals," by P.A. Friberg and C.A.T. Susch, 11/15/90, (PB91-171272, A03, MF-A01).

NCEER-90-0025   "A Three-Dimensional Analytical Study of Spatial Variability of Seismic Ground Motions," by L-L. Hong and A.H.-S. Ang, 10/30/90, (PB91-170399, A09, MF-A01).

NCEER-90-0026   "MUMOID User's Guide - A Program for the Identification of Modal Parameters," by S. Rodriguez-Gomez and E. DiPasquale, 9/30/90, (PB91-171298, A04, MF-A01).

NCEER-90-0027   "SARCF-II User's Guide - Seismic Analysis of Reinforced Concrete Frames," by S. Rodriguez-Gomez, Y.S. Chung and C. Meyer, 9/30/90, (PB91-171280, A05, MF-A01).

NCEER-90-0028   "Viscous Dampers: Testing, Modeling and Application in Vibration and Seismic Isolation," by N. Makris and M.C. Constantinou, 12/20/90 (PB91-190561, A06, MF-A01).

NCEER-90-0029   "Soil Effects on Earthquake Ground Motions in the Memphis Area," by H. Hwang, C.S. Lee, K.W. Ng and T.S. Chang, 8/2/90, (PB91-190751, A05, MF-A01).

NCEER-91-0001 "Proceedings from the Third Japan-U.S. Workshop on Earthquake Resistant Design of Lifeline Facilities and Countermeasures for Soil Liquefaction, December 17-19, 1990," edited by T.D. O'Rourke and M. Hamada, 2/1/91, (PB91-179259, A99, MF-A04).

NCEER-91-0002 "Physical Space Solutions of Non-Proportionally Damped Systems," by M. Tong, Z. Liang and G.C. Lee, 1/15/91, (PB91-179242, A04, MF-A01).

NCEER-91-0003 "Seismic Response of Single Piles and Pile Groups," by K. Fan and G. Gazetas, 1/10/91, (PB92-174994, A04, MF-A01).

NCEER-91-0004 "Damping of Structures: Part 1 - Theory of Complex Damping," by Z. Liang and G. Lee, 10/10/91, (PB92-197235, A12, MF-A03).

NCEER-91-0005 "3D-BASIS - Nonlinear Dynamic Analysis of Three Dimensional Base Isolated Structures: Part II," by S. Nagarajaiah, A.M. Reinhorn and M.C. Constantinou, 2/28/91, (PB91-190553, A07, MF-A01). This report has been replaced by NCEER-93-0011.

NCEER-91-0006 "A Multidimensional Hysteretic Model for Plasticity Deforming Metals in Energy Absorbing Devices," by E.J. Graesser and F.A. Cozzarelli, 4/9/91, (PB92-108364, A04, MF-A01).

NCEER-91-0007 "A Framework for Customizable Knowledge-Based Expert Systems with an Application to a KBES for Evaluating the Seismic Resistance of Existing Buildings," by E.G. Ibarra-Anaya and S.J. Fenves, 4/9/91, (PB91-210930, A08, MF-A01).

NCEER-91-0008 "Nonlinear Analysis of Steel Frames with Semi-Rigid Connections Using the Capacity Spectrum Method," by G.G. Deierlein, S-H. Hsieh, Y-J. Shen and J.F. Abel, 7/2/91, (PB92-113828, A05, MF-A01).

NCEER-91-0009 "Earthquake Education Materials for Grades K-12," by K.E.K. Ross, 4/30/91, (PB91-212142, A06, MF-A01). This report has been replaced by NCEER-92-0018.

NCEER-91-0010 "Phase Wave Velocities and Displacement Phase Differences in a Harmonically Oscillating Pile," by N. Makris and G. Gazetas, 7/8/91, (PB92-108356, A04, MF-A01).

NCEER-91-0011 "Dynamic Characteristics of a Full-Size Five-Story Steel Structure and a 2/5 Scale Model," by K.C. Chang, G.C. Yao, G.C. Lee, D.S. Hao and Y.C. Yeh," 7/2/91, (PB93-116648, A06, MF-A02).

NCEER-91-0012 "Seismic Response of a 2/5 Scale Steel Structure with Added Viscoelastic Dampers," by K.C. Chang, T.T. Soong, S-T. Oh and M.L. Lai, 5/17/91, (PB92-110816, A05, MF-A01).

NCEER-91-0013 "Earthquake Response of Retaining Walls; Full-Scale Testing and Computational Modeling," by S. Alampalli and A-W.M. Elgamal, 6/20/91, to be published.

NCEER-91-0014 "3D-BASIS-M: Nonlinear Dynamic Analysis of Multiple Building Base Isolated Structures," by P.C. Tsopelas, S. Nagarajaiah, M.C. Constantinou and A.M. Reinhorn, 5/28/91, (PB92-113885, A09, MF-A02).

NCEER-91-0015 "Evaluation of SEAOC Design Requirements for Sliding Isolated Structures," by D. Theodossiou and M.C. Constantinou, 6/10/91, (PB92-114602, A11, MF-A03).

NCEER-91-0016 "Closed-Loop Modal Testing of a 27-Story Reinforced Concrete Flat Plate-Core Building," by H.R. Somaprasad, T. Toksoy, H. Yoshiyuki and A.E. Aktan, 7/15/91, (PB92-129980, A07, MF-A02).

NCEER-91-0017 "Shake Table Test of a 1/6 Scale Two-Story Lightly Reinforced Concrete Building," by A.G. El-Attar, R.N. White and P. Gergely, 2/28/91, (PB92-222447, A06, MF-A02).

NCEER-91-0018 "Shake Table Test of a 1/8 Scale Three-Story Lightly Reinforced Concrete Building," by A.G. El-Attar, R.N. White and P. Gergely, 2/28/91, (PB93-116630, A08, MF-A02).

NCEER-91-0019 "Transfer Functions for Rigid Rectangular Foundations," by A.S. Veletsos, A.M. Prasad and W.H. Wu, 7/31/91, to be published.

NCEER-91-0020   "Hybrid Control of Seismic-Excited Nonlinear and Inelastic Structural Systems," by J.N. Yang, Z. Li and A. Danielians, 8/1/91, (PB92-143171, A06, MF-A02).

NCEER-91-0021   "The NCEER-91 Earthquake Catalog: Improved Intensity-Based Magnitudes and Recurrence Relations for U.S. Earthquakes East of New Madrid," by L. Seeber and J.G. Armbruster, 8/28/91, (PB92-176742, A06, MF-A02).

NCEER-91-0022   "Proceedings from the Implementation of Earthquake Planning and Education in Schools: The Need for Change - The Roles of the Changemakers," by K.E.K. Ross and F. Winslow, 7/23/91, (PB92-129998, A12, MF-A03).

NCEER-91-0023   "A Study of Reliability-Based Criteria for Seismic Design of Reinforced Concrete Frame Buildings," by H.H.M. Hwang and H-M. Hsu, 8/10/91, (PB92-140235, A09, MF-A02).

NCEER-91-0024   "Experimental Verification of a Number of Structural System Identification Algorithms," by R.G. Ghanem, H. Gavin and M. Shinozuka, 9/18/91, (PB92-176577, A18, MF-A04).

NCEER-91-0025   "Probabilistic Evaluation of Liquefaction Potential," by H.H.M. Hwang and C.S. Lee," 11/25/91, (PB92-143429, A05, MF-A01).

NCEER-91-0026   "Instantaneous Optimal Control for Linear, Nonlinear and Hysteretic Structures - Stable Controllers," by J.N. Yang and Z. Li, 11/15/91, (PB92-163807, A04, MF-A01).

NCEER-91-0027   "Experimental and Theoretical Study of a Sliding Isolation System for Bridges," by M.C. Constantinou, A. Kartoum, A.M. Reinhorn and P. Bradford, 11/15/91, (PB92-176973, A10, MF-A03).

NCEER-92-0001   "Case Studies of Liquefaction and Lifeline Performance During Past Earthquakes, Volume 1: Japanese Case Studies," Edited by M. Hamada and T. O'Rourke, 2/17/92, (PB92-197243, A18, MF-A04).

NCEER-92-0002   "Case Studies of Liquefaction and Lifeline Performance During Past Earthquakes, Volume 2: United States Case Studies," Edited by T. O'Rourke and M. Hamada, 2/17/92, (PB92-197250, A20, MF-A04).

NCEER-92-0003   "Issues in Earthquake Education," Edited by K. Ross, 2/3/92, (PB92-222389, A07, MF-A02).

NCEER-92-0004   "Proceedings from the First U.S. - Japan Workshop on Earthquake Protective Systems for Bridges," Edited by I.G. Buckle, 2/4/92, (PB94-142239, A99, MF-A06).

NCEER-92-0005   "Seismic Ground Motion from a Haskell-Type Source in a Multiple-Layered Half-Space," A.P. Theoharis, G. Deodatis and M. Shinozuka, 1/2/92, to be published.

NCEER-92-0006   "Proceedings from the Site Effects Workshop," Edited by R. Whitman, 2/29/92, (PB92-197201, A04, MF-A01).

NCEER-92-0007   "Engineering Evaluation of Permanent Ground Deformations Due to Seismically-Induced Liquefaction," by M.H. Baziar, R. Dobry and A-W.M. Elgamal, 3/24/92, (PB92-222421, A13, MF-A03).

NCEER-92-0008   "A Procedure for the Seismic Evaluation of Buildings in the Central and Eastern United States," by C.D. Poland and J.O. Malley, 4/2/92, (PB92-222439, A20, MF-A04).

NCEER-92-0009   "Experimental and Analytical Study of a Hybrid Isolation System Using Friction Controllable Sliding Bearings," by M.Q. Feng, S. Fujii and M. Shinozuka, 5/15/92, (PB93-150282, A06, MF-A02).

NCEER-92-0010   "Seismic Resistance of Slab-Column Connections in Existing Non-Ductile Flat-Plate Buildings," by A.J. Durrani and Y. Du, 5/18/92, (PB93-116812, A06, MF-A02).

NCEER-92-0011   "The Hysteretic and Dynamic Behavior of Brick Masonry Walls Upgraded by Ferrocement Coatings Under Cyclic Loading and Strong Simulated Ground Motion," by H. Lee and S.P. Prawel, 5/11/92, to be published.

NCEER-92-0012   "Study of Wire Rope Systems for Seismic Protection of Equipment in Buildings," by G.F. Demetriades, M.C. Constantinou and A.M. Reinhorn, 5/20/92, (PB93-116655, A08, MF-A02).

NCEER-92-0013 "Shape Memory Structural Dampers: Material Properties, Design and Seismic Testing," by P.R. Witting and F.A. Cozzarelli, 5/26/92, (PB93-116663, A05, MF-A01).

NCEER-92-0014 "Longitudinal Permanent Ground Deformation Effects on Buried Continuous Pipelines," by M.J. O'Rourke, and C. Nordberg, 6/15/92, (PB93-116671, A08, MF-A02).

NCEER-92-0015 "A Simulation Method for Stationary Gaussian Random Functions Based on the Sampling Theorem," by M. Grigoriu and S. Balopoulou, 6/11/92, (PB93-127496, A05, MF-A01).

NCEER-92-0016 "Gravity-Load-Designed Reinforced Concrete Buildings: Seismic Evaluation of Existing Construction and Detailing Strategies for Improved Seismic Resistance," by G.W. Hoffmann, S.K. Kunnath, A.M. Reinhorn and J.B. Mander, 7/15/92, (PB94-142007, A08, MF-A02).

NCEER-92-0017 "Observations on Water System and Pipeline Performance in the Limón Area of Costa Rica Due to the April 22, 1991 Earthquake," by M. O'Rourke and D. Ballantyne, 6/30/92, (PB93-126811, A06, MF-A02).

NCEER-92-0018 "Fourth Edition of Earthquake Education Materials for Grades K-12," Edited by K.E.K. Ross, 8/10/92, (PB93-114023, A07, MF-A02).

NCEER-92-0019 "Proceedings from the Fourth Japan-U.S. Workshop on Earthquake Resistant Design of Lifeline Facilities and Countermeasures for Soil Liquefaction," Edited by M. Hamada and T.D. O'Rourke, 8/12/92, (PB93-163939, A99, MF-E11).

NCEER-92-0020 "Active Bracing System: A Full Scale Implementation of Active Control," by A.M. Reinhorn, T.T. Soong, R.C. Lin, M.A. Riley, Y.P. Wang, S. Aizawa and M. Higashino, 8/14/92, (PB93-127512, A06, MF-A02).

NCEER-92-0021 "Empirical Analysis of Horizontal Ground Displacement Generated by Liquefaction-Induced Lateral Spreads," by S.F. Bartlett and T.L. Youd, 8/17/92, (PB93-188241, A06, MF-A02).

NCEER-92-0022 "IDARC Version 3.0: Inelastic Damage Analysis of Reinforced Concrete Structures," by S.K. Kunnath, A.M. Reinhorn and R.F. Lobo, 8/31/92, (PB93-227502, A07, MF-A02).

NCEER-92-0023 "A Semi-Empirical Analysis of Strong-Motion Peaks in Terms of Seismic Source, Propagation Path and Local Site Conditions, by M. Kamiyama, M.J. O'Rourke and R. Flores-Berrones, 9/9/92, (PB93-150266, A08, MF-A02).

NCEER-92-0024 "Seismic Behavior of Reinforced Concrete Frame Structures with Nonductile Details, Part I: Summary of Experimental Findings of Full Scale Beam-Column Joint Tests," by A. Beres, R.N. White and P. Gergely, 9/30/92, (PB93-227783, A05, MF-A01).

NCEER-92-0025 "Experimental Results of Repaired and Retrofitted Beam-Column Joint Tests in Lightly Reinforced Concrete Frame Buildings," by A. Beres, S. El-Borgi, R.N. White and P. Gergely, 10/29/92, (PB93-227791, A05, MF-A01).

NCEER-92-0026 "A Generalization of Optimal Control Theory: Linear and Nonlinear Structures," by J.N. Yang, Z. Li and S. Vongchavalitkul, 11/2/92, (PB93-188621, A05, MF-A01).

NCEER-92-0027 "Seismic Resistance of Reinforced Concrete Frame Structures Designed Only for Gravity Loads: Part I - Design and Properties of a One-Third Scale Model Structure," by J.M. Bracci, A.M. Reinhorn and J.B. Mander, 12/1/92, (PB94-104502, A08, MF-A02).

NCEER-92-0028 "Seismic Resistance of Reinforced Concrete Frame Structures Designed Only for Gravity Loads: Part II - Experimental Performance of Subassemblages," by L.E. Aycardi, J.B. Mander and A.M. Reinhorn, 12/1/92, (PB94-104510, A08, MF-A02).

NCEER-92-0029 "Seismic Resistance of Reinforced Concrete Frame Structures Designed Only for Gravity Loads: Part III - Experimental Performance and Analytical Study of a Structural Model," by J.M. Bracci, A.M. Reinhorn and J.B. Mander, 12/1/92, (PB93-227528, A09, MF-A01).

NCEER-92-0030   "Evaluation of Seismic Retrofit of Reinforced Concrete Frame Structures: Part I - Experimental Performance of Retrofitted Subassemblages," by D. Choudhuri, J.B. Mander and A.M. Reinhorn, 12/8/92, (PB93-198307, A07, MF-A02).

NCEER-92-0031   "Evaluation of Seismic Retrofit of Reinforced Concrete Frame Structures: Part II - Experimental Performance and Analytical Study of a Retrofitted Structural Model," by J.M. Bracci, A.M. Reinhorn and J.B. Mander, 12/8/92, (PB93-198315, A09, MF-A03).

NCEER-92-0032   "Experimental and Analytical Investigation of Seismic Response of Structures with Supplemental Fluid Viscous Dampers," by M.C. Constantinou and M.D. Symans, 12/21/92, (PB93-191435, A10, MF-A03). This report is available only through NTIS (see address given above).

NCEER-92-0033   "Reconnaissance Report on the Cairo, Egypt Earthquake of October 12, 1992," by M. Khater, 12/23/92, (PB93-188621, A03, MF-A01).

NCEER-92-0034   "Low-Level Dynamic Characteristics of Four Tall Flat-Plate Buildings in New York City," by H. Gavin, S. Yuan, J. Grossman, E. Pekelis and K. Jacob, 12/28/92, (PB93-188217, A07, MF-A02).

NCEER-93-0001   "An Experimental Study on the Seismic Performance of Brick-Infilled Steel Frames With and Without Retrofit," by J.B. Mander, B. Nair, K. Wojtkowski and J. Ma, 1/29/93, (PB93-227510, A07, MF-A02).

NCEER-93-0002   "Social Accounting for Disaster Preparedness and Recovery Planning," by S. Cole, E. Pantoja and V. Razak, 2/22/93, (PB94-142114, A12, MF-A03).

NCEER-93-0003   "Assessment of 1991 NEHRP Provisions for Nonstructural Components and Recommended Revisions," by T.T. Soong, G. Chen, Z. Wu, R-H. Zhang and M. Grigoriu, 3/1/93, (PB93-188639, A06, MF-A02).

NCEER-93-0004   "Evaluation of Static and Response Spectrum Analysis Procedures of SEAOC/UBC for Seismic Isolated Structures," by C.W. Winters and M.C. Constantinou, 3/23/93, (PB93-198299, A10, MF-A03).

NCEER-93-0005   "Earthquakes in the Northeast - Are We Ignoring the Hazard? A Workshop on Earthquake Science and Safety for Educators," edited by K.E.K. Ross, 4/2/93, (PB94-103066, A09, MF-A02).

NCEER-93-0006   "Inelastic Response of Reinforced Concrete Structures with Viscoelastic Braces," by R.F. Lobo, J.M. Bracci, K.L. Shen, A.M. Reinhorn and T.T. Soong, 4/5/93, (PB93-227486, A05, MF-A02).

NCEER-93-0007   "Seismic Testing of Installation Methods for Computers and Data Processing Equipment," by K. Kosar, T.T. Soong, K.L. Shen, J.A. HoLung and Y.K. Lin, 4/12/93, (PB93-198299, A07, MF-A02).

NCEER-93-0008   "Retrofit of Reinforced Concrete Frames Using Added Dampers," by A. Reinhorn, M. Constantinou and C. Li, to be published.

NCEER-93-0009   "Seismic Behavior and Design Guidelines for Steel Frame Structures with Added Viscoelastic Dampers," by K.C. Chang, M.L. Lai, T.T. Soong, D.S. Hao and Y.C. Yeh, 5/1/93, (PB94-141959, A07, MF-A02).

NCEER-93-0010   "Seismic Performance of Shear-Critical Reinforced Concrete Bridge Piers," by J.B. Mander, S.M. Waheed, M.T.A. Chaudhary and S.S. Chen, 5/12/93, (PB93-227494, A08, MF-A02).

NCEER-93-0011   "3D-BASIS-TABS: Computer Program for Nonlinear Dynamic Analysis of Three Dimensional Base Isolated Structures," by S. Nagarajaiah, C. Li, A.M. Reinhorn and M.C. Constantinou, 8/2/93, (PB94-141819, A09, MF-A02).

NCEER-93-0012   "Effects of Hydrocarbon Spills from an Oil Pipeline Break on Ground Water," by O.J. Helweg and H.H.M. Hwang, 8/3/93, (PB94-141942, A06, MF-A02).

NCEER-93-0013   "Simplified Procedures for Seismic Design of Nonstructural Components and Assessment of Current Code Provisions," by M.P. Singh, L.E. Suarez, E.E. Matheu and G.O. Maldonado, 8/4/93, (PB94-141827, A09, MF-A02).

NCEER-93-0014   "An Energy Approach to Seismic Analysis and Design of Secondary Systems," by G. Chen and T.T. Soong, 8/6/93, (PB94-142767, A11, MF-A03).

NCEER-93-0015   "Proceedings from School Sites: Becoming Prepared for Earthquakes - Commemorating the Third Anniversary of the Loma Prieta Earthquake," Edited by F.E. Winslow and K.E.K. Ross, 8/16/93, (PB94-154275, A16, MF-A02).

NCEER-93-0016   "Reconnaissance Report of Damage to Historic Monuments in Cairo, Egypt Following the October 12, 1992 Dahshur Earthquake," by D. Sykora, D. Look, G. Croci, E. Karaesmen and E. Karaesmen, 8/19/93, (PB94-142221, A08, MF-A02).

NCEER-93-0017   "The Island of Guam Earthquake of August 8, 1993," by S.W. Swan and S.K. Harris, 9/30/93, (PB94-141843, A04, MF-A01).

NCEER-93-0018   "Engineering Aspects of the October 12, 1992 Egyptian Earthquake," by A.W. Elgamal, M. Amer, K. Adalier and A. Abul-Fadl, 10/7/93, (PB94-141983, A05, MF-A01).

NCEER-93-0019   "Development of an Earthquake Motion Simulator and its Application in Dynamic Centrifuge Testing," by I. Krstelj, Supervised by J.H. Prevost, 10/23/93, (PB94-181773, A-10, MF-A03).

NCEER-93-0020   "NCEER-Taisei Corporation Research Program on Sliding Seismic Isolation Systems for Bridges: Experimental and Analytical Study of a Friction Pendulum System (FPS)," by M.C. Constantinou, P. Tsopelas, Y-S. Kim and S. Okamoto, 11/1/93, (PB94-142775, A08, MF-A02).

NCEER-93-0021   "Finite Element Modeling of Elastomeric Seismic Isolation Bearings," by L.J. Billings, Supervised by R. Shepherd, 11/8/93, to be published.

NCEER-93-0022   "Seismic Vulnerability of Equipment in Critical Facilities: Life-Safety and Operational Consequences," by K. Porter, G.S. Johnson, M.M. Zadeh, C. Scawthorn and S. Eder, 11/24/93, (PB94-181765, A16, MF-A03).

NCEER-93-0023   "Hokkaido Nansei-oki, Japan Earthquake of July 12, 1993, by P.I. Yanev and C.R. Scawthorn, 12/23/93, (PB94-181500, A07, MF-A01).

NCEER-94-0001   "An Evaluation of Seismic Serviceability of Water Supply Networks with Application to the San Francisco Auxiliary Water Supply System," by I. Markov, Supervised by M. Grigoriu and T. O'Rourke, 1/21/94, (PB94-204013, A07, MF-A02).

NCEER-94-0002   "NCEER-Taisei Corporation Research Program on Sliding Seismic Isolation Systems for Bridges: Experimental and Analytical Study of Systems Consisting of Sliding Bearings, Rubber Restoring Force Devices and Fluid Dampers," Volumes I and II, by P. Tsopelas, S. Okamoto, M.C. Constantinou, D. Ozaki and S. Fujii, 2/4/94, (PB94-181740, A09, MF-A02 and PB94-181757, A12, MF-A03).

NCEER-94-0003   "A Markov Model for Local and Global Damage Indices in Seismic Analysis," by S. Rahman and M. Grigoriu, 2/18/94, (PB94-206000, A12, MF-A03).

NCEER-94-0004   "Proceedings from the NCEER Workshop on Seismic Response of Masonry Infills," edited by D.P. Abrams, 3/1/94, (PB94-180783, A07, MF-A02).

NCEER-94-0005   "The Northridge, California Earthquake of January 17, 1994: General Reconnaissance Report," edited by J.D. Goltz, 3/11/94, (PB94-193943, A10, MF-A03).

NCEER-94-0006   "Seismic Energy Based Fatigue Damage Analysis of Bridge Columns: Part I - Evaluation of Seismic Capacity," by G.A. Chang and J.B. Mander, 3/14/94, (PB94-219185, A11, MF-A03).

NCEER-94-0007   "Seismic Isolation of Multi-Story Frame Structures Using Spherical Sliding Isolation Systems," by T.M. Al-Hussaini, V.A. Zayas and M.C. Constantinou, 3/17/94, (PB94-193745, A09, MF-A02).

NCEER-94-0008   "The Northridge, California Earthquake of January 17, 1994: Performance of Highway Bridges," edited by I.G. Buckle, 3/24/94, (PB94-193851, A06, MF-A02).

NCEER-94-0009   "Proceedings of the Third U.S.-Japan Workshop on Earthquake Protective Systems for Bridges," edited by I.G. Buckle and I. Friedland, 3/31/94, (PB94-195815, A99, MF-A06).

NCEER-94-0010   "3D-BASIS-ME: Computer Program for Nonlinear Dynamic Analysis of Seismically Isolated Single and Multiple Structures and Liquid Storage Tanks," by P.C. Tsopelas, M.C. Constantinou and A.M. Reinhorn, 4/12/94, (PB94-204922, A09, MF-A02).

NCEER-94-0011   "The Northridge, California Earthquake of January 17, 1994: Performance of Gas Transmission Pipelines," by T.D. O'Rourke and M.C. Palmer, 5/16/94, (PB94-204989, A05, MF-A01).

NCEER-94-0012   "Feasibility Study of Replacement Procedures and Earthquake Performance Related to Gas Transmission Pipelines," by T.D. O'Rourke and M.C. Palmer, 5/25/94, (PB94-206638, A09, MF-A02).

NCEER-94-0013   "Seismic Energy Based Fatigue Damage Analysis of Bridge Columns: Part II - Evaluation of Seismic Demand," by G.A. Chang and J.B. Mander, 6/1/94, (PB95-18106, A08, MF-A02).

NCEER-94-0014   "NCEER-Taisei Corporation Research Program on Sliding Seismic Isolation Systems for Bridges: Experimental and Analytical Study of a System Consisting of Sliding Bearings and Fluid Restoring Force/Damping Devices," by P. Tsopelas and M.C. Constantinou, 6/13/94, (PB94-219144, A10, MF-A03).

NCEER-94-0015   "Generation of Hazard-Consistent Fragility Curves for Seismic Loss Estimation Studies," by H. Hwang and J-R. Huo, 6/14/94, (PB95-181996, A09, MF-A02).

NCEER-94-0016   "Seismic Study of Building Frames with Added Energy-Absorbing Devices," by W.S. Pong, C.S. Tsai and G.C. Lee, 6/20/94, (PB94-219136, A10, A03).

NCEER-94-0017   "Sliding Mode Control for Seismic-Excited Linear and Nonlinear Civil Engineering Structures," by J. Yang, J. Wu, A. Agrawal and Z. Li, 6/21/94, (PB95-138483, A06, MF-A02).

NCEER-94-0018   "3D-BASIS-TABS Version 2.0: Computer Program for Nonlinear Dynamic Analysis of Three Dimensional Base Isolated Structures," by A.M. Reinhorn, S. Nagarajaiah, M.C. Constantinou, P. Tsopelas and R. Li, 6/22/94, (PB95-182176, A08, MF-A02).

NCEER-94-0019   "Proceedings of the International Workshop on Civil Infrastructure Systems: Application of Intelligent Systems and Advanced Materials on Bridge Systems," Edited by G.C. Lee and K.C. Chang, 7/18/94, (PB95-252474, A20, MF-A04).

NCEER-94-0020   "Study of Seismic Isolation Systems for Computer Floors," by V. Lambrou and M.C. Constantinou, 7/19/94, (PB95-138533, A10, MF-A03).

NCEER-94-0021   "Proceedings of the U.S.-Italian Workshop on Guidelines for Seismic Evaluation and Rehabilitation of Unreinforced Masonry Buildings," Edited by D.P. Abrams and G.M. Calvi, 7/20/94, (PB95-138749, A13, MF-A03).

NCEER-94-0022   "NCEER-Taisei Corporation Research Program on Sliding Seismic Isolation Systems for Bridges: Experimental and Analytical Study of a System Consisting of Lubricated PTFE Sliding Bearings and Mild Steel Dampers," by P. Tsopelas and M.C. Constantinou, 7/22/94, (PB95-182184, A08, MF-A02).

NCEER-94-0023   "Development of Reliability-Based Design Criteria for Buildings Under Seismic Load," by Y.K. Wen, H. Hwang and M. Shinozuka, 8/1/94, (PB95-211934, A08, MF-A02).

NCEER-94-0024   "Experimental Verification of Acceleration Feedback Control Strategies for an Active Tendon System," by S.J. Dyke, B.F. Spencer, Jr., P. Quast, M.K. Sain, D.C. Kaspari, Jr. and T.T. Soong, 8/29/94, (PB95-212320, A05, MF-A01).

NCEER-94-0025   "Seismic Retrofitting Manual for Highway Bridges," Edited by I.G. Buckle and I.F. Friedland, published by the Federal Highway Administration (PB95-212676, A15, MF-A03).

NCEER-94-0026   "Proceedings from the Fifth U.S.-Japan Workshop on Earthquake Resistant Design of Lifeline Facilities and Countermeasures Against Soil Liquefaction," Edited by T.D. O'Rourke and M. Hamada, 11/7/94, (PB95-220802, A99, MF-E08).

NCEER-95-0001 "Experimental and Analytical Investigation of Seismic Retrofit of Structures with Supplemental Damping: Part 1 - Fluid Viscous Damping Devices," by A.M. Reinhorn, C. Li and M.C. Constantinou, 1/3/95, (PB95-266599, A09, MF-A02).

NCEER-95-0002 "Experimental and Analytical Study of Low-Cycle Fatigue Behavior of Semi-Rigid Top-And-Seat Angle Connections," by G. Pekcan, J.B. Mander and S.S. Chen, 1/5/95, (PB95-220042, A07, MF-A02).

NCEER-95-0003 "NCEER-ATC Joint Study on Fragility of Buildings," by T. Anagnos, C. Rojahn and A.S. Kiremidjian, 1/20/95, (PB95-220026, A06, MF-A02).

NCEER-95-0004 "Nonlinear Control Algorithms for Peak Response Reduction," by Z. Wu, T.T. Soong, V. Gattulli and R.C. Lin, 2/16/95, (PB95-220349, A05, MF-A01).

NCEER-95-0005 "Pipeline Replacement Feasibility Study: A Methodology for Minimizing Seismic and Corrosion Risks to Underground Natural Gas Pipelines," by R.T. Eguchi, H.A. Seligson and D.G. Honegger, 3/2/95, (PB95-252326, A06, MF-A02).

NCEER-95-0006 "Evaluation of Seismic Performance of an 11-Story Frame Building During the 1994 Northridge Earthquake," by F. Naeim, R. DiSulio, K. Benuska, A. Reinhorn and C. Li, to be published.

NCEER-95-0007 "Prioritization of Bridges for Seismic Retrofitting," by N. Basöz and A.S. Kiremidjian, 4/24/95, (PB95-252300, A08, MF-A02).

NCEER-95-0008 "Method for Developing Motion Damage Relationships for Reinforced Concrete Frames," by A. Singhal and A.S. Kiremidjian, 5/11/95, (PB95-266607, A06, MF-A02).

NCEER-95-0009 "Experimental and Analytical Investigation of Seismic Retrofit of Structures with Supplemental Damping: Part II - Friction Devices," by C. Li and A.M. Reinhorn, 7/6/95, (PB96-128087, A11, MF-A03).

NCEER-95-0010 "Experimental Performance and Analytical Study of a Non-Ductile Reinforced Concrete Frame Structure Retrofitted with Elastomeric Spring Dampers," by G. Pekcan, J.B. Mander and S.S. Chen, 7/14/95, (PB96-137161, A08, MF-A02).

NCEER-95-0011 "Development and Experimental Study of Semi-Active Fluid Damping Devices for Seismic Protection of Structures," by M.D. Symans and M.C. Constantinou, 8/3/95, (PB96-136940, A23, MF-A04).

NCEER-95-0012 "Real-Time Structural Parameter Modification (RSPM): Development of Innervated Structures," by Z. Liang, M. Tong and G.C. Lee, 4/11/95, (PB96-137153, A06, MF-A01).

NCEER-95-0013 "Experimental and Analytical Investigation of Seismic Retrofit of Structures with Supplemental Damping: Part III - Viscous Damping Walls," by A.M. Reinhorn and C. Li, 10/1/95, (PB96-176409, A11, MF-A03).

NCEER-95-0014 "Seismic Fragility Analysis of Equipment and Structures in a Memphis Electric Substation," by J-R. Huo and H.H.M. Hwang, 8/10/95, (PB96-128087, A09, MF-A02).

NCEER-95-0015 "The Hanshin-Awaji Earthquake of January 17, 1995: Performance of Lifelines," Edited by M. Shinozuka, 11/3/95, (PB96-176383, A15, MF-A03).

NCEER-95-0016 "Highway Culvert Performance During Earthquakes," by T.L. Youd and C.J. Beckman, available as NCEER-96-0015.

NCEER-95-0017 "The Hanshin-Awaji Earthquake of January 17, 1995: Performance of Highway Bridges," Edited by I.G. Buckle, 12/1/95, to be published.

NCEER-95-0018 "Modeling of Masonry Infill Panels for Structural Analysis," by A.M. Reinhorn, A. Madan, R.E. Valles, Y. Reichmann and J.B. Mander, 12/8/95, (PB97-110886, MF-A01, A06).

NCEER-95-0019 "Optimal Polynomial Control for Linear and Nonlinear Structures," by A.K. Agrawal and J.N. Yang, 12/11/95, (PB96-168737, A07, MF-A02).

NCEER-95-0020   "Retrofit of Non-Ductile Reinforced Concrete Frames Using Friction Dampers," by R.S. Rao, P. Gergely and R.N. White, 12/22/95, (PB97-133508, A10, MF-A02).

NCEER-95-0021   "Parametric Results for Seismic Response of Pile-Supported Bridge Bents," by G. Mylonakis, A. Nikolaou and G. Gazetas, 12/22/95, (PB97-100242, A12, MF-A03).

NCEER-95-0022   "Kinematic Bending Moments in Seismically Stressed Piles," by A. Nikolaou, G. Mylonakis and G. Gazetas, 12/23/95, (PB97-113914, MF-A03, A13).

NCEER-96-0001   "Dynamic Response of Unreinforced Masonry Buildings with Flexible Diaphragms," by A.C. Costley and D.P. Abrams," 10/10/96, (PB97-133573, MF-A03, A15).

NCEER-96-0002   "State of the Art Review: Foundations and Retaining Structures," by I. Po Lam, to be published.

NCEER-96-0003   "Ductility of Rectangular Reinforced Concrete Bridge Columns with Moderate Confinement," by N. Wehbe, M. Saiidi, D. Sanders and B. Douglas, 11/7/96, (PB97-133557, A06, MF-A02).

NCEER-96-0004   "Proceedings of the Long-Span Bridge Seismic Research Workshop," edited by I.G. Buckle and I.M. Friedland, to be published.

NCEER-96-0005   "Establish Representative Pier Types for Comprehensive Study: Eastern United States," by J. Kulicki and Z. Prucz, 5/28/96, (PB98-119217, A07, MF-A02).

NCEER-96-0006   "Establish Representative Pier Types for Comprehensive Study: Western United States," by R. Imbsen, R.A. Schamber and T.A. Osterkamp, 5/28/96, (PB98-118607, A07, MF-A02).

NCEER-96-0007   "Nonlinear Control Techniques for Dynamical Systems with Uncertain Parameters," by R.G. Ghanem and M.I. Bujakov, 5/27/96, (PB97-100259, A17, MF-A03).

NCEER-96-0008   "Seismic Evaluation of a 30-Year Old Non-Ductile Highway Bridge Pier and Its Retrofit," by J.B. Mander, B. Mahmoodzadegan, S. Bhadra and S.S. Chen, 5/31/96, (PB97-110902, MF-A03, A10).

NCEER-96-0009   "Seismic Performance of a Model Reinforced Concrete Bridge Pier Before and After Retrofit," by J.B. Mander, J.H. Kim and C.A. Ligozio, 5/31/96, (PB97-110910, MF-A02, A10).

NCEER-96-0010   "IDARC2D Version 4.0: A Computer Program for the Inelastic Damage Analysis of Buildings," by R.E. Valles, A.M. Reinhorn, S.K. Kunnath, C. Li and A. Madan, 6/3/96, (PB97-100234, A17, MF-A03).

NCEER-96-0011   "Estimation of the Economic Impact of Multiple Lifeline Disruption: Memphis Light, Gas and Water Division Case Study," by S.E. Chang, H.A. Seligson and R.T. Eguchi, 8/16/96, (PB97-133490, A11, MF-A03).

NCEER-96-0012   "Proceedings from the Sixth Japan-U.S. Workshop on Earthquake Resistant Design of Lifeline Facilities and Countermeasures Against Soil Liquefaction, Edited by M. Hamada and T. O'Rourke, 9/11/96, (PB97-133581, A99, MF-A06).

NCEER-96-0013   "Chemical Hazards, Mitigation and Preparedness in Areas of High Seismic Risk: A Methodology for Estimating the Risk of Post-Earthquake Hazardous Materials Release," by H.A. Seligson, R.T. Eguchi, K.J. Tierney and K. Richmond, 11/7/96, (PB97-133565, MF-A02, A08).

NCEER-96-0014   "Response of Steel Bridge Bearings to Reversed Cyclic Loading," by J.B. Mander, D-K. Kim, S.S. Chen and G.J. Premus, 11/13/96, (PB97-140735, A12, MF-A03).

NCEER-96-0015   "Highway Culvert Performance During Past Earthquakes," by T.L. Youd and C.J. Beckman, 11/25/96, (PB97-133532, A06, MF-A01).

NCEER-97-0001   "Evaluation, Prevention and Mitigation of Pounding Effects in Building Structures," by R.E. Valles and A.M. Reinhorn, 2/20/97, (PB97-159552, A14, MF-A03).

NCEER-97-0002   "Seismic Design Criteria for Bridges and Other Highway Structures," by C. Rojahn, R. Mayes, D.G. Anderson, J. Clark, J.H. Hom, R.V. Nutt and M.J. O'Rourke, 4/30/97, (PB97-194658, A06, MF-A03).

NCEER-97-0003   "Proceedings of the U.S.-Italian Workshop on Seismic Evaluation and Retrofit," Edited by D.P. Abrams and G.M. Calvi, 3/19/97, (PB97-194666, A13, MF-A03).

NCEER-97-0004   "Investigation of Seismic Response of Buildings with Linear and Nonlinear Fluid Viscous Dampers," by A.A. Seleemah and M.C. Constantinou, 5/21/97, (PB98-109002, A15, MF-A03).

NCEER-97-0005   "Proceedings of the Workshop on Earthquake Engineering Frontiers in Transportation Facilities," edited by G.C. Lee and I.M. Friedland, 8/29/97, (PB98-128911, A25, MR-A04).

NCEER-97-0006   "Cumulative Seismic Damage of Reinforced Concrete Bridge Piers," by S.K. Kunnath, A. El-Bahy, A. Taylor and W. Stone, 9/2/97, (PB98-108814, A11, MF-A03).

NCEER-97-0007   "Structural Details to Accommodate Seismic Movements of Highway Bridges and Retaining Walls," by R.A. Imbsen, R.A. Schamber, E. Thorkildsen, A. Kartoum, B.T. Martin, T.N. Rosser and J.M. Kulicki, 9/3/97, (PB98-108996, A09, MF-A02).

NCEER-97-0008   "A Method for Earthquake Motion-Damage Relationships with Application to Reinforced Concrete Frames," by A. Singhal and A.S. Kiremidjian, 9/10/97, (PB98-108988, A13, MF-A03).

NCEER-97-0009   "Seismic Analysis and Design of Bridge Abutments Considering Sliding and Rotation," by K. Fishman and R. Richards, Jr., 9/15/97, (PB98-108897, A06, MF-A02).

NCEER-97-0010   "Proceedings of the FHWA/NCEER Workshop on the National Representation of Seismic Ground Motion for New and Existing Highway Facilities," edited by I.M. Friedland, M.S. Power and R.L. Mayes, 9/22/97, (PB98-128903, A21, MF-A04).

NCEER-97-0011   "Seismic Analysis for Design or Retrofit of Gravity Bridge Abutments," by K.L. Fishman, R. Richards, Jr. and R.C. Divito, 10/2/97, (PB98-128937, A08, MF-A02).

NCEER-97-0012   "Evaluation of Simplified Methods of Analysis for Yielding Structures," by P. Tsopelas, M.C. Constantinou, C.A. Kircher and A.S. Whittaker, 10/31/97, (PB98-128929, A10, MF-A03).

NCEER-97-0013   "Seismic Design of Bridge Columns Based on Control and Repairability of Damage," by C-T. Cheng and J.B. Mander, 12/8/97, (PB98-144249, A11, MF-A03).

NCEER-97-0014   "Seismic Resistance of Bridge Piers Based on Damage Avoidance Design," by J.B. Mander and C-T. Cheng, 12/10/97, (PB98-144223, A09, MF-A02).

NCEER-97-0015   "Seismic Response of Nominally Symmetric Systems with Strength Uncertainty," by S. Balopoulou and M. Grigoriu, 12/23/97, (PB98-153422, A11, MF-A03).

NCEER-97-0016   "Evaluation of Seismic Retrofit Methods for Reinforced Concrete Bridge Columns," by T.J. Wipf, F.W. Klaiber and F.M. Russo, 12/28/97, (PB98-144215, A12, MF-A03).

NCEER-97-0017   "Seismic Fragility of Existing Conventional Reinforced Concrete Highway Bridges," by C.L. Mullen and A.S. Cakmak, 12/30/97, (PB98-153406, A08, MF-A02).

NCEER-97-0018   "Loss Asssessment of Memphis Buildings," edited by D.P. Abrams and M. Shinozuka, 12/31/97, (PB98-144231, A13, MF-A03).

NCEER-97-0019   "Seismic Evaluation of Frames with Infill Walls Using Quasi-static Experiments," by K.M. Mosalam, R.N. White and P. Gergely, 12/31/97, (PB98-153455, A07, MF-A02).

NCEER-97-0020   "Seismic Evaluation of Frames with Infill Walls Using Pseudo-dynamic Experiments," by K.M. Mosalam, R.N. White and P. Gergely, 12/31/97, (PB98-153430, A07, MF-A02).

NCEER-97-0021   "Computational Strategies for Frames with Infill Walls: Discrete and Smeared Crack Analyses and Seismic Fragility," by K.M. Mosalam, R.N. White and P. Gergely, 12/31/97, (PB98-153414, A10, MF-A02).

NCEER-97-0022   "Proceedings of the NCEER Workshop on Evaluation of Liquefaction Resistance of Soils," edited by T.L. Youd and I.M. Idriss, 12/31/97, (PB98-155617, A15, MF-A03).

MCEER-98-0001   "Extraction of Nonlinear Hysteretic Properties of Seismically Isolated Bridges from Quick-Release Field Tests," by Q. Chen, B.M. Douglas, E.M. Maragakis and I.G. Buckle, 5/26/98, (PB99-118838, A06, MF-A01).

MCEER-98-0002   "Methodologies for Evaluating the Importance of Highway Bridges," by A. Thomas, S. Eshenaur and J. Kulicki, 5/29/98, (PB99-118846, A10, MF-A02).

MCEER-98-0003   "Capacity Design of Bridge Piers and the Analysis of Overstrength," by J.B. Mander, A. Dutta and P. Goel, 6/1/98, (PB99-118853, A09, MF-A02).

MCEER-98-0004   "Evaluation of Bridge Damage Data from the Loma Prieta and Northridge, California Earthquakes," by N. Basoz and A. Kiremidjian, 6/2/98, (PB99-118861, A15, MF-A03).

MCEER-98-0005   "Screening Guide for Rapid Assessment of Liquefaction Hazard at Highway Bridge Sites," by T. L. Youd, 6/16/98, (PB99-118879, A06, not available on microfiche).

MCEER-98-0006   "Structural Steel and Steel/Concrete Interface Details for Bridges," by P. Ritchie, N. Kauhl and J. Kulicki, 7/13/98, (PB99-118945, A06, MF-A01).

MCEER-98-0007   "Capacity Design and Fatigue Analysis of Confined Concrete Columns," by A. Dutta and J.B. Mander, 7/14/98, (PB99-118960, A14, MF-A03).

MCEER-98-0008   "Proceedings of the Workshop on Performance Criteria for Telecommunication Services Under Earthquake Conditions," edited by A.J. Schiff, 7/15/98, (PB99-118952, A08, MF-A02).

MCEER-98-0009   "Fatigue Analysis of Unconfined Concrete Columns," by J.B. Mander, A. Dutta and J.H. Kim, 9/12/98, (PB99-123655, A10, MF-A02).

MCEER-98-0010   "Centrifuge Modeling of Cyclic Lateral Response of Pile-Cap Systems and Seat-Type Abutments in Dry Sands," by A.D. Gadre and R. Dobry, 10/2/98, (PB99-123606, A13, MF-A03).

MCEER-98-0011   "IDARC-BRIDGE: A Computational Platform for Seismic Damage Assessment of Bridge Structures," by A.M. Reinhorn, V. Simeonov, G. Mylonakis and Y. Reichman, 10/2/98, (PB99-162919, A15, MF-A03).

MCEER-98-0012   "Experimental Investigation of the Dynamic Response of Two Bridges Before and After Retrofitting with Elastomeric Bearings," by D.A. Wendichansky, S.S. Chen and J.B. Mander, 10/2/98, (PB99-162927, A15, MF-A03).

MCEER-98-0013   "Design Procedures for Hinge Restrainers and Hinge Sear Width for Multiple-Frame Bridges," by R. Des Roches and G.L. Fenves, 11/3/98, (PB99-140477, A13, MF-A03).

MCEER-98-0014   "Response Modification Factors for Seismically Isolated Bridges," by M.C. Constantinou and J.K. Quarshie, 11/3/98, (PB99-140485, A14, MF-A03).

MCEER-98-0015   "Proceedings of the U.S.-Italy Workshop on Seismic Protective Systems for Bridges," edited by I.M. Friedland and M.C. Constantinou, 11/3/98, (PB2000-101711, A22, MF-A04).

MCEER-98-0016   "Appropriate Seismic Reliability for Critical Equipment Systems: Recommendations Based on Regional Analysis of Financial and Life Loss," by K. Porter, C. Scawthorn, C. Taylor and N. Blais, 11/10/98, (PB99-157265, A08, MF-A02).

MCEER-98-0017   "Proceedings of the U.S. Japan Joint Seminar on Civil Infrastructure Systems Research," edited by M. Shinozuka and A. Rose, 11/12/98, (PB99-156713, A16, MF-A03).

MCEER-98-0018   "Modeling of Pile Footings and Drilled Shafts for Seismic Design," by I. PoLam, M. Kapuskar and D. Chaudhuri, 12/21/98, (PB99-157257, A09, MF-A02).

MCEER-99-0001   "Seismic Evaluation of a Masonry Infilled Reinforced Concrete Frame by Pseudodynamic Testing," by S.G. Buonopane and R.N. White, 2/16/99, (PB99-162851, A09, MF-A02).

MCEER-99-0002   "Response History Analysis of Structures with Seismic Isolation and Energy Dissipation Systems: Verification Examples for Program SAP2000," by J. Scheller and M.C. Constantinou, 2/22/99, (PB99-162869, A08, MF-A02).

MCEER-99-0003   "Experimental Study on the Seismic Design and Retrofit of Bridge Columns Including Axial Load Effects," by A. Dutta, T. Kokorina and J.B. Mander, 2/22/99, (PB99-162877, A09, MF-A02).

MCEER-99-0004   "Experimental Study of Bridge Elastomeric and Other Isolation and Energy Dissipation Systems with Emphasis on Uplift Prevention and High Velocity Near-source Seismic Excitation," by A. Kasalanati and M. C. Constantinou, 2/26/99, (PB99-162885, A12, MF-A03).

MCEER-99-0005   "Truss Modeling of Reinforced Concrete Shear-flexure Behavior," by J.H. Kim and J.B. Mander, 3/8/99, (PB99-163693, A12, MF-A03).

MCEER-99-0006   "Experimental Investigation and Computational Modeling of Seismic Response of a 1:4 Scale Model Steel Structure with a Load Balancing Supplemental Damping System," by G. Pekcan, J.B. Mander and S.S. Chen, 4/2/99, (PB99-162893, A11, MF-A03).

MCEER-99-0007   "Effect of Vertical Ground Motions on the Structural Response of Highway Bridges," by M.R. Button, C.J. Cronin and R.L. Mayes, 4/10/99, (PB2000-101411, A10, MF-A03).

MCEER-99-0008   "Seismic Reliability Assessment of Critical Facilities: A Handbook, Supporting Documentation, and Model Code Provisions," by G.S. Johnson, R.E. Sheppard, M.D. Quilici, S.J. Eder and C.R. Scawthorn, 4/12/99, (PB2000-101701, A18, MF-A04).

MCEER-99-0009   "Impact Assessment of Selected MCEER Highway Project Research on the Seismic Design of Highway Structures," by C. Rojahn, R. Mayes, D.G. Anderson, J.H. Clark, D'Appolonia Engineering, S. Gloyd and R.V. Nutt, 4/14/99, (PB99-162901, A10, MF-A02).

MCEER-99-0010   "Site Factors and Site Categories in Seismic Codes," by R. Dobry, R. Ramos and M.S. Power, 7/19/99, (PB2000-101705, A08, MF-A02).

MCEER-99-0011   "Restrainer Design Procedures for Multi-Span Simply-Supported Bridges," by M.J. Randall, M. Saiidi, E. Maragakis and T. Isakovic, 7/20/99, (PB2000-101702, A10, MF-A02).

MCEER-99-0012   "Property Modification Factors for Seismic Isolation Bearings," by M.C. Constantinou, P. Tsopelas, A. Kasalanati and E. Wolff, 7/20/99, (PB2000-103387, A11, MF-A03).

MCEER-99-0013   "Critical Seismic Issues for Existing Steel Bridges," by P. Ritchie, N. Kauhl and J. Kulicki, 7/20/99, (PB2000-101697, A09, MF-A02).

MCEER-99-0014   "Nonstructural Damage Database," by A. Kao, T.T. Soong and A. Vender, 7/24/99, (PB2000-101407, A06, MF-A01).

MCEER-99-0015   "Guide to Remedial Measures for Liquefaction Mitigation at Existing Highway Bridge Sites," by H.G. Cooke and J. K. Mitchell, 7/26/99, (PB2000-101703, A11, MF-A03).

MCEER-99-0016   "Proceedings of the MCEER Workshop on Ground Motion Methodologies for the Eastern United States," edited by N. Abrahamson and A. Becker, 8/11/99, (PB2000-103385, A07, MF-A02).

MCEER-99-0017   "Quindío, Colombia Earthquake of January 25, 1999: Reconnaissance Report," by A.P. Asfura and P.J. Flores, 10/4/99, (PB2000-106893, A06, MF-A01).

MCEER-99-0018   "Hysteretic Models for Cyclic Behavior of Deteriorating Inelastic Structures," by M.V. Sivaselvan and A.M. Reinhorn, 11/5/99, (PB2000-103386, A08, MF-A02).
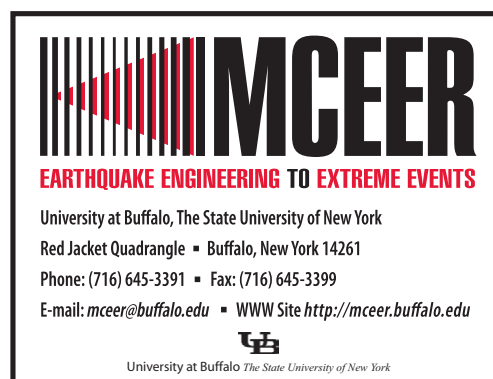
MCEER-99-0019 "Proceedings of the 7th U.S.- Japan Workshop on Earthquake Resistant Design of Lifeline Facilities and Countermeasures Against Soil Liquefaction," edited by T.D. O'Rourke, J.P. Bardet and M. Hamada, 11/19/99, (PB2000-103354, A99, MF-A06).

MCEER-99-0020 "Development of Measurement Capability for Micro-Vibration Evaluations with Application to Chip Fabrication Facilities," by G.C. Lee, Z. Liang, J.W. Song, J.D. Shen and W.C. Liu, 12/1/99, (PB2000-105993, A08, MF-A02).

MCEER-99-0021 "Design and Retrofit Methodology for Building Structures with Supplemental Energy Dissipating Systems," by G. Pekcan, J.B. Mander and S.S. Chen, 12/31/99, (PB2000-105994, A11, MF-A03).

MCEER-00-0001 "The Marmara, Turkey Earthquake of August 17, 1999: Reconnaissance Report," edited by C. Scawthorn; with major contributions by M. Bruneau, R. Eguchi, T. Holzer, G. Johnson, J. Mander, J. Mitchell, W. Mitchell, A. Papageorgiou, C. Scaethorn, and G. Webb, 3/23/00, (PB2000-106200, A11, MF-A03).

MCEER-00-0002 "Proceedings of the MCEER Workshop for Seismic Hazard Mitigation of Health Care Facilities," edited by G.C. Lee, M. Ettouney, M. Grigoriu, J. Hauer and J. Nigg, 3/29/00, (PB2000-106892, A08, MF-A02).

MCEER-00-0003 "The Chi-Chi, Taiwan Earthquake of September 21, 1999: Reconnaissance Report," edited by G.C. Lee and C.H. Loh, with major contributions by G.C. Lee, M. Bruneau, I.G. Buckle, S.E. Chang, P.J. Flores, T.D. O'Rourke, M. Shinozuka, T.T. Soong, C-H. Loh, K-C. Chang, Z-J. Chen, J-S. Hwang, M-L. Lin, G-Y. Liu, K-C. Tsai, G.C. Yao and C-L. Yen, 4/30/00, (PB2001-100980, A10, MF-A02).

MCEER-00-0004 "Seismic Retrofit of End-Sway Frames of Steel Deck-Truss Bridges with a Supplemental Tendon System: Experimental and Analytical Investigation," by G. Pekcan, J.B. Mander and S.S. Chen, 7/1/00, (PB2001-100982, A10, MF-A02).

MCEER-00-0005 "Sliding Fragility of Unrestrained Equipment in Critical Facilities," by W.H. Chong and T.T. Soong, 7/5/00, (PB2001-100983, A08, MF-A02).

MCEER-00-0006 "Seismic Response of Reinforced Concrete Bridge Pier Walls in the Weak Direction," by N. Abo-Shadi, M. Saiidi and D. Sanders, 7/17/00, (PB2001-100981, A17, MF-A03).

MCEER-00-0007 "Low-Cycle Fatigue Behavior of Longitudinal Reinforcement in Reinforced Concrete Bridge Columns," by J. Brown and S.K. Kunnath, 7/23/00, (PB2001-104392, A08, MF-A02).

MCEER-00-0008 "Soil Structure Interaction of Bridges for Seismic Analysis," I. PoLam and H. Law, 9/25/00, (PB2001-105397, A08, MF-A02).

MCEER-00-0009 "Proceedings of the First MCEER Workshop on Mitigation of Earthquake Disaster by Advanced Technologies (MEDAT-1), edited by M. Shinozuka, D.J. Inman and T.D. O'Rourke, 11/10/00, (PB2001-105399, A14, MF-A03).

MCEER-00-0010 "Development and Evaluation of Simplified Procedures for Analysis and Design of Buildings with Passive Energy Dissipation Systems," by O.M. Ramirez, M.C. Constantinou, C.A. Kircher, A.S. Whittaker, M.W. Johnson, J.D. Gomez and C. Chrysostomou, 11/16/01, (PB2001-105523, A23, MF-A04).

MCEER-00-0011 "Dynamic Soil-Foundation-Structure Interaction Analyses of Large Caissons," by C-Y. Chang, C-M. Mok, Z-L. Wang, R. Settgast, F. Waggoner, M.A. Ketchum, H.M. Gonnermann and C-C. Chin, 12/30/00, (PB2001-104373, A07, MF-A02).

MCEER-00-0012 "Experimental Evaluation of Seismic Performance of Bridge Restrainers," by A.G. Vlassis, E.M. Maragakis and M. Saiid Saiidi, 12/30/00, (PB2001-104354, A09, MF-A02).

MCEER-00-0013 "Effect of Spatial Variation of Ground Motion on Highway Structures," by M. Shinozuka, V. Saxena and G. Deodatis, 12/31/00, (PB2001-108755, A13, MF-A03).

MCEER-00-0014 "A Risk-Based Methodology for Assessing the Seismic Performance of Highway Systems," by S.D. Werner, C.E. Taylor, J.E. Moore, II, J.S. Walton and S. Cho, 12/31/00, (PB2001-108756, A14, MF-A03).

MCEER-01-0001   "Experimental Investigation of P-Delta Effects to Collapse During Earthquakes," by D. Vian and M. Bruneau, 6/25/01, (PB2002-100534, A17, MF-A03).

MCEER-01-0002   "Proceedings of the Second MCEER Workshop on Mitigation of Earthquake Disaster by Advanced Technologies (MEDAT-2)," edited by M. Bruneau and D.J. Inman, 7/23/01, (PB2002-100434, A16, MF-A03).

MCEER-01-0003   "Sensitivity Analysis of Dynamic Systems Subjected to Seismic Loads," by C. Roth and M. Grigoriu, 9/18/01, (PB2003-100884, A12, MF-A03).

MCEER-01-0004   "Overcoming Obstacles to Implementing Earthquake Hazard Mitigation Policies: Stage 1 Report," by D.J. Alesch and W.J. Petak, 12/17/01, (PB2002-107949, A07, MF-A02).

MCEER-01-0005   "Updating Real-Time Earthquake Loss Estimates: Methods, Problems and Insights," by C.E. Taylor, S.E. Chang and R.T. Eguchi, 12/17/01, (PB2002-107948, A05, MF-A01).

MCEER-01-0006   "Experimental Investigation and Retrofit of Steel Pile Foundations and Pile Bents Under Cyclic Lateral Loadings," by A. Shama, J. Mander, B. Blabac and S. Chen, 12/31/01, (PB2002-107950, A13, MF-A03).

MCEER-02-0001   "Assessment of Performance of Bolu Viaduct in the 1999 Duzce Earthquake in Turkey" by P.C. Roussis, M.C. Constantinou, M. Erdik, E. Durukal and M. Dicleli, 5/8/02, (PB2003-100883, A08, MF-A02).

MCEER-02-0002   "Seismic Behavior of Rail Counterweight Systems of Elevators in Buildings," by M.P. Singh, Rildova and L.E. Suarez, 5/27/02. (PB2003-100882, A11, MF-A03).

MCEER-02-0003   "Development of Analysis and Design Procedures for Spread Footings," by G. Mylonakis, G. Gazetas, S. Nikolaou and A. Chauncey, 10/02/02, (PB2004-101636, A13, MF-A03, CD-A13).

MCEER-02-0004   "Bare-Earth Algorithms for Use with SAR and LIDAR Digital Elevation Models," by C.K. Huyck, R.T. Eguchi and B. Houshmand, 10/16/02, (PB2004-101637, A07, CD-A07).

MCEER-02-0005   "Review of Energy Dissipation of Compression Members in Concentrically Braced Frames," by K.Lee and M. Bruneau, 10/18/02, (PB2004-101638, A10, CD-A10).

MCEER-03-0001   "Experimental Investigation of Light-Gauge Steel Plate Shear Walls for the Seismic Retrofit of Buildings" by J. Berman and M. Bruneau, 5/2/03, (PB2004-101622, A10, MF-A03, CD-A10).

MCEER-03-0002   "Statistical Analysis of Fragility Curves," by M. Shinozuka, M.Q. Feng, H. Kim, T. Uzawa and T. Ueda, 6/16/03, (PB2004-101849, A09, CD-A09).

MCEER-03-0003   "Proceedings of the Eighth U.S.-Japan Workshop on Earthquake Resistant Design f Lifeline Facilities and Countermeasures Against Liquefaction," edited by M. Hamada, J.P. Bardet and T.D. O'Rourke, 6/30/03, (PB2004-104386, A99, CD-A99).

MCEER-03-0004   "Proceedings of the PRC-US Workshop on Seismic Analysis and Design of Special Bridges," edited by L.C. Fan and G.C. Lee, 7/15/03, (PB2004-104387, A14, CD-A14).

MCEER-03-0005   "Urban Disaster Recovery: A Framework and Simulation Model," by S.B. Miles and S.E. Chang, 7/25/03, (PB2004-104388, A07, CD-A07).

MCEER-03-0006   "Behavior of Underground Piping Joints Due to Static and Dynamic Loading," by R.D. Meis, M. Maragakis and R. Siddharthan, 11/17/03, (PB2005-102194, A13, MF-A03, CD-A00).

MCEER-03-0007   "Seismic Vulnerability of Timber Bridges and Timber Substructures," by A.A. Shama, J.B. Mander, I.M. Friedland and D.R. Allicock, 12/15/03.

MCEER-04-0001   "Experimental Study of Seismic Isolation Systems with Emphasis on Secondary System Response and Verification of Accuracy of Dynamic Response History Analysis Methods," by E. Wolff and M. Constantinou, 1/16/04 (PB2005-102195, A99, MF-E08, CD-A00).

MCEER-04-0002   "Tension, Compression and Cyclic Testing of Engineered Cementitious Composite Materials," by K. Kesner and S.L. Billington, 3/1/04, (PB2005-102196, A08, CD-A08).

MCEER-04-0003   "Cyclic Testing of Braces Laterally Restrained by Steel Studs to Enhance Performance During Earthquakes," by O.C. Celik, J.W. Berman and M. Bruneau, 3/16/04, (PB2005-102197, A13, MF-A03, CD-A00).

MCEER-04-0004   "Methodologies for Post Earthquake Building Damage Detection Using SAR and Optical Remote Sensing: Application to the August 17, 1999 Marmara, Turkey Earthquake," by C.K. Huyck, B.J. Adams, S. Cho, R.T. Eguchi, B. Mansouri and B. Houshmand, 6/15/04, (PB2005-104888, A10, CD-A00).

MCEER-04-0005   "Nonlinear Structural Analysis Towards Collapse Simulation: A Dynamical Systems Approach," by M.V. Sivaselvan and A.M. Reinhorn, 6/16/04, (PB2005-104889, A11, MF-A03, CD-A00).

MCEER-04-0006   "Proceedings of the Second PRC-US Workshop on Seismic Analysis and Design of Special Bridges," edited by G.C. Lee and L.C. Fan, 6/25/04, (PB2005-104890, A16, CD-A00).

MCEER-04-0007   "Seismic Vulnerability Evaluation of Axially Loaded Steel Built-up Laced Members," by K. Lee and M. Bruneau, 6/30/04, (PB2005-104891, A16, CD-A00).

MCEER-04-0008   "Evaluation of Accuracy of Simplified Methods of Analysis and Design of Buildings with Damping Systems for Near-Fault and for Soft-Soil Seismic Motions," by E.A. Pavlou and M.C. Constantinou, 8/16/04, (PB2005-104892, A08, MF-A02, CD-A00).

MCEER-04-0009   "Assessment of Geotechnical Issues in Acute Care Facilities in California," by M. Lew, T.D. O'Rourke, R. Dobry and M. Koch, 9/15/04, (PB2005-104893, A08, CD-A00).

MCEER-04-0010   "Scissor-Jack-Damper Energy Dissipation System," by A.N. Sigaher-Boyle and M.C. Constantinou, 12/1/04 (PB2005-108221).

MCEER-04-0011   "Seismic Retrofit of Bridge Steel Truss Piers Using a Controlled Rocking Approach," by M. Pollino and M. Bruneau, 12/20/04 (PB2006-105795).

MCEER-05-0001   "Experimental and Analytical Studies of Structures Seismically Isolated with an Uplift-Restraint Isolation System," by P.C. Roussis and M.C. Constantinou, 1/10/05 (PB2005-108222).

MCEER-05-0002   "A Versatile Experimentation Model for Study of Structures Near Collapse Applied to Seismic Evaluation of Irregular Structures," by D. Kusumastuti, A.M. Reinhorn and A. Rutenberg, 3/31/05 (PB2006-101523).

MCEER-05-0003   "Proceedings of the Third PRC-US Workshop on Seismic Analysis and Design of Special Bridges," edited by L.C. Fan and G.C. Lee, 4/20/05, (PB2006-105796).

MCEER-05-0004   "Approaches for the Seismic Retrofit of Braced Steel Bridge Piers and Proof-of-Concept Testing of an Eccentrically Braced Frame with Tubular Link," by J.W. Berman and M. Bruneau, 4/21/05 (PB2006-101524).

MCEER-05-0005   "Simulation of Strong Ground Motions for Seismic Fragility Evaluation of Nonstructural Components in Hospitals," by A. Wanitkorkul and A. Filiatrault, 5/26/05 (PB2006-500027).

MCEER-05-0006   "Seismic Safety in California Hospitals: Assessing an Attempt to Accelerate the Replacement or Seismic Retrofit of Older Hospital Facilities," by D.J. Alesch, L.A. Arendt and W.J. Petak, 6/6/05 (PB2006-105794).

MCEER-05-0007   "Development of Seismic Strengthening and Retrofit Strategies for Critical Facilities Using Engineered Cementitious Composite Materials," by K. Kesner and S.L. Billington, 8/29/05 (PB2006-111701).

MCEER-05-0008   "Experimental and Analytical Studies of Base Isolation Systems for Seismic Protection of Power Transformers," by N. Murota, M.Q. Feng and G-Y. Liu, 9/30/05 (PB2006-111702).

MCEER-05-0009   "3D-BASIS-ME-MB: Computer Program for Nonlinear Dynamic Analysis of Seismically Isolated Structures," by P.C. Tsopelas, P.C. Roussis, M.C. Constantinou, R. Buchanan and A.M. Reinhorn, 10/3/05 (PB2006-111703).

MCEER-05-0010   "Steel Plate Shear Walls for Seismic Design and Retrofit of Building Structures," by D. Vian and M. Bruneau, 12/15/05 (PB2006-111704).

MCEER-05-0011   "The Performance-Based Design Paradigm," by M.J. Astrella and A. Whittaker, 12/15/05 (PB2006-111705).

MCEER-06-0001   "Seismic Fragility of Suspended Ceiling Systems," H. Badillo-Almaraz, A.S. Whittaker, A.M. Reinhorn and G.P. Cimellaro, 2/4/06 (PB2006-111706).

MCEER-06-0002   "Multi-Dimensional Fragility of Structures," by G.P. Cimellaro, A.M. Reinhorn and M. Bruneau, 3/1/06 (PB2007-106974, A09, MF-A02, CD A00).

MCEER-06-0003   "Built-Up Shear Links as Energy Dissipators for Seismic Protection of Bridges," by P. Dusicka, A.M. Itani and I.G. Buckle, 3/15/06 (PB2006-111708).

MCEER-06-0004   "Analytical Investigation of the Structural Fuse Concept," by R.E. Vargas and M. Bruneau, 3/16/06 (PB2006-111709).

MCEER-06-0005   "Experimental Investigation of the Structural Fuse Concept," by R.E. Vargas and M. Bruneau, 3/17/06 (PB2006-111710).

MCEER-06-0006   "Further Development of Tubular Eccentrically Braced Frame Links for the Seismic Retrofit of Braced Steel Truss Bridge Piers," by J.W. Berman and M. Bruneau, 3/27/06 (PB2007-105147).

MCEER-06-0007   "REDARS Validation Report," by S. Cho, C.K. Huyck, S. Ghosh and R.T. Eguchi, 8/8/06 (PB2007-106983).

MCEER-06-0008   "Review of Current NDE Technologies for Post-Earthquake Assessment of Retrofitted Bridge Columns," by J.W. Song, Z. Liang and G.C. Lee, 8/21/06 06 (PB2007-106984).

MCEER-06-0009   "Liquefaction Remediation in Silty Soils Using Dynamic Compaction and Stone Columns," by S. Thevanayagam, G.R. Martin, R. Nashed, T. Shenthan, T. Kanagalingam and N. Ecemis, 8/28/06 06 (PB2007-106985).

MCEER-06-0010   "Conceptual Design and Experimental Investigation of Polymer Matrix Composite Infill Panels for Seismic Retrofitting," by W. Jung, M. Chiewanichakorn and A.J. Aref, 9/21/06 (PB2007-106986).

MCEER-06-0011   "A Study of the Coupled Horizontal-Vertical Behavior of Elastomeric and Lead-Rubber Seismic Isolation Bearings," by G.P. Warn and A.S. Whittaker, 9/22/06 (PB2007-108679).

MCEER-06-0012   "Proceedings of the Fourth PRC-US Workshop on Seismic Analysis and Design of Special Bridges: Advancing Bridge Technologies in Research, Design, Construction and Preservation," Edited by L.C. Fan, G.C. Lee and L. Ziang, 10/12/06.

MCEER-06-0013   "Cyclic Response and Low Cycle Fatigue Characteristics of Plate Steels," by P. Dusicka, A.M. Itani and I.G. Buckle, 11/1/06 06 (PB2007-106987).

MCEER-06-0014   "Proceedings of the Second US-Taiwan Bridge Engineering Workshop," edited by W.P. Yen, J. Shen, J-Y. Chen and M. Wang, 11/15/06.

MCEER-06-0015   "User Manual and Technical Documentation for the REDARS^{TM} Import Wizard," by S. Cho, S. Ghosh, C.K. Huyck and S.D. Werner, 11/30/06.

MCEER-06-0016   "Hazard Mitigation Strategy and Monitoring Technologies for Urban and Infrastructure Public Buildings: Proceedings of the China-US Workshops," edited by X.Y. Zhou, A.L. Zhang, G.C. Lee and M. Tong, 12/12/06.

MCEER-07-0001   "Static and Kinetic Coefficients of Friction for Rigid Blocks," by C. Kafali, S. Fathali, M. Grigoriu and A.S. Whittaker, 3/20/07.

MCEER-07-0002   "Hazard Mitigation Investment Decision Making: Organizational Response to Legislative Mandate," by L.A. Arendt, D.J. Alesch and W.J. Petak, 4/9/07.

MCEER-07-0003   "Seismic Behavior of Bidirectional-Resistant Ductile End Diaphragms with Unbonded Braces in Straight or Skewed Steel Bridges," by O. Celik and M. Bruneau, 4/11/07.

MCEER-07-0004   "Modeling Pile Behavior in Large Pile Groups Under Lateral Loading," by A.M. Dodds and G.R. Martin, 4/16/07.

MCEER-07-0005   "Experimental Investigation of Blast Performance of Seismically Resistant Concrete-Filled Steel Tube Bridge Piers," by S. Fujikura, M. Bruneau and D. Lopez-Garcia, 4/20/07.

MCEER-07-0006   "Seismic Analysis of Conventional and Isolated Liquefied Natural Gas Tanks Using Mechanical Analogs," by I.P. Christovasilis and A.S. Whittaker, 5/1/07.

MCEER-07-0007   "Experimental Seismic Performance Evaluation of Isolation/Restraint Systems for Mechanical Equipment – Part 1: Heavy Equipment Study," by S. Fathali and A. Filiatrault, 6/6/07.

MCEER-07-0008   "Seismic Vulnerability of Timber Bridges and Timber Substructures," by A.A. Sharma, J.B. Mander, I.M. Friedland and D.R. Allicock, 6/7/07.

MCEER-07-0009   "Experimental and Analytical Study of the XY-Friction Pendulum (XY-FP) Bearing for Bridge Applications," by C.C. Marin-Artieda, A.S. Whittaker and M.C. Constantinou, 6/7/07.

MCEER-07-0010   "Proceedings of the PRC-US Earthquake Engineering Forum for Young Researchers," Edited by G.C. Lee and X.Z. Qi, 6/8/07.

MCEER-07-0011   "Design Recommendations for Perforated Steel Plate Shear Walls," by R. Purba and M. Bruneau, 6/18/07.

MCEER-07-0012   "Performance of Seismic Isolation Hardware Under Service and Seismic Loading," by M.C. Constantinou, A.S. Whittaker, Y. Kalpakidis, D.M. Fenz and G.P. Warn, 8/27/07.

MCEER

EARTHQUAKE ENGINEERING TO EXTREME EVENTS